Università degli Studi dell'Insubria
Dipartimento di Scienza ed Alta Tecnologia
Doctoral Programme in Physics and Astrophysics

Population properties, dissipation and radiative processes in GRBs

Doctoral Dissertation of:
Alessio Pescalli

Supervisors:
Prof. Giancarlo Ghirlanda
Prof. Gabriele Ghisellini

2017 – XXX Cycle

Abstract

Gamma Ray Bursts (GRBs) are short and intense flashes of γ–rays with typical energies between keV and a few MeV. They reach luminosities (assuming isotropy) of 10^{54} erg/s. The γ–ray emission, called "prompt", is highly variable (with timescales as short as few milliseconds) and can last a fraction of a second (short GRBs, $T_{90} < 2$ s) or few tens of seconds (long GRBs, $T_{90} > 2$ s). The prompt is followed by the "afterglow" emission, at lower frequencies (in the X–ray, Optical and Radio band) which has been detected also up to several months after the trigger and is typically smooth and decaying as a function of time. GRBs are cosmological sources having average redshift $\langle z \rangle \sim 2.5$. The progenitors of long GRBs are thought to be very massive stars that collapse at the end of their life, while the progenitors of short GRBs are though to be the merging of two neutron stars.

Two of the key properties characterizing the population of GRBs are their cosmic formation rate $\psi(z)$ (GRBFR) and their luminosity function $\phi(L)$ (LF). Recovering $\psi(z)$ and $\phi(L)$ of GRBs allows us to test the nature of their progenitor (e.g. through the comparison with the cosmic star formation rate), to study the possible presence of sub–classes of GRBs and to infer intrinsic properties such as the structure of their jetted outflows. The knowledge of the intrinsic population properties is becoming even more compelling with the recent association of short GRBs with gravitational wave signals produced by the merger of two neutron stars.

Samples comprising all GRBs with measured redshifts are affected by several selection effects and cannot be used *directly* to infer $\psi(z)$ and $\phi(L)$. Specific methods accounting for such biases should be adopted. Most of the past studies adopted either heterogeneous

samples (i.e. including GRBs detected by different satellites/detectors which have different sensitivities) and/or incomplete samples. Incompleteness can be induced by several effects such as the variation (for a given detector) of the trigger efficiency and/or the efficiency in measuring the redshift through optical spectroscopy. Modeling individually these instrumental and observational biases may be extremely difficult, if not impossible, in practice. Possible solutions are working with complete samples and/or adopting direct inversion methods accounting for the selection effects.

In this thesis I worked on deriving the luminosity function and formation rate of the population of short and long GRBs. For long GRBs I studied the C^- method (Lynden-Bell, 1971), originally applied to quasars and recently to GRBs. This method consists in counting GRBs within cells defined in the redshift – luminosity plane and in reconstructing the true population number within that cell. Through Monte Carlo simulations I found that the C^- method can correctly recover the LF and the GRBFR only if it is applied to sample of GRBs which is complete in flux and redshift. Using incomplete samples in redshift and/or in flux, as it has been done in the literature recently, the found GRBFR and LF can be misleading. Motivated by these results, I applied the C^- method for the first time to a complete, flux–limited, sample of *Swift* long GRBs (Pescalli et al., 2016). This sample includes all long GRBs with peak flux greater than 6 times the *Swift*/BAT flux detection threshold: of these GRBs 82% have the redshift measured. The found luminosity function $\phi(L)$ is a broken power–law with slopes $a = -1.32 \pm 0.21$ and $b = -1.84 \pm 0.24$ below and above, respectively, a break luminosity $L_{\rm b} = 10^{51.45 \pm 0.15}$ erg/s. These results are in agreement with those already obtained with different methods reported in the literature, but I found that, at odd with recent claims obtained with incomplete samples (Yu et al., 2015a; Petrosian et al., 2015), the GRB formation rate increases with redshift up to $z \sim 2$, where it peaks, and then decreases. My result is in agreement with the shape of the cosmic star formation rate and the GRBFR inferred from host galaxies.

The recent detection of gravitational waves in concert with a short GRB (170817A), poses new questions related to the SGRB population (e.g. local SGRB rate, properties of the progenitors and of the outflow). For the population of short GRBs (SGRB), $\phi(L)$ and $\psi(z)$ have

been derived in the past by several authors through small/incomplete samples of events with measured L and z. SGRB complete samples with measured z are composed by too few events for reliably apply direct methods. The alternative approach consists in assuming population properties (e.g. $\phi(L)$, $\psi(z)$) and fitting the observed flux distribution of large sample of GRBs detected by present and past instruments (e.g. *Swift*, *Fermi* and BATSE). Specifically, I collaborated to a project (Ghirlanda et al., 2016) where we derive $\phi(L)$, $\psi(z)$ and the local rate of SGRBs by fitting all the available observer–frame constraints (i.e. peak flux, fluence, peak energy and duration distributions) of the large population of *Fermi* SGRBs and the rest–frame properties of a small complete sample of bright SGRBs detected by *Swift*.

We find that a steep single power–law $\phi(L) \propto L^{-2}$ (as found in past works, e.g. Guetta and Piran 2006) is excluded if the full set of constraints is considered. We implement a Monte Carlo Markov Chain method to derive the free parameters of the $\phi(L)$ and $\psi(z)$ functions assuming intrinsic $E_{\rm p} - L$ and $E_{\rm p} - E$ correlations to hold also for the population of short GRBs. To make our results independent from assumptions on the progenitor (NS–NS binary mergers or other channels) and from uncertainties on the star formation history, we assume a parametric form for the cosmic formation rate of the population of SGRBs. We find that a relatively flat luminosity function with slope ~ -0.5 below a characteristic break luminosity $\sim 3 \times 10^{52}$ erg s^{-1} and quite steep above (slope ~ -4.0) and a redshift distribution of SGRBs peaking at $z \sim 1.5 - 2$ satisfy all our constraints. The latter results is consistent with the star formation history of Madau and Dickinson (2014) retarded with a power–law delay time distribution $\propto \tau^{-1}$. Similar results also hold if no $E_{\rm p} - L$ and $E_{\rm p} - E$ correlations are assumed or if the minimum luminosity of the LF increased from 10^{47} erg/s to 10^{50} erg/s . We estimate, within ~ 200 Mpc (i.e. the design aLIGO range for the detection of gravitational waves produced by NS–NS merger events), that there should be 0.007–0.03 SGRBs yr^{-1} with their jet pointing towards the Earth and detectable as γ–ray events. Assuming current estimates of NS–NS merger rates and that all NS–NS mergers lead to a SGRB event, we derive a conservative estimate of the average opening angle of SGRBs $\langle \theta_{\rm jet} \rangle \sim 9^{\circ}$–$17^{\circ}$. The luminosity function implies a prompt emission average luminosity $\langle L \rangle \sim 1.5 \times 10^{52}$ erg s^{-1},

higher by nearly two orders of magnitude than previous findings in the literature. This greatly enhances the chance of observing off–beam events as proposed for GW/GRB170817A (Ligo Collaboration, 2017).

GRBs have jets and several observed properties (e.g. the rate and the true energetic) are affected by the jet structure. During my PhD I studied how the luminosity function of GRBs is affected by the structure of their jets (Pescalli et al., 2015). The jet of GRBs can be uniform, with constant energy per unit solid angle within the jet aperture θ_j, or it can be structured, namely with energy and velocity which depend on the angular distance from the axis of the jet. I derived the analytical expressions for the luminosity function of GRBs assuming uniform and structured jet models and compared them to the LF. Uniform jets can reproduce the entire luminosity function with average opening angle $\langle\theta_j\rangle = 3^\circ$ and bulk Lorentz factor $\langle\Gamma\rangle = 30$. These values are reasonably consistent with estimates of opening angles from afterglow observations. A structured jet can also fit adequately the LF, provided that the energy within the jet is relatively strongly structured, i.e. $E \propto \theta^{-k}$ with $k \geq 4$ (best fit for $k \sim 8$). The "classical" $E \propto \theta^{-2}$ structured jet model (Zhang and Mészáros, 2002; Rossi et al., 2002) is excluded. In this work I showed also that low luminosity (LL – 10^{46-48} erg/s) and high luminosity (HL – $L \geq 10^{50}$ erg/s) bursts can be described by a unique luminosity function suggesting that they belong to the same population.

The works described above consider only the population of bright GRBs detected in the γ–ray band which are expected to be mostly due to jets observed within their opening angles. However, the bulk of the GRB population is expected to be oriented off-axis and their number should be quite large for small typical GRB opening angles. GRBs not pointing at us can still be seen as Orphan Afterglows (OA – i.e. afterglows with an extremely weak or undetected prompt emission). OAs should outnumber (by a factor $\sim 2/\theta_j^2$) the current population of bursts detected in the γ–ray band but they have not been conclusively observed so far at any frequency (except for the possible weak GRB170817A which could be a 5° jet observed at $\sim 30^\circ$). For the population of long GRBs, we compute the expected flux of orphan afterglows in the mm, optical, and X-ray bands combining

a population synthesis code with the standard afterglow emission model (Ghirlanda et al., 2015b). We estimate the detection rate of OAs with ongoing and forthcoming surveys. The average duration of OAs as transients above a given limiting flux is derived and described with analytical expressions: in general OAs should appear as daily transients in optical surveys and as monthly/yearly transients in the mm/Radio band. We find that up to $\sim$20 OA yr^{-1} could be observed by the ZTF survey and a larger number of $\sim$50 OA yr^{-1} should be detected by LSST in the optical band. For the X–ray band, $\sim$ 26 OA yr^{-1} could be detected by the eROSITA. For the large population of OA detectable by LSST, we show that the X–ray and optical follow up of the light–curve (for the brightest cases) and/or the extensive follow up of their emission in the mm and Radio band could be the key to disentangling their GRB nature from other extragalactic transients of comparable flux density. What is new in our model is that we predict the properties of OA based on the observed properties of GRBs in the γ–ray band considering as constraints the flux and fluence distribution of the population of GRBs detected by *Swift*, BATSE and *Fermi*. Since the γ–ray energy detected in the prompt emission is a proxy of the kinetic energy driving the afterglow deceleration, our simulated population of bursts includes both high and low kinetic power bursts.

During the last year of my thesis I also concentrated on the prompt emission dissipation and radiation mechanism operating in GRBs. According to the standard fireball model (Paczynski, 1986; Piran, 2004), the prompt emission of GRBs is generated by relativistic internal shocks (IS) produced by shells (i.e. the fireballs) ejected by the inner engine with random velocities. In these shocks, a fraction of the total kinetic energy of the fireballs is converted into radiation. Shocks produced by the deceleration of the relativistic outflow by the interstellar medium, external shocks (ES), have been invoked to explain the afterglow emission. However, if over–densities characterize the circum burst medium, ES could also produce a variable light–curve. However, IS (expected to occur at a constant radius) should differ from ES (occurring at an increasing radius) in producing pulses whose duration is not correlated with their time of occurrence.

The duration of prompt γ–ray pulses is rather constant while the width of X–ray flares correlates with their peak time ($\Delta t \propto t$ – Chin-

carini et al. 2010) suggesting a possible different origin. However, pulses and flares have similar spectral properties. One leading question is whether X–ray flares and prompt emission pulses share the same origin and if they are preferentially produced by IS or ES. To answer these questions, I derived how the energy and duration of pulses scale with their time of occurrence in both IS and ES scenarios (Pescalli et al. 2017). Then I compared these analytical models with existing data. The absence of an observed correlation between prompt emission pulse duration and its time of occurrence favours an "internal" origin and confirms the earlier results present in the literature (Ramirez-Ruiz and Fenimore, 2000). We show that also the energetic and temporal properties of X–ray flares are consistent with being produced by internal shocks between slow fireballs with a small contrast between their bulk Lorentz factors, confirming what has been previously found by Barraud et al. (2005) through numerical simulations. These results relax the requirement of a long lasting central engine to explain the latest X–ray flares.

Fireballs are initially extremely dense and highly opaque to Thomson scattering. Due to the high internal pressure, they expand and accelerate to relativistic velocities while converting their internal energy into bulk kinetic energy. The fireballs' expansion decreases their opacity until they become transparent. At this stage they release their internal radiation with a typical black body spectrum because, during the opaque phase, radiation and matter have reached thermal equilibrium.

Despite this model predicts thermal emission from GRBs, the spectra of these sources are typically non–thermal. GRBs with thermal spectra are extremely rare ($\sim$ 3% – Ghirlanda et al. 2003) but very precious since they allow us to analytically estimate some fundamental parameters describing the fireball dynamics.

I collaborated to a multi–wavelenght paper on the brigh GRB 151027A (Nappo et al., 2017) by performing the time–resolved spectral analysis of its prompt emission. A remarkable feature of the prompt emission is the presence of a bright flare $\sim$ 100 s after the trigger, lasting $\sim$ 70 s in the soft X–ray band, which was simultaneously detected from the optical band up to the MeV energy range. By combining *Swift*–BAT/XRT and *Fermi*/GBM data, the broadband ($[0.3 - 1000]$ keV) time resolved spectral analysis of the flare reveals the coexistence of a non–thermal (cutoff power–law) and a statis-

tically significant and particularly bright thermal black body components. The latter contributes up to 35% of the luminosity in the $[0.3 - 1000]$ keV band. In this work we discussed the possible origin of this thermal radiation. The γ–ray emission observed in *Swift*/BAT and *Fermi*/GBM anticipates and lasts less than the soft X–ray emission as observed by *Swift*/XRT, arguing against a Comptonization origin. Such late time black body component could be explained as due to the collision of a fast shell with a slow and heavy fireball ejected during the quiescent time interval between the initial and late flares of the burst.

Despite these few cases of GRBs with a thermal black body component, one of the major issues related to the prompt emission mechanism is the inconsistency of observed spectra with the predictions of synchrotron emission. Hard GRB spectra at low energies could be obtained still within the synchrotron theory (Daigne et al., 2011) at the expense of some ad–hoc configuration of the physical conditions. In a recent study, Oganesyan et al. (2017) extended the investigation of the prompt emission spectra down to the soft X–ray band finding consistency with synchrotron radiation from (moderately) fast–cooling electrons. We asked if also GRBs observed by *Fermi* have a break. I collaborated to a work (Ravasio et al. 2017) where we present the time–resolved spectral analysis of the prompt emission of GRB 160625B. This is one of the brightest bursts detected by *Fermi*. Standard empirical functions fail in providing an acceptable fit to the GBM spectral data. The goodness of the fit significantly improves when a low-energy break is added in the fitting function. The spectral break is located around $E_{\rm break} \sim 100\,{\rm keV}$, while at $0.5 - 6\,{\rm MeV}$ the spectrum displays the usual νF_ν peak energy feature $E_{\rm peak}$. The slopes below and above $E_{\rm break}$ are consistent with the values –0.7 and –1.5, respectively, expected from synchrotron emission produced by a population of electrons in a "moderately" fast–cooling regime. The small ratio between $E_{\rm peak}$ and $E_{\rm break}$ implies that the radiative cooling is incomplete, contrary to what expected in strongly magnetized and compact emitting regions. These results demand a revision of the radiation mechanism in the prompt phase of GRBs.

List of publications:

1. *From the earliest pulses to the latest flares in long GRBs*
   Pescalli, **A.**, Ronchi, M., Ghirlanda, G., Ghisellini, G., 2017, Submitted to Monthly Notices of the Royal Astronomical Society

2. *Consistency with synchrotron emission in the bright GRB 160625B observed by Fermi*
   Ravasio, M. E., Oganesyan, G., Ghirlanda, G., Nava, L., Ghisellini, G., **Pescalli**, **A.**, Celotti, A., 2017, Submitted to Astronomy & Astrophysics

3. *The 999th Swift gamma-ray burst: Some like it thermal*
   Nappo, F., **Pescalli**, **A.**, Oganesyan, G., Ghirlanda, G., Giroletti, M., Melandri, A., Campana, S., Ghisellini, G., Salafia, O. S., D'Avanzo, P., Bernardini, M. G., Covino, S., Carretti, E., Celotti, A., D'Elia, V., Nava, L., Palazzi, E., Poppi, S., Prandoni, I., Righini, S., Rossi, A., Salvaterra, R., Tagliaferri, G., Testa, V., Venturi, T., Vergani, S. D., 2017, Astronomy & Astrophysics, 598, A23

4. *Light curves and spectra from off–axis gamma–ray bursts*
   Salafia, O.S., Ghisellini, G., **Pescalli**, **A.**, Ghirlanda, G., Nappo, F., 2016, Monthly Notices of the Royal Astronomical Society, 461, 3607

5. *Short gamma-ray bursts at the dawn of the gravitational wave era*
   Ghirlanda, G., Salafia, O. S., **Pescalli**, **A.**, Ghisellini, G., Salvaterra, R., Chassande-Mottin, E., Colpi, M., Nappo, F., D'Avanzo, P., Melandri, A., Bernardini, M. G., Branchesi, M., Campana, S., Ciolfi, R., Covino, S., Götz, D., Vergani, S. D., Zennaro, M., Tagliaferri, G., 2016, Astronomy & Astrophysics, 594, 84,

6. *Searching for narrow absorption and emission lines in XMM–Newton spectra of gamma–ray bursts*
   Campana, S., Braito, V., D'Avanzo, P., Ghirlanda, G., Melandri, A., **Pescalli**, **A.**, Salafia, O. S., Salvaterra, R., Tagliaferri, G., Vergani, S. D., 2016, Astronomy & Astrophysics, 592, 85

7. *Are long gamma–ray bursts biased tracers of star formation? Clues from the host galaxies of the Swift/BAT6 complete sample of bright LGRBs. II. Star formation rates and metallicities at $z < 1$*
   Japelj, J., Vergani, S. D., Salvaterra, R., D'Avanzo, P., Mannucci, F., Fernandez–Soto, A., Boissier, S., Hunt, L. K., Atek, H., Rodriguez-Munoz, L., Scodeggio, M., Cristiani, S., Le Floc'h, E., Flores, H.,

Gallego, J., Ghirlanda, G., Gomboc, A., Hammer, F., Perley, D. A., **Pescalli**, **A.**, Petitjean, P., Puech, M., Rafelski, M., Tagliaferri, G., 2016, Astronomy & Astrophysics, 590, 129

8. *The rate and luminosity function of long gamma ray bursts*
Pescalli, **A.**, Ghirlanda, G., Salvaterra, R., Ghisellini, G., Vergani, S. D., Nappo, F., Salafia, O. S., Melandri, A., Covino, S., Götz, D., 2016, Astronomy & Astrophysics, 587, A40

9. *Structure of gamma–ray burst jets: intrinsic versus apparent properties*
Salafia, O.S., Ghisellini, G., **Pescalli**, **A.**, Ghirlanda, G., Nappo, F., 2015, Monthly Notices of the Royal Astronomical Society, 450, 3549

10. *Unveiling the population of orphan γ-ray bursts*
Ghirlanda, G., Salvaterra, R., Campana, S., Vergani, S. D., Japelj, J., Bernardini, M. G., Burlon, D., D'Avanzo, P., Melandri, A., Gomboc, A., Nappo, F., Paladini, R., **Pescalli**, **A.**, Salafia, O. S., Tagliaferri, G., 2015, Astronomy & Astrophysics, 578, A71

11. *Luminosity function and jet structure of Gamma-Ray Burst*
Pescalli, **A.**, Ghirlanda, G., Salafia, O.S., Ghisellini, G., Nappo, F., Salvaterra, R., 2015, Monthly Notices of the Royal Astronomical Society, 447, 1911

12. *Gamma-ray burst jets: uniform or structured?*
Salafia, O. S., **Pescalli**, **A.**, Nappo, F., Ghisellini, G., Ghirlanda, G., Salvaterra, R., Tagliaferri, G., 2014, Proceedings of Swift: 10 Years of Discovery (SWIFT 10)

13. *Photospheric emission throughout GRB 100507 detected by Fermi*
Ghirlanda, G., **Pescalli**, **A.** and Ghisellini, G., 2013, Monthly Notices of the Royal Astronomical Society, 432, 3237

Contents

1 GRB overview **1**
- 1.1 Temporal properties . . . 2
- 1.2 Spectral properties . . . 4
- 1.3 Correlations . . . 7
- 1.4 Redshift . . . 11
- 1.5 Progenitors . . . 12

2 The Fireball Standard Model **15**
- 2.1 The compactness argument . . . 15
- 2.2 Fireball dynamics . . . 17
- 2.3 Photospheric emission . . . 21
- 2.4 Internal shocks . . . 23
- 2.5 External shocks . . . 26
- 2.6 Synchrotron emission . . . 27
  - 2.6.1 Single particle emission . . . 27
  - 2.6.2 Single particle spectrum . . . 28
  - 2.6.3 Emission from a distribution of electrons . . . 30
- 2.7 Inverse Compton emission . . . 33
  - 2.7.1 Single particle emission . . . 33
  - 2.7.2 Single particle spectrum . . . 35
  - 2.7.3 Emission from a distribution of electrons . . . 36

3 The luminosity function and formation rate of GRBs **39**
- 3.1 Introduction . . . 39

3.2 General theoretical model 43

4 Reconstructing $\phi(L)$ and $\psi(z)$ of GRBs **47**
4.1 The C^- method 50
4.1.1 Test of $L - z$ independence 56
4.1.2 The relevance of sample completeness 57
4.2 The Maximum Likelihood Estimator method 58
4.3 The redshift integrated luminosity function 60
4.3.1 Application to the BAT6ext complete sample . . 62

5 Redshift dependent formation rate of long GRBs – $\psi(z)$ **65**
5.1 Monte Carlo test of the C^- method 70
5.2 The BAT6ext complete sample 72

6 Constraints on the GRB jet structure through the luminosity function – $\phi(L)$ **79**
6.1 Uniform jet 80
6.1.1 Uniform jet with unique $\theta_{\rm jet}$ observed on–axis . . 83
6.1.2 Uniform Jet with luminoisty dependent aperture $\theta_{\rm jet}(L)$ observed on–axis 85
6.1.3 Uniform jet observed at different viewing angles 86
6.1.4 Apparent vs intrinsic structure 89
6.2 Structured jet 93
6.2.1 The structured jet model LF 98
6.3 The observed luminosity function 99
6.4 What $\phi(L)$ tells us about the jet structure of long GRBs 103

7 Orphan GRBs Afterglows (OA) **113**
7.1 OA emission model 115
7.1.1 Setting the micro–physical shock parameters . . 117
7.2 OA distinguishing properties and predictions 119
7.2.1 OA flux densities 122
7.2.2 OA timescalses 123
7.2.3 OA detection rate 125

8 Short GRBs at the dawn of the Gravitational Wave era **131**
8.1 Observational constraints 133
8.1.1 From population properties to observables 134
8.2 Monte Carlo Markov Chain approach 137
8.2.1 MC simulation of the SGRB population 138
8.2.2 MCMC results 141

8.3 Results 143
8.3.1 SGRBs luminosity function $\phi(L)$ 145
8.3.2 SGRBs formation rate $\psi(z)$ 146
8.3.3 SGRBs local rate 148

9 Dissipation mechanism in GRBs **153**
9.1 Pulses duration–occurrence time relation 154
9.1.1 Correlation analysis 157
9.2 Internal vs External Shocks scenario 161
9.3 What is the origin of pulses in GRBs? 165

10 Radiative mechanism in GRBs **169**
10.1 GRB 151027A: some like it thermal 173
10.1.1 Observational data 173
10.1.2 Prompt emission analysis and results 175
10.1.3 Understanding the thermal component: a reborn fireball 182
10.2 GRB 160625B: consistency with synchrotron emission . 186
10.2.1 Observational data 188
10.2.2 Evidence of a spectral break 189
10.2.3 Time–resolved spectral analysis 193
10.2.4 Interpretation of synchrotron emission 194

11 Conclusions **203**

List of publications **225**

Acknowledgments **237**

Bibliography **237**

List of Figures

1.1 Examples of prompt light–curves 2
1.2 T_{90} distribution for BATSE GRB 3
1.3 Prompt spectrum of GRB 990123 4
1.4 GRB 951228: exemplum of class–I thermal burst 6
1.5 GRB 970111: exemplum of class–II thermal burst 7
1.6 GRB 100724: exemplum of class–III thermal burst . . . 8
1.7 Amati and Ghirlanda correlations compared 9
1.8 Yonetoku correlation of the BAT6et complete sample . 10
1.9 Redshift distribution of (pre–) *Swift* GRBs – Gehrels et al. (2009) 11
1.10 Schematic view of GRB progenitors. 13

2.1 Fireball $\Gamma(R)$ profile. 20
2.2 Internal shock radiative efficiency 24
2.3 Single particle synchrotron spectrum 29
2.4 Electron–photon scattering in two different frames. . . 34
2.5 Inverse Compton single particle spectrum 36
2.6 Limits of integration in Inverse Compton emission . . . 37

3.1 Sky distribution of 2704 BATSE GRBs 40
3.2 Intensity distribution of BATSE bursts – (Pendleton et al., 1996) 41
3.3 L and z distributions for long and short GRBs 43
3.4 Schematic view of a solid angle 44

4.1 Understanding the C^- method with a simulated sample – I 52
4.2 Understanding the C^- method with a simulated sample – II 55
4.3 Resulting vs. parent $\Phi(L)$ and $\psi(z)$ using C^- method . 56
4.4 BAT6ext redshift integrated luminosity function 62

5.1 Excess of GRBs at low redshifts – Petrosian et al. (2015); Yu et al. (2015a) 67
5.2 BAT6ext $\psi(z)$ and $\phi(L)$ derived with C^- method 69
5.3 C^- method applied to incomplete samples. 71

6.1 Achromatic jet–break of GRB 990510 81
6.2 Schematic view of a bipolar conical jet 82
6.3 Schematic view of the beaming effect 83
6.4 $L(\theta_v)$ for an off–axis uniform jet 87
6.5 Model LF for an off–axis uniform jet 88
6.6 The two possible jet structure scenario by Lipunov et al. (2001) 90
6.7 Uniform jet apparent vs. intrinsic structure 92
6.8 E_{iso} and L_{iso} distributions 94
6.9 Power–law structured jet apparent structure 95
6.10 Model LF for a power–law structured jet 95
6.11 Gaussian structured jet apparent structure 97
6.12 The observed (redshift integrated) luminosity function 99
6.13 The observed LF fit – on–axis UJ $\theta_j = const$ 105
6.14 The observed LF fit – on–axis UJ $\theta_j(L)$ 107
6.15 The observed LF fit – off–axis UJ 108
6.16 The observed LF fit – SJ 109
6.17 The observed LF fit – GJ 110

7.1 Schematic representation off–axis observer 114
7.2 Flux density cumulative distributions for the BAT6 complete sample 118
7.3 SED comparison between OA GRBs and potential competitors extragalactic sources 120
7.4 OAs peak fluxes distribution 124
7.5 OAs timescales distribution 125

8.1 SGRBs prompt properties distributions 135
8.2 Monte Carlo simulation scheme 139

8.3 MCMC resulting distributions and contour plots 142
8.4 Comparison of SGRBs $\psi(z)$ 147
8.5 Local SGRBs rate 149

9.1 Example of light–curve deconvolution from Bhat et al. (2012) 155
9.2 Pulse duration $\Delta t^{\rm obs}$ vs peak time $t^{\rm obs}_{\rm peak}$ 156
9.3 Average Peak Alignment of *Fermi* pulses 159
9.4 Average evolution of the normalized *Fermi* pulse width with time 160
9.5 XRFs $E_{\rm iso}$ versus $t^{\rm rest}_{\rm peak}$. 164
9.6 XRFs $\Delta t^{\rm rest}$ versus $t^{\rm rest}_{\rm peak}$. 165

10.1 Spectral index α distribution from Ghirlanda et al. (2002, 2003). 170
10.2 GRB 151027A: prompt light–curve and spectra 176
10.3 GRB 151027A: spectral parameters evolution – third peak 179
10.4 GRB 151027A: X/γ – Optical emission comparison – third peak 181
10.5 GRB 151027A: luminosity temporal evolution during the bursts 184
10.6 GRB 160625B: GBM (NaI and BGO) and LAT (LLE) light–curve 187
10.7 GRB 160625B: main episode time–integrated SBPL (standard) fit 190
10.8 GRB 160625B: main episode time–integrated fit with SBPL and 2SBPL 192
10.9 Comparison between different fitting models 194
10.10 Histograms of the 2SBPL F–test significance 198
10.11 GRB 160625B: fit of the brightest time–resolved spectrum 198
10.12 GRB 160625B: temporal evolution of spectral parameters 199
10.13 GRB 160625B: correlation between $E_{\rm break}$ and $E_{\rm peak}$ . . . 200
10.14 GRB 160625B: 2SBPL indexes distributions 201
10.15 GRB 160625B: temporal evolution of the $E_{\rm p}/E_{\rm b}$ ratio. . 202

List of Tables

1.1 $E_{\rm p} - L$ correlation for the BAT6ext complete sample . . 10

5.1 BAT6ext sample 75

6.1 Intermediate luminosity GRBs for the observed LF . . . 101

7.1 Transient surveys in the optical and X–ray bands 121
7.2 OAs average duration fit parameters. 125

8.1 MCMC results 144
8.2 Short GRB rate 151

9.1 Mean values of the normalized width $W/\langle W \rangle$ 161

10.1 GRB 151027A: Prompt emission fit parameters 180
10.2 GRB 160625B: SBPL best fit parameters. 195
10.3 GRB 160625B: 2SBPL best fit parameters 196
10.4 GRB 160625B: SBPL+BB best fit parameters. 197

CHAPTER 1

GRB overview

Gamma Ray Bursts (GRBs) are powerful emitters of γ–photons situated at cosmological distances and an almost isotropic distribution in the sky.

Prompt The main emission is characterized by typical energy going from a few keV up to some dozens of MeV (GeV in rare cases), it can last from the fraction up to thousands of seconds and its variability can reach the ms timescale.

Afterglow The latter is generally followed by another emission at lower frequencies (X, Optical/IR, Radio bands), less variable and lasting even up to months.

The several observational properties are explained in the so–called fireball standard model (see Chp.2). Within this model, the prompt radiation is produced by *internal shocks* (IS – see Sec.2.4) generated in collisions between relativistic shells of plasma (the fireballs) ejected by the inner engine with random velocities. In these shocks, a fraction of the total kinetic energy of the fireballs is converted into radi-

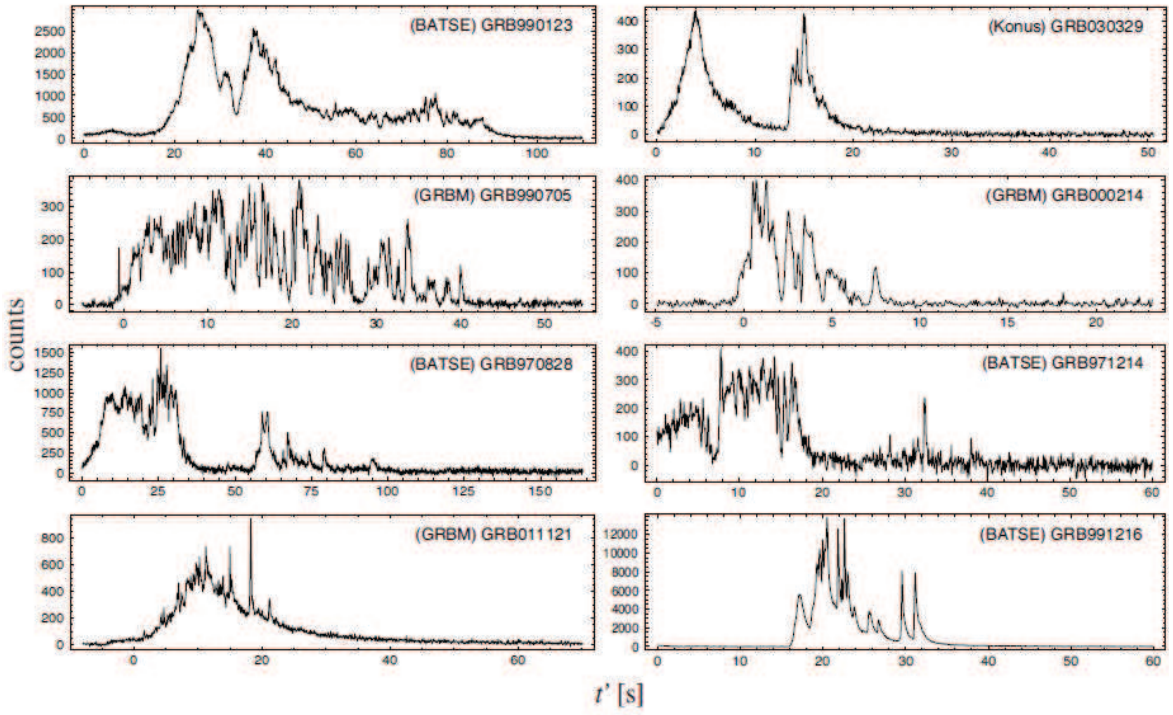

Figure 1.1: Some GRB prompt light–curve shown as example of the great diversity of temporal profiles (Borgonovo et al. 2007)

ation through synchrotron (see Sec.2.6) and inverse Compton emission (see Sec.2.7). Shocks produced by the deceleration of the merged relativistic outflow by the interstellar medium, *external shocks* (ES – see Sec.2.5), have been invoked to explain the long lasting, smoothly decaying, broad band afterglow emission.

1.1 Temporal properties

GRBs prompt emission is characterized by irregular temporal profile (see Fig.1.1). The light–curves are highly variable, on characteristic timescales as short as few milliseconds (Walker et al., 2000; Bhat et al., 1992; MacLachlan et al., 2013), appearing as a sequence and/or superposition of pulses (Fishman et al., 1993; Bhat et al., 2012). Some bursts contain distinct, well–separated emission episodes or can even have a single smooth pulse (e.g. GRB 980425 Galama et al., 1998). The individual pulse of which the light–curve is constituted typically shows an asymmetric structure with a Fast Rise and Exponentially Decay behavior (FRED shape – Fishman et al., 1994) and are indeed well described by the so–called Norris function (Norris et al., 1996). Their width δt vary in a wide range with the shortest pulses

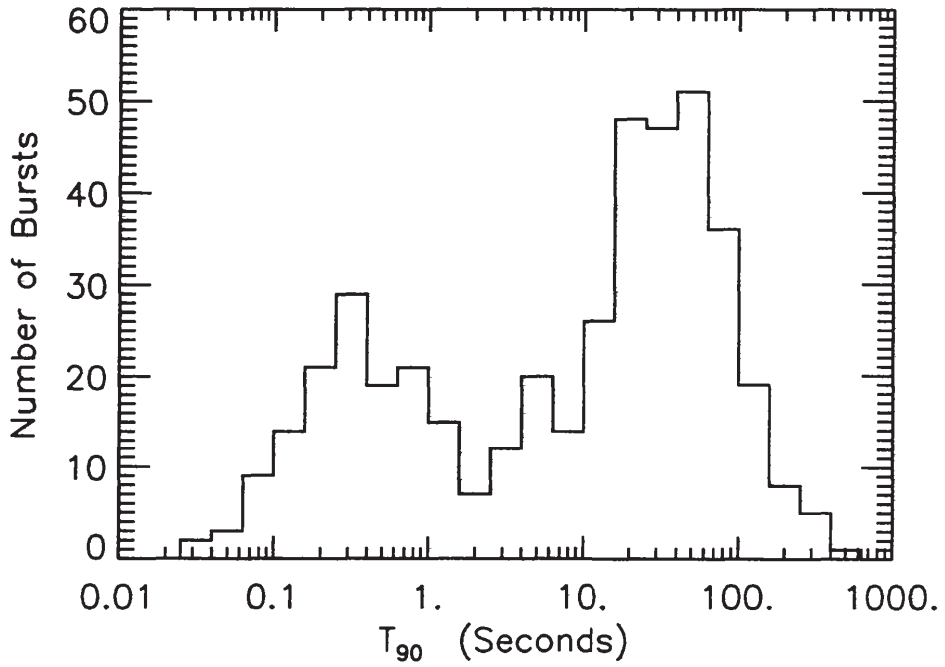

Figure 1.2: Distribution of T_{90} for 427 GRBs from the 3rd BATSE Catalog (Meegan et al., 1996).

having sub–ms width. If normalized with the burst duration ($\delta t/T$) they could reach values as low as $10^{-3} - 10^{-4}$.

The burst duration is typically defined through the T_{90} (T_{50}) being the time interval within which 90% (50%) of the burst fluence is detected. More precisely, T_{90} is defined as the time corresponding to an increment of the cumulative counts from 5% up to 95% above the background. The values of T_{90} span over 5 orders of magnitude, i.e. from $\sim 10^{-2}$ s to 10^3 s. Based on the bimodality of the duration distribution (see Fig.1.2), GRBs are conventionally divided GRBs in two classes:

- *Short* GRBs: having $T_{90} < 2$ s ($\langle T_{90} \rangle \sim 0.2$ s)
- *Long* GRBs: having $T_{90} > 2$ s ($\langle T_{90} \rangle \sim 20$ s)

This distinction is made on the basis of the observed durations and not the rest frame one. Moreover, T_{90} strongly depends on the assumed energy band on which the light–curve is calculated and the instrumental sensitivity. Moreover, according to Bromberg et al. (2013), for both the *Fermi* and *CGRO*/BATSE short GRB populations, this duration threshold should limit the contamination from collapsar–GRBs to less than 10%.

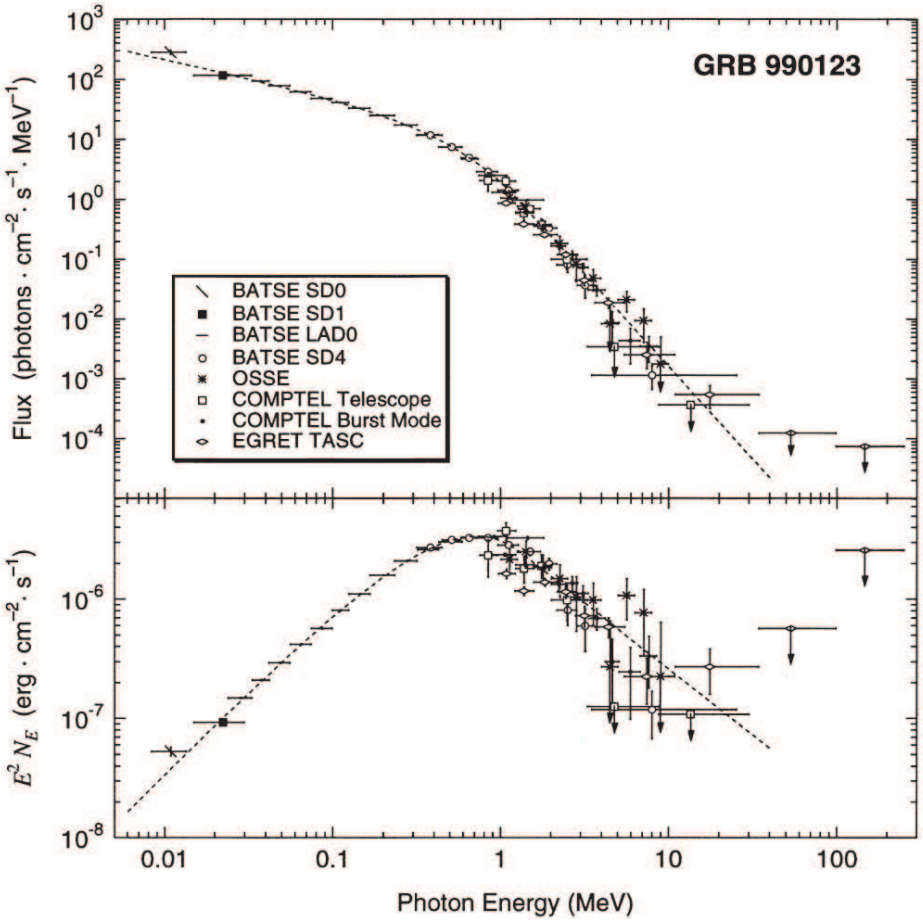

Figure 1.3: Prompt spectrum of GRB 990123 (Briggs et al., 1999). The spectrum is modelled with a Band function (Band et al., 1993) with $\alpha = -0.67$, $\beta = -3.0$, $E_{\rm p} = 720$ keV. *Upper panel*: photon spectrum. *Lower panel*: $\nu F(\nu)$ spectrum.

1.2 Spectral properties

The GRB prompt emission spectrum is typically non–thermal (i.e. well described by single or combinatons of power–laws), as expected if their emission is produced by shock accelerated relativistic electrons which radiate via synchrotron/inverse Compton (see Sec.2.6 and Sec.2.7). The photon spectrum $N(\nu)$ (or equivalently $N(E)$) represents the number of photons per unit area and time in function of the frequency (energy) of photons. Generally, also the $\nu F(\nu)$ ($E^2 N(E)$) representation is employed in order to describe prompt spectra (see. Fig.1.3). The majority of GRBs has a $\nu F(\nu)$ spectrum extending, without evidences of spectral lines, from keV to Mev typically peaking at few hundreds keV (in rare cases it can even extend up to GeV). It can be well described by the following empirical func-

tion (the so–called Band model):

$$N(\nu) = N_0 \begin{cases} (h\nu)^{\alpha} \exp(-h\nu/E_0) & \text{if } h\nu < (\alpha-\beta)E_0 \\ [(\alpha-\beta)E_0]^{\alpha-\beta}(h\nu)^{\beta}\exp(\beta-\alpha) & \text{if } h\nu < (\alpha-\beta)E_0 \end{cases} \tag{1.1}$$

which was introduced by Band et al. (1993). This is one of the most used model in spectral analysis since its formulation. α and β are the power–law spectral indices (at low and high energies, respectively) and E_0 is a parameter linked to the break energy through the relation $E_{\rm b} = (\alpha-\beta)E_0$. Only if $\alpha > -2$ and $\beta < -2$ the $\nu F(\nu)$ spectrum shows a peak at $E_{\rm p} = (\alpha+2)E_0$. This function is essentially a broken power–law with an exponential smoothing of the break.Typical values for the parameters are $\alpha = -1.0$, $\beta = -2.5$ and $E_{\rm p} \simeq 250$ keV.

There are, however, a few bursts which show a thermal black body (BB) spectrum. Thermal emission is naturally expected in the so–called standard fireball model of GRBs when the relativistically expanding plasma becomes transparent (e.g. Goodman, 1986; Paczynski, 1986; Daigne and Mochkovitch, 2002). Thermal photons can be either those of the initial fireball or they can be created at some stage of the fireball evolution, when it is still moderately opaque, due to some dissipation mechanism (e.g. Rees and Mészáros, 2005). In this case photons are expected to be distributed according to the Planck function:

$$N(\nu) = \frac{h\nu}{e^{\frac{h\nu}{kT}} - 1} \tag{1.2}$$

Evidences of thermal components in GRB prompt spectra could be divided into three classes, as follows:

- **Class–I** Bursts with a pure BB component for the entire duration of their prompt emission phase. These are only four cases and they have all been detected by BATSE: GRB 930214, 941023, 951228 (Ryde, 2004) and GRB 990413 (Bosnjak et al., 2006). An example of this class is shown in Fig.1.4;
- **Class–II** Bursts with a pure BB component only in the first few seconds of their emission which is overtaken by a dominating non–thermal component afterwards. Ghirlanda et al. (2003), performing the time–resolved spectral analysis of bright BATSE bursts, revealed a thermal component at the beginning of GRB 910807, 910927, 911118, 970111, 980306. An example is shown in Fig.1.5;

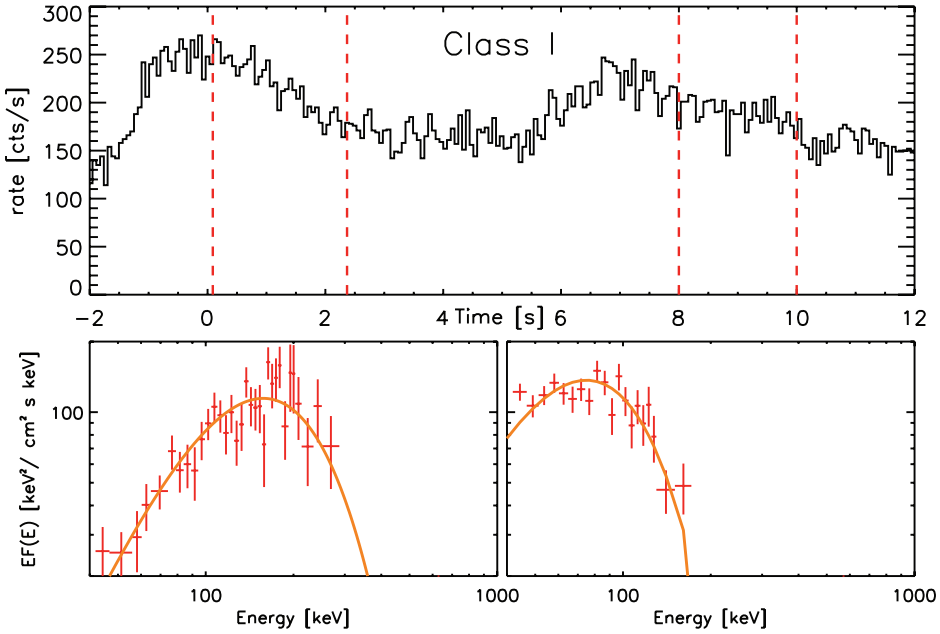

Figure 1.4: Example of class–I bursts. GRB 951228 (Ryde, 2004) which has a thermal spectrum throughout its duration. *Top panel*: light–curve (not background subtracted). *Bottom panels*: two spectra (accumulated in the time intervals marked by the dashed vertical lines in the top panel). Both spectra are fitted with a BB component (solid orange lines in the two bottom panels).

- **Class–III** Bursts with a BB plus a non–thermal component. Recently, GRB 110721A (Axelsson et al., 2012), GRB 100724B (Guiriec et al., 2011)and GRB 120323A (Guiriec et al., 2013), detected by the *Fermi* satellite, showed the compresence of a BB, contributing $\sim 5\%$ of the total flux and a dominating non–thermal component. GRB 090902B (Ryde et al., 2010), also detected by *Fermi*, has a prominent broadened BB component and a non–thermal sub–dominant power–law. An example of this class is shown in Fig.1.6.

Typically, the temperature characterizing the thermal component evolves with time approximately as $k\mathcal{T} \propto t^{-2/3}$ (Ryde, 2004) or $k\mathcal{T} \propto t^{-1/4}$ (Ghirlanda et al., 2003) after an initial rising or constant phase. The flux of the thermal component decreases $\propto t^{-2}$ at late times. Such temporal behaviors at late times have been interpreted (Pe'er, 2008) as high–latitude emission from the optically thick surface of the expanding plasma when it becomes transparent. Possible interpretations of class–II and III bursts propose that the non–thermal component is produced by Compton scattering of the photospheric photons by relativistically accelerated electrons (e.g.

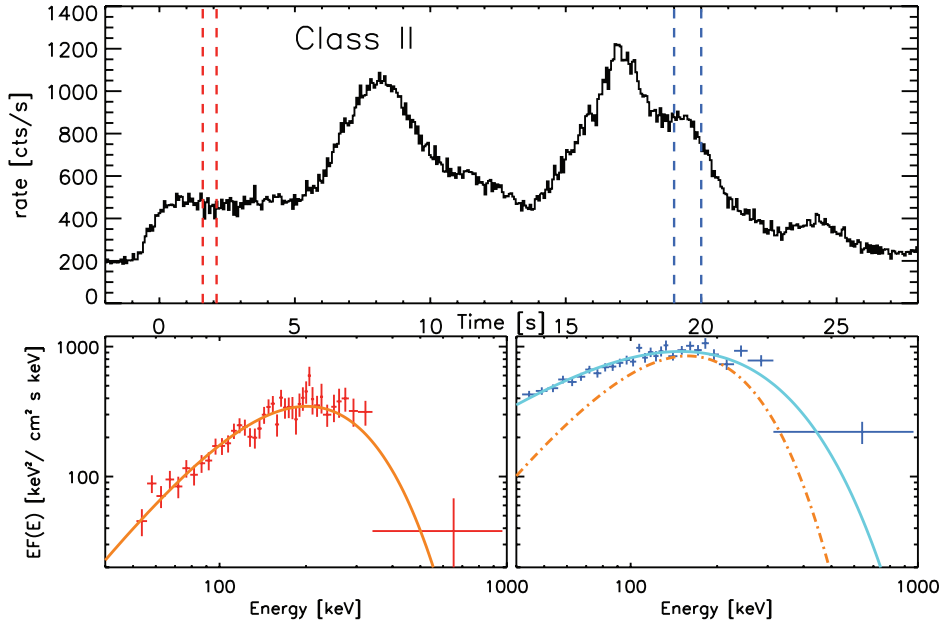

Figure 1.5: Example of class–II bursts. GRB 970111 (Ghirlanda et al., 2003) has a thermal spectrum at the beginning and a non–thermal spectrum at later times. *Top panel*: light–curve (not background subtracted). *Bottom panels*: two spectra (accumulated in the time intervals marked by the dashed vertical lines in the top panel). The first spectrum is fitted with a BB (solid orange line) the second spectrum is fitted with a non–thermal component (a cutoff–power-law model in this case) shown by the solid cyan line. For comparison the BB spectrum fitted to the early time spectrum (normalized to the peak of the late time spectrum) is shown by the dash–dotted orange line.

Pe'er, 2008) or that photons of the two component have indipendent origin with the thermal component being the photospheric emission and with the non–thermal component being produced in the optically thin region (e.g. through internal shocks) so that the relative strength of these two components is regulated by the thermal/magnetic content of the jet (Hascoët et al., 2013).

1.3 Correlations

There are empirical relations between the GRB observational properties. Such relations are useful because pose important constraints on the theoretical models and can be potentially helpful in deriving sum unknown parameters. Here, I will list the most remarkable ones:

- **Amati correlation** (Amati et al., 2002)
  The peak energy E_p of the $\nu F(\nu)$ spectrum correlate with the

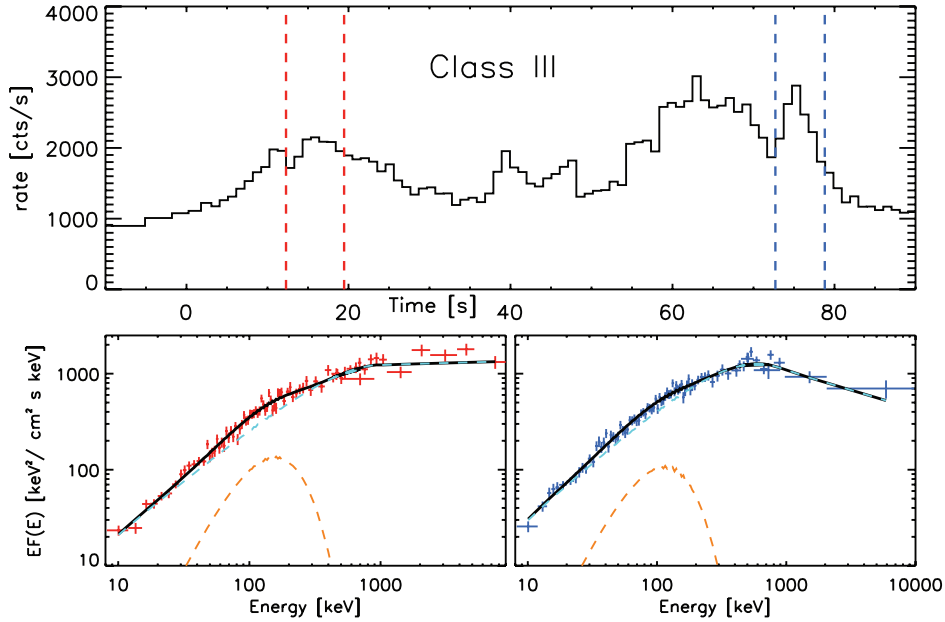

Figure 1.6: Example of class-III bursts. GRB 100724 (Guiriec et al. 2012) which has a thermal component (contributing only the 5% of the total flux) and a dominating non–thermal component throughout its duration. *Top panel*: light–curve. *Bottom panels*: early and late time spectrum (corresponding to the time intervals of the dashed vertical lines in the top panel) de–convoluted into a non–dominating BB component (dashed orange line) and a Band function (the dashed cyan line). The total spectrum is shown by the solid black line.

isotropic equivalent energy $E_{\rm iso}$ through the relation $E_{\rm p} \propto E_{\rm iso}^{0.5}$. An updated version of this correlation is shown, compared to the Ghirlanda correlation, in Fig.1.7. Mochkovitch and Nava (2015) studied the validity of this correlation within the internal shock scenario.

- **Ghirlanda correlation** (Ghirlanda et al., 2004)
  Only for those bursts whose jet opening angle $\theta_{\rm jet}$ is measured, it is possible to derive the true energy E_γ correcting the isotropic energies for the collimation factor: $E_\gamma = E_{\rm iso}(1-\cos(\theta_{\rm jet}))$. The collimation–corrected energy correlate with the peak energy as $E_{\rm p} \propto E_{\rm iso}^{G}$ with a slope depending on the assumption on the circumburst medium made in order to derive $\theta_{\rm jet}$. $G = 0.7$ for a homogeneous density and $G = 1$ for a wind profile (Nava et al., 2006). An updated version of this correlation ($G = 1$) is shown, compared to the Amati correlation, in Fig.1.7.

- **Yonetoku correlation** (Yonetoku et al., 2004)
  The peak energy $E_{\rm p}$ of the $\nu F(\nu)$ spectrum correlate with the

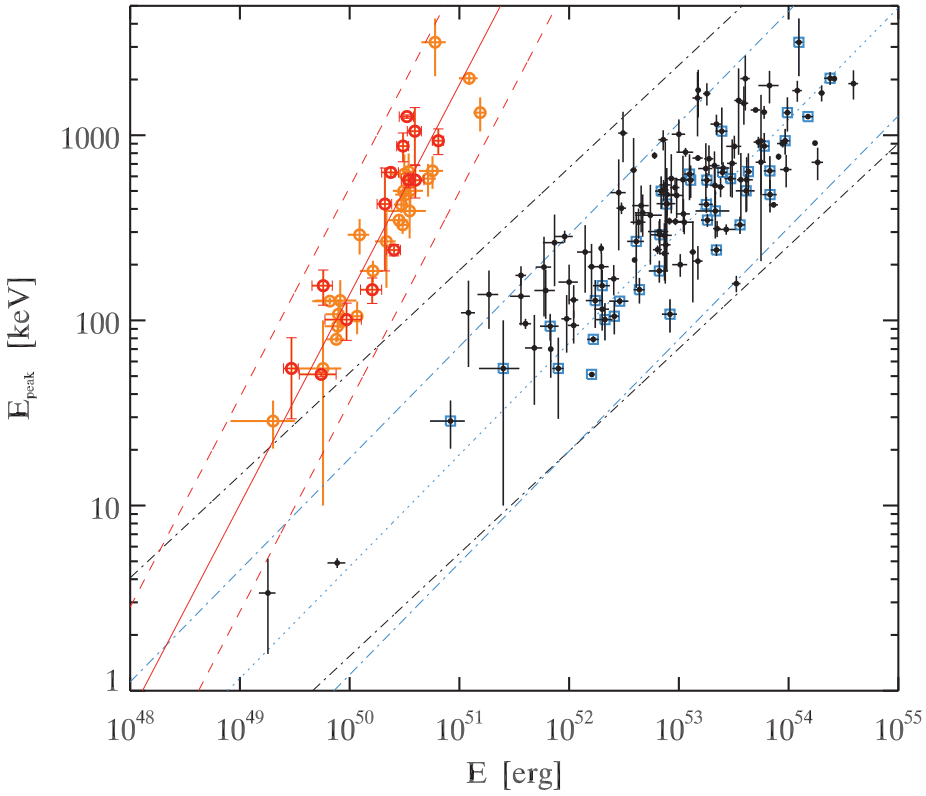

Figure 1.7: The so–called Amati and Ghirlanda correlation are shown. Black points represent the GRBs composing the Amati correlation $E_p \propto E_{iso}^{0.5}$ with 3σ dispersion (black dot–dashed lines). Points in the blue squares correspond to those GRBs with measured θ_{jet}. The blue dotted and dash–dotted lines represent, respectively, the fit and the dispersion associated to the blue points. These have been employed to obtain the red (original) and orange (added later) points of the Ghirlanda correlation ($G = 1$ wind medium). The red solid line and the red dashed lines represent the correlation and its dispersion, respectively.

isotropic equivalent luminosity L_{iso} through the relation $E_p \propto L_{iso}^{0.5}$. I personally studied this relation using the extended version (see Sec.5.2) of the complete (in flux and in redshift) BAT6 originally defined in Salvaterra et al. (2012). I calculated the isotropic equivalent luminosities for all bursts with z measured and well constrained spectral parameters: 81 out of the total 99 objects have both L, z and well–constrained E_p. Fig.1.8 shows the correlation based on the updated sample. This has been also compared with the the total sample of all bursts with L and z measured (187 objects – updated to GRB 140907A). The correlation was fitted using the bisector method (Isobe et al., 1990) in the barycentre of points for both the total and the BAT6ext sam-

Table 1.1: Results of the analysis for the $E_p - L$ correlation. The columns report in order: the analyzed sample and its size, the Spearman's rank correlation coefficient, the associated chance probability, the slope and the normalization of the bisector fit in the barycentre and the 1σ estimate of the scatter of the sample distribution around the correlation.

Sample	*#Bursts*	ρ	$P_{\rm chance}$	Slope	Norm.	σ
Total	187	0.74	6×10^{-33}	0.50 ± 0.03	$-2.3 \times 10^{-7} \pm 0.024$	0.29
BAT6ext	81	0.72	5×10^{-14}	0.54 ± 0.05	$-2.2 \times 10^{-8} \pm 0.036$	0.28

ple, respectively. I also estimated the scatter of the distribution of the points around the correlation (computed perpendicular to the correlation itself), the Spearman's rank correlation coefficient and the associated chance probability. These results are reported in Tab.1.1.

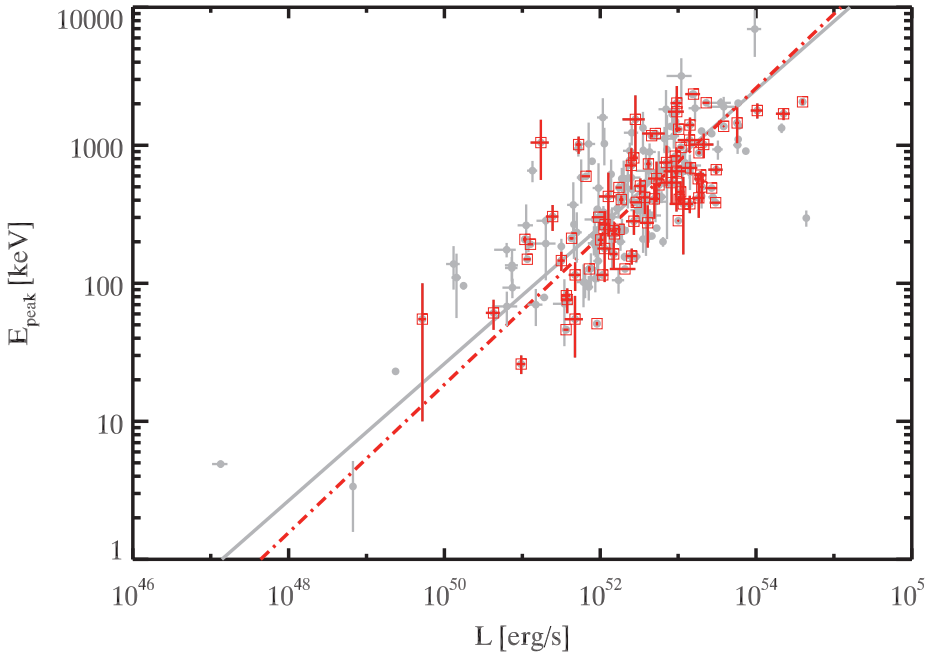

Figure 1.8: $E_p - L$ correlation. Grey points and the red empty squares represent the total (all long bursts with L and z measured) and BAT6ext complete sample, respectively. The solid gray line and the dot–dashed line are the best fit (obtained with the bisector method applied in the barycentre of points) results for the total and BAT6ext complete sample, respectively.

The cited correlations have largely been studied for the population of long GRBs but only the Yonetoku correlations has be confirmed to be valid also for short GRBs (D'Avanzo et al., 2014).

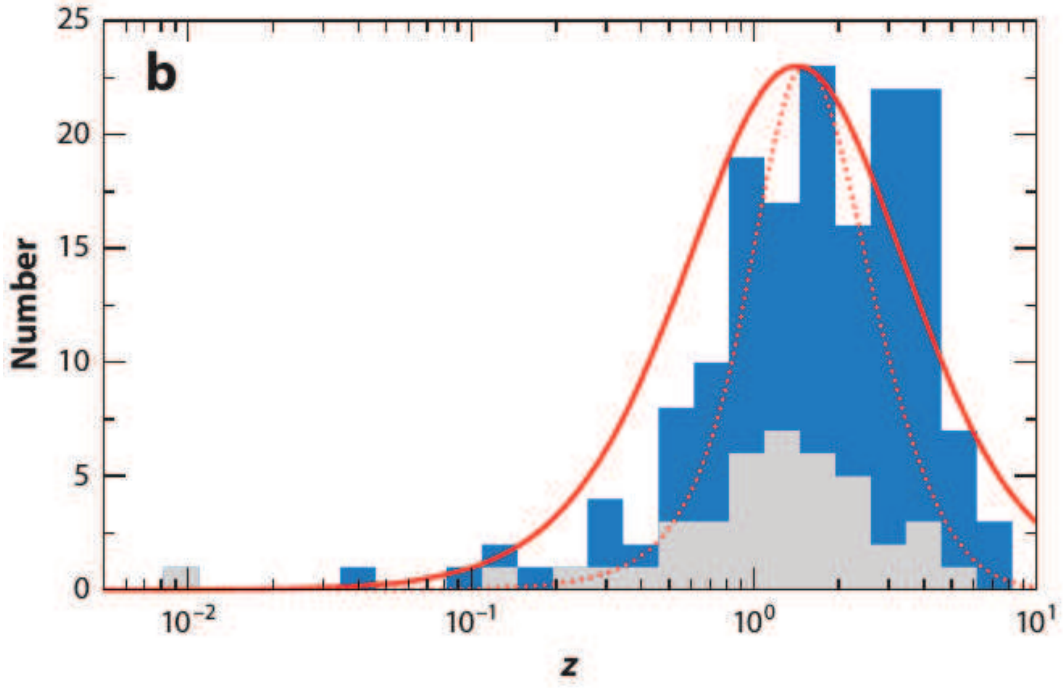

Figure 1.9: Redshift distribution for *Swift* GRBs (blue histogram) and pre–*Swift* GRBs (grey histogram). The thick solid red curve illustrates the evolution of a comoving volume element of the Universe; the thin dotted red curve is a convolution of the comoving volume with a model for the star-formation rate as calculated by Porciani and Madau (2001). Figure from Gehrels et al. (2009).

1.4 Redshift

The first redshift measurement was obtained immediately after the detection of the X and optical afterglow emission (Costa et al., 1997; van Paradijs et al., 1997) with the detection of GRB 970508. The early detection of its optical emission and the relative brightness of the event allowed to perform the optical spetroscopy (Metzger et al., 1997). The redshift was estimated to be $z = 0.835$ based on the presence of FeII and MgII absorption lines in the optical spectrum demonstrating that GRBs are cosmological sources.

The knowledge of the redshift allow to account for the expansion of the Universe and establish the distance and the rest frame properties of the source. In general, the measure of the redshift is affected by selection effects due to instrumental and/or observational biases (since the late afterglow is typically faint, the brightest bursts are favored). Initially the redshift measurement required a great deal of effort because of the needed cooperation between satellites (helpful in finding the source sky position) and ground–based telescopes

(employed to observe the late afterglow emission).

Recently, the rapid burst localization and pinpointing of the GRB afterglow, made available by the fast slewing of the *Swift* satellite (Gehrels et al., 2004), combined with the intense efforts to acquire early time optical spectra from the ground, allowed us to measure the redshifts z of GRBs with an average efficiency of 30%. GRBs with measured z are distributed from the local Universe up to very high redshift: GRB 090423 (with a spectroscopic $z = 8.2$ Salvaterra et al., 2009a; Tanvir et al., 2009) and GRB 090429B (with photometric redshift $z = 9.4$ Cucchiara et al., 2011) represent the furthest objects of stellar origin known to date.

Fig.1.9 shows the measured redshift distributions obtained by *Swift* events (blue) and by the pre–*Swift* events (grey). GRBs detected by *Swift* have a higher average redshift: $\langle z \rangle = 2.5$ for *Swift* bursts while $\langle z \rangle = 1.2$ for pre–*Swift* events. The reason for this difference is the higher sensitivity of *Swift* with respect to Beppo–SAX and HETE–II.

1.5 Progenitors

The inner engine powering GRBs must to be able to release amount of energy (10^{51-53} erg) on timescales as short as the duration of the γ–ray emission. Moreover, it must be a compact object in order to justify the short variability timescale. For these reasons the standard model of GRBs attributes their origin to relativistic jets produced by the accretion onto a fast–rotating black hole (BH) of stellar origin. Such a system can be generated in different ways (schematically represented in Fig.1.10):

- Collapsar
  The core collapse of a massive star ($\sim 30 - 50 M_{\odot}$) is thought to be the production channel of long GRBs. The BH formation is nearly instantaneous, while accretion of the surrounding stellar material can last tens of seconds consistently with the duration of long GRBs. The core collapse can alternatively lead to the formation of a magnetar (Bernardini et al., 2013). The best candidate stars are the Wolf–Rayet stars that lose most of their envelope mass because of their intense stellar winds.Moreover, observations of long GRBs indicate that they are located in small star forming galaxies, supporting the association of the progenitor with massive stars. Another fundamental issue for the

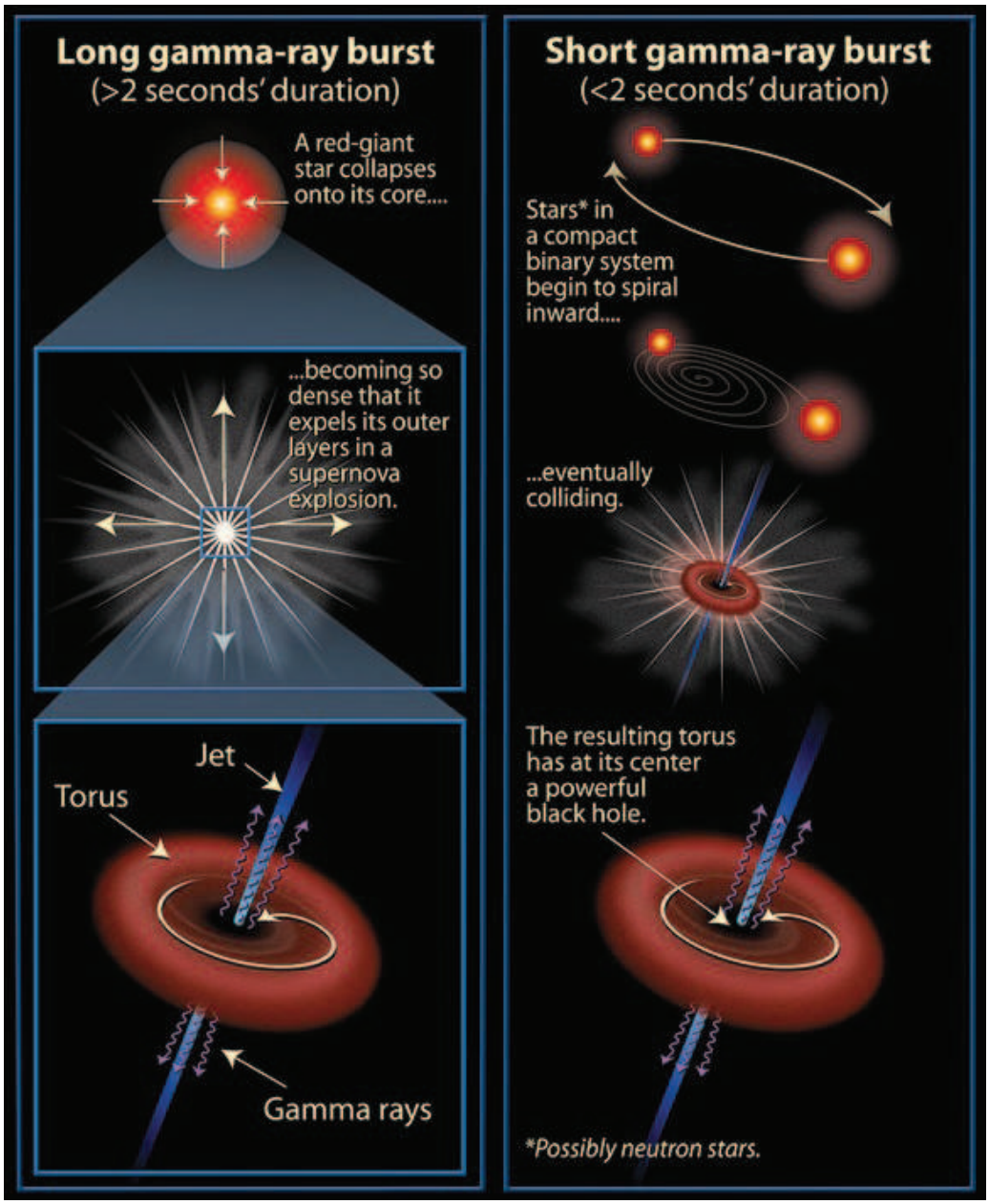

Figure 1.10: Schematic representation of GRB progenitors: a collapsar (associated to long burst – left) and a merging NS–NS binary system (associated to short bursts – right).

identification of long GRB progenitors is the association with supernovae (SN) Ib/c explosion. Signatures of such emission have been found for the first time in GRB 980425 (SN1998bw Ic type, $z = 0.0085$ – Galama et al., 1998). Another important SN–GRB connections were GRB 030329–SN 2003dh ($z = 0.1685$ – Stanek et al. 2003) and GRB 060218–SN 2006aj ($z = 0.0335$ – Mirabal et al. 2006). At the moment, the long GRBs with an as-

sociated supernova are ~ 50 (Cano, 2016). According to Soderberg et al. (2006b) less than 10% of type Ib/c SNe are associated with GRBs.

- NS–NS binary system
  For short GRBs the best candidates are the binary systems of compact objects (NS–NS or BH–NS), that lose their orbital angular momentum because of the emission of gravitational waves and merge. Their short duration is probably due to the low density of the close circumburst medium (Fong and Berger, 2013; Fong et al., 2015) leading to a lean accretion disc. Short GRBs were found in a variety of galaxy morphologies (D'Avanzo, 2015): from the elliptical galaxies to the young galaxies with ongoing star formation. No event of supernova was ever associated to the formation of short GRBs (this is compatible with the binary system scenario since the supernova explosion that formed the neutron star can be happened also $10^8 - 10^9$ years before the merger responsible for the GRB) while recently there was a possible detection of a "kilonova" signature (Eichler et al., 1989; Li and Paczyński, 1998; Jin et al., 2015, 2016).

CHAPTER 2

The Fireball Standard Model

In this chapter I will briefly introduce the key ingredients of the standard GRB fireball shock model that has been proposed, in its simplest version, by Paczynski (1986) and Goodman (1986). Over the years this model has been refined with the aim of explaining the increasing observational results collected e.g. by the *Swift* satellite (Gehrels et al., 2004) on the prompt and the afterglow emission (see the reviews Piran, 1999, 2004; Zhang and Mészáros, 2004).

2.1 The compactness argument

The inner engine of GRBs, most likely a fast rotating and accreting Black Hole (BH), is able to produce, in its polar region, a fireball, i.e. a plasma essentially composed by photons, electron/positron pairs and a small amount of baryons. This is the what is typically called the GRB "outflow". The request of a small amount of baryons, i.e. of a "light" outflow, comes from the requirement that it reaches relativistic bulk velocities. The latter condition was realized early in the field and is clearly formulated in the so–called *compactness argument* (e.g. Lithwick and Sari, 2001). This is an argument because

it is used to solve an apparent paradox which is briefly summarized below.

For a typical GRB fluence $S \sim 10^{-6}$ erg cm^{-2} and assuming a luminosity distance $d_L \sim 16$ Gpc (corresponding to $z \sim 2$), the total isotropic γ–ray energy released is $E_{\rm iso} = 4\pi d_L^2 S/(1+z) \sim 10^{52}$ erg. Given the short variability timescale δt (few milliseconds) observed in the prompt emission (Bhat et al., 1992; Walker et al., 2000; MacLachlan et al., 2013), the size of the emission region is approximately $R \sim c\delta t \simeq 3 \times 10^8 (\delta t/10\ {\rm ms})$ cm. Such high energy confined in a relatively small volume makes the fireball extremely opaque due to the process of pair production. Indeed, the optical depth for pair production can be estimated as:

$$\tau_{\gamma\gamma} = f_p \frac{\sigma_T \mathcal{S} d^2}{R^2 m_e c^2} \sim$$
$$\sim 10^{16} f_p \left(\frac{\mathcal{S}}{10^{-6}\ {\rm erg\ cm^{-2}}}\right) \left(\frac{d}{16\ {\rm Gpc}}\right)^2 \left(\frac{\delta t}{10\ {\rm ms}}\right)^{-2} \gg 1 \quad (2.1)$$

This value has been calculated assuming an approximated pair production cross section of the order of the Thomson cross section $\sigma_T = 6.25 \times 10^{-25}$ cm^2, and assuming that a fraction $f_{\rm p}$ of photons is above the photon–photon pair production ($\gamma\gamma \to e^+e^-$) threshold defined by the relation:

$$\epsilon_1 \epsilon_2 (1 - \cos\theta_{1,2}) \geq 2(m_e c^2)^2,$$

where $m_{\rm e}$ is the electron mass, ϵ_1 and ϵ_2 are the energies of two photons, and $\theta_{1,2}$ is the angle between the momenta of the two photons.

Despite these gross approximations, the order of magnitude estimate presented above shows that for typical GRB parameters (i.e. source size and energetics), the γ–rays with energies above a few hundreds of keV should be strongly absorbed. Therefore, contrary to what is observed, the spectrum of GRBs should be characterized by an abrupt cutoff at high energies where instead it seems to extend by far in the MeV energy range. This is the apparent paradox.

A possible way of out of this paradox consists in invoking the relativistic bulk motion of the emitting region (e.g. Lithwick and Sari, 2001). The relativistic Doppler effect has two main consequences. (i) Photons are blue–shifted by a factor Γ so that in the shell comoving frame they have lower energies. This reduces the number of photons above the pair production threshold which can produce pairs

(i.e. the fraction f_p is reduced by a factor $\Gamma^{2(\alpha-1)}$, where α is the photon spectral index in the γ–ray band). (ii) The real physical scale of the emission region is $R \sim \Gamma^2 c\delta t$. Accounting for these relativistic scalings, the pair production optical depth $\tau_{\gamma\gamma}$ is reduced by a factor $\Gamma^{2\alpha+2} \sim \Gamma^6$. Therefore, a bulk Lorentz factor of the order of 10^{2-3} reduced the pair production opacity $\tau_{\gamma\gamma} < 1$. Other methods have been proposed to estimate lower limits through the compactness argument applied to GeV photons detected by the LAT on board *Fermi* (Abdo et al., 2009a,b; Ackermann et al., 2010) and more detailed calculation have been presented (see Hascoët et al., 2011; Zhao et al., 2011; Zou et al., 2011). Finally, upper limits (Zou and Piran, 2010) can be obtained.

Based on the compactness argument, $\Gamma > 100$ has been obtained for a few GRBs (Lithwick and Sari, 2001). Independently, an almost unique probe that GRBs outflows are relativistic comes from the ceasing of the radio flux scintillation (observed few weeks after the detection of GRB 970508; Frail et al., 1997) which allowed us to estimate the source expansion pointing to a bulk Lorentz factor of a few ($\Gamma \sim 10$). This value, corresponding to the late phases of the deceleration, suggests that in the early phases (i.e. during the coasting phase) Γ should have been much larger.

The direct estimate of the bulk Lorentz factor during the coasting phase (Γ_0, i.e. the maximum value attained by the fireball during its dynamical evolution) is possible through the peak of the afterglow (Sari and Piran, 1999b) and has been extensively used (e.g. Molinari et al., 2007; Gruber et al., 2011; Liang et al., 2010). (Ghirlanda et al., 2012b) showed, with a sample of 31 GRBs with a measured peak of the optical light curve, that the bulk Lorentz factor in GRBs is correlated with their energetic and luminosity (but see Hascoët et al., 2014).

2.2 Fireball dynamics

Creation Let's consider a fireball created at a radius R_0 (with respect the central engine) containing N photons. Assuming a 10 $M_\odot$ black hole, $R_0 \sim 6GM/c^2 \sim 10^7$ cm (considering further that the length–scale is 3 gravitational radii). The total number of photons N is conserved until the fireball is opaque and the only internal mechanism acting on N is pair creation and there is equilibrium between creation and annihilation (e.g. Piran, 2004). As a consequence, internal

photons thermalize assuming a thermal black body (BB) spectrum. The initial state is substantially a hot plasma, with photons and pairs in equilibrium at a temperature $\mathcal{T}'_0 = (L'/4\pi R_0^2\sigma)^{1/4} \sim 10^{10}$ K assuming a comoving injected luminosity $L' = 10^{51}$ erg/s and $R_0 = 10^7$ cm (σ is the Stefan–Boltzmann constant). The BB energy density $n_{\rm BB}$ can be expressed as $a\mathcal{T}_0'^4$ (where $a = 4\sigma/c = 7.57 \times 10^{-15}$ erg/cm^3 K^4 is the radiation constant) so that the total internal energy is $E_{\rm tot} = n_{\rm BB}(4/3)\pi R_0^3 \sim 10^{52}$ erg.

Acceleration The dynamic of the GRB outflow during the acceleration phase has been presented in several works (Shemi and Piran, 1990; Meszaros and Rees, 1993a; Piran et al., 1993; Kobayashi et al., 1999). The high internal radiation pressure drives the accelerated expansion of the fireball. During this phase internal energy is converted into the fireball kinetic energy. Being $k\mathcal{T}'$ the typical photons' energy, the conservation of the photon number N leads to:

$$\frac{4}{3}\pi R_0^3 \frac{a\mathcal{T}_0'^4}{k\mathcal{T}'_0} \simeq N \simeq \frac{4}{3}\pi R^3 \frac{a\mathcal{T}'^4}{k\mathcal{T}'} \Rightarrow \mathcal{T}_0'^3 R_0^3 = \mathcal{T}'^3 R^3 \qquad (2.2)$$

Threfore, during the acceleration phase the scaling relation relating the temperature and radius of the fireball is $\mathcal{T}' \propto R^{-1}$ (Paczynski, 1986; Meszaros and Rees, 1993a). The volume increases $\propto R^3$ because the fireball is uniformly expanding. The comoving temperature $\mathcal{T}'$ and the volume V satisfy the relation $\mathcal{T}'V^{1/3} = constant$. If the expansion is adiabatic the fireball energy remains constant during the acceleration. If $E' \propto \Gamma\mathcal{T}'$ (see Shemi and Piran, 1990) then $\Gamma \propto R$.

Due to the increase of the fireball volume, the optical depth $\tau_{\gamma\gamma}$ decrease during the expansion. The acceleration lasts until all the available energy is converted into kinetic (at the saturation radius $R_{\rm s}$ with $\Gamma_{\rm max}$) or until the fireball is opaque. Oversimplyfing this evolution we can think of two source of opacity: pair production and electron scattering. For the typical conditions of the evolution of the fireball, the opacity for pair production is the first to be lost (i.e. $\tau_{\gamma\gamma} \lesssim 1$) when the fireball comoving temperature is $k\mathcal{T}' \sim 21$ keV. This happens when the bulk Lorentz factor is approximately $\Gamma_{\gamma\gamma} = 84 L_{52}^{1/4} R_{0,7}^{-1/2}$. In the absence of baryons a fireball of pure pairs would reach a relatively small bulk terminal velocity, inconsistent with the larger values derived from the observations (see above)

and would stop accelerating at a relatively small distance from the central engine ($R_{\gamma\gamma} \sim R_0\Gamma_{\gamma\gamma} \sim 10^9 L_{52}^{1/4} R_{0,7}^{1/2}$ cm). If (even a small amount) of baryons are present the opacity is sustained, due to electron scattering, after the pairs "freeze out" of equilibrium. When $\tau_{\rm es} \sim 1$ at the photospheric radius $R_{\rm p}$ (see below) the fireball becomes transparent. This transition can occur during the acceleration phase so that the fraction of internal energy not yet converted into kinetic energy is released as BB radiation with a rest frame temperature equal to the initial comoving one ($\Gamma\mathcal{T}' = \mathcal{T}'_0$). If the transparency occurs after the end of the acceleration the BB emission will be fainter and with a smaller temperature (see e.g. Daigne and Mochkovitch, 2002; Kumar and Smoot, 2014).

Coasting When the acceleration ends, the fireball enters in the so–called coasting phase in which its velocity is constant. The maximum reachable Lorentz factor $\Gamma_{\rm max} \sim 10^5$ (Piran, 1999). This value is reached in the case that all the internal energy is transferred to the baryons and it is equivalent to the maximum possible baryon loading $\varrho = E_{\rm tot}/M_0c^2$, where M_0 is the initial fireball mass. During the coasting phase the fireball volume increases $\propto R^2\Delta R$. If, during the coasting phase the fireball is still opaque to electron scattering, the number of internal photons is conserved so that:

$$4\pi R_{\rm s}^2 \Delta R \frac{a\mathcal{T}_{\rm s}'^4}{k\mathcal{T}_{\rm s}'} \simeq N \simeq 4\pi R^2 \Delta R \frac{a\mathcal{T}'^4}{k\mathcal{T}'} \Rightarrow \mathcal{T}_{\rm s}'^3 R_{\rm s}^2 = \mathcal{T}'^3 R^2 \qquad (2.3)$$

Thus, after the saturation radius (i.e. the end of the acceleration) the internal comoving temperature decreases $\mathcal{T}' \propto R^{-2/3}$ and the Lorentz factor remains constant. In this phase, energy dissipation may occur through, e.g., the development of relativistic shocks (*internal shocks*) between portion (fireballs or patches) of the outflow which underwent independent accelerations and attained different terminal velocities (Rees and Meszaros, 1992, 1994; Meszaros and Rees, 1993a).

Deceleration As the fireball expands into the circumburst medium, it collects matter and decelerates. The kinetic energy is transformed into random internal energy and partially radiated through the development of what is typically referred to as the *external shock*. Thus, the motion is characterized by a decreasing Lorentz factor with time.

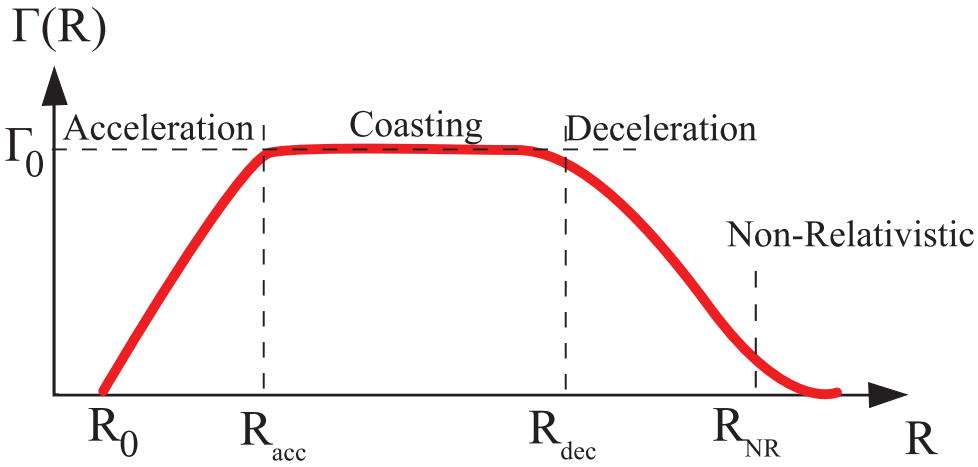

Figure 2.1: Schematic representation of the bulk Lorentz factor $\Gamma(R)$ evolution.

Blandford and McKee (1976) derived this relation analytically in the adiabatic regime (i.e. assuming that the fraction of energy dissipated as radiation is negligible): $\Gamma(t) \propto E_{\rm kin}^{1/8} n^{-1/8} t^{-3/8}$, where $E_{\rm kin}$ is the kinetic isotropic equivalent energy and n is the circumburst medium density (usually assumed constant). However, the ISM density profile can vary with the distance from the source. Typically it is described as $n(r) = n_0 r^{-\alpha}$ ($\alpha \gtrsim 0$) where n_0 represents the particle density at some characteristic radius r_0 close to the GRB progenitor (Panaitescu and Kumar, 2000; Chevalier and Li, 1999). Threfore, the general equation describing the bulk Lorentz factor decrease with distance r from the central engine is (Blandford and McKee, 1976; Nava et al., 2013):

$$\Gamma(r) = \left[\frac{E_{\rm kin}(17-4\alpha)}{16\pi n_0 m_{\rm p} c^2}\right]^{1/2} r^{-(3-\alpha)/2} \tag{2.4}$$

A general treatment of the fireball dynamics which considers both the fully adiabatic and radiative regime (as extreme cases) and the intermediate cases and smoothly joins the transition from the coasting phase to the deceleration one has been presented in Nava et al. (2013).

During the interaction between the fireball and the medium, two different shock waves are generated: a reverse shock propagating into the fireball (Uhm and Beloborodov, 2007; Genet et al., 2007), and a forward shock propagating through the ISM (Blandford and McKee, 1976). Usually, the deceleration radius ($R_{\rm dec}$) is defined as

the radius where the reverse shock crosses the fireball shell. For a standard fireball this corresponds to the instant when the total ISM collected mass is a factor $1/\Gamma$ of the initial fireball mass, i.e. $M_{\rm ISM} = (4/3)\pi R_{\rm dec}^3 n m_{\rm p} = M_0/\Gamma$. If we also consider the density variation with the radius the expression of the deceleration radius is:

$$R_{\rm dec} = \left(\frac{(3-\alpha)E_{\rm kin}}{4\pi n_0 \Gamma^2 m_{\rm p} c^2}\right)^{1/(3-\alpha)} \tag{2.5}$$

that corresponds to $R_{\rm dec} \simeq 10^{16}$ cm for standard parameters.

2.3 Photospheric emission

As the fireball shell expands, the photon number density and the typical photon energy drop. At a certain radius, the fireball becomes optically thin and, although much of the initial energy is converted to the kinetic energy of the shell, some energy will be radiated away as BB emission. This is the first electromagnetic emission that a single fireball can produce. In this case the peak energy of the spectrum and the observed BB temperature are linked by the relation $E_{\rm peak} = 3.93k\mathcal{T}$ (e.g. Zhang et al., 2012a). This emission, however, is characterized by a BB spectrum unless some dissipation process, occurring below the photosphere, modifies the spectral energy distribution of the trapped–in photons (e.g. Pe'er, 2008; Beloborodov, 2010).

The comoving frame (isotropic equivalent) luminosity of the photons trapped in the fireball is $L' = 4\pi R^2 \sigma \mathcal{T}'^4$, where $\mathcal{T}'$ is the comoving temperature of these photons. Adopting approximate transformations from the comoving to the rest frame, i.e. $L = 4/3\Gamma^2 L'$ and $\mathcal{T} = 5/3\Gamma\mathcal{T}'$ (Ghirlanda et al., 2012b), we can estimate the ratio between the fireball radius and its bulk Lorentz factor at the transparency:

$$\frac{R_T}{\Gamma_T} = 2.406 \frac{d_L(z)}{(1+z)^2}\left(\frac{F_{BB}}{\sigma \mathcal{T}_{\rm obs}}\right)^{1/2} \tag{2.6}$$

where F_{BB} and $\mathcal{T}_{\rm obs}$ are the flux and the observer–frame temperature of the BB spectrum and z is the source redshift.

The transparency can be reached:

(i) during the *acceleration phase* i.e. when the fireball is still accelerating with a bulk Lorentz factor $\Gamma \propto R$ ($\mathcal{T}' \propto R^{-1}$). Eq.2.6 allows

us to derive R_0/Γ_0 and, assuming that the fireball is created at R_0 with $\Gamma_0 = 1$, this gives the radius at the base of the jet where the fireball is created. In this case, the rest–frame temperature $\mathcal{T}$ ($= \mathcal{T}_{\rm obs}(1+z)$) is the same of the "fossil" photons, i.e. those that were injected at R_0;

(ii) during the *coasting phase*, i.e. when most of the internal energy has been converted to bulk motion and the fireball, because of the end of the acceleration, has a constant Lorentz factor, the transparency radius, is given by the following equation (valid for geometrically thin shells – Daigne and Mochkovitch 2002):

$$R_T = \frac{L_0 \sigma_T}{8\pi m_{\rm p} c^3 \Gamma^3} \tag{2.7}$$

where σ_T is the Thomson cross–section and L_0 represents the initial total luminosity injected by the central engine in the fireball at R_0. Only a fraction $L = \eta L_0$ with $\eta < 1$ is released as radiation at the transparency. The value $\eta \sim 20\%$ (derived from the modeling of GRB afterglows) is typically assumed. Combining Eq.2.6 and Eq.2.7 we can separately obtain the transparency radius R_T and the corresponding bulk Lorentz factor Γ_T (see Ghirlanda et al. 2013b for details):

$$R_T = 1.624 \left(\frac{\sigma_T}{m_{\rm p} c^3 \eta}\right)^{1/4} \frac{d_L^{5/4}(z)}{(1+z)^{3/2}} \frac{F_{BB}^{5/8}}{(\sigma \mathcal{T}_{\rm obs}^4)^{3/8}} \tag{2.8}$$

$$\Gamma_T = 0.675 \left(\frac{\sigma_T}{m_{\rm p} c^3 \eta}\right)^{1/4} \left[d_L(z)(1+z)^2\right]^{1/4} (F_{BB} \sigma \mathcal{T}_{\rm obs}^4)^{1/8} \tag{2.9}$$

recalling the expression for the energy density of the fossil BB photons (those ones injected at R_0), i.e. $a\mathcal{T}_0'^4 = L_0/4\pi c R_0^2$, and adopting the scaling relations valid for the acceleration ($\Gamma \propto R$, $\mathcal{T}' \propto R^{-1}$) and coasting phase ($\Gamma = const$, $\mathcal{T}' \propto R^{-2/3}$), it is possible to derive the radius R_0 where the fireball is created if the transparency is reached during the coasting phase:

$$R_0 = 12.5 \eta^{3/2} \frac{d_L(z)}{(1+z)^2} \left(\frac{F_B B}{\sigma \mathcal{T}_{\rm obs}^4}\right)^{1/2} \tag{2.10}$$

Therefore, the detection of a BB spectrum in GRB emission is of fundamental importance because through the measurement of the

BB temperature $k\mathcal{T}_{\rm obs}$ and flux F_{BB} allow us to estimate some fundamental parameters of the fireball. I applied all these arguments during the study of the pure thermal burst GRB 100507 (Ghirlanda et al., 2013b) and during my PhD to the case of GRB 151027A (Nappo et al., 2017, see Sec.10.1) with evidence of a thermal black body component.

2.4 Internal shocks

What has been described in the previous section is the theoretical dynamical evolution of a single fireball. Most likely, the inner engine is able to produce a sequence of fireballs, ejected intermittently, each one with a different initial energy and/or baryon loading and evolving independently. The fireballs, characterized by different bulk Lorentz factors, can collide and generate the so–called *internal shocks* (Rees and Meszaros, 1994). A fraction of the colliding fireballs' kinetic energy is given to electrons and positrons through their acceleration at e.g. relativistic shocks. Also a fraction of the kinetic energy can amplify the magnetic field. Given this configuration, the presence of relativistic electrons and of an intense magnetic field allows the dissipation of the energy through synchrotron radiation (see Sec.2.6).

Consider, for the sake of simplicity, two fireballs of mass m_2 and m_1 and comparable thickness ΔR, moving with Lorentz factors $\Gamma_2 > \Gamma_1 \gg 1$, respectively. Assuming that the two shells are separated by a distance comparable to their thickness, the collision time is (see Lazzati et al., 1999):

$$t_{\rm c} = 2\frac{\Delta R}{c}\frac{\alpha_\Gamma^2}{\alpha_\Gamma^2 - 1}\Gamma_1^2 \tag{2.11}$$

where $\alpha_\Gamma = \Gamma_2/\Gamma_1$. Then, the collision radius is $R_{\rm c} = \beta_2 c t_{\rm c}$. Following Lazzati et al. (1999) let's assume anelastic collision, so that the faster shell (m_2,Γ_2), catching up the slower one (m_1,Γ_1), forms the merged shell system ($M = m_1 + m_2 + \epsilon/c^2$,$\Gamma_{\rm m}$). Here ϵ represents the internal (random) energy of the merged shells. The dynamic of the collision is regulated by the energy–momentum conservation:

$$\begin{cases} \Gamma_1 m_1 + \Gamma_2 m_2 = \Gamma_{\rm m} M \\ \Gamma_1 m_1 \beta_1 + \Gamma_2 m_2 \beta_2 = \Gamma_{\rm m} M \beta_m \end{cases} \tag{2.12}$$

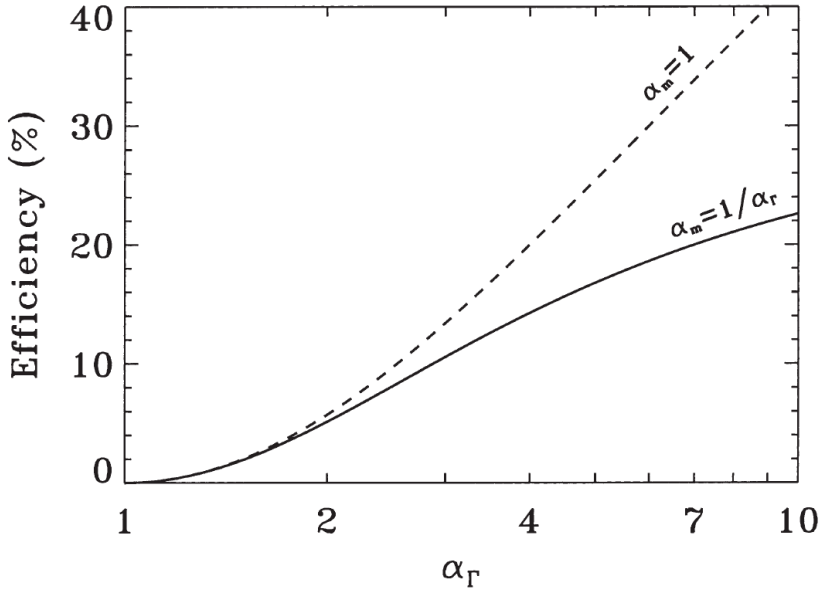

Figure 2.2: Internal shock efficiency as a function of the ratio of Lorentz factor α_Γ. Solid line represents the solution for shells of equal energy ($\Gamma_1 m_1 c^2 = \Gamma_2 m_2 c^2$), while dashed line represents the case of maximum efficiency with shells of equal mass (Figure from Lazzati et al., 1999).

The final bulk Lorentz factor of the merged shells is (Daigne and Mochkovitch, 1998):

$$\Gamma_{\rm m} = \sqrt{\frac{\Gamma_1 m_1 + \Gamma_2 m_2}{\frac{m_1}{\Gamma_1} + \frac{m_2}{\Gamma_2}}} \tag{2.13}$$

A useful asymptotic limit adopted when deriving the last equation is $\sqrt{1 - 1/\Gamma^2} \simeq 1 - 1/2\Gamma^2$. Moreover, assuming that all of the internal energy ϵ is converted into radiation, we obtain, independently of the emission mechanism, an upper limit for the radiative efficiency defined as $\eta = \frac{\Gamma_m \frac{\epsilon}{c^2}}{\Gamma_1 m_1 + \Gamma_2 m_2}$.

$$\eta = 1 - \frac{\Gamma_m (1 + \alpha_m)}{\Gamma_1 (1 + \alpha_\Gamma \alpha_m)} \tag{2.14}$$

where $\alpha_m = m_2/m_1$.

In the further approximation of shells of equal initial mass ($m_1 = m_2 = m$) Eq.2.13 and Eq.2.14 reduce to:

$$\Gamma_{\rm m} = \sqrt{\Gamma_1 \Gamma_2} \tag{2.15}$$

and

$$\eta = 1 - \frac{2\sqrt{\alpha_\Gamma}}{1 + \alpha_\Gamma} \tag{2.16}$$

In this case, the efficiency depends on the relative speed of the colliding shells (as shown in Fig.2.2). Suppose also that the width of the merged shell does not increase substantially during the merger and that a single pulse of radiation is produced during one merger. An observer located along the direction of the shells' motion will see a pulse whose duration is given by two contributions (e.g. Sari and Piran, 1997; Kocevski et al., 2007):

(i) the *curvature* timescale $t_{\rm curv}$ due to the different travel paths of photons emitted simultaneously by the spherical surface

$$t_{\rm curv} = \frac{R_{\rm c}}{2c\Gamma_{\rm m}^2} \tag{2.17}$$

Here, a spherical shell with an angular scale larger than $\Gamma_{\rm m}^{-1}$ has been assumed;

(ii) the *merging* timescale $t_{\rm merge}$, i.e. the difference of arrival times of photons, emitted along the line of sight, during the time necessary for the two shell to cross one another (also accounting for the relativistic Doppler effect);

$$t_{\rm merge} = \frac{\Delta R}{c}\frac{\alpha_\Gamma}{\alpha_\Gamma^2 - 1} \tag{2.18}$$

For small α_Γ this timescale is of the order of $\Delta R/c$.

Therefore, the duration in the rest frame of the source is $\Delta t = t_{\rm curv} + t_{\rm merge}$. Within the standard model, fireballs are commonly assumed to be ultra relativistic thin shells with $\alpha_\Gamma \gtrsim 2$ (e.g. Rees and Meszaros, 1994) so that $R_{\rm c} \gg \Delta R$. As a consequence the main contribution to the pulse duration is due to the curvature effect.

The typical case has $\alpha_\Gamma \sim 2(5)$, corresponding to a very low efficiency $\eta \sim 5\%(20\%)$. Thus, IS allows to dissipate only a small fraction of the total kinetic energy acquired during the acceleration phase. Most of the kinetic energy is conserved into the merged shell and will be eventually dissipated through the interaction with the interstellar medium. More sophysticated estimates (e.g. Kobayashi et al., 1997; Kumar, 1999; Maxham and Zhang, 2009) of the radiative efficiency of internal shocks (also considering the fraction of the bolometric energy dissipated within the observer frame band of a given detector) produced by shells with possible different bulk Lorentz factors' distributions, agree on a typically small radiative efficiency (but see Beloborodov, 2000).

2.5 External shocks

As the fireball interacts with the Inter Stellar Medium (ISM) it starts to decelerate and a strong forward shock also forms and propagates through the ISM. These are the so–called *external shocks* (ES) which similarly to IS, accelerating the electrons and amplifying the magnetic field, produce, via synchrotron, the GRB afterglow emission.

According to Ghisellini et al. (2010a) the behavior of the afterglow bolometric luminosity, assuming the fast–cooling regime (independently of the emission mechanism), is:

$$L_{\rm iso} \propto t^2 \Gamma^8 n \tag{2.19}$$

Therefore, dynamic strongly depends on the density profile n of the ISM and it may change from one collision to another one. For a homogeneous medium ($n = const$), during the deceleration phase ($t > t_{\rm dec}$), $\Gamma \propto t^{-3/8}$ so that $L_{\rm iso} \propto t^2\Gamma^8 \propto t^2 t^{-3} \propto t^{-1}$. The flux decreases with time in agreement with the observed afterglow light–curves. In the case of wind profile ISM ($n \propto R^{-2}$) Eq.2.4 gives $\Gamma \propto R^{-1/2}$ and since $R = 2\Gamma^2 ct$, Eq.2.19 results in the same scaling $L_{\rm iso} \propto t^{-1}$.

However, within the ES model, there is also the possibility to produce pulses when, for instance, the expanding relativistic fireball collides with extended over–density regions (e.g. Dermer and Böttcher, 2000), at rest with respect to the central engine. The exact effects of these regions on the fireball dynamics have been studied recently by Nava et al. (2013) and specifically considered for their emissivity in specific bursts (e.g. Lazzati et al., 2002). The main difference with respect to the IS case is that the shell now collides with targets (the clumps) at rest so that the dissipation is by far more efficient. Assume that such CBM clumps (having a shell–like structure) have width ΔL and are distributed at increasing distances from the central engine. We consider that such over–densities are superimposed to a generic density profile $n = n_0 R^{-\alpha}$ ($\alpha \gtrsim 0$ – Panaitescu and Kumar 2000; Chevalier and Li 1999). If the clumps are extended enough (with dimension similar or grater than the jet aperture), the duration of the pulses will be dominated by the curvature term (see Eq.2.17), scaling with the collision radius which increases linearly with time. Even considering the dynamic effect of deceleration (Eq.2.4), the leading term in the pulse duration is due to the curvature effect (if the dissipation radius is larger than ΔL).

Computing the radius R of fireball at a time t, we derive the expression of the pulse duration:

$$\Delta t \simeq \frac{R}{2c\Gamma(R)^2} \simeq (4-\alpha)t \tag{2.20}$$

Therefore, considering the ES scenario of a shell decelerated by the CBM where pulses are due to over–densities encountered along its path, the pulse width Δt should increase linearly with time. The application of these arguments to real data will be the subject of a specific chapter (Chp.9) where most of the content of a recently submitted paper will be presented.

2.6 Synchrotron emission

The synchrotron is thought to be the principal radiation mechanism originating the GRBs emission (Rees and Meszaros, 1994; Katz, 1994; Tavani, 1996; Sari et al., 1998; Paczynski and Rhoads, 1993). Such radiation is expected to be produced by energized electrons accelerated to ultrarelativistic speed into strong magnetic fields. In this section I will outline a simplified description of this radiative process (Rybicki and Lightman, 1986; Ghisellini, 2013).

2.6.1 Single particle emission

The power emitted by an electron of mass m and charge e moving at speed $\vec{v}$ in a magnetic field $\vec{B}$ can be expressed generalizing the Larmor formula:

$$P = P' = \frac{2e^2}{3c^3}\left[a'^2_{\parallel} + a'^2_{\perp}\right] = \frac{2e^2}{3c^3}\gamma^4\left[\gamma^2 a^2_{\parallel} + a^2_{\perp}\right] \tag{2.21}$$

where e is the electron charge, $\gamma = 1/\sqrt{1-\beta^2}$ is the electron Lorentz factor ($\beta = v/c$) and the (not) primate quantities refer to the (observer) comoving frame. The emitted power is Lorentz invariant so we can take the advantage to work in the comoving frame. On the contrary the received power is not the same in the two frames and we must account for the relativistic transformations.

The Lorentz force acting on it is:

$$\vec{F}_{\rm L} = \frac{d}{dt}(\gamma m\vec{v}) = \frac{e}{c}\vec{v}\times\vec{B} \tag{2.22}$$

Solving the equation of motion (Rybicki and Lightman, 1986) it is possible to obtain the acceleration components $a_{\parallel}$ and $a_{\perp}$ which substituted in Eq.2.21 give:

$$P(\theta) = 2\sigma_{\rm T} c U_{\rm B} \gamma^2 \beta^2 \sin^2\theta \tag{2.23}$$

where $\sigma_{\rm T} = 8\pi r_0^2/3 = 6.65 \times 10^{-25}$ cm^2 ($r_0 = e^2/mc^2$ is the classical electron radius) is the Thomson cross section, $U_{\rm B} \equiv B^2/8\pi$ is the magnetic field density, and θ is the so–called "pitch angle", i.e. the angle between $\vec{v}$ and $\vec{B}$.

Assuming an isotropic distribution of pitch angles , i.e. a random motion of the particles, we can average the term $sin^2(\theta)$ over the solid angle obtaining:

$$\langle P \rangle = \frac{4}{3}\sigma_{\rm T} c U_{\rm B} \gamma^2 \beta^2 \tag{2.24}$$

The fundamental frequency associated to this emission the the inverse of the time occurring to complete one orbit:

$$\nu_{\rm B} = \frac{c\beta \sin\theta}{2\pi r_{\rm L}} = \frac{eB}{2\pi\gamma mc} = \frac{\nu_{\rm L}}{\gamma} \tag{2.25}$$

where $\nu_{\rm L}$ is the Larmor frequency, namely the gyration frequency for sub–relativistic particles and the orbit radius, i.e. the Larmor radius $r_{\rm L}$ con be easily derived by setting $a_{\perp} = v_{\perp}^2/r_{\rm L}$.

2.6.2 Single particle spectrum

There exists a typical frequency associated to the synchrotron process. If the electron is relativistic, this frequency results the inverse of the fraction of revolution period during which the observer receives the radiation. This is not the inverse of the whole revolution period (as the ciclotron case) because the radiation is strongly collimated in the direction of the electron motion within a cone of semiaperture $1/\gamma$ ($\gamma \gg 1$). At each orbit the observer receives the radiation only for a small time interval. According to Rybicki and Lightman (1986) this typical frequency is:

$$\nu_{\rm s} = \gamma^2 \frac{eB}{2\pi mc} = \gamma^3 \nu_{\rm B} = \gamma^2 \nu_{\rm L} \tag{2.26}$$

We expect that the particle emits most of its power at this frequency. The power per unit frequency (integrated over the emission pattern)

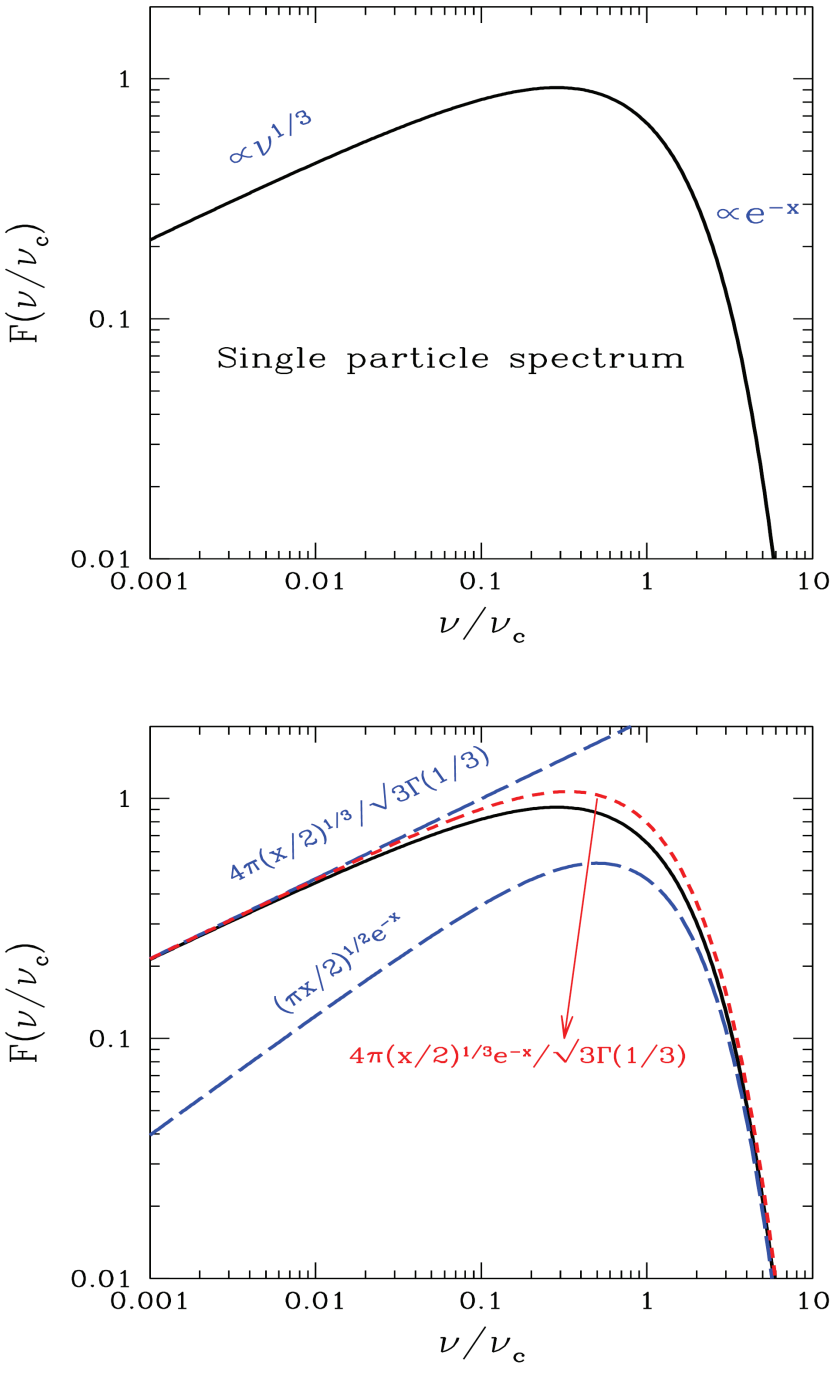

Figure 2.3: *Upper panel*: function $F(\nu/\nu_c)$ describing the single particle synchrotron spectrum. *Lower panel*: comparison between $F(\nu/\nu_c)$ and approximating formulae indicated in the text. $x \equiv \nu/\nu_c$. Figure from Ghisellini (2013).

emitted by an electron of given Lorentz factor γ and "pitch angle" θ is:

$$P_s(\nu,\gamma,\theta) = \frac{\sqrt{3}e^3 B\sin\theta}{mc^2}F(\nu/\nu_c) \tag{2.27}$$

$$F(\nu/\nu_c) \equiv \frac{\nu}{\nu_c}\int_{\nu/\nu_c}^{\infty} K_{5/3}(y)\,dy$$

$$\nu_c \equiv \frac{3}{2}\nu_s \sin\theta$$

where $K_{5/3}(y)$ is the modified Bessel function of order $5/3$. The single particle spectrum thus depends upon frequency through the function $F(\nu/\nu_c)$ (see Fig.2.3). This function peaks at $\nu \simeq 0.29\nu_c$. At low frequencies it is well approximated by a power–law with slope $1/3$

$$F(\nu/\nu_c) \longrightarrow \frac{4\pi}{\sqrt{3}\Gamma(1/3)}\left(\frac{\nu}{2\nu_c}\right)^{1/3} \qquad (\nu \ll \nu_c)$$

while at high frequencies ($\nu \gg \nu_c$) it exponentially decays and can be approximated by

$$F(\nu/\nu_c) \longrightarrow \left(\frac{\pi}{2}\right)^{1/2}\left(\frac{\nu}{\nu_c}\right)^{1/2} e^{-\nu/\nu_c} \qquad (\nu \gg \nu_c)$$

An useful formula well approximating the spectrum at all frequencies (but overestimating it a little around the peak) is:

$$F(\nu/\nu_c) \sim \frac{4\pi}{\sqrt{3}\Gamma(1/3)}\left(\frac{\nu}{2\nu_c}\right)^{1/3} \exp^{-\nu/\nu_c}$$

All these arguments hold under the hypothesis that the energy emitted by the single electron is sufficiently smaller than its total energy so that the electron trajectory is not sensibly modified. Therefore, we must have

$$P_s\frac{2\pi r_L}{\beta c} < \gamma mc^2 \Longrightarrow B < \frac{2e}{\gamma^2 \sin\theta^3 \sigma_T}$$

2.6.3 Emission from a distribution of electrons

In the previous sub–sections we defined the properties of the single particle emission. now we are interested in the emission coming from more particles. Let $N(\gamma)$ be the function describing the Lorentz

γ function distribution of the electrons population responsible of the synchrotron emission. This is typically assumed to be a power–law distribution like

$$N(\gamma) = K\gamma^{-p} = N(E)\frac{dE}{d\gamma} \qquad \gamma_{\min} < \gamma < \gamma_{\max} \tag{2.28}$$

In order to obtain the specific emissivity (i.e. the power emitted per unit solid angle and frequency produced within 1 cm^3 of source) of this distribution of particles, assuming that the distribution of pitch angles is the same for at every γ, we have to integrate Eq.2.27 (related to the single electron) along with $N(\gamma)$

$$\begin{aligned} \epsilon_{\rm s}(\nu,\theta) &= \frac{1}{4\pi}\int_{\gamma_{\min}}^{\gamma_{\max}} N(\gamma)P_{\rm s}(\gamma,\nu,\theta)\,d\gamma \\ &\propto KB^{(p+1)/2}\nu^{-(p-1)/2} \end{aligned} \tag{2.29}$$

A Lorentz factor power–law distribution implies a power–law spectrum and the slopes of this two functions are correlated. Writing $\epsilon_{\rm s} \propto \nu^{-\alpha}$ we have $\alpha = (p-1)/2$.

The synchrotron flux received from a homogeneus and optically thin source of volume $V \propto R^3$ at a luminosity distance d_L is:

$$\begin{aligned} F_{\rm s}(\nu) &= 4\pi\epsilon_{\rm s}(\nu)\frac{V}{4\pi d_{\rm L}^2} \\ &\propto \frac{R^3}{d_{\rm L}^2}KB^{1+\alpha}\nu^{-\alpha} \\ &\propto \theta_{\rm s}^2 RKB^{1+\alpha}\nu^{-\alpha} \end{aligned} \tag{2.30}$$

where θ_s is the angular dimension of the source. Observing the source at two different frequencies allows to determine α and, consequently, the slope p characterizing the particle distribution. Moreover, if R and the distance are known, the normalization only depends on the particle density K and on the magnetic field intensity B. Thus, we need a further relation (provided by the self–absorbed flux) to close the system and find the two unknowns K and B.

Synchrotron self–absorption

All emission processes have their absorption counterpart. in the case of a non–thermal particles distribution (i.e. power–law like) we need, in principle, to calculate the Einstein coefficients linking the

spontaneous and stimulated emission and "true" absorption. However, an alternative way exists.

We can think to our power law energy distribution as a superposition of Maxwellians at different temperatures. In this way, the electron energy γmc^2 and the typical energy $k\mathcal{T}$ of the Maxwellian are related. Assuming that a particular frequency ν is preferentially absorbed by those electrons that can emit it, we have:

$$k\mathcal{T} \sim \gamma mc^2 \sim mc^2 \left(\frac{\nu}{\nu_L}\right)^{1/2}$$

Taking advantage of the definition of the brightness temperature $\mathcal{T}_\mathrm{b}$ of a source we can write the intensity as

$$I(\nu) \equiv 2k\mathcal{T}\frac{\nu^2}{c^2} \sim 2m\nu^2 \left(\frac{\nu}{\nu_L}\right)^{1/2} \propto \frac{\nu^{5/2}}{B^{1/2}} \tag{2.31}$$

Note that the spectrum is $\propto \nu^{5/2}$, not ν^2, as a consequence of having different (fake) temperatures. Moreover, the result does not more depend on the electrons density: greater the number of particles grater the emission and also greater the absorption. Even the slope p is no more important.

The above is valid as long as we can associate a specific γ to any ν. If we can not do this we can not associate different temperatures to different frequencies. In this case we recover the self–absorbed intensity $I(\nu) \propto \nu^2$ (i.e. Raleigh–Jeans like).

The expression of the flux is simply obtained integrating the intensity over the angular dimension of the source, obtaining:

$$F(\nu) \propto \theta_\mathrm{s}^2 \frac{\nu^{5/2}}{B^{1/2}} \tag{2.32}$$

The observation of a self–absorbed source of known angular size should allow us to derive its magnetic field even without knowing its distance

Ghisellini and Svensson (1991) computed the synchrotron self–absorption cross section:

$$\sigma_\mathrm{s}(\nu,\gamma) = \frac{3\pi}{\sqrt{10}}\frac{\sigma_\mathrm{T} B_\mathrm{c} x}{\alpha_\mathrm{F} B\gamma^5}\left[K_{4/3}^2\left(\frac{x}{2}\right) - K_{1/3}^2\left(\frac{x}{2}\right)\right] \tag{2.33}$$

where $\alpha_\mathrm{F} = 1/137$ is the fine structure constant, $B_\mathrm{c} = \alpha_\mathrm{F}(mc^2/r_0^3)^{1/2}$ $\approx 4.4 \times 10^{13}\,\mathrm{G}$ is the critical magnetic field (for $B \gtrsim B_\mathrm{c}$ the quan-

tum effects become important). The optical depth $\tau_s(\nu)$ for synchrotron self–absorption is obtained integrating the cross section $\sigma_s(\nu, \gamma)$ with the particle density distribution $N(\gamma)$ over $d\gamma$ and multiplying it for the thickness ΔR of the emitting region. The self–absorption frequency ν_a is obtained for $\tau_s(\nu) = 1$.

2.7 Inverse Compton emission

When a relativistic electron has an energy greater than the typical one associated to the photons in which is moving, it is possible to have a transfer of energy from the electron to the photons. This process is called Inverse Compton scattering to distinguish it from the direct Compton scattering, in which the electron is at rest, and it is the photon to give part of its energy to the electron.. It is not a proper emission but rather the re–processing of the kinetic energy of the electron into radiation. For this reason the resulting emission will also depend on the characteristic of the pre–existent radiation.

If the energy of the incoming photon ($h\nu$, measured in the frame K' comoving with the electron) is lower than the rest energy of the electron ($h\nu \ll mc^2 \approx 511$ keV) we are in the Thomson regime in which the cross section is the Thomson one σ_T and the recoil of the electron can be neglected. In the opposite case ($h\nu > mc^2$) we are in the Klein–Nishina regime in which the cross section rapidly decreases as the frequency of the photon increases.

2.7.1 Single particle emission

in the frame K' comoving with the electron the energy of the incoming photon is:

$$x' = x\gamma(1 - \beta \cos\psi) \tag{2.34}$$

where ψ (Fig.2.4) is the angle between the electron and photon directions of motion. If $x' \ll 1$ we are in the Thomson regime. In the rest frame K the photon energy after the scattering x'_1 will be the same it had before the scattering:

$$x'_1 = x$$

ψ'_1 is the angle of the outgoing photon (Fig.2.4). The scattering in the comoving frame K' is a re–isotropization process: even if the incoming photons are all coming from the same direction, after the scattering they are distributed quasi–isotropically.

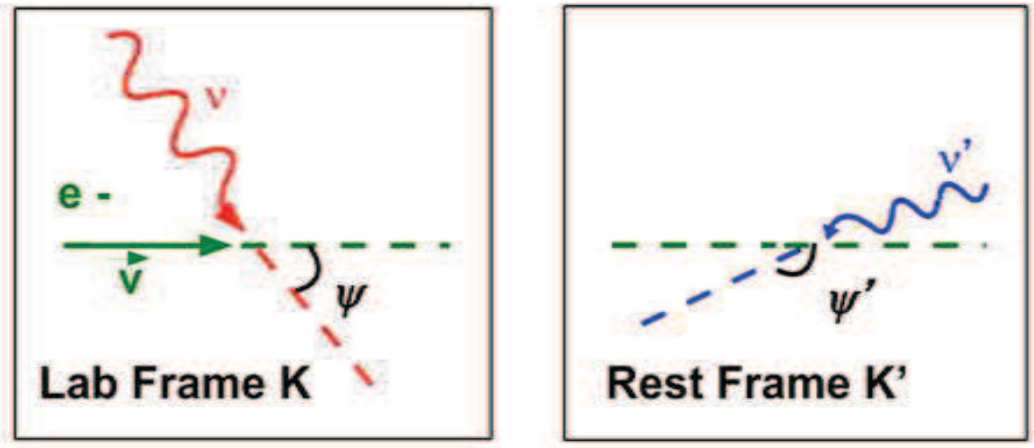

Figure 2.4: In the rest frame K the electron has velocity $\vec{v}$. This forms an angle ψ with the incoming photon of frequency ν. In the comoving frame K' the photon has a frequency ν' and forms an angle ψ' with the direction of motion of the electron.

In the rest frame K the observer will see an energy:

$$x_1 = x\frac{1-\beta\cos\psi}{1-\beta\cos\psi_1}$$

We have the maximum for the energy when $\psi = \pi$ (head–on collision) and $\psi_1 = 0$ (the photon is scattered along the electron direction of motion). In this case:

$$x_1 = x\frac{1+\beta}{1-\beta} \approx 4\gamma^2 x$$

The minimum is for $\psi = 0$ (tail-on collision) and $\psi_1 = \pi$. In this case:

$$x_1 = x\frac{1-\beta}{1+\beta} \approx \frac{x}{4\gamma^2}$$

For an isotropic distribution of photons and assuming $\gamma \gg 1$ the average energy after the scattering is:

$$\langle x_1 \rangle = \frac{4}{3}\gamma^2 x \tag{2.35}$$

If we assume an energy density $U_{\rm rad}$ associated to the radiation, the power emitted through the IC scattering is (Rybicki and Lightman, 1986):

$$\langle P \rangle = \frac{4}{3}\sigma_{\rm T} c U_{\rm rad}\gamma^2\beta^2 \tag{2.36}$$

that is identical to Eq.2.24 obtained for the synchrotron emission.Such relation can be expresse in a more intuitive way multiplying and dividing for the average energy of photons after the scattering $\langle h\nu \rangle$:

$$\langle P \rangle = \left(\frac{\#\text{collisions}}{s} \right) (\text{average energy}) = \left(\sigma_{\text{T}} c \frac{U_{\text{rad}}}{\langle h\nu \rangle} \right) \left(\frac{4}{3} \langle h\nu \rangle \gamma^2 \right) \tag{2.37}$$

2.7.2 Single particle spectrum

Let's assume that the incoming radiation (in the comoving frame K') is monochromatic with intensity I. The exact derivation of the spectrum made in Rybicki and Lightman (1986) and in Blumenthal and Gould (1970) lead to the following result:

$$\frac{I(x)}{x} = \frac{I_0}{x} \delta(x - x_0) \tag{2.38}$$

where $I(x)/x$ is the specific intensity. For n electrons per cm^3 then the emissivity is:

$$\epsilon_{\text{IC}}(x_1) = \frac{\sigma_{\text{T}} n I_0 (1+\beta)}{4\gamma^2 \beta^2 x_0} F_{\text{IC}}(x_1) \tag{2.39}$$

where the function F_{IC} (Fig.2.5) contains all the dependence on the frequency:

$$F_{\text{IC}}(x_1) = \frac{x_1}{x_0} \left[\frac{x_1}{x_0} - \frac{1}{(1+\beta)^2 \gamma^2} \right] \qquad \frac{1}{(1+\beta)^2 \gamma^2} < \frac{x_1}{x_0} < 1$$

In this range the function corresponds to the down–scattering: after the scattering the outgoing photons have less energy than the incoming ones. In this case $F_{\text{IC}}(x_1) \propto x_1^2$.

$$F_{\text{IC}}(x_1) = \frac{x_1}{x_0} \left[1 - \frac{x_1}{x_0} \frac{1}{(1+\beta)^2 \gamma^2} \right] \qquad 1 < \frac{x_1}{x_0} < (1+\beta)^2 \gamma^2$$

In this other case, instead, the function corresponds to the up–scattering: $F_{\text{IC}}(x_1) \propto x_1$.

The average frequency of the energy spectrum is $\langle x_1 \rangle = 2\gamma^2 x_0$ while $\langle x_1 \rangle = 4\gamma^2 x_0/3$ for the photon spectrum.

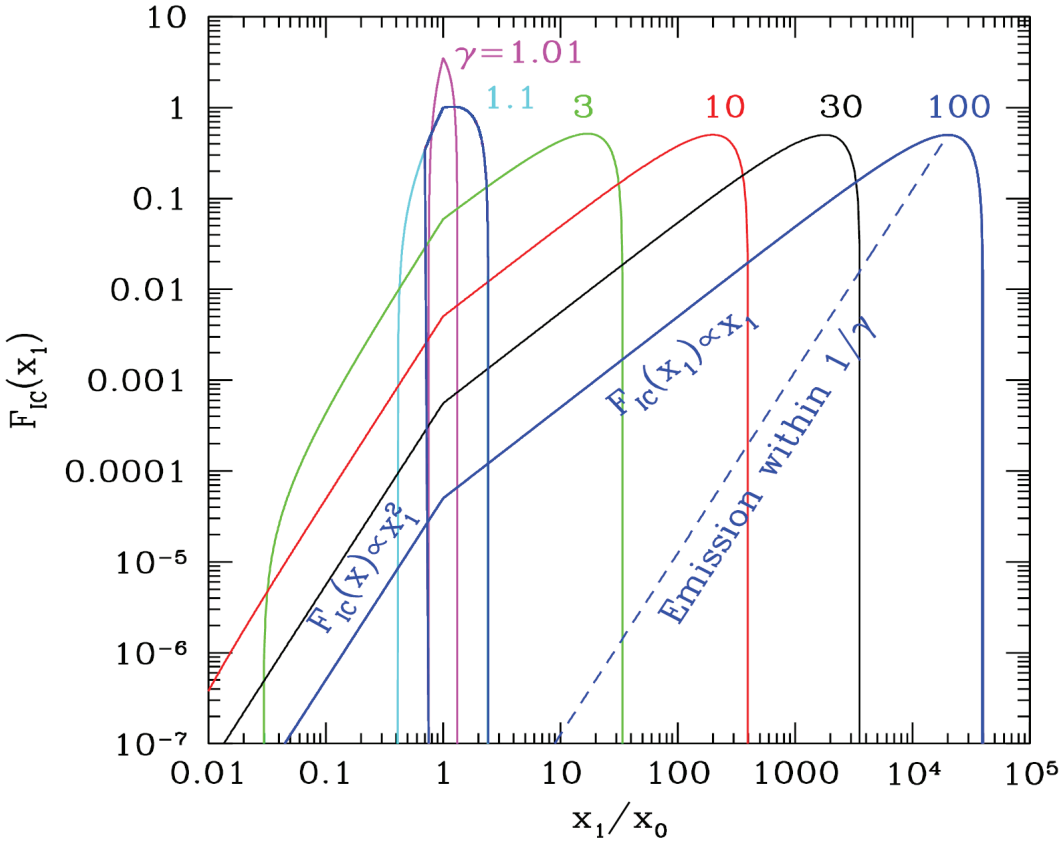

Figure 2.5: Inverse Compton spectrum emitted by electrons having different γ moving in a monochromatic radiation of frequency x_0. The dashed line corresponds to te spectrum emitted within the beaming cone $\theta \sim 1/\gamma$ (it contains the 75% of the emitted power independently from the value of γ). $x_1 < x_0$ correspond to the down–scattering regime (photons lose energy in the process). For $\gamma \gg 1$ $F_{\rm IC}(x_1) \propto x_1^2$ (down–scattering regime) and $F_{\rm IC}(x_1) \propto x_1$ (up–scattering regime). Figure from Ghisellini (2013).

2.7.3 Emission from a distribution of electrons

The single particle spectrum is peaked and the typical frequency is amplified by a factor γ^2 (as the synchrotron case). It is possible thus to derive the emissivity for the Inverse Compton scattering in the same way adopted for the synchrotron case (see previous section). Let $N(\gamma)$ be the function describing the distribution of Lorentz factor γ of the isotropic population of electrons:

$$N(\gamma) = K\gamma^{-p} = N(E)\frac{dE}{d\gamma} \qquad \gamma_{\rm min} < \gamma < \gamma_{\rm max} \tag{2.40}$$

Assuming, for the sake of simplicity, that also the photons in which electrons are moving are isotropic and monochromatic (with

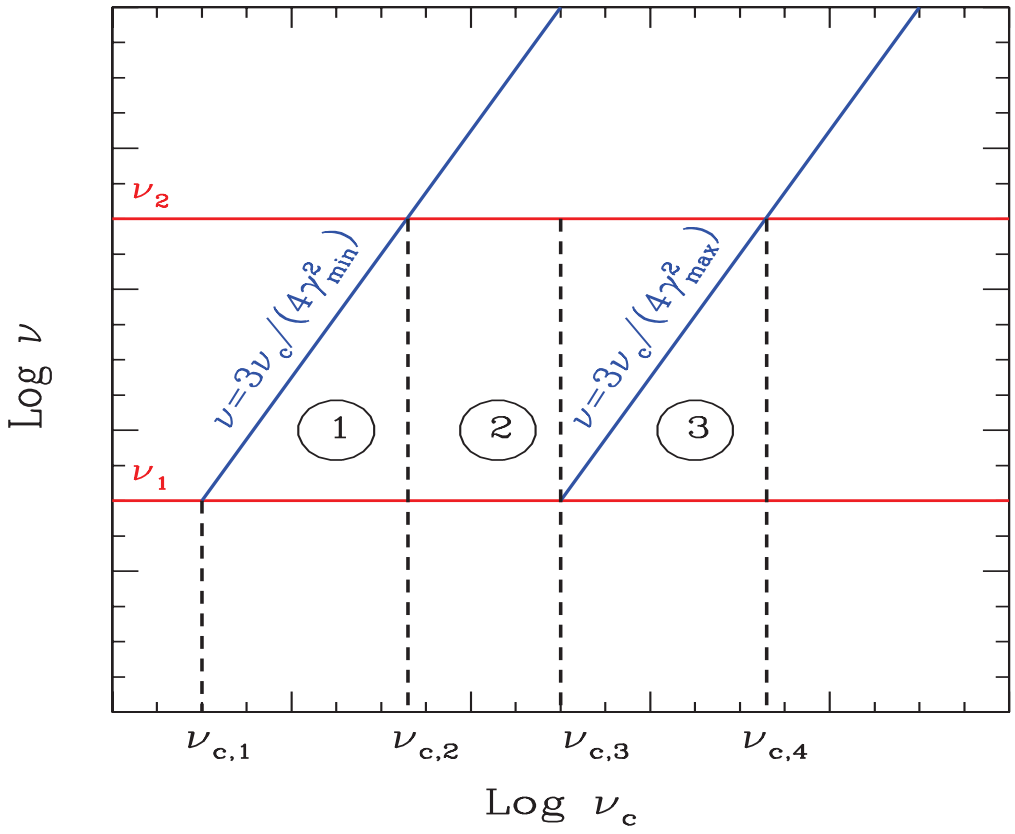

Figure 2.6: Limits of integration in Compton emission computation. Figure from Ghisellini (2013).

frequency ν_0) the emissivity can be expressed as:

$$\epsilon(\nu_c) = \frac{1}{4\pi}\frac{(4/3)^\alpha}{2}\sigma_T c K \frac{U_{rad}}{\nu_0}\left(\frac{\nu_c}{\nu_0}\right)^{-\alpha} \tag{2.41}$$

Even in this case we obtain a power–law whose slope con be related to the index p characterizing the electrons distributions through $\alpha = \frac{p-1}{2}$ (the same relation holds for the synchrotron). This is not a coincidence, in fact, this happens because both the emission processes spectra are peaked at a typical frequency that is a factor γ^2 greater than the starting one.

Consider now the more realistic case in which the seed photons are not monochromatic. We have to integrate Eq.2.41 over the frequency distribution of the seed photons.

$$\epsilon(\nu_c) = \frac{1}{4\pi}\frac{(4/3)^\alpha}{2}\sigma_T c K \nu_c^{-\alpha}\int_{\nu_{min}}^{\nu_{max}} \frac{U_{rad}(\nu)}{\nu}\nu^\alpha\, d\nu \tag{2.42}$$

where $U_{\rm rad}(\nu)$ [erg cm^{-3} Hz^{-1}] is the specific radiation energy density at the frequency ν. . Interestingly, if the electrons population producing IC emission is also producing synchrotron emission then the slopes of the two spectra are the same. More specifically, when $U_{\rm rad}(\nu)$ is made by synchrotron photons, then $U_{\rm rad}(\nu) \propto \nu^{-\alpha}$ and the result of the integral will be $\ln(\nu_{\rm max}/\nu_{\rm min})$.

The correct limits of the integration depend, in principle, on $\nu_{\rm c}$ (see Fig.2.6). Assuming that the seed photon frequency distribution extends from ν_1 to ν_2 and that $\gamma_{\rm min}$ and $\gamma_{\rm max}$ are the minimum and maximum energies of the electrons distribution, Fig.2.6 shows the right limit on $\nu_{\rm max}$ and $\nu_{\rm min}$. Following Ghisellini (2013) we define $\nu_{\rm c,1} = (4/3)\gamma^2_{\rm min}\nu_1$, $\nu_{\rm c,2} = (4/3)\gamma^2_{\rm min}\nu_2$, $\nu_{\rm c,3} = (4/3)\gamma^2_{\rm max}\nu_1$, $\nu_{\rm c,4} = (4/3)\gamma^2_{\rm max}\nu_2$. There are four possible cases:

Case (1)

$$\begin{cases} \nu_{\rm min} = \nu_1 \\ \nu_{\rm max} = 3\nu_{\rm c}/(4\gamma^2_{\rm min}) \end{cases} \quad \text{if } \nu_{\rm c,1} < \nu_{\rm c} < \min(\nu_{\rm c,2}, \nu_{\rm c,3}) \tag{2.43}$$

$$\tag{2.44}$$

Case (2)

$$\begin{cases} \nu_{\rm min} = \nu_1 \\ \nu_{\rm max} = \nu_2 \end{cases} \quad \text{if } \nu_{\rm c,2} < \nu_{\rm c} < \nu_{\rm c,3} \tag{2.45}$$

$$\tag{2.46}$$

Case (3)

$$\begin{cases} \nu_{\rm min} = 3\nu_{\rm c}/(4\gamma^2_{\rm max}) \\ \nu_{\rm max} = 3\nu_{\rm c}/(4\gamma^2_{\rm min}) \end{cases} \quad \text{if } \nu_{\rm c,3} < \nu_{\rm c} < \nu_{\rm c,2} \tag{2.47}$$

$$\tag{2.48}$$

Case (4)

$$\begin{cases} \nu_{\rm min} = 3\nu_{\rm c}/(4\gamma^2_{\rm max}) \\ \nu_{\rm max} = \nu_2 \end{cases} \quad \text{if } \max(\nu_{\rm c,2}, \nu_{\rm c,3}) < \nu_{\rm c} < \nu_{\rm c,4} \tag{2.49}$$

CHAPTER 3

The luminosity function and formation rate of GRBs

3.1 Introduction

One of the first issues about GRBs concerned the description of their population in terms of physical properties and spatial distribution. It was early realized that the knowledge of their distance scale (i.e. whether galactic or cosmological), given the observed fluxes, had very different macroscopic implications on their luminosities and energetics.

At the beginning, coarse sky localizations were obtained only for the brightest events and no counterpart was identified through which to measure the distance of the event. The Compton Gamma-Ray Observatory (*CGRO*), launched in 1991, was equipped with the Burst and Transient Experiment (BATSE) detector for GRBs. One of the most famous results of BATSE is the evidence of an isotropic sky distribution of GRBs (see Fig.3.1 – *CGRO*/BATSE team). No singificant clustering was found even considering possible flux classes (as shown by the color coding in Fig. 3.1). This result was considered,

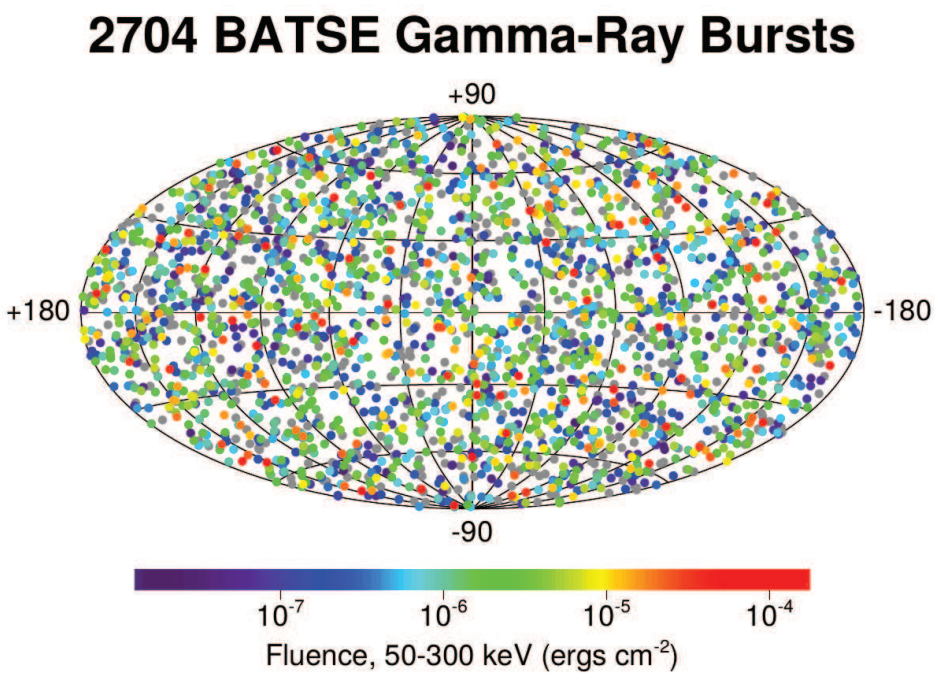

Figure 3.1: Sky distribution of 2704 BATSE GRBs (*CGRO*/BATSE team). Different colors refer to different values of fluence (see the colorbar)

in some scientific discussion, as an evidence supporting the cosmological origin of GRBs but yet the evidence was not conclusive as also a local (close by) distribution of soruces within a sphere of radius comparable to the Galactic scale height could produce such an isotropic sky distribution.

There are two classical method for studying the homogeneity of the spatial distribution of astrophysical sources.

1. The cumulative flux distribution (i.e. so–called $\log(N) - \log(F)$ distribution). The number of objects distributed within a certain radius r increases as $N(< r) \propto r^3$. Since the observed flux $F \propto r^{-2}$, the number of sources with flux >F are $N(> F) \propto F^{-3/2}$. Considering BATSE GRBs, the flux distribution (Fig.3.2) is consistent with a slope $-3/2$ at high fluxes (dashed line in Fig.3.2), as expected for sources homogeneously distributed in an Euclidean space. Howecer, at lower fluxes, the distribution appears shallower (Pendleton et al., 1996, see Fig.3.2). Note that at the beginning the $\log(N) - \log(F)$ distribution was derived considering the fluence S (flux integrated over the burst duration), but it was soon clear that the use of the fluence introduces selection effects (Fishman and Meegan, 1995). In fact the peak flux can be more directly related to the trigger criteria

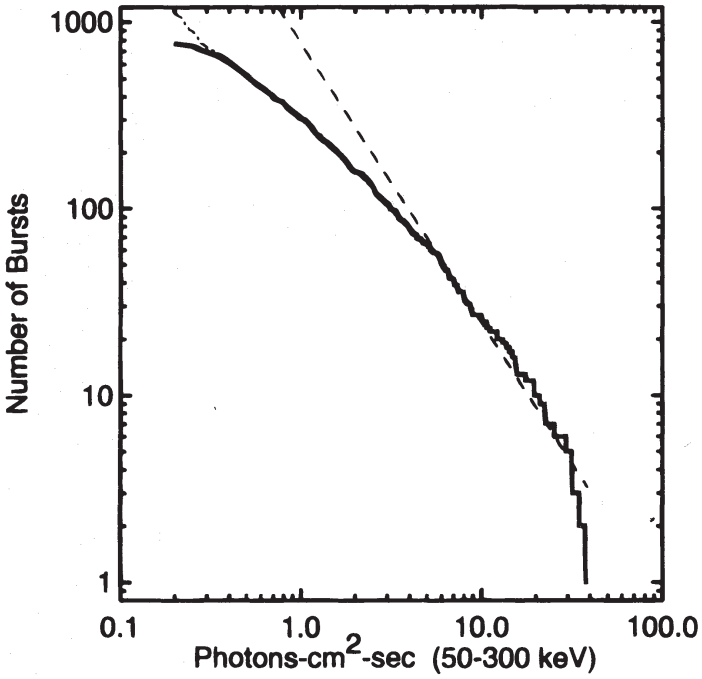

Figure 3.2: $\log(N) - \log(F)$ distribution of BATSE GRBS (Pendleton et al., 1996). The dashed line is the reference dependence $N \propto P^{-3/2}$.

typically employed by GRB detectors.

2. A second and more direct way is to find the average value of the ratio $V/V_{\max}$ (Schmidt, 1968; Schmidt et al., 1988), where V and $V_{\max}$ are the volume of space enclosed by the distance of the source and the maximum volume of space enclosed by the maximum distance at which the source could still be detected (given an instrumental flux threshold), respectively. For objects homogeneously distributed in a Euclidean space, the value of $V/V_{\max}$ should be uniformly distributed within the interval $[0,1]$ with the mean value $\langle V/V_{\max}\rangle = 1/2$. Conveniently enough, since this test directly uses the count rate threshold for each burst, it avoids errors in conversion from counts to fluxes and allows to combine samples of objects detected with different instrumetns. Paciesas et al. (1999) using 911 GRB of the revised fourth BATSE catalog found $\langle V/V_{\max}\rangle = 0.33 \pm 0.01$.

There is also another advantage in using this method. The ratio $V/V_{\max}$ computed through the count rate does not explicitly depend neither on the distance of the source, neither on the portion of the sky covered by the instrument. This fact allows to combine information coming from different instruments. If the source distance is

known the $V/V_{\rm max}$ can be computed directly.

The combined evidences of the isotropic sky distribution, of the flux distribution and of the classica $V/V_{\rm max}$ test suggest either that we are near the center of an isotropic distribution of burst sources whose space density decreases with distance or that the sources are at cosmological distances.

In order to solve this *debate* it is necessary to directly measure the source distance. With the detection of the X and optical afterglow emission (Costa et al., 1997; van Paradijs et al., 1997), the first redshift measurements were obtained and GRBs were definitively proven to be cosmological sources with large isotropic equivalent luminosities exceeding, in a few cases, 10^{54} erg/s. Recently, the pinpointing of the GRB afterglow, made available by the fast slewing of the *Swift* satellite (Gehrels et al., 2004), combined with the intense efforts to acquire early time optical spectra from the ground, allowed us to measure the redshifts z of GRBs with an average efficiency of 30%. GRBs with measured z are distributed from the local Universe up to very high redshift: GRB 090423 (with a spectroscopic $z = 8.2$ Salvaterra et al., 2009a; Tanvir et al., 2009) and GRB 090429B (with photometric redshift $z = 9.4$ Cucchiara et al., 2011) represent the furthest objects of stellar origin known to date.

The intensity distribution (typically represented in the $\log(N) - \log(F)$ distribution form) is what we observe as the combination of two fundamental intrinsic properties of the population of GRBs: (a) the cosmic formation rate $\psi(z)$ (GRB formation rate GRBFR, hereafter), representing the number of bursts per unit comoving volume and time as a function of redshift, and the luminosity function $\phi(L)$ (LF), which represents the relative fraction of bursts with a certain luminosity. Here, with $\phi(L)$ I will refer to the luminosity probability density function (PDF) defined as $dN(L)/dL/N_{\rm tot}$.

However, these intrinsic functions can not be "directly" derived from the observed luminosity and redshift distributions (see Fig.3.3). Fig.3.3 shows the luminosity and redshift cumulative distributions of short (red) and long (blue) GRBs as obtained collecting all the bursts with measured z and for which L can be derived. While the different average redshift of short and long GRBs and their different luminosity finds possible interpretations in the different progenitor nature and energy content available for the two classes, it is clear that these distributions are subject to several selection effects. For instance, the lower luminosity of short GRBs makes their detection

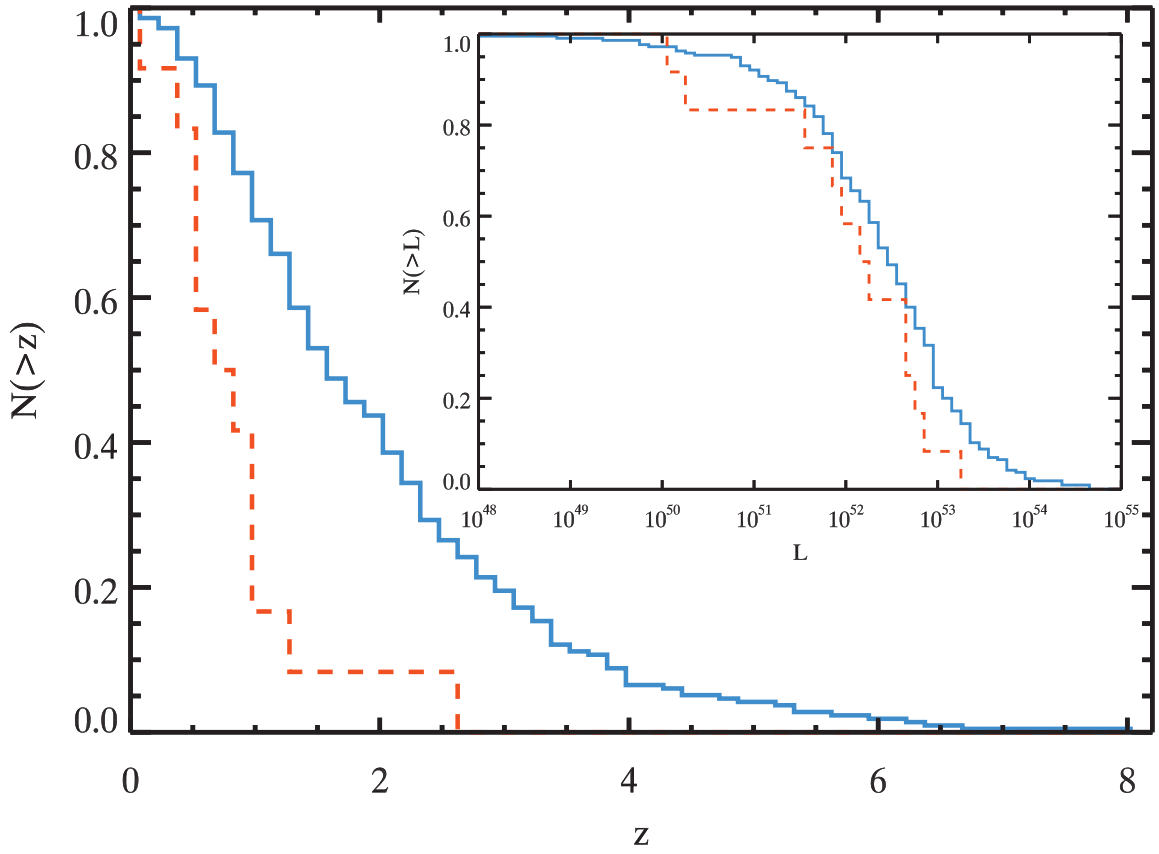

Figure 3.3: Luminosity (*insert*) and redshift distributions for long (blue solid line) and short (orange dashed line) GRBs.

strongly dependent on the instrumental sensitivity of current and past GRB detectors. Additionally, always for what concerns short bursts, the lower luminosity (with respect to long ones) makes their localization less efficient and therefore the number of measured z less uniform. For these reasons we need a method to reconstruct, starting from the observed distributions of luminosity and redshift, the intrinsic ones possibly accounting for the selection biases we can model. The final goal consists in describing the population of GRBs is to reconstruct the $\phi(L)$ and $\psi(z)$ adopting specific methods (see Chp.4).

3.2 General theoretical model

Thanks to the direct measure of the redshift it was possible to estimate the instrinc physical quantities (luminosity, total energy, true duration, ...) starting from the observables (flux, fluence, duration, ...). One of the key properties of GRBs as a cosmological popoula-

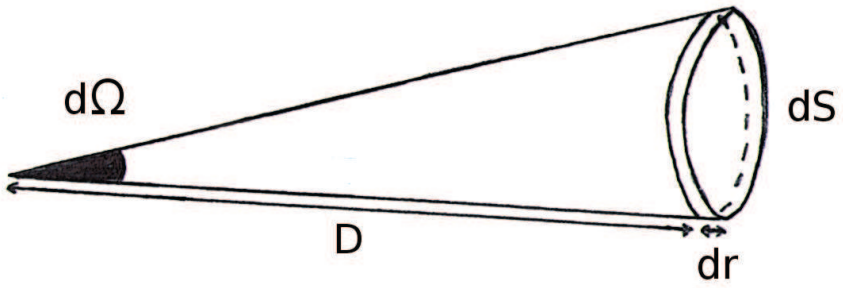

Figure 3.4: Infinitesimal volume element dV at a distance D within the solid angle $d\Omega$.

tion of sources (among the most luminous and farthest ever known) is their luminosity function. Additionally, their possible origin and role within a wider cosmological context can be explored if one knows also their intrinsic redshift distribution. In the following I will present the general (simplest) equations that related these two intrinsic properties to the observables.

The number of GRBs in a certain infinitesimal volume can be derived as follows. With reference to Fig.3.4, let dS be the portion of sky observed within a solid angle $d\Omega$ at the distance D and dr the thickness of the shell where the objects we dare to coint are distributed. The infinitesimal volume element is $dV = dSdr$ and, since $d\Omega = dS/D^2$, it reads $dV = d\Omega D^2 dr$. For the entire sky $dV = 4\pi D^2 dr$.

In the local Universe (well approximated by a Euclidean space), the redshift and the distance of a source are linked through the Hubble relation so that $D = cz/H_0$ (H_0 is the Hubble constant). When the source is at larger distance (higher redshift) it is necessary to consider how the Universe expanded in the time interval elapsed during the travel of photons. In this case, the luminosity distance is:

$$D_L(z) \equiv (1+z)\int_0^z \frac{cdz}{H(z)} = (1+z)\frac{c}{H_0}\int_0^z \frac{dz}{\sqrt{\Omega_m(1+z)^3+\Omega_\Lambda}} \tag{3.1}$$

In this thesis I will always assume a standard flat cosmology with $H_0 = 70$ km s^{-1}Mpc^{-1}, $\Omega_\Lambda = 0.7$, $\Omega_m = 0.3$.

In first approximation $dr = cdz/H(z)$ so we can write the infinitesimal element of comoving volume as

$$dV(z) = 4\pi D_L^2(z)\frac{cdz}{H(z)} \tag{3.2}$$

For each source it is convenient to define the comoving volume V, i.e. that part of the Universe nearest to the source at the current epoch. The comoving cubic giga parsec $(\mathrm{Gpc})^3$ volume is defined as that fraction of the Universe which, when expanded to the present cosmic epoch, fills one cubic giga parsec of the current Universe.

If we are interested in knowing how GRBs are distributed in function of their redshift we need to evaluate

$$\frac{dN}{dz} = \frac{dN}{dV}\frac{dV}{dz} \tag{3.3}$$

If we consider, for simplicity, that GRBs have a unique luminosity L, the total number of observed burst which have (in the observer frame) a flux larger than a certain threshold flux F_{lim} (fluxes are intended as defined over an energetic band $\Delta E = [E_1, E_2]$ in the observer reference frame) is:

$$N(> F_{\mathrm{lim}}) = \int_0^{z(L,F_{\mathrm{lim}})} \frac{dN}{dV}\frac{dV}{dz}\, dz \tag{3.4}$$

The maximum redshift at which it is possible to observe an object is a function of L and F_{lim} and it is defined by the relation $F_{\mathrm{lim}} K(z) = L/(4\pi D_L^2(z))$. The factor $K(z)$ corrects the observed flux into the bolometric one, i.e. integrated over all the frequencies. In practice, integration over the rest frame energy range $[1, 10^4]$ keV ensures to approximate reasonably well the bolometric flux given the typical 0.5 MeV peaked GRB spectra.

$$K(z) = \frac{\int_{1/(1+z)}^{10^4/(1+z)} EN(E)\, dE}{\int_{E_1}^{E_2} EN(E)\, dE} \tag{3.5}$$

where $N(E)$ is the observed photon spectrum.

The luminosity function $\phi(L)$ (defined as a PDF) and define N_{v} the true (unknown) number of GRB in the Universe. The number of GRBs within in a certain luminosity interval $N(L_1, L_2)$ can be obtained multiplying the true number for the probability to observe a GRB with $L \in [L_1, L_2]$.

$$N(L_1, L_2) = PN_{\mathrm{v}} = N_{\mathrm{v}} \int_{L_1}^{L_2} \phi(L)\, dL \tag{3.6}$$

Now, combining Eq.3.4 and Eq.3.6 we obtain:

$$N(> F_{\mathrm{lim}}) = \int_0^{z(L_{\mathrm{max}},F_{\mathrm{lim}})} \int_{L_{\mathrm{lim}}(F_{\mathrm{lim}},z)}^{L_{\mathrm{max}}} \phi(L)\frac{dN_{\mathrm{v}}}{dV}\frac{dV}{dz}\, dz \tag{3.7}$$

The associated rate of events can be obtained deriving this equation and taking into account the relation between the observed time t and the comoving one t_c. Since $t = (1+z)t_c$ then

$$\frac{dN(>F_{\rm lim})}{dt} = \int_0^{z(L_{\rm max},F_{\rm lim})} \int_{L_{\rm lim}(F_{\rm lim},z)}^{L_{\rm max}} \phi(L) \frac{dN_{\rm v}}{dV(1+z)dt_{\rm c}} \frac{dV}{dz}\, dz \quad (3.8)$$

$\psi(z) \equiv dN_{\rm v}/dVdt_c$ is defined the cosmic GRB formation rate, i.e. the true number of burst per unit of comoving volume and time.

Finally, considering an instrument with threshold flux $F_{\rm lim}$, a field of view Ω, operative for an observational time T, the number of detected GRBs can be write as:

$$N(>F_{\rm lim}) = \frac{\Omega T}{4\pi} \int_0^{z(L_{\rm max},F_{\rm lim})} \int_{L_{\rm lim}(F_{\rm lim},z)}^{L_{\rm max}} \phi(L) \frac{\psi(z)}{(1+z)} \frac{dV}{dz}\, dz \quad (3.9)$$

This is the typical approach of source counts adopted to link the observations, e.g. the flux distribution of the population GRBs detected by a given instrument above its limiting threshold, and their intrinsic properties, i.e. the luminosity function and redshift distribution.

CHAPTER 4

Reconstructing $\phi(L)$ and $\psi(z)$ of GRBs

Recovering the cosmic formation rate $\psi(z)$ and the luminosity function $\phi(L)$ of GRBs allows us to test the nature of their progenitor (e.g. by a comparison with the cosmic star formation rate) and to study the possible presence of sub–classes of GRBs at the low end of the luminosity function.

These two functions were derived for the population of long GRBs (e.g. Daigne et al., 2006; Firmani et al., 2004; Guetta and Della Valle, 2007; Salvaterra and Chincarini, 2007; Salvaterra et al., 2009b, 2012; Wanderman and Piran, 2010; Yu et al., 2015a; Petrosian et al., 2015) through different methods and samples of bursts. For the population of short GRBs, instead, these functions have been less securely constrained (e.g. Nakar et al., 2006; Berger, 2014; D'Avanzo et al., 2014; Guetta and Piran, 2006, 2005) because of the limited number of bursts with measured redshifts.

The typical approach consists in combining the $\psi(z)$ and $\phi(L)$ (assumed or known) to derive the flux distribution of the population of GRBs observable by a given detector, knowing its instrumental parameters (see Cap.3 Sec.3.2 Eq.3.9). Then, assuming functional forms for $\psi(z)$ and $\phi(L)$, it is possible to constrain their free parameters by

fitting the model flux distribution to the observed one. The number of free parameters, if both $\phi(L)$ and $\psi(z)$ are to be constrained, can be large when only the flux distribution of the population is used as a constrain (but see e.g. Ghirlanda et al., 2016). This is the reason why the formation rate is usually fixed a priori. One possibility for long bursts is to assume that, based on the massive collapsar progenitor scenario, the cosmic GRB formation rate traces the cosmic star formation rate, i.e. $\psi(z) \propto \psi_\star(z)$. Among the most accepted models for $\psi(z)$ is the one proposed by Li (2008). It is an extension at higher redshift of the model of Hopkins and Beacom (2006). Its functional form is based on the cosmic star formation rate of Cole et al. (2001)

$$\psi(z) = \frac{a + bz}{1 + (z/c)^d} \tag{4.1}$$

where $(a, b, c, d) = (0.0157, 0.118, 3.23, 4.66)$.

For short bursts, instead, since it is believed that the progenitors are likely compact object binary mergers (NS–NS or NS–BH; e.g. Giacomazzo et al., 2013), it is assumed a delayed cosmic star formation rate. In such a case the short GRBFR is given by the convolution of the cosmic star formation rate with the distribution $P_{\rm m}(\tau)$ of the delay time τ, i.e. $\psi(z) \propto \psi_\star(z) * P(\tau)$. This delay, tipically modeled with a power–law distribution with a minimum delay time (Piran, 1992), represents the time needed for the progenitor binary system to merge.

If $\psi(z)$ is fixed a priori, the approach described above allows us to to derive the free parameters of the luminosity function $\phi(L)$ by fitting the flux distribution of large, statistically significant, sample of observed GRBs. Then, the assumed $\psi(z)$, combined with the LF, is tested by computing the expected redshift distribution and by comparing it with the observed one of a sample of bursts with measured z.

The simplest hypothesis is to assume the luminosity function $\phi(L)$ to be independent from the redshift, but it does not provide a good representation of the observed redshift distribution. However, evolutionary scenarios are also considered: either the luminosity function or the GRB formation rate are allowed to change with redshift (Salvaterra et al., 2012; Daigne et al., 2006; Salvaterra and Chincarini, 2007; Salvaterra et al., 2009b; Qin et al., 2010; Wanderman and Piran, 2010; Firmani et al., 2004; Guetta et al., 2005; Virgili et al., 2011a; Natarajan et al., 2005; Butler et al., 2010; Campisi et al., 2010; Virgili

et al., 2011a; Robertson and Ellis, 2012). This kind of assumption is reasonable because the redshift distribution of GRBs is not uniform. In the case of luminosity evolution, the luminosity of GRBs may be simply parametrized (given the unknown a priori nature of this dependence from z) as $L(z) = L_0(1+z)^k$ (luminosity evolution scenario). The luminosity function at a particular redshift z can be constructed adopting the same functional form as at $z = 0$ and evolving all the luminosities, i.e. $\phi(L, z) = \phi(L_0(1+z)^k)$. Alternatively, the GRB formation rate $\psi(z)$ may be evolving with redshift with a similar analytic dependence $\psi(z) \propto \psi_\star(z)(1+z)^d$ (density evolution scenario). These two possibilities represent our lack of knowledge of the properties of the GRB population which may have changed (evolved) upon cosmic epochs. This means that the progenitor physical characteristics evolve with z (producing for example brighter GRBs at higher z) and/or that the GRBFR varies in normalization with respect to the cosmic star formation rate. Hybrid models, mixing both kind of evolution (i.e. in luminosity and in density), are possible in principle, even if it is preferable to test these two scenarios independently due to the degeneracy (see e.g. Salvaterra et al., 2012)..

The method described above is what we consider an *indirect method*. It has been recently applied to long GRBs by Salvaterra et al. (2012). They find, using a complete sample of GRBs detected by *Swift* (see sub–sec.4.1.2), that either a luminosity evolution with $k = 2.1 \pm 0.6$ or a density evolution with $d = 1.7 \pm 0.5$ can reproduce the flux distribution of BATSE bursts and the redshift distribution of the *Swift* complete sample. However, even if they cannot discriminate between these two scenarios (as previously mentioned), the indication is that GRBs must have experienced some sort of evolution implying either that they were brighter and/or in larger number in the past.

While the possible evolution of the LF or of the GRBFR with redshift is still a matter of debate, there seems to be a general consensus on describing the LF of long GRBs as a power–law, eventually with a break at some characteristic luminosity:

$$\phi(L) \propto \begin{cases} \left(\frac{L}{L_\mathrm{b}}\right)^{-a}, & L \leq L_\mathrm{b} \\ \left(\frac{L}{L_\mathrm{b}}\right)^{-b}, & L > L_\mathrm{b} \end{cases} \tag{4.2}$$

where L_b represents the break luminosity and a and b are the slopes

of the power–law below and above the break, respectively. Salvaterra et al. (2012) find $a = 0.74^{+1.42}_{-1.36}$, $b = 1.92^{+0.14}_{-0.11}$, $L_{\rm b} = 5.5^{+6.9}_{-3.4} \times 10^{50}$ erg/s in the case of the luminosity evolution scenario (parameters refer to LF at $z = 0$) and $a = 1.5^{+0.16}_{-0.32}$, $b = 2.32^{+0.32}_{-0.77}$, $L_{\rm b} = 3.8^{+6.3}_{-2.7} \times 10^{52}$ erg/s in the case of the density evolution scenario. Similar results ($a = 1.52$, $b = 2.00$, $L_{\rm b} = 10^{52.5}$ erg/s) are obtained by Jakobsson et al. (2012). Howell et al. (2014) derive a smaller low luminosity index $a = 0.95 \pm 0.09$ and consistent $b = 2.59 \pm 0.93$, $L_{\rm b} = 0.8 \pm 0.43 \times 10^{52}$ erg/s.

For short GRBs, the LF is typically modeled as a single or broken power–law, and in most cases it is found to be similar to that of long GRBs (i.e. proportional to L^{-1} and L^{-2} below and above a characteristic break luminosity of the order of 10^{51-52} erg/s; Guetta and Piran, 2006; Salvaterra et al., 2008; D'Avanzo et al., 2014; Virgili et al., 2011b) or even steeper (L^{-2} and L^{-3}; Wanderman and Piran, 2015).

The *indirect* method relies on assuming a parametric form for the luminosity function and the formation rate. There are, however, non–parametric methods that allow to directly determine $\phi(L)$ and $\psi(z)$ independently from a specific assumption of their analytic form. In the next sections I will outline these methods.

4.1 The C^- method

In this section I will describe the nonparametric statistical C^- method as originally proposed by Lynden-Bell (1971). This work was motivated by the will to study the luminosity function of quasars (in the 3CR sample) accounting for selection effects. Given the similarity in the observational bias affecting flux–limited samples, this method has been applied to GRBs by e.g. Yonetoku et al. (2004, 2014); Kocevski and Liang (2006); Wu et al. (2012) and more recently by Yu et al. (2015a); Petrosian et al. (2015). I have implemented and used this method to derive the properties of the long GRB population and present my main results in Sec.5. In the following sections I will describe the method and discuss its main advantages and limitations.

Faint sources can only be seen nearby and bright objects, for a typical decaying luminosity function, are rare. Therefore, we should account for the relative significance of these two type of sources populating the extremes of the flux distribution of a given sample of

events. Even more so in case we consider a complete sample of objects. Thus the luminosity function cannot be derived simply deriving the observed luminosity distribution. The problem is even more complicated if density of objects varies along the line of sight in an unknown manner.

Hence, the C^- method is based on two important requirements. First, the truncation limit below which no observations can be made must be well known. Second, the parent distributions can only be estimated assuming the independence between the luminosity and the redshift (this is, in general, a limitation of all non–parametric techniques that rely on the assumption of stochastic independence).

Before applying this method, it is necessary to determine the degree of correlation between the two variables L and z and then produce an uncorrelated data set by "de–evolving" the luminosities. Once obtained the uncorrelated sample, it is possible to apply the Lynden–Bell C^- method to derive the luminosity function (of de–evolved luminosities) and the GRB formation rate.

In order to estimate the degree of correlation of the luminosity with redshift induced by the flux in a flux–limited sample Efron and Petrosian (1992) proposed a non–parametric test, which is based in part on the C^- method. I will explain this test in the subsection 4.1.1 while now I will focus on the description of the C^- method.

Under the assumption that the luminosity function $\phi(L)$ is of the same form at all points along the line of sight but with a normalization that varies as the number density, the comoving number of GRBs with luminosity from L to $L + dL$, in the redshift bin between$z$ and $z + dz$, can be written as

$$dN(L, z) = D(z)\phi(L)dLdz \tag{4.3}$$

where $D(z) = \psi(z)[dV(z)/dz]/(1 + z)$ is the comoving number density (see Sec.3.2 Eq.3.8). Given a certain a sample of GRBs (with known L and z) selected adopting a well defined limiting flux $F_{\rm lim}$ (such that a GRB would not have been included in the sample unless its bolometric flux $F \geq F_{\rm lim}$) the question we want to tackle is whether we can derive the true luminosity and number density distribution of the GRB population.

In order to understand and test the C^-method I generated, through a Monte Carlo simulation, a small population of GRBs (Fig.4.1) distributed in redshift according to the GRB formation rate $\psi(z)$ of Li (2008) and adopting the luminosity function $\phi(L)$ (keeping it equal

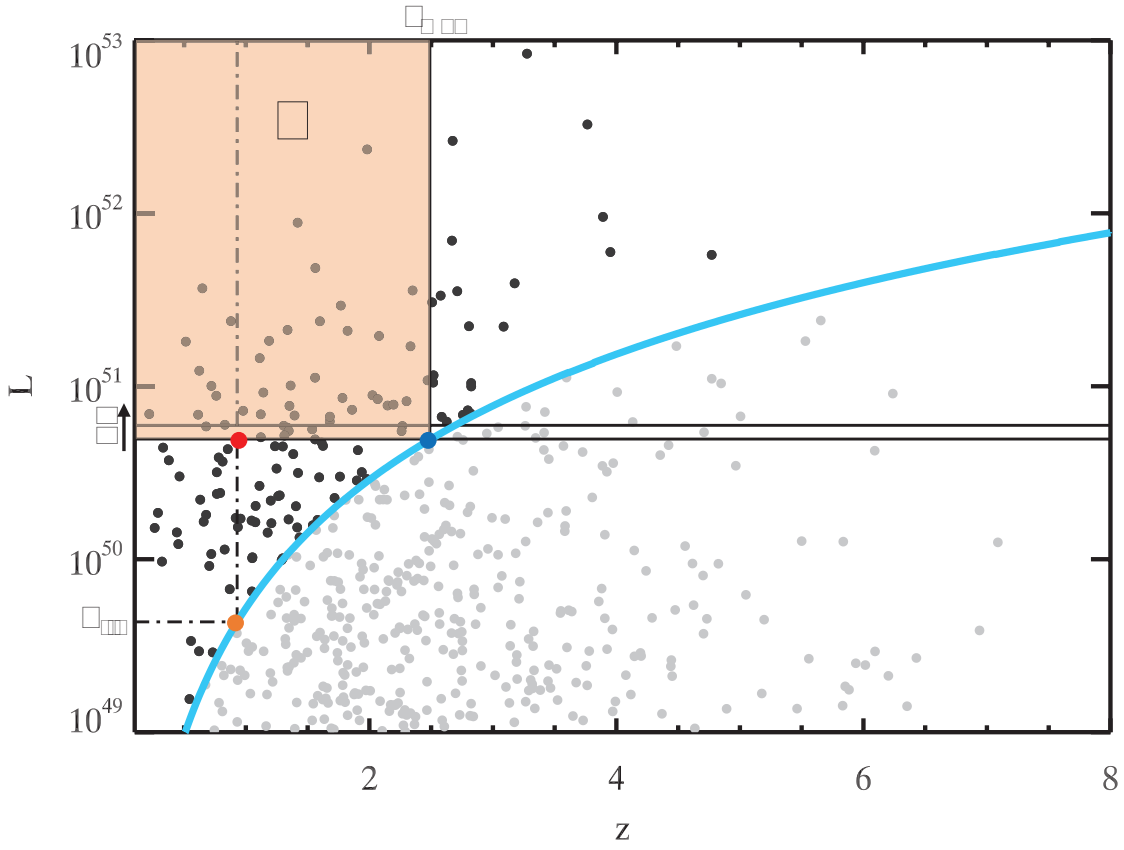

Figure 4.1: Simulated sample of GRBs (see the text for the parent distributions). The blue solid line is the adopted bolometric limiting flux $F_{\rm lim} = 10^{-8}$ erg cm^{-2} s^{-1}. Black and grey points represent those bursts having bolometric above and below the limiting flux. Blue and orange points represent, respectively, the maximum redshift and the minimum luminosity corresponding to the burst highlighted in red. The area C contains the cumulative fraction of observed burst in the volume within which a burst of luminosity L (red point) can be still detected.

at all redshift) obtained by Salvaterra et al. (2012). I then extracted a sample of GRBs (black points in Fig.4.1) by cutting the population with limiting flux $F_{\rm lim} = 10^{-8}$ erg cm^{-2} s^{-1}. It is important to understand that for the aim of the present test, any other assumption on the form of the two functions $\phi(L)$ and $\psi(z)$ would still be possible. Indeed, this simulation is only meant to understand the limitations of the C^- test.

For each GRB in the $L - z$ plane, $z_{\rm max}$ is defined as the maximum redshift at which the i–th GRB (with luminosity L_i) can still be observed because its flux is above the limit $F_{\rm lim}$. Similarly the limiting luminosity $L_{\rm lim}$ corresponds to the limiting flux $F_{\rm lim}$ at redshift z_i. The blue and the orange points in Fig.4.1 visually show $z_{\rm max}$ and

$L_{\rm lim}$ associated to the GRB identified by the red point.

Consider, as reference the luminosity of the i–th burst (shown by the red point in the $L-z$ plane) and call it $\tilde{L}$ and let $\Phi(\tilde{L})$ be the true cumulative luminosity function of GRBs with $L \geq \tilde{L}$ so that $-\Phi' = -d\Phi(L)/dL$ is the differential luminosity function ϕ we want to recover. Let's define $X(\tilde{L})$ as the observed number of burst with $L \geq \tilde{L}$. As the infinitesimal increment $d\tilde{L}$ is a positive defined quantity, the corresponding infinitesimal dX associated to the function $X(\tilde{L})$ is a negative quantity. $-dX$ thus represent the number of observed points in the infinitesimal column between $\tilde{L}$ and $\tilde{L}+d\tilde{L}$ (see Fig. 4.1). The ratio between this quantity and the number of objects $C(\tilde{L})$ in the rectangular area C in Fig.4.1, is equal to the ratio between the true cumulative distribution infinitesimal increment $-d\Phi$ (the number of object contained in the entire infinitesimal column, including the non detected events) and $\Phi(\tilde{L})$ itself. This relation is in general true at any luminosity so we can write:

$$\frac{dX}{C} = \frac{d\Phi}{\Phi} \tag{4.4}$$

Integrating this relation we obtain

$$\Phi(\tilde{L}) = A \exp\left\{\int \frac{dX}{C}\right\} = A \exp\left\{\int_{\tilde{L}}^{L_{\rm max}} \frac{1}{C(L)} \frac{dX}{dL}\, dL\right\} \tag{4.5}$$

where A comes from the integration constant. The set of observations is composed by distinct points so during the integration the value of X will change in a discrete manner at each i–th luminosity. Thus $-dX/dL$ can be expressed as a sum of Dirac delta functions

$$-\frac{dX}{dL} = \sum_i \delta(L - L_i) \tag{4.6}$$

Substituting this relation into Eq.4.5 it is clear that $C(L_i)$ has to be evaluated thus we are interested in knowing the behavior of $C(L)$ in a small neighborhood of L_i. When the number of points in C is not so large, the problem arises in the choice of whether to include, exclude, or half include the point on the edge (the one with $L = L_i$). In the neighborhood of L_i the i–th point contribution x can be written as

$$x = X(L) - X(L_i^+) \tag{4.7}$$

where L_i^+ is the luminosity barely greater than L_i .This expression allows us to define $C^-(L_i)$ as the value of C at L_i with the contribution of the i–th point omitted. So when L is close to L_i

$$C(L) = C^-(L_i) + x \tag{4.8}$$

The integral in Eq.4.5, evaluating the contribution of the i–th burst in a neighborhood of L_i, now becomes

$$A \exp\left\{\sum_i \int_0^1 \frac{dx}{C^- + x}\right\} = A \exp\left\{\sum_i \log\left(\frac{C^- + 1}{C^-}\right)\right\} \tag{4.9}$$

We can then write the solution to our initial problem:

$$\Phi(\tilde{L}) = A \prod_i \left(\frac{C^-(L_i) + 1}{C^-(L_i)}\right) \tag{4.10}$$

Here the product is over those bursts with $\tilde{L} < L_i < L_{\max}$ and the complete cumulative function can be evaluated step by step varying $\tilde{L}$ among the luminosities of the GRBs in the sample. This result is general and it is valid also in order to obtain the cumulative function associated to the comoving number density $D(z)$ (but defining different C areas in $L - z$ plane).

Consider the simulated sample in Fig.4.2. We want to to recover the luminosity function $\phi(L)$ and the cosmic formation rate $\psi(z)$ using the C^- method. To this aim, I created another sample adopting the same parent distributions and limiting flux of the previous one, but generating a larger number of GRBs (10000 in total) in order to have better statistic. Note that I assumed (as before) no luminosity evolution in the MC so I do not have to de–evolve the luminosities before apply the C^- method.

For the i–th GRB in the sample, described by its (L_i, z_i) (e.g. the red point in Fig.4.2), consider the subsample $J_i = \{j \mid L_j > L_i \wedge z_j < z_{\max,i}\}$ and call N_i the number of GRBs it contains (green rectangular area in Fig.4.2). Similarly, we define the subsample $J_i' = \{j \mid L_j > L_{\lim,i} \wedge z_j < z_i\}$ and call M_i the number of GRBs it contains (light blue rectangular area in Fig.4.2). Through M_i and N_i we can estimate the cumulative luminosity function $\Phi(L)$ and the cumulative GRB redshift distribution $\zeta(z)$:

$$\Phi(L_i) = \prod_{j\,:\,L_j > L_i} \left(1 + \frac{1}{N_j}\right) \tag{4.11}$$

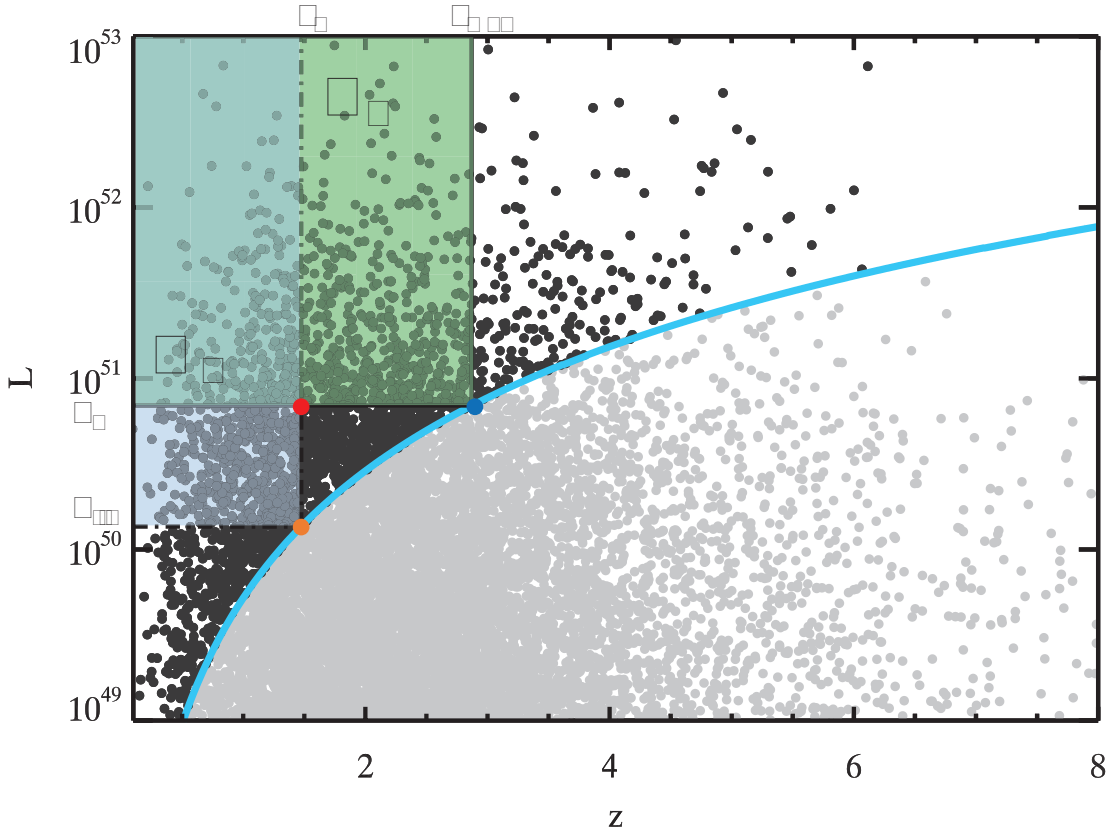

Figure 4.2: Simulated sample of GRBs (see the text for the assumptions). The blue solid line is the adopted bolometric limiting flux $F_{\rm lim} = 10^{-8}$ erg cm^{-2} s^{-1}. Black and grey points represent bursts having bolometric flux above and below the limiting value. Blue and orange points represent, respectively, the maximum redshift and the minimum luminosity corresponding to the burst highlighted in red. The light green and the light blue areas represent, respectively, the subsamples J (containing N_i) and J' (containing M_i) defined in order to apply the C^- method.

and

$$\zeta(z_i) = \prod_{j\,:\,z_j<z_i} \left(1 + \frac{1}{M_j}\right) \tag{4.12}$$

From the latter we can derive the GRB formation rate as

$$\psi(z) = \frac{d\zeta(z)}{dz}(1+z)\left[\frac{dV(z)}{dz}\right]^{-1} \tag{4.13}$$

The differential luminosity function $\phi(L)$ is obtained by deriving the cumulative one $\Phi(L)$. Note that M_j and N_j are equal to 0 for those bursts that are at the edge of the distribution in the $L - z$

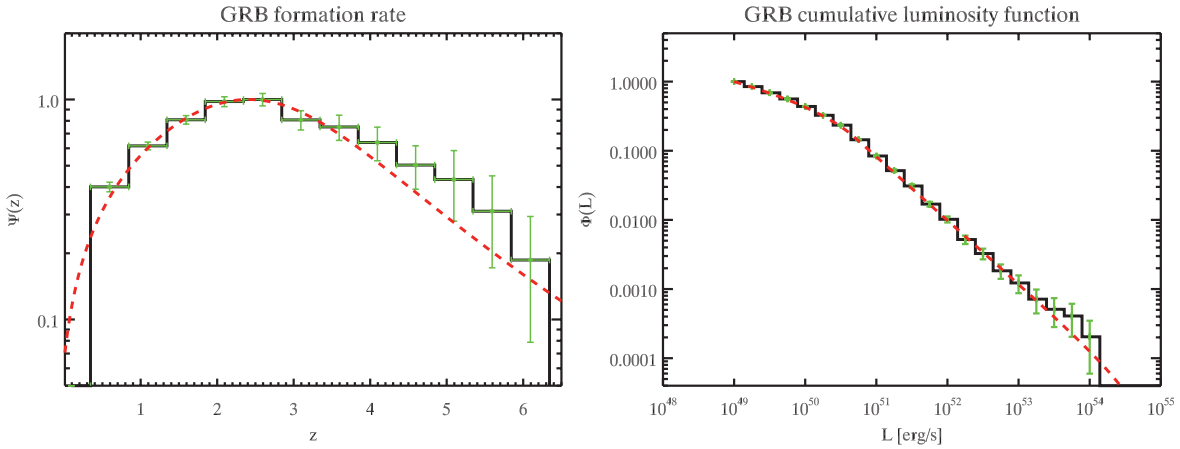

Figure 4.3: Resulting GRB formation rate and luminosity function (green points) obtained using the C^- method on the simulated sample. The red dashed lines represent the parent distributions used for the simulation.

plane. In these cases, the contribution has to be omitted in the products of Eqs. 4.11 and 4.13. The functions $\phi(L)$ and $\psi(z)$ are shown in Fig.4.3. Errors on $\phi(L)$ are computed by propagating the errors on the cumulative one and assuming Poisson statistics. The errors on the $\psi(z)$ are computed from the number n of GRBs within the redshift bin. I assumed that the relative error $\epsilon = 1/\sqrt{n}$ is the same as that affecting $\psi(z)$. Note that these function have an arbitrary normalization so that we can get information on their shape but not on the absolute numbers and densities.

4.1.1 Test of $L - z$ independence

The C^- method is based on the assumption that the luminosity is independent of redshift. However, as discussed in Petrosian et al. (2015), a strong luminosity evolution could be present in the GRB population. Efron and Petrosian (1992) proposed a non–parametric test in order to estimate the degree of correlation of the luminosity with redshift induced by the flux in a flux–limited sample.

If the two variables z and L are uncorrelated, then the rank r_i of z_i within the examined sample should be uniformly distributed between 1 and N, with an expected mean $E = (N+1)/2$ and variance $V = (N^2-1)/12$. The ranks are usually renormalized in a such a way that the mean and the variance become 0 and 1, respectively. This can be done by defining the new statistic $T_i = (r_i - E)/V$. The

modified Kendall correlation coefficient

$$\tau = \frac{\sum_i (r_i - E)}{\sqrt{\sum_i V}} \tag{4.14}$$

allow us to understand if directly reject or accept the hypothesis of independence. $\tau = 1$ indicates a 1σ correlation whereas $\tau = 0$ signifies a completely random data set.

This can be calculated considering the associated sets J and J' (defined in for the C^- method). The rank r_i of z_i is the number of elements within the associated set $R_i = J \cap J' = \{j \in J_i | z_j \leq z_i\}$ (see Fig.4.2). It is expected that this value is uniformly distributed between 1 and N_i (the number of points in the associated set J_i). Now, the expected mean and variance for the rank r_i are calculated separately in each associated subset R_i defined for the i–th GRBs and are $E_i = (N_i + 1)/2$ and $V = (N_i^2 - 1)/12$, respectively. The specialized version of Kendell's τ statistic is given by

$$\tau = \frac{\sum_i (r_i - E_i)}{\sqrt{\sum_i V_i}} \tag{4.15}$$

This parameter represents the degree of correlation for the entire sample with proper accounting for the data truncation.

The problem we are left with is how to describe the luminosity evolution. Let us, for example, define the luminosity evolution $L = L_0(1+z)^k$, where L_0 is the de–evolved luminosity. The right value for the parameter k is found de–evolving the luminosities of the sample and varying k until τ, calculated on the de–evolved sample, is 0.

4.1.2 The relevance of sample completeness

The main difficulty in obtaining the luminosity function $\phi(L)$ and the cosmic GRB formation rate $\psi(z)$ is accounting for the selection effects which affect the true GRB population detected by any instrument. These functions cannot be derived straightforwardly using all GRBs with known redshift since these samples are affected by observational biases. Independently from the method adopted, most of the previous studies used either heterogeneous samples (i.e. including GRBs detected by different satellites/detectors which do not have the same sensitivity) and/or incomplete samples (in flux and/or in redshift). In particular, incompleteness is induced by several effects, such as the variation of the trigger efficiency and the

redshift measurement. Accounting for such instrumental effects is extremely difficult. In practice it is much more rewarding to work with complete samples though at the expense of the sample size.

Salvaterra et al. (2012) constructed a flux–limited sample (BAT6) of bright GRBs detected by *Swift*/Burst Alert Telescope (BAT) which resulted 95% complete in redshift (BAT6). Despite containing a relatively small number of GRBs (58 in total), it has been extensively used to test various prompt and afterglow properties of GRBs in an unbiased way (Vergani et al., 2015; Nava et al., 2012; Melandri et al., 2014, 2012; Ghirlanda et al., 2012a; D'Avanzo et al., 2012; Covino et al., 2013; Campana et al., 2012). Salvaterra et al. (2012) applied the indirect method (explained at the beginning of this Chapter) on the BAT6 in order to obtain the luminosity function fixing a priori the form of the GRBFR. Similarly, Jakobsson et al. (2012) built the TOUGH sample, which extends to fainter luminosities, and derived the LF.

An alternative method (the C^-) is based on the direct derivation of the $\phi(L)$ and $\psi(z)$ from observed samples of GRBs with measured z and L. This method has been inherited from the studies of the luminosity function of quasars and blazars (e.g. Singal et al., 2013, 2012; Maloney and Petrosian, 1999; Chiang and Mukherjee, 1998) and it has been applied to GRBs (Kocevski and Liang, 2006; Lloyd and Petrosian, 1999). Wanderman and Piran (2010), instead, adopted a maximum likelihood estimator to derive the discrete luminosity function and cosmic formation rate.

In Chp.5 I will discuss why that Yu et al. (2015a) and Petrosian et al. (2015) obtained unreasonable results on the GRB formation rate through the C^- method. The main reason being the use of incomplete samples. For this reason, in Pescalli et al. (2016) we used the C^- on the BAT6 complete sample (updating and extending it) in order to correctly determine $\phi(L)$ and, above of all, $\psi(z)$ for long GRBs.

4.2 The Maximum Likelihood Estimator method

In this section I will describe the Maximum Likelihood Estimator (MLE) method as adopted by Wanderman and Piran (2010). This is a direct inversion method (similar to the C^- method) that allows us, by maximizing the likelihood function, to obtain simultaneously (and independently) $\phi(L)$ and $\psi(z)$ from a distribution of GRBs in the $L - z$ plane. As other non–parametric methods the unique key

assumption is that L and z are uncorrelated.

Let's consider a sample of GRBs having measured luminosity L and redshift z and, differently from before, let's define the logaritmic differential luminosity function $\phi(L) = dN/d\log(L)$. In this way the fraction of GRBs with luminosity in the interval $[\log(L), \log(L) + d\log(L)]$ and redshift between z and $z + dz$ is:

$$dN(L, z) = \phi(L)D(z)d\log(L)dz \tag{4.16}$$

where $D(z) = \psi(z)[dV(z)/dz]/(1+z)$ is the comoving number density (see Sec.3.2 Eq.3.8).

Such statistical model depends, in principle, on the set of parameters θ of the true parent functions. Define $X \equiv \{x_i\}_{i=1}^n$ the set of observational data and $P(\{x_i\}_{i=1}^n|\theta)$ the probability to observe the sample X given a specific set of parameter. The latter is equivalent to the probability $\mathcal{L}(\theta|\{x_i\}_{i=1}^n)$ that the given sample X has been generated by a set of parameter θ. The aim is to obtain the best set of parameter θ that describes the sample X, i.e. we want to maximize, in the parameter space, the probability $\mathcal{L}(\theta|X)$. This corresponds to find the maximum of the Likelihood function: $\hat{\theta} = \max_\theta\{\mathcal{L}(\theta|X)\}$. First we should evaluate the probability $P(X|\theta) = P(x_1|\theta) \times P(x_2|\theta) \times \cdots \times P(x_n|\theta)$. This allows us to obtain $\mathcal{L}(\theta|X) = P(X|\theta) = \prod_{i=1}^n P(x_1|\theta)$ which we have to maximize.

In order to apply this theoretical and general argument to our GRB sample we need to define the probability within luminosity and redshift intervals. To this aim it is convenient to define $\phi(L)$ and $D(z)$ as a step function with constant value within the corresponding luminosity and/or redshift bin:

$$\phi_i \equiv \phi(L_i < L < L_{i+1}) \tag{4.17}$$

$$D_j \equiv D(z_j < z < z_{j+1}) = \frac{1}{z_{j+1} - z_j} \int_{z_j}^{z_{j+1}} \frac{\psi(z)}{(1+z)} \frac{dV}{dz} dz \tag{4.18}$$

Wanderman and Piran (2010) also introduce weighting factors ω_{ij} which represent the probability to detect a burst with luminosity L and redshift z. These are:

$$\omega_{ij} = \int_{L_i}^{L_{i+1}} \int_{z_j}^{z_{j+1}} \delta(L, z) d\log(L) dz \tag{4.19}$$

where $\delta(L, z)$ is the probability to detect, and effectively measure, the redshift of a GRB with luminosity L at redshift z.

If N is the total number of objects in our sample, we call N_i the number of GRB in the luminosity interval $[L_i, L_{i+1}]$ and with N_j the number of bursts in the redshift interval $[z_j, z_{j+1}]$. N_{ij} is the number of objects belonging to both subset so that $N = \sum_{i,j} N_{ij}$. The probability to observe N_{ij} bursts in the corresponding $L - z$ interval is $P_{ij} = (\phi_i D_j \omega_{ij})^{N_{ij}}$. The logaritmic Likelihood function M (normalized to the probability to observe all N GRBs) is defined as:

$$M = \log \left(\frac{\prod_{i,j} (\phi_i D_j \omega_{ij})^{N_{ij}}}{(\sum_{i,j} \phi_i D_j \omega_{ij})^N} \right) \tag{4.20}$$

Computing the partial derivatives with respect to ϕ_i and D_j (in order to maximize M) we obtain:

$$\phi_i = \frac{N_i}{\sum_j R_j \omega_{ij}} \frac{\sum_{k,m} \phi_k D_m \omega_{km}}{N} \tag{4.21}$$

$$D_j = \frac{N_j}{\sum_i \phi_i \omega_{ij}} \frac{\sum_{k,m} \phi_k D_m \omega_{km}}{N} \tag{4.22}$$

This set of non–linear equations can be solved numerically and provides the values of the step functions ϕ e D.

4.3 The redshift integrated luminosity function

In this section I will show how it is possible to derive directly the luminosity function of GRBs integrated over all the redshift space. This is not the typical luminosity function that is derived through indirect methods, since it is free from any functional form and only uses the $1/V_{\max}$ concept, i.e. the maximum comoving volume within which a burst with an observed luminosity can be detected by a given instrument. This is a generalization of the $\langle V/V_{\max} \rangle$ method proposed by Schmidt (1968) and applied to quasars (see Avni and Bahcall, 1980).

However, the luminosity function obtained with this method is not the canonical $\phi(L)$, but it is the result of the integration of the latter together with the GRB formation rate $\psi(z)$ over z. We call this function the convolved luminosity function $\Sigma(L)$ (CLF). In theory, the luminosity function may evolve with redshift ($\phi(L, z)$). For this reason, the shape of the CLF contains both types of evolution (in luminosity and in density) and may be different from the shape of the

canonical $\phi(L)$. It could simply be proportional to $\phi(L)$ only if the luminosity function does not evolve in any way with the redshift. Indeed, it is possible to express $\Sigma(L)$ in terms of luminosity function and GRB formation rate:

$$\Sigma(L) = \int_0^\infty \phi(L, z)\psi(z)\, dz \tag{4.23}$$

The advantage is that this equation can be obtained directly from the data without any kind of assumption and it is extremely robust if derived through a flux–limited sample.

The method is the following. Given a complete sample, one should define $V_{\max}$ for each burst. Then, using the instrumental parameters it is possible to compute the rate ρ_i associated to the i–th GRB as $\rho_i = 4\pi/\Omega T V_{\max}$, where Ω is the field of view and T is the operating time of the instrument. The CLF can be easily derived in a discrete manner dividing the observed range of luminosities in bins of equal logarithmic width Δ and summing within each bin the rates of the corresponding bursts:

$$\Sigma_j(L_j) = \frac{1}{\Delta L_j} \sum_i \rho_i \tag{4.24}$$

where the sum is made over the bursts having luminosity $L_j - \Delta/2 \leq L_i \leq L_j + \Delta/2$.

When computing individual rates, we used the mission–elapsed time T . However, this is the time in the observer frame and the rate should be corrected for the cosmological time dilation. This means that, at higher z, the same subset of sources should occur with a larger frequency. Therefore, the elapsed time T has to be averaged out on the redshift interval $[0, z_{\max}]$

$$\langle T \rangle = \frac{\int_0^{z_{\max}} \frac{T}{1+z} dz}{\int_0^{z_{\max}} dz} \tag{4.25}$$

and then used in the computation of Eq.4.24 in order to obtain the true CLF. We can look at this function as a redshift–integrated luminosity distribution. This is the most direct information that we can obtain from the data. In fact, it is obtained without any type of assumption or observational constraints. As with the flux distribution $\log(N) - \log(P)$ and with the redshift distribution, it can be used as a constraint. The LF and the GRBFR obtained with other methods

should reproduce this CLF once convolved together and integrated over z.

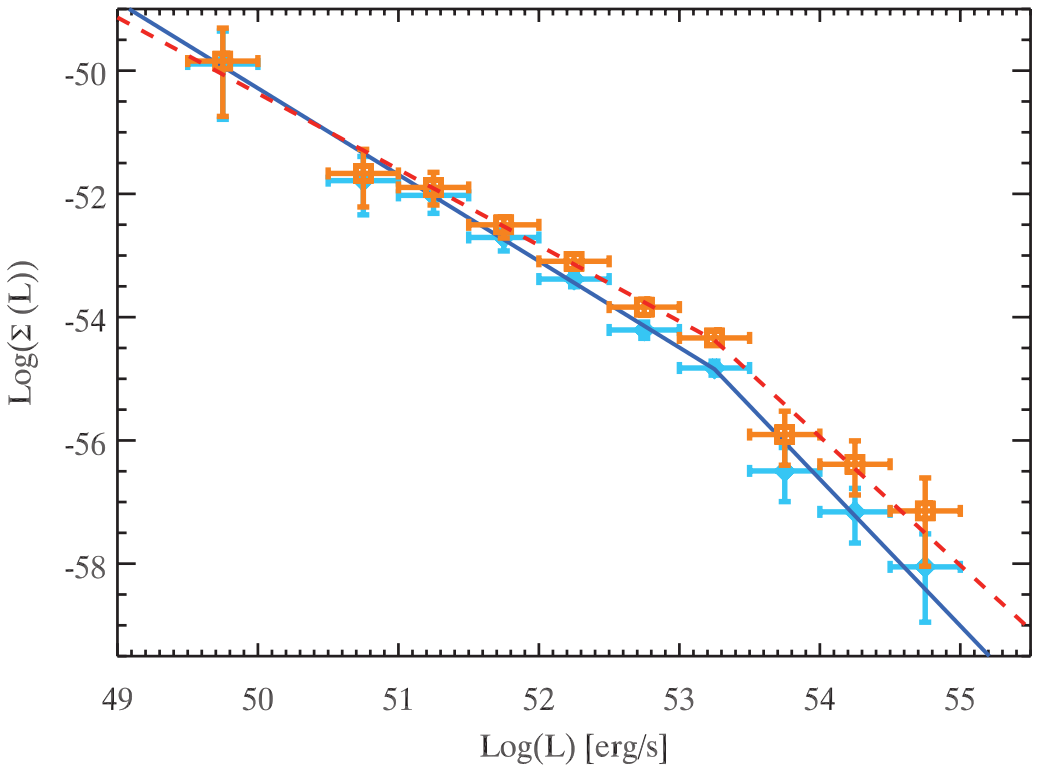

Figure 4.4: Blue–filled points represent the observed CLF $\Sigma(L)$ while the orange squares represent the true CLF $\tilde{\Sigma}(L)$ of the BAT6ext sample. The solid blue line ($a = -1.39 \pm 0.14$, $b = -2.38 \pm 0.41$, $L_b = 10^{53.3 \pm 0.3}$ erg/s) and the dashed orange line ($a = -1.22 \pm 0.1$, $b = -2.09 \pm 0.95$, $L_b = 10^{53.3 \pm 1}$ erg/s) are the best–fit BPL models of the observed and true CLF respectively.

4.3.1 Application to the BAT6ext complete sample

I adopted the method just described on the BAT6ext complete sample (see Sec.5.2). I considered 80 out of 99 GRBs with both measured z and L (see Tab.5.1 in Sec.5.2). For each GRB the $V_{\rm max}$ has been determined as the maximum volume within which the burst could still be detected because its flux is larger than the limiting flux, i.e. $P_{\rm lim} = 2.6$ ph cm^{-2} s^{-1} in the $[15 - 150]$ keV energy band. The observed photon flux in the *Swift*/BAT energy band as a function of the varying redshift is:

$$P(z) = \frac{L}{4\pi d_L^2(z)} \frac{\int_{15\ \rm keV}^{150\ \rm keV} N(E)\, dE}{\int_{1/(1+z)\ \rm keV}^{10^4/(1+z)\ \rm keV} EN(E)\, dE} \tag{4.26}$$

where $N(E)$ is the observed photon spectrum of each GRB and $d_L(z)$ is the luminosity distance at redshift z. The extremes of the integral in the denominator correspond to the same values adopted to compute L. The maximum redshift $z_{\rm max}$ corresponds to the redshift that satisfies $P(z_{\rm max}) = P_{\rm lim}$. The CLF has been computed considering the typical *Swift*/BAT field of view $\Omega = 1.33$ steradians and the time of activity of *Swift* $T \sim 9$.

The discrete (observed) CLF is shown in Fig.4.4. It can be adequately represented by a broken power law function with slopes -1.39 ± 0.14 and -2.38 ± 0.41 below and above the break luminosity $L_{\rm b} = 10^{53.3 \pm 0.3}$ erg/s (χ^2/d.o.f. $= 1.04$). The normalization is obtained by considering that the bursts in the BAT6ext sample represent approximately 1/3 of the total number of *Swift* detected GRBs with peak flux $P \geq 2.6$ ph cm^{-2} s^{-1}. I also verified that the BAT6ext sample (99 objects) is representative in terms of peak–flux distribution of the larger population. The error bar associated with the discrete CLF are mainly related to the Poissonian error on the count within the luminosity bin (see also e.g. Wolter et al., 1994).

Fig.4.4 also shows the true CLF obtained correcting the operating time for each burst using Eq.4.25. Correcting for the cosmological time dilation, the true CLF appears slightly flatter (slopes -1.22 ± 0.1 and -2.09 ± 0.95 below and above the break $L_{\rm b} = 10^{53.3 \pm 1}$ erg/s – χ^2/d.o.f.$= 0.99$). The true CLF is flatter than the observed one because, in general, the true elapsed time is less than the observed one. Moreover, the correction is more pronounced for high luminosity GRBs that are observable up to high redshifts.

CHAPTER 5

Redshift dependent formation rate of long GRBs – $\psi(z)$

The different methods and approaches that I described in Chp.4 agree on the shape of the luminosity function (typically represented by a broken power law) but lead to remarkably different results on the cosmic GRB rate (particularly at low redshifts).

Recently, Yu et al. (2015a, Y15 hereafter) and Petrosian et al. (2015, P15 hereafter) applied the C^- method (see Chp.4 Sec.4.1) to reconstruct the discrete $\phi(L)$ and $\psi(z)$ from a sample of *Swift* bursts with measured redshifts. Since this method requires the independence between the luminosity and the redshift, they applied the statistical method proposed by Efron and Petrosian (1992) in order to remove the $L - z$ correlation induced by the flux–cut in the selected GRB sample. They both find a strong luminosity evolution, parametrized as $L = L_0(1+z)^k$, with $k \sim 2.3$. They found, in agreement with previous works, that the cumulative luminosity function is well described by a broken power law (see Eq.**??**) with $\alpha = 0.14 \pm 0.02$, $\beta = 0.7 \pm 0.03$, $L_\mathrm{b} = 1.43 \times 10^{51}$ erg/s (Y15) and $\alpha = 0.5$, $\beta = 2.2$, $L_\mathrm{b} = 10^{51}$ erg/s (P15). These indices (α and β) are the slopes of

the cumulative luminosity function which is linked to the differential one through the integral $\Phi(L) = N(> L) = \int_L^{L_{\max}} \phi(L)\, dL$. Therefore, for a BPL luminosity function, the slopes of the differential form, if definite positive, are $(a, b) = (\alpha + 1, \beta + 1)$.

Intriguingly, they find that the cosmic GRB formation rate is flat or decreases from the local Universe up to $z = 1$, which is at odds with previous works. P15 and Y15 refer to this strange behavior as the excess of GRBs at low redshifts (when these functions are compared to the SFR once normalized to its peak – see Fig.5.1). This result is also puzzling because it is completely at odds with recent findings from host galaxy studies which show that the GRBFR is consistent or slightly steeper than SFR at low redshifts. Vergani et al. (2015); Perley et al. (2015b, 2016a,b); Schulze et al. (2015); Krühler et al. (2015), performed multi–wavelength and spectroscopic studies on the properties (stellar masses, luminosities, SFR, and metallicity) of GRB host galaxies of different complete GRB samples and compared them to those of the star–forming galaxies selected by galaxy surveys. All their results clearly indicate that at $z < 1$ only a small fraction of the star formation produces GRBs.

Motivated by these unexpected results reported by Yu et al. (2015a) and Petrosian et al. (2015) , I derived $\phi(L)$ and $\psi(z)$ applying, as P15 and Y15, the C^- method. All the results reported below have been published in Pescalli et al. (2016).

Independent of the method adopted, the key points are the definition of the sample and its completeness (as underlined by Salvaterra et al., 2012). For this reason, I started from the BAT6 complete sample, but, since it has been built in 2012, I extended it up to 2016. The new sample (BAT6ext) contains 99 bursts with $\sim 82\%$ redshift completeness (see Sec.5.2) and it is extensively described in the next section. I defined the luminosity evolution $L = L_0(1 + z)^k$ (as in Y15 and P15), whereL_0 is the de–evolved luminosity, and computed the modified Kendall correlation coefficient in order to test the independence between L and z in the sample (the details of this test are described in Sec.4.1.1). Consistently with the results of Y15 and P15, I found $k = 2.5$. However, this result should not be interpreted as the proof that GRBs had experienced a pure luminosity evolution because the test of Efron and Petrosian (1992) assigns the whole evolution to the luminosity.

A similar luminosity evolution were obtained by Salvaterra et al. (2012) applying the indirect method (see the beginning of Chp.4)

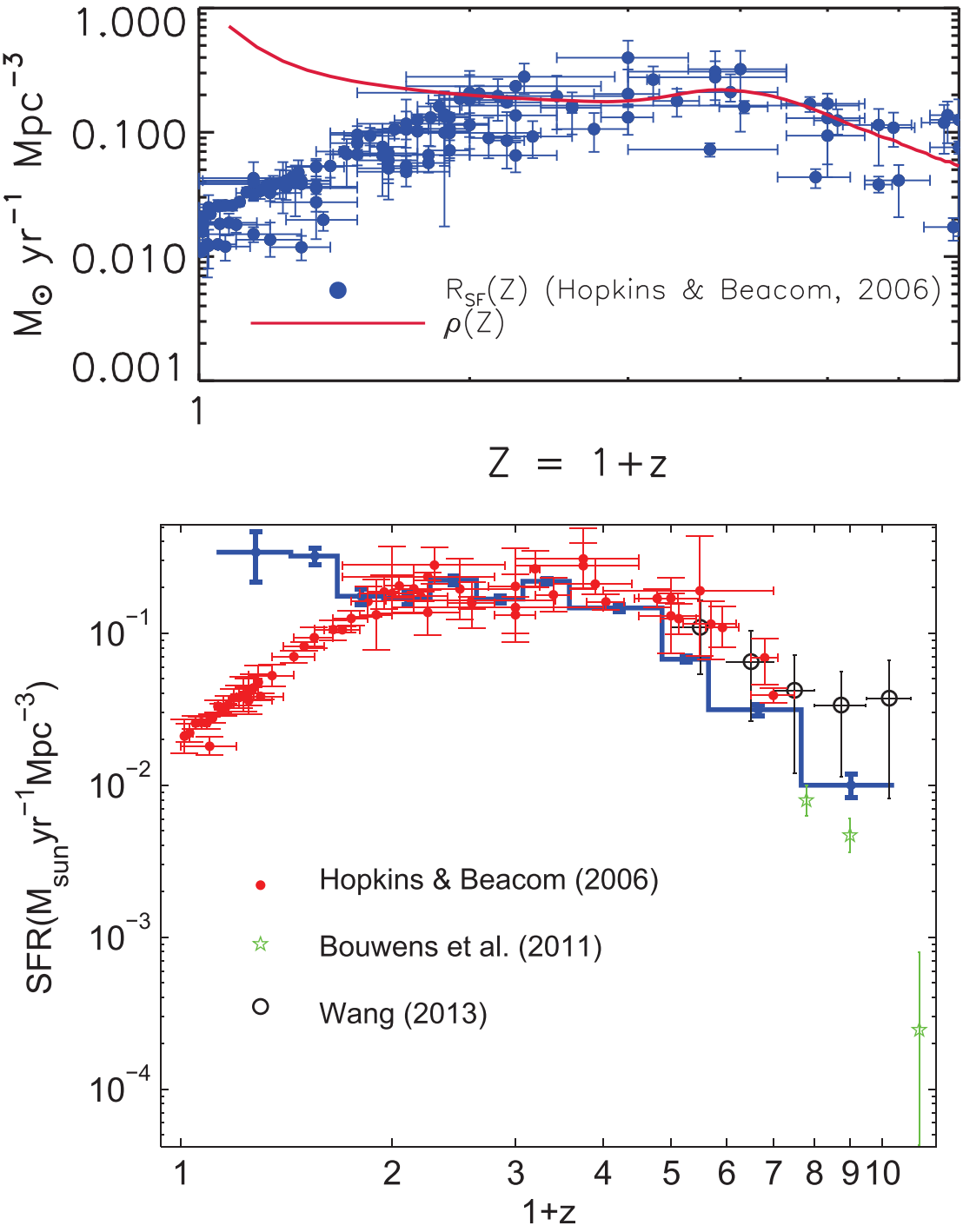

Figure 5.1: *Upper panel*: $\psi(z)$ found by Petrosian et al. (2015, red solid line) compared with the SFR obtained by Hopkins and Beacom (2006, blue points). *Lower panel*: $\psi(z)$ found by Yu et al. (2015a, blue solid line) compared with the SFR obtained by Hopkins and Beacom (2006, red points). The SFR of Bouwens et al. (2011, green stars) and Wang (2013, black open circles) are also shown. All error bars are 1σ error.

to the original BAT6 complete sample. Once the de–evolved luminosities $L_0 = L/(1+z)^k$ have been defined for every GRBs in the BAT6ext sample, I could apply the Lynden–Bell C^- method to derive the cumulative luminosity function $\Phi(L_0)$ and the cumulative redshift distribution $\zeta(z)$. In this case, since the BAT6 sample was selected according to the limiting flux computed in the observer frame *Swift*/BAT $[15-150]$ keV energy band, $L_{\rm lim}$ and $z_{\rm max}$ are computed by adopting for each GRB its own spectrum and applying the corresponding K–correction. Despite this approach introduces a small scatter in the cut in the $L-z$ plane (which means a non–unique equivalent bolometric limiting flux), it has a very small impact in the computation of $L_{\rm lim}$ and $z_{\rm max}$ and, consequently, in the definition of sub–set J and J' (see Sec.4.1 in Chp.4).

From the cumulative functions obtained through the C^- it is possible to derive the cosmic GRB formation rate as:

$$\psi(z) = \frac{d\zeta(z)}{dz}(1+z)\left[\frac{dV(z)}{dz}\right]^{-1} \tag{5.1}$$

where $dV(z)/dz$ is the differential comoving volume. The differential luminosity function $\phi(L_0)$ can be obtained simply deriving the cumulative one. These two functions, normalized to their maximum, are shown in Fig.5.2.

The best–fit model for the LF (green dashed line in Fig.5.2 – right panel) is represented by a broken power–law function with $a = 1.32 \pm 0.21$, $b = 1.84 \pm 0.24$, $L_{\rm b} = 10^{51.45\pm0.15}$ erg/s (where a and b represent the slopes of the power–law above and below the break luminosity $L_{\rm b}$ – $\chi^2/{\rm d.o.f.} = 0.47$). In Fig.5.2 is also shown, for comparison, the luminosity function derived in Salvaterra et al. (2012) assuming pure luminosity evolution ($a = 0.74^{+1.42}_{-1.36}$, $b = 1.92^{+0.14}_{-0.11}$, $L_{\rm b} = 5.5^{+6.9}_{-3.4} \times 10^{50}$ erg/s). The GRBFR (black symbols in Fig.5.2 – left panel) increases from low redshifts to higher values, peaking at $z \sim 2$ and decreases at higher redshifts. This trend is consistent with the shape of the SFR of Hopkins and Beacom (2006, green dashed line) and Cole et al. (2001, cyan dotted–dashed line) and also with the independent estimates obtained through host galaxy studies.

The result regarding $\psi(z)$ is in contrast with the GRBFR recently found by P15 and Y15, who report the existence of an excess of low redshift GRBs when applying the same C^- method but to differently selected GRB samples. Therefore, the reason of this inconsistency

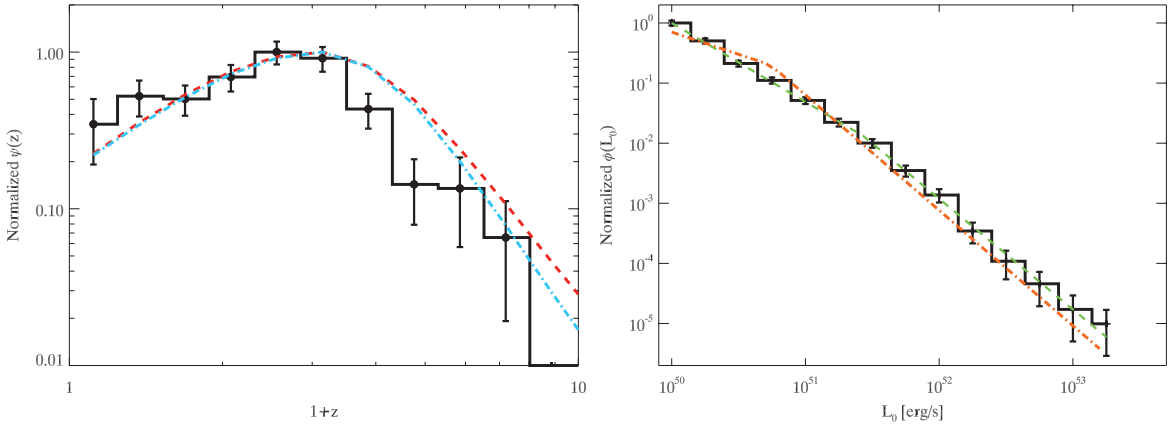

Figure 5.2: *Left panel:* GRB formation rate $\psi(z)$ obtained with the C^- method using the BAT6ext sample (black solid line). The dashed red line and the dot–dashed cyan line are the SFR models of Hopkins and Beacom (2006) and Cole et al. (2001) shown here for reference. All the curves are normalized to their maxima. *Right panel*: luminosity function $\phi(L_0)$ obtained with the C^- method using the BAT6ext sample (black solid line). The best fit model describing this function is a broken power–law (dashed green line) with ($a = 1.32 \pm 0.21$, $b = 1.84 \pm 0.24$, $L_b = 10^{51.45 \pm 0.15}$ erg/s). The orange dot–dashed line is the luminosity function obtained by Salvaterra et al. (2012) in the case of pure luminosity evolution.

should be searched in the definition of their samples. Both used GRBs detected by *Swift* with measured redshifts. However, while Y15 worked with the bolometric luminosity of GRBs, P15 adopted the luminosity calculated in the *Swift*/BAT $[15 - 150]$ keV energy band. Y15 used all GRBs detected by *Swift* with a measured redshift and well constrained spectral parameters (from *Fermi*/GBM and *Konus*/Wind spectra). Despite the number of objects in their sample is relatively large (127), their sample is highly incomplete in flux. In fact, they used as limiting flux the lowest of the bolometric fluxes in their sample ($F_{\rm lim} = 2 \times 10^{-8}$ erg cm^{-2} s^{-1}) resulting in a completeness $\sim$ 15%. P15 account for incompleteness by cutting their sample to a relatively large flux level ($F_{\rm lim} = 2 \times 10^{-8}$ erg cm^{-2} s^{-1}, as Y15 for coincidence), at the expense of the total number of bursts, i.e. working with 207 out of 253 events with measured z. Despite this the completeness in flux of their sample is $\sim$ 25%.

The BAT6ext sample is by definition complete in flux and has a higher completeness in redshift ($\sim$ 82%) which is, however, smaller than the completeness in redshift of the revised BAT6 ($\sim$ 97%). For this reason I checked if this slightly lower completeness could in some way affect the shape of $\psi(z)$. I computed the $\psi(z)$ using only

the 56 objects of the revised BAT6 sample. It turns out to be slightly steeper both at low and high redshifts than the one obtained with the BAT6ext, but it is totally consistent within the errors. It is possible to conclude from this simple test that the lower completeness in redshift of the BAT6ext does not introduce any strong bias in the obtained $\psi(z)$ and $\phi(L_0)$. Moreover, all these results tell us that the C^- method can correctly recover the LF and the GRBFR but only if the sample of GRBs it is applied to is complete in flux and has a high level of completeness in redshift. Using incomplete samples, the resulting GRBFR and LF can turn out different from the real ones.

5.1 Monte Carlo test of the C^- method

We tested the C$^-$ method used to derive $\psi(z)$ and $\phi(L_0)$. Through a Monte Carlo simulation (similar to e.g. Ghirlanda et al., 2015b) we explore how well the method adopted above can recover the input assumptions, i.e. the parent GRBFR $\psi(z)$ and LF $\phi(L)$. In particular, we show that if the used sample is highly incomplete, the resulting GRBFR and LF can differ significantly from those that were input. In particular, incomplete samples (either in flux and/or redshift) may produce a misleading excess of low redshift GRBs with respect to the assumed $\psi(z)$.

We simulate GRBs that are distributed in redshift according to the GRB formation rate $\psi(z)$ of Li (2008, see also Hopkins and Beacom 2006):

$$\psi(z) = \frac{0.0157 + 0.118z}{1 + (z/3.23)^{4.66}} \tag{5.2}$$

where $\psi(z)$, in units of $M_\odot$ yr^{-1} Mpc^{-3}, represents the formation rate of GRBs and we assume it can extend to $z \leq 10$. We stress that for the scope of the present test any other functional form of $\psi(z)$ could be assumed.

We adopt a luminosity function $\phi(L)$, as obtained by Salvaterra et al. (2012), from a complete sample of *Swift* GRBs:

$$\phi(L) \propto \begin{cases} \left(\frac{L}{L_\mathrm{b}}\right)^a & , L \leq L_\mathrm{b} \\ \left(\frac{L}{L_\mathrm{b}}\right)^b & , L > L_\mathrm{b} \end{cases} \tag{5.3}$$

composed of two power laws with a break atL_b. We adopt arbitrary parameter values: $a = -1.2$, $b = -1.92$ and $L_\mathrm{b} = 5 \times 10^{50}$

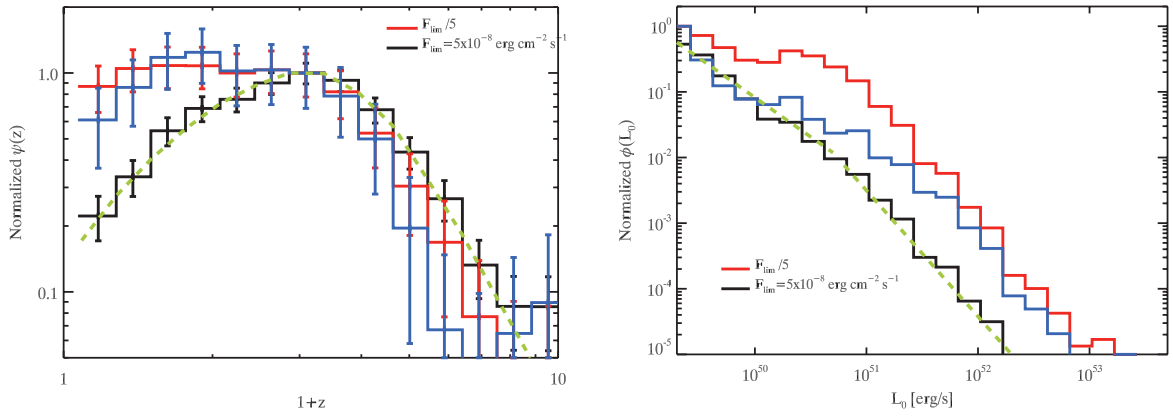

Figure 5.3: *Left panel*: GRB formation rate (normalized to its peak) for the simulated population of GRBs with flux limit 5×10^{-8} erg cm^{-2} s^{-1} (black symbols). The GRB formation rate assumed in the simulation is shown by the dashed green line. The red symbols show the results obtained from the same sample using, for the analysis, a flux limit factor of 5 smaller than the real one. Blue symbols are obtained by mimicking the sample incompleteness by removing some GRBs randomly near the flux threshold adopted for the sample selection. *Right panel*: cumulative luminosity function, normalized to the first bin. The black, red, and blue symbols are the same as for the left panel. The assumed luminosity function is shown by the dashed green line.

erg/s. We further assume an evolution in the luminosity proportional to $(1+z)^k$ with $k = 2.2$. Here, L is the bolometric luminosity of the simulated bursts, and therefore $L/4\pi d_L^2(z)$ is the corresponding bolometric flux. For this reason we do not need to assume any spectral shape for the simulated GRBs to obtain the values of $L_{\rm lim}$ and $z_{\rm max}$. Also for $\phi(L)$ we use this functional form but any other function could be assumed for the scope of the present test. With these two assumptions, we simulate a sample of GRBs with a flux limit $F_{\rm lim} = 5 \times 10^{-8}$ erg cm^{-2} s^{-1} and we analyze it with the C^- method. Accounting for the truncation of the sample, we recover the luminosity evolution in the form $(1+z)^k$, with $k \sim 2.2$, using the statistical method of Efron and Petrosian (1992). Then we work with the de–evolved GRB luminosities $L_0 = L/(1+z)^2.2$ and derive the GRB formation rate $\psi(z)$ and the luminosity function $\phi(L_0)$ through the C^- method proposed by Lynden-Bell (1971). The left–hand panel of Fig.5.3 shows that we recover the GRB formation rate adopted in the simulation (Eq.5.2 – green dashed line). Similarly, the right–hand panel of Fig.5.3 shows that we also recover the luminosity function that we adopted in the simulated sample (Eq.5.3 – dashed green line).

We then tested what happens if we apply the same method to an incomplete sample. Firstly we applied the C^- method to the same simulated sample, which is built to be complete to $F_{\rm lim} = 5 \times 10^{-8}$ erg cm^{-2} s^{-1}, from which we randomly removed a fraction of the bursts close to $F_{\rm lim}$. This new sample is clearly incomplete to $F_{\rm lim}$. The results are shown in Fig.5.3. We find that the GRB formation rate $\psi(z)$ is flat at low redshifts (i.e. below $z = 2$), which shows a clear excess with respect to the assumed function. The luminosity function is flatter than the assumed one (see the right–hand panel of Fig.5.3). Similar results were obtained by assuming for the derivation of $\psi(z)$ and $\phi(L_0)$ a flux limit which is a factor of five smaller than that used to construct the simulated sample, which is an- other way to make the sample artificially incomplete. The results are shown in the panels of Fig.5.3. We note that in this second test, the sample used is the same but it is analyzed through the C^- method, assuming it is complete with respect to a flux limit which is smaller (a factor of five) than the one corresponding to its real completeness (i.e. 5×10^{-8} erg cm^{-2} s^{-1}). These simulations show that if the samples adopted are highly incomplete in flux, an excess at the low redshift end of the GRB formation rate and a flatter luminosity function are obtained.

5.2 The BAT6ext complete sample

The BAT6 complete sample as defined in Salvaterra et al. (2012) was composed of 58 Swift GRBs with (i) optimal orientation in the sky and favourable observing conditions for their redshift determination as proposed in Jakobsson et al. (2006):

- well localized by *Swift*/XRT
- low Galactic extinction ($A_V < 0.5$)
- GRB declination $-70^\circ < \delta < 70^\circ$
- Sun–to–field distance $\theta_{\rm sun} > 55^\circ$
- no nearby bright star

and (ii) a peak photon flux $P \geq 2.6$ ph cm^{-2} s^{-1} (integrated over the $[15 - 150]$ keV *Swift*/BAT energy band). This sample, which is complete in flux by definition, after selection turned out to be also highly complete ($\sim$ 90%) in redshift (i.e. 52 out of 58 bursts have z). The study of the isotropic equivalent luminosity L of the bursts of the

BAT6 sample requires the knowledge of their broad–band prompt emission spectrum. Nava et al. (2012) collected 46 out of 52 GRBs, within the BAT6, with well constrained $E_{\rm p}$ and z. The remaining six bursts with measured z did not have $E_{\rm p}$ measurements. One of the main drawbacks of the narrow/soft energy range of the BAT instrument is the difficulty in measuring the peak $E_{\rm p}$ of the $\nu F(\nu)$ spectrum for the several bursts it detects. Other instruments (e.g. *Konus*/*Wind* – Aptekar et al. (1995), *Fermi*/GBM – Meegan et al. (2009) or *Suzaku*/WAM – Yamaoka et al. (2009)) compensate for this deficiency, by means of their wide energy range, and measuring a spectrum that extends from few keV to several MeV.

Sakamoto et al. (2009) showed that for *Swift* bursts with measured $E_{\rm p}$ there is a correlation between the slope of the spectrum $\alpha_{\rm PL}$ (when fitted with a single power–law model) and the peak energy $E_{\rm p}$ (measured by fitting a curved model). With the aim of enlarging the sample of Nava et al. (2012), I estimated the $E_{\rm p}$ of those six bursts of the BAT6, whose BAT spectrum is fitted by a single power law, through this relation. I also verified that estimates $E_{\rm p}$ were consistent with those of the other bursts (I performed the K–S test finding a probability of $\sim 70\%$ that the two sets of peak energies originate from the same distribution). I found that all but one GRB, i.e. 070306, have $E_{\rm p}^{\rm rest} = E_{\rm p}^{\rm obs}(1+z)$, which is consistent with the upper/lower limit reported in Nava et al. (2012). Therefore, I was the first to extend the number of burst with measured z and L in the original BAT6 sample to 50 out of 58 bursts.

Since the construction of the BAT6 on 2012, other bursts that satisfy its selection criteria were detected by *Swift*. Moreover, some bursts that were already present in the original BAT6 sample were re–analyzed and either their redshifts and/or their spectral properties were revised. Therefore, the first aim was to revise the BAT6 sample. In particular, the revision of eight redshifts is included in the revised sample (marked in *italics* in the table – with their luminosity updated). The revised BAT6 sample then contains 56 out of 58 GRBs with measured z and 54 out of 58 that also have a bolometric isotropic luminosity L. Taking only the redshift into consideration, the sample is $\sim 97\%$ complete while, if the knowledge of L is also required, the completeness level is only slightly smaller ($\sim 93\%$).

Then, I extended the BAT6 revised sample with new events that have been detected since 2012, and which satisfy the same selection criteria of the burst already present in the sample. The extended

sample contains 99 GRBs. Spectral parameters of the new GRBs have been collected in the existing literature. For events (6 out of 41 bursts) with only a *Swift* single power–law spectrum, I estimated $E_{\rm p}$ through the Sakamoto et al. (2009) relation. The BAT6 extended (BAT6ext) counts 82 out of 99 GRBs with z (and 81 out of 99 with z and L). Its completeness in redshift is $\sim 82\%$.

The BAT6ext is presented in Tab.5.1. The first 58 bursts are the original BAT6, while the others constitute the extension. For each GRB, Tab.5.1 shows the redshift z, the spectral parameters (high and low photon indexes α and β, and the rest frame peak energy $E_{\rm p}$), the peak flux with the relative energy band, and the isotropic equivalent luminosity L. The spectrum is a cut–off power–law (CPL) if only the low energy photon index α is reported and a band function, if the high energy photon index β is also given. When z is not measured, we report the observed peak energy. The luminosities reported in the table are only calculated in the $[1 - 10^4]$ keV rest frame energy range for those GRBs having both z and $E_{\rm p}$.

Table 5.1: BAT6ext (BAT6 extended) GRB complete sample. Columns report, in order, the redshift z, the spectral photon indices α and β, the peak flux in units of 10^{-7} erg cm^{-2} s^{-1} (except for those with the * which are in units of photons cm^{-2} s^{-1}), the respective energy band, the rest-frame peak energy $E_{\rm p}$ and the bolometric equivalent isotropic luminosity L (calculated in the $[1-10^4]$ rest-frame energy range). For L we also give the 1σ error. [b] Bursts with missing z are reported with their observer frame $E_{\rm p}^{\rm obs}$ for completeness, they are not used in the present work. [c] The peak energy has been estimated with the relation of Sakamoto et al. (2009). The eight GRBs (already present in the compilation of Nava et al. 2012) with an updated redshift estimate are marked in italics. In the last column we report the references, in order, for the spectral parameters and for the redshift: 1) Nava et al. (2012), 2) Covino et al. (2013), 3) Krühler et al. (2015), 4) GCN#12133, 5) GCN#12135-12137, 6) GCN#12190, 7) GCN#12352, 8) GCN#12424, 9) GCN#12431, 10) GCN#12749, 11) GCN#12761, 12) GCN#12801, 13) GCN#12839, 14) GCN#12874, 15) GCN#12865, 16) GCN#13120, 17) GCN#13118, 18) GCN#13412, 19) GCN#13536, 20) GCN#13532, 21) GCN#13559, 22) GCN#13562, 23) GCN#13634, 24) GCN#13628, 25) GCN#13721, 26) GCN#13723, 27) GCN#13990, 28) GCN#13992, 29) GCN#13997, 30) GCN#14052, 31) GCN#14419, 32) GCN#14437, 33) GCN#14487, 34) GCN#14491, 35) GCN#14469, 36) GCN#14493, 37) GCN#14545, 38) GCN#14575, 39) GCN#14567, 40) GCN#14720, 41) GCN#14808, 42) GCN#14796, 43) GCN#14869, 44) GCN#14959, 45) GCN#14956, 46) GCN#15064, 47) GCN#15145, 48) GCN#15144, 49) GCN#15203, 50) GCN#15187, 51) GCN#15413, 52) GCN#15407, 53) GCN#15452, 54) GCN#15450, 55) GCN#15669, 56) GCN#15805, 57) GCN#15800, 58) GCN#15853, 59) GCN#16134, 60) GCN#16125, 61) GCN#16220, 62) GCN#16217, 63) GCN#16262, 64) GCN#16310, 65) GCN#16423, 66) GCN#16473, 67) GCN#16495, 68) GCN#16489, 69) GCN#16512, 70) GCN#16505.

GRB	z	$\alpha[\beta]$	Peak flux 10^{-7} erg cm^{-2} s^{-1} * phot cm^{-2} s^{-1}	Range (keV)	$E_{\rm p}$ (keV)	L ($\times 10^{51}$ erg/s)	Ref
050318	1.44	-1.34 ± 0.32	2.20 ± 0.17	$[15-150]$	115 ± 27	4.76 ± 0.86	1,1
050401	2.9	$-1.0[-2.45]$	24.5 ± 1.2	$[20-2000]$	499 ± 117	201 ± 11	1,1
050416A	0.653	$-1.0[-3.4]$	$5.0 \pm 0.5^\star$	$[15-150]$	26 ± 4	0.97 ± 0.12	1,1
050525A	0.606	-0.99 ± 0.11	$47.7 \pm 1.2^\star$	$[15-350]$	127 ± 6	7.24 ± 0.28	1,1
050802[c]	1.71	-1.6 ± 0.1	2.21 ± 0.35	$[15-150]$	301	9.51 ± 1.71	1,1
050922C	2.198	-0.83 ± 0.24	45 ± 7	$[20-2000]$	416 ± 118	187 ± 30	1,1
060206	4.048	-1.12 ± 0.30	2.02 ± 0.13	$[15-150]$	409 ± 116	49.6 ± 7.1	1,1
060210	3.91	-1.12 ± 0.26	$2.8 \pm 0.3^\star$	$[15-150]$	574 ± 187	52.8 ± 11.1	1,1
060306	1.55	-1.2 ± 0.5	4.71 ± 0.28	$[15-150]$	178.5 ± 76.5	11.49 ± 2.26	1,2
060614	0.125	-1.5	$11.6 \pm 0.7^\star$	$[15-150]$	55 ± 45	0.05 ± 0.01	1,1
060814	1.92	-1.43 ± 0.16	21.3 ± 3.5	$[20-1000]$	750 ± 245	71.7 ± 13.1	1,1
060904A	–	-1.22 ± 0.05	13 ± 3	$[20-10\,000]$	235 ± 25[b]	–	1,1
060908	1.88	-0.93 ± 0.25	2.81 ± 0.23	$[15-150]$	426 ± 207	12.7 ± 3.1	1,1
060912A[c]	0.94	-1.85 ± 0.08	25 ± 9	$[20-10\,000]$	127	20.6 ± 7.4	1,1
060927	5.47	-0.81 ± 0.36	2.47 ± 0.17	$[15-150]$	459 ± 90	108.7 ± 13.1	1,1
061007	1.261	-0.75 ± 0.02 $[-2.79 \pm 0.09]$	120 ± 10	$[20-10\,000]$	965 ± 27	109.2 ± 8.9	1,1
061021	0.346	-1.22 ± 0.13	37.2 ± 9.3	$[20-2000]$	1046 ± 485	1.77 ± 0.46	1,1

GRB	z	$\alpha[\beta]$	Peak flux 10^{-7} erg cm^{-2} s^{-1} * phot cm^{-2} s^{-1}	Range (keV)	E_p (keV)	L ($\times 10^{51}$ erg/s)	Ref
061121	1.314	-1.32 ± 0.05	128 ± 17	$[20-5000]$	1402 ± 185	142 ± 19	1,1
061222A	2.09	-1.00 ± 0.05	48 ± 13	$[20-10\,000]$	1091 ± 167	140 ± 38	1,1
		$[-2.32 \pm 0.38]$					
070306[c]	1.50	-1.67 ± 0.1	3.04 ± 0.16	$[15-150]$	> 263	> 9.99	1,1
070328	2.063	-1.11 ± 0.04	59 ± 12	$[20-10\,000]$	2349	157.6 ± 37.6	1,3
		$[-2.33 \pm 0.24]$					
070521	2.087	-0.93 ± 0.12	41.2 ± 9.1	$[20-1000]$	685.6 ± 73.6	144.1 ± 32.6	1,3
071020	2.145	-0.65 ± 0.29	60.4 ± 20.8	$[20-2000]$	1013 ± 204	213 ± 73	1,1
071112C[c]	0.82	-1.09 ± 0.07	$8.0 \pm 1.0^\star$	$[15-150]$	596	6.57 ± 0.86	1,1
071117	1.331	-1.53 ± 0.15	66.6 ± 18.3	$[20-1000]$	648 ± 317	95.4 ± 28.4	1,1
080319B	0.937	-0.86 ± 0.01	226 ± 21	$[20-7000]$	1307 ± 43	101.6 ± 9.4	1,1
		$[-3.59 \pm 0.45]$					
080319C	1.95	-1.20 ± 0.10	33.5 ± 7.4	$[20-4000]$	1752 ± 504	96.1 ± 21.7	1,1
080413B	1.10	-1.23 ± 0.25	14.0 ± 0.6	$[15-150]$	163 ± 34	14.9 ± 1.8	1,1
080430[c]	0.77	-1.73 ± 0.08	1.82 ± 0.13	$[15-150]$	149	1.16 ± 0.13	1,1
080602[c]	1.820	-0.96 ± 0.63	19.2 ± 5.8	$[20-1000]$	1216	51 ± 17	1,3
080603B	2.69	-1.23 ± 0.64	15.1 ± 3.9	$[20-1000]$	376 ± 214	116.6 ± 38.9	1,1
080605	1.64	-1.03 ± 0.07	160 ± 33	$[20-2000]$	665 ± 48	308.7 ± 62.8	1,1
080607	3.036	-1.08 ± 0.06	269 ± 54	$[20-4000]$	1691 ± 169	2260 ± 446	1,1
080613B	–	-1.05 ± 0.18	47.6 ± 13.1	$[20-3000]$	33 ± 239[b]	–	1,1
080721	2.591	-0.96 ± 0.07	211 ± 35	$[20-7000]$	1785 ± 223	1039 ± 173	1,1
		$[-2.42 \pm 0.29]$					
080804	2.20	-0.72 ± 0.04	7.30 ± 0.88	$[8-35\,000]$	810 ± 45	27.0 ± 3.2	1,1
080916A	0.689	-0.99 ± 0.05	4.87 ± 0.27	$[8-35\,000]$	208 ± 11	1.08 ± 0.06	1,1
081007	0.53	-1.4 ± 0.4	$2.2 \pm 0.2^\star$	$[25-900]$	61 ± 15	0.43 ± 0.09	1,1
081121	2.512	-0.46 ± 0.08	51.7 ± 8.3	$[8-35\,000]$	608 ± 42	195.4 ± 33.7	1,1
		$[-2.19 \pm 0.07]$					
081203A	2.10	-1.29 ± 0.14	$2.9 \pm 0.2^\star$	$[15-150]$	1541 ± 756	28.3 ± 8.9	1,1
081221	2.26	-0.83 ± 0.01	24.2 ± 0.5	$[8-35\,000]$	284 ± 2	101 ± 2	1,3
081222	2.77	-0.90 ± 0.03	17.6 ± 0.58	$[8-35\,000]$	630 ± 31	95 ± 6	1,1
		$[-2.33 \pm 0.10]$					
090102	1.547	-0.97 ± 0.01	29.3 ± 0.91	$[8-35\,000]$	1174 ± 38	45.7 ± 1.4	1,1
090201	2.1	-0.97 ± 0.09	73.0 ± 12.6	$[20-2000]$	489.8	269.5 ± 47.6	1,2
		$[-2.80 \pm 0.52]$					
090424	0.544	-1.02 ± 0.01	91.2 ± 1.4	$[8-35\,000]$	250.0 ± 3.4	11.16 ± 0.18	1,1
		$[-3.26 \pm 0.18]$					
090709A	1.8	-0.85 ± 0.08	39 ± 6	$[20-3000]$	834.4	91.9 ± 13.9	1,2
		$[-2.7 \pm 0.24]$					
090715B	3.00	-1.1 ± 0.37	9.0 ± 2.5	$[20-2000]$	536 ± 164	82.6 ± 25.2	1,1
090812	2.452	-1.03 ± 0.07	$2.77 \pm 0.28^\star$	$[100-1000]$	2023 ± 663	96.3 ± 16.0	1,1
090926B	1.24	-0.19 ± 0.06	4.73 ± 0.28	$[8-35\,000]$	212.0 ± 4.3	4.28 ± 0.25	1,1
091018	0.971	-1.53 ± 0.48	4.32 ± 0.95	$[20-1000]$	55 ± 26	4.75 ± 1.33	1,1
091020	1.71	-1.20 ± 0.06	18.8 ± 2.6	$[8-35\,000]$	507 ± 68	32.7 ± 5.2	1,1
		$[-2.29 \pm 0.18]$					
091127	0.49	-1.25 ± 0.05	93.8 ± 2.3	$[8-35\,000]$	51.0 ± 1.5	9.09 ± 0.24	1,1
		$[-2.22 \pm 0.01]$					
091208B	1.063	-1.29 ± 0.04	25.6 ± 0.97	$[8-35\,000]$	246 ± 15	17.5 ± 0.7	1,1
100615A	1.4	-1.24 ± 0.07	$8.3 \pm 0.2^\star$	$[8-1000]$	206.4 ± 20.4	10.15 ± 0.87	1,2
		$[-2.27 \pm 0.11]$					
100621A	0.542	-1.70 ± 0.13	17.0 ± 1.3	$[20-2000]$	146 ± 23	3.17 ± 0.34	1,1
		$[-2.45 \pm 0.15]$					
100728B	2.106	-0.90 ± 0.07	5.43 ± 0.35	$[8-35\,000]$	404 ± 29	18.7 ± 1.3	1,1
110205A	2.22	-1.52 ± 0.14	5.1 ± 0.7	$[20-1200]$	715 ± 238	25.1 ± 4.3	1,1
110503A	1.613	-0.98 ± 0.08	100 ± 10	$[20-5000]$	572 ± 50	180.7 ± 19.7	1,1
		$[-2.7 \pm 0.3]$					
110709A	–	-1.16 ± 0.02	$15.4 \pm 1.7^\star$	$[10-1000]$	533 ± 37[b]	–	4,–
110709B	< 4	$-1.0^{+0.14}_{-0.13}$	11 ± 1	$[20-5000]$	$278^{+43\,\mathrm{b}}_{-32}$	–	5,6
110915A	–	-0.94 ± 0.23	$3.3 \pm 0.2^\star$	$[15-150]$	124.8 ± 41.4[b]	–	7,–
111008A[c]	4.989	-1.86 ± 0.09	$6.4 \pm 0.7^\star$	$[15-150]$	384	303.3 ± 48.8	8,9
111228A[c]	0.715	$-1\,[-2.27 \pm 0.06]$	$12.4 \pm 0.5^\star$	$[15-150]$	46	3.64 ± 0.27	10,11

GRB	z	$\alpha[\beta]$	Peak flux 10^{-7} erg cm^{-2} s^{-1} * phot cm^{-2} s^{-1}	Range (keV)	$E_{\rm p}$ (keV)	L ($\times 10^{51}$ erg/s)	Ref
120102A	–	-1.19 ± 0.03	$22.8 \pm 1.6^\star$	$[10-1000]$	$380 \pm 33^{\rm b}$	–	12,–
120116A	–	-1.31 ± 0.41	$4.1 \pm 0.3^\star$	$[15-150]$	–	–	13,–
120119A	1.728	-0.98 ± 0.03 $[-2.36 \pm 0.09]$	$16.9 \pm 0.4^\star$	$[10-1000]$	189.2 ± 8.3	56.9 ± 2.7	14,15
120326A	1.798	-1.41 ± 0.34	$4.6 \pm 0.2^\star$	$[15-150]$	115 ± 19	10.8 ± 1.8	16,17
120703A	–	$-0.81^{+0.3}_{-0.25}$	54 ± 13	$[20-10\,000]$	$295^{+88\,\rm b}_{-56}$	–	18,–
120729A[c]	0.8	-1.62 ± 0.08	$2.9 \pm 0.2^\star$	$[15-150]$	192	1.27 ± 0.11	19,20
120802A	3.796	-1.21 ± 0.47	$3.0 \pm 0.2^\star$	$[15-150]$	274.3 ± 93.0	40.7 ± 5.7	21,22
120811C	2.671	-1.4 ± 0.3	$4.1 \pm 0.2^\star$	$[15-150]$	157.5 ± 20.9	25.4 ± 4.5	23,24
120907A	0.97	-0.75 ± 0.25	$4.3 \pm 0.4^\star$	$[10-1000]$	304.4 ± 64.8	2.45 ± 0.27	25,26
121123A	2.7	-0.96 ± 0.2	2.6 ± 0.2	$[15-150]$	240.5 ± 18.9	14.9 ± 1.4	27,28
121125A	–	-1.38 ± 0.06	4.2 ± 0.3	$[10-1000]$	$196 \pm 26^{\rm b}$	–	29,–
121209A[c]	2.1	-1.43 ± 0.08	$3.4 \pm 0.3^\star$	$[15-150]$	494	17.4 ± 1.6	30,3
130420A	1.297	-1.52 ± 0.25	$3.4 \pm 0.2^\star$	$[15-150]$	76.3 ± 15.6	3.77 ± 0.65	31,32
130427A	0.339	-0.958 ± 0.006 $[-4.17 \pm 0.16]$	6900 ± 100	$[20-1200]$	1371.3 ± 10.7	384.1 ± 5.7	33,34
130427B[c]	2.78	-1.64 ± 0.15	3.0 ± 0.4	$[15-150]$	386	29 ± 5	35,36
130502A	–	-1.0 ± 0.3	7 ± 1	$[8-1000]$	$83 \pm 17^{\rm b}$	–	37,–
130505A	2.27	-0.69 ± 0.04 $[-2.03 \pm 0.03]$	690 ± 30	$[20-1200]$	2063.4 ± 101.4	3959 ± 172	38,39
130527A	–	1.04 ± 0.04	500 ± 30	$[20-10\,000]$	$1380 \pm 120^{\rm b}$	–	40,–
130606A[c]	5.913	-1.14 ± 0.15	$2.6 \pm 0.2^\star$	$[15-150]$	2032	229.5 ± 24.3	41,42
130609B	–	-0.66 ± 0.22 $[-2.6 \pm 0.2]$	$13.6 \pm 0.4^\star$	$[10-1000]$	$491 \pm 20^{\rm b}$	–	43,–
130701A	1.555	-0.9 ± 0.21	17.1 ± 0.7	$[15-150]$	227.9 ± 31.6	28.9 ± 1.5	44,45
130803A	–	0.85 ± 0.09	$7.1 \pm 0.3^\star$	$[10-1000]$	$141.6 \pm 12.2^{\rm b}$	–	46,–
130831A	0.479	-1.61 ± 0.06 $[-3.3 \pm 0.3]$	25 ± 3	$[20-10\,000]$	81.3 ± 5.9	3.68 ± 0.45	47,48
130907A	1.238	-0.91 ± 0.02 $[-2.34 \pm 0.07]$	220 ± 10	$[20-10\,000]$	881.8 ± 24.6	185.6 ± 8.8	49,50
131030A	1.293	-0.71 ± 0.12 $[-2.95 \pm 0.28]$	100 ± 10	$[20-10\,000]$	405.9 ± 22.9	103 ± 11	51,52
131105A	1.686	-0.88 ± 0.38 $[-2.33 \pm 0.33]$	20 ± 2	$[20-10\,000]$	419 ± 102	37.4 ± 4.9	53,54
140102A	–	-0.71 ± 0.02 $[-2.49 \pm 0.07]$	$49.7 \pm 0.5^\star$	$[10-1000]$	$186 \pm 5^{\rm b}$	–	55,–
140206A	2.73	-1.04 ± 0.15	$19.4 \pm 0.5^\star$	$[15-150]$	376.4 ± 54.1	141.5 ± 4.8	56,57
140215A	–	-0.66 ± 0.11 $[-2.94 \pm 0.35]$	35.7 ± 3.5	$[20-10\,000]$	$214 \pm 14^{\rm b}$	–	58,–
140419A	3.956	$-0.63^{+0.36}_{-0.22}$ $[-2.3^{+0.4}_{-2.5}]$	47^{+18}_{-19}	$[20-10\,000]$	1452.1 ± 416.3	572.6 ± 25.2	59,60
140506A	0.889	-0.9 ± 0.2 $[-2.0 \pm 0.1]$	$14.2 \pm 0.7^\star$	$[10-1000]$	266 ± 68	11.5 ± 1.3	61,62
140512A	0.72	-1.33 ± 0.03	$11.0 \pm 0.3^\star$	$[10-1000]$	1011 ± 145	5.28 ± 0.47	63,64
140619A	–	-1.45 ± 0.14	$4.6 \pm 0.2^\star$	$[15-150]$	$117.8 \pm 46.2^{\rm b}$	–	65,–
140628A	–	-1.56 ± 0.09	$2.8 \pm 0.2^\star$	$[15-150]$	–	–	66,–
140629A	2.275	-1.42 ± 0.54	4.7 ± 0.7	$[20-10\,000]$	281.7 ± 57.4	27.1 ± 5.5	67,68
140703A	3.14	-1.10 ± 0.06	$4.1 \pm 0.2^\star$	$[10-1000]$	732.8 ± 58.0	41.6 ± 2.2	69,70

CHAPTER 6

Constraints on the GRB jet structure through the luminosity function – $\phi(L)$

There are clear evidences that lead us to think that the emission of long GRBs is collimated in relativistic jets. There are somehow more observational evidences and theoretical arguments supporting this scenario for long GRBs. The direct measure of the steepening of the afterglow light curve at few days post burst has been interpreted as a signature of the collimated outflow. From the measure of this break time (more often observed in long GRBs than in short – most likely for the different afterglow flux in the two populations) the jet opening angles have been inferred. While long GRBs seem to have a log–normal jet distribution peaked between 3 and 5 degrees, there are fewer estimates of $\theta_{\rm jet}$ for the population of short GRBs. Jets in GRBs are thought to be the most extreme in terms of typical power (10^{50-54} erg/s) and of Lorentz factor ($\Gamma \sim 10^2 - 10^3$).

One compelling question on GRB jets is what is their structure. With "structure" we mean the way the energy and the velocity of the outflow are distributed within the jet. There are two main types of jets: uniform, where both the energy and the bulk Lorentz factor

are constant within the jet aperture $\theta_{\rm jet}$ and a structured jet, where these two properties depend on the angle from the jet axis. Several GRB properties are affected by the jet structure: both the prompt and afterglow emission properties depend on the jet structure having a strong dependence on the relativistic effects induced by the geometry and dynamics of the jet and the energy content. Globally also the luminosity function $\phi(L)$ and the GRB rates are strongly dependent on the intrinsic jet structure. Moreover, the possibility to observe GRBs without (or with a very dim) prompt emission and a late–peaked afterglow (so called orphan afterlgows) depend on the jet structure.

In this chapter I will show how it is possible to get some insight on the still unknown structure of GRBs by studying their luminosity function. For this purpose I used the so–called observed luminosity function, i.e. the LF (at $z = 0$ or not evolving in redshift) normalized at the density of bursts at $z = 0$ (see Sec.6.3). What I have done is to derive, given a specific jet model, the associated expected LF and then I compared it with the LF obtained by observational data. The results presented in this chapter have been published in the papers Pescalli et al. (2015) and Salafia et al. (2015).

6.1 Uniform jet

Understanding the structure of GRB jets is a key step forward in unveiling the origin of jets in these sources. In fact, what is still under intense study is the way jets are lunched from the central engine and collimated (see e.g. Granot, 2007). One of the crucial points in understanding the nature of this phenomena is the geometrical configuration of the outflow . At the beginning, for simplicity and lack of observational evidences, it was assumed that the outflow in GRBs is isotropic. Jets are a common feature of high-energy astrophysical sources powered by accretion on to compact objects, as Active Galactic Nuclei (AGN) and Quasars (QSO). Moreover, The large isotropic equivalent energy $E_{\gamma,\rm iso}$ of the prompt emission can easily exceed a solar mass rest energy, unless the radiation is collimated (Tan et al., 2001). For this reason and by analogy with other kind of sources, the idea that the emission could be collimated was born.

The first evidence was the steepening of the X, Optical and Radio afterglow flux light–curve a few days after the burst. This behavior, is interpreted as due to the collimation of the relativistic outflow.

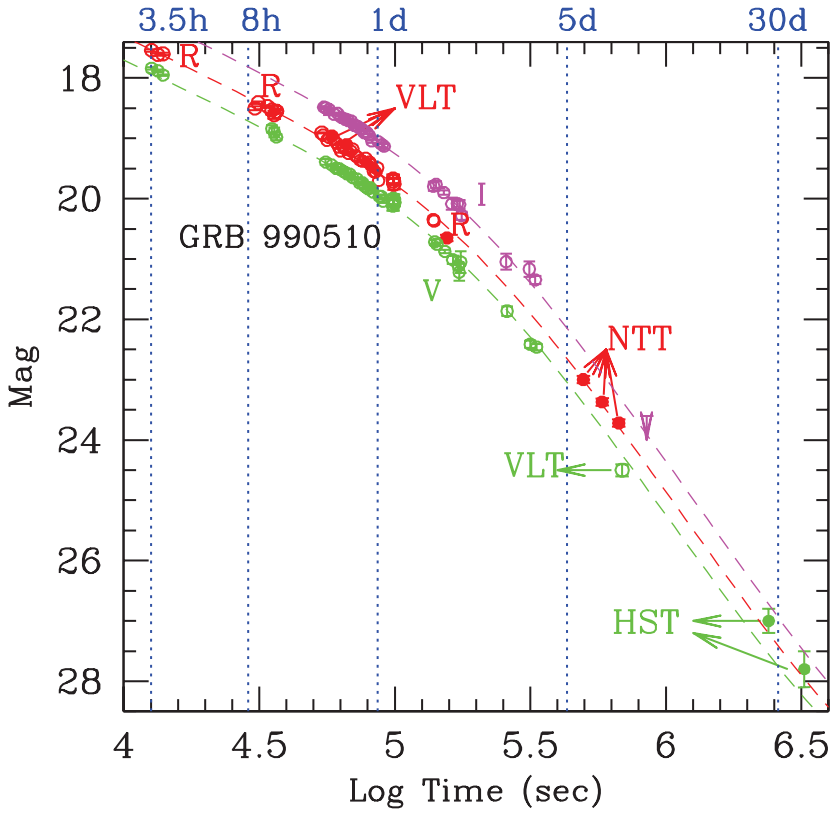

Figure 6.1: Afterglow light–curve of GRB 990510 in band V, R, I. The achromatic steepening can be interpreted as a jet–break.

An example of the so–called achromatic jet–break is given in Fig.6.1 where it is shown the afterglow light–curve (in V, R, I bands) with jet–break of GRB 990510. The fact that the time of the steepening is the same at different frequencies supports the jet–break as due to a geometrical effect.

It has been typically assumed that GRBs have a *Uniform Jet* (UJ): The ejecta are collimated along the black hole rotational axis into a bipolar conical jet of semi–aperture $\theta_{\rm jet}$ (Fig.6.2).

The energy per unit solid angle $\epsilon \equiv dE/d\Omega$ and the ejecta Lorentz factor Γ are constant within the jet and zero outside (sharp–edged jet). Typically, it is assumed that the radiation can be observed only if the viewing angle $\theta_{\rm v} \leq \theta_{\rm jet}$, i.e. if the GRB is pointing towards the observer. Due to the relativistic transformation applied to photons, the radiation is collimated along the direction of motion within an angle $1/\Gamma < \theta_{\rm jet}$. For this reason, it is possible to observe the radiation coming from those element of fireball at an angle θ (with respect to the rotational axis) such that $|\theta - \theta_{\rm v}| \lesssim 1/\Gamma$ (see Fig.6.3). Only a small fraction is then accessible to the observer who

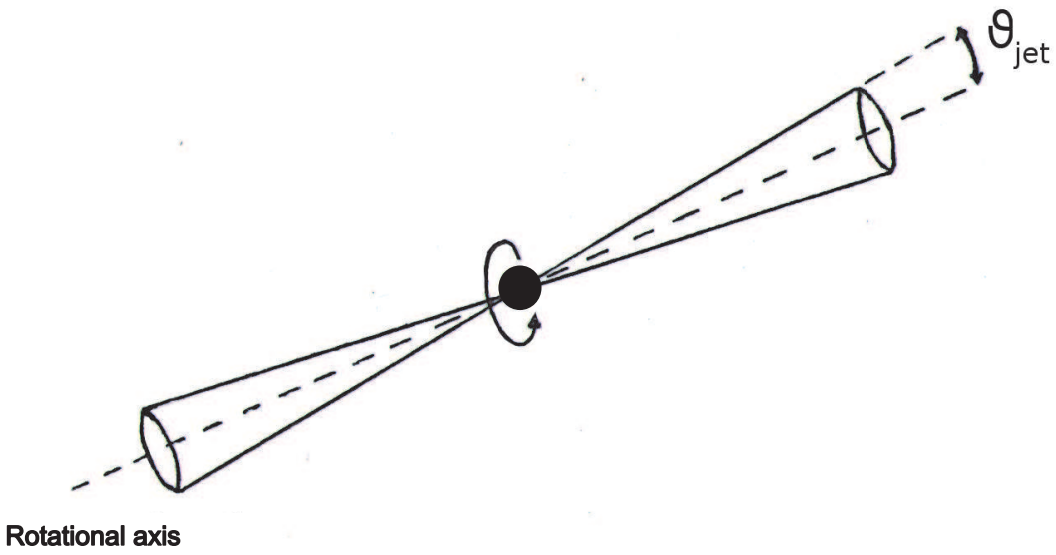

Figure 6.2: caption

cannot distinguish between a collimated jet and a spherical expansion. These assumptions are valid only in the ultrarelativistic case when $\Gamma \gg 1/\theta_{\rm jet}$. During the afterglow phase, when the emission is produced by the deceleration of the relativistic jet by the interstellar medium, Γ decreases allowing to observe an ever larger emitting surface.

Despite in this phase the visible area is increasing, the afterglow light–curve is however decreasing because each point of the fireball is decelerating. When $\Gamma \sim 1/\theta_{\rm jet}$ the contribution given by the increase of the area disappears and a steepening of the afterglow flux is observed (Rhoads, 1997).

According to the UJ model, the energetic released during the burst is smaller than the isotropic estimate because of the collimation. All the radiation that before was supposed to be emitted isotropically (solid angle equal to 4π) is now distributed into a bipolar conical jet whose solid angle is $4\pi(1-\cos(\theta_{\rm jet}))$. The true energy $E_\gamma = E_{\gamma,\rm iso}(1-\cos(\theta_{\rm jet})) \approx E_{\gamma,\rm iso}\theta^2_{\rm jet}$ in the approximation of small opening angle. This correction implies, for an average $\theta_{\rm jet} \sim 0.1$ rad, a reduction of the energetic and luminosity by a factor ~ 100 and a reduction of the dispersion of these quantities for the population of GRBs (Fig.6.8). The beaming factor $f_{\rm b} = (1-\cos(\theta_{\rm jet}))$ also af-

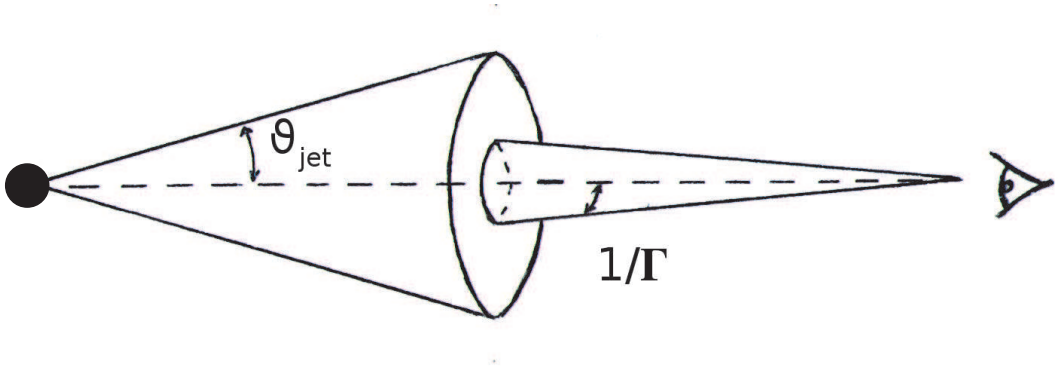

Figure 6.3: caption

fects the rate of events. In the case of isotropic emission, given a sufficiently sensitive instrument, a GRB is always detectable, while within the UJ model we can detect only those bursts pointing towards us. The number of observed burst $N^{\rm obs}$ does not correspond to the number of those effectively exploded in the Universe $N = f_{\rm b} N^{\rm obs}$.

In the following sub–sections I will derive the expected luminosity function associated to the uniform jet.

6.1.1 Uniform jet with unique $\theta_{\rm jet}$ observed on–axis

In the UJ model, one of the main assumptions is that the emission can be seen only if the observer line of sight intercepts the jet aperture angle, i.e. $\theta_{\rm v} \leq \theta_{\rm jet}$. This is valid in the ultrarelativistic approximation when $1/\Gamma \ll \theta_{\rm jet}$. Another important condition is that, to be observed, the jet must emerge from the progenitor star. This implies that the central engine has to provide a minimum energy $E_\star$ as enough to allow the jet to successfully drill through the stellar envelope. In a recent work, Kumar and Smoot (2014) find that such required energy must be at least the energy contained in the cocoon which, based on Mészáros and Rees (2001), can be assumed $\simeq 10^{51}$ erg. Therefore, if the inner engine provides enough energy $E_{\rm kin} > E_\star$, the jet can escape the star and the GRB can be observed. The residual energy $E_{\rm kin} - E_\star$ will be the total energetic reservoir of the burst. The brightest GRBs are those with $E_{\rm kin} \gg E_\star$ while if $E_{\rm kin}$ is only slightly larger than $E_\star$ the burst will be under–luminous.

Let assume that the central engines of GRBs provide a total kinetic energy distributed as a power–law $P(E_{\rm kin}) = dN(E_{\rm kin})/dE_{\rm kin} \propto E_{\rm kin}^{-k}$. Of the energy left after the jet break–out $E_{\rm kin} - E_\star$, only a frac-

tion η can be converted into radiation. The radiative efficiency η is typically a few per cent in the standard internal shock model (Rees and Meszaros, 1994). If $E_\gamma = \eta(E_{\rm kin} - E_\star)$ is the collimated energy that will be converted into radiation, we can define its isotropic equivalent as

$$E_{\rm iso} = \frac{\eta(E_{\rm kin} - E_\star)}{1 - \cos(\theta_{\rm jet})} \tag{6.1}$$

The probability to detect a GRB with isotropic energy $E_{\rm iso}$ is equivalent to the probability to have the inner engine providing the corresponding $E_{\rm kin}$ so we can write

$$P(E_{\rm iso}) = P(E_{\rm kin})\frac{dE_{\rm kin}}{dE_{\rm iso}} \tag{6.2}$$

Assuming a typical duration and that the prompt emission light–curve can be approximated by a triangular shape we can define the isotropic luminosity through the simple relation $E_{\rm iso} \approx (t \times L_{\rm iso})/s$. Then, the LF in the UJ model is

$$\begin{aligned}
\phi(L) &\propto P(L_{\rm kin})\frac{dL_{\rm kin}}{dL_{\rm iso}} \\
&\propto \frac{(1 - \cos(\theta_{\rm jet}))}{\eta} L_{\rm kin}^{-k} \\
&\propto \frac{(1 - \cos(\theta_{\rm jet}))}{\eta} \left[\frac{(1 - \cos(\theta_{\rm jet}))L_{\rm iso}}{\eta} + L_\star\right]^{-k}
\end{aligned} \tag{6.3}$$

where $L_\star$ is the collimation corrected (i.e. true) kinetic luminosity necessary to punch the star, while $L_{\rm iso}$ is the observed, isotropically equivalent radiative luminosity. The latter we obtained is the LF of all bursts including also those ones non detectable, i.e. not pointing to the Earth. In first approximation, if the opening angle is the same for all bursts, we will see only a fraction $(1 - \cos(\theta_{\rm jet}))$, independent from the luminosity. Therefore, the LF of the observed population is

$$\phi(L) \propto \frac{(1 - \cos(\theta_{\rm jet}))^2}{\eta} \left[\frac{(1 - \cos(\theta_{\rm jet}))L_{\rm iso}}{\eta} + L_\star\right]^{-k} \tag{6.4}$$

The luminosity function of the uniform jet has basically two regimes:

$$\phi(L) \propto \begin{cases} const, & L_{\rm iso} \ll \eta L_\star/(1 - \cos(\theta_{\rm jet})) \\ L_{\rm iso}^{-k}, & L_{\rm iso} \gg \eta L_\star/(1 - \cos(\theta_{\rm jet})) \end{cases} \tag{6.5}$$

When the inner engine provides a collimated kinetic luminosity $L \gg L_\star$ it will produce successful GRBs that build up the power–law behavior of the LF, otherwise for $L \simeq L_\star$, the LF becomes flat under a characteristic equivalent isotropic luminosity. The transition between these two regimes corresponds to the characteristic luminosity $L_{\rm iso} \sim \eta L_\star/(1-\cos(\theta_{\rm jet}))$.

Bromberg et al. (2012) derived similar consequences concerning the GRB duration distribution adopting the same arguments. If the central engine lasts much longer than the time necessary for the jet to drill through the star (break–out time), the resulting GRB will be a long one. If the central engine duration is comparable to the break–out time, but slightly longer, the GRB will be short and the time distribution results flat below the characteristic time.

6.1.2 Uniform Jet with luminoisty dependent aperture $\theta_{\rm jet}(L)$ observed on–axis

In the last subsection we assumed that all GRBs have the same jet angle. However, there is the possibility that the different luminosities we observe are in some way linked to the dimension of the jet in which the inner engine injects the energy. In this case one should expect an anti–correlation between $L_{\rm iso}$ and $\theta_{\rm jet}$. Indeed, it has been shown that such a relation exists for GRBs with measured $\theta_{\rm jet}$ (e.g. Lloyd-Ronning et al., 2004; Firmani et al., 2005; Ghirlanda et al., 2005).

The peak energy $E_{\rm peak}$ is correlated with the equivalent isotropic energy through the relation $E_{\rm peak} = k_{\rm A} E_{\rm iso}^{A}$ (Amati et al., 2002). A similar correlation also exists with the equivalent isotropic luminosity: $E_{\rm peak} = k_{\rm Y} E_{\rm iso}^{Y}$ (Yonetoku et al., 2004). The slopes of these two correlations are similar: $A \sim Y \sim 0.5$ (see Sec.1.3).

If $E_{\rm iso}$ is corrected for the jet collimation obtaining $E_\gamma = (1-\cos(\theta_{\rm jet}))E_{\rm iso}$, the correlation becomes tighter and steeper: $E_{\rm peak} = k_{\rm G} E_{\rm iso}^{G}$ (Ghirlanda et al., 2004, see Sec.1.3). The slope depends on the density profile of the circumburst medium, being $G = 0.7$ for a homogeneous density and $G = 1$ for a wind profile (Nava et al., 2006). Since the difference between the so–colled Amati and Ghirlanda correlations relies on the collimation factor (i.e. $1-\cos(\theta_{\rm jet})$), their different slopes suggest that a relation between the average jet opening angle and the energy of GRBs may exist: more energetic (luminous) bursts should have a smaller $\theta_{\rm jet}$.

Such relation can be derived by combining the correlations in this way:

$$1 - \cos(\theta_{\rm jet}) = \left(\frac{k_{\rm A}}{k_{\rm G}}\right)^{1/G} E_{\rm iso}^{(A-G)/G} = C L_{\rm iso}^{-\xi} \tag{6.6}$$

where $\xi = (G - A)/G$ and the conversion from energies to luminosities is incorporated in the normalization constant C. This relation also establishes that there is a characteristic minimum luminosity (corresponding to $\theta_{\rm jet} = 90^\circ$) $\sim 7 \times 10^{46}$ erg/s.

We can introduce this relation at the beginning of Eq.6.3 (including the bursts not pointing at us) in order to derive the model LF corresponding to this scenario:

$$\phi(L) \propto \frac{C(1-\xi) L_{\rm iso}^{-\xi}}{\eta} \left[\frac{C L_{\rm iso}^{1-\xi}}{\eta} + L_\star\right]^{-k} \tag{6.7}$$

Also in this case we can individuate two fundamental regimes:

$$\phi(L) \propto \begin{cases} L_{\rm iso}^{-\xi}, & C L_{\rm iso}^{1-\xi} \ll \eta L_\star \\ L_{\rm iso}^{-\xi-k(1-\xi)}, & C L_{\rm iso}^{1-\xi} \gg \eta L_\star \end{cases} \tag{6.8}$$

The luminosity function is a power–law that smoothly changes slope from high to low luminosity with the break at $L_{\rm iso} \sim (\eta L_\star / C)^{1/(1-\xi)}$.

6.1.3 Uniform jet observed at different viewing angles

Until now, we have described the UJ model in the ultrarelativistic approximation so that it is possible to detect the burst only if the viewing angle $\theta_{\rm v} \leq \theta_{\rm jet}$. More realistically, if Γ is not extreme, even if the jet is uniform it's possible to observe some radiation beyond the jet edges (see sub–sections 6.1.4). Moreover, we are going to describe the most probable case since it is much more likely to observe the jet at large viewing angle.

We have to take into account the relativistic beaming factor $\delta \equiv [\Gamma(1 - \beta\cos(\theta_{\rm v}))]^{-1}$ of the radiation. Assuming a population of bursts having all the same luminosity $L_{\rm iso}^{\rm on}$ on–axis, the corresponding off-axis observed luminosity varies as a function of the viewing angle (see Ghisellini et al. (2006) for GRBs; Urry and Shafer (1984); Celotti et al. (1993) for blazars). Within the jet opening angle the luminosity is constant while at larger angles the luminosity rapidly decreases

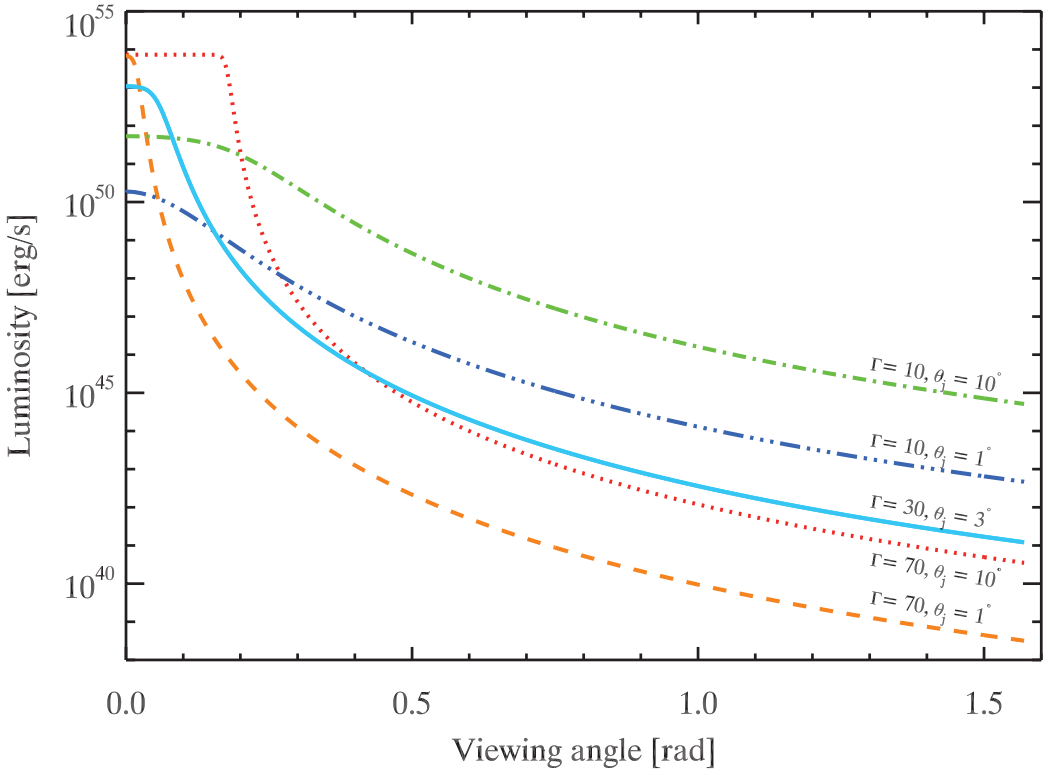

Figure 6.4: Luminosity as a function of the viewing angle for different combinations of the bulk Lorentz factor Γ and jet opening angle θ_j.The comoving frame luminosity L' is assumed to be the same for all curves. The different line–styles (colors) show different assumed combinations of θ_j and Γ. For all the curves, we have assumed a unique intrinsic comoving luminosity $L' = 10^{49}$ erg/s.

and the number of bursts seen at different viewing angles will depend on the corresponding solid angle.

$$N(L, L_{\rm iso}^{\rm on})dL = \frac{d\Omega}{2\pi} \Longrightarrow N(L, L_{\rm iso}^{\rm on})dL = \left(\frac{dL}{d\cos(\theta)}\right)^{-1} \tag{6.9}$$

The observed luminosity is the sum of the contributions of different portions of the emitting surface, each observed under a different angle (Ghisellini et al., 2006):

$$L(\theta_{\rm v}) = \int_{\max(0,\theta_{\rm v}-\theta_{\rm j})}^{\theta_{\rm v}+\theta_{\rm j}} \Delta\varphi\delta^4 L' \sin(\theta)d\theta \tag{6.10}$$

where L' is the comoving luminosity per unit solid angle (assumed constant), θ is the angle between the line of sight and the emitting element of the jet, and $\Delta\varphi$ takes into account the geometry of the emitting surface. If the observer is perfectly aligned with thew jet

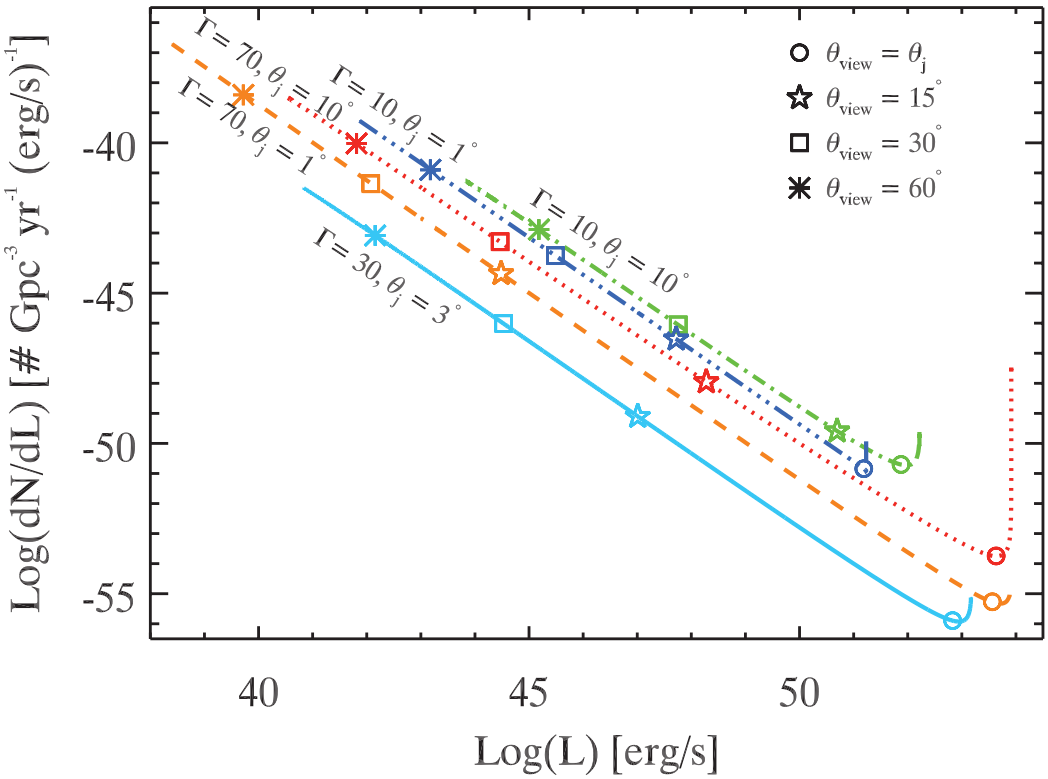

Figure 6.5: LF corresponding to the different assumptions of θ_j and Γ of Fig.6.4. The different symbols show different viewing angles as detailed in the labels.

axis, the emitting surface is a circular corona ($\Delta\varphi = 2\pi$), while for off-axis observers this results in a portion of a circular corona whose center depends on θ_v (Ghisellini and Lazzati, 1999):

$$\Delta\varphi = \begin{cases} 2\pi, & \text{if } \theta < \theta_{jet} - \theta_v \\ \pi + 2\sin\left(\frac{\theta_j^2 - \theta_v^2 - \theta^2}{2\theta_v\theta}\right), & \text{if } \theta \geq \theta_{jet} - \theta_v \end{cases} \tag{6.11}$$

Fig.6.4 (upper panel) shows the observed luminosity varies in function of the viewing angle for different jet opening angles and on–axis luminosities. The corresponding shape of the LF (assuming $L' = 10^{49}$ erg/s) is shown in Fig.6.5 (same line–styles and colors of Fig.6.4 with highlighted particular viewing angle) and can be easily explained.

Small viewing angles: $\theta_v < \theta_j$ Within the jet the observed luminosity is not perfectly constant but slightly decreases by increasing θ_v (starting from the center of the jet). This describes the high luminosity part of the LF, in which $\phi(L)$ presents a burst accumulation which height depends on the jet aperture (Fig.6.5)

Intermediate viewing angles: $\theta_j < \theta_v \leq 2\theta_j$ Slightly beyond the jet edges ($\theta_v \geq \theta_j$) the observed luminosity drops by a large factor if Γ is large. For smaller Γ this drop is, of course, smoother. However, for $\theta_j \leq \theta_v \leq \theta_j$ (namely, within the chasm, and before reaching the large viewing angle regime $L \propto \delta^4$), we can approximate the scaling of the luminosity as $L \propto \theta_v^{-f}$. According to equation , we have

$$\Phi(L) \propto \left[\frac{dL}{d\sin(\theta_v)d\theta_v}\right]^{-1} \propto \theta_v^{f+2} \propto L^{-(1+2/f)} \tag{6.12}$$

Note that the slope $1 + 2/f$ tends to unity for large f.

Large viewing angles: $\theta_v \gg \theta_j$ The burst can be considered as a single punctiform source with mono–directional velocity, along the jet axis. In this case, the observed luminosity depends from the beaming factor as δ^4. Therefore, taking into account Eq.6.9, $\phi(L) \propto (dL/d\cos\theta)^{-1} \propto \delta^{-5} \propto L^{-5/4}$. This results is general, as demonstrated by Urry and Shafer (1984): for beaming amplification factors dependence like $L \propto \delta^p$, the resulting low luminosity branch of the observed LF is $\phi(L) \propto L^{-(1+1/p)}$.

6.1.4 Apparent vs intrinsic structure

In this sub–section I want to better describe and deepen the concept of *apparent* structure of a GRB, as opposed to its *intrinsic* structure. I will outline some of the arguments developed in Salafia et al. (2015, to which I have collaborated). These topics are fundamental in order to understand the basis on which the predictions for the luminosity function are obtained in the previous two sections for different jet models. The intrinsic structure is defined as the energy emitted by different portions of the jet at different angular distances θ from the jet axis, while the apparent structure describes the energy received by observers under different viewing angles θ_v. While the intrinsic structure is linked to the way the inner engine distributes the energy during the jet formation process (e.g. Blandford and Znajek, 1977, process) or to the subsequent interaction with the stellar envelope (in the collapsar scenario), the apparent structure depends on how relativistic beaming effects shape the emission from each part of the jet. On the one hand, it is the apparent structure that defines the observational properties; on the other, one is interested in knowing,

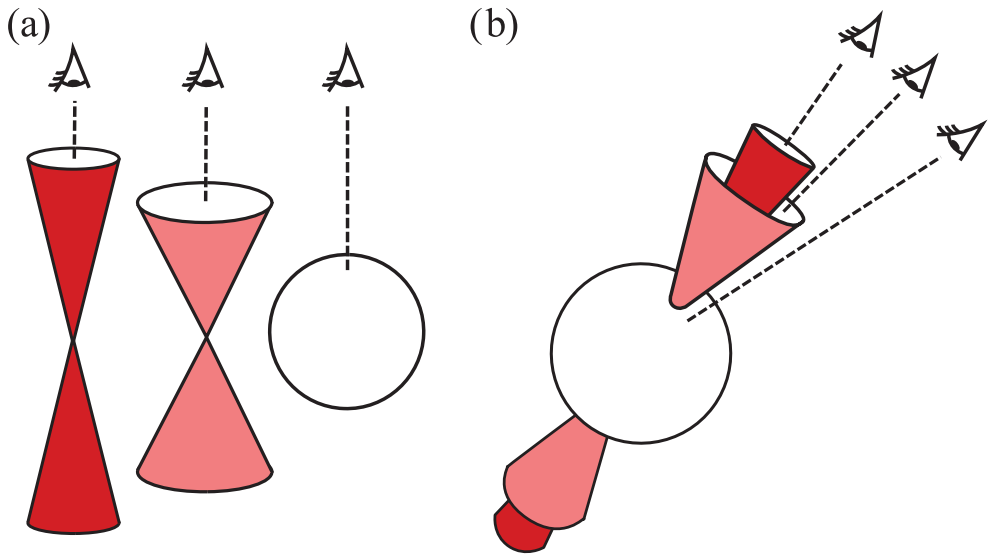

Figure 6.6: Sketch of the two possible scenarios described in Lipunov et al. (2001). In (a) GRB jets are seen on–axis, and they differ by their semi–aperture and consequently their observed energy, with the brightest being the most collimated; in (b) the jet configuration is such that the viewing angle determines which component contributes most significantly to the received energy.

from a theoretical point of view, the intrinsic structure to find out e.g. the actual energy emitted by the jet and, through the efficiency, the total energy (kinetic plus internal and possibly magnetic) and its distribution within the jet itself. Thus it is useful to make a clear distinction and establish their interdependence.

Originally, a first version of a structure for the jet was proposed in Lipunov et al. (2001). Triggered by the idea that the GRBs could be standard energy explosions with universal energy reservoir $\sim 5 \times 10^{51}$ erg (a similar result was found by Frail et al., 2001) they proposed two different scenarios: (i) the standard energy collimated into conical jet with semi–aperture $\theta_{\rm jet}$ varying from one GRB to another (Fig.6.6 – a); (ii) the jet configuration, made up of two coaxial conical components and an isotropic component, is the same for all GRBs (Fig.6.6 – b).

Intrinsic Following Rossi et al. (2002)and Zhang and Mészáros (2002) we define the intrinsic structure of the jet specifying the functions describing the radiative energy distribution $\epsilon_{\rm r}(\theta)$ and the Lorentz factor $\Gamma(\theta)$.

- $\epsilon_{\rm r}(\theta)$ is the energy that the portion of the jet comprised between

θ and $\theta + d\theta$ emits during the prompt phase, divided by the corresponding solid angle, i.e. $\epsilon_{\rm r}(\theta) = \eta\epsilon(\theta) = \eta dE(\theta)/d\Omega$. Here $\epsilon(\theta)$ is the intrinsic distribution of the total energy provided by the inner engine E (kinetic plus internal and magnetic) within the jet portion, and η is the prompt emission radiative efficiency, which might as well depend on θ;

- $\Gamma(\theta)$ is the Lorentz factor of the emitting material in the jet portion comprised between θ and $\theta + d\theta$ during the prompt phase.

Apparent We define apparent structure the function $E_{iso}(\theta_{\rm v})$ ($L(\theta_{\rm v})$) describing the isotropic equivalent energy (luminosity) inferred by the observer as a function of the viewing angle $\theta_{\rm v}$. Fore the sake of clarity let apply this definition to simple examples.

An isotropic explosion, defined by $\epsilon(\theta) = \epsilon\ \forall\theta \in [0, \pi]$, has $E_{\rm iso} = \eta 4\pi\epsilon\ \forall\theta_{\rm v}$. The classical uniform (top–hat) jet (previously introduced in this section) has:

$$\epsilon(\theta) = \begin{cases} \epsilon, & \theta \leq \theta_{\rm jet} \\ 0, & \theta > \theta_{\rm jet} \end{cases} \tag{6.13}$$

and

$$\Gamma(\theta) = \begin{cases} \Gamma, & \theta \leq \theta_{\rm jet} \\ 1, & \theta > \theta_{\rm jet} \end{cases} \tag{6.14}$$

In the ultrarelativistic approximation ($\Gamma \to \infty$) the apparent structure almost perfectly reproduces the intrinsic one. Thus, the uniform jet is indistinguishable from an isotropic explosion as long as $\theta_{\rm v} \leq \theta_{\rm jet}$ (the relativistic beaming does not allow to observe anything not expanding exactly along the line of sight). For the same reason, within the UJ model, we can not detect the GRB if $\theta_{\rm v} > \theta_{\rm jet}$. The corresponding apparent structure is

$$E_{\rm iso}(\theta_{\rm v}) = \begin{cases} \eta 4\pi\epsilon, & \theta \leq \theta_{\rm jet} \\ 0, & \theta > \theta_{\rm jet} \end{cases} \tag{6.15}$$

This is the picture typically adopted when the UJ model is assumed in works on GRBs (dashed line in Fig.6.7, see sub–section 6.1.1).

If we relax the ultrarelativistic assumption one must take into account the contribution to the observed flux coming from the different portions of the jet not aligned with the line of sight. The result

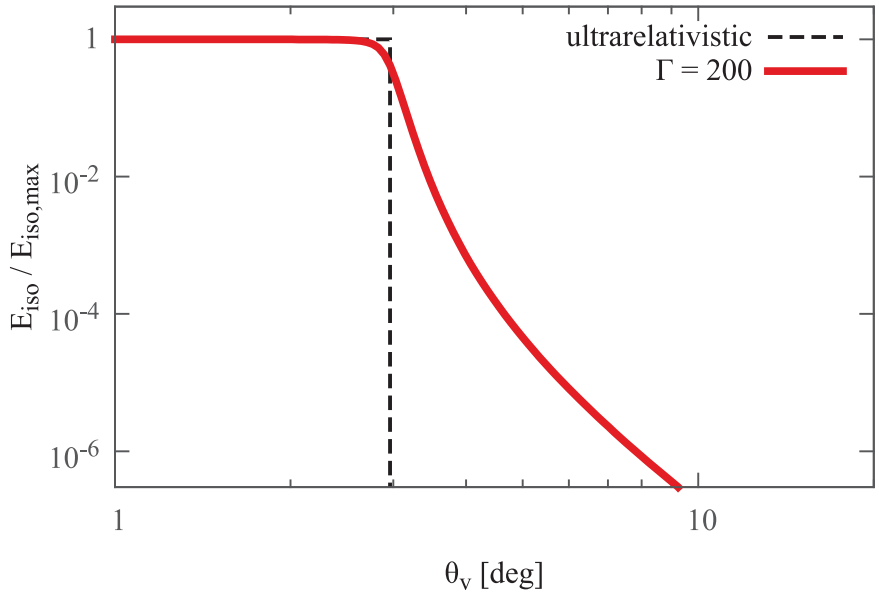

Figure 6.7: Apparent structure of a uniform jet in the ultrarelativistic limit (black dashed line) and for $\Gamma = 200$ (red solid line). The isotropic equivalent energy is normalized to its maximum value, corresponding to the jet observed on–axis. An opening angle $\theta = 3°$ has been assumed.

of such calculation for the uniform jet is usually dubbed off–axis jet model (e.g. Ghisellini et al., 2006; Yamazaki et al., 2003; Eichler and Levinson, 2004; Donaghy, 2006, see sub–section 6.1.3). The transition from the on–axis ($\theta_v \ll \theta_{jet}$) to the off–axis ($\theta_v > \theta_{jet}$) regime is smoother than the ultrarelativistic case, and a non–zero energy is received from the observer even at large viewing angles (red solid line in Fig.6.7).

Given an axisymmetric intrinsic structure defined by the couple $\{\epsilon(\theta), \Gamma(\theta)\}$ it is possible to derive the apparent structure $E_{iso}(\theta_v)$ through the following formula (full derivation in Salafia et al., 2015):

$$E_{iso}(\theta_v) = \int \frac{\delta^3(\theta, \varphi, \theta_v)}{\Gamma(\theta)} \eta \epsilon(\theta)\, d\Omega \tag{6.16}$$

This equation is valid under the assumptions that the emission comes from a geometrically and optically thin volume whose surface does not change significantly during the emission. Here the equivalent isotropic energy E_{iso} can be expressed as $4\pi d_L^2(z)/(1+z)$ times the bolometric fluence S ($d_L(z)$ is the luminosity distance). Given a spectrum characterizing the burst emission it is possible to calculate its

time integral as:

$$S(\nu,\theta_{\rm v}) = \frac{1+z}{4\pi d_L^2(z)} \int \frac{\delta^2(\theta,\varphi,\theta_{\rm v})}{\Gamma(\theta)} \frac{f(x,\alpha)}{\nu_0' f_\alpha} \eta\epsilon(\theta)\, d\Omega \tag{6.17}$$

where we have set $x = (1+z)\nu/(\delta\nu_0')$. $f(x,\alpha)$ is the (dimensionless) comoving spectral shape, which depends on a set of parameters α and ν_0' is the typical frequency of the comoving spectrum. f_α is the spectrum normalization

$$f_\alpha = \int_0^\infty f(x,\alpha)\, dx \tag{6.18}$$

Eq. 6.17 it is also useful to calculate the isotropic equivalent energy in a specific band:

$$E_{\rm iso}(\theta_{\rm v})|_{[\nu_1,\nu_2]} = \frac{4\pi d_L^2(z)}{1+z} \int_{\nu_1/(1+z)}^{\nu_2/(1+z)} S(\nu,\theta_{\rm v})\, d\nu \tag{6.19}$$

6.2 Structured jet

The measure of the jet opening angle $\theta_{\rm jet}$ through the jet–break allowed to estimate the true collimated energy E_γ associated to a burst (see Fig.6.8). This energy turned out to be clustered around a typical value $\sim 10^{51}$ erg with a dispersion of less than a decade (Frail et al., 2001; Panaitescu and Kumar, 2001). The small dispersion of E_γ and the possibility that GRBs can have a standard energy reservoir (implying the correlation $E_{\rm iso} \propto \theta_{\rm jet}^{-2}$) led to the idea that the jet is not uniform, but structured (Lipunov et al., 2001; Zhang and Mészáros, 2002; Rossi et al., 2002). This scenario assumes that what was believed to be the jet opening angle $\theta_{\rm jet}$ is actually the viewing angle $\theta_{\rm v}$. The direct implication is that the burst energetic has to vary proportionally to θ^{-2} in order to recover the clustering of E_γ. More recently, relativistic hydrodynamical simulations (e.g. Zhang et al., 2004a; Morsony et al., 2007) showed that the interaction of the jet with the stellar envelope (in the collapsar scenario of long GRBs) leads inevitably to the formation of some structure in the jet, even if it remains unclear from these studies if this structure is likely to have any degree of universality.

While within the uniform jet model GRBs distribute their energy into jet with different opening angles, within the structured jet model

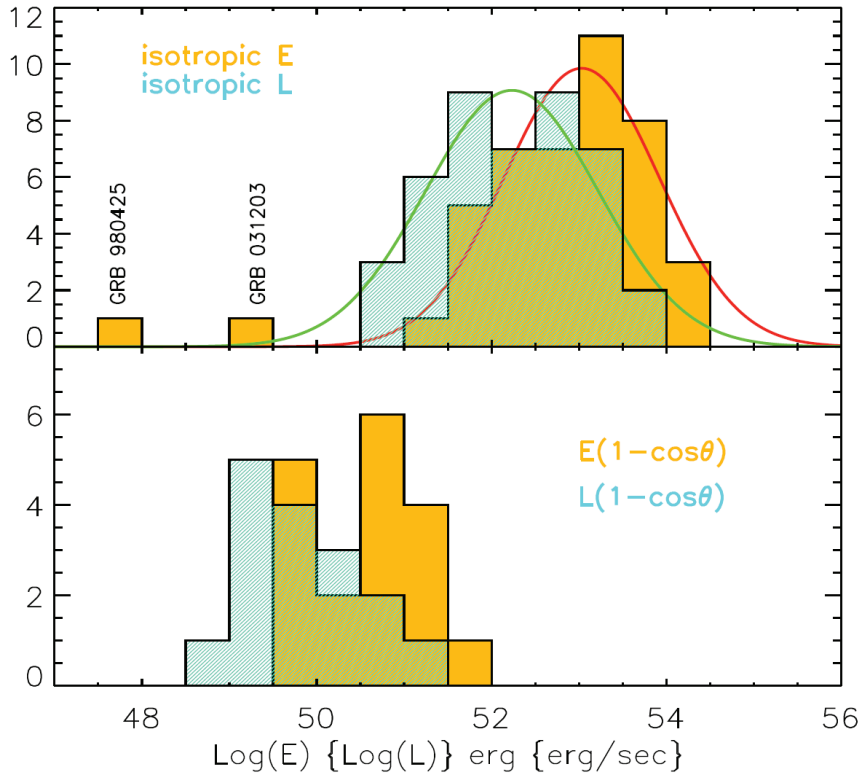

Figure 6.8: Caption

bursts have a quasi–universal jet configuration with a standard energy reservoir. This can lead to a unification scheme in which all bursts are intrinsically equal, but they appear different only because are seen under different angles.

The principal assumption of this model is that the energy distribution within the jet is strongly anisotropic and depending on the angular distance θ from the jet axis (around which it is reasonable to assume that most of the energy is concentrated). It is assumed that the distribution of the energy per unit solid angle $\epsilon(\theta)$ is constant within a core of small aperture θ_c and decaying as a power–law of slope k at larger angles:

$$\epsilon(\theta) = \frac{dE}{d\Omega} = \begin{cases} \epsilon_c, & \theta \leq \theta_c \\ \epsilon_c \left(\frac{\theta}{\theta_c}\right)^{-s}, & \theta > \theta_c \end{cases} \tag{6.20}$$

where there is not a maximum opening angle because in principle the jet can extend up to $\pi/2$. The integral of $\epsilon(\theta)$ is the total jet energy E which is a free parameter.

Also the Lorentz factor might not be the same in each point of the fireball. For simplicity it is assumed the same kind of angular

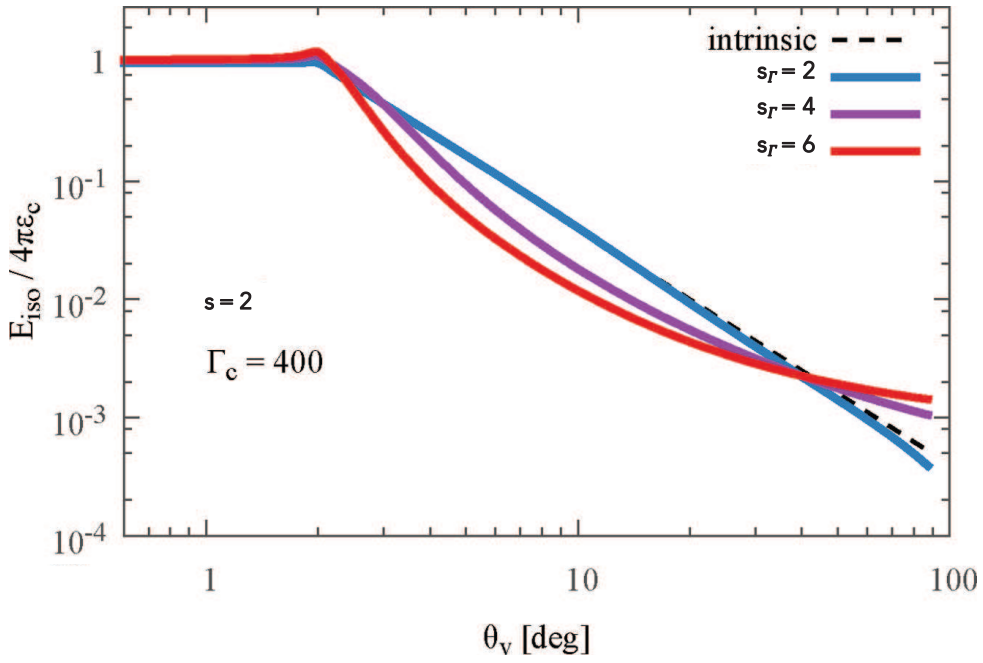

Figure 6.9: Apparent structures of three power–law structured jet models. All power–law models have $\theta_c = 2°$, $\Gamma_c = 400$, $s = 2$ and different values of the s_Γ parameter. The corresponding intrinsic energy structure is shown (black dashed lines).

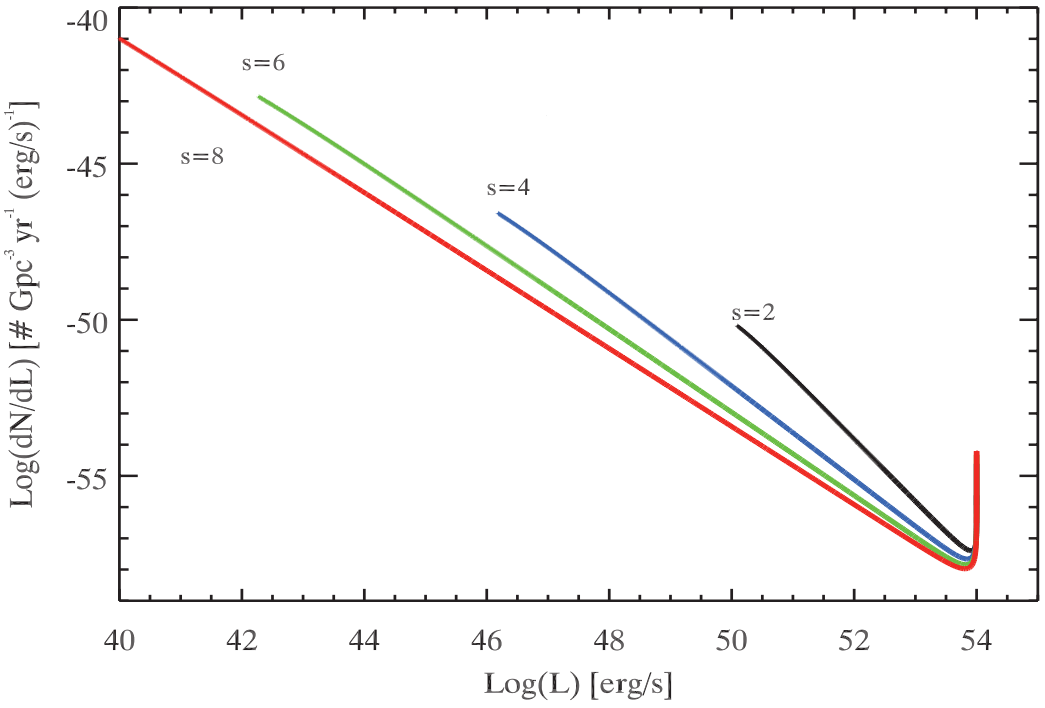

Figure 6.10: Power–law SJ model LF (solid lines) for different values of the power–law energy structure slope s (as labeled) assuming a core angle of 1°.

dependence of the energy:

$$\Gamma(\theta) = \frac{d\Gamma}{d\Omega} = \begin{cases} \Gamma_c, & \theta \leq \theta_c \\ 1 + (\Gamma_c - 1)\left(\frac{\theta}{\theta_c}\right)^{-s_\Gamma}, & \theta > \theta_c \end{cases} \tag{6.21}$$

where Γ_c is the Lorentz factor of the core of the jet. The slope s_Γ strongly depends on the baryon loading. In principle also this property can have an angular dependence but if it were constant within the fireball then Γ should have the same profile of the energy and $s_\Gamma = s$.

Fig.6.9 shows the computed apparent structures of three power–law structured jet models. The more the Lorentz factor varies, the less the apparent structure mimics the underlying intrinsic structure. For the sake of simplicity we adopted the ultrarelativistic approximation in obtaining the LF (Fig.6.10, see the following sub–section) so that the apparent structure could reproduce the intrinsic one (note that a similar effect is reproduced by choosing $\Gamma \sim 10^{2-3}$ and $s_\Gamma = 2$).

Despite this jet model does not assume the presence of sharp edges it is however possible to explain the jet–break. In the hypothesis of ultrarelativistic motion it is possible to observe only a small portion of fireball centered along the line of sight. Due to the deceleration, the observer will see a even larger portion of fireball and jet–break happen when the accessible area overcome the core of the jet ($\Gamma_c(t) \sim 1/\theta_v$).

Gaussian structured jet An interesting and maybe more realistic kind of jet structure is the Gaussian one. We reformulate the original structure (see Kumar and Granot, 2003) allowing for the Lorentz factor structure and intrinsic energy structure to fall off over different angular scales. The Gaussian intrinsic structure is defined by

$$\epsilon(\theta) = \epsilon_c e^{-\left(\frac{\theta}{\theta_c}\right)^2} \tag{6.22}$$

$$\Gamma(\theta) = 1 + (\Gamma_c - 1) e^{-\left(\frac{\theta}{\theta_\Gamma}\right)^2} \tag{6.23}$$

In principle, θ_c might differ from θ_Γ because of the following argument: $\epsilon(\theta)$ is related to the jet energy density $u = \rho c^2 + p + u_B$ (where u_B is the magnetic energy density) according to

$$\epsilon(\theta) \equiv \frac{dE(\theta)}{d\Omega} = \frac{4\pi R^2(\theta)\Delta(\theta)}{4\pi} u(\theta) \tag{6.24}$$

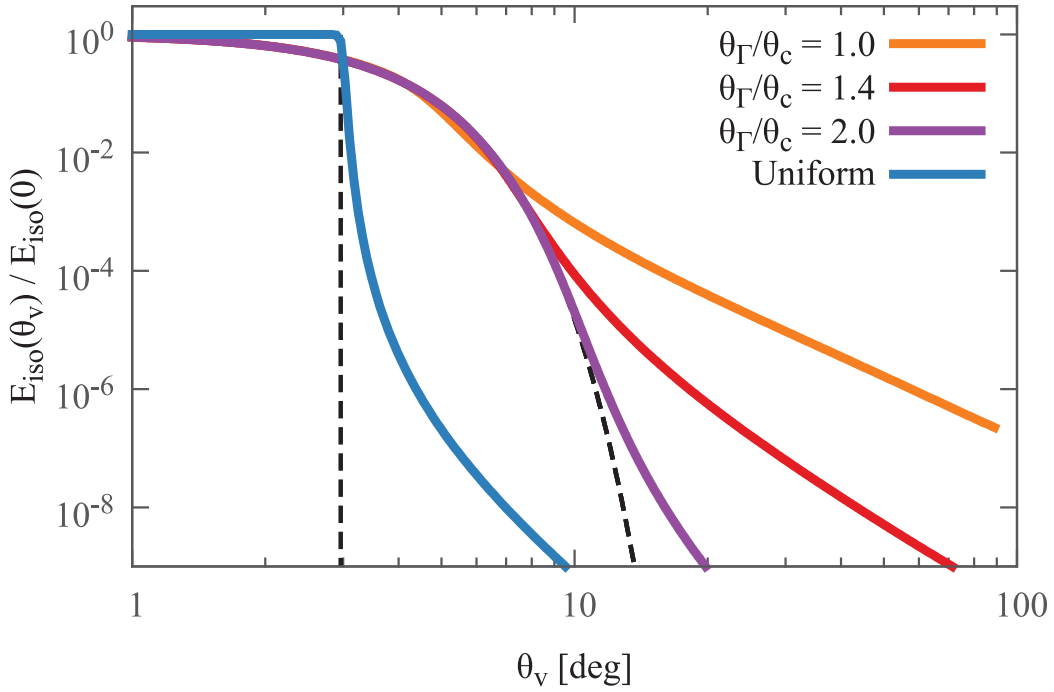

Figure 6.11: Apparent structures of three Gaussian jets with different values of θ_Γ/θ_c, together with the apparent structure of a uniform jet for comparison (blue solid line). The corresponding intrinsic structures are also shown (dashed lines). The Gaussian jets have $\theta_c = 3^\circ$ and $\Gamma_c = 400$; the uniform jet has $\theta_{jet} = 3^\circ$ and $\Gamma = 400$.

where $\Delta(\theta)$ is the width of the emitting volume and $R(\theta)$ the radius defining its surface. The energy density u is related to the comoving one by $u(\theta) = \Gamma^2(\theta)u'(\theta)$. Let us take the simplest picture as an example: let the emitting volume be a portion of a spherical shell, with fixed width Δ and radius R, and let the efficiency η be the same at all angles. One then gets $\epsilon(\theta) \propto u(\theta) = \Gamma^2(\theta)u'(\theta)$. If u' is constant, this implies $\theta_\Gamma = \sqrt{2}\theta_c$. The efficiency, geometry and energy density all play a role in determining the ratio θ_Γ/θ_c. Some mixing is likely to occur between the jet borders and the stellar envelope (Rossi et al., 2002), and indeed simulations indicate (e.g. Morsony et al., 2007) that the jet plasma density increases with the distance from the axis. This suggests a ratio $\theta_\Gamma/\theta_c \lesssim \sqrt{2}$ (we thus take $\theta_\Gamma/\theta_c = 1$ for simplicity). This ratio is the main parameter affecting the slope of the power–law tail of the apparent structure. Fig.6.11 shows the apparent structure of the Gaussian jet for three values of θ_Γ/θ_c, along with the uniform jet for comparison.

6.2.1 The structured jet model LF

In the hypothesis of ultrarelativistic jets with constant baryon loading the energy observed at a certain θ_v is defined as $E_{iso}(\theta_v) = 4\pi\eta\epsilon(\theta_v)$ where η is the radiative efficiency. Assuming a typical duration we can define the luminosity as $L_{iso} \propto \epsilon(\theta_v)$. The maximum observable luminosity is $L_{iso,max} \propto \epsilon_c$ (for $\theta_v \leq \theta_v$) while the minimum luminosity is for $\theta_v = \pi/2$ with consequent ratio

$$\frac{L_{max}}{L_{min}} = \left(\frac{\pi}{2\theta_c}\right)^s \tag{6.25}$$

which fix the extension of the luminosity function.

Since within the structured jet model GRBs are intrinsically equal, the different luminosities are linked to different viewing angles. What is observed only depends on the viewing angle (jet orientation) probability distribution. The fraction of object observed with a viewing angle in the interval $[\theta v, \theta v + d\theta v]$ is the ratio between the solid angle corresponding to the infinitesimal solid angle and half sky (since there are two opposite jets):

$$N(\theta v, \theta v + d\theta v) = \frac{\int_0^{2\pi} d\varphi \int_{\theta v}^{\theta v + d\theta v} \sin(\theta)\, d\theta}{2\pi} \tag{6.26}$$

Therefore, the probability to observe between θv and $\theta v + d\theta v$ is $P(\theta_v) = dN(\theta_v)/d\theta_v = \sin(\theta_v)$. At this point we can easily calculate the luminosity function:

$$\phi(L) = \frac{dN}{dL} = \frac{dN}{d\theta}\frac{d\theta}{dL} \tag{6.27}$$

Inverting the relation in Eq.6.20 and derivating we obtain

$$\begin{aligned} \phi(L) &\propto \sin\left\{\left(\frac{L}{L_{max}}\right)^{-\frac{1}{s}}\theta_c\right\}\left(\frac{L}{L_{max}}\right)^{-1-\frac{1}{s}} \\ &\approx \theta_c\left(\frac{L}{L_{max}}\right)^{-(1+\frac{2}{s})} \end{aligned} \tag{6.28}$$

since the argument of the sine is always small for reasonable values of θ_c. The slope of the LF directly depends on the shape of the jet structure s which also regulates the extension of the LF (see Fig.6.10).

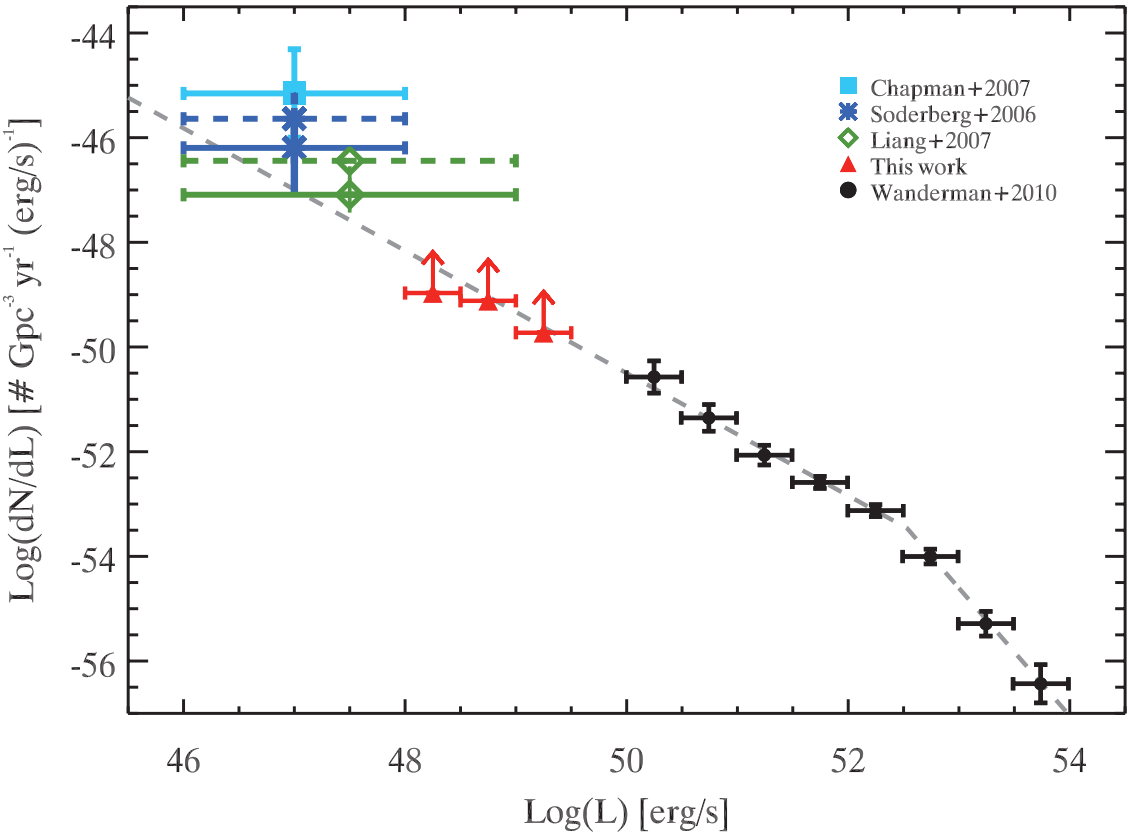

Figure 6.12: Long GRB LF representing the number of GRBs per unit volume, time and luminosity bin. Black symbols represent the discrete LF of WP10.The grey dashed line is the empirical fit of WP10 with a broken power law with $a = 1.2$, $b = 2.4$ and $L_b = 3.2 \times 10^{52}$ erg s^{-1}. The rate of LL GRBs is shown with different symbols according to the different sources in the literature: asterisk (Soderberg et al., 2006b), diamond (Liang et al., 2007), filled square (Chapman et al., 2007). The Soderberg et al. (2006b) and Liang et al. (2007) rates were calculated assuming a time bin corresponding to the *Swift* lifetime in 2006 (points with dashed horizontal bars). Since then, no other burst in the same luminosity bin has been discovered, so we added the rates corrected for the current *Swift* lifetime (points shown with solid horizontal bars). The lower limits on the rate of IL GRBs added in this work are shown with the filled (red) triangles.

6.3 The observed luminosity function

Our aim is to test the theoretical luminosity function obtained assuming different jet models in order to get some insight on the configuration of the GRB jet. In order to get as much information as possible we want that the compared LF covers the maximum range possible of luminosities. Since reliable LF cannot be constructed down to very low luminosites due to statistical and completeness matters, there is the need of exploit the rates calculated for the few observed

faint bursts. For this reason I constructed the observed luminosity function, i.e. the LF (at $z = 0$ or not evolving in redshift) normalized at the density of bursts at $z = 0$ (see Fig.6.12). In this way it is possible to extend the LF of high luminosity GRBs (HL – black points in Fig.6.12) towards lower luminosities using the rate of low luminosity GRBs (LL – blue asterisks and green diamonds in Fig.6.12). I also added lower limits in the region of intermediate luminosity (IL – red triangles in Fig.6.12).

HL GRBs Wanderman and Piran (2010, WP10 hereafter) adopted a direct inversion method (explained in Sec.4.2) on the distribution of GRBs in the $L - z$ space obtaining simultaneously $\phi(L)$ and $\psi(z)$ independently. They selected a sample of long GRBs with spectroscopically measured redshift and isotropic equivalent luminosities $L_{\rm iso} \geq 10^{50}$ erg/s detected by *Swift*/BAT. The derived LF is represented by a discrete series of data points (Fig.3 of WP10) in eight equal logarithmic bins of luminosity and it is represented by a broken power law with best fit parameters $a = 1.2^{+0.2}_{-0.1}$ and $b = 2.4^{+0.3}_{-0.6}$, with the break at $L_{\rm b} = 10^{52.5\pm0.2}$ erg/s (note that WP10 use $dN/d\log(L)$, whereas the common differential LF is defined as $dN/dL = dN/(Ld\log(L))$ so that the WP10 slopes are here increased by 1). These parameter values are consistent with those derived with the classical indirect approach described at the beginning of Chp.4. This function has been normalized at the local GRB rate $\rho_0 \simeq 1.3$ Gpc^{-3} yr^{-1} (WP10). Black points in Fig.6.12 show the renormalized discrete LF of WP10 which covers the luminosity range between 10^{50} and 10^{54} erg/s. The best fit obtained by WP10 is shown as a grey long dashed line.

IL GRBs In the luminosity range between HL and LL bursts (see Fig.6.12), it is possible to add some constraints. Firstly, I have searched all GRBs with measured redshift z and with $L_{\rm iso} \in [10^{48}, 10^{50}]$ erg/s. In order to have $L_{\rm iso}$ well determined we need that the peak energy and all other parameters of the spectrum at the peak of the light–curve has constrained. Only in this case it is possible to compute the bolometric isotropic luminosity. The bursts having such properties (grouped in three luminosity bin) are: GRB 051109B with $L_{\rm iso} \in [10^{48}, 3 \times 10^{48}]$ erg/s; GRB 020903, 031203, 060505 with $L_{\rm iso} \in [3 \times 10^{48}, 10^{49}]$ erg/s; GRB 120422A, 130702 with $L_{\rm iso} \in [10^{49}, 3 \times 10^{49}]$

GRB	z	Ref[a]	α	β	$E_{\rm peak}$ keV	P ph cm^{-2}s^{-1}	ΔE keV	Ref[b]	$P_{\rm bol}$ ph cm^{-2}s^{-1}	$L_{\rm iso}(\times 10^{48})$ erg/s	Instr.	$P_{\rm lim,bol}$ ph cm^{-2}s^{-1}
020903	0.25	1	-1.0	–	3.37	2.8	$[2-400]$	7	6.52	4.86	*Hete–II*	3.0
031203	0.105	2	-1.63	–	144	2.2	$[15-150]$	8,9,10	17.9	10	*Integral*	3.0
051109B	0.08	3	-1.90	–	50†	0.5	$[15-150]$	11,12,13	9.43	1.64	*Sxift*	1.3
060505	0.089	4	-1.8	–	239†	1.9	$[15-150]$	11	8.0	7.14	*Sxift*	0.8
120422A	0.283	5	-1.94	–	53	0.6	$[15-150]$	14	11.35	27	*Sxift*	2.5
130702A	0.145	6	-1.0	-2.5	20	7.03	$[10-1000]$	15	7.03	28.7	*Sxift*	2.5

Table 6.1: Intermediate Luminosity (IL) GRBs. [a] References for the redshift: (1) GCN #1554 Soderberg et al. (2002); (2) GCN #2482 Prochaska et al. (2003); (3) GCN #5387 Perley et al. (2005); (4) GCN #5161 Thoene et al. (2006); (5) GCN #13251 Tanvir et al. (2012); (6) GCN #14983 Leloudas et al. (2013); [b] References for the spectral parameters: (7) Sakamoto et al. (2004); (8) Bošnjak et al. (2014); (9) Sazonov et al. (2004); (10) Ulanov et al. (2005); (11) Troja et al. (2006); (12) Sakamoto et al. (2009); (13) Butler et al. (2007); (14) Zhang et al. (2012b); (15) von Kienlin et al. (2014). † $E_{\rm peak}$ computed through the $\alpha - E_{\rm peak}$ correlation of Sakamoto et al. (2009) for *Swift* GRBs (for GRB 051109B consistent also with the estimate of Butler et al. (2007)).

erg/s. The associated rate ρ_{LL} has been computed adopting the same method described for LL GRBs in Soderberg et al. (2006b). The prompt emission spectral parameters and flux of these bursts, through which I have computed their bolometric flux, are reported in Tab.6.1. In triggering these events were involved three different instruments (Column 10 in Tab.6.1), which have the following instrumental parameters: $\Omega = 1.33$ sr and $T = 8$ yr for *Swift*, $\Omega = 0.1$ sr and $T = 10$ yr for *Integral* and $\Omega = 0.802$ sr and $T = 4$ yr for *Hete–II*. The last column in Tab.6.1 reports the limiting flux of the corresponding detectors as computed by Band (2002, 2006) which depends on the burst peak spectral energy $E_{\rm peak}$ (in the observer frame). These limiting flux $P_{\rm lim}$ (computed in the $[1-1000]$ energy band) are used to compute the maximum distance (and therefore $V_{\rm max}$) out to which these events could have been detected. The rates ρ_{LL} calculated for these events (red triangles in Fig.6.12) should be considered as lower limits: I only selected GRBs with measured redshifts and well–constrained spectral parameters. These are most likely only a fraction of the bursts, with similar luminosities, which effectively triggered the corresponding detector.

LL GRBs At the low end of the luminosity distribution of GRBs, i.e. $L_{\rm iso} \sim 10^{46-48}$ erg/s, two particular events (GRB 980425 and GRB 060218) have been detected in the local Universe. Such events are extremely rare but their high proximity makes them representative of a large number of events. Moreover, these bursts are associated to SN events and have been intensively studied as direct evidences of the massive star progenitor of long GRBs. Their luminosity is more than three/four orders of magnitude smaller than HL bursts, and their rate is larger (e.g. Soderberg et al., 2006b). GRB 980425 ($z = 0.008$, associated with SN1998bw – Galama et al., 1998) was detected by *CGRO*/BATSE and had $L_{\rm iso} \sim 7 \times 10^{46}$ erg/s (as computed from its prompt emission spectrum – Jimenez et al., 2001). Similarly, GRB 060218 ($z = 0.0331$, associated with SN2006aj – Sollerman et al., 2006), detected by *Swift*/BAT, had $L_{\rm iso} \sim 1.3 \times 10^{47}$ erg/s (Campana et al., 2006). The rate of these LL events can be singularly computed as:

$$\rho_{LL} = 4\pi \frac{N_{LL}}{V_{\rm max} T \Omega} \tag{6.29}$$

where $V_{\rm max}$ is the maximum volume within which they could be detected by an instrument with an assigned sensitivity, with a field

of view Ω and operating for a time T. Based on GRB 980425 and GRB 060218, Soderberg et al. (2006, see also Pian et al., 2006) derived the rate of LL events by conservatively averaging over $V_{\rm max}$ and Ω for different detectors (*Beppo*SAX/Wide Field Camera, *Hete–II*/Wide Field X–ray Monitor and *Swift*/BAT). They obtained a rate $\rho_{LL} \sim 230^{+490}_{-190}$ Gpc^{-3} yr^{-1}. This rate has been converted dividing for the for width of the corresponding luminosity interval $[10^{46}, 10^{48}]$ erg/s and obtaining $\tilde{\rho}_{LL} \sim 2.3 \times 10^{-46}$ Gpc^{-3} yr^{-1} erg^{-1} s (blue asterisk in Fig.6.12). Since originally ρ_{LL} has been computed in 2006, it has also been corrected (blue asterisk with solid horizontal bar in Fig.6.12) for the larger time interval elapsed since the detection of these two LL events. These results are consistent with other numerical studies: Virgili et al. (2009) estimate $\rho_{LL} = 200$ Gpc^{-3} yr^{-1} for events with $\langle L \rangle = 10^{47}$ erg/s based on the BATSE GRB population. Chapman et al. (2007) obtained a slightly larger rate $\rho_{LL} \sim 700 \pm 360$ Gpc^{-3} yr^{-1} (shown by the cyan filled square symbol in Fig.6.3) from the cross–correlation of a subsample of low–fluence smooth single–peaked BATSE bursts with nearby galaxies. Liang et al. (2007) also derived $\rho_{LL} = 325^{+352}_{-177}$ Gpc^{-3} yr^{-1} (shown as green diamonds in Fig.6.12 also corrected for the current lifetime of *Swift*). I show these rates only for consistency with the others because, for the sake of simplicity, I will take into account only the rate of Soderberg et al. (2006b) in the calculations .

The grey dashed line in Fig.6.12 represents the fit performed by WP10 only to HL data points and it can be noted that its extrapolation to low luminosities is consistent with both the lower limits of IL bursts and the rate of LL events. This is a direct indication that LL and HL have a common progenitor, i.e. they form a *unique population*. Apparently there is no need to invoke a different origin for the LL events as they are consistent with the extension to low luminosities of the LF of HL bursts.

6.4 What $\phi(L)$ tells us about the jet structure of long GRBs

Our aim is to get some insights on the jet structure of GRBs through the comparison between the theoretical LF expected within different jet models (see Sec.6.1 and Sec.6.2) and the observed LF reconstructed in this work (see Sec.6.3 – Fig.6.12). The latter is consis-

tent down to the low luminosities with a broken power–law model with LL bursts lying on the extrapolation of the LF that describes HL events. This suggests that LL and HL bursts belong to the same population (spreading over almost seven order of magnitude in luminosity). Is the very large range of observed luminosities produced by the different intrinsic GRB power? Or is it, instead, the result of viewing the same intrinsic phenomenon under different lines of sight? Now I will discuss the problem case by case.

On–axis UJ – unique $\theta_{\rm jet}$ If the jets of GRBs are homogeneous and all bursts have the same opening angle $\theta_{\rm jet}$, then the observed luminosity is proportional to the energetic of the bursts after it has spent part of its initial energy to punch the progenitor star. This implies that the model LF (which expression in given in Eq.6.4) must be flat at low luminosities. Fig.6.13 shows the fit of the LF with the model of Eq.6.4 . We fit the HL rates (black symbols) and the LL rate (blue asterisk) as derived by Soderberg et al. (2006b, corrected in this work for the elapsed time, see Sec.6.3). The lower limits of IL bursts (red triangles in Fig.6.13) are used only for a consistency check of the fitted model. Fixing $L_\star = 10^{50}$ erg/s, the free parameters are the normalization, the slope k and the characteristic luminosity $L_\star \eta / (1 - \cos(\theta_{\rm jet}))$. Since the model depends on the ratio between the efficiency η and the beaming factor $(1 - \cos(\theta_{\rm jet}))$, there is degeneracy between these two quantities. The fit can constrain this ratio rather than the two factors independently. We can consider two cases:

(i) $\eta = 0.2$ (as typically found from the modeling of the GRB afterglows – e.g. Panaitescu and Kumar (2002)): the fit is shown by the solid cyan line in Fig.6.13. HL bursts can be reproduced with a unique LF which has a slope $k = 1.62 \pm 0.08$ (1σ confidence) and is also marginally consistent with the IL lower limits. The fit has $\chi^2 = 33.5$ for 6 degrees of freedom (d.o.f.) corresponding to a goodness of fit probability of 8×10^{-6}. However, the LL bursts cannot be reproduced by this model. Indeed, the characteristic luminosity $L_\star \eta / (1 - \cos(\theta_{\rm jet}))$, with $\eta = 0.2$ and $L_\star = 10^{50}$ erg/s, corresponds to $\sim 2 \times 10^{49} / (1 - \cos(\theta_{\rm jet}))$ erg/s. This expression has a minimum for $\theta_{\rm jet} = 90^\circ$. In this case, all GRBs would be isotropic and still LL events should be a different population;

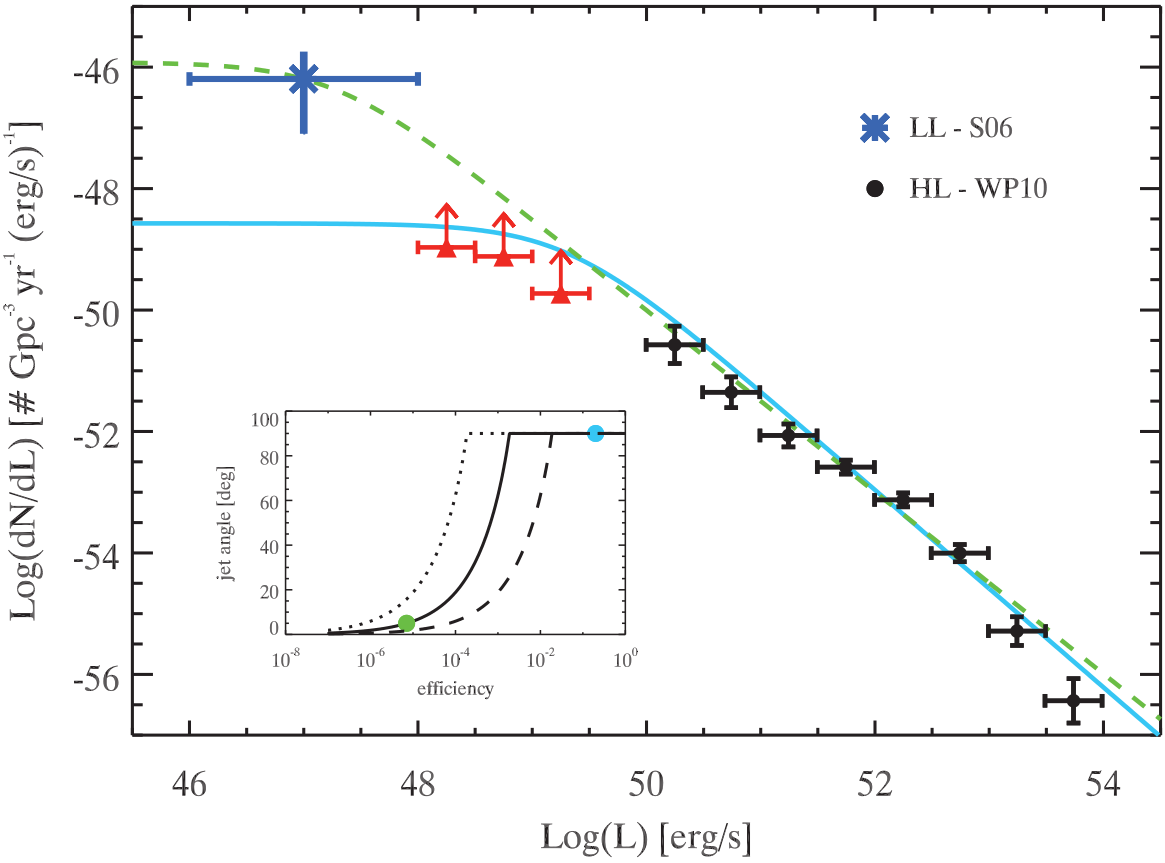

Figure 6.13: LF fitted with the UJ model (Eq.6.4) with fixed opening angle. For the models shown in the main plot (solid cyan and dashed green curves), $L_\star = 10^{50}$ erg/s is fixed. The solid cyan line shows the case with $\eta = 0.2$ (which gives $\theta_{\rm jet} = 90°$) and the dashed green line is the case with $\theta_{\rm jet} = 5°$ (which gives $\eta \sim 10^{-5}$). *Inset*: curves showing the degeneracy of the model in the angle and efficiency parameters. Dotted, solid and dashed curves correspond to different choices of $L_\star = 10^{49}, 10^{50}, 10^{51}$ erg/s, respectively. The green and cyan dots show the choice of η and $\theta_{\rm jet}$ corresponding to the model curves shown in the main panel, respectively.

(ii) $\theta_{\rm jet} = 5°$ (i.e. corresponding to the typical opening angle of GRBs – Frail et al. (2001); Ghirlanda et al. (2007)): the fit is shown by the dashed green line in Fig.6.13 and can reproduce all the bursts (with a $\chi^2 = 16$ for 6 d.o.f., i.e. probability 0.01). The resulting $k = 1.49 \pm 0.08$ is consistent with the previous one, but the efficiency $\eta \sim 10^{-5}$ is unreasonably low.

The above results are independent from the choice of the particular value for $L_\star$: if we fix this parameter to any value in the interval $[10^{49}, 10^{51}]$ erg/s, we still find an unreasonably low efficiency $\eta < 10^{-5}$ for reasonable values of $\theta_{\rm jet}$; or too large $\theta_{\rm jet}$ for reasonable

efficiencies. This is shown in the inset of Fig.6.13 where all the curves saturate at 90° (for the three different choices of $L_\star$) for $\eta > 0.01$. The conclusion is that, since the UJ model (assuming a unique angle for all bursts) does not reproduce the entire LF, we can exclude this simple case.

On–axis UJ – $\theta_{\rm jet}(L)$ In this case the jet angle is related to the GRB energetics: smaller $\theta_{\rm jet}$ correspond to larger $E_{\rm iso}$ and $L_{\rm iso}$. Since LL bursts have larger $\theta_{\rm jet}$ the probability that they intercept our line of sight is greater then that for HL bursts: therefore, the fraction of GRBs that we detect at lower luminosities is greater than at large luminosities (with respect the total number of event). For this reason, also the observed luminosity function has to be corrected in normalization according to the different beaming factor characterizing each luminosity bin. Fig.6.14 shows the corrected points (black dots and red triangles) together with the observed ones (grey dots): the higher the luminosity, the larger is the applied correction, according to Eq.6.6.

There is degeneracy between the parameters η and $L_\star$: changing $L_\star$ in the range $[10^{49},10^{51}]$ erg/s the fit always favors an efficiency $\eta = 1$ which is unrealistic (e.g. all the energy is converted in prompt radiation and there would be no energy left for the afterglow emission). Only for $L_\star \geq 10^{52}$ erg/s, we find reasonable values of η. Therefore, in Fig.6.14 is shown the fit with both η and $L_\star$ fixed to their typical values (0.2 and 10^{50} erg/s, respectively – cyan solid line). With these assumptions the fit is consistent with the lower limits of the IL (triangles in Fig.6.14) and only marginally consistent with the LL bursts.

Since the slopes of the correlations are $A = 0.5$, $G = 1$, we have the slope at low luminosities $\xi = (G - A)/G = 0.5$ in the case of a circumburst wind density profile (or $\xi \simeq 0.3$ being $A = 0.5$, $G = 0.7$ – homogeneous circumburst density). The slope of the distribution of energies provided by the inner engine found by the fit is $k = 1.5 \pm 0.15$, corresponding to a high–luminosities slope $\xi + k(1 - \xi) \simeq 1.25$ for $\phi(L)$. Fig.6.14 also shows (shaded region) the 3σ boundaries of the LF obtained accounting for the scatter of the $E_{\rm peak} - E_{\rm iso}$ (0.22 dex), $E_{\rm peak} - E_\gamma$ (0.12 dex) correlations in deriving the correlation of Eq.6.6.

In this case, we can obtain a reasonable agreement with the data in the entire luminosity range but the very low luminosities, where the model shows a small deficit.

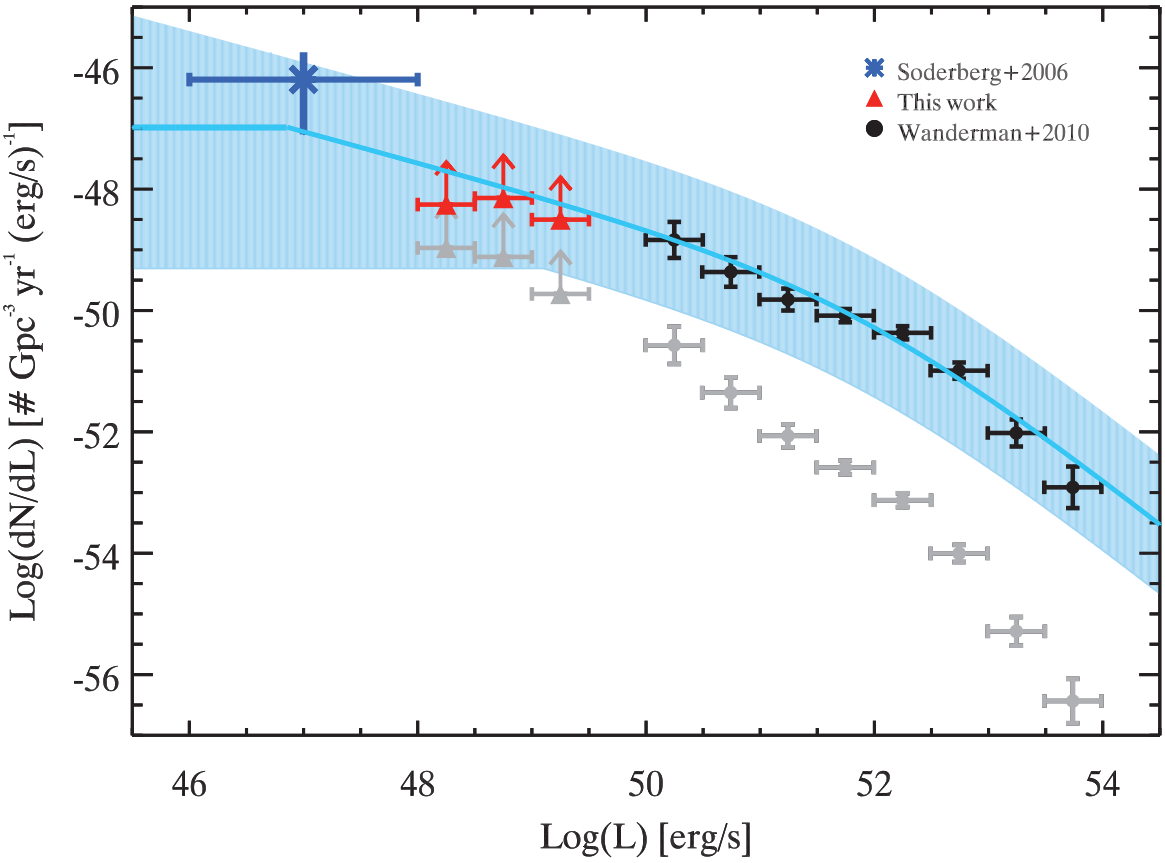

Figure 6.14: UJ with jet angle dependent from the luminosity. The LF of the entire GRB population (i.e. corrected for the collimation factor, which depends on the luminosity in this case) is shown by the black symbols. Original points (grey symbols) are also shown. The model is shown by the solid cyan line and the 3σ confidence interval of the model, obtained accounting for the scatter of the $\theta_{\rm jet} - L_{\rm iso}$ correlation (see text) is shown by the azure shaded region.

Also off–axis UJ In the third case the jet is still uniform, but we allow the observer to detect radiation also off–axis, i.e. for viewing angles $\theta_{\rm v} > \theta_{\rm jet}$. This is possible for Γ not extreme, as illustrated in Fig.6.4: the luminosity drop at $\theta_{\rm v} \gtrsim \theta_{\rm jet}$ is more pronounced for larger Γ. The LF (see Fig.6.5) is a power–law with a slope $-5/4$ which smoothly turns into a peak at high luminosities corresponding to the maximum observable luminosity (for $\theta_{\rm v} < \theta_{\rm jet}$). The observed LF (shown in Fig.6.12) has a slope -1.2 (WP10) and breaks into a steeper (-2.4) power–law for $L_{\rm iso} > 10^{52.5}$ erg/s, thus there is very good agreement with the theoretical LF (before the break).

However, the model LF does not fit the data above the break because it has been obtained assuming single value of $\theta_{\rm jet}$ and Γ (and for this reason the LF show an upturn at HL instead of a steepening).

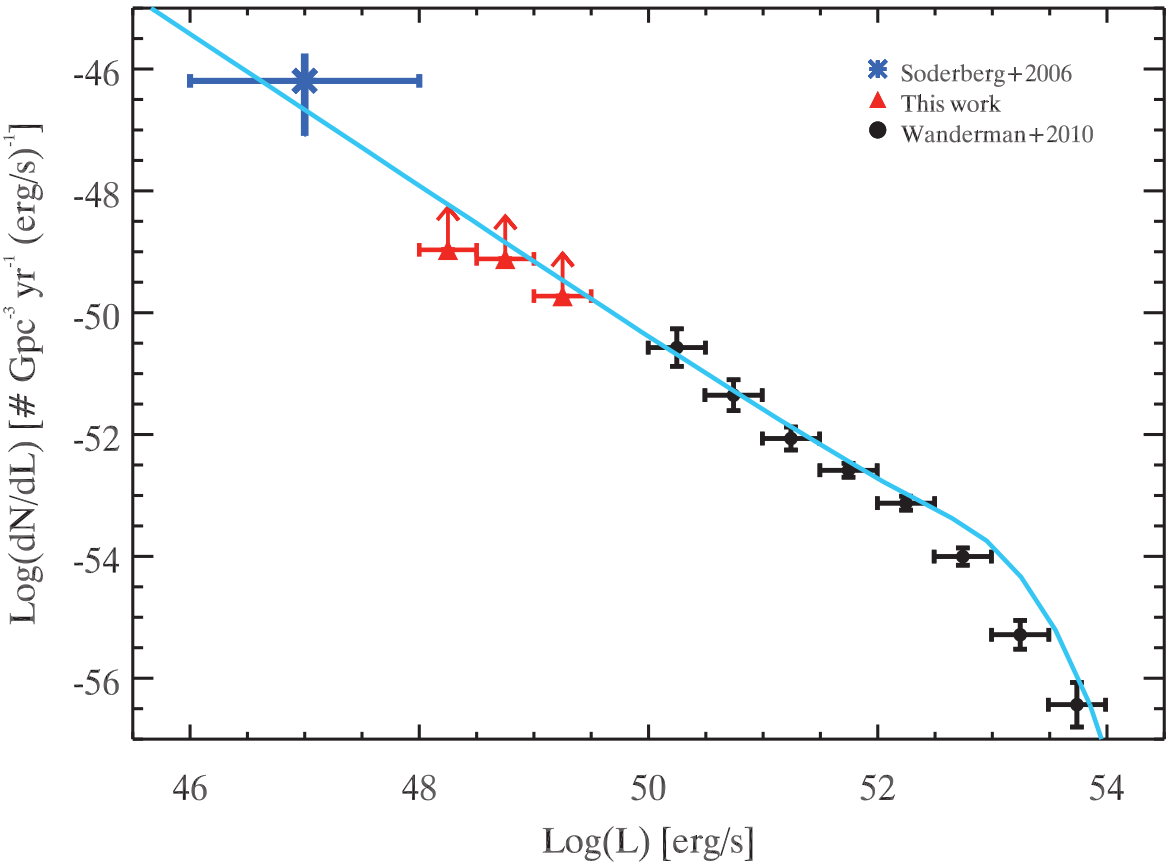

Figure 6.15: Uniform jet model LF allowing to observe the jet also off–axis. Blue solid line is obtained assuming dispersion for the jet parameter $\theta_{\rm jet}$ and Γ (see text).

In order to smooth this peak and obtain a break in the LF model, we need to introduce some dispersions of the values of Γ and $\theta_{\rm jet}$. We find good agreement with the data as shown in Fig.6.15 by the solid line assuming $\theta_{\rm jet}$ centred around 3° with a log–normal dispersion of width 0.2 and Γ centered at a value of 30 with a log–normal dispersion of width 0.14. What is remarkable in this case is that the analytically predicted slope at intermediate luminosities is very close to what seen.

SJ The slope of the LF assuming a power–law structured jet (Eq.6.28) depends on the shape of the jet structure s which also regulates the extension of the LF (i.e. the ratio of the minimum and maximum observable luminosity, see Eq.6.25) as shown by the different curves of Fig.6.10.

In the first formulations of the SJ, the parameter s was fixed to 2 in order to re–obtain and explain the clustering of the collimation

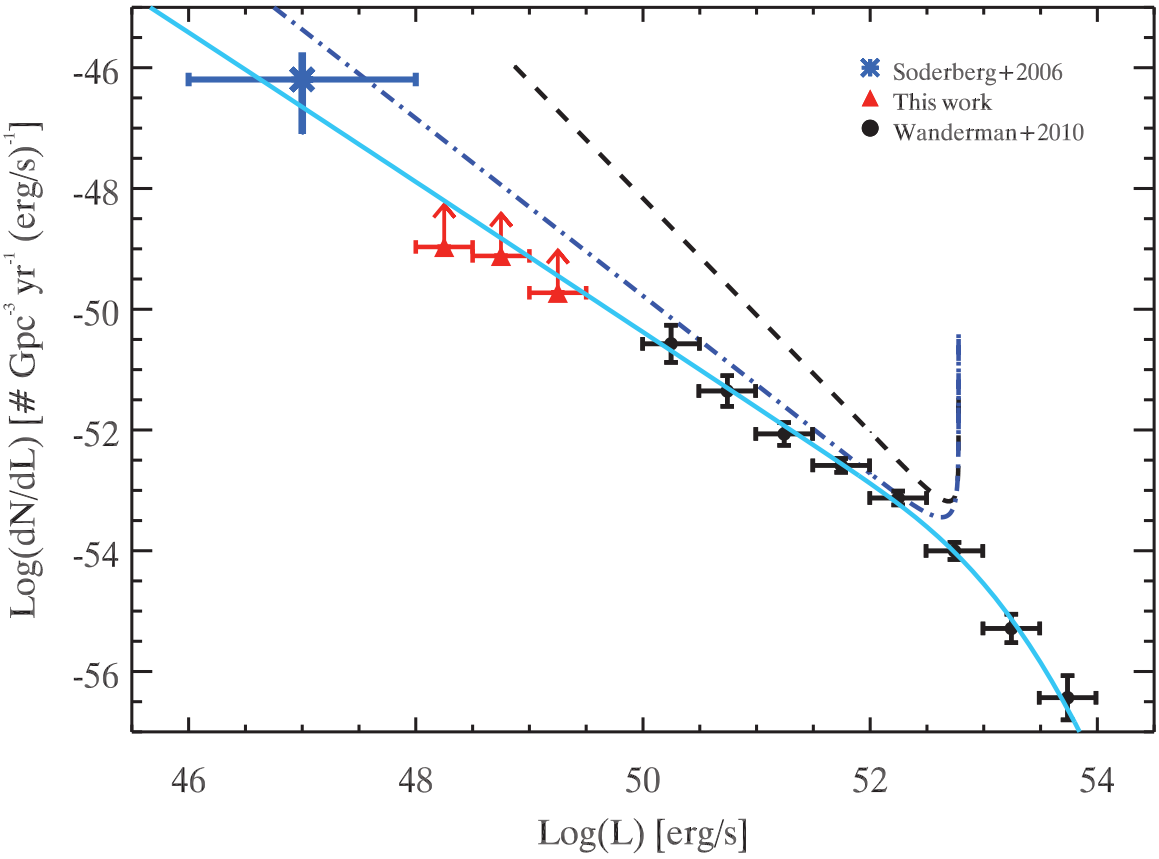

Figure 6.16: SJ model assuming a jet core energy per unit solid angle $\epsilon_c = 6 \times 10^{52}$ erg with a dispersion (log–normal) around this value with $\sigma = 0.5$, $s = 8.1$ and $\theta_c \sim 5°$. For comparison are also shown the LF obtained with $s = 2$ and 4 (from Fig.6.10) by the dashed and dot–dashed lines, respectively.

corrected energy found by Frail et al. (2001); Panaitescu and Kumar (2001). However, in order to explain the range of observed luminosities ($\sim$ 8 dex) wee need that the slope s is rather steep ($s > 4$ assuming a core angle $\theta_c = 1°$). This simple argument excludes the value $s = 2$ commonly adopted in literature. Formally, in order to reproduce the slope 1.25 of the observed LF of Fig.6.12 we need $s = 8$. The upturn at large luminosities shown in Fig.6.10 corresponds to the jets observed within the core which all have the same luminosity. Instead, the observed LF (Fig.6.12) is steeper after a break corresponding to $L_{iso} \sim 3 \times 10^{52}$ erg/s. To reproduce this smooth break, we have to introduce some dispersion of the parameters. Fig.6.16 shows that we can reproduce the LF if we assume a jet core energy per unit solid angle $\epsilon_c = 6 \times 10^{52}$ erg with a dispersion (log–normal) around this value with $\sigma = 0.5$, $s = 8.1$ and $\theta_c \sim 5°$. The obtained LF is also consistent with the lower limits corresponding to the IL burst.

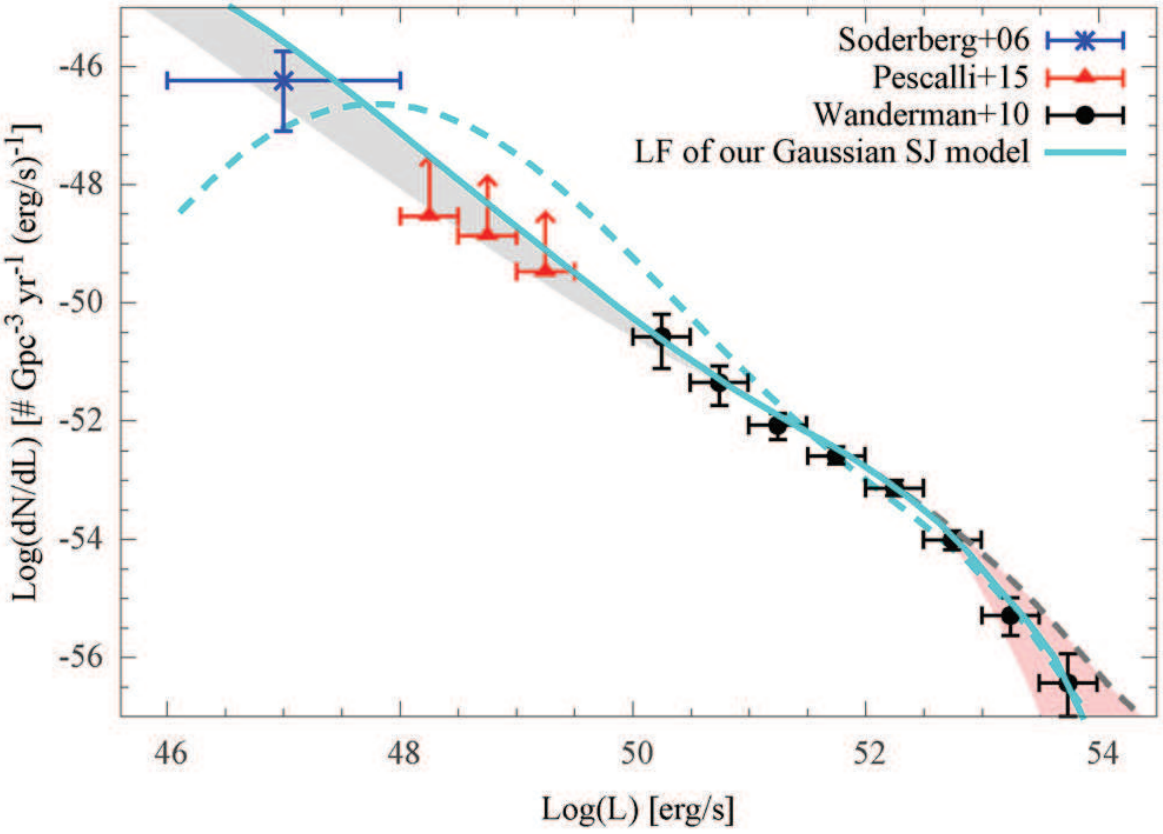

Figure 6.17: The light blue line represents the LF for a Gaussian structured jet. There are two shaded areas obtained by varying one parameter and leaving the others fixed: the grey one refers to $1 \leq \theta_\Gamma/\theta_c \leq 2$, while the pink one refers to a intrinsic dispersion σ between 0.35 and 0.78 dex. The dashed grey line (visible on the bottom–right corner) is the LF for $\theta_c = 5°$, while the dashed light blue line is the LF for $\theta_\Gamma/\theta_c = 0.5$, both with all other parameters fixed.

In Salafia et al. (2015)we also tested the Gaussian structured jet finding equivalently good agreement (see.Fig.6.17). The exact value of Γ_c has little effect on the apparent structure of the Gaussian jet (as long as it is > 100), so it is a secondary parameter for what concerns the LF and we fixed it to 800. In order to obtain the cluster of the collimation corrected energy around 10^{51} we adopted central values $\theta_c = 3°$ and $\epsilon_c \sim 2 \times 10^{52}$ erg.

All these comparisons indicate that the jet must have a relatively sharp cut–off. Even if an abrupt one is nonphysical (all the energy contained within the jet, and zero outside), the energy must in any case decrease rapidly with the angle from the jet axis, once it becomes greater than the core angle θ_{rmc}. Thus the over all conclusion is that the jet can be considered universal, all GRBs have the same

steep structure (with very little dispersion) that can eventually be well approximated by a uniform jet.

CHAPTER 7

Orphan GRBs Afterglows (OA)

GRB jets are among the most powerful in the Universe. Their typical luminosity is about $10^{50} - 10^{54}$ erg/s and there are theoretical arguments (e.g. Sari and Piran, 1999a) and direct observational evidence (e.g. Molinari et al., 2007) suggesting that the highly relativistic ejected plasma has typical bulk Lorentz factors $\Gamma_0 \sim 10^{2-3}$. The most luminous and energetic GRBs seem to have larger Γ_0 (e.g. Ghirlanda et al., 2012b; Liang et al., 2010). If the energy/luminosity and the bulk Lorentz factors are constant within the jet (with the velocities pointed radially as the expansion of the outflow), we can only detect those bursts whose jet is pointing towards the Earth. Indeed, since the emitted radiation is strongly beamed, the flux directed at the Earth is dramatically reduced when $\theta_{\rm v} > \theta_{\rm jet}$, where $\theta_{\rm v}$ is the viewing angle between the jet axis and the line of sight. The events observed at large viewing angle, which are the most numerous since the jet orientation probability is $\propto \sin\theta_{\rm v}$, go easily undetected as prompt GRBs. However, during the afterglow phase, being the outflow decelerated by the external medium, the bulk Lorentz factor may decrease enough to make the afterglow radiation visible to the observer. This happens on a characteristic timescale when the rela-

tivistic beaming $\propto 1/\Gamma$ equals θ_v (see Fig.7.1).

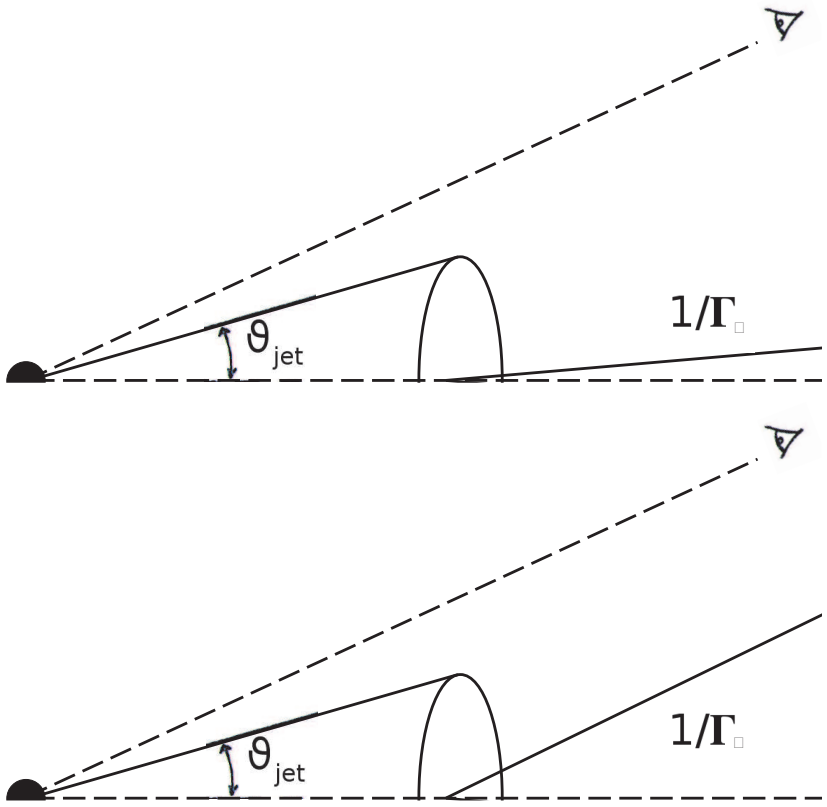

Figure 7.1: Schematic representation of the de–beaming due to the fireball deceleration. Only when $1/\Gamma \sim \theta_v$ the off–axis observer detect the radiation.

Such events, missing the prompt emission but detected as afterglows, are called orphan afterglows (OAs) and, for typical opening angles of a few degrees, e.g. $\theta_{jet} \sim 0.1$ rad, they should outnumber the population of observed GRBs by a factor $(1 - \cos(\theta_{jet}))^{-1} \sim 200$. Despite their expected numerosity and despite specific studies designed in order to search them in X–ray surveys (Grindlay, 1999; Greiner et al., 2000), in optical surveys (Rau et al., 2007, 2006; Malacrino et al., 2007), and in the Radio band (Levinson et al., 2002; Gal-Yam et al., 2006; Bannister et al., 2011; Bower and Saul, 2011; Bell et al., 2011; Croft et al., 2010; Frail et al., 2012; Carilli et al., 2003; Matsumura et al., 2009; Lazio et al., 2010), no OA have been conclusively detected so far. Nondetections of OA are in agreement with current theoretical predictions (Totani and Panaitescu, 2002; Nakar et al., 2002; Zou et al., 2007; Rossi et al., 2008; Metzger et al., 2015).

Such predictions are based on works that either simply extrapolated the properties of a few known GRB afterglows to the orphans (e.g. Totani and Panaitescu, 2002) either assumed too basic prescriptions

for the known GRB population properties or for the afterglow emission model. Thus, there is the necessity of specific predictions on the detection rate that are based on the true rate (duration, fluxes) of the population of OAs (derived from the population properties of observed GRBs) and on the survey characteristics (area of the sky covered, timescales, limiting flux). Only recently, Ghirlanda et al. (2014) studied the properties of OAs in the Radio considering the Square Kilometer Array (SKA) limiting flux ($\sim \mu$Jy) and predicting up to $\sim 0.2 - 1.5$ OA deg^{-2}yr^{-1}.

I collaborated to Ghirlanda et al. (2015b) in which we derive the flux distribution of OAs in the X–ray, optical, and mm Radio band exploiting the population synthesis code recently developed in Ghirlanda et al. (2013a). In this work we also studied the average duration of the population of OAs as a function of the survey limiting flux and made predictions for ongoing and forthcoming surveys.

7.1 OA emission model

Basically, OAs are normal GRBs but observed with a viewing angle so that $\theta_{\rm v} > \theta_{\rm jet}$. We can exploit the known population properties of GRBs detected in the γ–ray band (with well–studied afterglow emission) and infer the OA emission properties taking into account their different orientation of the jet. Thus, we first need a model describing the GRB population.

We used the population code developed recently in Ghirlanda et al. (2013a) and extended in Ghirlanda et al. (2014), called PSYCHE (Population SYnthesis Code and Hydrodynamic Emission model). Using PSYCHE we generated a population of GRBs having:

- redshift z assigned following the GRBFR of Hopkins and Beacom (2008);
- viewing angle $\theta_{\rm v}$ according to the jet orientation probability $\sin(\theta_{\rm v})$ with respect the line of sight (see Eq.6.26);
- jet opening angle $\theta_{\rm jet}$ drawn from a log–normal distribution with median value 5.7°;
- bulk Lorentz factor Γ_0 drawn from a log–normal distribution with median value 90.

The latter two distributions have been obtained (Ghirlanda et al., 2013a) reproducing:

- the $E_{\rm p} - E_{\rm iso}$ correlation of the BAT6 complete sample (Salvaterra et al., 2012; Nava et al., 2012);
- the flux distribution of GRBs detected by BATSE and *Fermi*/GBM;
- the detection rate of GRBs by *Swift*, *Fermi*, and BATSE;

assuming universal comoving frame properties (see Ghirlanda et al., 2013a, for more details).

Whitin the simulated population, we considered only the fraction of burst that could be detected as OA ,i.e. those ones having $\theta_{\rm v} > \theta_{\rm jet}$. At this point, we also need to simulate the afterglow emission since this is most probably the only one that can be detected from an off–axis ultrarelativistic GRB. To this aim we used *BOXFIT* (van Eerten et al., 2012; van Eerten and MacFadyen, 2011, implemented in PSYCHE) which is based on numerical 2D simulations of the jet dynamics and assumes synchrotron emission from shock accelerated electrons as the radiation mechanisms of the afterglow phase.

The GRBs generated using PSYCHE have a jet with a top–hat uniform structure, i.e., the kinetic energy and the bulk Lorentz factor are constant within the jet opening angle (see Sec.6.1). Alternatively, (Rossi et al., 2002; Zhang and Mészáros, 2002) GRB jets could be structured (see Sec.6.2), i.e., the kinetic energy (and possibly also) the bulk Lorentz factor vary within the jet depending on the angular distance from the jet axis.

In the former (UJ) scenario considered in this work, orphan afterglows are naturally expected to largely exceed the number of GRBs in the Universe (considering a typical jet opening angle of few degrees). Even if the top–hat uniform jet emission can be seen when off–axis ($\theta_{\rm v} \geq \theta_{\rm jet}$, its flux should decreases so much that it is difficult for the observer to detect the prompt emission. This justify the approximation that we can only see prompt emission from GRBs whose uniform jet is pointed toward the Earth (i.e., when $\theta_{\rm v} \leq \theta_{\rm jet}$). In the structured jet model, instead, there is always a portion of the jet that is pointing toward the observer. Therefore, the observed GRB properties strongly depend (if Γ is large enough) on the viewing angle $\theta_{\rm v}$ such that orphan afterglows should not exist in principle, since jet emission can be seen even at large angles from the jet (Salafia et al., 2015). However, also in this scenario OAs could still be present if either the prompt emission at large angles is below any detector threshold or if the jet is uniform within a relatively

narrow core and highly structured (i.e., with a steeply decreasing energy profile) outside it, as suggested by the modeling of the luminosity function (Pescalli et al. 2015 – see Chp.6). In this model, the detection rates of OA would, at any rate, be lower than in the top–hat model adopted here as shown in Rossi et al. (2008).

7.1.1 Setting the micro–physical shock parameters

In the standard afterglow model, the external shock emission depends on a set of micro–physical parameters: the index p of the power–law energy distribution of the shock accelerated electrons ($N(\gamma) \propto \gamma^{-p}$), the fraction of the dissipated energy distributed to electrons ϵ_e and to the magnetic field ϵ_B. Finally, we also need to assign a value to the circumburst medium density n (assumed constant in *BOXFIT*).

Distributions of the microphysical shock parameters (p, ϵ_e, ϵ_B) are poorly constrained directly from the observations. These parameters are typically derived through the modeling the afterglow light–curves (Panaitescu and Kumar, 2000). However, dense multi–wavelength sampling of the afterglow light–curve from early times to days after the burst explosion is available for a limited number of bursts.

For this reason, we used the average values of the micro–physical parameters (p, ϵ_e, ϵ_B) derived from the entire simulated GRB population. We considered the afterglow emission of those bursts seen on–axis (having $\theta_v \leq \theta_{jet}$) with the aim to reproduce, assigning to this sub–sample a set of values for the micro–physical parameters, the observed afterglow flux distributions. Fig.7.2 shows the cumulative distribution of the optical flux (at 12 h after the burst) of the BAT6 sample (red solid line, adapted from Melandri et al. 2014), the cumulative distribution of the X–ray flux (at 3 keV and at 11 h) of the BAT6 (blue solid line, adapted from D'Avanzo et al. 2012), and the cumulative distribution of the radio flux (at 8.4 GHz between 1 and 6 days) of the BAT6 (green solid line, adapted from Ghirlanda et al. 2013c).

We selected among the sub–sample of on–axis bursts only the bright events adopting the same limiting flux defining the BAT6, i.e., we choose those bursts with a peak flux larger than 2.6 ph cm^{-2} s^{-1} integrated in the $[15 - 150]$ keV energy band. We assigned to each simulated burst a value for the circumburst density n randomly ex-

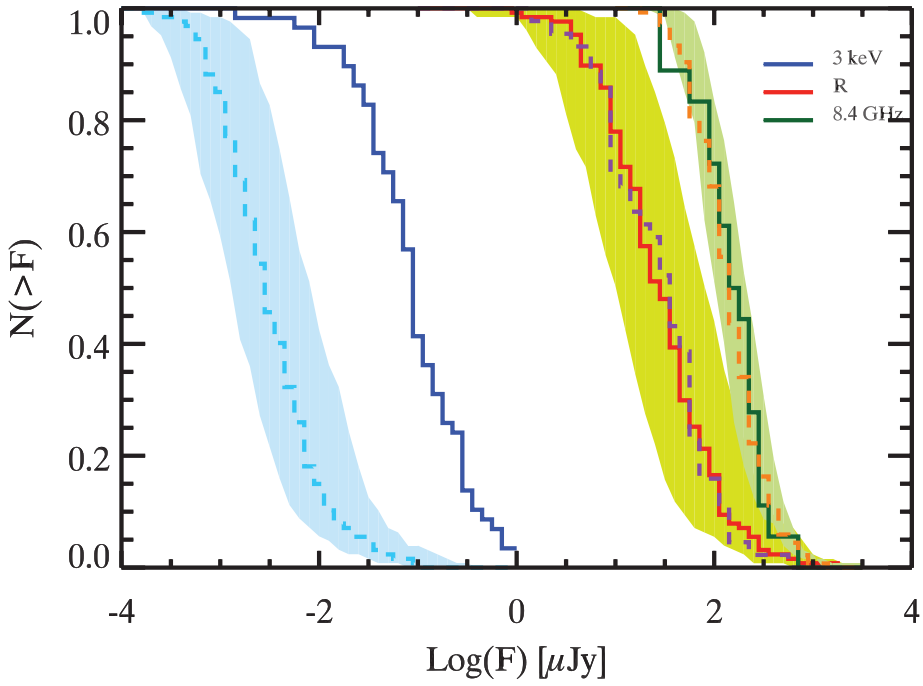

Figure 7.2: Flux density cumulative distributions in the optical (R, solid red line), X–ray (at 3 keV, solid blue line) computed at 11 h after the start of the GRB emission for the BAT6 *Swift* complete sample (adapted from Melandri et al., 2014; D'Avanzo et al., 2012, for the optical and X-ray band, respectively). The radio (at 8.4 GHz – solid green line) is from Ghirlanda et al. (2013c), also for the BAT6 sample. The results of the population synthesis code with $p = 2.3$, $\epsilon_e = 0.02$ and $\epsilon_B = 0.008$ are shown with the dashed lines. The shaded regions represent, for each band, the results obtained with $(p, \epsilon_e, \epsilon_B) = (2.3, 0.01, 0.001)$ for the lower boundary and $(p, \epsilon_e, \epsilon_B) = (2.3, 0.05, 0.01)$ for the upper boundary. The X–ray and R band fluxes of the *Swift* BAT6 sample (solid blue and red line respectively) have been corrected for absorption (D'Avanzo et al., 2012; Campana et al., 2012) and for dust extinction (Melandri et al., 2014; Covino et al., 2013), respectively.

tracted from a uniform distribution between 0.1 and 30 cm^{-3}. We keep the other three parameters (p, ϵ_e, ϵ_B) fixed and fiducial values will be obtained reproducing the flux distributions of the BAT6 sample shown with the solid lines in Fig.7.2.

With the obtained value $p = 2.3$, $\epsilon_e = 0.02$ and $\epsilon_B = 0.008$ we can nicely match the radio and optical flux distributions (solid lines in Fig.7.2) of the real GRBs of the BAT6 sample. If we assume lower/higher values for ϵ_e and ϵ_B, we obtain lower/higher fluxes in both bands (solid shaded regions in Fig.7.2). The obtained micro–physical parameter values (that well reproduce the optical and radio fluxes) underestimate the X–ray flux by more than one order of mag-

nitude. This is not unexpected since the fact that X–ray emission of GRBs could be dominated at early times (typically up to half a day after the explosion) by an extra component, which is apparently unrelated to the standard afterglow forward shock emission (e.g., Ghisellini et al., 2009; D'Avanzo et al., 2012), has already been discussed in the literature. Therefore, we assume the micro–physical parameters values that reproduce the optical and radio flux distribution of a flux limited sample of real bursts.

7.2 OA distinguishing properties and predictions

One of the problems in the OA detection concerns how to distinguish them from other similar transients detected in large sky surveys. According to our simulations, OAs appear as daily transients in optical and X–ray band (see Fig.7.5 and sub–sec.7.2.2), given the typical flux limits of current and forthcoming surveys (see Tab.7.1). The problem is that many other extragalactic sources show similar duration.

OA lightcurve has the same typical temporal behavior of a GRB afterglow, i.e. $\propto t^{-\delta}$ with $\delta \sim 1-2$, but it is not enough to unambiguously distinguish them. For this reason, a dedicated optical photometric and spectroscopic follow–up program is fundamental in order to successfully classify them. The optical/X–ray light curves, especially if the detected OA is still quite bright and/or before its lightcurve peak, can be a very useful tool for a preliminary classification. Indeed, its shape and its decay power–law index should be at least different from those of SNe or blazars. A further key information should be provided by the optical spectroscopy since the he spectral continuum and the absorption lines present in the optical–Near–IR (NIR) spectra of the afterglow are very different from those typically found in SNe or blazars (Fynbo et al., 2009; Christensen et al., 2011). Nonetheless, also spectra with a sufficient signal–to–noise ratio are needed. To date this requirement is fulfilled down to $R \sim 22$ with a reasonable amount of integration time (~ 2 h, e.g., with X–Shooter at ESO/VLT), but future larger telescopes will also make possible to obtain similar results for fainter objects.

Another useful way to discriminate between OAs and other transients comes from the analysis of the broad spectral energy distribution (SED). Fig.7.3 shows the typical overall SED of OAs (i.e., the convolution of the SEDs of all OAs detectable by the LSST survey

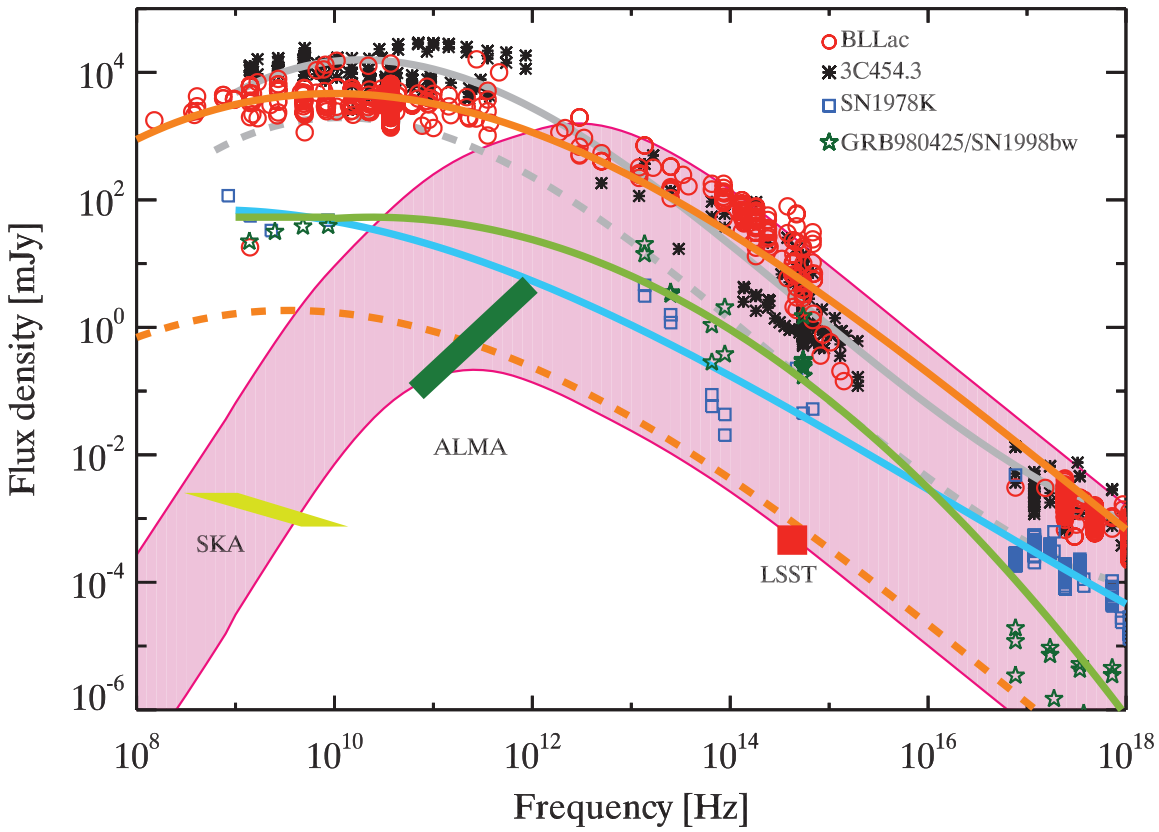

Figure 7.3: Spectral energy distribution of the OAs that can be detected by the LSST (pink filled region). The SED of the low–power blazar BLLac (open circles), the FSRQ 3C 454.3 (asterisks), and of two supernovae, SN1978K (open squares) and the GRB–SN associated GRB980425/SN1998bw (open stars), are shown with different symbols. The solid lines provide an interpolation of the data points and do not represent any physical model. For the two blazars, we also show, with a dashed gray line for 3C 454.3 and dashed orange line for BLLac, how their spectra would appear if they were at $z = 2$ (typical of GRBs). The (5σ) limits for a 12 h continuum observation with the SKA is shown by the yellow shaded region. The green shaded region marks the limiting flux of an ALMA observation (32 antennas of 12 m for 3 h of observation in dual mode, from https://almascience.eso.org/proposing/sensitivity-calculator). The LSST limiting flux (see Tab.7.1) is shown by the red square symbol.

Table 7.1: Transient surveys in the optical and X–ray bands. On–going and future surveys are marked in boldface. Parameters of the optical surveys, field of view (FOV), cadence, limiting flux $F_{\rm lim}$, coverage and lifetime are from the compilation of Rau et al. (2009). The rate of orphan afterglow R_{OA} above the survey limiting flux is obtained through the flux density distribution reported in Fig.7.4. The average OA duration above this flux limit $\langle T \rangle$ is derived from Fig.7.5 and from the parameters of the linear fits reported in Tab.7.2 (the minimum and maximum durations are shown in square parentheses). The last column shows the number of OA per year detectable by the reported surveys. For the X–ray the sky coverage is intended for 24 h. * see `http://www.ptf.caltech.edu/ztf` and Bellm (2014).

Survey	FOV ($\deg^2$)	Cadence	F_{lim} (mJy)	Coverage ($\deg^2$ night^{-1})	Lifetime days	R_{OA} ($\deg^{-2}$ yr^{-1})	$\langle T \rangle$ days	# OA yr^{-1}
PTF	7.8	1m–5d	1.17×10^{-2}	1000		1.5×10^{-3}	1[0.2-3.8]	1.5
ROTSE–II	3.4	1d	1.17×10^{-1}	450		5.2×10^{-4}	0.4[0.1-1.7]	0.1
CIDA–QUEST	5.4	2d–1yr	4.60×10^{-2}	276		8.0×10^{-4}	0.5[0.1-2.3]	0.1
Palomar–Quest	9.4	0.5h–1d	1.17×10^{-2}	500	2003–2008	1.5×10^{-3}	1[0.2-3.8]	0.8
SDSS–II SS	1.5	2d	2.68×10^{-3}	150	2005–2008	3.2×10^{-3}	1.6[0.4-6.3]	0.8
Catilina	2.5	10m–1yr	4.60×10^{-2}	1200		8.0×10^{-4}	0.6[0.1-2.4]	0.6
SLS	1.0	3d–5yr	5.60×10^{-4}	2	2003–2008	5.2×10^{-3}	2.8[0.8-11]	0.03
SkyMapper	5.7	0.2d–1yr	7.39×10^{-2}	1000	2009–...	6.4×10^{-4}	0.5[0.2-2.0]	0.3
Pan–STARRS1	7.0	3d	7.39×10^{-3}	6000	2009–...	2.0×10^{-3}	1[0.3-4.4]	12
LSST	9.6	3d	4.66×10^{-4}	3300	2022–...	5.1×10^{-3}	3[0.8-11]	50
Gaia	0.5x2	20d	3.00×10^{-2}	2000	2014–2019	10^{-3}	1[0.5-5]	2
ZTF *	42.0	1d	2.00×10^{-2}	22500	2017–...	1.1×10^{-3}	0.8[0.4-4.8]	20
RASS	3.1	...	4.00×10^{-5}	12000	6 months	8.0×10^{-4}	1[0.3-4.4]	10
eROSITA	0.8	6 months	2.00×10^{-6}	4320*	4 years	3.0×10^{-3}	2[0.5-6.5]	26

– hatched pink region) compared with that of potential competitors extragalactic sources like SNe and blazars. We chose to consider only the OAs that will be detected by the forthcoming LSST survey (Ivezic et al., 2008a, – see Tab.7.1) since it is the most promising (we predict a rate $\sim$ 50 OAs per year). The typical SED of OAs detectable by LSST peaks in the 1011–13 Hz range. The spectrum below the peak, in the GHz down to the MHz range scales $\propto \nu^2$.

Fig.7.3 also shows the SED of two blazars: the Flat Spectrum Radio Quasar (FSRQ) 3C454.3 and BLLac itself as representative of the respective classes (see Ghisellini et al., 2010b). Two supernovae are also shown: SN 1978K as a possible representative of highly luminous supernovae and the GRB980425/SN1998bw (Galama et al., 1998) for the class of associated GRB–SNe. The SED are reported as obtained by multifrequency observational campaigns and retrieved from Italian Space Agency (ASI) Science Data Center SED Builder tool. The corresponding solid curves in Fig.7.3 are not physical models, and only illustrative of the overall broadband SED of these classes of objects. The blazar SED is also shown as it would be like if positioned at $z = 2$, i.e., at the typical distance of long GRBs. Red square symbol represents the LSST flux limit. The OAs that LSST can detected when their jet emission is fully visible by the off–axis observer already have their peak frequency below the optical band, in the mm region. This is because the peak of the OA emission is reached several months after the burst (see sub–sec.7.2.2 and see also Ghirlanda et al., 2014). Furthermore, Fig.7.3shows that their emission in the MHz/GHz region is still in the self–absorbed regime. In contrast, BLLacs and SN emission like 1998bw or 1978 K are characterized by a softer spectrum in the radio band than the typical OA detected in an optical survey like the LSST. Therefore, the follow up of these transients in the mm and GHz bands will characterize their different SED.

7.2.1 OA flux densities

The peak flux associated to the OA is by definition the OA flux at the time of the lightcurve peak. The cumulative peak flux density distributions of OAs are shown in Fig.7.4. The range of variation of the flux density distributions has been obtained by varying the micro–physical parameters.

X–ray Flux density is computed at 3 keV where the photoelectric absorption by metals in the Galaxy and host galaxy is negligible (Campana et al., 2012).

Optical In order to obtain the Optical R flux density, the dust extinctions A_V has been assumed according to the distribution obtained in Covino et al. (2013). Such distribution has been obtained by the analysis of the BAT6 sample, i.e. bursts detected in γ–rays. It is possible that the GRB X–ray/UV emission might partially destruct the dust and then reduce the optical absorption along the line of sight that in this case isclose to the jet axis Perna et al. (2003). Since OAs are observed at larger viewing angles, they could therefore have a larger A_V than the assumed one. This would further reduce the optical fluxes of OAs observed at large viewing angles and consequently reduce the predicted rates of OAs in the Optical band. Moreover, we only considered OAs at $z < 4.5$ because at higher z the optical emission is expected to be fully absorbed by the Lyα absorption.

Radio We also computed the OA flux cumulative distribution at the reference frequency of 443 GHz. Such frequency has been adopted because, considering the typical timescales when OA are detectable, the few hundred GHz range is where OAs are brightest. Frequencies in this range are covered by, e.g., ALMA.

7.2.2 OA timescalses

For off–axis observers, the OA lightcurve starts to rise when $\Gamma \sim 1/\sin(\theta_{\rm v} - \theta_{\rm jet})$ and peaks when $\Gamma \sim 1/\sin(\theta_{\rm v} + \theta_{\rm jet})$, i.e. when the entire jet is visible. After this time the OA will follow the same light curve detected by an on–axis observer. According to our simulations, the time when the OA peaks, which depends on the burst parameters and on the viewing angle, has a broad distribution with a typical value of few hundred days after the GRB (note that this reference is purely theoretical, since the GRB start time is missed in the real case of an OA).

The necessary condition for the OA to be detected is that its flux is above the survey limiting flux. This determines how much time the OAs are visible, i.e. their characteristic duration $\langle T \rangle$, and affects their rate. Fig.7.5 shows the average duration of OA for the three frequencies we considered for the flux (X at 3 keV, Optical R band,

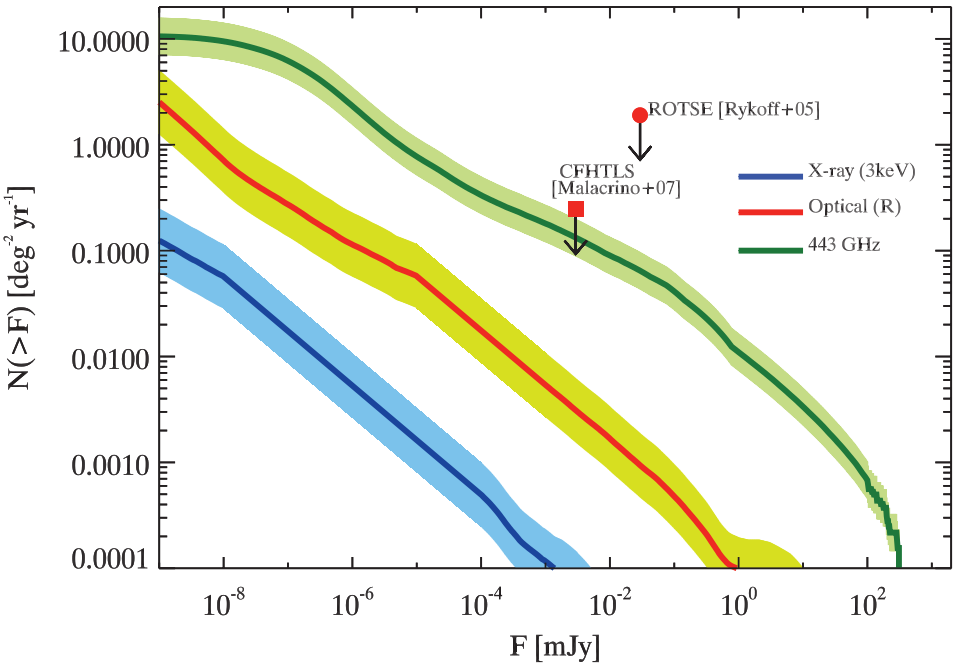

Figure 7.4: Cumulative flux density distribution of OAs at three characteristic frequencies: R band for the Optical (red line), 3 keV for the X–ray (blue line), and 443 GHz for the mm band (green line is representative of ALMA frequency range). Upper limits of past searches of OAs in the optical band are shown by the red symbols (to be compared with the red solid line). The optical R flux distribution is representative of the OAs at $z \leq 4.5$ because, at higher redshift, their R band flux suffers from Lyα suppression. An optical extinction (according to the distribution of Covino et al., 2013) has been applied to the optical fluxes.

Radio at 443 GHz). In general, considering the typical flux limits of Optical and X–ray surveys, OAs will appear as daily transients. At GHz frequencies, they will instead be much more durable transients lasting for even tens to hundreds of days (see also Ghirlanda et al., 2014).

These timescales should not be confused with the peak timescale the OA. The latter depends on the combination of geometrical (opening angle and jet orientation) and hydrodynamics (describing how the fireball decelerates in dependence of the kinetic energy, initial bulk Lorentz factor, and circumburst density) properties and the corresponding distribution is centered around a few hundred days.

Fig.7.5 shows that, at any frequency, the OA duration $\langle T \rangle$ increases as the survey limiting flux decreases. Tab.7.2 shows the parameters (slope m and normalization q) of the linear fit (dotted lines in Fig.7.5) to the data shown in Fig.7.5 for the three characteristic

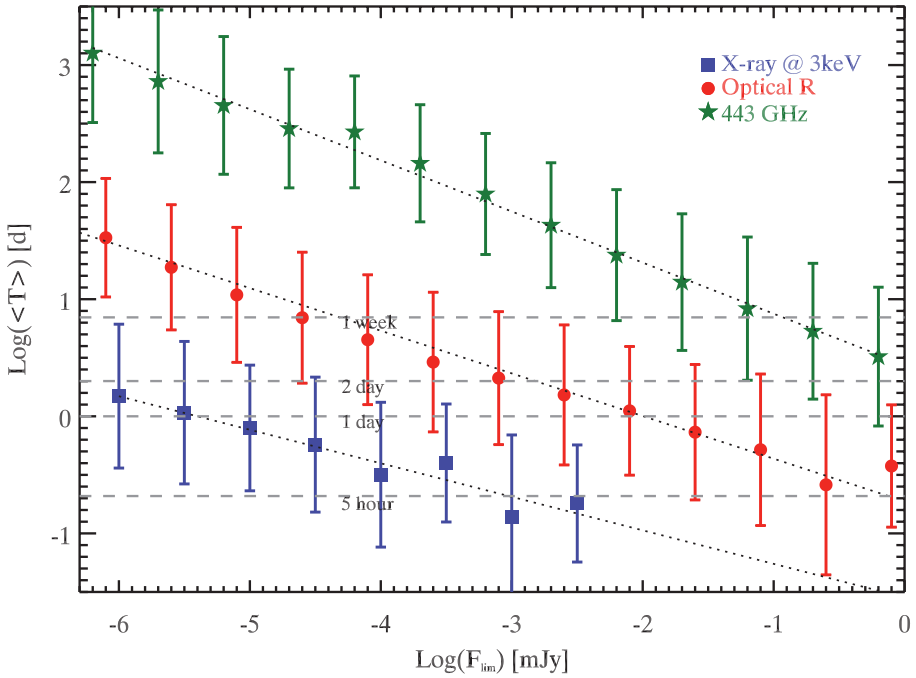

Figure 7.5: Average duration of the simulated population of OAs with flux above the corresponding x–axis value. The bars represent the 1σ scatter around the average. Typical timescales are shown by the dashed horizontal lines (as labeled). Linear fits are shown by the dotted lines. Fit parameters are reported in Tab.7.2.

Band	m	q
X–ray (3 keV)	-0.28	-1.54
R (7000)	-0.36	-0.72
443 Ghz	-0.44	0.44

Table 7.2: Parameters of the linear fits to the average duration of OAs above flux threshold (Fig.7.5. Fit parameters refers to the formula: $\log(\langle T \rangle_{\rm days}) = q + m \log(F_{\rm lim,mJy})$.

frequencies.

7.2.3 OA detection rate

In this sub–section I will compare our results with past searches for OAs mainly in the optical and X–ray band and show specific predictions for ongoing or planned surveys in these bands.

Optical surveys Among past searches for orphan afterglows in the optical, Rykoff et al. (2005) used the Robotic Optical Transients Search

Experiment III (ROTSE–III). Over a period of 1.5 year, they identified no credible GRB afterglow. They place a 95% upper limit on the OA rate of 1.9 deg^{-2} yr^{-1} at $R = 20$. The Deep Lensing Survey (DLS; Becker et al., 2004) provides a (less constraining) limit of 5.2 deg^{-2} day^{-1} for transients with typical duration of a few ks and $19.5 < R < 23.4$. Malacrino et al. (2007) obtained a more stringent upper limit from the CFHTLS Very Wide survey: excluding that the three transient they find are GRBs (Malacrino et al., 2007), an upper limit of 0.24 deg^{-2} yr^{-1} down to $R = 23$ can be placed. The ROTSE–III and CFHTLS limits are shown in Fig.7.4 (filled red symbols) and they are consistent with the rate for the optical band predicted by our model (solid red line in Fig.7.4). Also, no credible OA was found in the Faint Sky Variability Survey project (Vreeswijk 2002).

Present and future major surveys in the optical are shown in Tab.7.1. Most of the optical survey parameters are obtained from Rau et al. (2009). In Tab.7.1, we report the survey name (Col. 1), its field of view (FOV) and its cadence (Cols. 2 and 3). The limiting flux density and the coverage, representing the sky area covered per night, are reported in Cols. 3 and 4, respectively. Through Fig.7.4 we can derive the rate ROA of OAs that have their peak flux density above each survey limiting flux. This is reported in units of deg^{-2} yr^{-1} in Col. 7 of Tab.7.1. Similarly, from Fig.7.5 it is possible to estimate the average duration $\langle T \rangle$ of the OA above the survey limiting flux (Col. 8 in Tab.7.1). In brackets, we indicate the upper and lower estimates of the average duration (i.e., corresponding to the 1σ error bars in Fig.7.5). We derive the rate of OAs (expressed in number of OA per year, last column of Tab.7.1) in a given survey as $N_{\mathrm{OA}} = R_{\mathrm{OA}} \times C \times \langle T \rangle$, where C is the fraction of the sky covered by the survey per night (coverage in Tab.7.1).

Most past and ongoing optical surveys have a small chance of of detecting OAs. Among these, the Palomar Transient Factory (PTF; Law et al., 2009) could marginally see one OA per year (consistent with Rau et al. (2009), predictions) given its relatively low sensitivity compensated by the large portion of the sky covered per night (103 deg^2). Instead, according to our model, an optical survey like that of Pan–STARRS1, which will cover 6000 deg^2 per night could already detect a dozen of OAs per year. Higher detection rates are expected for the forthcoming development of the PTF survey. The Zwicky Transient Facility (Bellm, 2014), which is designed specifically for transients discovery, will cover about 22 500 deg^2 per night

down to a limiting magnitude ~ 20.5. We expect that it will detect ~ 20 OA yr^{-1}. A considerably larger number of OAs will be accessible with the Large Synoptic Sky Telescope survey (LSST; Ivezic et al., 2008b). The telescope will have a 9.6 deg^2 FOV and will be able to survey 104 deg^2 of the sky every three nights down to a limiting magnitude for point sources $R \sim 24.5$. With these parameters, we estimate it could detect 50 OA yr^{-1}. An interesting prediction concerns the *Gaia* satellite (Lindegren, 2010). It will carry two telescopes each one with a FOV of $0.7^\circ \times 0.7^\circ$ and will scan an angle of 360° every six hours. Therefore, it will cover ~ 2000 deg^2 per day performing a survey down to a limiting flux of 0.03 mJy. According to our model, $R_O A \sim 10^{-3}$ deg^{-2} yr^{-1} at this flux limit so that we predict that *Gaia* will detect about 10–15 OAs in its 5 year mission. This estimate is consistent with that reported in Japelj and Gomboc (2011). Given the depth of forthcoming optical surveys, we expect that OAs will have a typical redshift $z \sim 2$. At these distances, the typical GRB host galaxy should be fainter than the LSST limiting magnitude (Hjorth et al., 2012).

X–ray surveys Searching for GRB afterglows in X–ray surveys led to the discovery of few flare stars (Grindlay, 1999; Greiner et al., 2000). The 27 X–ray transients, detected in the 5.5 year survey of Ariel V (Pye and McHardy, 1983), provide a conservative upper limit of 1.15×10^{-3} deg^{-2} yr^{-1}, corresponding to a flux ≈ 0.06 mJy (Grindlay, 1999). This is consistent with our predictions for the X–ray band (solid blue line in Fig.7.4) at the same flux limit. Among the widest X–ray surveys, the ROSAT All–Sky Survey covered the full sky reaching a limiting flux of 4×10^{-13} erg cm^{-2} s^{-1} (0.5–2 keV) in almost six months. This flux limit (assuming a spectrum with photon index -2) corresponds to a flux density of $\sim 4 \times 10^{-5}$ mJy which, according to our estimates, gives a rate $R_{OA} \sim 8 \times 10^{-4}$ deg^{-2} yr^{-1}. The RASS scan procedure covered a full–sky circle of width 2 deg every orbit corresponding to ~ 12000 deg^{-2} day^{-1}. According to our estimates (Fig.7.4 and Tab.7.1), the typical duration of the OA above the RASS flux limit should be ~ 1 day so that the expected OA number should be ~ 4.8 during the six month lifetime of the survey. This result is consistent with the estimate of Greiner et al. (2000). They effectively searched in the RASS for GRB afterglows and concluded that of the 23 candidates only a few could be

due to GRBs, finding that most of the others are flare stars. The second release of the RASS, 2RXS2 has been extended to a flux limit a factor of 4 deeper than the first release. Therefore, we expect to have $\sim$ 12 OAs in the 2RXS. In the X-ray band *Chandra* and *XMM–Newton* have performed deep surveys but, because of their small FOV, at the expense of a relatively small portion of the sky explored (see Brandt and Hasinger, 2005). The observing strategy in these surveys was not a scanning mode as in the RASS, but rather the combination of pointed repeated observations of the same field. Therefore, it is difficult to reconstruct the overall sky coverage. As a gross estimate, we can compute the expected number of OAs by multiplying the predicted rate (according to our results of Fig.7.4) times the area of the sky covered. We stress that this is an overestimate of the number of OAs that could be detected by these surveys. Among the deepest surveys, the 2 Ms *Chandra* Deep Field North covered 0.13 deg^2 in the 0.5–8.0 keV band down to a flux limit of $\sim 10^{-16}$ erg cm^{-2} s^{-1} (Alexander et al., 2003). To such a flux limit, we predict less than 10^{-2} OA yr^{-1}. Similar rates are expected in the *XMM–Newton* Large Scale Survey (Pierre et al., 2004) which, with a sensitivity of $\sim 5 \times 10^{-15}$ erg cm^{-2} s^{-1} (0.5–2 keV) and a 10 deg^2 of sky coverage, should detect at most 0.1 OA yr^{-1}. Both *Chandra* and *XMM–Newton* have performed several other surveys, however, despite larger sky coverage than those mentioned above, this was at the expense of their sensitivity (e.g., the *XMM–Newton* Bright Serendipitous Survey – Della Ceca et al. 2004). Among forthcoming X–ray surveys, we consider the extended ROentgen Survey with the Imaging Telescope Array (eROSITA – Merloni 2012), which will cover the full sky up to 10 keV with a flux limit $\sim 2 \times 10^{-14}$ erg^{-1} cm^{-2} s^{-1} in the 0.5–2 keV band. Therefore, $\sim 3 \times 10^{-3}$ deg^{-2} day^{-1} OA should be reachable by this survey (Tab.7.1). According to the planned scanning strategy, a full circle of width 2 degree will be covered every four hours. This corresponds to $\sim$ 4320 deg^2 day^{-1}. The expected OA number is $\sim$ 26 yr^{-1} (but see also Khabibullin et al., 2012). A larger number of OAs (by a factor 2) could be reached by the WFXT survey (e.g. Rosati et al., 2011).

Therefore, according to our predictions, there does not seem like there is an opportunity to detect any orphan afterglow in current deep X–ray surveys.

Radio For the radio band, Ghirlanda et al. (2014) showed that the OA rates are consistent with the (upper) limits of past radio surveys, which did not detect any credible orphan afterglow. Forthcoming radio surveys like the VAST/ASKAP at 1.4 GHz or the MeerKAT or EVLA at 8.4 GHz could detect 3×10^{-3} and 3×10^{-1} OA deg^{-2} yr^{-1}, respectively. The deeper SKA survey, reaching the μJy flux limit, could detect up to 0.2–1.5 OA deg^{-2} yr^{-1} (Ghirlanda et al., 2014). The Herschel/SPIRE survey ATLAS[1], one of the widest covering a total of 500 deg^2, is limited by the confusion limit of 5–7 mJy at 250–500 μm so that we expect less than 0.1 OA yr^{-1}. *Spitzer* SWIRE[2] observed six fields in the northern and southern sky with typical areas between $\sim$ 4.2 deg^2 and $\sim$ 12 deg^2 with higher sensitivities of few tens of μJy in the low frequency channels (IRAC) at 3.6 μm and 4.5 μm. These fields were covered on different timescales between one and six days. According to our model we expect a rate of less than one OA per year in such fields above the deepest flux limits of this survey.

Among previous works in the literature, which estimated the detection rate of OAs, Totani and Panaitescu (2002) considered 10 GRB of the pre–*Swift* era with well–monitored afterglow light–curves as templates. By assuming different off–axis viewing angles, they estimated the rate of OAs in the X–ray, optical, and Radio band. Their predictions were based on a very small number of afterglows mostly representative of the bright afterglow population of GRBs. Since our code is calibrated with the entire GRB prompt emission flux distribution and includes a more representative sample of afterglows (thanks to which we fixed the micro–physical parameters), we consider that our estimates better represent the low flux end of the OA distribution. Moreover, what is new in our model is that we predict the properties of OAs based on the observed properties of GRBs in the γ–ray band, considering as constraints the flux and fluence distribution of the population of GRBs detected by *Swift*, BATSE, and *Fermi*. Since the γ–ray energy detected in the prompt emission is a proxy of the kinetic energy driving the afterglow deceleration, our simulated population of bursts includes both high and low kinetic power bursts. The choice to reproduce the afterglow flux dis-

[1] http://www.h-atlas.org/\http://www.h-atlas.org/survey/fields

[2] http://swire.ipac.caltech.edu/swire/astronomers/program.html\http://swire.ipac.caltech.edu/swire/public/faqs.html#where

tribution of the complete BAT6 sample of *Swift* bursts, despite being composed by relatively bright events, ensures that we are extending the flux distribution of the synthetic GRB population to the low end better than what could be done with the limited number of GRBs detected in the pre–*Swift* era.

CHAPTER 8

Short GRBs at the dawn of the Gravitational Wave era

It is believed that short GRBs have a different origin with respect the long ones. Their progenitor is most likely a compact object binary system (NS–NS or NS–BH e.g. Giacomazzo et al. 2013 but also see Perna et al. 2016) which merge and lead to the formation of a BH–torus system. In fact, they are characterized by a low density of the close circumburst medium (Fong and Berger, 2013; Fong et al., 2015), are not associated to SNe events and recently a kilonova signature has been detected (Eichler et al., 1989; Li and Paczyński, 1998; Yang et al., 2015; Jin et al., 2015, 2016). Despite this, the prompt γ–ray emission properties of SGRBs (Ghirlanda et al., 2009, 2015a), the sustained long–lasting X–ray emission (although not ubiquitous in short GRBs; Sakamoto and Gehrels, 2009) and the flaring activity suggest that the central engine and the radiation mechanisms are similar to long GRBs.

Because of their link with coalescing binary systems of compact objects, SGRBs are one of the most promising electromagnetic counterparts of gravitational waves (GW) events.

The rate of association of GW events with SGRBs is mainly determined by the rate of SGRBs within the relatively small horizon set by the sensitivity of the updated interferometers aLIGO and Advanced Virgo (Abbott et al., 2016a). However, current estimates of local SGRB rates range from $0.1 - 0.6$ Gpc^{-3} yr^{-1} (e.g. Guetta and Piran, 2005, 2006) to $1 - 10$ Gpc^{-3} yr^{-1} (Guetta and Piran, 2006; Guetta and Stella, 2009; Coward et al., 2012; Siellez et al., 2014; Wanderman and Piran, 2015) to even larger values, e.g. $40 - 240$ Gpc^{-3} yr^{-1} (Guetta and Piran, 2006; Nakar et al., 2006). Note that these rates do not take into account the correction for the jet collimation, i.e. they are representative of the observed population. Moreover, such rate estimates mainly depend on the luminosity function $\phi(L)$ and the cosmic formation rate $\psi(z)$ of SGRBs. These functions have been derived for SGRBs by using the indirect method (see the beginning of Chp.4 for more details) on small samples of bursts. $\psi(z)$, in particular, has always been assumed to follow the cosmic star formation rate $\psi_\star(z)$ with a delay τ which is due to the time necessary for the progenitor binary system to merge:

$$\psi(z) = \int_z^\infty \psi_\star(z') P[t(z) - t(z')] \frac{dt}{dz'} dz' \tag{8.1}$$

The common approach consists in assuming parametric forms for the compact binary merger delay time distribution $P(\tau)$ and for the SGRB luminosity function; free parameters of such functions are then constrained through the small sample of SGRBs with measured redshifts and luminosities and through the distribution of the γ–ray peak fluxes of SGRBs. The delay time τ distribution has been derived by various authors typically assuming a single power–law $P(\tau) \propto \tau^{-\delta}$ (e.g. with $\delta = 1 - 2$; Guetta and Piran, 2005, 2006; D'Avanzo et al., 2014; Wanderman and Piran, 2015) with a minimum delay time $\tau_{\rm min} = 10 - 20$ Myr, or a peaked (log–normal) distribution with a considerably large delay (e.g. 2–4 Gyr, Wanderman and Piran, 2015; Nakar and Gal-Yam, 2005). However, theoretical considerations and population synthesis (Portegies Zwart and Yungelson, 1998; Schneider et al., 2001; O'Shaughnessy et al., 2008; Belczynski et al., 2006; Dominik et al., 2013) suggest that compact binary coalescence should typically follow a delay time distribution $P(\tau) \propto \tau^{-1}$ with $\tau \gtrsim 10$ Myr. A power–law or a BPL (normalized to their integral) are usually assumed for $\phi(L)$.

Since there are relatively few events with $L - z$ measured (see

e.g. Berger, 2014; D'Avanzo, 2015, for recent reviews) constituting incomplete samples, it is not possible to apply direct inversion methods (e.g. C^- method or the MLE – see Chp.4) in order to obtain $\phi(L)$ and $\psi(z)$. For this reason we considered, for the first time, all the available observational constraints for the short GRB population (detected by *Fermi*/GBM) and adopted a Markov Chain Monte Carlo (MCMC) approach in order to derive the parameters describing the $\phi(L)$ and $\psi(z)$ of SGRBs. These constraints are:

1. the peak flux distribution;
2. the redshift distribution of the SGRBs with measured z;
3. the peak energy $E_{\rm p,o}$ of the observed $\nu F(\nu)$ spectrum;
4. the fluence S;
5. the duration T_{90};
6. isotropic luminosity L;
7. isotropic energy E.

8.1 Observational constraints

For the distributions of the observer frame prompt emission properties (constraints 1, 3, 4, 5) we considered the sample of 1767 GRBs detected by *Fermi*/GBM (from GRB 080714 to GRB 160118) as reported in the online spectral catalogue. Of these bursts, 295 in the sample are SGRBs (i.e. with $T_{90} \leq 2$ s). We only select bursts with a peak flux (computed on 64 ms timescale in the $[10-1000]$ keV energy range) larger than 5 ph cm^{-2} s^{-1} in order to work with a well–defined sample, less affected by the possible incompleteness close to the detector threshold flux. With this selection, our sample reduces to 211 SGRBs detected by *Fermi*/GBM in 7.5 yr within its field of view of $\sim 70\%$ of the sky. We defined the observer–frame constraints as follows:

1 the distribution of the 64 ms peak flux P_{64} (integrated in the $[10-1000]$ keV energy range). Black symbols in the top left panel of Fig.8.1;

3 the distribution of the observed peak energy of the prompt emission spectrum $E_{\rm p,o}$. Black symbols in the bottom left panel of Fig.8.1;

4 the distribution of the fluence S (integrated in the $[10-1000]$ keV energy range). Black symbols in the bottom middle panel of Fig.8.1;

5 the distribution of the duration T_{90} of the prompt emission. Black symbols in the bottom right panel of Fig.8.1.

The errors on these distributions (shown in Fig.8.1) have been computed by resampling each measurement (P_{64}, S, $E_{\rm p,o}$, and T_{90}) within its error with a normal distribution. For each bin, the vertical error bars represent the standard deviation of the bin heights of the resampled distributions.

We adopted here the peak flux P_{64} and the fluence S computed in the wide $[10-1000]$ keV energy range (provided in the *Fermi* spectral catalog) rather than the typically adopted $[50-300]$ keV peak flux (e.g. from the BATSE catalog) because the typical observer frame peak energy $E_{\rm p,o}$ distribution (e.g. Ghirlanda et al., 2009; Nava et al., 2011; Gruber et al., 2014) is centered at relatively large values ($\sim 0.5-1$ MeV). In this way we are more confident to sample a greater portion of the prompt spectrum.

In order to get the rest frame properties (constraints 2, 6, 7) we considered the SBAT4 complete sample defined in D'Avanzo et al. (2014). It consists of bursts detected by *Swift*, selected with criteria similar to those adopted for the BAT6 complete sample of long GRBs defined in Salvaterra et al. (2012, see however Sec.5.2), with a peak flux (integrated in the $[15-150]$ keV energy range and computed on a 64 ms timescale) $P_{64} \geq 3.5$ photons cm^{-2} s^{-1}.

2 The redshift distribution of the SBAT4 sample is shown in the top right panel of Fig.8.1 (solid black line). The grey shaded region is spanned by the distribution when the five SGRBs in the sample with unknown z are all assigned the minimum or the maximum redshift of the sample.

6-7 Within the SBAT4 sample we considered the 11 GRBs with known z and determined L and E (the distributions of these quantities are shown in the inset of Fig.8.1, top right panel, with black and grey lines respectively).

8.1.1 From population properties to observables

We can exploit the general theoretical model describing a population of sources (see Sec.3.2) in order to obtain their observational proper-

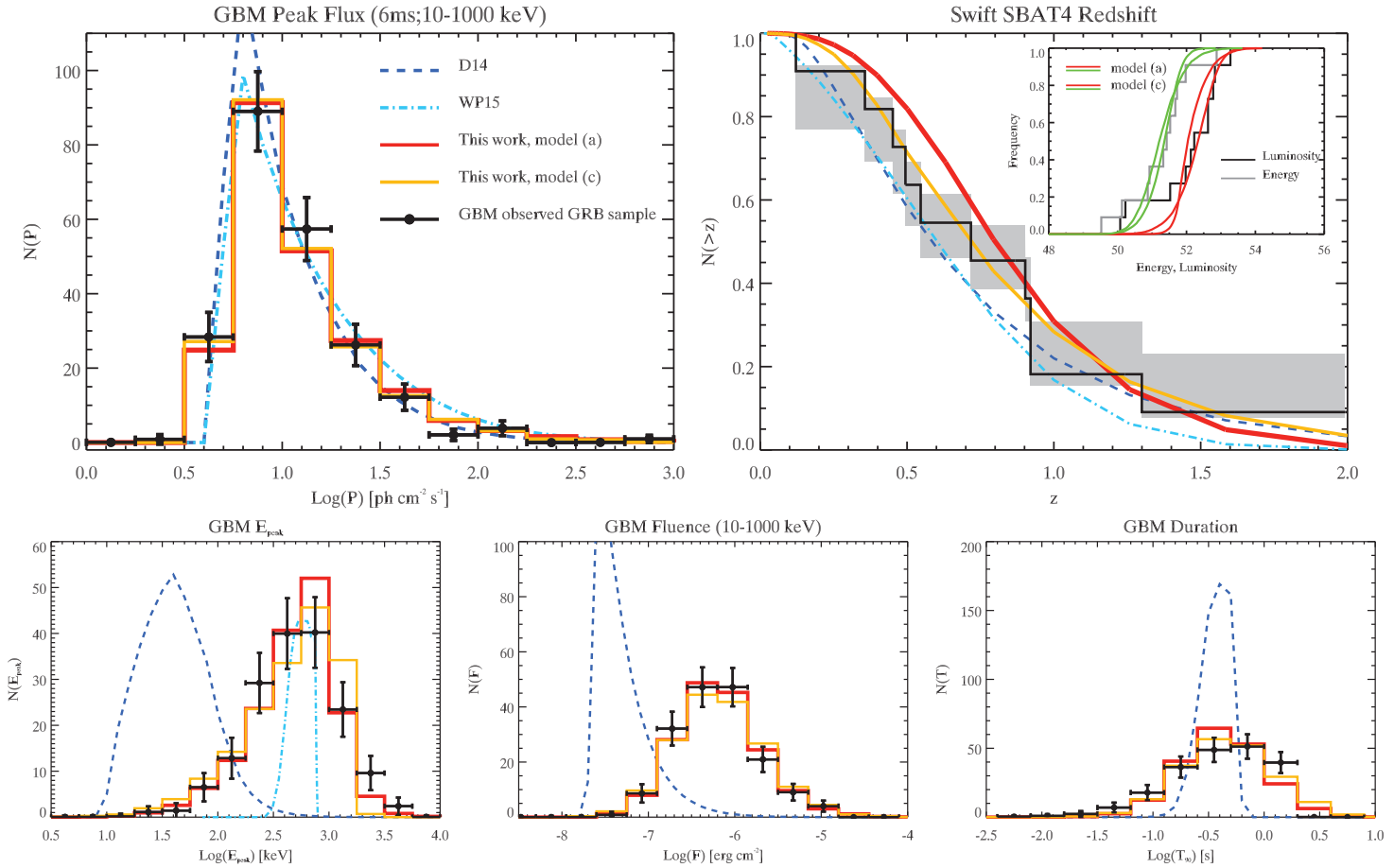

Figure 8.1: Black dots show the distributions obtained from our *Fermi*/GBM and *Swift* SBAT4 samples. Horizontal error bars are the bin widths, while vertical error bars are 1σ errors on the bin heights accounting for experimental errors on single measurements. The results of our MC population synthesis code are shown by solid red lines (assuming $E_{\rm p} - L$ and $E_{\rm p} - E$ correlations to hold for SGRBs) and by triple dot–dashed orange lines (assuming no correlation). Predictions based on the models of D'Avanzo et al. (2014) and (Wanderman and Piran, 2015) are shown by dashed blue and dot–dashed cyan lines, respectively (the latter only in the first three panels; see text). These are obtained by the analytic methods of sub–Sec.8.1.1. *Top left panel*: distribution of the peak flux P of the *Fermi*/GBM sample. *Top right panel*: normalized cumulative redshift distribution of the SBAT4 sample. The grey shaded area represents the range spanned by the distribution if the remaining bursts with unknown z are assigned the largest or the lowest z of the sample. The inset shows the cumulative distributions of the isotropic luminosity (solid black line) and energy (solid grey line) of the same sample. *Bottom panels*: from left to right, distributions of peak energy $E_{\rm p,o}$, fluence, and duration of SGRBs of our *Fermi*/GBM sample.

ties. Given the two parent distributions $\phi(L)$ and $\psi(z)$, the peak flux distribution can be derived as:

$$N(P_1 < P < P_2) = \frac{\Omega T}{4\pi} \int_0^\infty \frac{\psi(z)}{(1+z)} \frac{dV}{dz} dz \int_{L(P_1,z)}^{L(P_2,z)} \phi(L)\, dL \quad (8.2)$$

where $\Omega/4\pi$ is the fraction of sky covered by the instrument/detector, $dV(z)/dz$ is the differential comoving volume and the flux P (observed in the energy range $[E_1, E_2]$) corresponding to the luminosity L at redshift z is given by

$$P(L, z, E_{\rm peak}, \alpha) = \frac{L}{4\pi d_L(z)^2} \frac{\int_{E_1(1+z)}^{E_2(1+z)} EN(E|E_{\rm peak}, \alpha)\, dE}{\int_0^\infty EN(E|E_{\rm peak}, \alpha)\, dE} \quad (8.3)$$

being $N(E|E_{\rm peak}, \alpha)$ the rest frame photon spectrum of the GRB. In order to compare the model peak flux distribution obtained from Eq.8.2 with the real peak flux distribution obtained by the observed population of GRBs, only those events with peak flux above a certain threshold $P_{\rm lim}$ have been considered. The integral in Eq.8.2 is thus performed over the (L, z) range where the corresponding flux is larger than $P_{\rm lim}$.

The assumption of the an $E_{\rm p} - L$ correlation (see D'Avanzo et al., 2014) allows us to derive the expected distribution of the observer frame peak energy $E_{\rm p,o}$:

$$N(E_{1,\rm p,o} < E_{\rm p,o} < E_{2,\rm p,o}) = \frac{\Omega T}{4\pi} \int_0^\infty \frac{\psi(z)}{(1+z)} \frac{dV}{dz} dz \int_{L(E_{1,\rm p,o},z)}^{L(E_{2,\rm p,o},z)} \phi(L)\, dL \quad (8.4)$$

where the limits of the luminosity integral are computed by using the rest frame correlation $E_{\rm p} = YL^{m_y}$, namely

$$L(E_{\rm p,o}, z) = \left(\frac{E_{\rm p}}{Y}\right)^{1/m_y} = \left(\frac{(1+z)E_{\rm p,o}}{Y}\right)^{1/m_y} \quad (8.5)$$

Similarly to the previous case the integral in Eq.8.4 is performed over values of $L(E_{\rm p,o}, z)$ corresponding to fluxes above the limiting flux adopted to define the real GRB sample. Now, assuming also an $E_{\rm p} - E$ correlation to hold for SGRBs (see D'Avanzo et al., 2014; Tsutsui et al., 2013; Amati, 2006; Calderone et al., 2015), i.e. $E_{\rm p} = AE^{m_a}$, we can derive the following relation between E and L:

$$L(E) = \left(\frac{A}{Y}\right)^{1/m_y} E^{m_a/m_y} \quad (8.6)$$

The latter is then used to define the integral needed in obtaining the fluence S distribution through the following formula:

$$N(S_1 < S < S_2) = \frac{\Omega T}{4\pi} \int_0^\infty \frac{\psi(z)}{(1+z)} \frac{dV}{dz}\, dz \int_{L(E_1)}^{L(E_2)} \phi(L)\, dL \qquad (8.7)$$

again by limiting the integral to luminosities corresponding to fluxes above the given limiting flux.

Finally, considering the spiky light–curves of SGRBs, we can assume a triangular shape and thus let $2E/L \approx T$ in the rest frame of the source. Therefore, it is possible to combine the $E_\mathrm{p} - E$ and $E_\mathrm{p} - L$ correlations to derive the model predictions for the distribution of the duration to be compared with the observed distribution,

$$N(T_{1,\mathrm{o}} < T < T_{1,\mathrm{o}}) = \frac{\Omega T}{4\pi} \int_0^\infty \frac{\psi(z)}{(1+z)} \frac{dV}{dz}\, dz \int_{L(T_{1,\mathrm{o}},z)}^{L(T_{2,\mathrm{o}},z)} \phi(L)\, dL \qquad (8.8)$$

where

$$L(T_\mathrm{o}, z) = \left[\left(\frac{Y}{A} \right)^{1/m_a} \frac{2(1+z)}{T_\mathrm{o}} \right]^{1/(1-m_y/m_a)} \qquad (8.9)$$

8.2 Monte Carlo Markov Chain approach

In this section I will describe the MCMC implemented in order to find the best $\phi(L)$ and $\psi(z)$ for short GRBs that reproduce all the seven constraints defined in the previous section. We employed a MCMC approach based on the Metropolis-Hastings algorithm (Hastings, 1970). At each step of the MCMC, a Monte Carlo simulation is run to generate a model population (depending on a set p of parameters) that is then compared with the real SGRB samples.

- we displace each parameter p_i from the last accepted value. The displacement is sampled from a uniform distribution whose maximum width is carefully tuned in order to avoid the random walk remaining stuck in local maxima; For parameters corresponding to slopes m_i, we actually displace the corresponding angle $\varphi_i = \arctan(m_i)$ (in order to avoid a bias towards high slopes;
- we compute the Kolmogorov–Smirnov (KS) probability $P_{\mathrm{KS,j}}$ of each observed distribution to be drawn from the corresponding model distribution;

- we define the goodness of fit $\mathcal{G}$ of the model as the sum of the logarithms of these KS probabilities, i.e. $\mathcal{G} = \sum_{j=1}^{7} \log(P_{\mathrm{KS,j}})$. This is clearly only an approximate likelihood, since it implies an assumption of independence of each distribution from the others, but we tested that its maximization gives consistent results;

- Finally, we compare $g = \exp(\mathcal{G})$ with a random number r sampled from a uniform distribution within 0 and 1: if $g > r$ the set of parameters is accepted, otherwise it is rejected.

We tested the MCMC adopting different sets of initial parameters with the aim to verify that a unique global maximum of $\mathcal{G}$ could be found. Once properly set up, 200 000 steps of the MCMC were run. After removing the initial burn in, the auto–correlation length of each parameter in the chain was computed, and the posterior density distribution of each parameter (and the joint distribution of each couple of parameters) were calculated.

8.2.1 MC simulation of the SGRB population

The Monte Carlo we performed in order to simulate the SGRBs population (at each MCMC step) is schematically represented in Fig.8.2 and it is based on the following choices:

- Usually the SGRB cosmic formation rate $\psi(z)$ is modeled retarding the SFR $\psi_\star$ assuming a delay time distribution $P(\tau)$(see. Eq.8.1). However, it is possible to directly describe the formation rate of SGRBs adopting a generic parametric form for $\psi(z)$. A posteriori, if one believes the progenitors to be compact binaries, the delay time distribution can be recovered by direct comparison of our result with the star formation history of choice. We parametrized $\psi(z)$ following Cole et al. (2001), namely:

$$\psi(z) = \frac{1 + p_1 z}{1 + (z/z_p)^{p_2}} \tag{8.10}$$

  for $p_1 > 0$ and $p_2 > 1$ this function peaks around z_p.

- In order to have a proper set of simulated parameters, it is convenient, rather than directly extract the luminosities, to extract E_{p} from an assumed probability distribution. We assumed a

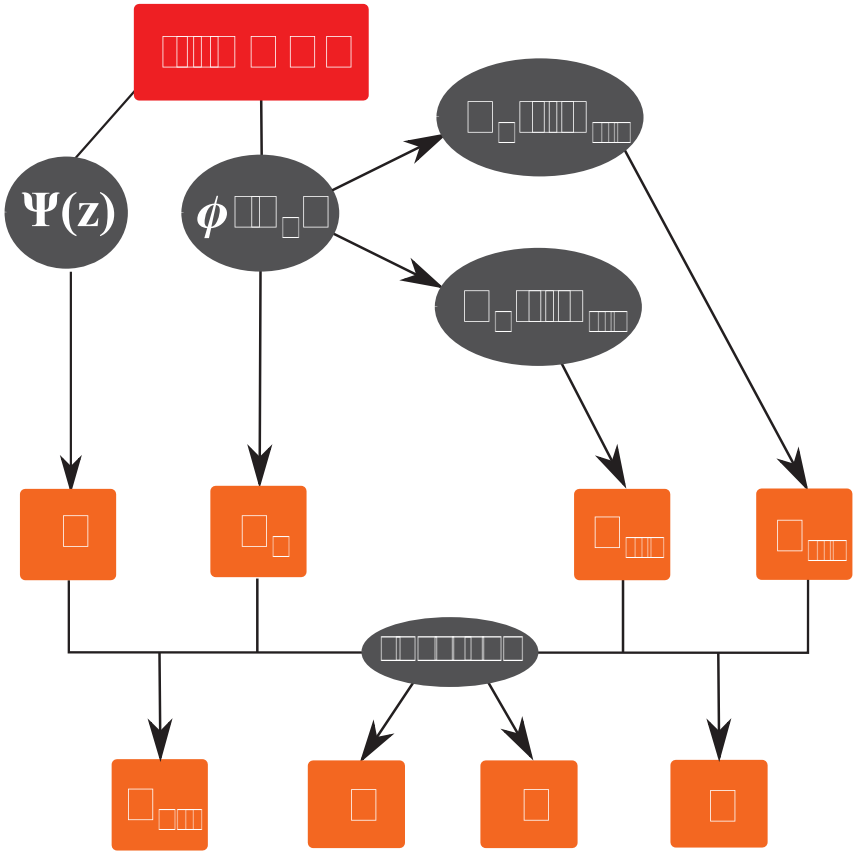

Figure 8.2: Scheme of the procedure followed in the MC to generate the observables of each synthetic GRB.

BPL shape for this distribution:

$$\phi(E_{\rm p}) \propto \begin{cases} (E_{\rm p}/E_{\rm p,b})^{-a_1}, & E_{\rm p} \leq E_{\rm p,b} \\ (E_{\rm p}/E_{\rm p,b})^{-a_2}, & E_{\rm p} > E_{\rm p,b} \end{cases} \tag{8.11}$$

Once extracted the peak energy it is possible to assign a luminosity and an energy through the $E_{\rm p} - L$ (aka Yonetoku) and $E_{\rm p} - E$ (aka Amati) correlations (also accounting for their scatter – see Sec.1.3). Recent evidence supports the existence of such a correlation among SGRBs (see e.g. Calderone et al., 2015; D'Avanzo et al., 2014; Ghirlanda et al., 2009; Tsutsui et al., 2013) with similar parameters to those present in the population of long GRBs (Amati et al., 2002; Yonetoku et al., 2004). The luminosity function is then reconstructed using the assigned luminosities.

- We employed the Yonetoku and Amati correlations in the fol-

lowing form:

$$\log_{10}(E_{\rm p}/670\,{\rm keV}) = q_Y + m_Y \log_{10}(L/10^{52}\,{\rm erg/s}) \qquad (8.12)$$

$$\log_{10}(E_{\rm p}/670\,{\rm keV}) = q_A + m_A \log_{10}(E/10^{51}\,{\rm erg}) \qquad (8.13)$$

We did not assume the observed correlation but assumed that such a kind of correlations exist for SGRBs. The latter equations represent the central values of the correlations. Since there are still too few SGRBs with measured redshift in order to properly define an intrinsic scatter, we assumed the scatter affecting the correlations holding for the population of long GRBs, i.e. $\sigma = 0.2$ (Nava et al., 2012).

- The spectrum of SGRBs is often assumed to be a cut–off power–law, or a Band function (Band et al., 1993). Typical values for the low energy spectral index $\alpha \sim 0.6$ (relative to the population of SGRBs detected by BATSE and *Fermi* – Ghirlanda et al. 2009; Gruber et al. 2014; Nava et al. 2011 and, in the case of the Band function, $\beta \sim 2.3 - 2.5$. The peak energy is either assumed fixed (e.g. 800 keV in Wanderman and Piran, 2015) or derived through the SGRBs $E_{\rm p} - L$ correlation analogously to long bursts (D'Avanzo et al., 2014; Virgili et al., 2011b). We assumed that the prompt spectrum is described by typical Band function having low and high photon spectral index equals to -0.6 and -2.5, respectively. We kept these two parameters fixed after checking that our results were unaffected by sampling them from distributions centered around these values or either centered around other reasonable values.

The MC simulation is resumed in the scheme shown in Fig.8.2. We considered and tested three different scenarios:

(a) a redshift z and a peak energy $E_{\rm p}$ are sampled from the corresponding distribution $\psi(z)$ and $\phi(E_{\rm p})$, respectively. Then, a luminosity (energy) is assigned through the $E_{\rm p} - L$ ($E_{\rm p} - E$) correlation having log–normal scatter. Using L (E) and z, the peak flux P (fluence S) in the observer frame energy range $[10 - 1000]$ keV is derived via the assumed spectral shape. The observer frame duration T is obtained, approximating the light–curve with a triangle, through the relation $T = 2(1+z)E/L$;

(b) The minimum and the maximum values of $E_{\rm p}$ admitted are 0.1 keV and 10^5 keV, respectively. These limiting values correspond to a minimum luminosity $L_{\rm min}$ and a maximum luminosity $L_{\rm max}$ which are obtained through the $Ep - L$ correlation. While the maximum luminosity is inessential, the existence of a minimum luminosity might affect the observed distributions. Differently with respect the case (a) we consider $L_{\rm min}$ as a parameter and we reject values of $E_{\rm p}$ corresponding to smaller luminosities.

(c) There is the possibility that the results obtained in case (a) and (b) depend on the assumption of the Amati and Yonetoku correlations. Therefore in this third case we consider independent probability distributions for the luminosity and duration. A broken power–law

$$\phi(E_{\rm p}) \propto \begin{cases} (L/L_{\rm b})^{-\alpha_1}, & L \leq L_{\rm b} \\ (L/L_{\rm b})^{-\alpha_2}, & L > L_{\rm b} \end{cases} \tag{8.14}$$

is assumed for the luminosity distribution, and a log–normal shape

$$P(T_{\rm r}) \propto \exp\left[-\frac{1}{2}\left(\frac{\log(T_{\rm r}) - \log(T_{\rm c})}{\sigma_{\rm Tc}}\right)^2\right] \tag{8.15}$$

is assumed for the rest frame duration $T_{\rm r} = T/(1+z)$ probability distribution. The energy of each GRB is computed as $E = LT_{\rm r}/2$.

8.2.2 MCMC results

We explored three different cases:

(a) We assumed that the correlations $E_{\rm p} - L$ and $E_{\rm p} - E$ are valid for SGRBs as for the long ones and we did not imposed a minimum value for the luminosity. In total there are ten free parameters: three (p_1, z_p, p_2) define the SGRB formation rate (Eq.8.10), three (a_1, a_2, $E_{\rm p,b}$) define the peak energy distribution (Eq.8.11), and four (q_Y, m_Y, q_A, m_A) define the correlations (Eq.8.12 and Eq.8.13);

(b) We assumed also in this case the presence of both the correlations but imposing a minimum value for the luminosity. Since

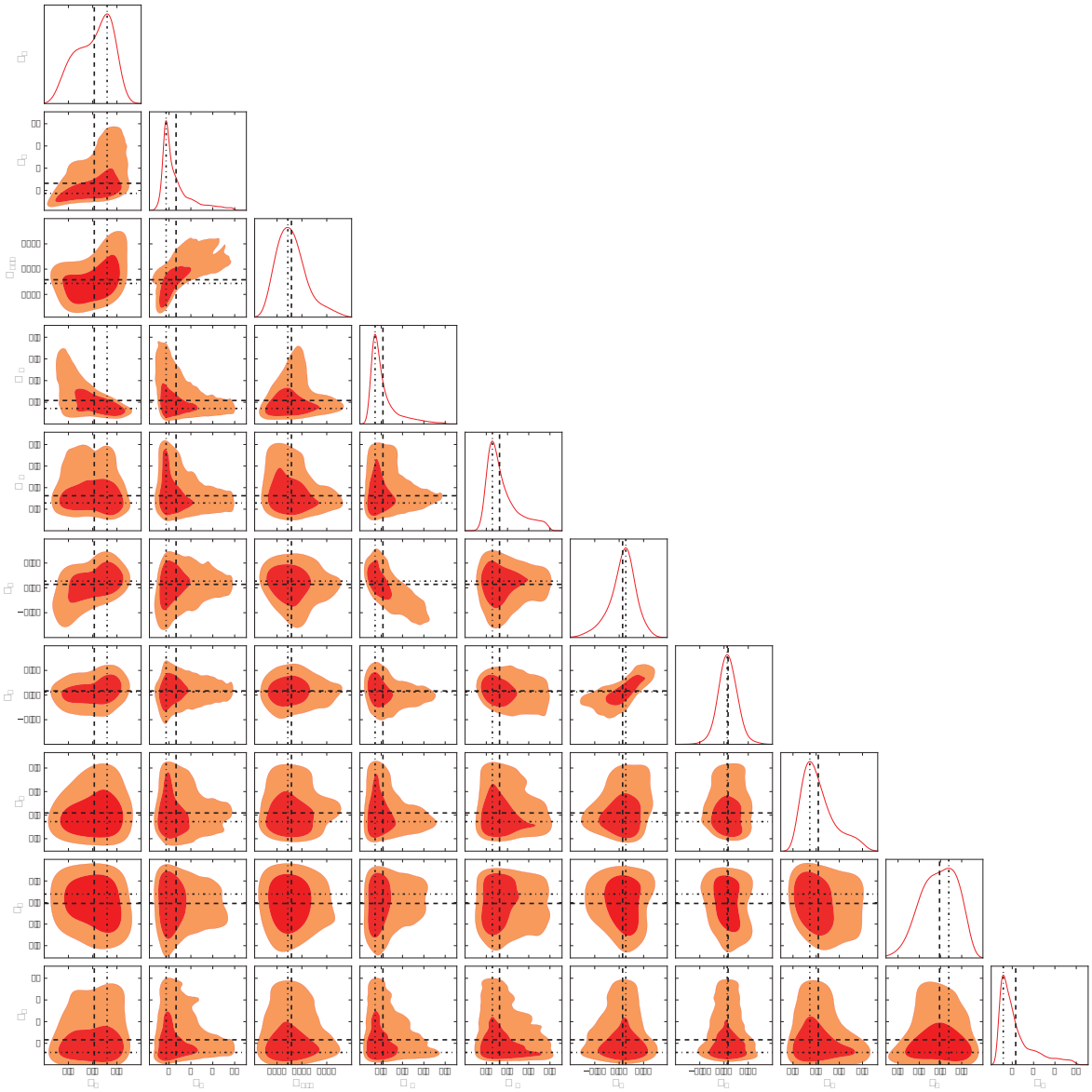

Figure 8.3: Marginalized densities of our MCMC parameters for the case (a) (i.e. with correlations and no minimum luminosity). Black dashed lines indicate the means and black dot–dashed lines indicate the modes of the distributions.

$L_{\rm min}$ is assumed a priori the free parameter are the same of the case (a);

(c) We did non assume any correlations and thus directly generated luminosity L and rest frame duration $T_{\rm r}$ from which indirectly we obtained the energy E. In this case we lose the four parameters related to the correlations but we gain five more (eleven in total): (α_1, α_2, $L_{\rm b}$) for the luminosity function (Eq.8.14) and ($T_{\rm c}$, σ_{Tc}) for the duration distribution (Eq.8.15).

The resulting 1D and 2D marginalized distributions are shown, for case (a), in Fig.8.3, where black dashed (black dot–dashed) lines indicate the position of the mean (mode) of the marginalized density of each parameter. The filled contours represent the 68% (darker red) and 95% (lighter red) probability areas of the joint density distributions. In Fig.8.1 the resulting distributions are shown, for case (a – red lines) and case (c – orange lines), superimposed to the constraints distributions. Are also shown, for comparison, the results of D'Avanzo et al. (2014); Wanderman and Piran (2015) and the derived observables distributions (blue dashed lines and cyan dot–dashed lines, respectively). The means, modes, and 68% probability intervals of the 1D marginalized distributions are summarized in Tab.8.1, where the corresponding luminosity function parameters are also reported.

8.3 Results

Among the most recent studies of the $\phi(L)$ and $\psi(z)$ of SGRBs we considered, as a comparison work, the work of D'Avanzo et al. (2014) and Wanderman and Piran (2015) (see Fig.8.1).

D'Avanzo et al. (2014) assumed a power–law shape for both the $\phi(L)$ and the delay time distribution $P(\tau)$, and assumed the cosmic SFR of Hopkins and Beacom (2006). Similarly to our case (a) and (b) they assumed the correlation $E_{\rm p} - L$ to be valid for SGRBs (in the form $E_{\rm p} = 337{\rm keV}(L_{\rm iso}/(2\times10^{52}{\rm erg/s}))^{0.49}$ as reported in their paper). They also assumed a Band spectrum (Band et al., 1993) with low and high energy photon spectral indexes -0.6 and -2.3, respectively. They used two constrains: the BATSE peak flux distribution and the redshift distribution of bright *Swift* short bursts with measured z.

Table 8.1: Summary of Monte Carlo Markov Chain results. C.I. = confidence interval. $E_{\rm peak,b}$, L_b and T_c are in units of keV, 10^{52} erg s^{-1} and s, respectively. Double horizontal lines separate different cases. From top to bottom: (a) case with correlations and no minimum luminosity, (b) case with correlations and minimum luminosity, (c) case with no correlations.

Parameter	Mean	Mode	68% C.I.
a_1	0.53	0.8	$(0.2, 1)$
a_2	4	2.6	$(1.9, 4.4)$
$E_{\rm peak,b}$	1600	1400	$(880, 2000)$
m_Y	0.84	0.69	$(0.58, 0.88)$
m_A	1.1	0.91	$(0.76, 1.2)$
q_Y	0.034	0.068	$(-0.069, 0.18)$
q_A	0.042	0.033	$(-0.061, 0.13)$
p_1	2.8	1.8	$(0.59, 3.7)$
z_p	2.3	2.7	$(1.7, 3.2)$
p_2	3.5	1.7	$(0.94, 4)$
α_1	0.53	0.88	$(0.39, 1.0)$
α_2	3.4	2.2	$(1.7, 3.7)$
L_b	2.8	2.1	$(0.91, 3.4)$
a_1	0.39	0.24	$(-0.15, 0.8)$
a_2	3.5	2.5	$(1.9, 3.7)$
$E_{\rm peak,b}$	1400	1100	$(730, 1700)$
m_Y	0.88	0.76	$(0.61, 0.97)$
m_A	1.1	0.95	$(0.77, 1.2)$
q_Y	0.045	0.077	$(-0.039, 0.17)$
q_A	0.043	0.053	$(-0.037, 0.14)$
p_1	3.1	2.4	$(1, 4.2)$
z_p	2.5	3	$(1.9, 3.3)$
p_2	3	1.3	$(0.9, 3.1)$
α_1	0.38	0.47	$(0.034, 0.98)$
α_2	3	2.1	$(1.7, 3.2)$
L_b	2.3	1.5	$(0.71, 2.8)$
a_1	-0.61	-0.55	$(-0.73, -0.41)$
a_2	2.8	2.5	$(2.1, 2.9)$
$E_{\rm peak,b}$	2200	2100	$(1900, 2500)$
α_1	-0.15	-0.32	$(-1.5, 0.81)$
α_2	2.0	1.8	$(1.2, 2.8)$
L_b	0.63	0.79	$(0.32, 1.6)$
T_c	0.11	0.11	$(0.084, 0.13)$
$\sigma_{\rm Tc}$	0.91	0.90	$(0.79, 1.0)$
p_1	3.1	2.0	$(0.51, 4.1)$
z_p	2.5	2.8	$(2.0, 3.3)$
p_2	3.6	2.0	$(1.1, 3.7)$

They find that the luminosity function of SGRBs is $\phi(L) \propto L^{-2.17}$ between 10^{49} erg/s and 10^{55} erg/s, and that $P(\tau) \propto \tau^{-1.5}$ with a minimum delay of 20 Myr. The dashed blue lines in Fig.8.1 show the distributions corresponding to the results of D'Avanzo et al. (2014) obtained through the equations derived in sub–Sec.8.1.1): they correctly reproduce the peak flux distribution (top *left panel* of Fig.8.1) of *Fermi* SGRBs and the redshift distribution of the bright SGRBs detected by *Swift* (*top right* panel), but are not in agreement with the other additional constraints (*bottom panels* of Fig.8.1) that we consider in this work. We limited their model to the limiting flux 5 ph cm^{-2} s^{-1} in order to make their distributions comparable with the sample selected in this work.

Also the results from WP15 (dot–dashed cyan lines in Fig.8.1 – log–normal $P(\tau)$ case) correctly reproduce the constraints they adopted while badly match the other ones. Differently from D'Avanzo et al. (2014) they assigned to all SGRBs a fixed rest frame $E_{\rm p}^{\rm rest} = 800$ keV, thus it is not possible to derive the fluence and duration of their model unless independent functions for these parameters are assumed. Their preferred model for $\phi(L)$ is a broken power–law, with a break at 2×10^{52} erg/s having slopes of -1.9 and -3.0 before and above the break, respectively. Their preferred models for the delay time are either a power–law $P(\tau) \propto \tau^{-0.81}$ with a minimum delay of 20 Myr or a log–normal delay time distribution with central value 2.9 Gyr and sigma ≤ 0.2.

In conclusion, a steep $\phi(L)$ with either a power–law distribution of delay times favouring short delays (as in D'Avanzo et al., 2014) or a nearly unique long delay time (as in the log–normal model adopted by Wanderman and Piran, 2015) correctly reproduce the observer frame peak flux distribution of *Fermi* GRBs and the redshift distribution of *Swift* bright short bursts. However, they do not reproduce the peak energy, fluence, and duration distributions of the same population of *Fermi* SGRBs.

8.3.1 SGRBs luminosity function $\phi(L)$

The luminosity obtained in the case (a) is a BPL (Eq.8.14) with $\alpha_1 = 0.53^{+0.47}_{-0.14}$ (i.e. and flatter than 1.0 within the 68% confidence interval) below a break luminosity $L_{\rm b} = 2.8^{+0.6}_{-1.89} \times 10^{52}$ erg/s and much steeper, $\alpha_2 = 3.4^{+0.3}_{-1.7}$, above this characteristic luminosity. Here, the

minimum luminosity $\sim 5 \times 10^{47}$ erg/s is set by the minimum $E_{\rm p}$ coupled with the $E_{\rm p} - L$ correlation. In the case (b), despite a minimum luminosity has been introduced a priori, we obtain similar parameters for $\phi(L)$. This tells us that $\phi(L)$ is not almost independent on the assumption of a minimum luminosity.

If we assume no correlations to hold (case (c)), we obtain (independent) peaked distributions for the peak energy and the luminosity. These distributions are wider and leads to more dispersed parameters than cases (a) and (b). In particular, the slope α_1 of the luminosity function below the break is poorly constrained, although this cannot be steeper than 0.81 (at the 68% confidence level). We believe that the larger uncertainty on the best fit parameters in case (c) is due to the higher freedom allowed by the uncorrelated luminosity function, peak energy distribution, and duration distribution.

Moreover, such a luminosity function implies an average isotropic equivalent luminosity $\langle L \rangle = 1.5 \times 10^{52}$ erg/s (or 3×10^{52} erg/s in case (c)) which is much larger than e.g. $\langle L \rangle \approx 3 \times 10^{50}$ erg/s from D'Avanzo et al. (2014) or $\langle L \rangle \approx 4.5 \times 10^{50}$ erg/s from Wanderman and Piran (2015).

8.3.2 SGRBs formation rate $\psi(z)$

Our predicted cosmic formation rate for short GRBs (case (a) – red solid line; and case (c) – orange triple dot–dashed line) are shown in Fig.8.4 compared with the following redshift distributions (arbitrary normalization):

- The SFR from Madau and Dickinson (2014) retarded according to the delay time distribution $P(\tau) \propto \tau^{-1}$ with $\tau > 20$ Myr (grey dashed line);
- the redshift distribution of NS–NS mergers as predicted by Dominik et al. (2013) in the case of standard binary evolution. Their formation rate is obtained on the basis of sophisticated binary population synthesis, assuming two different metallicity evolution scenarios: *high–end* (pink solid line) and *low–end* (pink dotted line);
- The SGRBs formation rate from D'Avanzo et al. (2014), which is the SFR by Hopkins and Beacom (2006) retarded according to the delay time distribution $P(\tau) \propto \tau^{-1.5}$ with $\tau > 20$ Myr (blue dashed line);

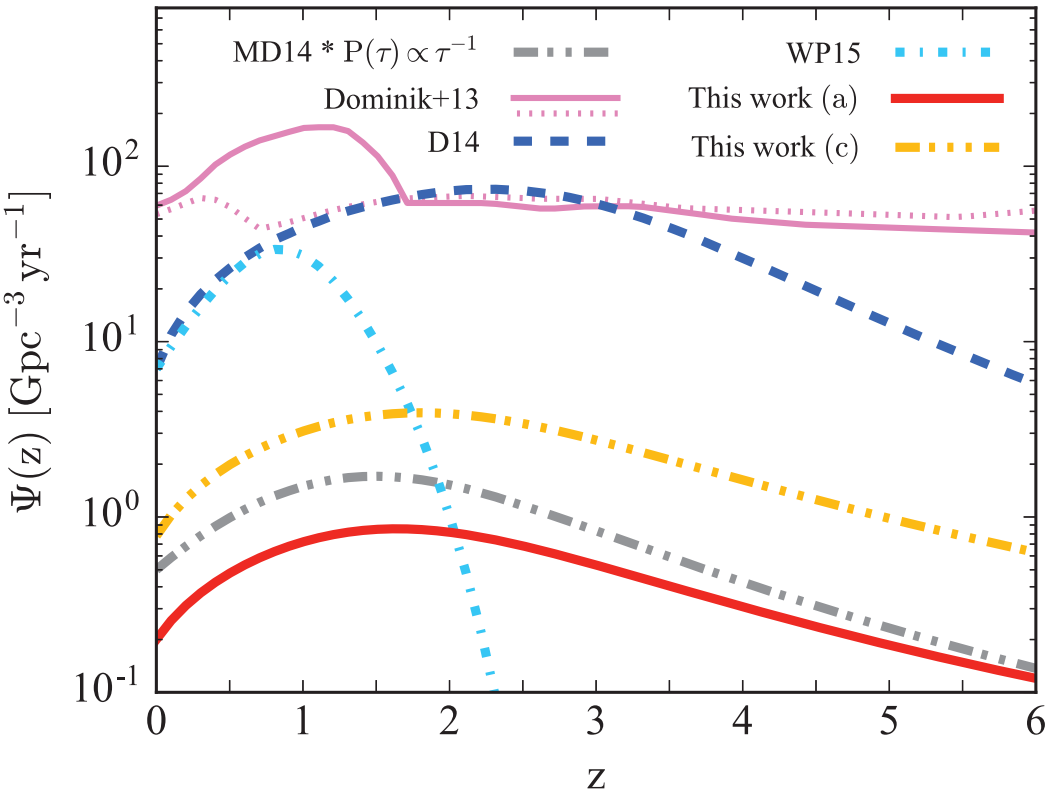

Figure 8.4: Comparison between various predicted SGRB redshift distributions. The grey dashed line represents the convolution of the cosmic SFH from Madau and Dickinson (2014) with a delay time distribution $P(\tau) \propto \tau^{-1}$ with $\tau > 20$ Myr (the normalization is arbitrary). The pink solid line (pink dotted line) represents the redshift distribution of NS–NS binary mergers predicted by Dominik et al. (2013) in their high end (low end) metallicity evolution scenario (standard binary evolution model). The blue dashed line and cyan dot–dashed line are the SGRB redshift distributions according to D'Avanzo et al. (2014) and to Wanderman and Piran (2015), respectively. The red solid line is our result in case (a), while the orange triple dot–dashed line is our result in case (c). In both cases we used the mean parameter values as listed in Tab.8.1.

- The SGRBs formation rate from Wanderman and Piran (2015), obtained convolving a SFR based on Planck results (extended halo model – Planck Collaboration et al. 2014) with a log–normal delay time distribution $P(\tau) \propto \exp\left[-(\ln\tau - \ln\tau_0)/(2\sigma^2)\right]$, where $\tau_0 = 2.9$ Gyr and $\sigma < 0.2$ (we adopted $\sigma = 0.1$ – cyan dot–dashed line).

The redshift distribution of SGRBs $\psi(z)$ in case (a) peaks at $z \sim 1.5$ and falls rapidly above the peak. It seems to be compatible with the SFR from Madau and Dickinson (2014) delayed with $P(\tau) \propto \tau^{-1}$

with $\tau > 20$ Myr. In case (c), on the other hand, the redshift distribution we find seems to be indicative of a slightly smaller average delay with respect to case (a). However, since the errors on our parameters (p_1, z_p, p_2) of the resulting formation rate (Eq.8.10) are rather large, no strong and detailed conclusion about the delay time distribution can be drawn.

The redshift distribution by D'Avanzo et al. (2014) peaks between $z \sim 2$ and $z \sim 2.5$ (at a higher redshift with respect our results). This because their assumed SFR (peaking a priori at higher redshift) is not much delayed by the assumed $P(\tau) \propto \tau^{-1.5}$ delay time distribution. On the other hand, the result of Wanderman and Piran (2015) peaks at very low redshift (~ 0.8) and predicts essentially no SGRBs with redshift $z \sim 2$ because of the extremely large delay implied by their delay time distribution.

8.3.3 SGRBs local rate

The local rate of SGRBs is particularly important due to the connection with gravitational wave events to be detected by the advanced interferometers: Advanced LIGO (LIGO Scientific Collaboration et al., 2015) and Advanced Virgo (Acernese et al., 2015). There is a considerable number of predictions for the rate of SGRBs within the horizon of GW detectors in the literature. The rather wide range of predictions, extending from $0.1\,\mathrm{Gpc^{-3}\,yr^{-1}}$ to $> 200\,\mathrm{Gpc^{-3}\,yr^{-1}}$ (e.g. Guetta and Piran, 2005, 2006), can be tested and further constrained by forthcoming GW–SGRB associations (Coward et al., 2014; Branchesi et al., 2012). If SGRBs have a jet, one must account for the collimation factor, i.e. multiply the rate by $f_b = (1 - \cos\theta_{jet})^{-1}$, in order to compare such predictions with the compact binary merger rate.

The fraction of SGRBs detectable above a limiting flux P_{lim} within a given redshift z is:

$$N(<z) = \int_0^z \frac{\psi(z)}{(1+z)} \frac{dV}{dz}\, dz \int_{L \geq L(P_{lim},z)} \phi(L)\, dL \tag{8.16}$$

where $L(P_{lim}, z)$ represents the minimum luminosity corresponding to the flux limit P_{lim} at redshift z.

Fig.8.5 shows the rate of SGRBs within a given redshift z (zoomed up to $z < 0.1$). The different curves are obtained using the formation rate $\psi(z)$ and luminosity function $\phi(L)$ by D'Avanzo et al. (2014) and Wanderman and Piran (2015) (shown by the dashed blue and

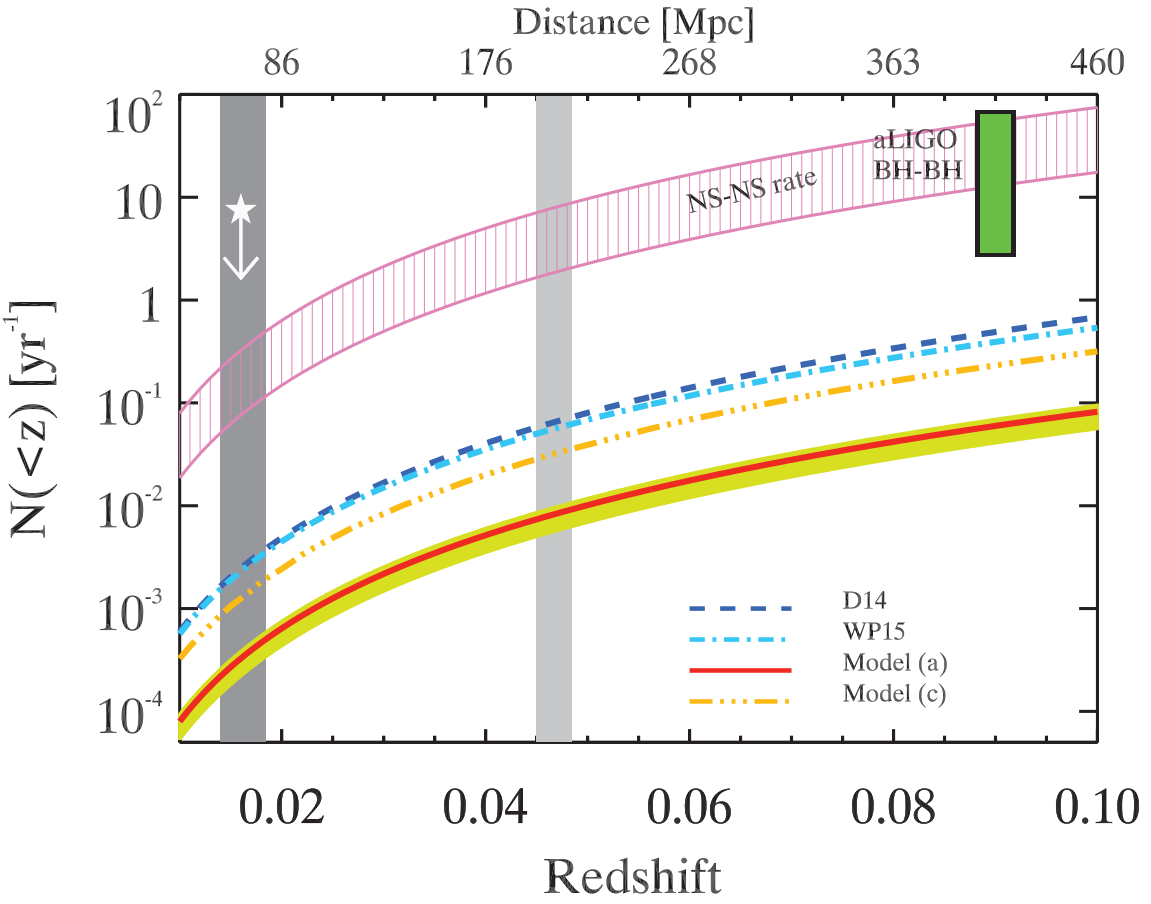

Figure 8.5: Event rates within redshift z: Solid red line and triple dot–dashed orange line represent the SGRB rates for case (a) and case (c) of this work, respectively. The yellow shaded region represents the 68% confidence level on the rate (red line) of case (a). SGRB rates according to the models of D'Avanzo et al. (2014) and Wanderman and Piran (2015) are shown by the dashed blue and dot–dashed cyan lines, respectively. The rate of NS–NS mergers is shown by the hatched pink region where the lower (upper) boundary corresponds to the rate derived from population synthesis models (Galactic binaries) in Dominik et al. (2015) and Kim et al. (2015). The vertical grey shaded regions show the present and design ranges of aLIGO for NS–NS mergers. The upper limit (white star) corresponds to the non–detection of NS–NS mergers in the first 48.6 days of the "O1" run of aLIGO. The green vertical bar is the rate of binary BH mergers derived by Abbott et al. (2016b) and shown here at the distance of GW150914 and GW151226.

dot–dashed cyan lines, respectively) and the results of our case (a) (solid red line) and case (c) (triple dot–dashed orange line). These curves represent the population of SGRBs detectable in γ–rays by current flying instruments. At such low redshifts (as those in Fig.8.5), even the bursts populating the lowest end of the luminosity function

can be observed above the flux limits of available GRB detectors (e.g. the *Fermi*/GBM). The $\psi(z)$ that we derive (see Fig.8.4) rises, below the peak, in a way similar to those adopted in the literature (e.g. D'Avanzo et al., 2014; Wanderman and Piran, 2015). The lower rates predicted by our models with respect to those of D'Avanzo et al. (2014) and Wanderman and Piran (2015) are thus mainly due to our flatter $\phi(L)$.

The dark grey shaded region in Fig.8.5 represents the distance within which aLIGO should have been able to detect NS–NS mergers during "O1" (Martynov et al. 2016 – estimated to be 60–80 Mpc, which corresponds to redshift $z \sim 0.014 - 0.0185$). We use this distance to define an upper limit on the NS–NS merger rate (white star symbol in Fig.8.5), given the non–detection of any such events in the 48.6 days of "O1" data (Martynov et al., 2016).

Fig.8.5 also shows the predictions of population synthesis models for double NS merger (Dominik et al., 2015) or the estimates based on the Galactic population of NS (Kim et al., 2015) which bracket the pink dashed region in Fig.8.5.

By comparing our SGRB rate models in Fig.8.5 with these putative progenitor curves and assuming that all NS–NS binary mergers yield a SGRB, we estimate the average jet opening angle of SGRBs as $\langle\theta_{\rm jet}\rangle \sim 3^\circ - 6^\circ$ in case (a – red solid line) and $\langle\theta_{\rm jet}\rangle \sim 5^\circ - 10^\circ$ in case (c – triple dot–dashed orange line). Using the local rates by D'Avanzo et al. (2014, dashed blue line) and Wanderman and Piran (2015, dot–dashed cyan line) we obtain a slightly larger $\langle\theta_{\rm jet}\rangle \sim 7^\circ - 14^\circ$. These estimates represent minimum values of the average jet opening angle, because they have been obtained under the assumption that all NS–NS binary mergers lead to a SGRB. We note that our range is consistent with the very few SGRBs with an estimated jet opening angle: GRB 051221A ($\theta_{\rm jet} = 7^\circ$, Soderberg et al. 2006a), GRB 090426 ($\theta_{\rm jet} = 5^\circ$, Nicuesa Guelbenzu et al. 2011), GRB 111020A ($\theta_{\rm jet} = 3^\circ - 8^\circ$, Fong et al. 2012), GRB 130603B ($\theta_{\rm jet} = 4^\circ - 8^\circ$, Fong et al. 2014), and GRB 140903A (Troja et al., 2016).

If the jet is preferentially launched in the same direction as the orbital angular momentum, the inspiral of the progenitor binary, when associated to a SGRB, could be detected up to a larger distance (up to a factor 2.26 larger, see Chassande–Mottin 2016) because the binary is more likely to be face–on.

We can define the SGRB rate in function of the following three typical distances:

	R	D	H
NS–NS	$\leq$200 Mpc	$\leq$300 Mpc	$\leq$450 Mpc
Model (a)	$0.007^{+0.001}_{-0.003}$	$0.024^{+0.004}_{-0.007}$	$0.077^{+0.014}_{-0.028}$
Model (c)	$0.028^{+0.005}_{-0.010}$	$0.095^{+0.017}_{-0.034}$	$0.299^{+0.054}_{-0.108}$
NS–BH	$\leq$410 Mpc	$\leq$615 Mpc	$\leq$927 Mpc
Model (a)	$0.060^{+0.011}_{-0.022}$	$0.20^{+0.035}_{-0.07}$	$0.572^{+0.103}_{-0.206}$
Model (c)	$0.232^{+0.042}_{-0.083}$	$0.605^{+0.109}_{-0.218}$	$1.158^{+0.208}_{-0.417}$

Table 8.2: Short GRB rates in yr^{-1} (68% errors) within the volume corresponding to different distances: R = limiting distance for binary inspiral detection by aLIGO, averaged over sky location and binary inclination, D = limiting distance for a face–on binary, averaged on sky location, H = limiting distance (*horizon*) for a face–on binary. Limiting distances are obtained considering the aLIGO design sensitivity to NS–NS or NS–BH inspirals (top and bottom portions of the table, respectively).

- we indicate by R (*range*) the limiting distance for the detection of a compact binary inspiral, averaged over all sky locations and over all binary inclinations with respect to the line of sight;
- we indicate by D (*distance to face–on*) the limiting distance for the detection of a *face–on* compact binary inspiral, averaged over all sky locations;
- we indicate by H (*horizon*) the maximum limiting distance for the detection of a *face–on* compact binary inspiral, i.e. the limiting distance at the best sky location.

Tab.8.2 shows R, D, and H for both NS–NS binaries and BH–NS binaries, corresponding to the design sensitivity of Advanced LIGO, together with the expected rates of SGRBs (according to our models (a) and (c)) within the corresponding volumes. The local rate of SGRBs predicted by our model (a) is $\rho_{0,a} = 0.20^{+0.04}_{-0.07}$ Gpc^{-3} yr^{-1} and for model (c) $\rho_{0,c} = 0.8^{+0.3}_{-0.15}$ Gpc^{-3} yr^{-1}. The distance R for NS–NS binary inspiral at design aLIGO sensitivity, which corresponds to 200 Mpc ($z \approx 0.045$), is shown by the vertical light grey shaded region in Fig. 8.5.

Finally, considering the detections resulting from the analysis of the "O1" aLIGO interferometers, the rate of BH–BH merger is 9–240 Gpc^{-3} yr^{-1}, assuming different BH mass distributions (Abbott et al.,

2016b). For the sake of comparison, in Fig.8.5 we show this range of rates (vertical green bar) in yr^{-1} computed at the distance of GW 150914. The first such detection, named GW150914, has been interpreted according to general relativity as the space–time perturbation produced by the merger of two black holes (with masses $M_1 \sim 29$ $M_\odot$ and $M_2 \sim 36$ $M_\odot$) at a distance of ∼410 Mpc (z =0.09). The full analysis of the aLIGO first run cycle revealed a second binary black hole merger event, GW151226 (Abbott et al., 2016b). In this case the involved masses are smaller ($M_1 \sim 14.2$ $M_\odot$ and $M_2 \sim 7.5$ $M_\odot$) and the associated distance is only slightly larger (∼440 Mpc).

CHAPTER 9

Dissipation mechanism in GRBs

GRBs light–curves appear as a sequence of prompt emission pulses (PP herafter) (Fishman et al., 1993; Bhat et al., 2012) and exhibit a variability on timescales as short as few milliseconds (Bhat et al., 1992; Walker et al., 2000; MacLachlan et al., 2013). Thanks to the early follow up by the X Ray Telescope (XRT - 0.3–10 keV) onboard of *Swift* (Gehrels et al., 2004), it has been shown that large amplitude X–ray flares (XRF, hereafter) are often superimposed to the "canonical" afterglow emission (Chincarini et al., 2007, 2010; Falcone et al., 2007). Sometimes, X–ray flares can occur even one day after the γ–ray trigger (Bernardini et al., 2011).

According to the fireball model, the prompt emission of GRBs is generated by relativistic *internal* shocks (IS) produced by shells ejected by the inner engine with random velocities (e.g. Rees and Meszaros, 1994, see Chp.**??**). In these shocks, a fraction of the total kinetic energy of the fireballs is converted into radiation through synchrotron and inverse Compton emission. This scenario can produce the highly variable light–curve of the prompt emission (Kobayashi et al., 1997). Shocks produced by the deceleration of the relativistic outflow by the interstellar medium, *external* shocks (ES),

have been invoked to explain the long lasting, smoothly decaying, broad band (from the optical to the radio) afterglow emission. However, over–densities of the circum burst medium (CBM) could also produce a variable light–curve (e.g. Nakar and Piran, 2003).

While IS, being produced by shells with slightly different random velocities, are expected to occur at a constant distance from the central engine, in ES the radius where shocks occur increases due to the expansion of the outflow in the CBM. As a consequence, IS should differ from ES in producing pulses whose duration is not correlated with their time of occurrence. No correlation between the duration and the occurrence time of a pulse of BATSE GRBs was found (Ramirez-Ruiz and Fenimore, 2000). This favored the IS mechanism.

Swift observed X–ray flares in the $[0.3 - 10]$ keV energy range which show a duration increasing with time (Chincarini et al., 2010; Yi et al., 2016; Kocevski et al., 2007). This property may be consistent with an ES scenario. However, XRFs have spectral properties (e.g. hard to soft evolution and harder spectral shape than the underlying afterglow component) similar to those of PP (Chincarini et al., 2006, 2007, 2010; Falcone et al., 2006; Margutti et al., 2010) and might be due to IS (Chincarini et al., 2007; Curran et al., 2008). The nature of XRFs is challenging for current models: they might demand a long–lived (hours) central engine (e.g. Yu et al., 2015c) or they could hint to short lived central engine emitting slower shells which dissipate their energy via IS at later times (e.g. Lazzati and Perna, 2007). Distinguishing between these two scenarios leads to important implications for the physics of the GRB central engine.

One leading question is whether X–ray flares and prompt emission pulses share the same origin and if they are preferentially produced by IS or ES (the latter due to the interaction with over–densities in the CBM). To answer these questions we derived in Sec.2.4 and Sec.2.5, under the simplest IS and ES scenarios, the expected relation between the pulse duration and its time of occurrence and we will compare them with observations in the following section. This work has recently been submitted for the publication (Pescalli et al. 2017).

9.1 Pulses duration–occurrence time relation

Within the standard IS model, if the collision radius of the fireballs R_c is almost constant (assuming $\alpha_\Gamma = 2 - 5$, $\Gamma_1 = 50 - 200$ and

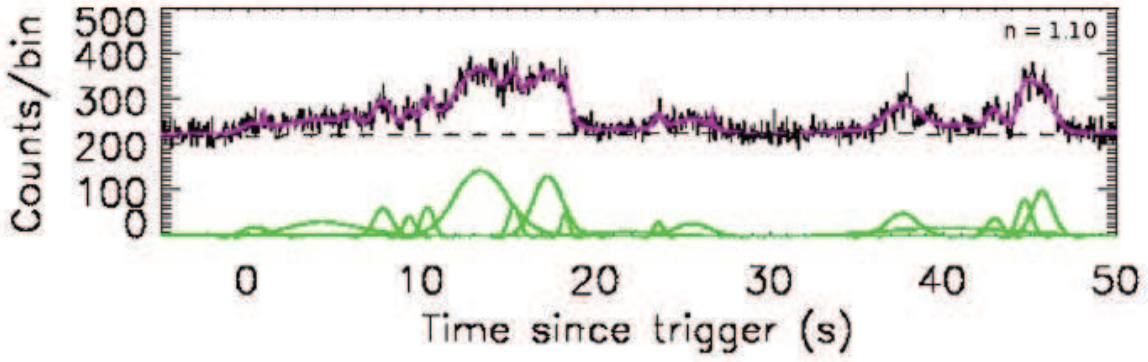

Figure 9.1: Example of deconvolution of the light–curve of GRB 080723D in single log–normal pulses. Figure from Bhat et al. (2012).

$\Delta R = 10^9$ cm, $R_c \simeq ct_c$ is 10^{13-14} cm – see Eq.2.11 in Sec.2.4 – see also Lazzati et al. 1999) the duration of pulses Δt (Eq.2.17 and Eq.2.18) is of the order of 0.1 s and it should be uncorrelated with the time t_p of occurrence of the pulses. In the ES scenario pulses can be produced by collisions between a relativistic fireball and over–density regions encountered along its path (e.g. Dermer and Böttcher, 2000), at rest with respect the central engine. If such over–densities are positioned at increasing distances, the pulse width Δt should increase linearly with t_p (see Sec.2.5). In summary, internal shock and external shock scenarios predict a pulse duration which should be constant or increasing with time, respectively.

In this section we compare these simple predictions with available observations. We consider both the pulses of the prompt emission phase as observed by the *Fermi*/GBM and the X–ray flares (XRF) observed by *Swift*/XRT in the $[0.3 - 10]$ keV energy range.

For the prompt pulses (PP) we consider the sample of bright GRBs analyzed in Bhat et al. (2012, B12 hereafter). They selected 32 bright long GRBs (only 7 with measured redshift), detected by *Fermi* in its first year of activity, which have the product of their fluence and peak flux larger than 10^{-4} erg photons cm^{-4} s^{-1}. B12 decompose the observed light–curves (considering both the data of the NaI [8 keV–1 MeV] and BGO [200 keV–10 MeV] detectors) as the superposition of log–normal pulses obtaining, for each GRB in their sample, a set of pulse duration, peak time and intensity (see Fig.9.1).

B12 analyzed light–curves with a variable time resolution between 25 and 50 milliseconds in order to maximize the number of fitted pulses. Since we are interested in the pulse duration, we considered only the pulses with duration $>$25 ms, i.e. reasonably larger than the

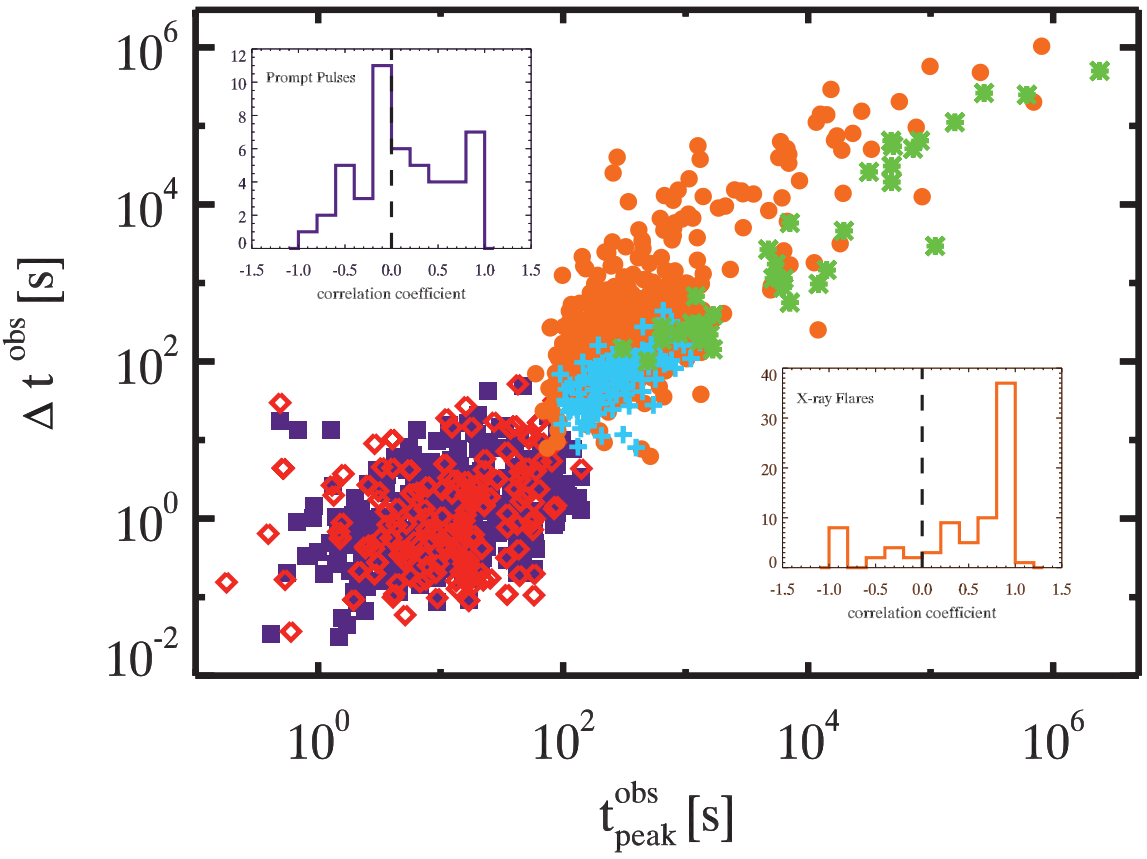

Figure 9.2: Observer frame pulse duration $\Delta t^{\rm obs}$ versus the pulse occurrence time (peak time - $t^{obs}_{\rm peak}$). Times are refereed to the trigger time. Prompt emission pulses of *Fermi*/GBM bursts (from Bhat et al. 2012) are shown with different symbols: purple squares show pulses obtained from the analysis of the GBM/NaI [8 keV–1 MeV] light–curves and red diamonds are pulses from GBM/BGO [200 keV–10 MeV] light–curves. Orange points, green asterisks and cyan crosses show X–ray Flares (from Yi et al. 2016, Bernardini et al. 2011 and Chincarini et al. 2010). The top–left and bottom–right inserts show the distribution of the correlation coefficients between the duration and pulse time within single GRBs with $>$ 2 pulses. Top left insert refers to pulses and the bottom right insert is for flares. Dashed lines in the inserts show the case of no correlation.

time resolution of the light–curves analyzed by B12. We extracted from their compilation 374 pulses obtained from the analysis of the light–curves of the NaI detectors, and 228 pulses from the data of the BGO detectors.

For the X–Ray Flares (XRF) there are different samples published in the literature: Chincarini et al. (2010, C10), Bernardini et al. (2011, B11), Yi et al. (2016, Y16). C10 analyzed 113 early flares ($t_{\rm peak} < 1000$ s) detected by *Swift* between April 2005 and March 2008. B11, ex-

tending to flares detected up to December 2009, considered 36 late flares ($t_{\rm peak} > 1000$ s). Joining these two samples, the total number of flares amounts to 149 of which 59 belongs to GRBs with measured redshift. Recently, Y16 enlarged the sample of XRFs considering all GRBs up to March 2015. Their catalog contains 468 bright and significant XRFs of which 200 with redshift. We collected the flares from these three works.

Fig.9.2 shows the (observed) duration $\Delta t^{\rm obs}$ of pulses as a function of the observed time of the pulse peak $t^{\rm obs}_{\rm peak}$. Prompt emission pulses obtained from B12 are shown by the purple squares and red diamonds (corresponding to BGO and NaI data, respectively) and XRFs are shown by the orange range points (Y16), green asterisks (B11) and cyan crosses (C10). Peak times are referred to the trigger time of individual GRBs they belong to.

The distribution of PP and XRF in the plane of Fig.9.2 seems to describe an overall, almost linear, continuum extending from short duration (e.g. 0.01 seconds) early (1 s post trigger) pulses to extremely long and late flares (up to 11 days after the trigger and with comparable duration). We note that a possible selection effect on X–ray flares is due to the time needed for XRT to repoint the GRB. Typically this time is 1 minute which is close to the division between PP and XRF in Fig.9.2.

9.1.1 Correlation analysis

We studied the possible correlation between the pulse duration and its peak time in Fig.9.2. Considering PP and XRF as two distinct populations we find the presence of a correlation (stronger and more significant for flares) between the pulse duration $\Delta t^{\rm obs}$ and the peak time $t^{\rm obs}_{\rm peak}$. The Spearman's correlation coefficient and its chance probability are $r = 0.31$ and $P \sim 10^{-15}$, respectively, for prompt pulses (considering NaI and BGO pulses together, i.e. purple squares and red diamonds in Fig.9.2). For XRF, distributed in a larger region of the $\Delta t^{\rm obs}$–$t^{\rm obs}_{\rm peak}$ plane with respect to PP, we find $r = 0.60$ ($P \sim 10^{-61}$).

Since we are searching for the possible signature of the IS or ES as a process within individual bursts, we explore if there is a correlation (either for PP and XRF) between the pulses duration $\Delta t^{\rm obs}$ and their peak time $t^{\rm obs}_{\rm peak}$ *within single GRBs*. We restricted our analysis

to GRBs with more than two PP and we compute the Spearman's correlation coefficient for each GRB. The distribution of r for the PP is shown in the top–left inset of Fig.9.2. Similarly, we compute the correlation coefficient within individual GRBs with more than two XRF: the distribution of r is shown by the orange histogram in the bottom–right inset of Fig.9.2.

For PP we find that the correlation coefficient is distributed around 0 while for XRF there is a clustering around positive values of r. This suggests that, on average, no correlation is present between the pulse width and its time of appearance in prompt emission pulses (PP) as originally found by Ramirez-Ruiz and Fenimore (2000) while a positive correlation exists in XRF (Chincarini et al., 2010; Yi et al., 2016; Kocevski et al., 2007).

Since both $\Delta t^{\rm obs}$–$t^{\rm obs}_{\rm peak}$ are computed in the observer frame we verified that the correlations are not induced by the common redshift dependence. Since only few bursts in B12 sample have measured z, we performed a Monte Carlo simulation randomly generating redshifts from the GRB formation rate (as reported by Li 2008; Pescalli et al. 2016). We created 10^4 random samples for which we computed the correlation coefficient. For XRFs we considered the 259 bursts with measured redshifts. We computed the partial correlation coefficient accounting for the common dependence on z of $\Delta t^{\rm obs}$ and $t^{\rm obs}_{\rm peak}$. Also this test shows the correlation found in XRF is solid and not induced by z. For PP we again find no significant correlation.

The absence of a correlation between the pulse duration and the time of the peak during the prompt emission was originally reported by Ramirez-Ruiz and Fenimore (2000). They considered GRBs detected by BATSE, aligned the light–curves to the time of the the brightest peak during individual bursts and normalized the peak–aligned light–curves. However, their analysis missed the possible corrections for the redshift on the energy and time.

In order to verify their results including the corrections for z, we select a sample of *Fermi* long GRBs ($T_{90} > 2$ s) with redshift measurement in the *Fermi* database. We find 100 bursts (from GRB 080804 to GRB 160629). We excluded 32 bursts having SNR lower than 3[1], GRB 130427 which saturated the *Fermi*/GBM detectors and GRB 120624 because the TTE data (necessary to produce high–resolution light–curves) were only partially available due to the instrument slewing

[1]SNR was calculated as $\overline{(S-B)}/\bar{B}^{0.5}$, where S is the signal and B the background.

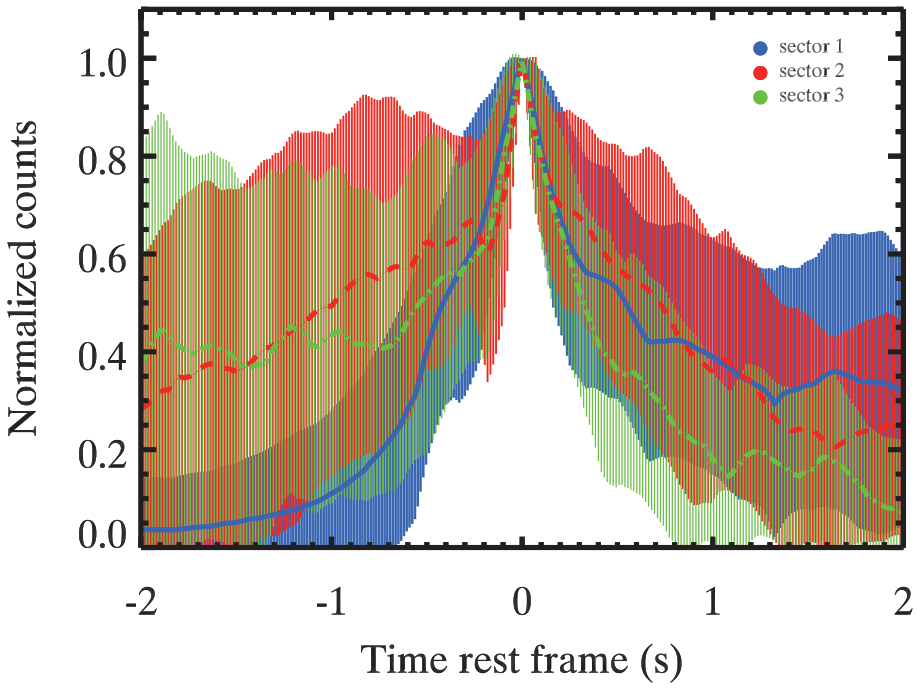

Figure 9.3: Peak time aligned signal for the three sectors identified within each GRB. Different combinations of colors and line–styles refer to different sectors.

(Gruber et al., 2012, GCN #13377). For the 64 remaining bursts we extracted the light–curves in the common $[72, 800]$ keV *rest frame energy range*[2] with 256 ms temporal resolution, from the most illuminated NaI detector.

The light–curves are converted to rest frame times and resampled on a common time grid. The resolution of the new time grid has been chosen in order to faithfully reproduce the original light–curves without losing any information on the time structure and variability.

We applied the Average Peak Alignment (APA) method (**?**) dividing light–curves in three equal parts (according to the rest frame T_{90} of each bursts). These are the sectors shown in Fig.9.3 with different colors. The uncertainty on the pulse aligned signal (solid line in Fig.9.3) is computed as the standard deviation of the signal in each bin. Since secondary peaks are not aligned in time this results in a large dispersion of the curve aside of the main (aligned) peak.

Following Ramirez-Ruiz and Fenimore (2000) we also analyzed separately with the APA method GRBs with $T_{90} > 20$ s and GRBs with $T_{90} < 20$ s. Even considering these subsamples, we find similar

[2]In this energy range NaI detectors have an almost constant response efficiency.

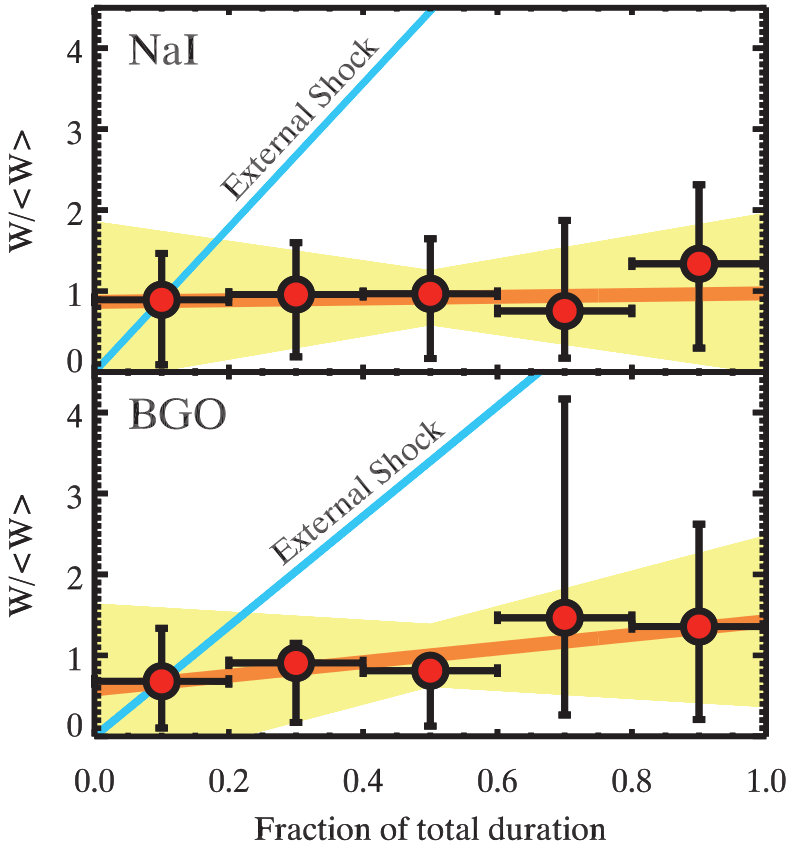

Figure 9.4: Average evolution of the normalized pulse width with time. The orange solid line represents the linear fit and the yellow shadow the associated uncertainty region. The blue line is the expected behavior assuming as emission mechanism external shocks happening at increasing distance. Top and bottom panels show the results obtained using the pulses of B12 obtained from the NaI and BGO BATSE light–curves respectively.

results to those shown in Fig.9.3.

By visual inspection of Fig. 9.3 we confirm, even accounting for the energy and time redshift corrections, that there is no evolution of the pulse width with time during the prompt emission phase of GRBs. However, the pulse alignment method has some limitations: it allows us to compare preferentially the main emission episodes of different light–curves and it is rather less sensitive to the whole emission (and weaker pulses) of the GRB. The wings of the profiles in Fig.9.3 show the large uncertainties due to the great diversity of temporal profiles.

In order to further support these results, we also compute the average pulse duration evolution along the GRB. To this aim, we study the average evolution of the normalized pulse width $W/\langle W\rangle$ of every single prompt pulse in B12 (purple squares and red diamonds

Sector	mean $W/\langle W\rangle$ (NaI)	mean $W/\langle W\rangle$ (BGO)
1	$0.89^{+0.57}_{-0.80}$	$0.68^{+0.66}_{-0.58}$
2	$0.96^{+0.64}_{-0.77}$	$0.91^{+0.24}_{-0.73}$
3	$0.97^{+0.68}_{-0.80}$	$0.81^{+0.15}_{-0.69}$
4	$0.75^{+1.12}_{-0.58}$	$1.46^{+2.70}_{-1.20}$
5	$1.34^{+0.98}_{-1.04}$	$1.36^{+1.26}_{-1.15}$

Table 9.1: Mean values of the normalized width $W/\langle W\rangle$ in each sector with associated superior and inferior estimated errors. Data refers to pulses coming from NaI and BGO light–cuves.

in Fig.9.2). We divide each light–curve into five sectors, which are fractions of the total GRB duration. For each sector we re–normalize every single pulse to the average duration of all the pulses belonging to the same GRB. So we averaged all the normalized pulses in the same sector. Fig.9.4 shows the evolution with time of $W/\langle W\rangle$ for the NaI and BGO pulses. Errors represent the 68% confidence interval of the normalized pulse width.

We fitted, in the barycentre of the data points, a linear function $W/\langle W\rangle = mt + q$ finding $m = 0.1 \pm 1.3$, $q = -0.06 \pm 0.34$ ($\chi^2 = 0.24$) and $m = 0.8 \pm 1.3$, $q = -0.04 \pm 0.39$ ($\chi^2 = 0.15$) for NaI and BGO pulses, respectively. The fits and their uncertainty are shown by the orange lines and yellow shaded regions in Fig.9.4. These results confirm that the pulse width remains constant with time. The average values of $W/\langle W\rangle$ of the five sectors and their errors are reported in Tab.9.1.

9.2 Internal vs External Shocks scenario

The blue lines (normalized to the first data point) in Fig.9.4 show how the pulse width should increase with time in the ES scenario (see Eq.2.20 in Sec.2.5). The absence of correlation between the pulse width and the peak time (shown by the correlation analysis presented in the previous section) and the almost constant average pulse width along the GRB light–curves (as found in Fig.9.3) favours IS as the leading mechanism for the origin of the dissipation associated with the γ–ray emission of GRBs.

The linear increase of XRF duration with time (Fig.9.2) has been interpreted as a signature of their origin from external shocks generated by the interaction of the blast wave with shell–like over–dense

regions located at increasing distance from the central engine (see also Wang and Loeb, 2000; Lazzati et al., 2002; Heyl and Perna, 2003). Chincarini et al. (2007) also discuss this mechanism considering the global fireball deceleration which could produce the superposition of flares with a monotonically decaying continuum emission (i.e. the standard afterglow).

The relative position of PP and XRF in Fig.9.2 define a unique distribution. This motivates us to explore also the possibility that XRF can have an internal origin. The IS scenario predicts a constant pulse width and would apparently be disfavoured. However, for the IS case we assumed that the shock is produced at a constant distance from the central engine. If we relax this assumption, as we show below, it is possible to explain also XRF through IS produced by shells with different bulk velocities. Additionally, another property of XRF which should be consistent with this interpretation is their energetic. Early flares show a possible decreasing isotropic equivalent energy as a function of their time of occurrence as pointed out by Margutti et al. (2011). We have computed the isotropic equivalent energy of XRFs as $E_{\rm iso} = 4\pi d_{\rm L}^2 S/(1+z)$, where S is the fluence in the XRT energy range. Fig.9.5 shows $E_{\rm iso}$ for XRFs with measured z as a function of the rest frame peak time $t_{\rm peak}^{\rm rest}$ (different combination of colors and symbols refer to different samples - see Fig.9.2).

Fig.9.5 shows that there is a trend: flares occurring later are less energetic. We have investigated if this trend can be the result of a decreasing efficiency of internal shocks. Suppose that two shells are created at two different times, and have very similar velocities. The smaller the velocity difference, the longer it takes for them to collide, and the smaller the produced energy, because their relative kinetic energy is small. In this case we do expect a trend: the flare $E_{\rm iso}$ should decrease with $t_{\rm peak}$. In order to born this out, we derive how the energy, released during the flare, scales with the time of occurrence of the flare.

The collision time $t_{\rm c}$ (Eq.2.11 in Sec.2.4) has been calculated for an observer at 90 degree with respect the direction of motion of the shells. We need to calculate the time interval between the flare and the trigger time.

Assume that the first γ–ray photon that triggers the instrument is at $R_{\rm c,p}$ and time $t_{\rm c,p}$. Suppose also that the shells producing the flare were ejected from the inner engine with a delay time ΔT with respect to the shells that produced the prompt emission. Their collision oc-

curs at a radius $R_{c,f}$ and time $t_{c,f}$ (these parameters set the emission radius and time of the first photon of the flare). The observer will see the flare after a time $(R_{c,p} + (\Delta T + t_{c,f} - t_{c,p})c - R_{c,f})/c$ respect to the trigger of the first prompt photon. The peak time of the flare t_{peak} is further increased of $\Delta t/2$ (assuming a simple flare triangular shape). The rest frame peak time is:

$$t_{peak}^{rest} \simeq \frac{R_{c,p}}{c} - t_{c,p} + \Delta T + \frac{\Delta R}{c}\frac{1}{\alpha_\Gamma - 1} \tag{9.1}$$

To evaluate $R_{c,p}$ and $t_{c,p}$ we assumed typical parameters for the prompt emission: $\alpha_\Gamma = 5$, $\Delta R = 10^9$ cm, $\Gamma_1 = 100$. Such assumption lead to $R_{c,p} \simeq c t_{c,p}$ so that the contribution of the first two terms cancels out. To evaluate the time of occurrence of flares t_{peak}^{rest} we allow ΔT, ΔR and α_Γ to vary in the other two terms.

An upper limit on the isotropic energy E_{iso} released in form of radiation during the flare can be derived applying the efficiency factor η (see Eq.2.16 in Sec.2.4) to an initial isotropic equivalent kinetic energy E_{kin} (fixed at 10^{54} erg). Thus, knowing how the peak time and the efficiency vary with respect to α_Γ (fixing all other parameters), we can find how the emitted energy changes with respect to the time when the pulse occurs.

Fig.9.5 shows the curves obtained assuming $\Delta R = 3 \times 10^{10}$ (7×10^{12}) cm and $\Delta T = 30$ (1000) s as the solid (dashed) red line. Interestingly, independently from the parameter choice, for relatively small values of α_Γ (in the limit of shells with slightly different bulk Lorentz factors) the energy released in the flares scales as t^{-2}. These curves shows that for some particular combination of parameters, it is possible to produce flares and also to consistently produce an energy of the flares which decreases with the flare occurrence time.

The same scenario allows us to derive the width of the flares as a function of their peak time. Summing Eq.2.17 and Eq.2.18 we obtain the rest frame pulse duration:

$$\Delta t^{rest} \simeq \frac{2\Delta R}{c}\frac{\alpha_\Gamma}{\alpha_\Gamma^2 - 1} \tag{9.2}$$

This is shown in Fig.9.6: points show the data in the rest frame (for XRFs with measured redshifts) and the curve is obtained assuming $\Delta R = 3 \times 10^{10}$ cm and $\Delta T = 30$ s. We are able to justify the increasing duration of the flares with time.

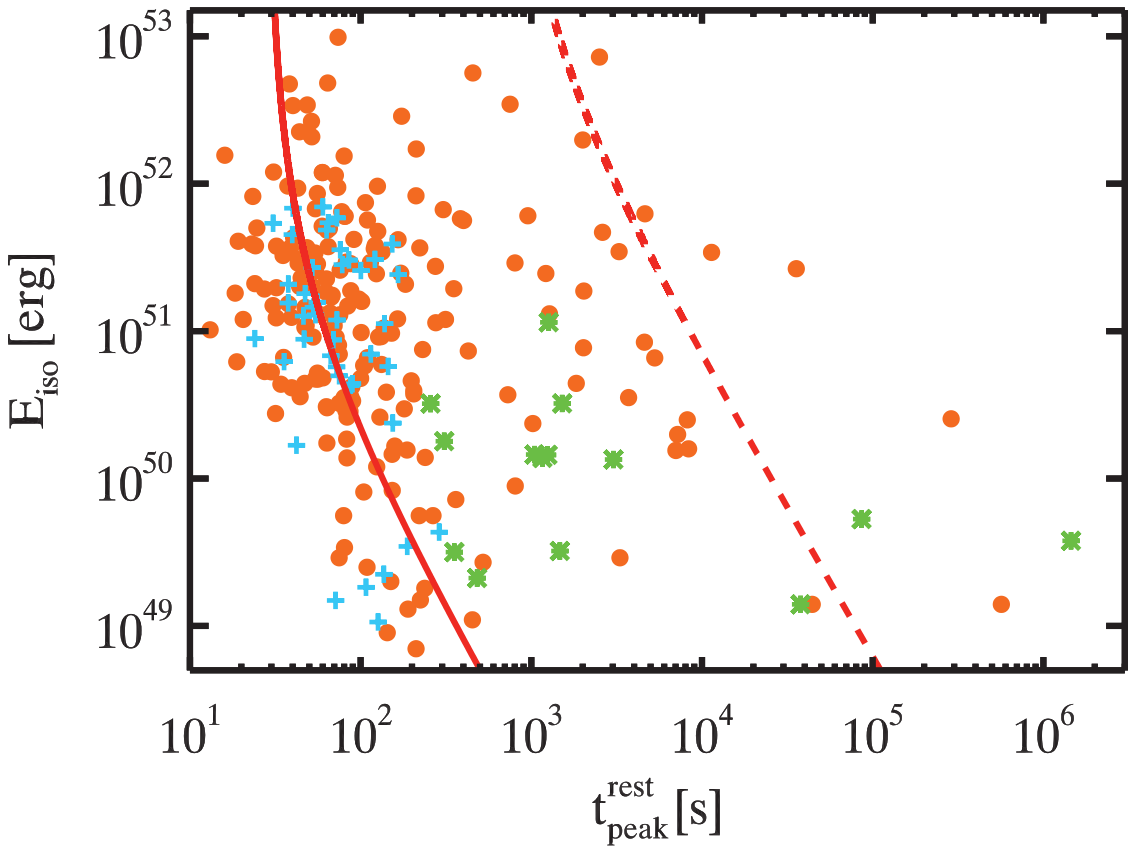

Figure 9.5: Isotropic energy (computed in the XRT energy range) of XRF versus their rest frame peak time. Different combinations of symbols and colors refer to different samples collected from the literature. Orange points, green asterisks and cyan crosses are associated to X–ray Flares (only those ones having measured redshift) from Yi et al.(2016), Bernardini et al.(2011) and Chincarini et al.(2010), respectively. The solid (dashed) red line shows the behaviour of the isotropic energy versus flare peak time predicted considering two shells emitted with a delay ΔT with respect to the start of the prompt emission and with a separation ΔR. These are free parameters, see the text for the values adopted to obtain the curves shown here.

The leading dependence of the flare properties (temporal and energetic) is from α_Γ. The smaller is α_Γ (i.e. shells with only slightly different bulk Lorentz factors) the larger is the flare duration and its occurrence time and the smaller is the released energy. With this simple model we do not aim to derive the parameters of the shells which is out of the scopes of the present work. Our simple approach considers only two shells encounters. It can explain the overall temporal and energetic tendency of the majority of flares as a succession of IS with decreasing values of α_Γ. Allowing for some dispersion of free parameters it might be possible to account for the dispersion of

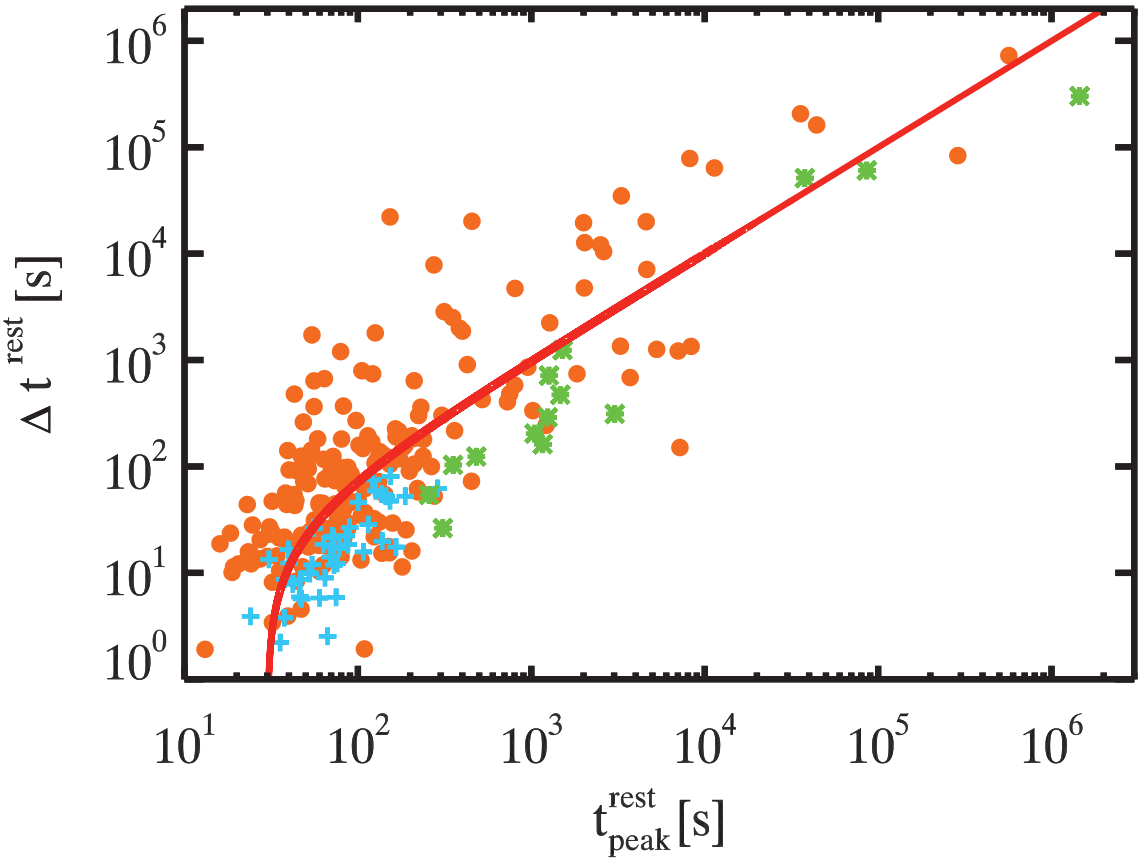

Figure 9.6: Rest frame duration versus occurrence time for XRFs. Different combinations of symbols and colors refer to different sources found in the literature for these parameters. Orange points, green asterisks and cyan crosses are associated to X–ray Flares (only those ones having measured redshift) from Yi et al.(2016), Bernardini et al.(2011) and Chincarini et al.(2010), respectively. The red solid line shows the expected relation between the flare width and the time of the flare in the IS shock model (see the text for the adopted set of parameter).

the XRF in Fig.9.5 and Fig.9.6. Very late flares could still be explained choosing a particular set of parameters (maybe extreme values) so it seems reasonable also to consider the possibility that their origin may be different.

9.3 What is the origin of pulses in GRBs?

In the previous sections we considered the possible dependence of the pulse width with time along GRBs combining prompt emission pulses with X–ray flares. It is known that prompt emission pulses do not show an increase of the pulse width with time (Ramirez-Ruiz and Fenimore, 2000). XRF, instead, show a nearly linear increase of

their width with time (Chincarini et al., 2010; Yi et al., 2016; Kocevski et al., 2007). Fig.9.2 shows prompt emission pulses (from the sample of B12) and XRFs (from the samples of C10, B11, Y16).

Internal shocks predict that the dissipation of energy between shells coasting with slightly different bulk Lorentz factor should produce random pulses with duration uncorrelated with their time of occurrence. On the other hand, the flare width has been observed to increase with time and considered so far a signature in favour of an external origin. In this scenario, the production of flares occurs in the interaction of a decelerating blast wave with ISM over–densities located at increasing distance from the central engine. In these two scenarios, what determines whether the pulse duration increases with time or not is the dissipation at increasing radii (as in external shocks) or at a constant distance (as in internal shocks).

We verified in Sec.9.1 with three different methods (Fig.9.2 - top left inset, Fig.9.3 and Fig.9.4) and with two independent samples of prompt emission pulses (pulses obtained by the deconvolution of bright *Fermi* bursts - from B12 - and a sample of 100 GRBs with redshift whose light–curves were analyzed in this work) that prompt emission pulses show no correlation between their duration and their time of occurrence. Our results fully confirm those obtained with the BATSE data by Ramirez-Ruiz and Fenimore (2000). Despite the emission during the prompt phase is highly variable, it can be described as the emission due to internal shocks occurring almost at the same distance from the central engine.

XRFs exhibit an (almost linear) increase of their duration with time. Moreover, their peak luminosity $L_{\rm p}$ anti–correlates with the peak time $t_{\rm peak}$: for early flares ($t_{\rm peak} < 1000$ s, Chincarini et al., 2010; Margutti et al., 2011) $L_{\rm p} \propto t^{-2.7}$ and becomes shallower $L_{\rm p} \propto t^{-1.7}$ for late flares (Bernardini et al., 2011). As a consequence, (as noted by Margutti et al., 2011) the energy released during the flares should scale as $t^{-1.7}$ ($t^{-0.7}$ for late time flares).

The origin of XRF has been debated in the literature. Temporal and spectral properties of XRFs lead different authors to ascribe them to internal–like dissipation due to the late time activity of the inner engine (Falcone et al., 2006, 2007; Lazzati and Perna, 2007; Maxham and Zhang, 2009; Lazzati et al., 2011). Alternatively, XRFs could be produced by external shocks with over–dense regions of the ISM (e.g. Wang and Loeb, 2000; Lazzati et al., 2002; Heyl and Perna, 2003) or by the long–lived reverse shock interacting with the

tail of the ejecta (Hascoet et al., 2015).

Based on the distribution of prompt emission pulses and XRF in the plane of Fig.9.2 we considered the possibility that also XRF are produced by internal shocks between shells emitted with a certain initial separation and a certain (even small) temporal delay with respect the prompt shell. If these shells are characterized by small values of α_Γ, the time of their encounter is delayed (and therefore the shock development). Later flares last longer and are less efficient in emitting radiation. These results, shown by the red model curves in Fig.9.5 and Fig.9.6, are consistent with the distribution of data in these planes. In this scenario the leading parameter is the relatively low ratio between the shells' Lorentz factors, parametrized by α_Γ. The asymptotic behaviour, for small α_Γ, is approximately t^{-2} in agreement with the $E \propto L_p \Delta t \propto t^{-1.7}$ also marginally shown by the early flares in Fig.9.5. This behavior also seems to explain the shape of the left boundary of the distribution in the region populated by XRF with low energies and peak time.

We showed that it is possible to explain the energetic and temporal properties of X–ray flares as the result (under appropriate assumptions) of classical internal shocks between fireball ejected during the prompt emission phase. We do not require that the inner engine is active until late times: late flares, characterized by smaller energies, can be produced by relativistic shocks between fireballs with Lorentz factor ratio α_Γ very close to one. This result confirms what has been previously found by Barraud et al. (2005) through numerical simulations.

CHAPTER 10

Radiative mechanism in GRBs

The spectrum characterizing the prompt emission of GRBs is typically non–thermal. Within the standard model, synchrotron is the leading radiation mechanism proposed to interpret and explain GRB prompt emission (Meszaros and Rees, 1993a,b; Rees and Meszaros, 1994; Sari et al., 1996, 1998). This is the most natural mechanism involving accelerated electrons into intense magnetic fields and it is found to successfully interpret the afterglows emission (Paczynski and Rhoads, 1993; Katz, 1994) and many other astrophysical phenomena.

Despite many of the observed GRB spectra are consistent with this interpretation (Tavani, 1996; Cohen et al., 1997), the synchrotron model encounters difficulties in explaining some cases that violate the so–called synchrotron line–of–death (Preece et al., 1998). The standard synchrotron spectrum in the fast–cooling regime (see Sec.2.6) is expected to have, below the $\nu F(\nu)$ peak, a power–law photon spectral index $-3/2$. An harder spectrum could be reached at lower energies with the limiting value $-2/3$ below the cooling break frequency (Preece et al., 1998; Ghisellini et al., 2000). Despite these theoretical limits a large fraction of GRBs seem to violate them

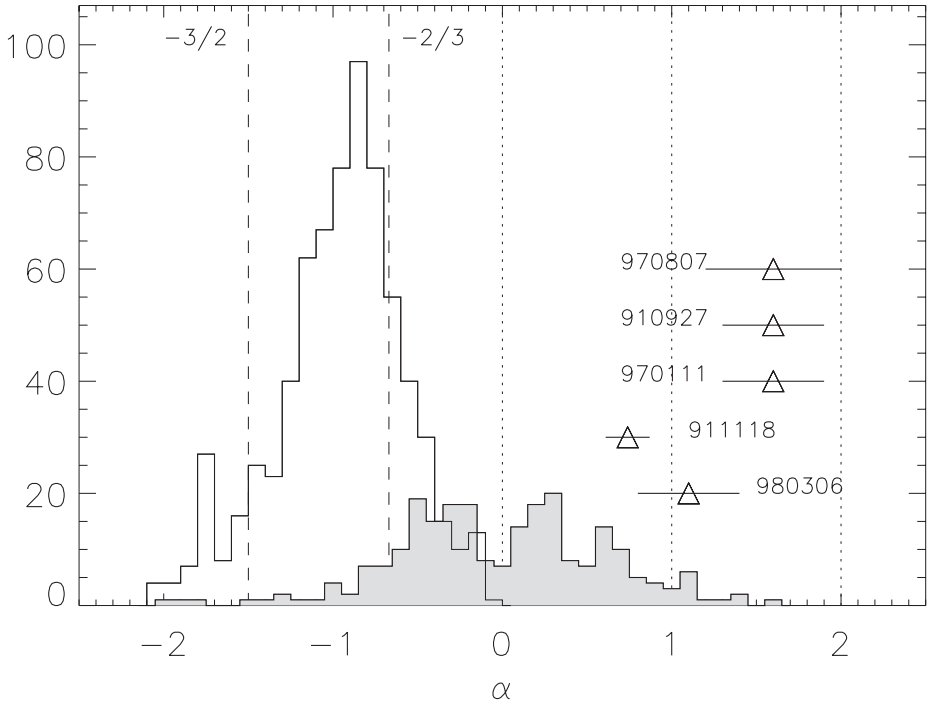

Figure 10.1: Low energy spectral index distribution from Ghirlanda et al. (2002). The Synchrotron violating region is bounded by the death line $\alpha = -2/3$ and the acceptable region is bounded by the $\alpha = -3/2$ line (dashed). The triangles represent the maximum values found from the spectral analysis of the bursts presented in this work along with their 90% confidence interval (horizontal bars). The gray histogram shows the distribution of the low energy spectral index found from the time resolved spectral analysis of the thermal bursts presented in Ghirlanda et al. (2003).

(Preece et al. 1998; Ghirlanda et al. 2003, 2002; Kaneko et al. 2006; Nava et al. 2011; Goldstein et al. 2012; Lien et al. 2016 – see Fig.10.1), having on average spectral indexes ~ -1 or even harder than $-2/3$ in some cases.

There are many solutions proposed in the literature that interpret the observed hard spectra of GRB prompt emission adopting anyway the synchrotron. It is possible to reproduce the observed hard spectra through a fine tuning of the parameters characterizing the distribution of the emitting electrons, the magnetic field and the ambient medium. One possibility is that the magnetic field decays on a timescale which is shorter than dynamical timescale not allowing electrons to cool efficiently (Pe'er and Zhang, 2006; Zhao et al., 2014b,a). Alternatively an highly anisotropic magnetic fields (Medvedev, 2000) combined with a synchrotron self–absorption frequency in the X–ray range (Lloyd and Petrosian, 2000) can explain hard low–

energy spectra with photon indexes that can be as hard as $\alpha \sim 0$. When the energy density of the photons is larger than in the magnetic field, the inverse Compton scattering in Klein–Nishina regime can reduce the amount of lower energy photons making the observed spectra harder than expected in a synchrotron scenario (Derishev et al., 2001; Nakar et al., 2009; Daigne et al., 2011). Another possible solution to the inconsistency between the expected and measured photon index is to consider a marginally fast–cooling regime in which the cooling frequency of electrons ν_c is close to the typical synchrotron frequency ν_m, i.e. with $\nu_c \lesssim \nu_m$ rather than $\nu_c \ll \nu_m$ as in the normal fast–cooling (as proposed by Daigne et al., 2011; Beniamini and Piran, 2013).

Unfortunately, all these modifications of the standard synchrotron model are almost indistinguishable by observations, since tuned physical properties are required, making the origin of prompt emission still debated. Although the synchrotron model continues to be the main paradigm, some other alternative radiation mechanisms have been proposed to interpret GRB prompt emission. The most natural extension to this model is given by considering the Inverse Compton scattering (see Sec.2.7). Then, the GRB prompt emission could be due to synchrotron self–inverse–Compton (SSIC) emission (Panaitescu and Mészáros, 2000), with the caveat that the typical synchrotron emission frequency has to be much below the MeV band.

Another important emission, naturally predicted within the standard fireball scenario, is the thermal one. Such thermal emission is predicted when the relativistically expanding fireball releases the internal photons at the transparency radius (e.g. Goodman, 1986; Paczynski, 1986; Daigne and Mochkovitch, 1998). Nevertheless, the GRBs spectrum is found to be consistent with a black body spectrum only in rare cases (Ghirlanda et al., 2003; Bosnjak et al., 2006; Ryde, 2004) and the majority of GRBs present a non–thermal spectrum. The few GRBs exhibiting BB spectrum represent a fundamental tool to investigate the origin of the thermal component, its evolution and the basic properties of the relativistic outflow. The detection of a BB spectrum in GRBs allows us to estimate (Pe'er et al., 2007) fundamental parameters of the fireball like the transparency radius R_T, the bulk Lorentz factor Γ_T at transparency and the radius at the base of the relativistic flow R_0 where the acceleration began (see. Sec.2.3). Clearly, when only the thermal component is observed these estimates depend on a lower number of free param-

eters (since no modeling of the non–thermal component is required in these cases). Interestingly, it should be explained why in this kind of bursts the non–thermal emission (typically ascribed to synchrotron/inverse Compton emission at internal shocks) is absent: either it could be highly inefficient or there should be a mechanism suppressing this process.

The analysis and study of the prompt (and also of the afterglow) emission in GRBs is required for a complete understanding of their central engine, the nature and properties of the outflow (magnetic or matter dominated) and emission processes. The *Fermi* satellite has shown the presence of long–lasting emission extending up to the GeV energy range (e.g. Abdo et al., 2009b; Ackermann et al., 2010; Ghirlanda et al., 2010; Ghisellini et al., 2010a; Ackermann et al., 2013) and a sometimes complex coexistence of thermal and non–thermal components during the prompt phase observed between 8 keV and a few MeV (Guiriec et al., 2011, 2013; Burgess et al., 2014). The *Swift* satellite has been enriching the observational picture of the prompt and afterglow emission either directly, by systematic monitoring of the X–ray $[0.3 - 10]$ keV light–curve on average from a few tens of seconds to months after the trigger (see e.g. Gehrels et al., 2009), or indirectly, by triggering ground based follow up programs/telescopes in the optical band.

Either statistical studies of well–defined GRB samples (Salvaterra et al., 2012; Hjorth et al., 2012; Perley et al., 2016a) or single–event modeling like GRB 130427A (Maselli et al., 2014; Vestrand et al., 2014; van der Horst et al., 2014; Perley et al., 2014; Bernardini et al., 2014; Ackermann et al., 2014; Panaitescu et al., 2013; Kouveliotou et al., 2013; Laskar et al., 2013) seem to be the best approaches to compare theory and observations. However, the latter case is possible only in a handful of bursts and still the wealth of information (as for GRB 130427A) does not completely break some parameters degeneracy. Nevertheless, it is still important to study in detail any new single event which presents peculiar properties of either the prompt and/or afterglow emission, especially if with good data quality and coverage.

In the following sections I will present two interesting cases, GRB 151027A (see Sec.10.1) and GRB 160625B (see Sec.10.2) that I analyzed during my PhD.

10.1 GRB 151027A: some like it thermal

GRB 151027A, the 999th burst detected by the *Swift* satellite, is a long bright event lasting about 130 s which was followed in the X–ray and in the optical and radio bands until five months after the prompt emission. The event presents unique properties in the prompt emission due to the presence of a bright flare (see e.g. Burrows et al., 2005b; Chincarini et al., 2010; Margutti et al., 2010; Bernardini et al., 2011), which has been observed from 0.3 keV to $>$ MeV (by *Swift*/XRT and *Swift*/BAT and by *Fermi*/GBM).

In Nappo et al. (2017) we presented a multi–wavelength study of this particular burst. In the following I will describe in detail the prompt spectral analysis which I have lead whithin this work. The multi–wavelength light–curve from 500 s to 140 days can be modelled through a standard forward shock afterglow, but it requires an additional emission component to reproduce the early X-ray and optical emission. We presented and analyzed optical observations performed with the Telescopio Nazionale *Galileo* (TNG) and the Large Binocular Telescope (LBT) 19.6, 33.9, and 92.3 days after the trigger which show a bump with respect to a standard afterglow flux decay and are interpreted as possibly due to the underlying supernova and host galaxy (at a level of ~ 0.4 μJy in the optical R band, $R_{AB} \sim 25$). Radio observations, performed with the Sardinia Radio Telescope (SRT) and Medicina in single–dish mode and with the European Very Long Baseline Interferometer (VLBI) Network and the Very Long Baseline Array (VLBA), between day 4 and 140 suggest that the burst exploded in an environment characterized by a density profile scaling with the distance from the source (wind profile).

10.1.1 Observational data

In this sub–section I will describe the data reduction and analysis of the prompt emission of GRB 151027A and the main results.

γ–ray and X–ray data GRB 151027A (Maselli et al., 2015, GCN #18478) was detected and located at 03:58:24 UT by the *Swift* Burst Alert Telescope (BAT; Barthelmy et al., 2005). The *Swift* X–ray Telescope (XRT; Burrows et al., 2005a) and the Ultra Violet Optical Telescope (UVOT; Roming et al., 2005) started acquiring data 87 s and 95 s post trigger, respectively, and detected a bright X–ray and optical transient. The prompt XRT light–curve (limited to the first 200 s since the trigger)

is shown in Fig.10.2 (blue line). The $[15-350]$ keV energy band BAT light–curve has a duration of $T_{90} = 130 \pm 6$ s (Palmer et al., 2015, GCN #18496) with two main emission episodes (the first composed of two peaks) separated by a quiescent phase of ~ 80 s (see Fig.10.2 – red line). The $[15-150]$ keV band peak flux (corresponding to the first peak at 0.2 s) is 6.8 ± 0.6 ph cm^{-2} s^{-1} and the fluence is $(7.8 \pm 0.2) \times 10^{-6}$ erg cm^{-2}.

The burst was also detected by the Gamma Burst Monitor (GBM; Meegan et al., 2009) on board the *Fermi* satellite (Toelge et al., 2015, GCN #18492) and by Konus/Wind (Golenetskii et al., 2015, GCN #18516). The *Swift*/BAT, *Fermi*/GBM (red and green line in the middle panel of Fig.10.2, respectively), and Konus/Wind light–curves show similar temporal properties. The wide energy ranges of the GBM ([8 keV -1 MeV]) and Konus/Wind ([20 keV -5 MeV]) show that the time–averaged spectrum is best fit by a cutoff power–law model with low energy spectral index $\alpha = 1.41 \pm 0.04$ and $E_{\rm peak} = 340 \pm 63$ keV (GBM; Toelge et al., 2015, GCN #18492) or $E_{\rm peak} = 173^{+135}_{-46}$ (Konus/Wind; Golenetskii et al., 2015, GCN #18516). The GRB fluence in the [10 keV -1 MeV] energy range, as measured by the GBM spectrum, is $(1.94 \pm 0.09) \times 10^{-5}$ erg cm^{-2} and the photon peak flux is 11.37 ± 0.34 ph cm^{-2} s^{-1} .

The redshift $z = 0.81$ was measured through the MgII doublet in absorption from the Keck/HIRES spectrum (Perley et al., 2015a, GCN #18487). The isotropic equivalent energy of the burst inferred from GBM spectral data analysis in Toelge et al. (2015, GCN #18492) is $E_{\gamma,\rm iso} = 3.98 \times 10^{52}$ erg.

***Fermi*/GBM data extraction** We selected and downloaded from the official *Fermi* website (`http://fermi.gsfc.nasa.gov/`) the GBM CSPEC data (having 1.024 s time resolution) of the brightest detectors: NaI#0, NaI#3, and BGO#0. Data filtering, background spectrum extraction, and timeslice selection was performed with the software RMFIT v.4.3.2 using standard procedures (see e.g. Gruber et al., 2014; Nava et al., 2011). Channels with energy $\in [10, 800]$ keV and $\in [300, 2000]$ keV were considered for the NaI and BGO detectors, respectively. GBM spectra and background files were exported to XSPEC (v12.7.1) format (see Arnaud, 1996) in order to fit them jointly with *Swift*/BAT and XRT data. Details on the spectral analysis and models adopted are given in sub–sec.10.1.2.

***Swift*/BAT and XRT data extraction** We extracted and reduced the *Swift*/BAT spectra and light–curve[1] with the *Swift* software included in the HEASoft package (ver.6.17), using standard procedures. We also retrieved[2] the *Swift*/XRT count rate light–curve (Fig.10.2 – blue line). In order to correct for the extinction we used intrinsic $N_H = 4.4 \times 10^{21}$ cm^{-2} inferred from late time XRT spectra and galactic $N_{H,\mathrm{gal}} = 3.7 \times 10^{20}$ cm^{-2}. XRT spectra[3] were corrected for pile–up following the procedure in Romano et al. (2006). Windowed Timing mode (WT) counts below 0.5 keV were excluded owing to the abnormal photon redistribution. Count spectra were rebinned requiring a minimum of 20–30 counts per bin.

***XMM–Newton* data** *XMM–Newton* started observing GRB 151027A on 2015 October 28 at 01:19:34.00 UT (21.3 h after the burst). The observation lasted for 51.5 ks without interruption. Data reduction was performed with the *XMM–Newton* Science Analysis Software (SAS) version xmmsas_20131209_1901-13.0.0 and the latest calibration files. Data were first locally reprocessed with `epproc`, `emproc`, and `rgsproc`. The RGS data contained too few photons and were not considered any further. MOS and pn data were searched for high–background intervals, and none were found. EPIC data were grade filtered using pattern 0–12 (0–4) for MOS (pn) data, and FLAG==0 and #XMMEA_EM(P) options. The pn and MOS events were extracted from a circular region of 870 pixels centered on source. Background events were extracted from similar regions close to the source and free of sources. MOS and pn data were rebinned to have 20 counts per energy bin. MOS data were summed and fitted within the $[0.3 - 10]$ keV range, pn data within the $[0.2 - 10]$ keV range.

10.1.2 Prompt emission analysis and results

- **First and second peak**
  During the first two peaks of the light–curve, corresponding to the time interval $\sim 0 - 24$ s, we extracted three spectra: #1 and #2 corresponding respectively to the rise and decay phase of the first peak and #3 for the entire duration of the second (dim-

[1] downloaded from *Swift* data archive: `http://heasarc.gsfc.nasa.gov/cgi-bin/W3Browse/swift.pl`

[2] from the *Swift* Science Data Center at the University of Leicester website: `http://www.swift.ac.uk/xrt_curves/` – Evans et al. (2009)

[3] retrieved from the archive of the *Swift*/XRT website: `http://www.swift.ac.uk/archive/`

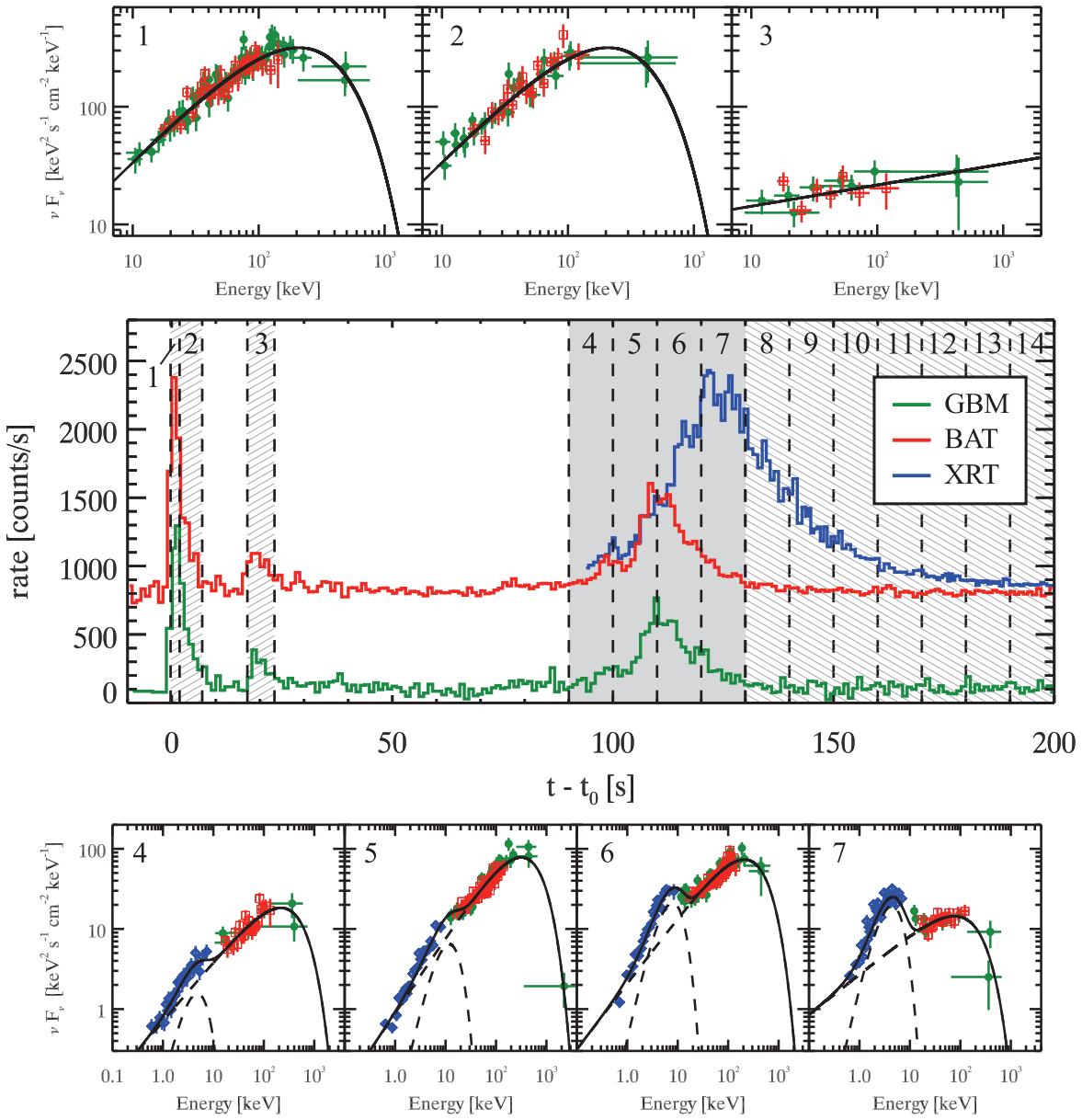

Figure 10.2: GRB 151027A rate light curve (*middle panel*). The *Fermi*/GBM NaI(0) data ([8 keV −1 MeV]) are shown by the green line. The *Swift*/BAT ([15 − 150] keV) light–curve is shown by the red line. The rescaled *Swift*/XRT ([0.3 − 10] keV) light–curve is shown by the blue line. Vertical dashed lines represent the start and stop times of the intervals selected for the spectral analysis. *Top panels*: $\nu F(\nu)$ spectra of the rise (left, #1) and decay (middle, #2) phase of the first peak and of the second peak (right, #3), corresponding to the first three hatched regions in the *middle panel*. Green and red symbols show the GBM and BAT data, respectively, and the solid line is the best fit model (see Tab.10.1). *Bottom panels*: $\nu F(\nu)$ spectra of the third peak corresponding to the shaded regions of the light–curve (*middle panel*, #4–#7). The blue symbols show the XRT spectra. The two model components (cutoff power–law and blackbody) are shown by the dashed lines and their sum by the solid line.

mer) peak (referring to the labeled regions in the *middle panel* of Fig.10.2). We jointly fit the *Fermi*/GBM (NaI and BGO) and the *Swift*/BAT spectra with a cutoff power–law model (CPL) with a free normalization constant between *Fermi* and *Swift*. Start and stop times and the best fit parameters (with 68% confidence errors) and the χ^2(d.o.f.) are given in Tab.10.1. Spectrum #3 can be fitted only with a simple power–law model (i.e. the $E_{\rm peak}$ of the cutoff power–law model is unconstrained). These three spectra are shown in the top panels of Fig.10.2 where the data (green and red for the GBM and BAT, respectively) and the best fit model (solid black line) are shown.

- **Third peak: evidence of a thermal component**
  The third peak of the light–curve was observed by BAT and GBM above 10 keV and simultaneously by XRT in the $[0.5-10]$ keV energy range. The light–curves (see *middle panel* of Fig.10.2) show that the XRT peak is delayed with respect to that observed by BAT and GBM. This peak has been divided in four time intervals (from 90 s to 130 s after the trigger) where the data from three instruments overlap, and over which we jointly fitted the spectra. This allows us to perform a time–resolved spectral analysis over a wide energy range, namely from 0.5 keV to a few MeV. Spectra have been fit with a CPL model.

  Since the data extend down to 0.5 keV, it is necessary to take into account the galactic and intrinsic absorption. The Tuebingen–Boulder ISM absorption model (Wilms et al., 2000) encoded in the `tbabs` and `ztbabs` models of XSPEC (Arnaud, 1996) is used. We assume the galactic absorption $N_{H,\rm gal} = 3.7 \times 10^{20}$ cm^{-2} and keep it fixed, and we also allow for an intrinsic (at $z = 0.81$) absorption. Also in this case we allow a free normalization constant between the *Swift*/BAT spectrum and the *Fermi*/GBM (NaI plus BGO) spectra. In all the fits we find that this constant is within a factor of 2 and is consistent with 1.0.

  If the intrinsic N_H is treated as a free parameter, we find that it varies dramatically (by more than one order of magnitude) describing a peak over a 30 s timescale coincident with the flare. We interpret this nonphysical feature as being indicative of the possible presence of an additional component during the flare. We therefore fixed the intrinsic $N_H = 0.44 \times 10^{22}$ cm^{-2} which is the value found by fitting the XRT spectra at very late times

(i.e. > 5 days – compatible with the N_H accurately estimated from *XMM–Newton* data analysis). The fit with the CPL model is unacceptable since the fitted spectra and their residuals show a systematic deviation from the model in the XRT $[0.5 - 10]$ keV energy range. We therefore tried to model this excess by adding the simplest two–parameter thermal black body (BB) component. We refitted the data and compared the new fit (i.e. absorbed cutoff power–law plus blackbody – CPL+BB) with the old one (i.e. absorbed CPL) through an F–test. We find that there is statistically significant evidence for the presence of a thermal black body component in all of the four spectra describing the third emission episode of GRB 151027A. The probability associated to the F–test (representing the probability that the fit is not significantly improved by the additional BB component) is given in Tab.10.1, along with the spectral parameters of the CPL+BB fit. The four spectra are shown in the bottom panels of Fig.10.2.

The addition of the BB component to the CPL is the minimal assumption that can produce a curvature of the spectrum which adapts to the data points. However, we also verified whether the systematic deviation of the data from a simple CPL could also be accommodated by a second CPL. In order to have a similar number of free parameters of the BB, in this case we fixed the second CPL low energy photon index to the value predicted for single electron synchrotron emission, i.e. $2/3$. In spectra #3 and #4, when the peaked component is less dominant, the fits performed using CPL+CPL or CPL+BB are statistically equivalent. Afterwards, when the component at low energies represents a considerable fraction of the total flux, the CPL+BB model is statistically preferable. The evolution of the spectral parameters is shown in Tab.10.1 and Fig.10.3.

- **Third peak: X–ray emission in the interval 130–200 s**
  After 130 s, there is no more sufficient signal in GBM and BAT data and thus they cannot be used for the spectral analysis. Then, we analyzed seven XRT spectra (corresponding to regions 8-14 in the *middle panel* of Fig.10.2) corresponding to the time interval $[130 - 200]$ s and fit with an absorbed power–law (PL) or an absorbed power–law plus a black body component (PL+BB). Given the limited energy range $[0.5 - 10]$ keV we can-

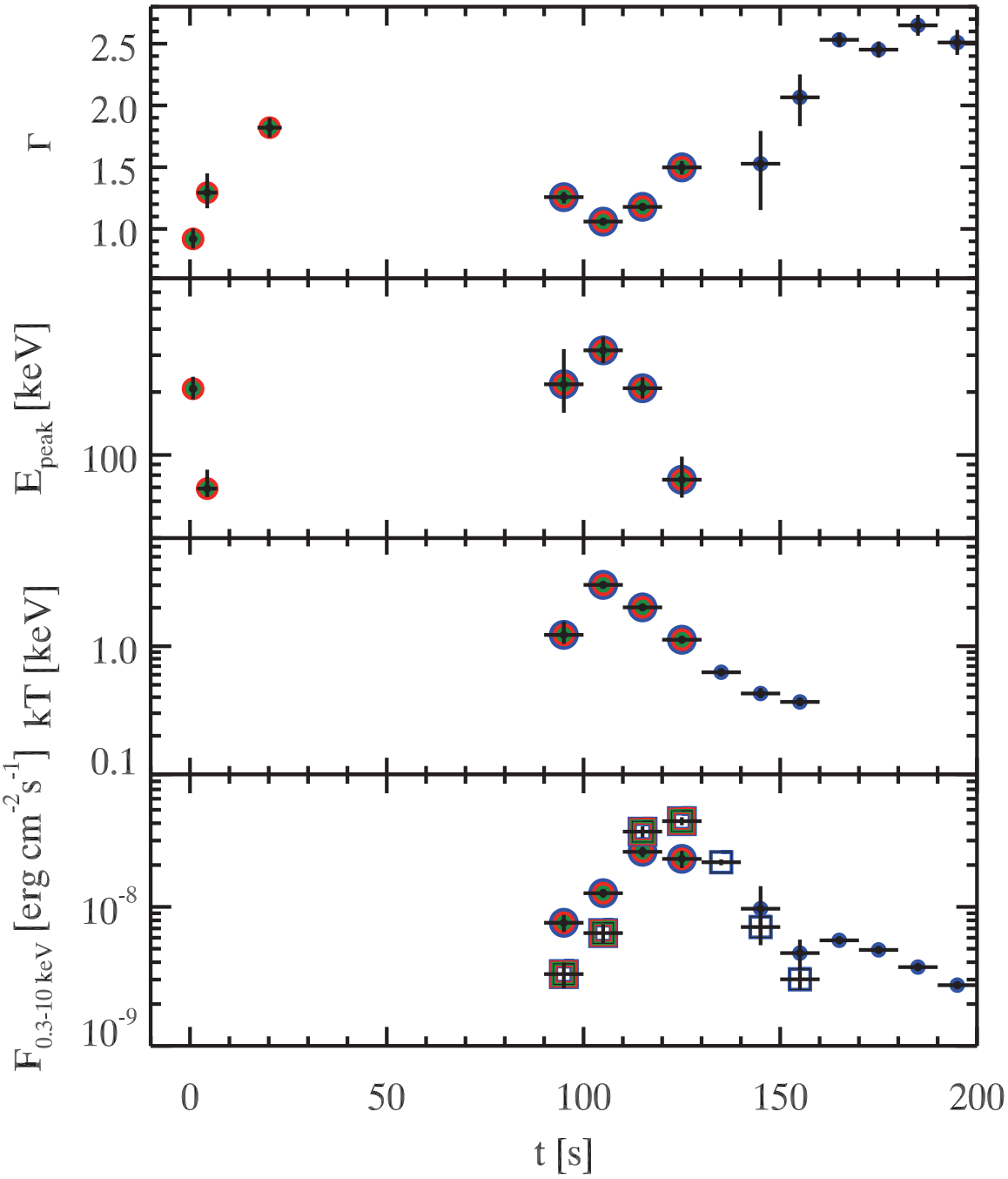

Figure 10.3: Spectral evolution of GRB 151027A parameters through the entire burst duration. Panel a) shows the temporal evolution of the non–thermal component spectral index. Panel b) shows the evolution of the peak energy when the non–thermal component is described by a CPL. Panel c) shows the BB temperature evolution. The last panel d) shows the comparison between the fluxes, integrated in the $[0.3 - 10]$ keV energy range, associated with the thermal (squares) and non–thermal component (points). The color codes of the different symbols corresponds to the spectral data sets (the same color coding) shown in Fig.10.2.

Data[a]	#	start[b] s	stop[b] s	Model[c]	Γ	$E_{\rm peak}$ keV	A[d] ph cm^{-2} s^{-1}	$k\mathcal{T}$ keV	$A_{\rm BB}$ ph cm^{-2} s^{-1}	χ^2(dof)	$P^{\rm F-test}_{CPL-CPLBB}$
B+G	1	-0.256	1.792	CPL	$0.92^{+0.08}_{-0.08}$	207^{+29}_{-23}	$2.93^{+0.84}_{-0.68}$	-	-	164(244)	-
...	2	1.792	6.912	CPL	$1.29^{+0.15}_{-0.13}$	69^{+16}_{-6}	$6.09^{+2.84}_{-1.38}$	-	-	192(272)	-
...	3	17.152	23.296	PL	$1.82^{+0.08}_{-0.08}$	-	$9.43^{+3.26}_{-2.43}$	-	-	168(286)	-
X+B+G	4	90	100	CPL+BB	$1.26^{+0.04}_{-0.05}$	218^{+103}_{-59}	$0.71^{+0.09}_{-0.10}$	$1.23^{+0.33}_{-0.19}$	$0.041^{+0.009}_{-0.008}$	211(256)	3.8×10^{-7}
...	5	100	110	CPL+BB	$1.06^{+0.02}_{-0.02}$	316^{+51}_{-41}	$0.89^{+0.06}_{-0.06}$	$3.02^{+0.21}_{-0.20}$	$0.17^{+0.02}_{-0.02}$	279(301)	8.0×10^{-13}
...	6	110	120	CPL+BB	$1.18^{+0.02}_{-0.03}$	209^{+27}_{-22}	$2.08^{+0.16}_{-0.16}$	$2.01^{+0.07}_{-0.08}$	$0.55^{+0.05}_{-0.04}$	257(296)	6.3×10^{-35}
...	7	120	130	CPL+BB	$1.50^{+0.05}_{-0.06}$	76^{+22}_{-14}	$2.71^{+0.37}_{-0.37}$	$1.12^{+0.07}_{-0.06}$	$0.51^{+0.03}_{-0.03}$	284(293)	8.7×10^{-45}
X	8	130	140	BB	-	-	-	$0.63^{+0.02}_{-0.02}$	$0.25^{+0.01}_{-0.01}$	39(34)	-
...	9	140	150	PL+BB	$1.53^{+0.27}_{-0.38}$	-	$1.19^{+0.40}_{-0.47}$	$0.43^{+0.04}_{-0.03}$	$0.087^{+0.015}_{-0.013}$	30(26)	2.3×10^{-6}
...	10	150	160	PL+BB	$2.07^{+0.19}_{-0.23}$	-	$0.86^{+0.18}_{-0.21}$	$0.37^{+0.03}_{-0.03}$	$0.037^{+0.006}_{-0.005}$	36(46)	4.6×10^{-10}
...	11	160	170	PL	$2.53^{+0.06}_{-0.06}$	-	$1.19^{+0.04}_{-0.04}$	-	-	53(45)	(0.02)[e]
...	12	170	180	PL	$2.45^{+0.07}_{-0.06}$	-	$1.01^{+0.04}_{-0.04}$	-	-	50(40)	(0.01)[e]
...	13	180	190	PL	$2.65^{+0.09}_{-0.08}$	-	$0.76^{+0.09}_{-0.03}$	-	-	16(30)	-
...	14	190	200	PL	$2.51^{+0.10}_{-0.10}$	-	$0.57^{+0.03}_{-0.03}$	-	-	25(22)	-
XMM		7.8×10^5	1.3×10^6	PL+BB	$2.09^{+0.03}_{-0.04}$	-	$3.8^{+0.1}_{-0.2}\times10^{-4}$	$0.11^{+0.03}_{-0.02}$	$3.1^{+2.0}_{-1.1}\times10^{-6}$	398(345)	5.8×10^{-7}

Table 10.1: Prompt emission time resolved spectral analysis. [a]Spectral data used in the fit: B=*Swift*/BAT, G=*Fermi*/GBM and X=*Swift*/XRT. [b]Times refer to the trigger time of the burst. [c]Models adopted in the fit: CPL=power–law with exponential cutoff, PL=power–law, BB=black body; galactic ($N_{\rm H,gal}$=3.7×10^{20} cm^{-2}) and intrinsic ($N_H = 4.4\times10^{21}$ cm^{-2}) absorption is present in all models (using Tuebingen–Boulder ISM absorption model, Wilms et al. 2000). [d]Spectral normalization is computed at 1 keV. [e]In this case the addition of a BB component is not statistically significant, as suggested by the value of the null hypothesis probability associated with the F–test. The horizontal lines correspond to the differently shaded regions in Fig.10.2.

not determine the peak of a possible cutoff power–law model. For each spectrum the statistical significance of the addition of the thermal component has been estimated through the F-test. For spectrum #8 the best fit is obtained with a pure BB model since the addition of a power law component does not constrain the power–law fit parameters. In the following spectra the best fit model is PL+BB, in which the thermal component remains statistically significant up to 160 s. After that, the spectrum is best fitted by a single PL component. The evolution of the spectral parameters is shown in Tab.10.1 and Fig.10.3.

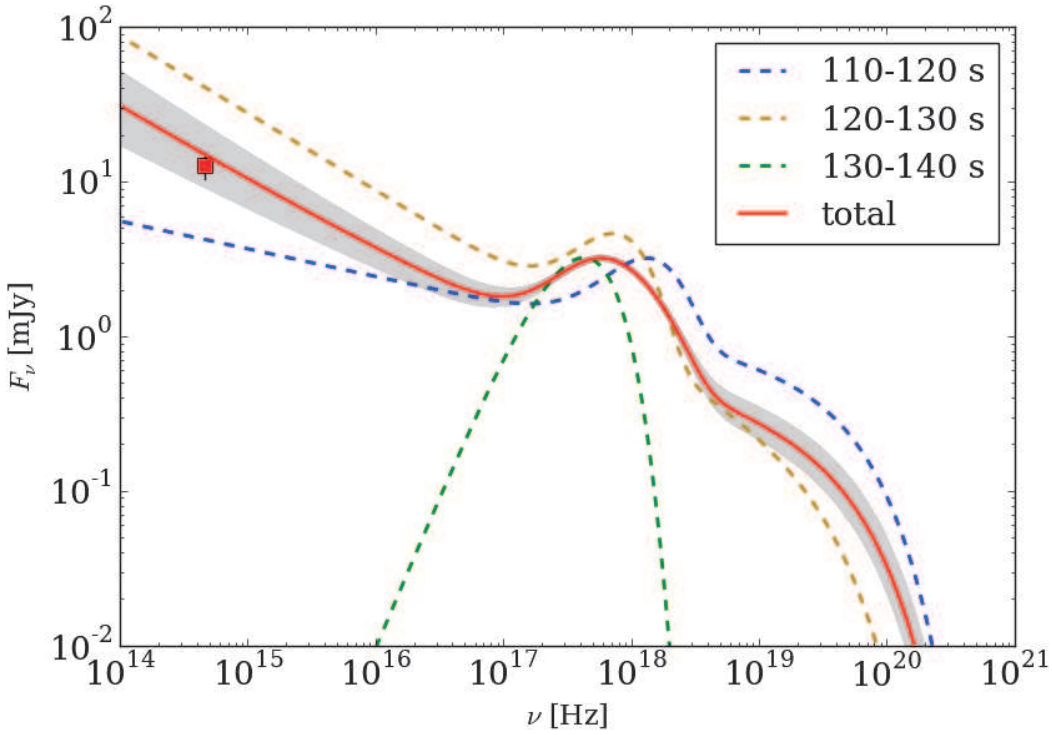

Figure 10.4: Comparison between the optical *R* band detection at 126 s (red square, Pozanenko et al., 2015, GCN #18635) and the fit of the composite XRT–BAT–GBM spectrum (red solid line). The grey shaded area represents the 1σ scatter from the best fit.

The results of the BAT–GBM–XRT joint spectral fits were compared with the optical *R* band detection at 126 s (Pozanenko et al., 2015, GCN #18635). An intriguing fact is that the optical detection is compatible with the low energy extrapolation of the model (Fig.10.4). This result suggests that the early optical emission could be produced by the same mechanism responsible for the high energy emission and therefore it should not be interpreted as standard afterglow.

- ***XMM–Newton* late spectrum**
  The *XMM–Newton* late time spectral analysis was performed in order to obtain a more accurate estimate of intrinsic N_H. We initially performed the fit using a PL model with free intrinsic absorption. From the residual, we noticed that a peaked component should be added to improve the fit. For this reason we refit the spectrum using a PL+BB model with free absorption. The XMM–Newton spectrum showed a still statistical significant thermal component that contributes to only $\sim$ 8% of the $[0.3 - 10]$ keV flux. The BB temperature was lower than the one obtained from XRT spectrum #10 (the last time interval where BB was detected). All the fit parameters are listed in Tab.10.1. From the *XMM–Newton* spectrum we obtained $N_H = (0.42 \pm 0.05) \times 10^{22}$ cm^{-}2 (in agreement within errors with the value obtained by the late time XRT spectrum).

10.1.3 Understanding the thermal component: a reborn fireball

The prompt light curve of GRB 151027A shows three isolated emission peaks. The first two peaks have a standard behavior with non–thermal spectra both characterized by a hard to soft evolution. The third peak shows a statistically significant BB component at low energies superimposed to a cutoff power–law.

Evidence of a thermal emission has also been found in other GRB spectra. Typically it has been detected in the early phases of the prompt emission (Class–II; Ghirlanda et al., 2003) or it can even be present throughout the entire burst duration (Class–I; Ryde, 2004; Bosnjak et al., 2006; Ghirlanda et al., 2013b). In some cases it has also been detected in X-ray flares (Peng et al., 2014). Furthermore, Starling et al. (2012) and Sparre and Starling (2012) have presented systematic research of thermal signatures in X–ray emission. According to the classification made in Ghirlanda et al. (2013b, see Sec.1.2), GRB 151027A belongs to Class–III of the thermal bursts because the thermal and non–thermal components coexist during the third episode.

The X–ray flare of GRB 151027A has a very luminous thermal component ($\sim 10^{50}$ erg/s near the peak) characterized by a low temperature ($k\mathcal{T} \sim 1$ keV, a factor of ~ 10 lower than the typical temperature observed in GRB prompt emission, e.g. Ryde 2004). The simultaneous evolution of the luminosities corresponding to the thermal (calculated in the $[0.3 - 10]$ keV energy range) and non–thermal

components (calculated in the $[0.3-1000]$ energy range) is shown in Fig.10.5. Fig.10.5 shows that the thermal luminosity peaks later than the non–thermal component and, at its maximum, it contributes primarily to the total luminosity in the $[0.3-10]$ keV and to 35% of the $[0.3-1000]$ keV luminosity. In addition, the thermal component is still detected in the *XMM–Newton* late time spectrum with a luminosity $\sim 5\times10^{44}$ erg/s, corresponding to $\sim 8\%$ of the $[0.3-10]$ keV emission. In the following, we discuss the possible origin of this black body emission.

The observed black body emission is very bright thus the hypothesis that it may be due to a Ib/c SN shock breakout has to be excluded. In fact, the X–ray luminosity of such emission is typically $\sim 10^{45}$ erg/s (see e.g. Matzner and McKee, 1999; Campana et al., 2006; Ghisellini et al., 2007b), which is much lower than the BB luminosity ($\sim 10^{50}$ erg/s) observed at the peak of the flare in GRB 151027A. Piro et al. (2014) proposed a model based on the emission of a hot plasma cocoon (based on Pe'er et al., 2006b) to explain the long–lasting thermal emission observed in the ultra–long GRB 130925A. Starling et al. (2012) also used the cocoon expansion to explain the presence of thermal emission in X–ray spectra of GRB associated with a SN explosion. Even these models cannot be applied to our case because of the brightness of the thermal component during the flare which is much larger than the expected $\sim 10^{47}$ erg/s.

However, we do not need to invoke sophisticated model in order to explain the thermal emission: it is, indeed, naturally predicted within the standard fireball scenario, when the relativistically expanding fireball releases the internal photons at the transparency radius (e.g. Goodman, 1986; Paczynski, 1986; Daigne and Mochkovitch, 2002). Owing to the initial huge opacity of the fireball (optical depth $\tau_{\gamma\gamma}\gg 1$), photons can reach the thermodynamic equilibrium and are characterized by a BB spectrum (see Chp.**??**).

Using the observables associated with the BB spectrum, i.e. the temperature $kT_{\rm BB}$ and the flux $F_{\rm BB}$, we can estimate the fundamental parameters of the fireball making a simple assumption on the trasparency occurring time (see Sec.2.3):

(i) It might happen when, owing to the high internal pressure the fireball is converting its internal energy to bulk motion energy, i.e. during the acceleration phase. In this case, it is possible

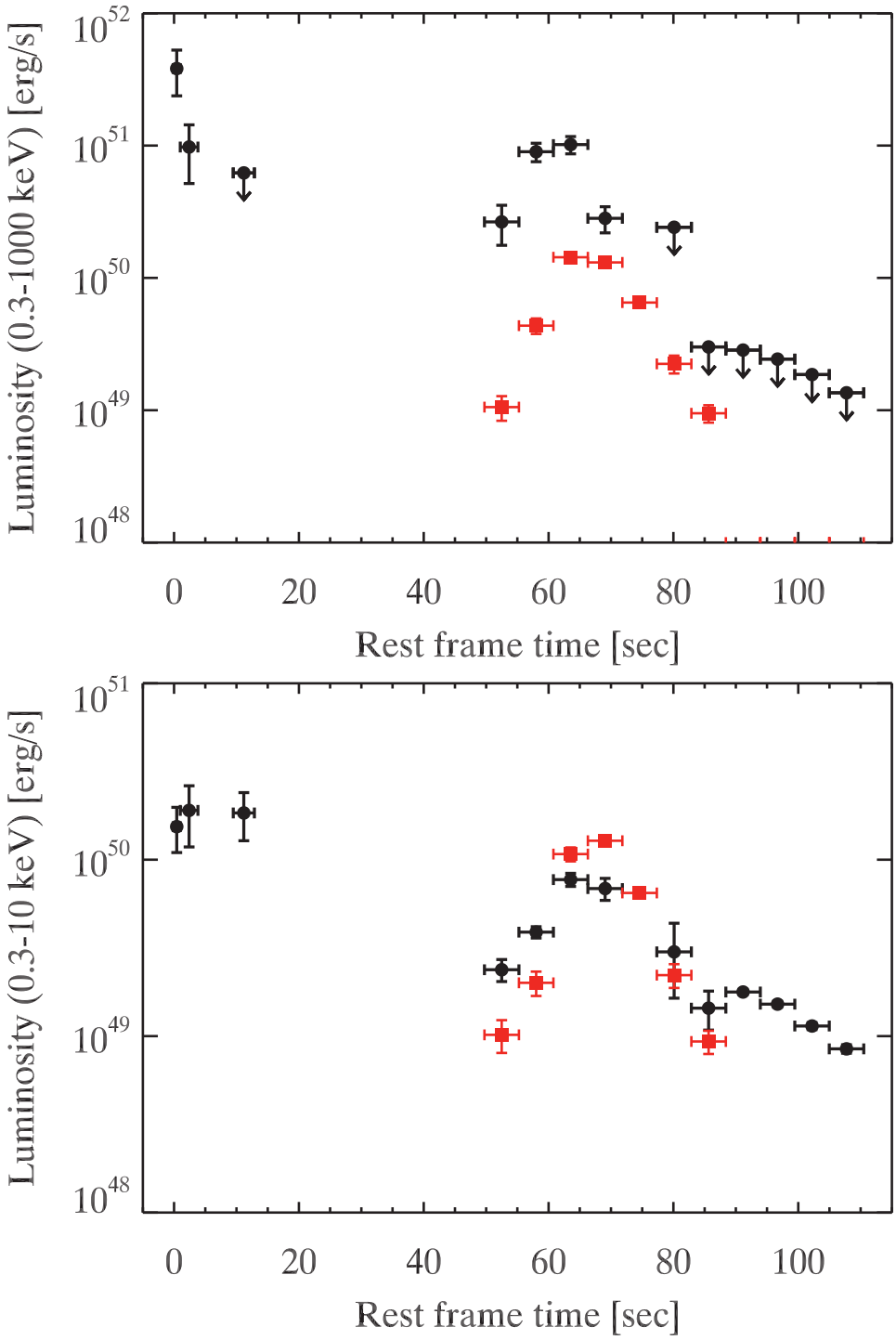

Figure 10.5: *Top panel*: $[0.3 - 1000]$ keV luminosity as a function of rest frame time divided into thermal (red squares) and non–thermal component (black circles). Upper limits to the non–thermal luminosity are shown when the peak energy of the cutoff power–law component is not constrained. *Bottom panel*: same as the top, but for luminosity in the range $[0.3 - 10]$ keV.

to estimate the distance from the central engine R_0, where the fireball is created, assuming an initial bulk Lorentz factor $\Gamma_0 = 1$. We obtain $R_0 \sim 10^{11-12}$ cm.

(ii) It might happen during the coasting phase. The internal pressure is no longer sufficient to accelerate the fireball that proceeds with constant bulk Lorentz factor. In this case we can obtain the parameters at the transparency R_T, Γ_T, and R_0 as well. Differently from the previous case, these values are not unequivocally determined because they depend on the black body radiative efficiency η_{BB}. As for GRB 100507, analyzed in Ghirlanda et al. (2013b), we use a radiative efficiency related to the thermal component of about $\eta_{BB} \sim 10^{-2}$, since the black body flux varies from 5% up to $\sim 50\%$ of the non–thermal flux. Then, we find $R_T = 10^{13-14}$ cm, $\Gamma_T \sim 60$, and $R_0 \sim 10^{9-10}$ cm.

In both cases the value of R_0 is much higher than expected one, i.e. $R_0 \sim 10^7$ cm (for a compact object of $5 - 10 M_\odot$, see Sec.2.2). In case (ii), the value we should use for η_{BB} in order to get $R_0 \sim 10^7$ cm is $\sim 10^{-4}$. Such a low radiative efficiency would imply an enormous amount of kinetic energy implying a very energetic afterglow that is in contrast with what we observe. Another possible explanation of the significant thermal emission of GRB 151027A is given by the so–called reborn fireball model (Ghisellini et al., 2007a). In this scenario the thermal emission is produced by plasma heated in the collision between the relativistic ejecta and the surrounding material released by the progenitor star during its final evolutionary stages.

If the optical depth after collision is large, a re–acceleration to relativistic speed due to the dissipated internal energy can take place. This process allows the creation of a reborn fireball with a larger initial radius $R_0 \sim 10^{11}$ cm consistent with the large values inferred for GRB 151027A. Ghisellini et al. (2007a) assume the target material to be at rest with respect to the central engine. Nevertheless, in our case the relativistic shells that produced the first two prompt emission peaks should have interacted with such material before. For this reason, we can conclude that the optically thick target material was not there when the first prompt photons were emitted.

A possible alternative is to assume the GRB central engine as responsible for the production of the target material. At the beginning, shells that produce the initial part of the prompt emission are ejected. Then a denser and slower shell is ejected, which does not

emit radiation since it is optically thick. After a quiescent period a quicker shell is ejected and it reaches the slower one. In this scenario the reborn fireball is actually like an internal shock between a thick, mildly relativistic, massive shell with a faster shell. The collision dissipates energy with non–negligible efficiency since the relative Lorentz factor of the dense/thick and fast shell can be large. The photons produced cannot escape because of the large opacity so that the internal thermal energy can be used to re–accelerate the shell. Beyond the photospheric radius the shell emits the black body radiation produced by the reprocessing of the trapped photons and a non–thermal component. The decreasing emission of the flare is then due to the quenching of the radiation of the shell and to the off latitude emission.

10.2 GRB 160625B: consistency with synchrotron emission

GRB 160625B is an exceptionally bright burst ($L_{\rm iso} \sim 2 \times 10^{53}$ erg/s, $E_{\rm iso} \sim 5 \times 10^{54}$ erg. – Svinkin et al. 2016 – GCN #19604) recently detected by the Gamma–ray Burst Monitor (GBM – Burns 2016 – GCN #19581) and the Large Area Telescope (LAT – Dirirsa et al. 2016 – GCN #19580) on board of the *Fermi* satellite. GRB 160625B is the third *Fermi* burst in order of fluence ($S = 5.7 \times 10^{-4}$ erg cm^{-2} in the [10–1000] keV energy range, according to the GBM catalog) and its redshift is $z = 1.406$ (Xu et al. 2016 – GCN #19600). Its prompt emission is composed by a precursor lasting ~ 0.8 s and anticipating of about ~ 180 s the two main events of duration ~ 35 s and ~ 210 s, respectively (see. Fig.10.6).

This burst has been extensively studied in the literature thanks to its extremely high photon statistic (Zhang et al., 2016; Wang et al., 2017; Lü et al., 2017) and the rich data sets covering its afterglow emission (Troja et al., 2017; Alexander et al., 2017). Zhang et al. (2016) claims, on the basis of the time–resolved spectral analysis, the presence of two different spectral components. They fitted the spectrum of the precursor using a BB while the main emission episode is well described by a non–thermal component. They interpreted the BB as photospheric emission and the transition to a non–thermal component as caused by the transition from a matter dominated to a magnetically dominated jet. Wang et al. (2017) also included LAT low–energy data (LLE) and adopted a mixed model, i.e. a composition of a Band function (Band et al., 1993) with a high energy cutoff

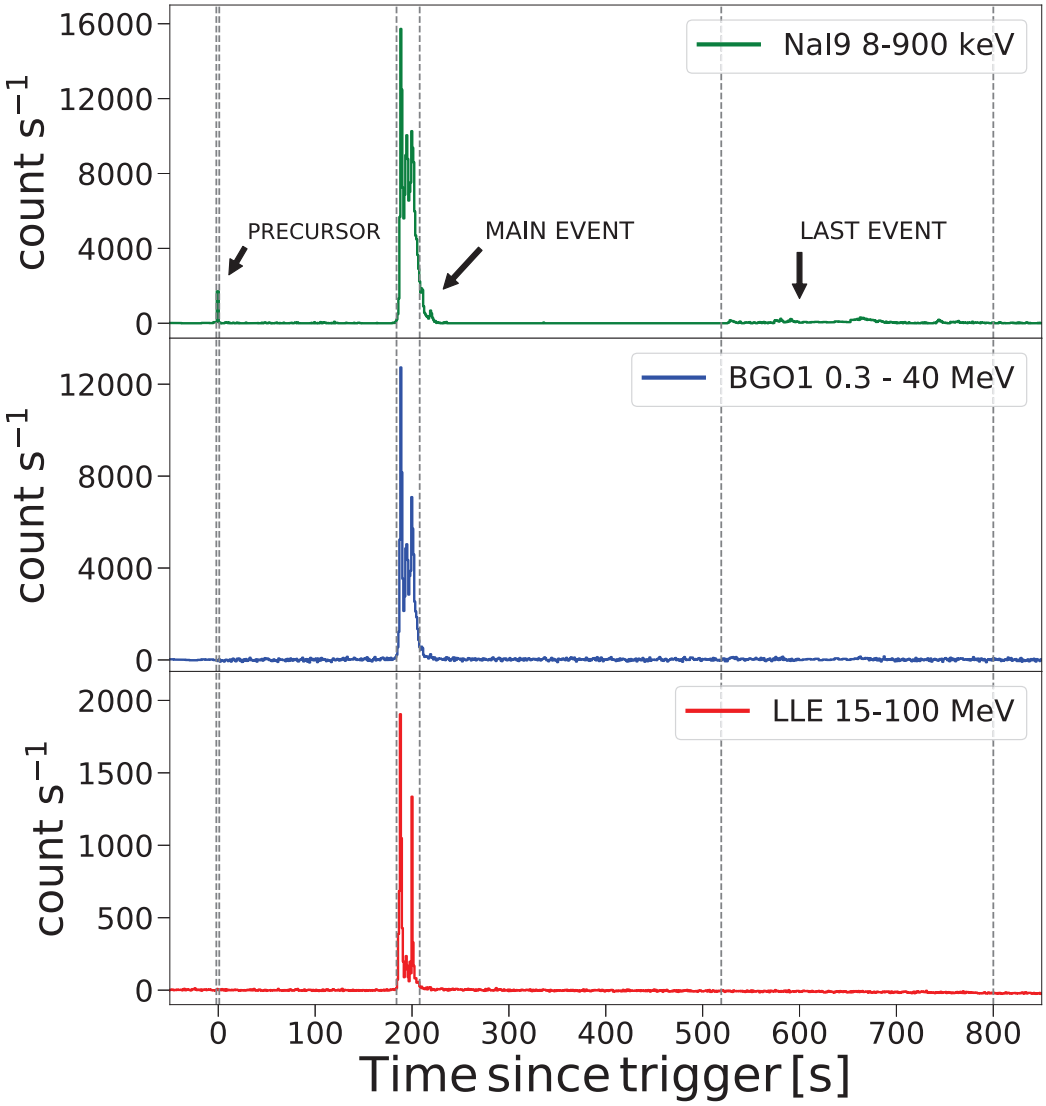

Figure 10.6: Background subtracted light–curve of GRB 160625B detected by different instruments on board of *Fermi*: GBM NaI (8 keV – 900 keV, *top panel*) BGO (350 keV – 40 MeV, mid panel) detectors and LAT Low Energy events (LLE, 40 MeV – 100 MeV, *bottom panel*)

and a black body component. A similar two–component model, but using a multi–color BB, is adopted by Lü et al. (2017). What appears common in these modeling is the presence, at different times (Zhang et al., 2016) or simultaneously (Wang et al., 2017; Lü et al., 2017), of a thermal BB and a non–thermal component.

Recently, Oganesyan et al. (2017) performed a systematic study of the prompt emission of 14 GRBs observed with the BAT $[15 - 150]$ keV and the XRT $[0.3 - 10]$ keV on board the *Swift* satellite. Extending the spectral analysis down to soft X–rays band allowed them to show the existence of a break in the spectrum at low energies (such

feature is required with high statistical significance in 67% of cases). The time–resolved XRT+BAT joint spectral analysis showed that the spectrum typically hardens below a break energy $E_{\rm break}$ of few keV while it shows the standard peak energy $E_{\rm peak} \sim 120$ keV (in $\nu F(\nu)$ representation). The typical ratio is $\rm E_{peak}/E_{break} \sim 30$. The photon index α_1 below the peak has a distribution peaked around –0.67, while the photon index α_2 describing the spectral segment between $\rm E_{break}$ and E_{peak} has mean value –1.5. These are consistent with expectations for synchrotron radiation of fast–cooling electrons.

A compelling question is whether bursts with such spectral properties, i.e. consistent with synchrotron predictions, also exist in the *Fermi* database. In Ravasio et al. (submitted to A&A), taking advantage of the wider energy range and the high spectral resolution of *Fermi*/GBM (8 keV – 40 MeV), we performed the prompt emission spectral analysis of GRB 160625B mostly focusing on the main event. The precursor and the third pulse are relatively weak. The main goal of this work relies on testing empirically to what extent the time resolved spectra of this bright burst are consistent with the synchrotron spectrum expected in the marginally fast–cooling synchrotron scenario.

10.2.1 Observational data

In order to perform the time–resolved spectral analysis we considered the detectors with the highest signal: NaI #6, NaI #9, and both BGO detectors (#0 and #1) given the extraordinary brightness of this burst. For the few spectra having poor signal we also added the data from the NaI #7 (see Tab.10.2, Tab.10.4 and Tab.10.3) in order to improve the photon statistics. We worked in the $[8, 900]$ keV and $[0.3, 40]$ MeV energy range for NaI and BGO detectors, respectively. For NaI detectors, we excluded the spectral channels with energies in the 25–45 keV interval due to the presence of the Iodine K–edge at 33.17 keV (see Bissaldi et al., 2009). In fitting spectra combining data from NaI and BGO detectors together we included an intercalibration constant as a free parameter.

We retrieved *Fermi* data from the public archive[4] and we analyzed them using the GBM official software for spectroscopy RMFIT (v. 4.3.2). We analyzed the CSPEC data which have 1.024 s temporal resolution and are composed by 128 energy channels logarithmically

[4] https://heasarc.gsfc.nasa.gov/W3Browse/fermi/fermigbrst.html

spaced in the whole energy range covered by the single detector, i.e. $\sim 8 - 1000$ keV for the NaI and $0.3 - 40$ MeV for the BGO. We used the detector response matrices .rsp2 which accounts for the satellite slew. The background has been fitted with a polynomial function over two time intervals selected after and before the temporal region containing the event of interest.

10.2.2 Evidence of a spectral break

According to the *Fermi*/GBM burst catalog, the model which best fits the spectrum of GRB 160625B, integrated over the entire duration of the burst ($T_{\rm start} = -44$ s, $T_{\rm stop} = 788$ s), is a Smoothly Broken Power–Law (SBPL) function with $\alpha = -1.021 \pm 0.004$, $E_{\rm peak} = (229 \pm 4)$ keV and $\beta = -2.096 \pm 0.014$, with an associated, extremely large, $\chi^2_{\rm red} = 4.195$. As mentioned before, we principally focused on the main event namely extending from 186.40 up to 207.91 s after trigger time T_0. This time interval has been selected on the basis of a S/N ratio > 20 in the BGO light–curve. This conservative approach ensures to have much larger S/N ratio in the NaI detectors (for a typical photon spectrum $N(E) \propto E^{-x}$ with $x > 0$). We performed a preliminary analysis fitting the time integrated spectrum adopting a SBPL function (solid line in Fig.10.7). We find $\alpha = -0.684 \pm 0.004$, $E_{\rm peak} = 207.2^{+2.2}_{-2.14}$ keV, $\beta = -2.242 \pm 0.006$ and a $\chi^2_{\rm red} = 2306.8/464 = 4.97$.

From the visual inspection of this spectrum (see Fig.10.7) and of the data–to–model residuals (in units of standard deviation– *bottom panel* in Fig.10.7), we notice the presence of a systematic trend, with broad excesses (possibly a break) peaking around 60 keV and 700 keV.

These features have been modeled in recent works (Zhang et al., 2016; Wang et al., 2017; Lü et al., 2017) adding a thermal black body component. Following their example we performed a fit using a two component model: SBPL+BB. In this case the fit significantly improves yielding $k\mathcal{T} = 33.27^{+0.421}_{-0.416}$ keV and a peak energy of the SBPL model $E_{\rm peak} = 449.4^{+8.11}_{-7.97}$ keV with $\alpha = -0.874 \pm -0.006$ and $\beta = -2.484^{+0.011}_{-0.012}$. The chi–square reduces to $\chi^2_{\rm red} = 810.93/462 = 1.75$. The addition of the BB component manages to model the excess at low energies allowing the SBPL function to better adapt to the high energy part of the spectrum (shifting the peak by a factor

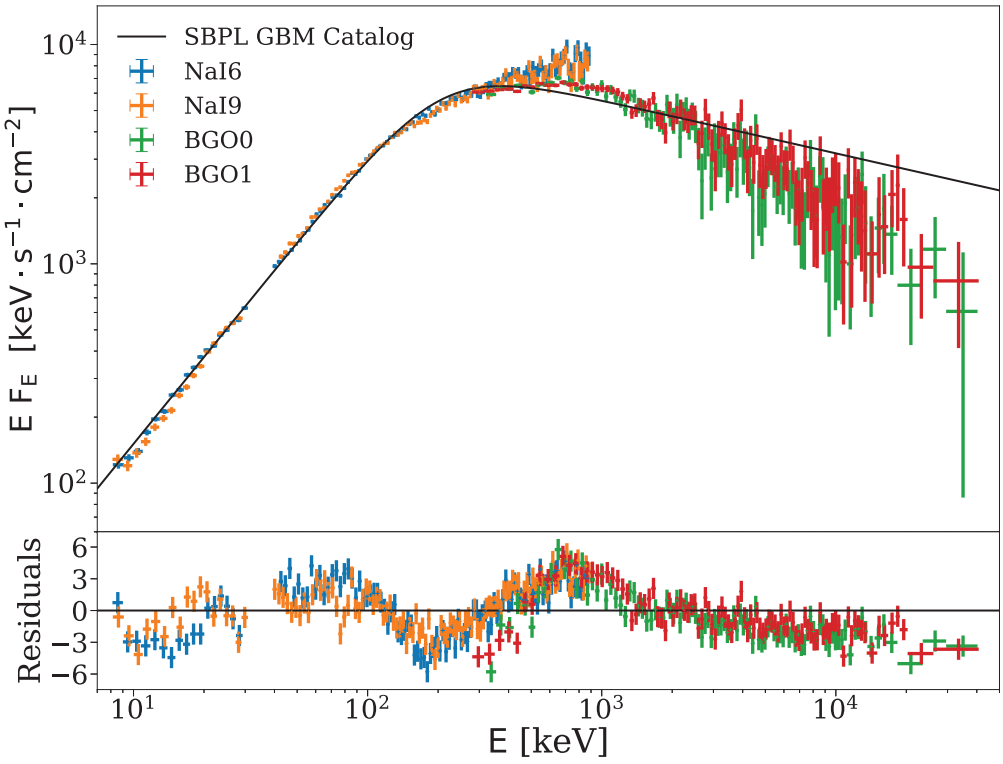

Figure 10.7: EF_E spectrum of the main episode (186.40–207.91) s fitted with the standard SBPL function (solid line). Error bars on the data points are at 1σ confidence level and 1σ upper limits are shown with downward arrows. Residuals in units of σ are shown in the *bottom panel*. Different colors show the spectra of different detectors (as labelled).

$\sim$ 2 with respect to the fit without the BB component). While this possibility is not excluded, the additional BB component (typically associated to the photospheric emission; Pe'er et al. 2006a) has to be explained.

Here, as suggested by (Oganesyan et al., 2017), we try to follow a different approach: in the following we will introduce a completely empirical function made of three power laws separated by two breaks to verify if it can cure the excesses shown by the residuals in Fig. 10.7. The advantage of our model is that it is a single component that also includes, within its parameters' space, the shape expected in the case of synchrotron emission from fast–cooling electrons or marginally cooled electrons allowing us to test these scenarios.

Since we need to account for two breaks (i.e. a low energy break and a second one – corresponding to the peak energy) we elaborate the simple SBPL model (as defined in Rhoads 1999) adding a second

break. The advantage of the SBPL with respect to the Band model is that it allows for the possibility to change the smoothness of the curvature (in the limit it can account for a sharp break or a smooth curvature as in the Band model). Here the models definition:

- The *basic* Smoothly Broken Power Law (SBPL)

$$N(E)\,[\mathrm{SBPL}] = AE_j^{-\alpha}\left[\left(\frac{E}{E_j}\right)^{\alpha n} + \left(\frac{E}{E_j}\right)^{\beta n}\right]^{-\frac{1}{n}} \tag{10.1}$$

where

$$E_j = E_{\mathrm{peak}} \cdot \left(\frac{2-\alpha}{\beta-2}\right)^{\frac{1}{(\alpha-\beta)n}} \tag{10.2}$$

$N(E)$ is the photon spectrum (in units of $\mathrm{cm}^{-2}\ \mathrm{s}^{-1}\ \mathrm{keV}^{-1}$). The four free parameters are the amplitude A, the low energy spectral index α, the peak energy E_{peak} of the $\nu F(\nu)$ spectrum and the high energy spectral index β. This model has a peak in $\nu F(\nu)$ only if $\alpha < 2$ and $\beta > 2$.

- The *double* Smoothly Broken Power Law (2SBPL)
It presents a second break and a third power law segment.

$$N(E)\,[\mathrm{2SBPL}] = AE_{\mathrm{b}}^{-\alpha_1}\{\left(\frac{E}{E_b}\right)^{\alpha_1 n} + \left(\frac{E}{E_b}\right)^{\alpha_2 n} + \\ + \left(\frac{E}{E_j}\right)^{\beta n} \cdot \left[\left(\frac{E_j}{E_b}\right)^{\alpha_1 n} + \left(\frac{E_j}{E_b}\right)^{\alpha_2 n}\right]\}^{-\frac{1}{n}} \tag{10.3}$$

where

$$E_j = E_{peak} \cdot \left(\frac{2-\alpha_2}{\beta-2}\right)^{\frac{1}{(\alpha_2-\beta)n}} \tag{10.4}$$

The five free parameter are the amplitude A, the low energy index α_1, the break energy E_{break}, α_2, namely the index of the power law between the break and the peak, the $\nu F\nu$ spectrum peak energy E_{peak} and the high-energy index β. As the previous model it peaks in $\nu F(\nu)$ only if $\alpha_2 < 2$ and $\beta > 2$. We kept the smoothness parameter n fixed in our analysis for both the break and the peak.

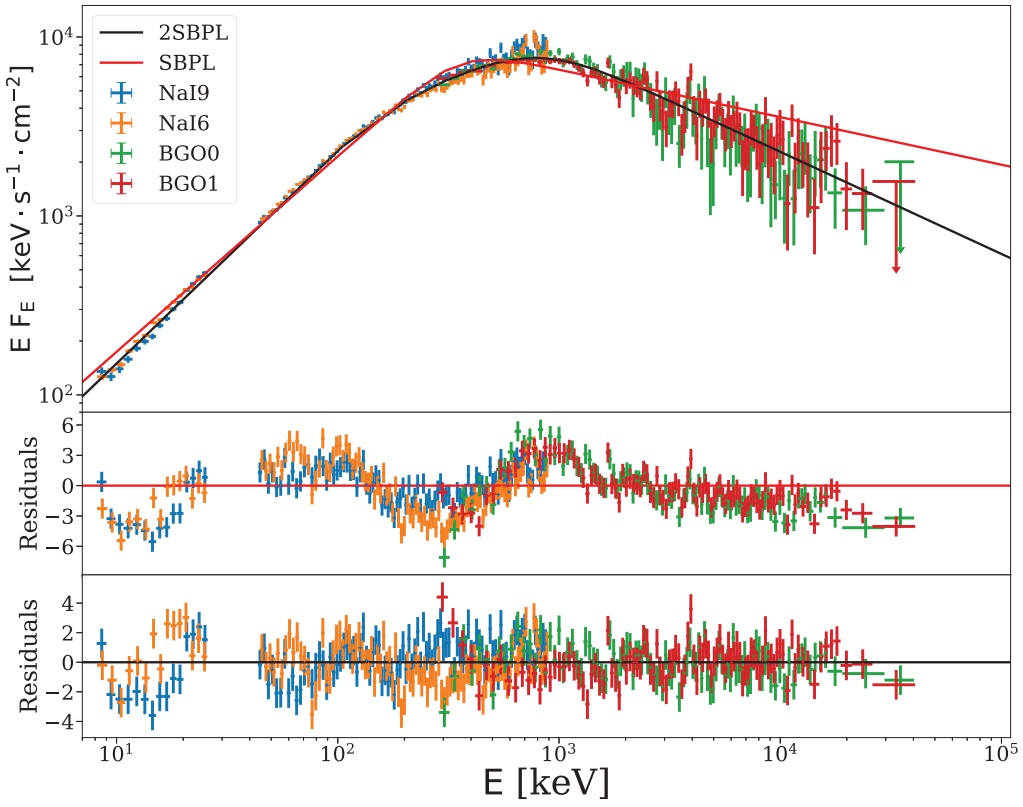

Figure 10.8: EF_E spectrum of the main episode (186.40–207.91 sec) fitted with the SBPL function (red line) and its residuals (*middle panel*). The fit with the 2SBPL function, allowing for a break, is shown with the solid black line. The residuals of the 2SBPL model are shown in the *bottom panel*. Symbols and color coding of data points are labeled.

with directly implemented $E_{\rm peak}$ as a free parameter so that the result of the fit is $E_{\rm peak}$ itself (see e.g. Calderone et al., 2015)). Moreover, being the 2SBPL nested into the SBPL, it is possible to compare the improvement of the fit with the 2SBPL over the SBPL through the F–test (Protassov et al., 2002).

The fit of the time–integrated spectrum with the new SBPL model (see Fig.10.8) gives similar results to the standard SBPL fit and has $\chi^2_{\rm red} = 1981/456 = 4.34$. Even the residuals (*middle panel* of Fig.10.8) are similar to those of the standard SBPL fit (*bottom panel* of Fig.10.7).

Despite some systematic deviations due to the possible spectral evolution remain (the spectrum is time–integrated), the 2SBPL greatly improves the fit ($\chi^2_{\rm red} = 771/454 = 1.69$) with a significance of 8.35σ as can be visually seen in the residuals (*bottom panel* of Fig.10.8). Intriguingly, fitting with the 2SBPL model, the slopes of the power–law component below and above the low energy break ($\alpha_1 = 0.81 \pm$

0.01 and $\alpha_2 = 1.59 \pm 0.03$, respectively) are near to the expected slopes of the synchrotron emission.

We performed an additional test adding a BB to the SBPL model, in order to compare it with the 2SBPL fit. Since the SBPL+BB and 2SBPL have the same number of degrees of freedom, they can be directly compared in terms of χ^2 and associated probability. The fit with SBPL+BB, $\chi^2_{\rm red} = 949/454 = 2.09$, is also improving over the SBPL with identical significance of 8.35σ as the 2SBPL case. However, the fit with 2SBPL ($\chi^2_{\rm red} = 1.69$) remains the best one.

To conclude, these results show that the spectrum of the main peak of GRB 160625B requires the addition of a low energy spectral break to a standard SBPL model. Though this can be accomplished by adding a black body component we prefer to add a break to the single non–thermal component (SBPL) since the 2SBPL may result consistent with synchrotron emission.

10.2.3 Time–resolved spectral analysis

In order to check if the low energy break seen in the time–integrated spectrum is present also in the time resolved spectra, we analyze the 21 time–resolved spectra (1.024 time bins) distributed in the 186.40–207.91 s time interval of the main episode (as reported in Tab.10.2, Tab.10.4 and Tab.10.3). We adopted the three models: SBPL, 2SBPL and SBPL+BB. Fig.10.9 shows the comparison between these models.

In almost all the time–resolved spectra (18/21 and 17/21 for the 2SBPL and SBPL+BB respectively) we find that the fit significantly improves when passing from the SBPL to the 2SPBL or SBPL+BB. Fig.10.10 shows the distributions of the F–test significance between the SBPL and 2SBPL with only three cases having significance lower than 3σ. 2SBPL and SBPL+BB models can be directly compared through the χ^2 (reported in Tab.10.3 and Tab.10.4, respectively). In all cases the probability of the 2SBPL and SBPL+BB is larger than 10^{-3} and we note that the probabilities of the 2SBPL are systematically larger than the SBPL+BB. The spectral results with the different models are reported in Tab.10.2 (SBPL), Tab.10.3 (2SBPL) and Tab.10.4 (SBPL+BB).

Fig.10.11 shows the spectrum of the brightest temporal bin of the main emission episode. Also in this spectrum we find systematic residuals in the SBPL fit (*top panel*of Fig.10.11) which are absorbed

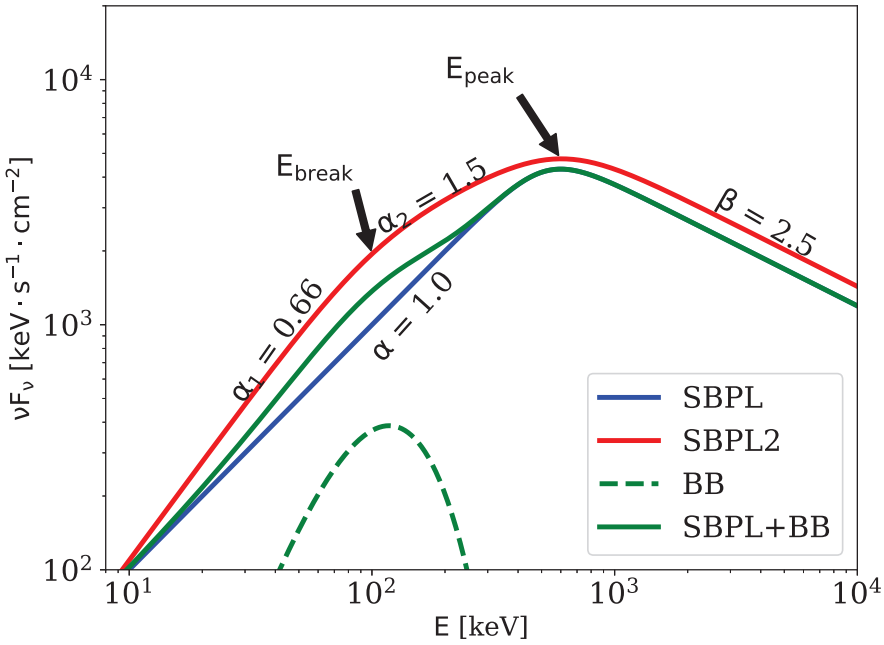

Figure 10.9: Comparison of the three spectral models SBPL, SBPL+BB and 2SBPL (see text) assuming typical parameters (as labeled).

by the 2SBPL (*mid panel* of Fig.10.11) or SBPL+BB (*bottom panel* of Fig.10.11). Notably, the break energy of the 2SBPL coincides with the peak of the BB. However, the 2SBPL fit has a larger probability of the fit ($P = 0.216$) compared to the SBPL+BB ($P = 0.012$).

The evolution of the spectral parameters of the 2SBPL is shown in Fig.10.12. Both $E_{\rm break}$ (blue symbols) and $E_{\rm peak}$ (red symbols) evolve simultaneously and monotonically soften during the beginning of the main emission episode and then keep constant (with a ratio of 5) after 190 s from the trigger. Fig.10.13 shows the correlation between $E_{\rm break}$ and $E_{\rm peak}$. We find a significant correlation with Spearman's correlation coefficient $\rho = 0.45$ and a chance probability $P = 0.06$. The fit of the correlation with a linear model (solid line in Fig.10.13) has slope 1.45 and intercept -0.28.

10.2.4 Interpretation of synchrotron emission

The time–resolved spectral analysis of the main peak of GRB 160625B (see previous sub–section) shows that in almost all the spectra the fit with the simple SBPL model is unsatisfactory and a low energy spectral break is required. Both adding a break (2SBPL model) or a black body (SBPL+BB model) significantly improves the fit in the majority

Time Bin (s)	Norm.	α	β	E_{peak}	Photon Flux	Energy Flux (10^{-5})	χ^2/DOF	Prob	NaI#7
186.40 - 187.43	$2.9^{+0.4}_{-0.5}$	$1.02^{+0.02}_{-0.04}$	$2.2^{+0.1}_{-0.2}$	$2917.0^{+28400.0}_{-223.0}$	19.7 ± 0.4	3.12 ± 0.18	555.16 / 564	0.60	x
187.43 - 188.45	$6.2^{+0.1}_{-0.2}$	$0.830^{+0.012}_{-0.001}$	$2.013^{+0.0428}_{-0.0113}$	$2014.0^{+227.0}_{-542.0}$	74.63 ± 0.68	9.45 ± 0.19	565.27 / 456	$3.55 \cdot 10^{-4}$	-
188.45 - 189.47	$17.38^{+0.799}_{-0.808}$	$0.826^{+0.008}_{-0.010}$	$2.167^{+0.0176}_{-0.0229}$	$918.5^{+20.6}_{-20.6}$	199.49 ± 1.03	19.46 ± 0.27	796.29 / 456	$7.09 \cdot 10^{-21}$	-
189.47 - 190.50	$21.06^{+1.07}_{-1.09}$	$0.865^{+0.011}_{-0.013}$	$2.165^{+0.0202}_{-0.0282}$	$663.6^{+22.7}_{-20.9}$	154.88 ± 0.96	11.32 ± 0.19	726.06 / 456	$1.14 \cdot 10^{-14}$	-
190.50 - 191.52	$16.81^{+1.14}_{-1.33}$	$0.858^{+0.017}_{-0.022}$	$2.177^{+0.0183}_{-0.0386}$	$379.0^{+21.1}_{-16.8}$	88.15 ± 0.79	4.32 ± 0.12	528.3 / 456	0.011	-
191.52 - 192.55	$19.7^{+1.47}_{-1.96}$	$0.901^{+0.025}_{-0.025}$	$2.204^{+0.02}_{-0.0542}$	$284.5^{+19.1}_{-11.8}$	69.14 ± 0.69	2.61 ± 0.88	453.94 / 456	0.52	-
192.55 - 193.57	$16.79^{+1.2}_{-1.3}$	$0.854^{+0.018}_{-0.019}$	$2.279^{+0.0234}_{-0.0414}$	$297.0^{+13.3}_{-10.7}$	83.62 ± 0.78	3.26 ± 0.092	475.8 / 456	0.25	-
193.57 - 194.59	$17.12^{+0.984}_{-1.08}$	$0.886^{+0.012}_{-0.018}$	$2.388^{+0.0253}_{-0.0579}$	$473.8^{+15.9}_{-22.5}$	111.77 ± 0.84	5.61 ± 0.13	564.98 / 456	$3.7 \cdot 10^{-4}$	-
194.59 - 195.62	$19.86^{+1.06}_{-1.19}$	$0.886^{+0.011}_{-0.017}$	$2.392^{+0.022}_{-0.0541}$	$447.6^{+14.3}_{-20.3}$	124.52 ± 0.89	5.97 ± 0.13	592.46 / 456	$1.6 \cdot 10^{-5}$	-
195.62 - 196.64	$18.62^{+1.08}_{-1.23}$	$0.883^{+0.013}_{-0.021}$	$2.399^{+0.0243}_{-0.0597}$	$419.2^{+15.0}_{-22.1}$	108.31 ± 0.83	4.93 ± 0.11	574.56 / 456	$1.3 \cdot 10^{-4}$	-
196.64 - 197.67	$17.6^{+1.01}_{-1.17}$	$0.928^{+0.013}_{-0.018}$	$2.361^{+0.0254}_{-0.0593}$	$381.6^{+14.8}_{-16.3}$	82.28 ± 0.64	3.40 ± 0.10	689.6 / 564	$2.2 \cdot 10^{-4}$	x
197.67 - 198.69	$18.38^{+0.997}_{-1.12}$	$0.930^{+0.011}_{-0.016}$	$2.345^{+0.0252}_{-0.058}$	$466.1^{+17.1}_{-19.2}$	88.27 ± 0.65	4.26 ± 0.12	618.15 / 564	0.057	x
198.69 - 199.71	$16.83^{+1.03}_{-1.09}$	$0.919^{+0.011}_{-0.016}$	$2.591^{+0.0353}_{-0.0891}$	$514.5^{+15.5}_{-23.9}$	94.33 ± 0.78	4.36 ± 0.11	552.84 / 456	0.0012	-
199.71 - 200.74	$17.25^{+0.951}_{-0.942}$	$0.866^{+0.010}_{-0.012}$	$2.239^{+0.0219}_{-0.0269}$	$678.7^{+19.4}_{-19.5}$	129.77 ± 0.88	9.41 ± 0.17	563.27 / 456	$4.4 \cdot 10^{-4}$	-
200.74 - 201.76	$18.33^{+1.04}_{-1.07}$	$0.868^{+0.012}_{-0.014}$	$2.23^{+0.0206}_{-0.0301}$	$548.1^{+18.8}_{-19.1}$	117.05 ± 0.88	7.26 ± 0.14	502.65 / 456	0.065	-
201.76 - 202.79	$24.15^{+1.31}_{-1.31}$	$0.956^{+0.011}_{-0.011}$	$2.631^{+0.0406}_{-0.0689}$	$525.1^{+16.3}_{-16.1}$	108.57 ± 0.84	4.80 ± 0.11	512.23 / 456	0.035	-
202.79 - 203.81	$21.05^{+1.17}_{-1.35}$	$0.985^{+0.012}_{-0.016}$	$2.434^{+0.0312}_{-0.0849}$	$424.5^{+18.3}_{-17.5}$	76.14 ± 0.63	3.063 ± 0.097	622.94 / 564	0.043	x
203.81 - 204.83	$17.0^{+1.13}_{-1.27}$	$0.999^{+0.014}_{-0.019}$	$2.313^{+0.0323}_{-0.0783}$	$477.3^{+27.0}_{-22.9}$	60.49 ± 0.57	2.78 ± 0.11	624.2 / 564	0.040	x
204.83 - 205.86	$15.96^{+1.05}_{-1.4}$	$0.961^{+0.016}_{-0.026}$	$2.369^{+0.0293}_{-0.0951}$	$364.5^{+18.0}_{-21.3}$	57.30 ± 0.55	2.201 ± 0.083	647.83 / 564	0.0082	x
205.86 - 206.88	$14.17^{+1.11}_{-1.55}$	$0.928^{+0.019}_{-0.025}$	$2.296^{+0.0288}_{-0.0834}$	$272.8^{+17.5}_{-10.5}$	46.53 ± 0.52	1.6 ± 0.073	576.01 / 564	0.35	x
206.88 - 207.91	$9.896^{+1.04}_{-1.22}$	$0.975^{+0.026}_{-0.036}$	$2.087^{+0.0304}_{-0.0854}$	$338.2^{+471.0}_{-26.9}$	39.2 ± 0.6	1.579 ± 0.097	500.58 / 456	0.073	-

Table 10.2: Best fit parameters for SBPL model for the main emission episode of GRB 160625B.

Time Bin (s)	Norm.	α_1	E_{break}	α_2	E_{peak}	β	Photon Flux	Energy Flux (10^{-5})	χ^2/DOF	Prob.	$\sigma(F_{test})$	NaI#7
186.40 - 187.43	$2.4^{+0.5}_{-0.34}$	$0.95^{+0.04}_{-0.03}$	$645.1^{+335.0}_{-163.0}$	$1.6^{+0.12}_{-0.1}$	$6711.0^{+1530.0}_{-1720.0}$	$3.77^{+0.83}_{-1.13}$	19.05 ± 0.39	2.6 ± 0.16	542.7/562	0.71	3.1	x
187.43 - 188.45	$4.53^{+0.56}_{-0.52}$	$0.72^{+0.03}_{-0.03}$	$276.5^{+52.8}_{-45.4}$	$1.52^{+0.08}_{-0.08}$	$2945.0^{+480.0}_{-375.0}$	$2.47^{+0.13}_{-0.11}$	73.11 ± 0.67	8.5 ± 0.19	489.6/454	0.12	7.8	-
188.45 - 189.47	$10.48^{+0.75}_{-0.75}$	$0.65^{+0.02}_{-0.02}$	$194.6^{+15.5}_{-15.8}$	$1.49^{+0.04}_{-0.04}$	$1754.0^{+105.0}_{-104.0}$	$2.56^{+0.05}_{-0.06}$	193.0 ± 1.08	16.6 ± 0.22	477.4/454	0.22	8.4	-
189.47 - 190.50	$12.92^{+1.07}_{-1.15}$	$0.7^{+0.02}_{-0.03}$	$163.9^{+15.3}_{-17.5}$	$1.55^{+0.05}_{-0.06}$	$1323.0^{+104.0}_{-111.0}$	$2.58^{+0.06}_{-0.08}$	151.86 ± 0.96	9.9 ± 0.16	499.6/454	0.07	8.4	-
190.50 - 191.52	$10.2^{+1.31}_{-1.47}$	$0.72^{+0.03}_{-0.04}$	$122.2^{+17.9}_{-21.7}$	$1.54^{+0.07}_{-0.1}$	$721.1^{+59.3}_{-68.8}$	$2.52^{+0.05}_{-0.11}$	88.17 ± 0.76	4 ± 0.11	455.5/454	0.47	7.9	-
191.52 - 192.55	$13.84^{+1.73}_{-1.89}$	$0.82^{+0.03}_{-0.04}$	$128.5^{+15.2}_{-18.2}$	$1.78^{+0.08}_{-0.11}$	$695.5^{+91.3}_{-127.0}$	$2.75^{+0.09}_{-0.25}$	69.45 ± 0.69	2.4 ± 0.09	416.7/454	0.89	5.9	-
192.55 - 193.57	$11.51^{+1.57}_{-2.03}$	$0.76^{+0.03}_{-0.06}$	$134.9^{+23.0}_{-36.0}$	$1.6^{+0.13}_{-0.2}$	$456.2^{+38.9}_{-51.0}$	$2.52^{+0.06}_{-0.12}$	83.72 ± 0.76	3.1 ± 0.1	446.6/454	0.59	5.0	-
193.57 - 194.59	$9.41^{+1.18}_{-1.29}$	$0.69^{+0.03}_{-0.04}$	$125.7^{+21.7}_{-24.7}$	$1.42^{+0.07}_{-0.09}$	$657.4^{+30.6}_{-35.9}$	$2.66^{+0.04}_{-0.08}$	109.62 ± 0.84	5 ± 0.11	451.8/454	0.52	8.4	-
194.59 - 195.62	$11.65^{+1.28}_{-1.48}$	$0.71^{+0.03}_{-0.04}$	$135.2^{+20.5}_{-25.2}$	$1.46^{+0.07}_{-0.09}$	$629.8^{+27.0}_{-36.3}$	$2.67^{+0.04}_{-0.08}$	122.52 ± 0.93	5.4 ± 0.12	478.5/454	0.21	8.4	-
195.62 - 196.64	$10.81^{+1.51}_{-1.23}$	$0.71^{+0.04}_{-0.04}$	$133.2^{+24.1}_{-22.0}$	$1.49^{+0.09}_{-0.09}$	$610.5^{+30.7}_{-35.8}$	$2.75^{+0.06}_{-0.1}$	106.67 ± 0.8	4.4 ± 0.1	470.4/454	0.29	8.4	-
196.64 - 197.67	$10.5^{+1.71}_{-2.09}$	$0.78^{+0.04}_{-0.07}$	$122.6^{+31.1}_{-39.7}$	$1.5^{+0.11}_{-0.14}$	$615.8^{+41.3}_{-53.8}$	$2.87^{+0.12}_{-0.2}$	81.82 ± 0.65	3 ± 0.1	616.1/562	0.06	7.7	x
197.67 - 198.69	$11.12^{+1.49}_{-2.3}$	$0.77^{+0.04}_{-0.08}$	$119.4^{+35.9}_{-48.4}$	$1.35^{+0.09}_{-0.12}$	$605.9^{+32.6}_{-30.7}$	$2.55^{+0.05}_{-0.08}$	87.37 ± 0.66	3.9 ± 0.11	561.6/562	0.5	7.0	x
198.69 - 199.71	$9.79^{+1.24}_{-2.12}$	$0.73^{+0.03}_{-0.08}$	$135.2^{+28.8}_{-46.9}$	$1.41^{+0.08}_{-0.13}$	$667.7^{+28.8}_{-41.0}$	$2.94^{+0.07}_{-0.16}$	92.29 ± 0.78	3.8 ± 0.11	466.9/454	0.33	8.4	-
199.71 - 200.74	$12.04^{+1.19}_{-1.31}$	$0.74^{+0.03}_{-0.03}$	$199.1^{+36.7}_{-42.1}$	$1.41^{+0.09}_{-0.1}$	$928.2^{+58.3}_{-55.7}$	$2.4^{+0.04}_{-0.04}$	127.62 ± 0.9	8.7 ± 0.16	490.4/454	0.12	7.6	-
200.74 - 201.76	$11.99^{+1.43}_{-1.57}$	$0.73^{+0.03}_{-0.04}$	$157.4^{+34.8}_{-38.8}$	$1.39^{+0.1}_{-0.11}$	$737.7^{+48.0}_{-43.2}$	$2.37^{+0.03}_{-0.04}$	115.49 ± 0.84	6.8 ± 0.14	439.2/454	0.68	7.5	-
201.76 - 202.79	$14.08^{+1.82}_{-2.44}$	$0.76^{+0.04}_{-0.06}$	$129.8^{+29.7}_{-39.0}$	$1.42^{+0.08}_{-0.11}$	$662.4^{+25.8}_{-36.4}$	$2.94^{+0.06}_{-0.13}$	106.19 ± 0.83	4.3 ± 0.09	416.7/454	0.89	8.4	-
202.79 - 203.81	$16.78^{+2.12}_{-2.05}$	$0.91^{+0.03}_{-0.04}$	$214.8^{+62.1}_{-73.0}$	$1.56^{+0.18}_{-0.22}$	$513.1^{+27.5}_{-91.5}$	$2.69^{+0.06}_{-0.18}$	75.69 ± 0.63	2.8 ± 0.1	605.9/562	0.1	3.5	x
203.81 - 204.83	$13.18^{+2.04}_{-3.27}$	$0.92^{+0.04}_{-0.12}$	$193.0^{+97.6}_{-141.0}$	$1.46^{+0.18}_{-0.28}$	$586.4^{+45.2}_{-62.6}$	$2.5^{+0.06}_{-0.15}$	60.19 ± 0.57	2.6 ± 0.11	613.2/562	0.07	2.7	x
204.83 - 205.86	$11.45^{+1.37}_{-1.81}$	$0.87^{+0.03}_{-0.05}$	$159.9^{+28.6}_{-44.2}$	$1.61^{+0.1}_{-0.18}$	$528.1^{+36.2}_{-64.1}$	$2.83^{+0.08}_{-0.26}$	56.88 ± 0.56	1.9 ± 0.08	617.7/562	0.05	4.8	x
205.86 - 206.88	0.0	0.0	0.0	0.0	0.0	0.0	0.0	0.0	0.0	0.0	0.0	x
206.88 - 207.91	0.0	0.0	0.0	0.0	0.0	0.0	0.0	0.0	0.0	0.0	0.0	-

Table 10.3: Best fit parameters for 2SBPL model for the main emission episode of GRB 160625B.

Time Bin (s)	Norm.	α	β	E_{peak}	BB Norm. (10^{-5})	kT	Photon Flux	Energy Flux(10^{-5})	χ^2/DOF	Prob	NaI7
186.40 - 187.43	$4.28^{+0.7}_{-0.64}$	$1.13^{+0.04}_{-0.03}$	$2.68^{+0.34}_{-0.37}$	$4465.0^{+909.0}_{-599.0}$	$0.049^{+0.024}_{-0.021}$	$123.6^{+21.8}_{-15.4}$	19.24 ± 0.38	2.76 ± 0.16	537.6/562	0.76	x
187.43 - 188.45	$6.17^{+0.07}_{-0.26}$	$0.85^{+0.05}_{-0.05}$	$2.01^{+0.0}_{-0.01}$	$2592.0^{+174.0}_{-411.0}$	$2.23^{+0.41}_{-0.63}$	$51.58^{+6.08}_{-0.52}$	72.8 ± 0.7	9.32 ± 0.17	530.1/454	0.01	-
188.45 - 189.47	$21.88^{+1.4}_{-1.32}$	$0.91^{+0.01}_{-0.01}$	$2.33^{+0.02}_{-0.03}$	$1170.0^{+39.1}_{-34.9}$	$9.5^{+1.14}_{-1.08}$	$54.84^{+2.28}_{-2.18}$	192.1 ± 1.06	16.71 ± 0.22	524.6/454	0.01	-
189.47 - 190.50	$25.29^{+2.23}_{-2.09}$	$0.95^{+0.02}_{-0.02}$	$2.35^{+0.03}_{-0.04}$	$882.0^{+39.4}_{-35.1}$	$14.35^{+2.44}_{-2.1}$	$44.28^{+2.84}_{-2.79}$	151.56 ± 0.97	10.10 ± 0.17	543.7/454	0.0	-
190.50 - 191.52	$20.95^{+2.42}_{-2.22}$	$1.0^{+0.02}_{-0.03}$	$2.41^{+0.04}_{-0.07}$	$613.8^{+37.3}_{-32.7}$	$16.01^{+3.35}_{-2.8}$	$36.41^{+2.76}_{-2.68}$	88.06 ± 0.76	4.10 ± 0.17	462.3/454	0.38	-
191.52 - 192.55	$13.28^{+0.0}_{-4.58}$	$0.84^{+0.07}_{-0.1}$	$2.22^{+0.03}_{-0.06}$	$293.7^{+27.9}_{-338.0}$	$183.2^{+302.0}_{-3390.0}$	$13.34^{+5.11}_{-2.6}$	69.46 ± 0.71	2.62 ± 0.09	444.3/454	0.62	-
192.55 - 193.57	$19.79^{+2.61}_{-2.49}$	$0.97^{+0.03}_{-0.04}$	$2.43^{+0.04}_{-0.07}$	$438.3^{+32.8}_{-36.9}$	$16.63^{+4.8}_{-3.57}$	$33.58^{+3.34}_{-3.71}$	83.72 ± 0.77	3.19 ± 0.10	451.9/454	0.52	-
193.57 - 194.59	$18.48^{+1.71}_{-1.77}$	$0.94^{+0.02}_{-0.02}$	$2.58^{+0.03}_{-0.07}$	$603.4^{+20.9}_{-23.9}$	$13.49^{+3.03}_{-2.29}$	$38.58^{+2.69}_{-2.96}$	109.57 ± 0.85	5.07 ± 0.11	455.8/454	0.47	-
194.59 - 195.62	$21.78^{+1.9}_{-2.0}$	$0.95^{+0.02}_{-0.02}$	$2.58^{+0.03}_{-0.07}$	$579.8^{+19.6}_{-23.4}$	$14.99^{+3.27}_{-2.49}$	$38.4^{+2.64}_{-2.92}$	122.41 ± 0.86	5.45 ± 0.12	484.1/454	0.16	-
195.62 - 196.64	$21.0^{+2.13}_{-2.08}$	$0.96^{+0.02}_{-0.02}$	$2.64^{+0.04}_{-0.08}$	$564.2^{+21.9}_{-24.8}$	$14.12^{+3.18}_{-2.48}$	$38.64^{+2.93}_{-3.08}$	106.69 ± 0.81	4.48 ± 0.11	480.6/454	0.19	-
196.64 - 197.67	$17.22^{+2.13}_{-1.81}$	$0.98^{+0.03}_{-0.03}$	$2.58^{+0.06}_{-0.1}$	$506.4^{+30.0}_{-30.7}$	$15.29^{+6.35}_{-4.49}$	$30.26^{+4.28}_{-3.71}$	81.99 ± 0.65	3.23 ± 0.10	638.0/562	0.01	x
197.67 - 198.69	$19.65^{+1.76}_{-1.72}$	$0.98^{+0.02}_{-0.02}$	$2.51^{+0.04}_{-0.08}$	$577.9^{+24.4}_{-26.0}$	$8.93^{+2.71}_{-2.04}$	$37.02^{+3.64}_{-3.78}$	87.33 ± 0.65	3.97 ± 0.11	567.6/562	0.43	x
198.69 - 199.71	$16.79^{+2.73}_{-1.62}$	$0.94^{+0.03}_{-0.02}$	$2.76^{+0.07}_{-0.09}$	$595.1^{+32.1}_{-21.9}$	$11.05^{+3.86}_{-3.57}$	$36.65^{+6.43}_{-4.06}$	92.38 ± 0.79	4.00 ± 0.10	483.9/454	0.16	-
199.71 - 200.74	$21.28^{+1.94}_{-1.9}$	$0.94^{+0.02}_{-0.02}$	$2.34^{+0.03}_{-0.03}$	$832.8^{+43.4}_{-41.3}$	$5.09^{+1.2}_{-0.94}$	$53.53^{+4.31}_{-4.93}$	127.4 ± 0.89	8.67 ± 0.15	505.6/454	0.05	-
200.74 - 201.76	$20.29^{+1.99}_{-1.86}$	$0.92^{+0.02}_{-0.02}$	$2.33^{+0.03}_{-0.03}$	$664.4^{+31.2}_{-28.2}$	$9.71^{+2.68}_{-2.02}$	$41.75^{+4.0}_{-4.06}$	115.35 ± 0.84	6.80 ± 0.14	443.1/454	0.63	-
201.76 - 202.79	$25.12^{+2.31}_{-2.37}$	$0.98^{+0.02}_{-0.02}$	$2.8^{+0.04}_{-0.09}$	$605.1^{+18.2}_{-23.3}$	$13.26^{+4.15}_{-2.86}$	$37.14^{+3.38}_{-3.72}$	106.25 ± 0.84	4.38 ± 0.10	428.4/454	0.8	-
202.79 - 203.81	$24.83^{+2.34}_{-3.03}$	$1.06^{+0.02}_{-0.03}$	$2.62^{+0.04}_{-0.15}$	$530.3^{+26.7}_{-43.3}$	$4.34^{+1.69}_{-1.2}$	$42.71^{+4.65}_{-6.99}$	75.71 ± 0.64	2.86 ± 0.10	606.9/562	0.09	x
203.81 - 204.83	$19.57^{+2.28}_{-2.2}$	$1.06^{+0.03}_{-0.03}$	$2.45^{+0.05}_{-0.11}$	$583.6^{+44.0}_{-43.6}$	$3.09^{+1.48}_{-0.97}$	$41.91^{+5.75}_{-7.24}$	60.16 ± 0.58	2.62 ± 0.11	613.4/562	0.07	x
204.83 - 205.86	$19.76^{+2.01}_{-2.29}$	$1.07^{+0.02}_{-0.03}$	$2.73^{+0.06}_{-0.19}$	$527.9^{+25.5}_{-38.6}$	$6.91^{+1.8}_{-1.45}$	$38.51^{+2.96}_{-3.58}$	56.86 ± 0.56	1.96 ± 0.09	614.2/562	0.06	x
205.86 - 206.88	$15.98^{+1.5}_{-2.54}$	$1.0^{+0.06}_{-0.06}$	$2.36^{+0.05}_{-0.65}$	$334.8^{+49.2}_{-190.0}$	$7.14^{+3.59}_{-4.07}$	$31.53^{+6.74}_{-8.23}$	46.48 ± 0.53	1.54 ± 0.08	573.6/562	0.36	x
206.88 - 207.91	0.0	0.0	0.0	0.0	0.0	0.0	0.0	0.0	0.0	0.0	-

Table 10.4: Best fit parameters for SBPL+BB model for the main emission episode of GRB 160625B.

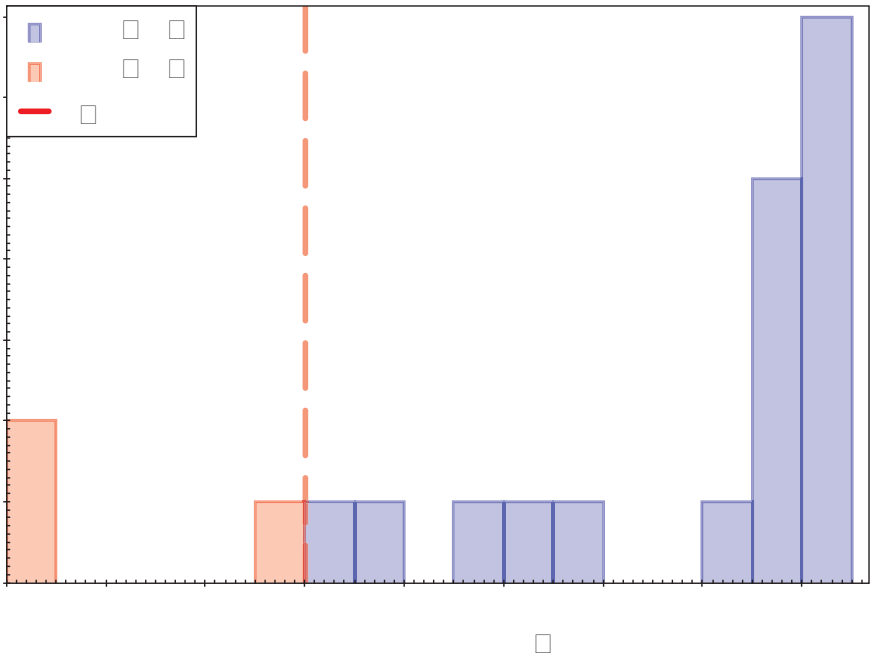

Figure 10.10: Histograms of the F–test significance of 2SBPL with respect to SBPL. The vertical dashed line shows the 3σ threshold.

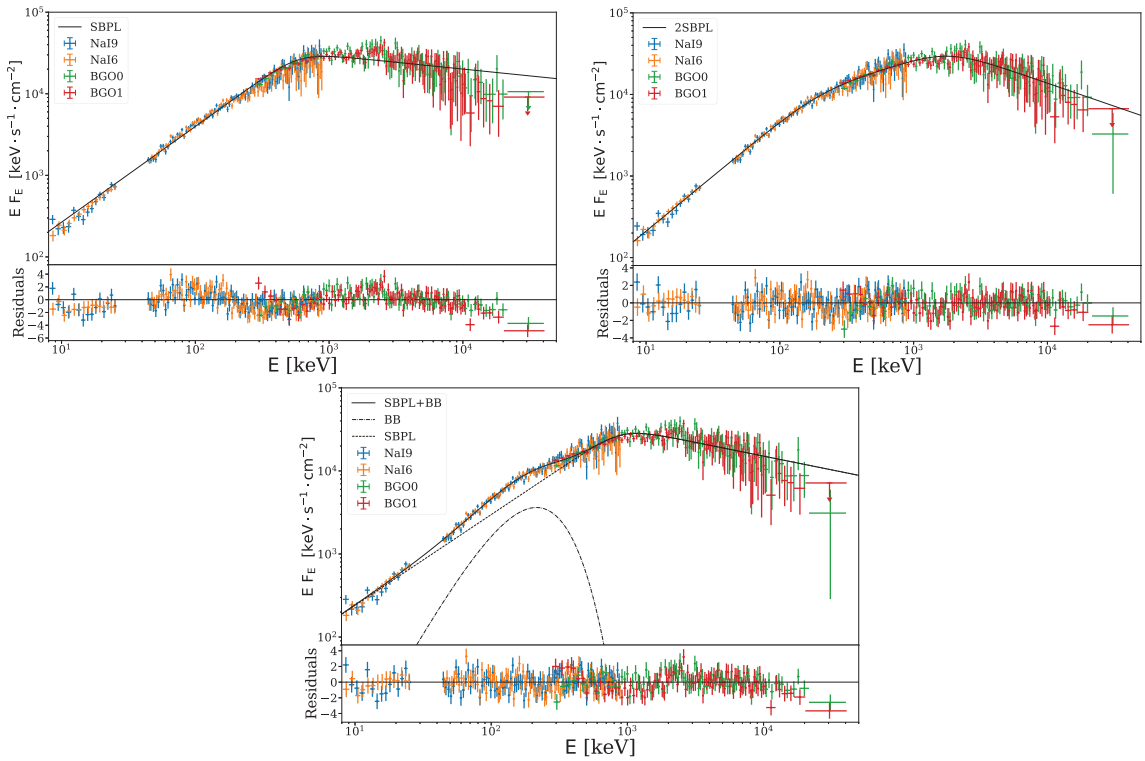

Figure 10.11: Spectrum of the brightest time bin (1.024 seconds width) of the main event fitted with different models: SBPL, SBPL+BB and 2SBPL.

of spectra.

We prefer the 2SBPL model over the SBPL+BB for three reasons:

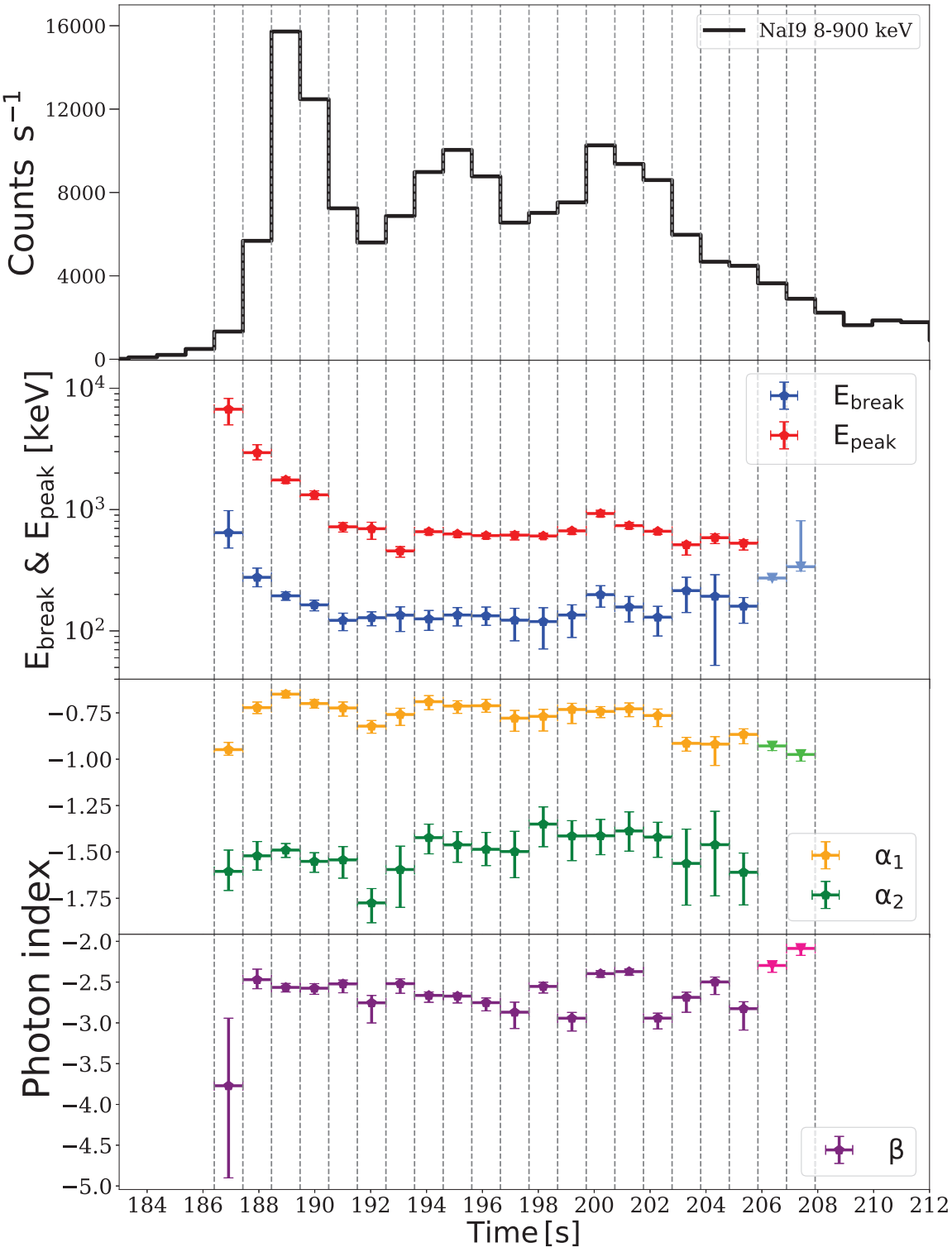

Figure 10.12: Time evolution of the spectral parameters of the 2SBPL model (Tab.10.2). From *top* to *bottom*: count rate (with 1.024 s time resolution), peak and break energy (red and blue symbols, respectively), photon index below and above the break (yellow and green symbols, respectively) and spectral index above the peak energy. The last two spectra could only be fitted with the SBPL model and its spectral parameters are represented with different symbols.

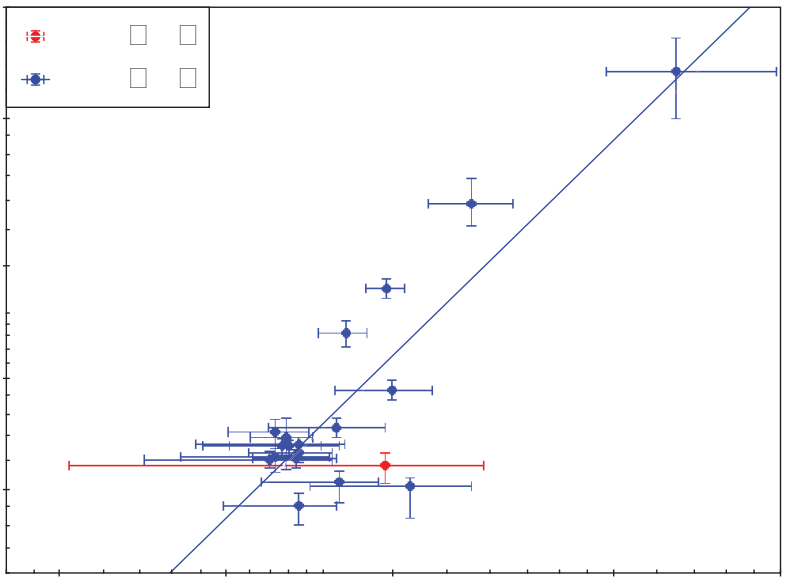

Figure 10.13: Correlation between the peak energy $E_{\rm peak}$ and the break energy $E_{\rm break}$ of the 2SBPL model. The red point is the only spectrum where the F–test probability of the fit improvement using 2SBPL over the SBPL is significant at 2.71σ. Error bars show uncertainties at 1σ.

(i) in the majority of the cases the fit with 2SBPL model has a larger probability (of the χ^2) than the SBPL+BB;

(ii) 2SBPL is a single component emission model;

(iii) the spectral indexes of the 2SBPL are remarkably consistent with standard synchrotron fast–cooling emission.

Indeed, the synchrotron fast–cooling model predicts photon index $\alpha_1 = -2/3$ and $\alpha_2 = -3/2$ and the mean values of our spectral analysis are $\alpha_1 = -0.76 \pm 0.02$ and $\alpha_2 = -1.51 \pm 0.02$. Fig.10.14 shows the distributions of the spectral indexes of the 2SBPL model fits.

Ghisellini et al. (2000) show that, between E_{break} and E_{peak}, the flux density should scale as $F(\nu) \propto \nu^{-1/2}$. This is the consequence of the radiative cooling timescale of electrons being shorter than the dynamical one.

Considering electrons of energy $\gamma m_{\rm e} c^2$, within a shell of bulk Lorentz factor Γ and with a magnetic field B, the radiative cooling

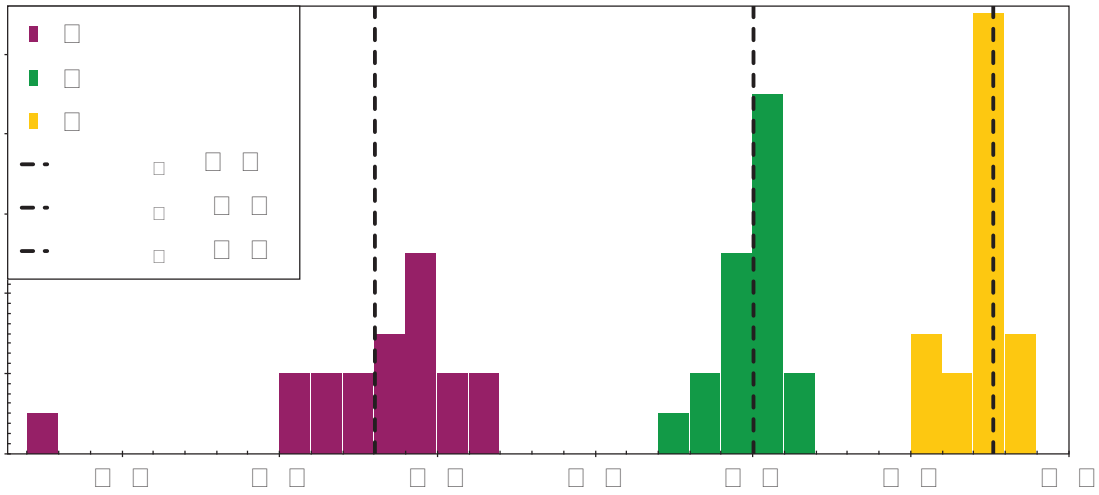

Figure 10.14: Distributions of the spectral indexes of the three power–law segments of the 2SBPL model (values in Tab.10.3). The vertical dashed lines show the median value of the three indexes α_1, α_2 and β.

timescale (in the observer frame) for synchrotron emission is:

$$t_{\rm cool}^{\rm obs} = \frac{\gamma}{\dot{\gamma}} \frac{(1+z)}{\Gamma} = \frac{6\pi m_{\rm e} c}{\sigma_{\rm T} B^2 \Gamma \gamma (1 + U_{\rm rad}/U_B)} \frac{(1+z)}{\Gamma} \tag{10.5}$$

where $U_{\rm rad}$ and $U_{\rm B}$ are the radiation and magnetic energy densities, respectively.

Our time–resolved spectral analysis was performed considering spectra with integration time of 1.024 seconds. Therefore, we can derive a limit on B by requiring $t_{\rm cool}^{\rm obs} \geq 1$ s. We can express γ as a function of the synchrotron frequency, $\nu_s = 3.6 \times 10^6 B \gamma^2 \Gamma/(1+z)$ Hz, obtaining:

$$B \leq \left[\frac{6\pi m_e c^2 (3.6 \times 10^6)^{1/2} (1+z)^{1/2}}{\sigma_{\rm T} c \Gamma^{1/2} \nu_s^{1/2}} \right]^{2/3} \tag{10.6}$$

Considering the typical value of $E_{\rm break} \sim 100$ keV found in our analysis we obtain:

$$B \lesssim 13 \;\; \Gamma_2^{-1/3} \nu_{100\,{\rm keV}}^{-1/3} \;\; \text{Gauss.} \tag{10.7}$$

Such a small value of B is at odd with the expectation at the GRB emission region unless it decayed substantially from the value it has at the shock front (Zhao et al., 2014a). In this case the observed slope

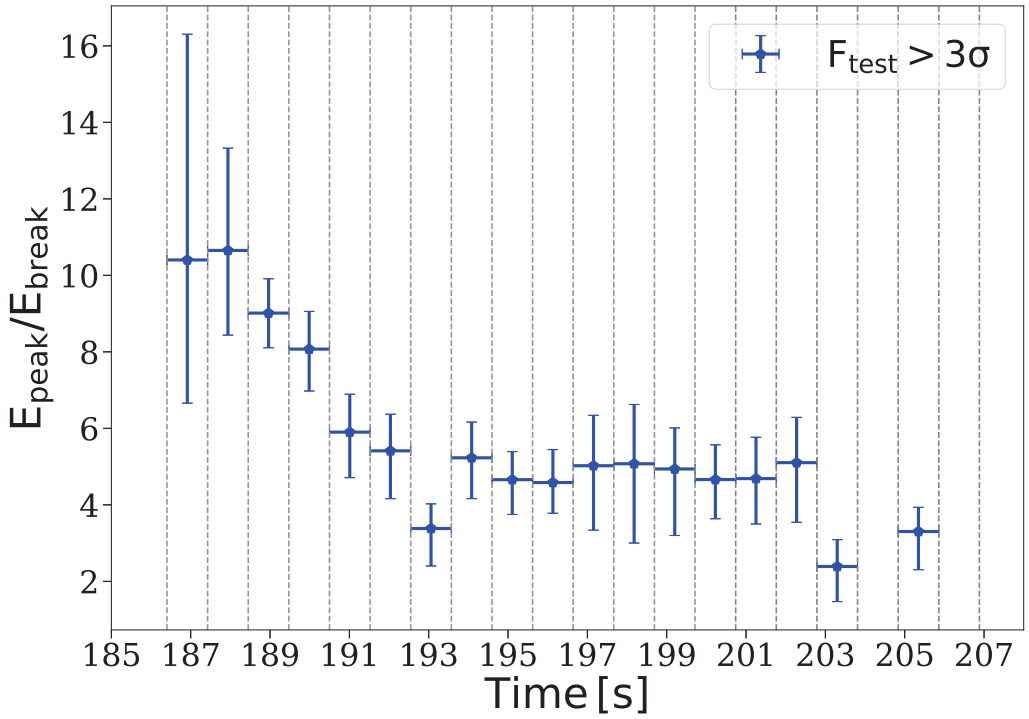

Figure 10.15: Temporal evolution of the ratio between the peak energy and the break energy of the 2SBPL model for the 18 spectra where this fit is significantly (at more than 3σ significance level) better than the SBPL model fit.

of GRB prompt emission spectra could still be attributed to synchrotron radiation, but in a moderately fast cooling regime (i.e., a situation in which $\nu_{cool} \lesssim \nu_{min}$).

Another analogous study on physical conditions leading to $\nu_{cool} \lesssim \nu_{min}$ was discussed in Beniamini and Piran (2013), finding reasonable synchrotron solutions for emission radii of the order of $10^{15}\,cm < R < 10^{17}\,cm$.

We show in Fig.10.12 that $E_{\rm break}$ (corresponding to ν_{cool}) and $E_{\rm peak}$ (corresponding to ν_{min}) are fairly close to each other. Fig.10.15 shows the time evolution of the ratio $E_{break}/E_{peak} \sim 5$. A similar analysis was performed also by Yu et al. (2015b), using a synchrotron plus black body model to fit 8 GRBs time–resolved spectra observed by *Fermi* GBM. They found that the break and the peak of their synchrotron model are close to one another, with a narrow distribution of E_{peak}/E_{break} centered at $3.77^{-1.53}_{+4.01}$.

To conclude, even if the two energies are not expected to be related and their ratio is not constrained by any theoretical prediction, their values and their ratio, as found in our analysis, seem to support the "moderately fast–cooling" scenario.

CHAPTER 11

Conclusions

Since the discovery of Gamma Ray Bursts (GRBs), one of the most important questions was related to their distance scale (i.e. whether galactic or cosmological) which had immediate implications on their associated luminosities and energetics. Through the afterglow detection (Costa et al., 1997; van Paradijs et al., 1997) and first redshift measurements, GRBs were proven to be cosmological sources with large isotropic equivalent luminosities exceeding, in few cases, 10^{54} erg/s. The pinpointing of the GRB afterglow, made available by the fast slewing of the *Swift* satellite (Gehrels et al., 2004), coupled with intense efforts to acquire early time optical spectra from ground, allowed us to measure the redshifts z of GRBs with an average efficiency of 30%. Among these, GRB 090423 (with a spectroscopic $z = 8.2$ – Salvaterra et al. 2009a; Tanvir et al. 2009) and GRB 090429B (with photometric redshift $z = 9.4$ – Cucchiara et al. 2011) represent the farthest objects of stellar origin known so far.

Two of the key properties characterising the population of GRBs are their cosmic formation rate $\psi(z)$, (i.e. the number of bursts per unit comoving volume and time as a function of redshift) and their luminosity function $\phi(L)$ (i.e. the fraction of bursts with a certain

luminosity). Recovering $\psi(z)$ and $\phi(L)$ of GRBs allows us to test the nature of their progenitor (e.g. through the comparison with the cosmic star formation rate) and to study the possible presence of sub–classes of GRBs at the low end of the luminosity function (e.g. Liang et al., 2007). This is becoming even more compelling with the advent of the detection of gravitational waves whose progenitors could produce also short GRBs.

These two functions were derived for the population of long GRBs (e.g. Daigne et al., 2006; Firmani et al., 2004; Guetta and Della Valle, 2007; Salvaterra and Chincarini, 2007; Salvaterra et al., 2009b, 2012; Wanderman and Piran, 2010; Yu et al., 2015a; Petrosian et al., 2015) through different methods and samples of bursts (see Chp.4 for more details). The population of short GRBs, instead, is still poorly understood owing to the relatively few events with measured redshift (see e.g. Berger, 2014; D'Avanzo, 2015, for recent reviews). For this reason, their $\psi(z)$ and $\phi(L)$ have been less securely constrained (e.g. Nakar et al., 2006; Berger, 2014; D'Avanzo et al., 2014; Guetta and Piran, 2006, 2005).

However, $\psi(z)$ and $\phi(L)$ cannot be derived straightforwardly using all GRBs with known redshift since these samples are affected by observational biases. Specific methods accounting for such biases should be adopted.

The main approaches that have been used so far (see Chp.4) agree on the shape of the luminosity function (typically represented by a broken power law) for but lead to remarkably different results on the cosmic GRB formation rate (particularly at low redshifts – see Chp.5). The above general consideration applies to the population of long GRBs. For short events no consensus has been found both on the shape and redshift distribution yet. Independently from the method used to recover these two functions, most of the previous studies (see however Salvaterra et al., 2012) adopted either heterogeneous samples (i.e. including GRBs detected by different satellites/GRB detectors which have different sensitivities) and/or incomplete samples. Incompleteness can be induced by several effects such as the variation (for a given detector) of the trigger efficiency and/or the efficiency in measuring the redshift through optical spectroscopy. Modeling individually these instrumental and observational biases may be extremely difficult, if not impossible, in practice.

A good solution is to work with complete samples despite the

number of GRBs with measured L and z is still small, particularly for the puplation of short GRBs. Salvaterra et al. (2012) defined a complete flux–limited sample of long GRBs (called BAT6) detected by *Swift* which, despite containing a relatively small number of GRBs, has a high redshift completeness ($\sim$ 95%) and has been extensively used to test various prompt and afterglow properties of GRBs in an unbiased way (Vergani et al., 2015; Nava et al., 2012; Melandri et al., 2014, 2012; Ghirlanda et al., 2012a; D'Avanzo et al., 2012; Covino et al., 2013; Campana et al., 2012).

Alternatively, one can adopt direct inversion methods that allow us to derive $\psi(z)$ and $\phi(L)$ from samples of GRBs with measured z and L. For example Wanderman and Piran (2010) adopted the Maximum Likelihood Estimator (explained in Sec.4.2). More recently, Yu et al. (2015a, Y15) and Petrosian et al. (2015, Y15) applied the C^- statistical method (Lynden-Bell, 1971) to reconstruct the discrete $\psi(z)$ and $\phi(L)$ from a sample of *Swift* bursts with measured redshifts. This method has been inherited from the studies of the luminosity function of quasars and blazars (e.g. Singal et al., 2013, 2012; Maloney and Petrosian, 1999; Chiang and Mukherjee, 1998) and it has been applied to GRBs (Kocevski and Liang, 2006; Lloyd and Petrosian, 1999). The key assumption of these non–parametric methods is that L and z must be uncorrelated. For this reason both P15 and Y15 apply a statistical method (Efron and Petrosian, 1992) to remove the redshift dependence of the luminosity induced by the flux–cut in the selected GRB sample.

Intriguingly, they find, at odd with respect to previous works, that the GRB rate is flat or decreases from the local Universe up to $z = 1$. If compared to the SFR, this behaviour would imply a relative excess of the GRB formation rate with respect to $\psi_\star(z)$ at $z \leq 1$ (if both are normalized to their respective peaks). They call this behaviour *the excess of GRBs at low redshifts*. This result is puzzling also because it is completely at odds with the findings of the works based on the properties of GRB host galaxies. In fact, Vergani et al. (2015); Perley et al. (2015b, 2016a,b); Schulze et al. (2015); Krühler et al. (2015), performed multi–wavelength and spectroscopic studies on the properties (stellar masses, luminosities, SFR and metallicity) of GRB host galaxies of different complete GRB samples and compared them to those of the star-forming galaxies selected by galaxy surveys. All their results clearly indicate that at $z < 1$ only a small fraction of the star–formation produces GRBs.

In Pescalli et al. (2016) we tested the the robustness of the C^- method performing Monte Carlo simulations (see Sec.4.1 and Sec.5.1). We showed that this method can correctly recover the LF and the GRBFR assumed in the simulation, but only if the sample of GRBs it is applied to is complete in flux and has a high level of completeness in redshift. Using incomplete samples in redshift and/or in flux (as Y15 and P15 did), the resulting GRBFR and LF can be different from the assumed ones. Indeed, this could account for the excess of the rate of GRBs at low redshift reported by Y15 and P15.

Motivated by these results, we applied the C^- direct method (in its specific version already applied to GRBs by e.g. Yonetoku et al. 2004, 2014; Kocevski and Liang 2006; Wu et al. 2012; P15; Y15) for the first time to a well–defined sample of GRBs, with the aim to derive the luminosity function of long GRBs and their formation rate (Pescalli et al., 2016).

We build our sample of long GRBs starting from the BAT6 complete sample (Salvaterra et al., 2012): this was composed by 58 GRBs detected by the *Swift* satellite satisfying the multiple observational selection criteria of Jakobsson et al. (2006) and having a peak photon flux $P \geq 2.6$ ph cm^{-2} s^{-1}. We updated the sample including GRB 140703A obtaining a total of 99 objects (see Sec.5.2) . We collected their redshift and spectral parameters from the literature and accordingly computed their luminosities. The BAT6ext sample has a redshift completeness of $\sim 82\%$ (82/99 burst with z measured) and contains 81/99 bursts with well determined L.

We analyzed the BAT6ext sample, searching for a possible luminosity evolution which is induced by the flux threshold. To this aim we use the method proposed by Efron and Petrosian (1992). We found that the $L - z$ correlation, which was introduced by the truncation at the limiting flux, can be described as $L = L_0(1+z)^k$ with $k = 2.5$. This result is in agreement with what found by other authors (Yonetoku et al., 2004; Wu et al., 2012, Y15; P15). Through the BAT6ext sample, after de–evolving the luminosities for their redshift dependence, we find that:

- the luminosity function $\phi(L_0)$ of long GRBs is a monotonic decreasing function well described by a broken power–law with slopes $a = -1.32 \pm 0.21$ and $b = -1.84 \pm 0.24$ below and above, respectively, a characteristic break luminosity $L_\mathrm{b} = 10^{51.45 \pm 0.15}$ erg/s. This result (shape, slopes and characteristic break – see

Fig.5.2) is consistent with the luminosity function found by Salvaterra et al. (2012).

- The cosmological GRB formation rate $\psi(z)$ increases from low redshifts to higher values peaking at $z \sim 2$ and decreases at higher redshifts (see Fig.5.2). This trend is consistent with the shape of the SFR of Hopkins and Beacom (2006) and Cole et al. (2001). Our results on $\psi(z)$ is in contrast with the GRBFR reported by P15 and Y15 and agrees with the results obtained from the studies of the hosts (e.g. Vergani et al., 2015; Krühler et al., 2015).

- We have shown that the latter inconsistency with the results of P15 and Y15 is due to their samples being incomplete in redshift and, more severely, in flux.

The luminosity evolution of the luminosity function $\phi(L)$ is huge (but in agreement with the findings of Yonetoku et al. 2004; Wu et al. 2012; P15; Y15). This might be difficult to be justified from a theoretical point of view (see also Daigne et al., 2006). In fact, this could imply an evolution with redshift of either the physical processes leading to the emission of γ–rays and/or an evolution in the physical properties of the progenitor (even if the GRB formation rate seems to follow the SFR, as obtained in this work).

However, the result that GRBs evolve in luminosity should not be interpreted as the proof that GRBs had experienced a pure luminosity evolution. It is beyond the scope of this work to demonstrate which type of evolution the GRBs experienced. In fact the C^- method assumes independence between L and z and the non–parametric method of Efron and Petrosian (1992), which was used to get the de–evolved luminosities, assigns the whole evolution to the luminosity. For this reason, we are not able to distinguish between a luminosity or density evolution (see also Salvaterra et al., 2012) and probably the true solution resides in a combination of the two.

For the popoulation of short GRBs (SGRB) the luminosity fucntion and redshift distribution have been derived with more uncertainties mainly based on the small size of the samples with measured L and z. Now with the first GW events detected it is mandatory to recover $\phi(L)$ and $\psi(z)$ in order to compare the local SGRB rate with that of GW events. This would constrain at the same time

the progenitor properties of short GRBs and in general the properties of the population of binary neutron stars. Such rate estimates mainly depend on the luminosity function $\phi(L)$ and redshift distribution $\psi(z)$ (assumed to follow the cosmic SFR with a delay which is due to the time necessary for the progenitor binary system to merge) of SGRBs. The common approach is to assume parametric forms for the compact binary merger delay time distribution and for the SGRB luminosity function; free parameters of such functions are then constrained through the small sample of SGRBs with measured redshifts and luminosities and through the distribution of the γ–ray peak fluxes of SGRBs detected by past and/or present GRB detectors (Guetta and Piran, 2005, 2006; Nakar et al., 2006; Salvaterra et al., 2008; Hopman et al., 2006; D'Avanzo et al., 2014; Wanderman and Piran, 2015). Given the incompleteness of the available SGRB samples, particularly with measured z, no direct method (as for the population of long GRBs) can be applied to straightforwardly derive the shape of the SGRB luminosity function $\phi(L)$ and redshift distribution $\psi(z)$ from the observations.

However, a number of other observer frame properties are available for SGRBs (fluence distribution, duration distribution, observer frame peak energy) and we considered them in Ghirlanda et al. (2016, see Chp.8).

We derived $\phi(L)$, $\psi(z)$ and the local rate of SGRBs. Similarly to previous works present in the literature, we fitted the properties of a synthetic SGRB population, described by the parametric $\phi(L)$ and $\psi(z)$, to a set of observational constraints derived from the population of SGRBs detected by *Fermi* and *Swift*, but our approach features a series of improvements:

- (observer frame) constraints: We extend the classical set of observational constraints (peak flux and – for a few events – redshift distribution) requiring that our model should reproduce the peak flux P, fluence S, peak energy $E_{\rm p,o}$, and duration T distributions of 211 SGRBs with $P_{64} \geq 5$ ph s^{-1} cm^{-2} as detected by the GBM instrument on board the *Fermi* satellite. The uniform response of the GBM over a wide energy range (10 keV – few MeV) ensures a good characterization of the prompt emission spectral properties of the GRB population and, therefore, of the derived quantities, i.e. the peak flux and the fluence;

- (rest frame) constraints: We also require that our model repro-

duces the distributions of redshift, luminosity, and energy of a small sample (11 events) of *Swift* SGRBs with $P_{64} \geq 3.5$ ph s^{-1} cm^{-2} (selected by D'Avanzo et al., 2014). This sample is 70% complete in redshift and therefore it ensures a less pronounced impact of redshift–selection biases in the results;

- method: We directly parametrize $\psi(z)$ following Cole et al. (2001) and derive the redshift distribution of SGRBs independently from their progenitor nature and their cosmic star formation history. Differently from our implementation, the classical approach assumes of a specific cosmic star formation history $\psi(z)$ and a delay time distribution $P(\tau)$ (i.e. works under the hypothesis of a specific progenitor type, i.e. NS-NS merger);
- method: We assume the existence of intrinsic $E_{\rm p} - L$ and $E_{\rm p} - E$ correlations in SGRBs (case (a)), similarly to what has been observed in the population of long GRBs. We also allow for a lower minimum luminosity $L_{\rm min} = 10^{50}$ erg/s (case (b)). However, since evidence of the existence of such correlations in the population of SGRBs is still based on a limited number of bursts (D'Avanzo et al., 2014; Tsutsui et al., 2013; Amati, 2006; Calderone et al., 2015), we also explore the case of uncorrelated peak energy, luminosity and energy (case (c)).

Our main results are as follows:

1. The luminosity function of SGRBs (case (a)), which we model with a broken power law, has a slope $\alpha_1 = 0.53^{+0.47}_{-0.14}$ (68% confidence interval) below the break luminosity of $L_{\rm b} = 2.8^{+0.6}_{-1.89} \times 10^{52}$ erg s^{-1} and falls steeply above the break with $\alpha_2 = 3.4^{+0.3}_{-1.7}$. This solution is almost independent from the specific assumption of the minimum luminosity of the $\phi(L)$ (case (b)). Moreover, it implies an average isotropic equivalent luminosity $\langle L \rangle \approx 1.5 \times 10^{52}$ erg s^{-1} (or 3×10^{52} erg s^{-1} in case (c)), which is much larger than e.g. $\langle L \rangle \approx 3 \times 10^{50}$ erg s^{-1} from D'Avanzo et al. (2014) or $\langle L \rangle \approx 4.5 \times 10^{50}$ erg s^{-1} from (Wanderman and Piran, 2015);
2. The redshift distribution of SGRBs $\psi(z)$ peaks at $z \sim 1.5$ and falls rapidly above the peak. This result is intermediate between those reported in the literature which assume either a constant large delay or a power–law distribution favouring small

delays. We find that our $\psi(z)$ is consistent with the SFH of Madau and Dickinson (2014) retarded with a power–law delay time distribution $P(\tau) \propto \tau^{-1}$;

3. As a by–product we find that, if SGRBs feature intrinsic $E_{\rm p} - L$ and $E_{\rm p} - E$ correlations, they could be slightly steeper than those derived with the current small sample of short bursts with redshift (e.g. Tsutsui et al., 2013), but still consistent within their 68% confidence intervals;

4. If we assume that there is no correlations between $E_{\rm p}$ and L (or E) (case (c)), we find similarly that the $\phi(L)$ is flat at low luminosities and the formation rate peaks at slightly larger redshift ($z \sim 2$);

5. We estimate the rate of SGRBs as a function of z within the explorable volume of advanced LIGO and Virgo for the detection of double NS mergers or NS–BH mergers (see Fig.8.5). Assuming the design aLIGO sensitivity averaged over sky location and over binary orbital plane orientation with respect to the line of sight, NS–NS mergers can be detected up to 200 Mpc (410 Mpc for NS–BH mergers). This is usually referred to as the detection range for these binaries. The rate of SGRBs within the corresponding volume is $\sim 7 \times 10^{-3}$ yr^{-1} (0.028 yr^{-1} for NS–BH merger distance), assuming the existence of $E_{\rm p} - L$ and $E_{\rm p} - E$ correlations for the population of short bursts (model (a)). Rates larger by a factor of $\sim$ 4 are obtained if no correlation is assumed (model (c)). If binaries producing observable SGRBs are preferentially face–on (which is the case if the GRB jet is preferentially aligned with the orbital angular momentum), then the actual explorable volume extends to a somewhat larger distance (a factor of $\sim$ 1.5 larger, see Schutz, 2011), increasing the rates of coincident SGRB–GWs of about a factor of 3.4 (Schutz, 2011);

6. We compare our SGRB rates with the rates of NS mergers derived from population synthesis models or from the statistics of Galactic binaries. This enables us to infer an average opening angle of the population of SGRBs of 9°–17° (assuming that all SGRBs are produced by the NS–NS mergers), which is consistent with the few bursts with $\theta_{\rm jet}$ measured from the break of their afterglow light curve.

Our SGRB rate estimates might seem to compromise the perspective of a joint GW–SGRB observation in the near future. We note, however, that these rates refer to those bursts whose jets point towards the Earth. Therefore these rates should increase if we also consider the bursts oriented in different directions.

GRB jets are extremely powerful (isotropic luminosity in γ-rays 10^{50-54} erg s^{-1}) and with large bulk Lorentz factors ($\Gamma \sim 10^2 - 10^3$). Jets are a common feature of high–energy astrophysical sources powered by accretion on compact objects, as Active Galactic Nuclei (AGN) and Quasars (QSO). Moreover, the large isotropic equivalent energy $E_{\gamma,\mathrm{iso}}$ of the GRB prompt emission can easily exceed a solar mass rest energy, unless the radiation is collimated (Tan et al., 2001). For this reason and by analogy with other kind of sources, the idea that the emission could be collimated was born.

Observational evidence of jets is the steepening of the X, Optical and Radio afterglow flux light–curve a few days after the burst. This behavior, predicted when $\Gamma \sim 1/\theta_\mathrm{j}$ (Rhoads, 1997; Sari et al., 1999), is interpreted as due to collimation. Although there are still few breaks in the optical light curves for short GRBs, it is believed that they also have jets (e.g. Berger, 2014; Fong et al., 2015).

Typically GRB jets are thought as conical with energy and ejecta velocity constant, within the jet aperture, and zero outside the jet opening angle (i.e. sharp–edged jet). This is the so called *Uniform Jet* (UJ).

Intriguingly, the true energetic of GRBs (i.e. accounting for their collimation) clusters around a typical value $E_\gamma = E_\mathrm{iso}(1 - \cos\theta_\mathrm{j}) \approx 10^{51}$ erg with a dispersion of less than a decade (Frail et al., 2001), correlating with the peak energy of the prompt emission spectrum E_peak (Ghirlanda et al., 2004; Nava et al., 2006).

For small jet angles, the collimation corrected $E_\gamma \propto \theta_\mathrm{j}^2 E_\mathrm{iso}$. The small dispersion of E_γ led to the idea that the jet is not uniform, but *structured*, where θ is the angular distance from the jet axis, and coincides with the viewing angle θ_v. This scenario assumes that what we believed to be the jet angle θ_j is actually the viewing angle θ_v. This can lead to a unification scheme in which all bursts are basically equal, but appear different only because they are seen under different angles. If the dependence of the burst energetics on θ is $E_\mathrm{iso} \propto \theta^{-2}$, one recovers the finding of Frail et al. (2001) of the clustering of E_γ. These GRBs with a universal structured jet (SJ) were first

proposed by Lipunov et al. (2001) and then studied by Rossi et al. (2002) and Zhang and Mészáros (2002). Some structure to the jet power and velocity could be imprinted, within the collapsar model, by the interaction of the jet with the star (e.g. Zhang et al., 2003, 2004b; Lazzati and Begelman, 2005; Morsony et al., 2007; Levinson and Eichler, 2003).

Several GRB properties are affected by the jet structure: the achromatic break in the afterglow light curve is smoother in the SJ model and it is related to $\theta_{\rm v}$ rather than $\theta_{\rm j}$ (Zhang and Mészáros, 2002); different degree of polarization of the afterglow emission (Rossi et al., 2004; Lazzati et al., 2004a,b) and different luminosity functions (and GRB rates) are expected in the two scenarios. The jet break measurements are hampered by the necessity of a follow up of the afterglow emission until late times, by the smoothing induced by viewing angle effects (e.g. van Eerten et al., 2012) and by the contamination of the afterglow emission at late times by the possible supernova and host galaxy emission (e.g. Ghirlanda et al., 2007). Despite all these diagnostics, there is no concluding evidence yet of the real jet structure.

In Pescalli et al. (2015) we show how the jet structure affects the luminosity function and we try to get some insight about the still unknown jet structure of long GRBs by comparing the expected LF calculated assuming different jet models with the observed one (see Chp.6).

Due to the increased capability to measure the redshift of long GBRs, we have now better determination of their luminosity function, and indeed the results of different groups and of different methods start to converge. The LF can be modeled as a broken power–law, with slopes $\sim$1.2–1.5 and $b > 2$, and a break above 10^{52} erg s^{-1} (Wanderman and Piran 2010 – also in agreement with the findings of Pescalli et al. 2016). The degree of cosmic evolution is instead still uncertain (see e.g. Salvaterra et al., 2012).

Another controversial issue concerns low luminosity GRBs. A few have been observed, but their proximity implies a large local density (e.g. Soderberg et al., 2006b; Pian et al., 2006). It was proposed that low luminosity GRBs could belong to a different population (e.g. Virgili et al., 2009; Daigne and Mochkovitch, 2007). We have shown in Pescalli et al. (2015) that instead they lie on the extrapolation of the luminosity function that describes high luminosity events. This suggests that bursts of low and high luminosity belong

to the same population.

Low luminosity bursts have luminosities of $\sim 10^{47}$ erg s^{-1} and therefore extend the range of observed GRB luminosities up to seven orders of magnitude. Is this very large range produced by the different intrinsic GRB power or is it instead the result of viewing the same intrinsic phenomenon under different lines of sight?

- Jets are homogeneous and have a unique opening angle. The observed luminosity is proportional to the energy left after some of it has been spent to punch the progenitor star (see Fig.6.13). This implies that the LF must be flat at low luminosities in contrast with the observed data. Therefore, we can exclude this simple scenario.

- Jets are homogeneous, but with an angle related to the GRB energy. We assume that smaller θ_j correspond to larger E_{iso} and L_{iso}. Since low luminosity bursts have larger θ_j the probability that they intercept our line of sight is larger then that for high luminosity bursts: therefore the fraction of GRBs that we detect at low luminosities is larger than at high luminosities. If the "true" LF is flat, the observed LF is instead decreasing towards larger L_{iso} with a slope that depends on the chosen relation between θ_j and L_{iso}. In this case we obtain a reasonable agreement with the data in the entire luminosity range but the very low luminosities, where the model shows a small deficit (see Fig.6.14).

- Jet is homogeneous, but it can be seen also off–axis, for viewing angles $\theta \gtrsim \theta_j$. This is possible if Γ is not extreme: the luminosity decreases as a function of θ_v showing a drop for $\theta_v \gtrsim \theta_j$ (more pronounced for larger Γ – see Fig.6.4). The LF constructed with a single value of θ_j and Γ do not fit the data, since they show an upturn at high luminosity instead of a steepening. On the other hand, assuming some dispersion of θ_j and Γ, we can obtain a reasonable agreement (see Fig.6.15). The required average values are $< \Gamma >= 30$ and $< \theta_j >= 3^\circ$. What is remarkable is that the analytically predicted slope at intermediate luminosities is very close to what observed.

- Jet is structured, of the form $\epsilon(\theta_v) \propto \theta_v^{-s}$ beyond a core angle θ_c. We have found that a good fit of the observed LF can be obtained, but only if the slope s is rather steep, $s > 4$, with a preferred value $s \sim 8$ (see Fig.6.16). This is much steeper than

the value $s = 2$ originally proposed to explain the clustering of E_γ found by Frail et al. (2001).

These studies indicate that the jet must have a relatively sharp cut–off. Even if an abrupt one is nonphysical (all the energy contained within θ_j, and zero outside), the energy must in any case decrease rapidly with the angle from the jet axis, once it it becomes greater than the core angle θ_c. The other important conclusion is that although the low luminosity bursts seem not to have enough energy to punch the progenitor star, they can nevertheless be explained within the same framework of large luminosity GRBs, as long as they have a larger jet angle, or they are seen off–axis. In the first case we see the little energy leftover after the jet breaks out, in the latter case the apparent low luminosity is due to the large viewing angle, but the real energetic of these burst is much larger.

The satellites/instruments deputed to the detection of GRBs observed hundreds/thousands of GRBs at an average rate of ~ 0.3 day^{-1}. Since GRBs are characterized by the presence of a relatively narrow jet (eventually well approximated by an uniform jet – Pescalli et al. 2015), we more probably detect only those bursts whose jet is pointing at the Earth.

Indeed, since the highly relativistic motion results in a strong forward beaming of the emitted radiation, the flux directed at the Earth is dramatically reduced when $\theta_v > \theta_j$. These events (which are the most numerous due to the jet orientation probability being $\propto \sin\theta_v$) go undetected as prompt γ–ray bursts. However, during the afterglow the bulk Lorentz factor decreases with time (as the outflow is decelerated by the external medium). There will be a characteristic timescale when the *relativistic beaming* $\propto 1/\Gamma$ equals the *observer viewing angle* θ_v and the (afterglow) radiation can be seen. These events, missing the prompt emission but detected as afterglows, are called *orphan afterglows* (OA – hereafter) and, for typical opening angles of GRBs of a few degrees, e.g. $\theta_j \sim 0.1$ rad, they should outnumber the population of GRBs (by a factor $\propto (1 - \cos\theta_j)^{-1} \sim 200$).

Therefore, OA should be detected as transients but their association with GRBs is made difficult due to the lack of a prompt high–energy emission. Despite specific studies have been searching for OA in X–ray surveys (Grindlay, 1999; Greiner et al., 2000) in optical surveys (Rau et al., 2006, 2007; Malacrino et al., 2007) and in the radio band (Levinson et al., 2002; Gal-Yam et al., 2006; Bannister et al.,

2011; Bell et al., 2011; Bower and Saul, 2011; Croft et al., 2010; Frail et al., 2012; Carilli et al., 2003; Matsumura et al., 2009; Lazio et al., 2010), no OA has been conclusively detected so far.

Non detections of OA are in agreement with current theoretical predictions (Totani and Panaitescu, 2002; Nakar et al., 2002; Zou et al., 2007; Rossi et al., 2008; Metzger et al., 2015). However, these works extrapolated the properties of a few known GRB afterglows (supposed to be observed on-axis) as a function of viewing angle (i.e. to the population of orphans) (e.g. Totani and Panaitescu, 2002). Another approach was to assume basic prescriptions for the known GRB population properties and/or for the afterglow emission model (e.g. Zou et al., 2007).

Ghirlanda et al. (2013a) recently developed a population synthesis code which, coupled with the most detailed model for the afterglow emission (van Eerten et al., 2012), allowed Ghirlanda et al. (2014) to predict the properties of the population of OA reproducing a large set of observed properties of the population of the "Earth–pointed" GRBs. They considered the radio band predicting that the Square Kilometer Array (SKA), reaching the μJy flux limit, could see up to $\sim$0.2–1.5 OA deg^{-2} yr^{-1} (Ghirlanda et al., 2014). Alternatively, the non detection of OA could be due to the structure of the jet (Rossi et al., 2008; Salafia et al., 2015).

We are entering the era of large synoptic surveys which will monitor large portions of the (if not the whole) sky with unprecedented sensitivities. OA are potentially in the list of transients that these surveys will detect, but specific predictions on the rate depend on the true rate of the population of OA (and also their duration) and on the survey characteristics (area of the sky covered, timescales, limiting flux). In Ghirlanda et al. (2015b, see Chp.7) we derive the flux distribution of OA in the X–ray, Optical and mm Radio band based on the recent population synthesis code developed in Ghirlanda et al. (2013a). We also study the average duration of the population of OA as a function of the survey limiting flux. We computed the emission properties of the population of orphan afterglows in the optical and X–ray band comparing our results with current limits of OA in these bands and make predictions for on–going and forthcoming surveys.

What is new in our model is that we predict the properties of OA based on the observed properties of GRBs in the γ–ray band considering as constraints the flux and fluence distribution of the pop-

ulation of GRBs detected by *Swift*, BATSE and *Fermi*. Since the γ–ray energy detected in the prompt emission is a proxy of the kinetic energy driving the afterglow deceleration, our simulated population of bursts includes both high and low kinetic power bursts. The choice to reproduce the afterglow flux distribution of the complete BAT6 sample of *Swift* bursts, despite being composed by relatively bright events, ensures that we are extending the flux distribution of the synthetic GRB population to the low end better than what could be done with the limited number of GRBs detected in the pre–*Swift* era.

We have assumed that GRBs have a jet with a top–hat uniform structure, i.e. the kinetic energy and the bulk Lorentz factor are constant within the jet opening angle. In this scenario, orphan afterglows are naturally expected to dominate the number of GRBs in the Universe (considering a typical jet opening angle of few degrees). Even if the top–hat uniform jet emission can be seen when $\theta_v \geq \theta_j$, its flux decreases drastically for off–axis observers so that we can consider valid the approximation so far understated that we do see the prompt emission only of GRBs whose uniform jet is pointed towards the Earth (i.e. when $\theta_v \leq \theta_j$). In the structured jet model, instead, there is always a portion of the jet that is pointing to the observer. Therefore, the observed GRB properties depend only on the viewing angle θ_v so that orphan afterglows should not exist in principle, since even at large angles from the jet there is jet emission that can be seen (Salafia et al., 2015). However, also in this scenario OA could still be present if either the prompt emission at large angles is below any detector threshold or if the jet is uniform within a relatively narrow core and highly structured (i.e. with a steeply decreasing energy profile) outside it, as suggested by recent results from the modelling of the luminosity function (Pescalli et al., 2015). In this model the detection rates of OA would be, anyway, smaller than in the top–hat model adopted here as shown in Rossi et al. (2008).

Our model allows us to predict the expected rate of detection of OA in past, current and future optical and X–ray surveys. For a similar work for the radio band see Ghirlanda et al. (2014) (see also Metzger et al. (2015)). Most past and on–going optical surveys have small chances to detect OA. Among these, the Palomar Transient Factory (PTF – Law et al. (2009)) could marginally see one OA per year (consistent with Rau et al., 2009, predictions) given its relatively

low sensitivity compensated by the large portion of the sky covered per night (10^3 deg^2). Instead, according to our model, an optical survey like that of Pan–STARRS1 which will cover 6000 deg^2 per night could already detect a dozen of OA per year. Larger detection rates are expected for the forthcoming development of the PTF survey. The Zwicky Transient Facility (Bellm, 2014), which is designed specifically for transients discovery, will cover about 22500 deg^{-2} per night down to a limiting magnitude $\sim$20.5. We expect that it will detect $\sim$20 OA yr^{-1}. A considerably larger number of OA will be accessible by the Large Synoptic Sky Telescope survey (LSST – Ivezic et al., 2008a). The telescope will have a 9.6 deg^2 field of view and will be able to survey 10^4 deg^2 of the sky every three nights down to a limiting magnitude for point sources $R \sim$24.5. With these parameters we estimate it could detect 50 OA yr^{-1}.

Given the depth of forthcoming optical surveys we expect that OA will have a typical redshift $z \sim 2$. At such distances the typical GRB host galaxy should be fainter than the LSST limiting magnitude (Hjorth et al., 2012).

The difficulty will be to disentangle these OA from other (galactic and extragalactic) transients that will be detected with similar flux and temporal behaviour. The follow up in the optical and X–ray will secure the sampling of the light curve which could be the first hint to the OA nature (with respect to potential other extragalactic transients like supernovae and blazars). The availability of dedicated facilities or assigned observing time at different ground based facilities will be crucial in this respect. Optical/NIR spectroscopy will discriminate extragalactic transients (e.g. Gorosabel et al., 2002), low frequency (mm and Radio bands) observations[1] could be used to distinguish among possible competing transients sources. For particularly low redshift transients, the search for the host galaxy could also provide further clues on their nature.

In this work, we also computed the OA flux cumulative distribution at the reference frequency of 443 GHz which is one of the frequencies covered by e.g. ALMA. We have verified that the few hundred GHz range is where OA are brightest considering the typical timescales when they become visible. The Herschel/SPIRE survey ATLAS, one of the widest covering a total of 500 deg^2, is limited by the confusion limit of 5–7 mJy at 250–500 μm so that we expect less

[1]The LSST will start operating approximately in the same period of the Square Kilometer Array (SKA).

than 0.1 OA yr^{-1}. Spitzer SWIRE observed six fields in the northern and southern sky with typical areas between $\sim$4.2 deg^2 and $\sim$12 deg^2 with higher sensitivities of few tens of μJy in the low frequencies channels (IRAC) at 3.6μm and 4.5μm. These fields were covered on different timescales between 1 and 6 days. According to our model we expect a rate of less than one OA per year in such fields above the deepest flux limits of this survey.

Among forthcoming X–ray surveys we consider the extended ROentgen Survey with the Imaging Telescope Array (eROSITA – Merloni 2012) which will cover the full sky up to 10 keV with a flux limit $\sim 2 \times 10^{-14}$ erg^{-1} cm^{-2} s^{-1} in the 0.5–2 keV band. Therefore, $\sim 3 \times 10^{-3}$ deg^{-2} yr^{-1} OA should be reachable by this survey. According to the planned scanning strategy, a full circle of width 2 degree will be covered every four hours. This corresponds to $\sim$ 4320 deg^2 day^{-1}. The expected OA number is $\sim$26 yr^{-1} (but see also Khabibullin et al., 2012). A larger number of OA (by a factor 2) could be reached by the WFXT survey (e.g. Rosati et al., 2011).

GRBs light–curves show variability timescales as short as few milliseconds (Bhat et al., 1992; Walker et al., 2000; MacLachlan et al., 2013), appearing as a sequence of "prompt emission pulses" (PP hereafter) (Fishman et al., 1993; Bhat et al., 2012). Thanks to the early follow up by the X Ray Telescope (XRT - 0.3–10 keV) onboard Swift (Gehrels et al., 2004), it has been shown that large amplitude "X–ray flares" (XRF, hereafter) are often superimposed to the "canonical" afterglow emission (Chincarini et al., 2007, 2010; Falcone et al., 2007). Sometimes, X–ray flares can occur even one day after the γ–ray trigger (Bernardini et al., 2011).

According to the fireball model, the prompt emission of GRBs is generated by relativistic *internal* shocks (IS – see Sec.2.4) produced by shells ejected by the inner engine with random velocities (e.g. Rees and Meszaros, 1994). In these shocks, a fraction of the total kinetic energy of the fireballs is converted into radiation through synchrotron and inverse Compton emission. This scenario can produce the highly variable light–curve of the prompt emission (Kobayashi et al., 1997). Shocks produced by the deceleration of the relativistic outflow by the interstellar medium, *external* shocks (ES – see Sec.2.5), have been invoked to explain the long lasting, smoothly decaying, broad band (from the optical to the radio) afterglow emission. However, over–densities of the circum burst medium (CBM) could also

produce a variable light–curve (e.g. Nakar and Piran, 2003).

While IS, being produced by shells with slightly different random velocities, are expected to occur at a constant distance from the central engine, in ES the radius where shocks occur increases due to the expansion of the outflow in the CBM. As a consequence, IS should differ from ES in producing pulses whose duration is not correlated with their time of occurrence. No correlation between the duration and the occurrence time of a pulse of BATSE GRBs was found (Ramirez-Ruiz and Fenimore, 2000). This favoured the IS mechanism.

Swift observed X–ray pulses in the 0.3–10 keV energy range (called flares) which show a duration increasing with time (Chincarini et al., 2010; Yi et al., 2016; Kocevski et al., 2007). This property may be consistent with an ES scenario. However, XRFs have spectral properties (e.g. hard to soft evolution and harder spectral shape than the underlying afterglow component) similar to those of PP (Chincarini et al., 2006, 2007, 2010; Falcone et al., 2006; Margutti et al., 2010) and might be due to IS (Chincarini et al., 2007; Curran et al., 2008). The nature of XRFs is challenging for current models: they might demand a long–lived (hours) central engine (e.g. Yu et al., 2015c) or they could hint to short lived central engine emitting slower shells which dissipate their energy via IS at later times (e.g. Lazzati and Perna, 2007). Distinguishing between these two scenarios leads to important implications for the physics of the GRB central engine.

One leading question is whether X–ray flares and prompt emission pulses share the same origin and if they are preferentially produced by IS or ES (the latter due to the interaction with over–densities in the CBM). To answer these questions, in Pescalli et al. (2017 – recently submited to MNRAS) we consider the possible dependence of the pulse width with time along GRBs combining prompt emission pulses with X–ray flares. We derive, under the simplest IS and ES scenarios, the expected relation between the pulse duration and its time of occurrence and compare with observations (see Chp.9).

It is known that prompt emission pulses do not show an increase of the pulse width with time (Ramirez-Ruiz and Fenimore, 2000). XRF, instead, show a nearly linear increase of their width with time (Chincarini et al., 2010; Yi et al., 2016; Kocevski et al., 2007).

Internal shocks predict that the dissipation of energy between shells coasting with slightly different bulk Lorentz factor should pro-

duce random pulses with duration uncorrelated with their time of occurrence. On the other hand, the flare width has been observed to increase with time and considered so far a signature in favour of an external origin. In this scenario, the production of flares occurs in the interaction of a decelerating blast wave with ISM over–densities located at increasing distance from the central engine. In these two scenarios, what determines whether the pulse duration increases with time or not is the dissipation at increasing radii (as in external shocks) or at a constant distance (as in internal shocks).

We verified (see Sec.9.1 for the results and the details of the methods adopted) using two independent samples of prompt emission pulses (pulses obtained by the deconvolution of bright *Fermi* bursts – from Bhat et al. (2012) – and a sample of 100 GRBs with redshift whose light–curves were analyzed in this work) that prompt emission pulses show no correlation between their duration and their time of occurrence. This confirms what obtained by Ramirez-Ruiz and Fenimore (2000) with the BATSE data. Despite the emission during the prompt phase is highly variable, it can be described as the emission due to internal shocks occurring almost at the same distance from the central engine.

XRFs, instead, exhibit an (almost linear) increase of their duration with time (see Fig.9.2). Moreover, their peak luminosity $L_{\rm p}$ anti–correlates with the peak time $t_{\rm peak}$: for early flares ($t_{\rm peak} < 1000$ s, Chincarini et al., 2010; Margutti et al., 2011) $L_{\rm p} \propto t^{-2.7}$ and becomes shallower $L_{\rm p} \propto t^{-1.7}$ for late flares (Bernardini et al., 2011). As a consequence, (as noted by Margutti et al., 2011) the energy released during the flares should scale as $t^{-1.7}$ ($t^{-0.7}$ for late time flares).

The origin of XRFs has been debated in the literature. Temporal and spectral properties of XRFs lead different authors to ascribe them to internal–like dissipation due to the late time activity of the inner engine (Falcone et al., 2006, 2007; Lazzati and Perna, 2007; Maxham and Zhang, 2009; Lazzati et al., 2011). Alternatively, XRFs could be produced by external shocks with over–dense regions of the ISM (e.g. Wang and Loeb, 2000; Lazzati et al., 2002; Heyl and Perna, 2003) or by the long–lived reverse shock interacting with the tail of the ejecta (Hascoet et al., 2015).

In this work we considered the possibility that also XRF are produced by internal shocks between shells emitted with a certain initial separation and a certain (even small) temporal delay with re-

spect the prompt shell. If these shells are characterized by small values of α_Γ, the time of their encounter is delayed (and therefore the shock development). Later flares last longer and are less efficient in emitting radiation. We derived the expected duration and released energy of flares in function of their occurrence time. We compared this theoretical model with the observational data finding good agreement. These results, shown by the red model curves in Fig.9.5 and Fig.9.6, are consistent with the distribution of data in these planes. In this scenario the leading parameter is the relatively low ratio between the shells' Lorentz factors, parametrized by α_Γ. The asymptotic behaviour of the model in the $E_{\rm iso} - t_{\rm peak}$ energy–occurrence time plane, for small α_Γ, is approximately t^{-2} in agreement with the $E \propto L_{\rm p}\Delta t \propto t^{-1.7}$ (also marginally shown by the data points). This behavior also seems to explain the shape of the left boundary of the distribution in the region populated by XRF with low energies and peak time.

In this way we showed that it is possible to explain the energetic and temporal properties of X–ray flares as the result (under appropriate assumptions) of "classical" internal shocks between fireball ejected during the prompt emission phase. We do not require that the inner engine is active until late times: late flares, characterized by smaller energies, can be produced by relativistic shocks between fireballs with Lorentz factor ratio α_Γ very close to one. This result confirms what has been previously found by Barraud et al. (2005) through numerical simulations.

The spectrum characterizing the prompt emission of GRBs is typically non–thermal. Within the standard model, the synchrotron is the leading radiation mechanism adopted to interpret and explain GRB prompt emission (Meszaros and Rees, 1993a,b; Rees and Meszaros, 1994; Sari et al., 1996, 1998). This is the most natural mechanism involving accelerated electrons into intense magnetic fields and it is found to successfully interpret the afterglows emission (Paczynski and Rhoads, 1993; Katz, 1994).

Despite many of the observed GRB spectra are consistent with this interpretation (Tavani, 1996; Cohen et al., 1997), the synchrotron model encounters difficulties in explaining some cases that violate the so–called synchrotron line–of–death (Preece et al., 1998). The predicted spectral index at low energy in the standard synchrotron model (in the fast–cooling regime) should not exceed the value $-3/2$

($-2/3$ if the cooling is inefficient – see Preece et al. 1998; Ghisellini et al. 2000). Despite this theoretical limit a good portion of GRBs seem to violate it (Preece et al., 1998; Ghirlanda et al., 2003, 2002; Kaneko et al., 2006; Nava et al., 2011; Goldstein et al., 2012; Lien et al., 2016), having in average spectral indexes ~ -1 or even harder than $-2/3$ in some cases.

There are many solutions proposed in the literature that interpret the observed hard spectra of GRB prompt emission adopting modifications of the synchrotron theory (Pe'er and Zhang, 2006; Zhao et al., 2014b,a; Medvedev, 2000; Lloyd and Petrosian, 2000; Derishev et al., 2001; Nakar et al., 2009; Daigne et al., 2011; Beniamini and Piran, 2013).

Unfortunately, all these modifications of the standard synchrotron model are almost indistinguishable by observations, since tuned physical properties are required, making the origin of prompt emission still debated. In a recent study, Oganesyan et al. (2017) extended the investigation of the prompt emission spectra down to the soft X–ray band finding consistency with synchrotron radiation from (moderately) fast–cooling electrons. The question being if there exist also GRBs observed by *Fermi* with a break in the low energy part of the spectrum.

In Ravasio et al. (recently submitted for the publication to A&A) we performed time–resolved spectroscopy of GRB 160625B (see Sec.10.2), one of the brightest GRB detected by *Fermi*. We find that almost all the spectra of the main episode are well described by a double Smoothly Broken Power–Law (2SBPL) consisting in three power laws connected by two smooth breaks (see Fig.10.11). The use of this model significantly improves ($F_{\rm test} > 3\sigma$) the fit obtained with the standard SBPL model showing that the addition of a low energy spectral break is required. Intriguingly, the indexes of the power–laws below and above the low energy break that we find are: $\alpha_1 = -0.76 \pm 0.02$ and $\alpha_2 = -1.51 \pm 0.02$ (see Fig.10.14). These values are remarkably consistent with those predicted for the synchrotron emission of a population of electrons that does not cool completely, and therefore presents a low energy cutoff. This is not the only possible explanation for the observed spectrum. In fact, the spectral hardening below $E_{\rm break}$ could be produced by adding a black body component to a typical single break spectrum (as also shown by Zhang et al., 2016; Wang et al., 2017; Lü et al., 2017). Despite this additional emission component is expected within the standard fire-

ball scenario, in such a case it must be fine tuned in order to mimic low energy break, and this fine tuning must be present in each of the time–resolved spectra we analyzed. Our results thus suggests that the observed GRB prompt spectrum is due to synchrotron emission. If we associate the $E_{\rm break}$ (typically ~ 100 keV) found in our analysis to the ν_{cool} of the electrons population, the implied magnetic field is too small with respect to the typically expected value in the emission region (see Sec.10.2.4). This problem can be alleviated considering e.g. a regime of "moderately" fast cooling and some solutions have been proposed such as a decaying magnetic field (Zhao et al., 2014a). However, further investigation and a revision of the standard prompt emission model seems necessary.

The thermal emission is predicted when the relativistically expanding fireball releases the internal photons at the transparency radius (e.g. Goodman, 1986; Paczynski, 1986; Daigne and Mochkovitch, 1998). Nevertheless, the GRBs spectrum is found to be consistent with a black body spectrum only in rare cases (Ghirlanda et al., 2003; Bosnjak et al., 2006; Ryde, 2004; Ghirlanda et al., 2013b) and the majority of GRBs present a non–thermal spectrum.

The few GRBs exhibiting BB spectrum represent a fundamental tool to investigate the origin of the thermal component, its evolution and the basic properties of the relativistic outflow. The detection of a BB spectrum in GRBs allows us to estimate (Pe'er et al., 2007) fundamental parameters of the fireball like the transparency radius R_T, the bulk Lorentz factor Γ_T at transparency and the radius at the base of the relativistic flow R_0 where the acceleration began (see. Sec.2.3). Clearly, when only the thermal component is observed, these estimates depend on a lower number of free parameters (since no modeling of the non–thermal component is required in these cases). Interestingly, it should be explained why in this kind of bursts the non–thermal emission (typically ascribed to synchrotron/inverse Compton emission at internal shocks) is absent: either it could be highly inefficient or there should be a mechanism suppressing this process.

In Nappo et al. (2017) we performed the time–resolved spectral analysis of the prompt emission of GRB 151027A (see Sec.10.1). The first two peaks have a standard non–thermal behaviour while the third peak shows a statistically significant BB component (providing up to 35% of the total luminosity in the $[0.3 - 1000]$ keV band) at low energies superimposed on a cutoff power–law. In this work

we discussed the possible origin of this thermal radiation. Since the radius and the luminosity of the blackbody emission were too large to be interpreted as the photospheric emission of a standard fireball model, we explored a reborn fireball scenario (Ghisellini et al., 2007a) in which the thermal radiation is produced by the energy dissipation due to the collision of a relativistic shell with a more massive, optically thick, slower one.

These bursts are exceptionally informative but open additional questions. GRB 160625B presents a spectrum consistent with synchrotron emission while GRB 151027A has a thermal component which evolves independently from the non-thermal one. These two cases suggest that both non–thermal and thermal emission may have a role in GRB prompt emission. The incidence of these emission component (which might point to different jet compositions) need still to be explored by extending the present analysis to larger samples and, as shown in the case of GRB 160625B, by implementing proper models (possibly more physically based) for the emission spectrum.

List of publications

1. *From the earliest pulses to the latest flares in long GRBs*
Pescalli, **A.**, Ronchi, M., Ghirlanda, G., Ghisellini, G., 2017, Submitted to Monthly Notices of the Royal Astronomical Society

   The prompt emission of Gamma Ray Bursts extends from the early pulses observed in γ–rays (> 15 keV) to very late flares of X–ray photons ($0.3 - 10$ keV). The duration of prompt γ–ray pulses is rather constant while the width of X–ray flares correlates with their peak time suggesting a possible different origin. However, pulses and flares have similar spectral properties. Considering internal and external shock scenarios, we derive how the energy and duration of pulses scale with their time of occurrence and we compare with observations. The absence of an observed correlation between prompt emission pulse duration and its time of occurrence favours an "internal" origin and confirms the earlier results of Ramirez–Ruiz & Fenimore. We show that also the energetic and temporal properties of X–ray flares are consistent with being produced by internal shocks between slow fireballs with a small contrast between their bulk Lorentz factors. These results relax the requirement of a long lasting central engine to explain the latest X–ray flares.

2. *Consistency with synchrotron emission in the bright GRB 160625B observed by Fermi*
Ravasio, M. E., Oganesyan, G., Ghirlanda, G., Nava, L., Ghisellini, G., **Pescalli**, **A.**, Celotti, A., 2017, Submitted to Astronomy & Astrophysics

   We present time resolved spectral analysis of the prompt emis-

sion from GRB 160625B, one of the brightest bursts detected by *Fermi* in its 9 years of operations. Standard empirical functions fail in providing an acceptable fit to the GBM spectral data. The goodness of the fit significantly improves when a low-energy break is added in the fitting function. The spectral break is located around $E_{\rm break} \sim$100 keV, while at $0.5 - 6$ MeV the spectrum displays the usual νF_ν peak energy feature $E_{\rm peak}$. The slopes below and above $E_{\rm break}$ are consistent with the values –0.7 and –1.5, respectively, expected from synchrotron emission produced by a relativistic electron population with a low energy cut–off. The small ratio between $E_{\rm peak}$ and $E_{\rm break}$ implies that the radiative cooling is incomplete, contrary to what expected in strongly magnetized and compact emitting regions. These results demand a revision of the so–called fireball standard model of Gamma–ray bursts.

3. *The 999th Swift gamma-ray burst: Some like it thermal*
Nappo, F., **Pescalli**, **A.**, Oganesyan, G., Ghirlanda, G., Giroletti, M., Melandri, A., Campana, S., Ghisellini, G., Salafia, O. S., D'Avanzo, P., Bernardini, M. G., Covino, S., Carretti, E., Celotti, A., D'Elia, V., Nava, L., Palazzi, E., Poppi, S., Prandoni, I., Righini, S., Rossi, A., Salvaterra, R., Tagliaferri, G., Testa, V., Venturi, T., Vergani, S. D., 2017, Astronomy & Astrophysics, 598, A23

   We present a multi–wavelength study of GRB 151027A. This is the 999th Gamma Ray Burst detected by the *Swift* satellite and it has a densely sampled emission in the X–ray and optical band and has been observed and detected in the radio up to 140 days after the prompt. The multi–wavelength light curve from 500 seconds to 140 days can be modeled through a standard forward shock afterglow but requires an additional emission component to reproduce the early X–ray and optical emission. We present TNG and LBT optical observations performed 19.6, 33.9 and 92.3 days after the trigger which show a bump with respect to a standard afterglow flux decay and are possibly interpreted as due to the underlying supernova and host galaxy (at a level of $\sim 0.4\,\mu$Jy in the optical R band, $R_{\rm AB} \sim 25$). Radio observations, performed with the Sardinia Radio Telescope and Medicina in single dish mode and with the European VLBI Network and Very Long Baseline Array, between day 4 and 140 suggest that the burst exploded in an environment characterized by a

density profile scaling with the distance from the source (wind profile). A remarkable feature of the prompt emission is the presence of a bright flare 100 s after the trigger, lasting $\sim$70 seconds in the soft X–ray band, which was simultaneously detected from the optical band up to the MeV energy range. By combining *Swift*–BAT/XRT and *Fermi*–GBM data, the broad-band (0.3–1000 keV) time resolved spectral analysis of the flare reveals the coexistence of a non–thermal (power law) and thermal blackbody components. The blackbody component contributes up to 35% of the luminosity in the 0.3–1000 keV band. The γ–ray emission observed in *Swift*–BAT and *Fermi*–GBM anticipates and lasts less than the soft X–ray emission as observed by *Swift*–XRT, arguing against a Comptonization origin. The blackbody component could either be produced by an outflow becoming transparent or by the collision of a fast shell with a slow, heavy and optically thick fireball ejected during the quiescent time interval between the initial and later flares of the burst.

4. *Light curves and spectra from off–axis gamma–ray bursts*
Salafia, O.S., Ghisellini, G., **Pescalli**, **A.**, Ghirlanda, G., Nappo, F., 2016, Monthly Notices of the Royal Astronomical Society, 461, 3607

   If gamma-ray burst prompt emission originates at a typical radius, and if material producing the emission moves at relativistic speed, then the variability of the resulting light curve depends on the viewing angle. This is due to the fact that the pulse evolution time-scale is Doppler contracted, while the pulse separation is not. For off-axis viewing angles $\theta_{\rm view} \gtrsim \theta_{\rm jet} + \Gamma^{-1}$, the pulse broadening significantly smears out the light-curve variability. This is largely independent of geometry and emission processes. To explore a specific case, we set up a simple model of a single pulse under the assumption that the pulse rise and decay are dominated by the shell curvature effect. We show that such a pulse observed off-axis is (i) broader, (ii) softer and (iii) displays a different hardness-intensity correlation with respect to the same pulse seen on-axis. For each of these effects, we provide an intuitive physical explanation. We then show how a synthetic light curve made by a superposition of pulses changes with increasing viewing angle. We find that a

highly variable light curve (as seen on-axis) becomes smooth and apparently single-pulsed (when seen off-axis) because of pulse overlap. To test the relevance of this fact, we estimate the fraction of off-axis gamma-ray bursts detectable by Swift as a function of redshift, finding that a sizeable fraction (between 10 per cent and 80 per cent) of nearby ($z < 0.1$) bursts are observed with $\theta_{\rm view} \gtrsim \theta_{\rm jet} + \Gamma^{-1}$. Based on these results, we argue that low-luminosity gamma-ray bursts are consistent with being ordinary bursts seen off-axis.

5. *Short gamma-ray bursts at the dawn of the gravitational wave era*
Ghirlanda, G., Salafia, O. S., **Pescalli**, **A.**, Ghisellini, G., Salvaterra, R., Chassande-Mottin, E., Colpi, M., Nappo, F., D'Avanzo, P., Melandri, A., Bernardini, M. G., Branchesi, M., Campana, S., Ciolfi, R., Covino, S., Götz, D., Vergani, S. D., Zennaro, M., Tagliaferri, G., 2016, Astronomy & Astrophysics, 594, 84,

   We derive the luminosity function $\phi(L)$ and redshift distribution $\Psi(z)$ of short gamma-ray bursts (SGRBs) using all the available observer-frame constraints (i.e. peak flux, fluence, peak energy and duration distributions) of the large population of Fermi SGRBs and the rest-frame properties of a complete sample of SGRBs detected by Swift. We show that a steep $\phi(L) \propto L^{-\alpha}$ with $\alpha \geq 2.0$ is excluded if the full set of constraints is considered. We implement a Markov chain Monte Carlo method to derive the $\phi(L)$ and $\Psi(z)$ functions assuming intrinsic $E_{\rm p} - L_{\rm iso}$ and $E_{\rm p} - E_{\rm iso}$ correlations to hold or, alternatively, that the distributions of intrinsic peak energy, luminosity, and duration are independent. To make our results independent from assumptions on the progenitor (NS-NS binary mergers or other channels) and from uncertainties on the star formation history, we assume a parametric form for the redshift distribution of the population of SGRBs. We find that a relatively flat luminosity function with slope ~ 0.5 below a characteristic break luminosity $\sim 3 \times 10^{52}$ erg s^{-1} and a redshift distribution of SGRBs peaking at $z \sim 1.5 - 2$ satisfy all our constraints. These results also hold if no $E_{\rm p} - L_{\rm iso}$ and $E_{\rm p} - E_{\rm iso}$ correlations are assumed and they do not depend on the choice of the minimum luminosity of the SGRB population. We estimate, within ~ 200 Mpc (i.e. the design aLIGO range for the detection of gravitational waves produced by NS-NS merger events), that there should be 0.007-

0.03 SGRBs yr^{-1} detectable as γ-ray events. Assuming current estimates of NS-NS merger rates and that all NS-NS mergers lead to a SGRB event, we derive a conservative estimate of the average opening angle of SGRBs $\langle\theta_{\rm jet}\rangle \sim 3^\circ - 6^\circ$. The luminosity function implies a prompt emission average luminosity $\langle L\rangle \sim 1.5 \times 10^{52}$ erg s^{-1}, higher by nearly two orders of magnitude than previous findings in the literature, which greatly enhances the chance of observing SGRB "orphan" afterglows. Effort should go in the direction of finding and identifying such orphan afterglows as counterparts of GW events.

6. *Searching for narrow absorption and emission lines in XMM–Newton spectra of gamma–ray bursts*
Campana, S., Braito, V., D'Avanzo, P., Ghirlanda, G., Melandri, A., **Pescalli**, **A.**, Salafia, O. S., Salvaterra, R., Tagliaferri, G., Vergani, S. D., 2016, Astronomy & Astrophysics, 592, 85

   We present the results of a spectroscopic search for narrow emission and absorption features in the X–ray spectra of long gamma–ray burst (GRB) afterglows. Using *XMM–Newton* data, both EPIC and RGS spectra, of six bright (fluence $> 10^{-7}$ erg cm^{-2}) and relatively nearby ($z = 0.54 - 1.41$) GRBs, we performed a blind search for emission or absorption lines that could be related to a high cloud density or metal–rich gas in the environment close to the GRBs. We detected five emission features in four of the six GRBs with an overall statistical significance, assessed through Monte Carlo simulations, of $\leq 3.0\sigma$. Most of the lines are detected around the observed energy of the oxygen edge at ~ 0.5 keV, suggesting that they are not related to the GRB environment but are most likely of Galactic origin. No significant absorption features were detected. A spectral fitting with a free Galactic column density (N_H) testing different models for the Galactic absorption confirms this origin because we found an indication of an excess of Galactic N_H in these four GRBs with respect to the tabulated values.

7. *Are long gamma–ray bursts biased tracers of star formation? Clues from the host galaxies of the Swift/BAT6 complete sample of bright LGRBs. II. Star formation rates and metallicities at $z < 1$*
Japelj, J., Vergani, S. D., Salvaterra, R., D'Avanzo, P., Mannucci, F., Fernandez–Soto, A., Boissier, S., Hunt, L. K., Atek, H., Rodriguez-

Munoz, L., Scodeggio, M., Cristiani, S., Le Floc'h, E., Flores, H., Gallego, J., Ghirlanda, G., Gomboc, A., Hammer, F., Perley, D. A., **Pescalli**, **A.**, Petitjean, P., Puech, M., Rafelski, M., Tagliaferri, G., 2016, Astronomy & Astrophysics, 590, 129

Aims: Long gamma–ray bursts (LGRBs) are associated with the deaths of massive stars and might therefore be a potentially powerful tool for tracing cosmic star formation. However, especially at low redshifts ($z < 1.5$) LGRBs seem to prefer particular types of environment. Our aim is to study the host galaxies of a complete sample of bright LGRBs to investigate the effect of the environment on GRB formation.

Methods: We studied host galaxy spectra of the *Swift*/BAT6 complete sample of 14 $z < 1$ bright LGRBs. We used the detected nebular emission lines to measure the dust extinction, star formation rate (SFR), and nebular metallicity (Z) of the hosts and supplemented the data set with previously measured stellar masses $M_\star$. The distributions of the obtained properties and their interrelations (e.g. mass–metallicity and $SFR--M_\star$ relations) are compared to samples of field star–forming galaxies.

Results: We find that LGRB hosts at $z < 1$ have on average lower SFRs than if they were direct star formation tracers. By directly comparing metallicity distributions of LGRB hosts and star–forming galaxies, we find a good match between the two populations up to $12 + \log\left(\frac{O}{H}\right) \sim 8.4 - 8.5$, after which the paucity of metal–rich LGRB hosts becomes apparent. The LGRB host galaxies of our complete sample are consistent with the mass–metallicity relation at similar mean redshift and stellar masses. The cutoff against high metallicities (and high masses) can explain the low SFR values of LGRB hosts. We find a hint of an increased incidence of starburst galaxies in the *Swift*/BAT6 $z < 1$ sample with respect to that of a field star–forming population. Given that the SFRs are low on average, the latter is ascribed to low stellar masses. Nevertheless, the limits on the completeness and metallicity availability of current surveys, coupled with the limited number of LGRB host galaxies, prevents us from investigating more quantitatively whether the starburst incidence is such as expected after taking into account the high–metallicity aversion of LGRB host galaxies.

8. *The rate and luminosity function of long gamma ray bursts*
Pescalli, **A.**, Ghirlanda, G., Salvaterra, R., Ghisellini, G., Vergani, S. D., Nappo, F., Salafia, O. S., Melandri, A., Covino, S., Götz, D., 2016, Astronomy & Astrophysics, 587, A40

   We derive, adopting a direct method, the luminosity function and the formation rate of long Gamma Ray Bursts through a complete, flux-limited, sample of Swift bursts which has a high level of completeness in redshift z ($\sim$ 82%). We parametrise the redshift evolution of the GRB luminosity as $L = L_0(1+z)^k$ and we derive $k = 2.5$, consistently with recent estimates. The de-evolved luminosity function $\phi(L_0)$ of GRBs can be represented by a broken power law with slopes $a = -1.32 \pm 0.21$ and $b = -1.84 \pm 0.24$ below and above, respectively, a break luminosity $L_{0,\mathrm{b}} = 10^{51.45 \pm 0.15}$ erg/s. Under the hypothesis of luminosity evolution we find that the GRB formation rate increases with redshift up to $z \sim 2$, where it peaks, and then decreases in agreement with the shape of the cosmic star formation rate. We test the direct method through numerical simulations and we show that if it is applied to incomplete (both in redshift and/or flux) GRB samples it can misleadingly result in an excess of the GRB formation rate at low redshifts.

9. *Structure of gamma–ray burst jets: intrinsic versus apparent properties*
Salafia, O.S., Ghisellini, G., **Pescalli**, **A.**, Ghirlanda, G., Nappo, F., 2015, Monthly Notices of the Royal Astronomical Society, 450, 3549

   With this paper we introduce the concept of apparent structure of a gamma-ray burst (GRB) jet, as opposed to its intrinsic structure. The latter is customarily defined specifying the functions $\epsilon(\theta)$ (the energy emitted per jet unit solid angle) and $\Gamma(\theta)$ (the Lorentz factor of the emitting material); the apparent structure is instead defined by us as the isotropic equivalent energy $E_{\mathrm{iso}}(\theta_{\mathrm{v}})$ as a function of the viewing angle θ_{v}. We show how to predict the apparent structure of a jet given its intrinsic structure. We find that a Gaussian intrinsic structure yields

a power-law apparent structure: this opens a new viewpoint on the Gaussian (which can be understood as a proxy for a realistic narrow, well-collimated jet structure) as a possible candidate for a quasi-universal GRB jet structure. We show that such a model (a) is consistent with recent constraints on the observed luminosity function of GRBs; (b) implies fewer orphan afterglows with respect to the standard uniform model; (c) can break out the progenitor star (in the collapsar scenario) without wasting an unreasonable amount of energy; (d) is compatible with the explanation of the Amati correlation as a viewing angle effect; (e) can be very standard in energy content, and still yield a very wide range of observed isotropic equivalent energies.

10. *Unveiling the population of orphan γ-ray bursts*
Ghirlanda, G., Salvaterra, R., Campana, S., Vergani, S. D., Japelj, J., Bernardini, M. G., Burlon, D., D'Avanzo, P., Melandri, A., Gomboc, A., Nappo, F., Paladini, R., **Pescalli**, **A.**, Salafia, O. S., Tagliaferri, G., 2015, Astronomy & Astrophysics, 578, A71

Gamma-ray bursts (GRBs) are detectable in the γ-ray band if their jets are oriented toward the observer. However, for each GRB with a typical $\theta_{\rm jet}$, there should be $\sim 2/\theta_{\rm jet}^2$ bursts whose emission cone is oriented elsewhere in space. These off-axis bursts can eventually be detected when, due to the deceleration of their relativistic jets, the beaming angle becomes comparable to the viewing angle. Orphan afterglows (OAs) should outnumber the current population of bursts detected in the γ-ray band even if they have not been conclusively observed so far at any frequency. We compute the expected flux of the population of orphan afterglows in the mm, optical, and X-ray bands through a population synthesis code of GRBs and the standard afterglow emission model. We estimate the detection rate of OAs with ongoing and forthcoming surveys. The average duration of OAs as transients above a given limiting flux is derived and described with analytical expressions: in general OAs should appear as daily transients in optical surveys and as monthly/yearly transients in the mm/radio band. We find that ~ 2 OA yr^{-1} could already be detected by Gaia and up to 20 OA yr^{-1} could be observed by the ZTF survey. A larger number of

50 OA yr^{-1} should be detected by LSST in the optical band. For the X-ray band,$\sim$ 26 OA yr^{-1} could be detected by the eROSITA. For the large population of OA detectable by LSST, the X-ray and optical follow up of the light curve (for the brightest cases) and/or the extensive follow up of their emission in the mm and radio band could be the key to disentangling their GRB nature from other extragalactic transients of comparable flux density.

11. *Luminosity function and jet structure of Gamma-Ray Burst*
Pescalli, **A.**, Ghirlanda, G., Salafia, O.S., Ghisellini, G., Nappo, F., Salvaterra, R., 2015, Monthly Notices of the Royal Astronomical Society, 447, 1911

    The structure of gamma-ray burst (GRB) jets impacts on their prompt and afterglow emission properties. The jet of GRBs could be uniform, with constant energy per unit solid angle within the jet aperture, or it could be structured, namely with energy and velocity that depend on the angular distance from the axis of the jet. We try to get some insight about the still unknown structure of GRBs by studying their luminosity function. We show that low (10^{46-48} erg s^{-1}) and high (i.e. with $L \geq 10^{50}$ erg s^{-1}) luminosity GRBs can be described by a unique luminosity function, which is also consistent with current lower limits in the intermediate luminosity range (10^{48-50} erg s^{-1}). We derive analytical expressions for the luminosity function of GRBs in uniform and structured jet models and compare them with the data. Uniform jets can reproduce the entire luminosity function with reasonable values of the free parameters. A structured jet can also fit adequately the current data, provided that the energy within the jet is relatively strongly structured, i.e. $E \propto \theta^{-k}$ with $k \geq 4$. The classical $E \propto \theta^{-2}$ structured jet model is excluded by the current data.

12. *Gamma-ray burst jets: uniform or structured?*
Salafia, O. S., **Pescalli**, **A.**, Nappo, F., Ghisellini, G., Ghirlanda, G., Salvaterra, R., Tagliaferri, G., 2014, Proceedings of Swift: 10 Years of Discovery (SWIFT 10)

    The structure of Gamma-Ray Burst (GRB) jets impacts on their prompt and afterglow emission properties. Insights into the

still unknown structure of GRBs can be achieved by studying how different structures impact on the luminosity function (LF): i) we show that low ($10^{46} < L_{\rm iso} < 10^{48}$ erg/s) and high (i.e. with $L_{\rm iso} > 10^{50}$ erg/s) luminosity GRBs can be described by a unique LF; ii) we find that a uniform jet (seen on- and off-axis) as well as a very steep structured jet (i.e. $\varepsilon(\theta) \propto \theta^{-s}$ with $s > 4$) can reproduce the current LF data; iii) taking into account the emission from the whole jet (i.e. including contributions from mildly relativistic, off-axis jet elements) we find that $E_{\rm iso}(\theta_{\rm v})$ (we dub this quantity "apparent structure") can be very different from the intrinsic structure $\varepsilon(\theta)$: in particular, a jet with a Gaussian intrinsic structure has an apparent structure which is more similar to a power law. This opens a new viewpoint on the quasi-universal structured jet hypothesis.

13. *Photospheric emission throughout GRB 100507 detected by Fermi*
Ghirlanda, G., **Pescalli**, **A.** and Ghisellini, G., 2013, Monthly Notices of the Royal Astronomical Society, 432, 3237

Gamma–ray bursts with black body spectra are only a few and in most cases this spectral component is accompanied by a dominating non–thermal one. Only four bursts detected by Burst And Transient Source Experiment have a pure black body spectrum throughout their duration. We present the new case of GRB 100507 detected by the Gamma Burst Monitor on board the *Fermi* satellite. GRB 100507 has a black body spectrum for the entire duration ($\sim$ 30 s) of the prompt emission. The black body temperature varies between 25 and 40 keV. The flux varies between 10^{-7} and 4×10^{-7} erg cm^{-2} s^{-1}. There is no clear evidence of a correlation between the temperature and the black body flux. If the thermal emission in GRB 100507 is due to the fireballs becoming transparent, we can estimate the radius R_T and bulk Lorentz factor Γ_T corresponding to this transition and the radius R_0 where the fireballs are created. We compare these parameters with those derived for the other four bursts with a pure black body spectrum. In all but one burst, for fiducial assumptions on the radiative efficiency and distance of the sources, $R_0 \sim 10^9 - 10^{10}$ cm, i.e. much larger than the gravitational radius of a few solar mass black hole. Possible solutions of this apparent inconsistency are tentatively discussed considering the dependence of R_0 on the unknown parameters. Alterna-

tively, such a large R_0 could be where the fireball, still opaque, converts most of its kinetic energy into internal energy (due to the impact with some material left over by the progenitor star) and starts to re–accelerate.

Bibliography

B. P. Abbott, R. Abbott, T. D. Abbott, M. R. Abernathy, F. Acernese, K. Ackley, C. Adams, T. Adams, P. Addesso, R. X. Adhikari, and et al. Prospects for Observing and Localizing Gravitational-Wave Transients with Advanced LIGO and Advanced Virgo. *Living Reviews in Relativity*, 19:1, February 2016a. doi: 10.1007/lrr-2016-1.

B. P. Abbott, R. Abbott, T. D. Abbott, M. R. Abernathy, F. Acernese, K. Ackley, C. Adams, T. Adams, P. Addesso, R. X. Adhikari, and et al. Binary Black Hole Mergers in the First Advanced LIGO Observing Run. *Physical Review X*, 6(4):041015, October 2016b. doi: 10.1103/PhysRevX.6.041015.

A. A. Abdo, M. Ackermann, M. Arimoto, K. Asano, W. B. Atwood, M. Axelsson, L. Baldini, J. Ballet, D. L. Band, G. Barbiellini, and et al. Fermi Observations of High-Energy Gamma-Ray Emission from GRB 080916C. *Science*, 323:1688, March 2009a. doi: 10.1126/science.1169101.

A. A. Abdo, M. Ackermann, K. Asano, W. B. Atwood, M. Axelsson, L. Baldini, J. Ballet, D. L. Band, G. Barbiellini, D. Bastieri, K. Bechtol, R. Bellazzini, B. Berenji, P. N. Bhat, E. Bissaldi, E. D. Bloom, E. Bonamente, A. W. Borgland, A. Bouvier, J. Bregeon, A. Brez, M. S. Briggs, M. Brigida, P. Bruel, T. H. Burnett, G. A. Caliandro, R. A. Cameron, P. A. Caraveo, J. M. Casandjian, C. Cecchi, V. Chaplin, A. Chekhtman, C. C. Cheung, J. Chiang, S. Ciprini, R. Claus, J. Cohen-Tanugi, L. R. Cominsky, V. Connaughton, J. Conrad, S. Cutini, C. D. Dermer, A. de Angelis, F. de Palma, S. W. Digel, E. d. C. e. Silva, P. S. Drell, R. Dubois, D. Dumora, C. Farnier, C. Favuzzi, W. B. Focke, M. Frailis, Y. Fukazawa, P. Fusco, F. Gargano, D. Gasparrini, N. Gehrels, S. Germani, L. Gibby, B. Giebels, N. Giglietto, F. Giordano, T. Glanzman, G. Godfrey, A. Goldstein, J. Granot, I. A. Grenier, M.-H. Grondin, J. E. Grove, L. Guillemot, S. Guiriec, Y. Hanabata, A. K. Harding, M. Hayashida, E. Hays, R. E. Hughes, G. Jóhannesson, A. S. Johnson, W. N. Johnson, T. Kamae, H. Katagiri, J. Kataoka, N. Kawai, M. Kerr, J. Knödlseder, D. Kocevski, N. Komin, C. Kouveliotou, F. Kuehn, M. Kuss, L. Latronico, F. Longo, F. Loparco, B. Lott, M. N. Lovellette, P. Lubrano, A. Makeev, M. N. Mazziotta, S. McBreen, J. E. McEnery, S. McGlynn, C. Meegan, C. Meurer, P. F. Michelson, W. Mitthumsiri, T. Mizuno, C. Monte, M. E. Monzani, E. Moretti, A. Morselli, I. V. Moskalenko, S. Murgia, T. Nakamori, P. L. Nolan, J. P. Norris, E. Nuss, M. Ohno, T. Ohsugi, N. Omodei,

E. Orlando, J. F. Ormes, M. Ozaki, W. S. Paciesas, D. Paneque, J. H. Panetta, D. Parent, V. Pelassa, M. Pepe, M. Pesce-Rollins, F. Piron, T. A. Porter, R. Preece, S. Rainò, R. Rando, M. Razzano, S. Razzaque, O. Reimer, T. Reposeur, S. Ritz, L. S. Rochester, A. Y. Rodriguez, M. Roth, F. Ryde, H. F.-W. Sadrozinski, D. Sanchez, A. Sander, P. M. Saz Parkinson, J. D. Scargle, C. Sgrò, E. J. Siskind, D. A. Smith, P. D. Smith, G. Spandre, P. Spinelli, M. Stamatikos, M. S. Strickman, D. J. Suson, H. Tajima, H. Takahashi, T. Tanaka, J. B. Thayer, J. G. Thayer, L. Tibaldo, D. F. Torres, G. Tosti, A. Tramacere, Y. Uchiyama, T. L. Usher, A. J. van der Horst, V. Vasileiou, N. Vilchez, V. Vitale, A. von Kienlin, A. P. Waite, P. Wang, C. Wilson-Hodge, B. L. Winer, K. S. Wood, T. Ylinen, and M. Ziegler. Fermi Observations of High-energy Gamma-ray Emission from GRB 080825C. *ApJ*, 707:580–592, December 2009b. doi: 10.1088/0004-637X/707/1/580.

F. Acernese, M. Agathos, K. Agatsuma, D. Aisa, N. Allemandou, A. Allocca, J. Amarni, P. Astone, G. Balestri, G. Ballardin, and et al. Advanced Virgo: a second-generation interferometric gravitational wave detector. *Classical and Quantum Gravity*, 32(2):024001, January 2015. doi: 10.1088/0264-9381/32/2/024001.

M. Ackermann, M. Ajello, L. Baldini, J. Ballet, G. Barbiellini, M. G. Baring, D. Bastieri, K. Bechtol, R. Bellazzini, B. Berenji, P. N. Bhat, E. Bissaldi, R. D. Blandford, E. Bonamente, A. W. Borgland, A. Bouvier, J. Bregeon, A. Brez, M. S. Briggs, M. Brigida, P. Bruel, R. Buehler, S. Buson, G. A. Caliandro, R. A. Cameron, P. A. Caraveo, S. Carrigan, J. M. Casandjian, C. Cecchi, Ö. Çelik, E. Charles, A. Chekhtman, J. Chiang, S. Ciprini, R. Claus, J. Cohen-Tanugi, V. Connaughton, J. Conrad, S. Cutini, C. D. Dermer, A. de Angelis, F. de Palma, S. W. Digel, E. d. C. e. Silva, P. S. Drell, R. Dubois, C. Favuzzi, S. J. Fegan, E. C. Ferrara, M. Frailis, Y. Fukazawa, P. Fusco, F. Gargano, D. Gasparrini, N. Gehrels, S. Germani, N. Giglietto, P. Giommi, F. Giordano, M. Giroletti, T. Glanzman, G. Godfrey, J. Granot, I. A. Grenier, J. E. Grove, L. Guillemot, S. Guiriec, D. Hadasch, E. Hays, D. Horan, R. E. Hughes, G. Jóhannesson, A. S. Johnson, W. N. Johnson, T. Kamae, H. Katagiri, R. M. Kippen, J. Knödlseder, D. Kocevski, M. Kuss, J. Lande, L. Latronico, S.-H. Lee, M. Llena Garde, F. Longo, F. Loparco, M. N. Lovellette, P. Lubrano, A. Makeev, M. N. Mazziotta, S. McBreen, J. E. McEnery, S. McGlynn, C. Meegan, J. Mehault, P. Mészáros, P. F. Michelson, T. Mizuno, A. A. Moiseev, C. Monte, M. E. Monzani, E. Moretti, A. Morselli, I. V. Moskalenko, S. Murgia, H. Nakajima, T. Nakamori, M. Naumann-Godo, P. L. Nolan, J. P. Norris, E. Nuss, M. Ohno, T. Ohsugi, A. Okumura, N. Omodei, E. Orlando, J. F. Ormes, M. Ozaki, W. S. Paciesas, D. Paneque, J. H. Panetta, D. Parent, V. Pelassa, M. Pepe, M. Pesce-Rollins, V. Petrosian, F. Piron, T. A. Porter, R. Preece, J. L. Racusin, S. Rainò, R. Rando, A. Rau, M. Razzano, S. Razzaque, A. Reimer, O. Reimer, J. Ripken, M. Roth, F. Ryde, H. F.-W. Sadrozinski, A. Sander, J. D. Scargle, T. L. Schalk, C. Sgrò, E. J. Siskind, P. D. Smith, G. Spandre, P. Spinelli, M. Stamatikos, M. S. Strickman, D. J. Suson, H. Tajima, H. Takahashi, T. Tanaka, J. B. Thayer, J. G. Thayer, L. Tibaldo, D. F. Torres, G. Tosti, A. Tramacere, T. Uehara, T. L. Usher, J. Vandenbroucke, A. J. van der Horst, V. Vasileiou, N. Vilchez, V. Vitale, A. von Kienlin, A. P. Waite, P. Wang, C. Wilson-Hodge, B. L. Winer, K. S. Wood, X. F. Wu, R. Yamazaki, Z. Yang, T. Ylinen, M. Ziegler, Fermi LAT Collaboration, and Fermi GBM Collaboration. Fermi Observations of High-energy Gamma-ray Emission from GRB 090217A. *ApJ*, 717:L127–L132, July 2010. doi: 10.1088/2041-8205/717/2/L127.

M. Ackermann, M. Ajello, K. Asano, M. Axelsson, L. Baldini, J. Ballet, G. Barbiellini, D. Bastieri, K. Bechtol, R. Bellazzini, P. N. Bhat, E. Bissaldi, E. D. Bloom, E. Bonamente, J. Bonnell, A. Bouvier, T. J. Brandt, J. Bregeon, M. Brigida, P. Bruel, R. Buehler, J. M. Burgess, S. Buson, D. Byrne, G. A. Caliandro, R. A. Cameron, P. A. Caraveo, C. Cecchi, E. Charles, R. C. G. Chaves, A. Chekhtman, J. Chiang, G. Chiaro, S. Ciprini, R. Claus,

J. Cohen-Tanugi, V. Connaughton, J. Conrad, S. Cutini, F. D'Ammando, A. de Angelis, F. de Palma, C. D. Dermer, R. Desiante, S. W. Digel, B. L. Dingus, L. Di Venere, P. S. Drell, A. Drlica-Wagner, R. Dubois, C. Favuzzi, E. C. Ferrara, G. Fitzpatrick, S. Foley, A. Franckowiak, Y. Fukazawa, P. Fusco, F. Gargano, D. Gasparrini, N. Gehrels, S. Germani, N. Giglietto, P. Giommi, F. Giordano, M. Giroletti, T. Glanzman, G. Godfrey, A. Goldstein, J. Granot, I. A. Grenier, J. E. Grove, D. Gruber, S. Guiriec, D. Hadasch, Y. Hanabata, M. Hayashida, D. Horan, X. Hou, R. E. Hughes, Y. Inoue, M. S. Jackson, T. Jogler, G. Jóhannesson, A. S. Johnson, W. N. Johnson, T. Kamae, J. Kataoka, T. Kawano, R. M. Kippen, J. Knödlseder, D. Kocevski, C. Kouveliotou, M. Kuss, J. Lande, S. Larsson, L. Latronico, S.-H. Lee, F. Longo, F. Loparco, M. N. Lovellette, P. Lubrano, F. Massaro, M. Mayer, M. N. Mazziotta, S. McBreen, J. E. McEnery, S. McGlynn, P. F. Michelson, T. Mizuno, A. A. Moiseev, C. Monte, M. E. Monzani, E. Moretti, A. Morselli, S. Murgia, R. Nemmen, E. Nuss, T. Nymark, M. Ohno, T. Ohsugi, N. Omodei, M. Orienti, E. Orlando, W. S. Paciesas, D. Paneque, J. H. Panetta, V. Pelassa, J. S. Perkins, M. Pesce-Rollins, F. Piron, G. Pivato, T. A. Porter, R. Preece, J. L. Racusin, S. Rainò, R. Rando, A. Rau, M. Razzano, S. Razzaque, A. Reimer, O. Reimer, T. Reposeur, S. Ritz, C. Romoli, M. Roth, F. Ryde, P. M. Saz Parkinson, T. L. Schalk, C. Sgrò, E. J. Siskind, E. Sonbas, G. Spandre, P. Spinelli, D. J. Suson, H. Tajima, H. Takahashi, Y. Takeuchi, Y. Tanaka, J. G. Thayer, J. B. Thayer, D. J. Thompson, L. Tibaldo, D. Tierney, M. Tinivella, D. F. Torres, G. Tosti, E. Troja, V. Tronconi, T. L. Usher, J. Vandenbroucke, A. J. van der Horst, V. Vasileiou, G. Vianello, V. Vitale, A. von Kienlin, B. L. Winer, K. S. Wood, M. Wood, S. Xiong, and Z. Yang. The First Fermi-LAT Gamma-Ray Burst Catalog. *ApJ*, 209:11, November 2013. doi: 10.1088/0067-0049/209/1/11.

M. Ackermann, M. Ajello, K. Asano, W. B. Atwood, M. Axelsson, L. Baldini, J. Ballet, G. Barbiellini, M. G. Baring, D. Bastieri, K. Bechtol, R. Bellazzini, E. Bissaldi, E. Bonamente, J. Bregeon, M. Brigida, P. Bruel, R. Buehler, J. M. Burgess, S. Buson, G. A. Caliandro, R. A. Cameron, P. A. Caraveo, C. Cecchi, V. Chaplin, E. Charles, A. Chekhtman, C. C. Cheung, J. Chiang, G. Chiaro, S. Ciprini, R. Claus, W. Cleveland, J. Cohen-Tanugi, A. Collazzi, L. R. Cominsky, V. Connaughton, J. Conrad, S. Cutini, F. D'Ammando, A. de Angelis, M. DeKlotz, F. de Palma, C. D. Dermer, R. Desiante, A. Diekmann, L. Di Venere, P. S. Drell, A. Drlica-Wagner, C. Favuzzi, S. J. Fegan, E. C. Ferrara, J. Finke, G. Fitzpatrick, W. B. Focke, A. Franckowiak, Y. Fukazawa, S. Funk, P. Fusco, F. Gargano, N. Gehrels, S. Germani, M. Gibby, N. Giglietto, M. Giles, F. Giordano, M. Giroletti, G. Godfrey, J. Granot, I. A. Grenier, J. E. Grove, D. Gruber, S. Guiriec, D. Hadasch, Y. Hanabata, A. K. Harding, M. Hayashida, E. Hays, D. Horan, R. E. Hughes, Y. Inoue, T. Jogler, G. Jóhannesson, W. N. Johnson, T. Kawano, J. Knödlseder, D. Kocevski, M. Kuss, J. Lande, S. Larsson, L. Latronico, F. Longo, F. Loparco, M. N. Lovellette, P. Lubrano, M. Mayer, M. N. Mazziotta, J. E. McEnery, P. F. Michelson, T. Mizuno, A. A. Moiseev, M. E. Monzani, E. Moretti, A. Morselli, I. V. Moskalenko, S. Murgia, R. Nemmen, E. Nuss, M. Ohno, T. Ohsugi, A. Okumura, N. Omodei, M. Orienti, D. Paneque, V. Pelassa, J. S. Perkins, M. Pesce-Rollins, V. Petrosian, F. Piron, G. Pivato, T. A. Porter, J. L. Racusin, S. Rainò, R. Rando, M. Razzano, S. Razzaque, A. Reimer, O. Reimer, S. Ritz, M. Roth, F. Ryde, A. Sartori, P. M. S. Parkinson, J. D. Scargle, A. Schulz, C. Sgrò, E. J. Siskind, E. Sonbas, G. Spandre, P. Spinelli, H. Tajima, H. Takahashi, J. G. Thayer, J. B. Thayer, D. J. Thompson, L. Tibaldo, M. Tinivella, D. F. Torres, G. Tosti, E. Troja, T. L. Usher, J. Vandenbroucke, V. Vasileiou, G. Vianello, V. Vitale, B. L. Winer, K. S. Wood, R. Yamazaki, G. Younes, H.-F. Yu, S. J. Zhu, P. N. Bhat, M. S. Briggs, D. Byrne, S. Foley, A. Goldstein, P. Jenke, R. M. Kippen, C. Kouveliotou, S. McBreen, C. Meegan, W. S. Paciesas, R. Preece, A. Rau, D. Tierney, A. J. van der Horst, A. von Kienlin, C. Wilson-Hodge, S. Xiong, G. Cusumano, V. La Parola, and J. R. Cummings. Fermi-LAT Observations of the Gamma-Ray Burst GRB 130427A.

Science, 343:42–47, January 2014. doi: 10.1126/science.1242353.

D. M. Alexander, F. E. Bauer, W. N. Brandt, D. P. Schneider, A. E. Hornschemeier, C. Vignali, A. J. Barger, P. S. Broos, L. L. Cowie, G. P. Garmire, L. K. Townsley, M. W. Bautz, G. Chartas, and W. L. W. Sargent. The Chandra Deep Field North Survey. XIII. 2 Ms Point-Source Catalogs. *Astronomical Journal*, 126:539–574, August 2003. doi: 10.1086/376473.

K. D. Alexander, T. Laskar, E. Berger, C. Guidorzi, S. Dichiara, W. Fong, A. Gomboc, S. Kobayashi, D. Kopac, C. G. Mundell, N. R. Tanvir, and P. K. G. Williams. A Reverse Shock and Unusual Radio Properties in GRB 160625B. *ArXiv e-prints*, May 2017.

L. Amati. The $E_{p,i}$-E_{iso} correlation in gamma-ray bursts: updated observational status, reanalysis and main implications. *MNRAS*, 372:233–245, October 2006. doi: 10.1111/j.1365-2966.2006.10840.x.

L. Amati, F. Frontera, M. Tavani, J. J. M. in't Zand, A. Antonelli, E. Costa, M. Feroci, C. Guidorzi, J. Heise, N. Masetti, E. Montanari, L. Nicastro, E. Palazzi, E. Pian, L. Piro, and P. Soffitta. Intrinsic spectra and energetics of BeppoSAX Gamma-Ray Bursts with known redshifts. *A&A*, 390:81–89, July 2002. doi: 10.1051/0004-6361:20020722.

R. L. Aptekar, D. D. Frederiks, S. V. Golenetskii, V. N. Ilynskii, E. P. Mazets, V. N. Panov, Z. J. Sokolova, M. M. Terekhov, L. O. Sheshin, T. L. Cline, and D. E. Stilwell. Konus-W Gamma-Ray Burst Experiment for the GGS Wind Spacecraft. *Space Sci. Rev.*, 71:265–272, February 1995. doi: 10.1007/BF00751332.

K. A. Arnaud. XSPEC: The First Ten Years. In G. H. Jacoby and J. Barnes, editors, *Astronomical Data Analysis Software and Systems V*, volume 101 of *Astronomical Society of the Pacific Conference Series*, page 17, 1996.

Y. Avni and J. N. Bahcall. On the simultaneous analysis of several complete samples - The V/Vmax and Ve/Va variables, with applications to quasars. *ApJ*, 235:694–716, February 1980. doi: 10.1086/157673.

M. Axelsson, L. Baldini, G. Barbiellini, M. G. Baring, R. Bellazzini, J. Bregeon, M. Brigida, P. Bruel, R. Buehler, G. A. Caliandro, R. A. Cameron, P. A. Caraveo, C. Cecchi, R. C. G. Chaves, A. Chekhtman, J. Chiang, R. Claus, J. Conrad, S. Cutini, F. D'Ammando, F. de Palma, C. D. Dermer, E. d. C. e. Silva, P. S. Drell, C. Favuzzi, S. J. Fegan, E. C. Ferrara, W. B. Focke, Y. Fukazawa, P. Fusco, F. Gargano, D. Gasparrini, N. Gehrels, S. Germani, N. Giglietto, M. Giroletti, G. Godfrey, S. Guiriec, D. Hadasch, Y. Hanabata, M. Hayashida, X. Hou, S. Iyyani, M. S. Jackson, D. Kocevski, M. Kuss, J. Larsson, S. Larsson, F. Longo, F. Loparco, C. Lundman, M. N. Mazziotta, J. E. McEnery, T. Mizuno, M. E. Monzani, E. Moretti, A. Morselli, S. Murgia, E. Nuss, T. Nymark, M. Ohno, N. Omodei, M. Pesce-Rollins, F. Piron, G. Pivato, J. L. Racusin, S. Rainò, M. Razzano, S. Razzaque, A. Reimer, M. Roth, F. Ryde, D. A. Sanchez, C. Sgrò, E. J. Siskind, G. Spandre, P. Spinelli, M. Stamatikos, L. Tibaldo, M. Tinivella, T. L. Usher, J. Vandenbroucke, V. Vasileiou, G. Vianello, V. Vitale, A. P. Waite, B. L. Winer, K. S. Wood, J. M. Burgess, P. N. Bhat, E. Bissaldi, M. S. Briggs, V. Connaughton, G. Fishman, G. Fitzpatrick, S. Foley, D. Gruber, R. M. Kippen, C. Kouveliotou, P. Jenke, S. McBreen, S. McGlynn, C. Meegan, W. S. Paciesas, V. Pelassa, R. Preece, D. Tierney, A. von Kienlin, C. Wilson-Hodge, S. Xiong, and A. Pe'er. GRB110721A: An Extreme Peak Energy and Signatures of the Photosphere. *ApJ*, 757:L31, October 2012. doi: 10.1088/2041-8205/757/2/L31.

D. Band, J. Matteson, L. Ford, B. Schaefer, D. Palmer, B. Teegarden, T. Cline, M. Briggs, W. Paciesas, G. Pendleton, G. Fishman, C. Kouveliotou, C. Meegan, R. Wilson, and P. Lestrade. BATSE observations of gamma-ray burst spectra. I - Spectral diversity. *ApJ*, 413:281–292, August 1993. doi: 10.1086/172995.

D. L. Band. A Gamma-Ray Burst Trigger Tool Kit. *ApJ*, 578:806–811, October 2002. doi: 10.1086/342661.

D. L. Band. Postlaunch Analysis of Swift's Gamma-Ray Burst Detection Sensitivity. *ApJ*, 644:378–384, June 2006. doi: 10.1086/503326.

K. W. Bannister, T. Murphy, B. M. Gaensler, R. W. Hunstead, and S. Chatterjee. Erratum: A 22-yr southern sky survey for transient and variable radio sources using the Molonglo Observatory Synthesis Telescope. *MNRAS*, 418:2813–2814, December 2011. doi: 10.1111/j.1365-2966.2011.19739.x.

C. Barraud, F. Daigne, R. Mochkovitch, and J. L. Atteia. On the nature of X-ray flashes. *A&A*, 440:809–817, September 2005. doi: 10.1051/0004-6361:20041572.

S. D. Barthelmy, L. M. Barbier, J. R. Cummings, E. E. Fenimore, N. Gehrels, D. Hullinger, H. A. Krimm, C. B. Markwardt, D. M. Palmer, A. Parsons, G. Sato, M. Suzuki, T. Takahashi, M. Tashiro, and J. Tueller. The Burst Alert Telescope (BAT) on the SWIFT Midex Mission. *Space Science Review*, 120:143–164, October 2005. doi: 10.1007/s11214-005-5096-3.

A. C. Becker, D. M. Wittman, P. C. Boeshaar, A. Clocchiatti, I. P. Dell'Antonio, D. A. Frail, J. Halpern, V. E. Margoniner, D. Norman, J. A. Tyson, and R. A. Schommer. The Deep Lens Survey Transient Search. I. Short Timescale and Astrometric Variability. *ApJ*, 611:418–433, August 2004. doi: 10.1086/421994.

K. Belczynski, R. Perna, T. Bulik, V. Kalogera, N. Ivanova, and D. Q. Lamb. A Study of Compact Object Mergers as Short Gamma-Ray Burst Progenitors. *ApJ*, 648:1110–1116, September 2006. doi: 10.1086/505169.

M. E. Bell, R. P. Fender, J. Swinbank, J. C. A. Miller-Jones, C. J. Law, B. Scheers, H. Spreeuw, M. W. Wise, B. W. Stappers, R. A. M. J. Wijers, J. W. T. Hessels, and J. Masters. An automated archival Very Large Array transients survey. *MNRAS*, 415:2–10, July 2011. doi: 10.1111/j.1365-2966.2011.18631.x.

E. Bellm. The Zwicky Transient Facility. In P. R. Wozniak, M. J. Graham, A. A. Mahabal, and R. Seaman, editors, *The Third Hot–wiring the Transient Universe Workshop*, pages 27–33, 2014.

A. M. Beloborodov. On the Efficiency of Internal Shocks in Gamma-Ray Bursts. *ApJ*, 539:L25–L28, August 2000. doi: 10.1086/312830.

A. M. Beloborodov. Collisional mechanism for gamma-ray burst emission. *MNRAS*, 407:1033–1047, September 2010. doi: 10.1111/j.1365-2966.2010.16770.x.

P. Beniamini and T. Piran. Constraints on the Synchrotron Emission Mechanism in Gamma-Ray Bursts. *ApJ*, 769:69, May 2013. doi: 10.1088/0004-637X/769/1/69.

E. Berger. Short-Duration Gamma-Ray Bursts. *A&A*, 52:43–105, August 2014. doi: 10.1146/annurev-astro-081913-035926.

M. G. Bernardini, R. Margutti, G. Chincarini, C. Guidorzi, and J. Mao. Gamma-ray burst long lasting X-ray flaring activity. *A&A*, 526:A27, February 2011. doi: 10.1051/0004-6361/201015703.

M. G. Bernardini, S. Campana, G. Ghisellini, P. D'Avanzo, D. Burlon, S. Covino, G. Ghirlanda, A. Melandri, R. Salvaterra, S. D. Vergani, V. D'Elia, D. Fugazza, B. Sbarufatti, and G. Tagliaferri. How to Switch a Gamma-Ray Burst On and Off through a Magnetar. *ApJ*, 775:67, September 2013. doi: 10.1088/0004-637X/775/1/67.

M. G. Bernardini, S. Campana, G. Ghisellini, P. D'Avanzo, G. Calderone, S. Covino, G. Cusumano, G. Ghirlanda, V. La Parola, A. Maselli, A. Melandri, R. Salvaterra, D. Burlon, V. D'Elia, D. Fugazza, B. Sbarufatti, S. D. Vergani, and G. Tagliaferri. A magnetar powering the ordinary monster GRB 130427A? *MNRAS*, 439:L80–L84, March 2014. doi: 10.1093/mnrasl/slu003.

P. N. Bhat, G. J. Fishman, C. A. Meegan, R. B. Wilson, M. N. Brock, and W. S. Paciesas. Evidence of sub-millisecond structure in a gamma-ray burst. *Nature*, 359:217, September 1992. doi: 10.1038/359217a0.

P. N. Bhat, M. S. Briggs, V. Connaughton, C. Kouveliotou, A. J. van der Horst, W. Paciesas, C. A. Meegan, E. Bissaldi, M. Burgess, V. Chaplin, R. Diehl, G. Fishman, G. Fitzpatrick, S. Foley, M. Gibby, M. M. Giles, A. Goldstein, J. Greiner, D. Gruber, S. Guiriec, A. von Kienlin, M. Kippen, S. McBreen, R. Preece, A. Rau, D. Tierney, and C. Wilson-Hodge. Temporal Deconvolution Study of Long and Short Gamma-Ray Burst Light Curves. *ApJ*, 744:141, January 2012. doi: 10.1088/0004-637X/744/2/141.

P. N. Bhat, Michael S. Briggs, Valerie Connaughton, Chryssa Kouveliotou, Alexander J. van der Horst, William Paciesas, Charles A. Meegan, Elisabetta Bissaldi, Michael Burgess, Vandiver Chaplin, Roland Diehl, Gerald Fishman, Gerard Fitzpatrick, Suzanne Foley, Melissa Gibby, Misty M. Giles, Adam Goldstein, Jochen Greiner, David Gruber, Sylvain Guiriec, Andreas von Kienlin, Marc Kippen, Sheila McBreen, Robert Preece, Arne Rau, Dave Tierney, and Colleen Wilson-Hodge. Temporal deconvolution study of long and short gamma-ray burst light curves. *The Astrophysical Journal*, 744(2):141, 2012. URL `http://stacks.iop.org/0004-637X/744/i=2/a=141`.

E. Bissaldi, A. von Kienlin, G. Lichti, H. Steinle, P. N. Bhat, M. S. Briggs, G. J. Fishman, A. S. Hoover, R. M. Kippen, M. Krumrey, M. Gerlach, V. Connaughton, R. Diehl, J. Greiner, A. J. van der Horst, C. Kouveliotou, S. McBreen, C. A. Meegan, W. S. Paciesas, R. D. Preece, and C. A. Wilson-Hodge. Ground-based calibration and characterization of the Fermi gamma-ray burst monitor detectors. *Experimental Astronomy*, 24:47–88, May 2009. doi: 10.1007/s10686-008-9135-4.

R. D. Blandford and C. F. McKee. Fluid dynamics of relativistic blast waves. *Physics of Fluids*, 19:1130–1138, August 1976. doi: 10.1063/1.861619.

R. D. Blandford and R. L. Znajek. Electromagnetic extraction of energy from Kerr black holes. *MNRAS*, 179:433–456, May 1977. doi: 10.1093/mnras/179.3.433.

G. R. Blumenthal and R. J. Gould. Bremsstrahlung, Synchrotron Radiation, and Compton Scattering of High-Energy Electrons Traversing Dilute Gases. *Reviews of Modern Physics*, 42:237–271, 1970. doi: 10.1103/RevModPhys.42.237.

Z. Bosnjak, A. Celotti, and G. Ghirlanda. GRB 990413: insight into the thermal phase evolution. *MNRAS*, 370:L33–L37, July 2006. doi: 10.1111/j.1745-3933.2006.00183.x.

R. J. Bouwens, G. D. Illingworth, I. Labbe, P. A. Oesch, M. Trenti, C. M. Carollo, P. G. van Dokkum, M. Franx, M. Stiavelli, V. González, D. Magee, and L. Bradley. A candidate redshift z˜10 galaxy and rapid changes in that population at an age of 500Myr. *Nature*, 469:504–507, January 2011. doi: 10.1038/nature09717.

Ž. Bošnjak, D. Götz, L. Bouchet, S. Schanne, and B. Cordier. The spectral catalogue of INTEGRAL gamma-ray bursts. results of the joint IBIS/SPI spectral analysis. *A&A*, 561: A25, January 2014. doi: 10.1051/0004-6361/201322256.

G. C. Bower and D. Saul. A Search for Radio Transients in Very Large Array Archival Images of the 3C 286 Field. *ApJ*, 728:L14, February 2011. doi: 10.1088/2041-8205/728/1/L14.

M. Branchesi, Ligo Scientific Collaboration, and Virgo Collaboration. Electromagnetic follow-up of gravitational wave transient signal candidates. In *Journal of Physics Conference Series*, volume 375 of *Journal of Physics Conference Series*, page 062004, July 2012. doi: 10.1088/1742-6596/375/1/062004.

W. N. Brandt and G. Hasinger. Deep Extragalactic X-Ray Surveys. *A&A*, 43:827–859, September 2005. doi: 10.1146/annurev.astro.43.051804.102213.

M. S. Briggs, D. L. Band, R. M. Kippen, R. D. Preece, C. Kouveliotou, J. van Paradijs, G. H. Share, R. J. Murphy, S. M. Matz, A. Connors, C. Winkler, M. L. McConnell, J. M. Ryan, O. R. Williams, C. A. Young, B. Dingus, J. R. Catelli, and R. A. M. J. Wijers. Observations of GRB 990123 by the Compton Gamma Ray Observatory. *ApJ*, 524:82–91, October 1999. doi: 10.1086/307808.

O. Bromberg, E. Nakar, T. Piran, and R. Sari. An Observational Imprint of the Collapsar Model of Long Gamma-Ray Bursts. *ApJ*, 749:110, April 2012. doi: 10.1088/0004-637X/749/2/110.

O. Bromberg, E. Nakar, T. Piran, and R. Sari. Short versus Long and Collapsars versus Non-collapsars: A Quantitative Classification of Gamma-Ray Bursts. *ApJ*, 764:179, February 2013. doi: 10.1088/0004-637X/764/2/179.

J. M. Burgess, R. D. Preece, F. Ryde, P. Veres, P. Mészáros, V. Connaughton, M. Briggs, A. Pe'er, S. Iyyani, A. Goldstein, M. Axelsson, M. G. Baring, P. N. Bhat, D. Byrne, G. Fitzpatrick, S. Foley, D. Kocevski, N. Omodei, W. S. Paciesas, V. Pelassa, C. Kouveliotou, S. Xiong, H.-F. Yu, B. Zhang, and S. Zhu. An Observed Correlation between Thermal and Non-thermal Emission in Gamma-Ray Bursts. *ApJ*, 784:L43, April 2014. doi: 10.1088/2041-8205/784/2/L43.

E. Burns. GRB 160625B: Fermi GBM initial observations. *GRB Coordinates Network, Circular Service, No. 19581, #1 (2016)*, 19581, 2016.

D. N. Burrows, J. E. Hill, J. A. Nousek, J. A. Kennea, A. Wells, J. P. Osborne, A. F. Abbey, A. Beardmore, K. Mukerjee, A. D. T. Short, G. Chincarini, S. Campana, O. Citterio, A. Moretti, C. Pagani, G. Tagliaferri, P. Giommi, M. Capalbi, F. Tamburelli, L. Angelini, G. Cusumano, H. W. Bräuninger, W. Burkert, and G. D. Hartner. The Swift X-Ray Telescope. *Space Science Review*, 120:165–195, October 2005a. doi: 10.1007/s11214-005-5097-2.

D. N. Burrows, P. Romano, A. Falcone, S. Kobayashi, B. Zhang, A. Moretti, P. T. O'Brien, M. R. Goad, S. Campana, K. L. Page, L. Angelini, S. Barthelmy, A. P. Beardmore, M. Capalbi, G. Chincarini, J. Cummings, G. Cusumano, D. Fox, P. Giommi, J. E. Hill, J. A.

Kennea, H. Krimm, V. Mangano, F. Marshall, P. Mészáros, D. C. Morris, J. A. Nousek, J. P. Osborne, C. Pagani, M. Perri, G. Tagliaferri, A. A. Wells, S. Woosley, and N. Gehrels. Bright X-ray Flares in Gamma-Ray Burst Afterglows. *Science*, 309:1833–1835, September 2005b. doi: 10.1126/science.1116168.

N. R. Butler, D. Kocevski, J. S. Bloom, and J. L. Curtis. A Complete Catalog of Swift Gamma-Ray Burst Spectra and Durations: Demise of a Physical Origin for Pre-Swift High-Energy Correlations. *ApJ*, 671:656–677, December 2007. doi: 10.1086/522492.

N. R. Butler, J. S. Bloom, and D. Poznanski. The Cosmic Rate, Luminosity Function, and Intrinsic Correlations of Long Gamma-Ray Bursts. *ApJ*, 711:495–516, March 2010. doi: 10.1088/0004-637X/711/1/495.

G. Calderone, G. Ghirlanda, G. Ghisellini, M. G. Bernardini, S. Campana, S. Covino, D. D'Avanzo, V., A. Melandri, R. Salvaterra, B. Sbarufatti, and G. Tagliaferri. There is a short gamma-ray burst prompt phase at the beginning of each long one. *MNRAS*, 448: 403–416, March 2015. doi: 10.1093/mnras/stu2664.

S. Campana, V. Mangano, A. J. Blustin, P. Brown, D. N. Burrows, G. Chincarini, J. R. Cummings, G. Cusumano, M. Della Valle, D. Malesani, P. Mészáros, J. A. Nousek, M. Page, T. Sakamoto, E. Waxman, B. Zhang, Z. G. Dai, N. Gehrels, S. Immler, F. E. Marshall, K. O. Mason, A. Moretti, P. T. O'Brien, J. P. Osborne, K. L. Page, P. Romano, P. W. A. Roming, G. Tagliaferri, L. R. Cominsky, P. Giommi, O. Godet, J. A. Kennea, H. Krimm, L. Angelini, S. D. Barthelmy, P. T. Boyd, D. M. Palmer, A. A. Wells, and N. E. White. The association of GRB 060218 with a supernova and the evolution of the shock wave. *Nature*, 442:1008–1010, August 2006. doi: 10.1038/nature04892.

S. Campana, R. Salvaterra, A. Melandri, S. D. Vergani, S. Covino, P. D'Avanzo, D. Fugazza, G. Ghisellini, B. Sbarufatti, and G. Tagliaferri. The X-ray absorbing column density of a complete sample of bright Swift gamma-ray bursts. *MNRAS*, 421:1697–1702, April 2012. doi: 10.1111/j.1365-2966.2012.20428.x.

M. A. Campisi, L.-X. Li, and P. Jakobsson. Redshift distribution and luminosity function of long gamma-ray bursts from cosmological simulations. *MNRAS*, 407:1972–1980, September 2010. doi: 10.1111/j.1365-2966.2010.17044.x.

Z. Cano. The Observer's Guide to the Gamma-Ray Burst-Supernova Connection. In *Eighth Huntsville Gamma-Ray Burst Symposium*, volume 1962 of *LPI Contributions*, page 4116, October 2016.

C. L. Carilli, R. J. Ivison, and D. A. Frail. Variability of Submillijansky Radio Sources. *ApJ*, 590:192–196, June 2003. doi: 10.1086/375005.

A. Celotti, L. Maraschi, G. Ghisellini, A. Caccianiga, and T. Maccacaro. Unified Model for X-Ray– and Radio-selected BL Lacertae Objects. *ApJ*, 416:118, October 1993. doi: 10.1086/173218.

R. Chapman, N. R. Tanvir, R. S. Priddey, and A. J. Levan. How common are long gamma-ray bursts in the local Universe? *MNRAS*, 382:L21–L25, November 2007. doi: 10.1111/j.1745-3933.2007.00381.x.

Roger A. Chevalier and Zhi-Yun Li. Gamma-ray burst environments and progenitors. *ApJ*, 520(1):L29, 1999. URL `http://stacks.iop.org/1538-4357/520/i=1/a=L29`.

J. Chiang and R. Mukherjee. The Luminosity Function of the EGRET Gamma-Ray Blazars. *ApJ*, 496:752–760, March 1998. doi: 10.1086/305403.

G. Chincarini, A. Moretti, P. Romano, A. D. Falcone, S. Campana, S. Covino, C. Guidorzi, G. Tagliaferri, D. N. Burrows, M. Capalbi, G. Cusumano, P. Giommi, V. Mangano, V. La Parola, T. Mineo, M. Perri, and E. Troja. Attributes of flares in gamma-ray bursts: Sample I. *Nuovo Cimento B Serie*, 121:1307–1316, October 2006. doi: 10.1393/ncb/i2007-10276-y.

G. Chincarini, A. Moretti, P. Romano, A. D. Falcone, D. Morris, J. Racusin, S. Campana, S. Covino, C. Guidorzi, G. Tagliaferri, D. N. Burrows, C. Pagani, M. Stroh, D. Grupe, M. Capalbi, G. Cusumano, N. Gehrels, P. Giommi, V. La Parola, V. Mangano, T. Mineo, J. A. Nousek, P. T. O'Brien, K. L. Page, M. Perri, E. Troja, R. Willingale, and B. Zhang. The First Survey of X-Ray Flares from Gamma-Ray Bursts Observed by Swift: Temporal Properties and Morphology. *ApJ*, 671:1903–1920, December 2007. doi: 10.1086/521591.

G. Chincarini, J. Mao, R. Margutti, M. G. Bernardini, C. Guidorzi, F. Pasotti, D. Giannios, M. Della Valle, A. Moretti, P. Romano, P. D'Avanzo, G. Cusumano, and P. Giommi. Unveiling the origin of X-ray flares in gamma-ray bursts. *MNRAS*, 406:2113–2148, August 2010. doi: 10.1111/j.1365-2966.2010.17037.x.

L. Christensen, J. P. U. Fynbo, J. X. Prochaska, C. C. Thöne, A. de Ugarte Postigo, and P. Jakobsson. A High Signal-to-noise Ratio Composite Spectrum of Gamma-ray Burst Afterglows. *ApJ*, 727:73, February 2011. doi: 10.1088/0004-637X/727/2/73.

E. Cohen, J. I. Katz, T. Piran, R. Sari, R. D. Preece, and D. L. Band. Possible Evidence for Relativistic Shocks in Gamma-Ray Bursts. *ApJ*, 488:330–337, October 1997. doi: 10.1086/304699.

S. Cole, P. Norberg, C. M. Baugh, C. S. Frenk, J. Bland-Hawthorn, T. Bridges, R. Cannon, M. Colless, C. Collins, W. Couch, N. Cross, G. Dalton, R. De Propris, S. P. Driver, G. Efstathiou, R. S. Ellis, K. Glazebrook, C. Jackson, O. Lahav, I. Lewis, S. Lumsden, S. Maddox, D. Madgwick, J. A. Peacock, B. A. Peterson, W. Sutherland, and K. Taylor. The 2dF galaxy redshift survey: near-infrared galaxy luminosity functions. *MNRAS*, 326:255–273, September 2001. doi: 10.1046/j.1365-8711.2001.04591.x.

Ligo Collaboration. Gravitational waves and gamma-rays from a binary neutron star merger: Gw170817 and grb 170817a. *The Astrophysical Journal Letters*, 848(2):L13, 2017. URL `http://stacks.iop.org/2041-8205/848/i=2/a=L13`.

E. Costa, F. Frontera, J. Heise, M. Feroci, J. in't Zand, F. Fiore, M. N. Cinti, D. Dal Fiume, L. Nicastro, M. Orlandini, E. Palazzi, M. Rapisarda#, G. Zavattini, R. Jager, A. Parmar, A. Owens, S. Molendi, G. Cusumano, M. C. Maccarone, S. Giarrusso, A. Coletta, L. A. Antonelli, P. Giommi, J. M. Muller, L. Piro, and R. C. Butler. Discovery of an X-ray afterglow associated with the γ-ray burst of 28 February 1997. *Nature*, 387:783–785, June 1997. doi: 10.1038/42885.

S. Covino, A. Melandri, R. Salvaterra, S. Campana, S. D. Vergani, M. G. Bernardini, P. D'Avanzo, V. D'Elia, D. Fugazza, G. Ghirlanda, G. Ghisellini, A. Gomboc, Z. P. Jin, T. Krühler, D. Malesani, L. Nava, B. Sbarufatti, and G. Tagliaferri. Dust extinctions for an unbiased sample of gamma-ray burst afterglows. *MNRAS*, 432:1231–1244, June 2013. doi: 10.1093/mnras/stt540.

D. M. Coward, E. J. Howell, T. Piran, G. Stratta, M. Branchesi, O. Bromberg, B. Gendre, R. R. Burman, and D. Guetta. The Swift short gamma-ray burst rate density: implications for binary neutron star merger rates. *MNRAS*, 425:2668–2673, October 2012. doi: 10.1111/j.1365-2966.2012.21604.x.

D. M. Coward, M. Branchesi, E. J. Howell, P. D. Lasky, and M. Böer. The detection efficiency of on-axis short gamma-ray burst optical afterglows triggered by aLIGO/Virgo. *MNRAS*, 445:3575–3580, December 2014. doi: 10.1093/mnras/stu1863.

S. Croft, G. C. Bower, R. Ackermann, S. Atkinson, D. Backer, P. Backus, W. C. Barott, A. Bauermeister, L. Blitz, D. Bock, T. Bradford, C. Cheng, C. Cork, M. Davis, D. DeBoer, M. Dexter, J. Dreher, G. Engargiola, E. Fields, M. Fleming, J. R. Forster, C. Gutierrez-Kraybill, G. Harp, T. Helfer, C. Hull, J. Jordan, S. Jorgensen, G. Keating, T. Kilsdonk, C. Law, J. van Leeuwen, J. Lugten, D. MacMahon, P. McMahon, O. Milgrome, T. Pierson, K. Randall, J. Ross, S. Shostak, A. Siemion, K. Smolek, J. Tarter, D. Thornton, L. Urry, A. Vitouchkine, N. Wadefalk, J. Welch, D. Werthimer, D. Whysong, P. K. G. Williams, and M. Wright. The Allen Telescope Array Twenty-centimeter Survey – A 690 deg^2, 12 Epoch Radio Data Set. I. Catalog and Long-duration Transient Statistics. *ApJ*, 719:45–58, August 2010. doi: 10.1088/0004-637X/719/1/45.

A. Cucchiara, A. J. Levan, D. B. Fox, N. R. Tanvir, T. N. Ukwatta, E. Berger, T. Krühler, A. Küpcü Yoldaş, X. F. Wu, K. Toma, J. Greiner, F. E. Olivares, A. Rowlinson, L. Amati, T. Sakamoto, K. Roth, A. Stephens, A. Fritz, J. P. U. Fynbo, J. Hjorth, D. Malesani, P. Jakobsson, K. Wiersema, P. T. O'Brien, A. M. Soderberg, R. J. Foley, A. S. Fruchter, J. Rhoads, R. E. Rutledge, B. P. Schmidt, M. A. Dopita, P. Podsiadlowski, R. Willingale, C. Wolf, S. R. Kulkarni, and P. D'Avanzo. A Photometric Redshift of z ˜ 9.4 for GRB 090429B. *ApJ*, 736:7, July 2011. doi: 10.1088/0004-637X/736/1/7.

P. A. Curran, R. L. C. Starling, P. T. O'Brien, O. Godet, A. J. van der Horst, and R. A. M. J. Wijers. On the nature of late X-ray flares in Swift gamma-ray bursts. *A&A*, 487:533–538, August 2008. doi: 10.1051/0004-6361:200809652.

F. Daigne and R. Mochkovitch. Gamma-ray bursts from internal shocks in a relativistic wind: temporal and spectral properties. *MNRAS*, 296:275–286, May 1998. doi: 10.1046/j.1365-8711.1998.01305.x.

F. Daigne and R. Mochkovitch. The expected thermal precursors of gamma-ray bursts in the internal shock model. *MNRAS*, 336:1271–1280, November 2002. doi: 10.1046/j.1365-8711.2002.05875.x.

F. Daigne and R. Mochkovitch. The low-luminosity tail of the GRB distribution: the case of GRB 980425. *A&A*, 465:1–8, April 2007. doi: 10.1051/0004-6361:20066080.

F. Daigne, E. M. Rossi, and R. Mochkovitch. The redshift distribution of Swift gamma-ray bursts: evidence for evolution. *MNRAS*, 372:1034–1042, November 2006. doi: 10.1111/j.1365-2966.2006.10837.x.

F. Daigne, Ž. Bošnjak, and G. Dubus. Reconciling observed gamma-ray burst prompt spectra with synchrotron radiation? *A&A*, 526:A110, February 2011. doi: 10.1051/0004-6361/201015457.

P. D'Avanzo. Short gamma-ray bursts: A review. *Journal of High Energy Astrophysics*, 7:73–80, September 2015. doi: 10.1016/j.jheap.2015.07.002.

P. D'Avanzo, R. Salvaterra, B. Sbarufatti, L. Nava, A. Melandri, M. G. Bernardini, S. Campana, S. Covino, D. Fugazza, G. Ghirlanda, G. Ghisellini, V. La Parola, M. Perri, S. D. Vergani, and G. Tagliaferri. A complete sample of bright Swift Gamma-ray bursts: X-ray afterglow luminosity and its correlation with the prompt emission. *MNRAS*, 425: 506–513, September 2012. doi: 10.1111/j.1365-2966.2012.21489.x.

P. D'Avanzo, R. Salvaterra, M. G. Bernardini, L. Nava, S. Campana, S. Covino, V. D'Elia, G. Ghirlanda, G. Ghisellini, A. Melandri, B. Sbarufatti, S. D. Vergani, and G. Tagliaferri. A complete sample of bright Swift short gamma-ray bursts. *MNRAS*, 442:2342–2356, August 2014. doi: 10.1093/mnras/stu994.

R. Della Ceca, T. Maccacaro, A. Caccianiga, P. Severgnini, V. Braito, X. Barcons, F. J. Carrera, M. G. Watson, J. A. Tedds, H. Brunner, I. Lehmann, M. J. Page, G. Lamer, and A. Schwope. Exploring the X-ray sky with the XMM-Newton bright serendipitous survey. *A&A*, 428:383–399, December 2004. doi: 10.1051/0004-6361:20040252.

E. V. Derishev, V. V. Kocharovsky, and V. V. Kocharovsky. Physical parameters and emission mechanism in gamma-ray bursts. *A&A*, 372:1071–1077, June 2001. doi: 10.1051/0004-6361:20010586.

C. D. Dermer and M. Böttcher. Flash Heating of Circumstellar Clouds by Gamma-Ray Bursts. *ApJ*, 534:L155–L158, May 2000. doi: 10.1086/312669.

F. Dirirsa, J. Racusin, J. McEnery, and R. Desiante. GRB 160625B: Fermi-LAT detection of a bright burst. *GRB Coordinates Network, Circular Service, No. 19580, #1 (2016)*, 19580, 2016.

M. Dominik, K. Belczynski, C. Fryer, D. E. Holz, E. Berti, T. Bulik, I. Mandel, and R. O'Shaughnessy. Double Compact Objects. II. Cosmological Merger Rates. *ApJ*, 779: 72, December 2013. doi: 10.1088/0004-637X/779/1/72.

M. Dominik, E. Berti, R. O'Shaughnessy, I. Mandel, K. Belczynski, C. Fryer, D. E. Holz, T. Bulik, and F. Pannarale. Double Compact Objects III: Gravitational-wave Detection Rates. *ApJ*, 806:263, June 2015. doi: 10.1088/0004-637X/806/2/263.

T. Q. Donaghy. The Importance of Off-Jet Relativistic Kinematics in Gamma-Ray Burst Jet Models. *ApJ*, 645:436–449, July 2006. doi: 10.1086/504255.

B. Efron and V. Petrosian. A simple test of independence for truncated data with applications to redshift surveys. *ApJ*, 399:345–352, November 1992. doi: 10.1086/171931.

D. Eichler and A. Levinson. An Interpretation of the hν_{peak}-E$_{iso}$ Correlation for Gamma-Ray Bursts. *ApJ*, 614:L13–L16, October 2004. doi: 10.1086/425310.

D. Eichler, M. Livio, T. Piran, and D. N. Schramm. Nucleosynthesis, neutrino bursts and gamma-rays from coalescing neutron stars. *Nature*, 340:126–128, July 1989. doi: 10.1038/340126a0.

P. A. Evans, A. P. Beardmore, K. L. Page, J. P. Osborne, P. T. O'Brien, R. Willingale, R. L. C. Starling, D. N. Burrows, O. Godet, L. Vetere, J. Racusin, M. R. Goad, K. Wiersema, L. Angelini, M. Capalbi, G. Chincarini, N. Gehrels, J. A. Kennea, R. Margutti, D. C. Morris, C. J. Mountford, C. Pagani, M. Perri, P. Romano, and N. Tanvir. Methods and results of an automatic analysis of a complete sample of Swift-XRT observations of GRBs. *MNRAS*, 397:1177–1201, August 2009. doi: 10.1111/j.1365-2966.2009.14913.x.

A. D. Falcone, D. N. Burrows, D. Lazzati, S. Campana, S. Kobayashi, B. Zhang, P. Mészáros, K. L. Page, J. A. Kennea, P. Romano, C. Pagani, L. Angelini, A. P. Beardmore, M. Capalbi, G. Chincarini, G. Cusumano, P. Giommi, M. R. Goad, O. Godet, D. Grupe, J. E. Hill, V. La Parola, V. Mangano, A. Moretti, J. A. Nousek, P. T. O'Brien, J. P. Osborne, M. Perri, G. Tagliaferri, A. A. Wells, and N. Gehrels. The Giant X-Ray Flare of GRB 050502B: Evidence for Late-Time Internal Engine Activity. *ApJ*, 641:1010–1017, April 2006. doi: 10.1086/500655.

A. D. Falcone, D. Morris, J. Racusin, G. Chincarini, A. Moretti, P. Romano, D. N. Burrows, C. Pagani, M. Stroh, D. Grupe, S. Campana, S. Covino, G. Tagliaferri, R. Willingale, and N. Gehrels. The First Survey of X-Ray Flares from Gamma-Ray Bursts Observed by Swift: Spectral Properties and Energetics. *ApJ*, 671:1921–1938, December 2007. doi: 10.1086/523296.

C. Firmani, V. Avila-Reese, G. Ghisellini, and A. V. Tutukov. Formation Rate, Evolving Luminosity Function, Jet Structure, and Progenitors for Long Gamma-Ray Bursts. *ApJ*, 611:1033–1040, August 2004. doi: 10.1086/422186.

C. Firmani, G. Ghisellini, G. Ghirlanda, and V. Avila-Reese. A new method optimized to use gamma-ray bursts as cosmic rulers. *MNRAS*, 360:L1–L5, June 2005. doi: 10.1111/j.1745-3933.2005.00023.x.

G. J. Fishman and C. A. Meegan. Gamma-Ray Bursts. *Annual Reviews A&A*, 33:415–458, 1995. doi: 10.1146/annurev.aa.33.090195.002215.

G. J. Fishman, C. A. Meegan, R. B. Wilson, W. S. Paciesas, G. N. Pendleton, B. A. Harmon, J. M. Horack, C. Kouveliotou, and M. Finger. Overview of Observations from BATSE on the Compton Observatory. *A&A*, 97:17, January 1993.

G. J. Fishman, C. A. Meegan, R. B. Wilson, M. N. Brock, J. M. Horack, C. Kouveliotou, S. Howard, W. S. Paciesas, M. S. Briggs, G. N. Pendleton, T. M. Koshut, R. S. Mallozzi, M. Stollberg, and J. P. Lestrade. The first BATSE gamma-ray burst catalog. *ApJ*, 92:229–283, May 1994. doi: 10.1086/191968.

W. Fong and E. Berger. The Locations of Short Gamma-Ray Bursts as Evidence for Compact Object Binary Progenitors. *ApJ*, 776:18, October 2013. doi: 10.1088/0004-637X/776/1/18.

W. Fong, E. Berger, R. Margutti, B. A. Zauderer, E. Troja, I. Czekala, R. Chornock, N. Gehrels, T. Sakamoto, D. B. Fox, and P. Podsiadlowski. A Jet Break in the X-Ray Light Curve of Short GRB 111020A: Implications for Energetics and Rates. *ApJ*, 756:189, September 2012. doi: 10.1088/0004-637X/756/2/189.

W. Fong, E. Berger, B. D. Metzger, R. Margutti, R. Chornock, G. Migliori, R. J. Foley, B. A. Zauderer, R. Lunnan, T. Laskar, S. J. Desch, K. J. Meech, S. Sonnett, C. Dickey, A. Hedlund, and P. Harding. Short GRB 130603B: Discovery of a Jet Break in the Optical and Radio Afterglows, and a Mysterious Late-time X-Ray Excess. *ApJ*, 780:118, January 2014. doi: 10.1088/0004-637X/780/2/118.

W. Fong, E. Berger, R. Margutti, and B. A. Zauderer. A Decade of Short-duration Gamma-Ray Burst Broadband Afterglows: Energetics, Circumburst Densities, and Jet Opening Angles. *ApJ*, 815:102, December 2015. doi: 10.1088/0004-637X/815/2/102.

D. A. Frail, S. R. Kulkarni, L. Nicastro, M. Feroci, and G. B. Taylor. The radio afterglow from the γ-ray burst of 8 May 1997. *Nature*, 389:261–263, September 1997. doi: 10.1038/38451.

D. A. Frail, S. R. Kulkarni, R. Sari, S. G. Djorgovski, J. S. Bloom, T. J. Galama, D. E. Reichart, E. Berger, F. A. Harrison, P. A. Price, S. A. Yost, A. Diercks, R. W. Goodrich, and F. Chaffee. Beaming in Gamma-Ray Bursts: Evidence for a Standard Energy Reservoir. *ApJ*, 562: L55–L58, November 2001. doi: 10.1086/338119.

D. A. Frail, S. R. Kulkarni, E. O. Ofek, G. C. Bower, and E. Nakar. A Revised View of the Transient Radio Sky. *ApJ*, 747:70, March 2012. doi: 10.1088/0004-637X/747/1/70.

J. P. U. Fynbo, P. Jakobsson, J. X. Prochaska, D. Malesani, C. Ledoux, A. de Ugarte Postigo, M. Nardini, P. M. Vreeswijk, K. Wiersema, J. Hjorth, J. Sollerman, H.-W. Chen, C. C. Thöne, G. Björnsson, J. S. Bloom, A. J. Castro-Tirado, L. Christensen, A. De Cia, A. S. Fruchter, J. Gorosabel, J. F. Graham, A. O. Jaunsen, B. L. Jensen, D. A. Kann, C. Kouveliotou, A. J. Levan, J. Maund, N. Masetti, B. Milvang-Jensen, E. Palazzi, D. A. Perley, E. Pian, E. Rol, P. Schady, R. L. C. Starling, N. R. Tanvir, D. J. Watson, D. Xu, T. Augusteijn, F. Grundahl, J. Telting, and P.-O. Quirion. Low-resolution Spectroscopy of Gamma-ray Burst Optical Afterglows: Biases in the Swift Sample and Characterization of the Absorbers. *ApJ*, 185:526–573, December 2009. doi: 10.1088/0067-0049/185/2/526.

A. Gal-Yam, E. O. Ofek, D. Poznanski, A. Levinson, E. Waxman, D. A. Frail, A. M. Soderberg, E. Nakar, W. Li, and A. V. Filippenko. Radio and Optical Follow-up Observations of a Uniform Radio Transient Search: Implications for Gamma-Ray Bursts and Supernovae. *ApJ*, 639:331–339, March 2006. doi: 10.1086/499157.

T. J. Galama, P. M. Vreeswijk, J. van Paradijs, C. Kouveliotou, T. Augusteijn, H. Böhnhardt, J. P. Brewer, V. Doublier, J.-F. Gonzalez, B. Leibundgut, C. Lidman, O. R. Hainaut, F. Patat, J. Heise, J. in't Zand, K. Hurley, P. J. Groot, R. G. Strom, P. A. Mazzali, K. Iwamoto, K. Nomoto, H. Umeda, T. Nakamura, T. R. Young, T. Suzuki, T. Shigeyama, T. Koshut, M. Kippen, C. Robinson, P. de Wildt, R. A. M. J. Wijers, N. Tanvir, J. Greiner, E. Pian, E. Palazzi, F. Frontera, N. Masetti, L. Nicastro, M. Feroci, E. Costa, L. Piro, B. A. Peterson, C. Tinney, B. Boyle, R. Cannon, R. Stathakis, E. Sadler, M. C. Begam, and P. Ianna. An unusual supernova in the error box of the γ-ray burst of 25 April 1998. *Nature*, 395: 670–672, October 1998. doi: 10.1038/27150.

N. Gehrels, G. Chincarini, P. Giommi, K. O. Mason, J. A. Nousek, A. A. Wells, N. E. White, S. D. Barthelmy, D. N. Burrows, L. R. Cominsky, K. C. Hurley, F. E. Marshall, P. Mészáros, P. W. A. Roming, L. Angelini, L. M. Barbier, T. Belloni, S. Campana, P. A. Caraveo, M. M. Chester, O. Citterio, T. L. Cline, M. S. Cropper, J. R. Cummings, A. J. Dean, E. D. Feigelson, E. E. Fenimore, D. A. Frail, A. S. Fruchter, G. P. Garmire, K. Gendreau, G. Ghisellini, J. Greiner, J. E. Hill, S. D. Hunsberger, H. A. Krimm, S. R. Kulkarni, P. Kumar, F. Lebrun, N. M. Lloyd-Ronning, C. B. Markwardt, B. J. Mattson, R. F. Mushotzky, J. P. Norris, J. Osborne, B. Paczynski, D. M. Palmer, H.-S. Park, A. M. Parsons, J. Paul, M. J. Rees, C. S. Reynolds, J. E. Rhoads, T. P. Sasseen, B. E. Schaefer, A. T. Short, A. P. Smale, I. A. Smith, L. Stella, G. Tagliaferri, T. Takahashi, M. Tashiro, L. K. Townsley, J. Tueller, M. J. L. Turner, M. Vietri, W. Voges, M. J. Ward, R. Willingale, F. M. Zerbi, and W. W. Zhang. The Swift Gamma-Ray Burst Mission. *ApJ*, 611:1005–1020, August 2004. doi: 10.1086/422091.

N. Gehrels, E. Ramirez-Ruiz, and D. B. Fox. Gamma-Ray Bursts in the Swift Era. *Annual Reviews A&A*, 47:567–617, September 2009. doi: 10.1146/annurev.astro.46.060407.145147.

F. Genet, F. Daigne, and R. Mochkovitch. Can the early X-ray afterglow of gamma-ray bursts be explained by a contribution from the reverse shock? *MNRAS*, 381:732–740, October 2007. doi: 10.1111/j.1365-2966.2007.12243.x.

G. Ghirlanda, A. Celotti, and G. Ghisellini. Time resolved spectral analysis of bright gamma ray bursts. *A&A*, 393:409–423, October 2002. doi: 10.1051/0004-6361:20021038.

G. Ghirlanda, A. Celotti, and G. Ghisellini. Extremely hard GRB spectra prune down the forest of emission models. *A&A*, 406:879–892, August 2003. doi: 10.1051/0004-6361:20030803.

G. Ghirlanda, G. Ghisellini, and D. Lazzati. The Collimation-corrected Gamma-Ray Burst Energies Correlate with the Peak Energy of Their νF_ν Spectrum. *ApJ*, 616:331–338, November 2004. doi: 10.1086/424913.

G. Ghirlanda, G. Ghisellini, and C. Firmani. Probing the existence of the E_{peak}-E_{iso} correlation in long gamma ray bursts. *MNRAS*, 361:L10–L14, July 2005. doi: 10.1111/j.1745-3933.2005.00053.x.

G. Ghirlanda, L. Nava, G. Ghisellini, and C. Firmani. Confirming the γ-ray burst spectral-energy correlations in the era of multiple time breaks. *A&A*, 466:127–136, April 2007. doi: 10.1051/0004-6361:20077119.

G. Ghirlanda, L. Nava, G. Ghisellini, A. Celotti, and C. Firmani. Short versus long gamma-ray bursts: spectra, energetics, and luminosities. *A&A*, 496:585–595, March 2009. doi: 10.1051/0004-6361/200811209.

G. Ghirlanda, G. Ghisellini, and L. Nava. The onset of the GeV afterglow of GRB 090510. *A&A*, 510:L7, February 2010. doi: 10.1051/0004-6361/200913980.

G. Ghirlanda, G. Ghisellini, L. Nava, R. Salvaterra, G. Tagliaferri, S. Campana, S. Covino, P. D'Avanzo, D. Fugazza, A. Melandri, and S. D. Vergani. The impact of selection biases on the E_{peak}-L_{ISO} correlation of gamma-ray bursts. *MNRAS*, 422:2553–2559, May 2012a. doi: 10.1111/j.1365-2966.2012.20815.x.

G. Ghirlanda, L. Nava, G. Ghisellini, A. Celotti, D. Burlon, S. Covino, and A. Melandri. Gamma-ray bursts in the comoving frame. *MNRAS*, 420:483–494, February 2012b. doi: 10.1111/j.1365-2966.2011.20053.x.

G. Ghirlanda, G. Ghisellini, R. Salvaterra, L. Nava, D. Burlon, G. Tagliaferri, S. Campana, P. D'Avanzo, and A. Melandri. The faster the narrower: characteristic bulk velocities and jet opening angles of gamma-ray bursts. *MNRAS*, 428:1410–1423, January 2013a. doi: 10.1093/mnras/sts128.

G. Ghirlanda, A. Pescalli, and G. Ghisellini. Photospheric emission throughout GRB 100507 detected by Fermi. *MNRAS*, 432:3237–3244, July 2013b. doi: 10.1093/mnras/stt681.

G. Ghirlanda, R. Salvaterra, D. Burlon, S. Campana, A. Melandri, M. G. Bernardini, S. Covino, P. D'Avanzo, V. D'Elia, G. Ghisellini, L. Nava, I. Prandoni, L. Sironi, G. Tagliaferri, S. D. Vergani, and A. Wolter. Radio afterglows of a complete sample of bright Swift GRBs: predictions from present days to the SKA era. *MNRAS*, 435:2543–2551, November 2013c. doi: 10.1093/mnras/stt1466.

G. Ghirlanda, D. Burlon, G. Ghisellini, R. Salvaterra, M. G. Bernardini, S. Campana, S. Covino, P. D'Avanzo, V. D'Elia, A. Melandri, T. Murphy, L. Nava, S. D. Vergani, and G. Tagliaferri. GRB Orphan Afterglows in Present and Future Radio Transient Surveys. *PASA*, 31:e022, May 2014. doi: 10.1017/pasa.2014.14.

G. Ghirlanda, M. G. Bernardini, G. Calderone, and P. D'Avanzo. Are short Gamma Ray Bursts similar to long ones? *Journal of High Energy Astrophysics*, 7:81–89, September 2015a. doi: 10.1016/j.jheap.2015.04.002.

G. Ghirlanda, R. Salvaterra, S. Campana, S. D. Vergani, J. Japelj, M. G. Bernardini, D. Burlon, P. D'Avanzo, A. Melandri, A. Gomboc, F. Nappo, R. Paladini, A. Pescalli, O. S. Salafia, and G. Tagliaferri. Unveiling the population of orphan γ-ray bursts. *A&A*, 578: A71, June 2015b. doi: 10.1051/0004-6361/201526112.

G. Ghirlanda, O. S. Salafia, A. Pescalli, G. Ghisellini, R. Salvaterra, E. Chassande-Mottin, M. Colpi, F. Nappo, P. D'Avanzo, A. Melandri, M. G. Bernardini, M. Branchesi, S. Campana, R. Ciolfi, S. Covino, D. Götz, S. D. Vergani, M. Zennaro, and G. Tagliaferri. Short gamma-ray bursts at the dawn of the gravitational wave era. *A&A*, 594:A84, October 2016. doi: 10.1051/0004-6361/201628993.

G. Ghisellini, editor. *Radiative Processes in High Energy Astrophysics*, volume 873 of *Lecture Notes in Physics, Berlin Springer Verlag*, 2013. doi: 10.1007/978-3-319-00612-3.

G. Ghisellini and D. Lazzati. Polarization light curves and position angle variation of beamed gamma-ray bursts. *MNRAS*, 309:L7–L11, October 1999. doi: 10.1046/j.1365-8711.1999.03025.x.

G. Ghisellini and R. Svensson. The synchrotron and cyclo-synchrotron absorption cross-section. *Monthly Notices of the Royal Astronomical Society*, 252:313–318, October 1991. doi: 10.1093/mnras/252.3.313.

G. Ghisellini, A. Celotti, and D. Lazzati. Constraints on the emission mechanisms of gamma-ray bursts. *MNRAS*, 313:L1–L5, March 2000. doi: 10.1046/j.1365-8711.2000.03354.x.

G. Ghisellini, G. Ghirlanda, S. Mereghetti, Z. Bosnjak, F. Tavecchio, and C. Firmani. Are GRB980425 and GRB031203 real outliers or twins of GRB060218? *MNRAS*, 372:1699–1709, November 2006. doi: 10.1111/j.1365-2966.2006.10972.x.

G. Ghisellini, A. Celotti, G. Ghirlanda, C. Firmani, and L. Nava. Re-born fireballs in gamma-ray bursts. *MNRAAS*, 382:L72–L76, November 2007a. doi: 10.1111/j.1745-3933.2007.00392.x.

G. Ghisellini, G. Ghirlanda, and F. Tavecchio. Did we observe the supernova shock breakout in GRB 060218? *MNRAS*, 382:L77–L81, November 2007b. doi: 10.1111/j.1745-3933.2007.00396.x.

G. Ghisellini, M. Nardini, G. Ghirlanda, and A. Celotti. A unifying view of gamma-ray burst afterglows. *MNRAS*, 393:253–271, February 2009. doi: 10.1111/j.1365-2966.2008.14214.x.

G. Ghisellini, G. Ghirlanda, L. Nava, and A. Celotti. GeV emission from gamma-ray bursts: a radiative fireball? *MNRAS*, 403:926–937, April 2010a. doi: 10.1111/j.1365-2966.2009.16171.x.

G. Ghisellini, F. Tavecchio, L. Foschini, G. Ghirlanda, L. Maraschi, and A. Celotti. General physical properties of bright Fermi blazars. *MNRAS*, 402:497–518, February 2010b. doi: 10.1111/j.1365-2966.2009.15898.x.

B. Giacomazzo, R. Perna, L. Rezzolla, E. Troja, and D. Lazzati. Compact Binary Progenitors of Short Gamma-Ray Bursts. *ApJ*, 762:L18, January 2013. doi: 10.1088/2041-8205/762/2/L18.

A. Goldstein, J. M. Burgess, R. D. Preece, M. S. Briggs, S. Guiriec, A. J. van der Horst, V. Connaughton, C. A. Wilson-Hodge, W. S. Paciesas, C. A. Meegan, A. von Kienlin, P. N. Bhat, E. Bissaldi, V. Chaplin, R. Diehl, G. J. Fishman, G. Fitzpatrick, S. Foley, M. Gibby, M. Giles, J. Greiner, D. Gruber, R. M. Kippen, C. Kouveliotou, S. McBreen, S. McGlynn, A. Rau, and D. Tierney. The Fermi GBM Gamma-Ray Burst Spectral Catalog: The First Two Years. *ApJ*, 199:19, March 2012. doi: 10.1088/0067-0049/199/1/19.

S. Golenetskii, R. Aptekar, D. Frederiks, V. Pal'Shin, P. Oleynik, M. Ulanov, D. Svinkin, A. Tsvetkova, A. Lysenko, A. Kozlova, and T. Cline. Konus-Wind observation of GRB 151027A. *GRB Coordinates Network, Circular Service, No. 18516, #1 (2015)*, 18516, 2015.

J. Goodman. Are gamma-ray bursts optically thick? *ApJ*, 308:L47–L50, September 1986. doi: 10.1086/184741.

J. Gorosabel, J. U. Fynbo, J. Hjorth, C. Wolf, M. I. Andersen, H. Pedersen, L. Christensen, B. L. Jensen, P. Möller, J. Afonso, M. A. Treyer, G. Mallén-Ornelas, A. J. Castro-Tirado, A. Fruchter, J. Greiner, E. Pian, P. M. Vreeswijk, F. Frontera, L. Kaper, S. Klose, C. Kouveliotou, N. Masetti, E. Palazzi, E. Rol, I. Salamanca, N. Tanvir, R. A. M. J. Wijers, and E. van den Heuvel. Strategies for prompt searches for GRB afterglows: The discovery of the <ASTROBJ>GRB 001011</ASTROBJ> optical/near-infrared counterpart using colour-colour selection. *A&A*, 384:11–23, March 2002. doi: 10.1051/0004-6361:20011598.

J. Granot. The Structure and Dynamics of GRB Jets. In *Revista Mexicana de Astronomia y Astrofisica, vol. 27*, volume 27 of *Revista Mexicana de Astronomia y Astrofisica Conference Series*, pages 140–165, March 2007.

J. Greiner, D. H. Hartmann, W. Voges, T. Boller, R. Schwarz, and S. V. Zharikov. Search for GRB X-ray afterglows in the ROSAT all-sky survey. *A&A*, 353:998–1008, January 2000.

J. E. Grindlay. Fast X-Ray Transients and Gamma-Ray Bursts: Constraints on Beaming. *ApJ*, 510:710–714, January 1999. doi: 10.1086/306617.

D. Gruber, T. Krühler, S. Foley, M. Nardini, D. Burlon, A. Rau, E. Bissaldi, A. von Kienlin, S. McBreen, J. Greiner, P. N. Bhat, M. S. Briggs, J. M. Burgess, V. L. Chaplin, V. Connaughton, R. Diehl, G. J. Fishman, M. H. Gibby, M. M. Giles, A. Goldstein, S. Guiriec, A. J. van der Horst, R. M. Kippen, C. Kouveliotou, L. Lin, C. A. Meegan, W. S. Paciesas, R. D. Preece, D. Tierney, and C. Wilson-Hodge. Fermi/GBM observations of the ultra-long GRB 091024. A burst with an optical flash. *A&A*, 528:A15, April 2011. doi: 10.1051/0004-6361/201015891.

D. Gruber, J. M. Burgess, and V. Connaughton. GRB 120624B: Fermi GBM detection. *GRB Coordinates Network, Circular Service, No. 13377, #1 (2012)*, 13377, 2012.

D. Gruber, A. Goldstein, V. Weller von Ahlefeld, P. Narayana Bhat, E. Bissaldi, M. S. Briggs, D. Byrne, W. H. Cleveland, V. Connaughton, R. Diehl, G. J. Fishman, G. Fitzpatrick, S. Foley, M. Gibby, M. M. Giles, J. Greiner, S. Guiriec, A. J. van der Horst, A. von Kienlin, C. Kouveliotou, E. Layden, L. Lin, C. A. Meegan, S. McGlynn, W. S. Paciesas, V. Pelassa, R. D. Preece, A. Rau, C. A. Wilson-Hodge, S. Xiong, G. Younes, and H.-F. Yu. The Fermi GBM Gamma-Ray Burst Spectral Catalog: Four Years of Data. *ApJ*, 211:12, March 2014. doi: 10.1088/0067-0049/211/1/12.

D. Guetta and M. Della Valle. On the Rates of Gamma-Ray Bursts and Type Ib/c Supernovae. *ApJ*, 657:L73–L76, March 2007. doi: 10.1086/511417.

D. Guetta and T. Piran. The luminosity and redshift distributions of short-duration GRBs. *A&A*, 435:421–426, May 2005. doi: 10.1051/0004-6361:20041702.

D. Guetta and T. Piran. The BATSE-Swift luminosity and redshift distributions of short-duration GRBs. *A&A*, 453:823–828, July 2006. doi: 10.1051/0004-6361:20054498.

D. Guetta and L. Stella. Short γ-ray bursts and gravitational waves from dynamically formed merging binaries. *A&A*, 498:329–333, May 2009. doi: 10.1051/0004-6361:200810493.

D. Guetta, T. Piran, and E. Waxman. The Luminosity and Angular Distributions of Long-Duration Gamma-Ray Bursts. *ApJ*, 619:412–419, January 2005. doi: 10.1086/423125.

S. Guiriec, V. Connaughton, M. S. Briggs, M. Burgess, F. Ryde, F. Daigne, P. Mészáros, A. Goldstein, J. McEnery, N. Omodei, P. N. Bhat, E. Bissaldi, A. Camero-Arranz, V. Chaplin, R. Diehl, G. Fishman, S. Foley, M. Gibby, M. M. Giles, J. Greiner, D. Gruber, A. von Kienlin, M. Kippen, C. Kouveliotou, S. McBreen, C. A. Meegan, W. Paciesas, R. Preece, A. Rau, D. Tierney, A. J. van der Horst, and C. Wilson-Hodge. Detection of a Thermal Spectral Component in the Prompt Emission of GRB 100724B. *ApJ*, 727:L33, February 2011. doi: 10.1088/2041-8205/727/2/L33.

S. Guiriec, F. Daigne, R. Hascoët, G. Vianello, F. Ryde, R. Mochkovitch, C. Kouveliotou, S. Xiong, P. N. Bhat, S. Foley, D. Gruber, J. M. Burgess, S. McGlynn, J. McEnery, and N. Gehrels. Evidence for a Photospheric Component in the Prompt Emission of the Short GRB 120323A and Its Effects on the GRB Hardness-Luminosity Relation. *ApJ*, 770: 32, June 2013. doi: 10.1088/0004-637X/770/1/32.

R. Hascoët, Z. L. Uhm, R. Mochkovitch, and F. Daigne. Was the "naked burst" GRB 050421 really naked? *A&A*, 534:A104, October 2011. doi: 10.1051/0004-6361/201117404.

R. Hascoët, F. Daigne, and R. Mochkovitch. Prompt thermal emission in gamma-ray bursts. *A&A*, 551:A124, March 2013. doi: 10.1051/0004-6361/201220023.

R. Hascoët, A. M. Beloborodov, F. Daigne, and R. Mochkovitch. Estimates for Lorentz Factors of Gamma-Ray Bursts from Early Optical Afterglow Observations. *ApJ*, 782:5, February 2014. doi: 10.1088/0004-637X/782/1/5.

R. Hascoet, A. M. Beloborodov, F. Daigne, and R. Mochkovitch. X-ray flares from dense shells formed in gamma-ray burst explosions. *ArXiv e-prints*, March 2015.

W. K. Hastings. Monte carlo sampling methods using markov chains and their applications. *Biometrika*, 57(1):97–109, 1970. ISSN 00063444. URL `http://www.jstor.org/stable/2334940`.

J. S. Heyl and R. Perna. Broadband Modeling of GRB 021004. *ApJ*, 586:L13–L17, March 2003. doi: 10.1086/374652.

J. Hjorth, D. Malesani, P. Jakobsson, A. O. Jaunsen, J. P. U. Fynbo, J. Gorosabel, T. Krühler, A. J. Levan, M. J. Michałowski, B. Milvang-Jensen, P. Møller, S. Schulze, N. R. Tanvir, and D. Watson. The Optically Unbiased Gamma-Ray Burst Host (TOUGH) Survey. I. Survey Design and Catalogs. *ApJ*, 756:187, September 2012. doi: 10.1088/0004-637X/756/2/187.

A. M. Hopkins and J. F. Beacom. On the Normalization of the Cosmic Star Formation History. *ApJ*, 651:142–154, November 2006. doi: 10.1086/506610.

A. M. Hopkins and J. F. Beacom. Erratum: "On the Normalization of the Cosmic Star Formation History" (ApJ, 651, 142 [20067]). *ApJ*, 682:1486, August 2008. doi: 10.1086/589809.

C. Hopman, D. Guetta, E. Waxman, and S. Portegies Zwart. The Redshift Distribution of Short Gamma-Ray Bursts from Dynamically Formed Neutron Star Binaries. *ApJ*, 643: L91–L94, June 2006. doi: 10.1086/505141.

E. J. Howell, D. M. Coward, G. Stratta, B. Gendre, and H. Zhou. Constraining the rate and luminosity function of Swift gamma-ray bursts. *MNRAS*, 444:15–28, October 2014. doi: 10.1093/mnras/stu1403.

T. Isobe, E. D. Feigelson, M. G. Akritas, and G. J. Babu. Linear regression in astronomy. *ApJ*, 364:104–113, November 1990. doi: 10.1086/169390.

Z. Ivezic, T. Axelrod, W. N. Brandt, D. L. Burke, C. F. Claver, A. Connolly, K. H. Cook, P. Gee, D. K. Gilmore, S. H. Jacoby, R. L. Jones, S. M. Kahn, J. P. Kantor, V. V. Krabbendam, R. H. Lupton, D. G. Monet, P. A. Pinto, A. Saha, T. L. Schalk, D. P. Schneider, M. A. Strauss, C. W. Stubbs, D. Sweeney, A. Szalay, J. J. Thaler, J. A. Tyson, and LSST Collaboration. Large Synoptic Survey Telescope: From Science Drivers To Reference Design. *Serbian Astronomical Journal*, 176:1–13, June 2008a. doi: 10.2298/SAJ0876001I.

Z. Ivezic, J. A. Tyson, B. Abel, E. Acosta, R. Allsman, Y. AlSayyad, S. F. Anderson, J. Andrew, R. Angel, G. Angeli, R. Ansari, P. Antilogus, K. T. Arndt, P. Astier, E. Aubourg, T. Axelrod, D. J. Bard, J. D. Barr, A. Barrau, J. G. Bartlett, B. J. Bauman, S. Beaumont, A. C. Becker, J. Becla, C. Beldica, S. Bellavia, G. Blanc, R. D. Blandford, J. S. Bloom, J. Bogart, K. Borne, J. F. Bosch, D. Boutigny, W. N. Brandt, M. E. Brown, J. S. Bullock, P. Burchat, D. L. Burke, G. Cagnoli, D. Calabrese, S. Chandrasekharan, S. Chesley, E. C. Cheu, J. Chiang, C. F. Claver, A. J. Connolly, K. H. Cook, A. Cooray, K. R. Covey, C. Cribbs, W. Cui, R. Cutri, G. Daubard, G. Daues, F. Delgado, S. Digel, P. Doherty, R. Dubois, G. P. Dubois-Felsmann, J. Durech, M. Eracleous, H. Ferguson, J. Frank, M. Freemon, E. Gangler, E. Gawiser, J. C. Geary, P. Gee, M. Geha, R. R. Gibson, D. K. Gilmore, T. Glanzman, I. Goodenow, W. J. Gressler, P. Gris, A. Guyonnet, P. A. Hascall, J. Haupt, F. Hernandez, C. Hogan, D. Huang, M. E. Huffer, W. R. Innes, S. H. Jacoby, B. Jain, J. Jee, J. G. Jernigan, D. Jevremovic, K. Johns, R. L. Jones, C. Juramy-Gilles, M. Juric, S. M. Kahn, J. S. Kalirai, N. Kallivayalil, B. Kalmbach, J. P. Kantor, M. M. Kasliwal, R. Kessler, D. Kirkby, L. Knox, I. Kotov, V. L. Krabbendam, S. Krughoff, P. Kubanek, J. Kuczewski, S. Kulkarni, R. Lambert, L. Le Guillou, D. Levine, M. Liang, K. Lim, C. Lintott, R. H. Lupton, A. Mahabal, P. Marshall, S. Marshall, M. May, R. McKercher, M. Migliore, M. Miller, D. J. Mills, D. G. Monet, M. Moniez, D. R. Neill, J. Nief, A. Nomerotski, M. Nordby, P. O'Connor, J. Oliver, S. S. Olivier, K. Olsen, S. Ortiz, R. E. Owen, R. Pain, J. R. Peterson, C. E. Petry, F. Pierfederici, S. Pietrowicz, R. Pike, P. A. Pinto, R. Plante, S. Plate, P. A. Price, M. Prouza, V. Radeka, J. Rajagopal, A. Rasmussen, N. Regnault, S. T. Ridgway, S. Ritz, W. Rosing, C. Roucelle, M. R. Rumore, S. Russo, A. Saha, B. Sassolas, T. L. Schalk, R. H. Schindler, D. P. Schneider, G. Schumacher, J. Sebag, G. H. Sembroski, L. G. Seppala, I. Shipsey, N. Silvestri, J. A. Smith, R. C. Smith, M. A. Strauss, C. W. Stubbs, D. Sweeney, A. Szalay, P. Takacs, J. J. Thaler, R. Van Berg, D. Vanden Berk, K. Vetter, F. Virieux, B. Xin, L. Walkowicz, C. W. Walter, D. L. Wang, M. Warner, B. Willman, D. Wittman, S. C. Wolff, W. M. Wood-Vasey, P. Yoachim, H. Zhan, and for the LSST Collaboration. LSST: from

Science Drivers to Reference Design and Anticipated Data Products. *ArXiv e-prints*, May 2008b.

P. Jakobsson, A. Levan, J. P. U. Fynbo, R. Priddey, J. Hjorth, N. Tanvir, D. Watson, B. L. Jensen, J. Sollerman, P. Natarajan, J. Gorosabel, J. M. Castro Cerón, K. Pedersen, T. Pursimo, A. S. Árnadóttir, A. J. Castro-Tirado, C. J. Davis, H. J. Deeg, D. A. Fiuza, S. Mikolaitis, and S. G. Sousa. A mean redshift of 2.8 for Swift gamma-ray bursts. *A&A*, 447: 897–903, March 2006. doi: 10.1051/0004-6361:20054287.

P. Jakobsson, J. Hjorth, D. Malesani, R. Chapman, J. P. U. Fynbo, N. R. Tanvir, B. Milvang-Jensen, P. M. Vreeswijk, G. Letawe, and R. L. C. Starling. The Optically Unbiased GRB Host (TOUGH) Survey. III. Redshift Distribution. *ApJ*, 752:62, June 2012. doi: 10.1088/0004-637X/752/1/62.

J. Japelj and A. Gomboc. Detectability of GRB Optical Afterglows with Gaia Satellite. *Publications of the Astronomical Society of Pacific*, 123:1034, September 2011. doi: 10.1086/661979.

R. Jimenez, D. Band, and T. Piran. Energetics of Gamma-Ray Bursts. *ApJ*, 561:171–177, November 2001. doi: 10.1086/323224.

Z.-P. Jin, X. Li, Z. Cano, S. Covino, Y.-Z. Fan, and D.-M. Wei. The Light Curve of the Macronova Associated with the Long-Short Burst GRB 060614. *ApJ*, 811:L22, October 2015. doi: 10.1088/2041-8205/811/2/L22.

Z.-P. Jin, K. Hotokezaka, X. Li, M. Tanaka, P. D'Avanzo, Y.-Z. Fan, S. Covino, D.-M. Wei, and T. Piran. The Macronova in GRB 050709 and the GRB-macronova connection. *Nature Communications*, 7:12898, September 2016. doi: 10.1038/ncomms12898.

Y. Kaneko, R. D. Preece, M. S. Briggs, W. S. Paciesas, C. A. Meegan, and D. L. Band. The Complete Spectral Catalog of Bright BATSE Gamma-Ray Bursts. *ApJ*, 166:298–340, September 2006. doi: 10.1086/505911.

J. I. Katz. Low-frequency spectra of gamma-ray bursts. *ApJ*, 432:L107–L109, September 1994. doi: 10.1086/187523.

I. Khabibullin, S. Sazonov, and R. Sunyaev. SRG/eROSITA prospects for the detection of GRB afterglows. *MNRAS*, 426:1819–1828, November 2012. doi: 10.1111/j.1365-2966.2012.21807.x.

C. Kim, B. B. P. Perera, and M. A. McLaughlin. Implications of PSR J0737-3039B for the Galactic NS-NS binary merger rate. *MNRAS*, 448:928–938, March 2015. doi: 10.1093/mnras/stu2729.

S. Kobayashi, T. Piran, and R. Sari. Can Internal Shocks Produce the Variability in Gamma-Ray Bursts? *ApJ*, 490:92, November 1997. doi: 10.1086/512791.

S. Kobayashi, T. Piran, and R. Sari. Hydrodynamics of a Relativistic Fireball: The Complete Evolution. *ApJ*, 513:669–678, March 1999. doi: 10.1086/306868.

D. Kocevski and E. Liang. Quantifying the Luminosity Evolution in Gamma-Ray Bursts. *ApJ*, 642:371–381, May 2006. doi: 10.1086/500816.

D. Kocevski, N. Butler, and J. S. Bloom. Pulse Width Evolution of Late-Time X-Ray Flares in Gamma-Ray Bursts. *ApJ*, 667:1024–1032, October 2007. doi: 10.1086/520041.

C. Kouveliotou, J. Granot, J. L. Racusin, E. Bellm, G. Vianello, S. Oates, C. L. Fryer, S. E. Boggs, F. E. Christensen, W. W. Craig, C. D. Dermer, N. Gehrels, C. J. Hailey, F. A. Harrison, A. Melandri, J. E. McEnery, C. G. Mundell, D. K. Stern, G. Tagliaferri, and W. W. Zhang. NuSTAR Observations of GRB 130427A Establish a Single Component Synchrotron Afterglow Origin for the Late Optical to Multi-GeV Emission. *ApJ*, 779:L1, December 2013. doi: 10.1088/2041-8205/779/1/L1.

T. Krühler, D. Malesani, J. P. U. Fynbo, O. E. Hartoog, J. Hjorth, P. Jakobsson, D. A. Perley, A. Rossi, P. Schady, S. Schulze, N. R. Tanvir, S. D. Vergani, K. Wiersema, P. M. J. Afonso, J. Bolmer, Z. Cano, S. Covino, V. D'Elia, A. de Ugarte Postigo, R. Filgas, M. Friis, J. F. Graham, J. Greiner, P. Goldoni, A. Gomboc, F. Hammer, J. Japelj, D. A. Kann, L. Kaper, S. Klose, A. J. Levan, G. Leloudas, B. Milvang-Jensen, A. Nicuesa Guelbenzu, E. Palazzi, E. Pian, S. Piranomonte, R. Sánchez-Ramírez, S. Savaglio, J. Selsing, G. Tagliaferri, P. M. Vreeswijk, D. J. Watson, and D. Xu. GRB hosts through cosmic time. VLT/X-Shooter emission-line spectroscopy of 96 γ-ray-burst-selected galaxies at $0.1 < z < 3.6$. *A&A*, 581:A125, September 2015. doi: 10.1051/0004-6361/201425561.

P. Kumar. Gamma-Ray Burst Energetics. *ApJ*, 523:L113–L116, October 1999. doi: 10.1086/312265.

P. Kumar and J. Granot. The Evolution of a Structured Relativistic Jet and Gamma-Ray Burst Afterglow Light Curves. *ApJ*, 591:1075–1085, July 2003. doi: 10.1086/375186.

P. Kumar and G. F. Smoot. Some implications of inverse-Compton scattering of hot cocoon radiation by relativistic jets in gamma-ray bursts. *MNRAS*, 445:528–543, November 2014. doi: 10.1093/mnras/stu1638.

T. Laskar, E. Berger, B. A. Zauderer, R. Margutti, A. M. Soderberg, S. Chakraborti, R. Lunnan, R. Chornock, P. Chandra, and A. Ray. A Reverse Shock in GRB 130427A. *ApJ*, 776:119, October 2013. doi: 10.1088/0004-637X/776/2/119.

N. M. Law, S. R. Kulkarni, R. G. Dekany, E. O. Ofek, R. M. Quimby, P. E. Nugent, J. Surace, C. C. Grillmair, J. S. Bloom, M. M. Kasliwal, L. Bildsten, T. Brown, S. B. Cenko, D. Ciardi, E. Croner, S. G. Djorgovski, J. van Eyken, A. V. Filippenko, D. B. Fox, A. Gal-Yam, D. Hale, N. Hamam, G. Helou, J. Henning, D. A. Howell, J. Jacobsen, R. Laher, S. Mattingly, D. McKenna, A. Pickles, D. Poznanski, G. Rahmer, A. Rau, W. Rosing, M. Shara, R. Smith, D. Starr, M. Sullivan, V. Velur, R. Walters, and J. Zolkower. The Palomar Transient Factory: System Overview, Performance, and First Results. *Publications of the Astronomical Society of Pacific*, 121:1395, December 2009. doi: 10.1086/648598.

T. J. W. Lazio, T. E. Clarke, W. M. Lane, C. Gross, N. E. Kassim, P. S. Ray, D. Wood, J. A. York, A. Kerkhoff, B. Hicks, E. Polisensky, K. Stewart, N. Paravastu Dalal, A. S. Cohen, and W. C. Erickson. Surveying the Dynamic Radio Sky with the Long Wavelength Demonstrator Array. *AJ*, 140:1995–2006, December 2010. doi: 10.1088/0004-6256/140/6/1995.

D. Lazzati and M. C. Begelman. Universal GRB Jets from Jet-Cocoon Interaction in Massive Stars. *ApJ*, 629:903–907, August 2005. doi: 10.1086/430877.

D. Lazzati and R. Perna. X-ray flares and the duration of engine activity in gamma-ray bursts. *MNRAS*, 375:L46–L50, February 2007. doi: 10.1111/j.1745-3933.2006.00273.x.

D. Lazzati, G. Ghisellini, and A. Celotti. Constraints on the bulk Lorentz factor in the internal shock scenario for gamma-ray bursts. *MNRAS*, 309:L13–L17, October 1999. doi: 10.1046/j.1365-8711.1999.02970.x.

D. Lazzati, E. Rossi, S. Covino, G. Ghisellini, and D. Malesani. The afterglow of GRB 021004: Surfing on density waves. *A&A*, 396:L5–L9, December 2002. doi: 10.1051/0004-6361:20021618.

D. Lazzati, S. Covino, J. Gorosabel, E. Rossi, G. Ghisellini, E. Rol, J. M. Castro Cerón, A. J. Castro-Tirado, M. Della Valle, S. di Serego Alighieri, A. S. Fruchter, J. P. U. Fynbo, P. Goldoni, J. Hjorth, G. L. Israel, L. Kaper, N. Kawai, E. Le Floc'h, D. Malesani, N. Masetti, P. Mazzali, F. Mirabel, P. Moller, S. Ortolani, E. Palazzi, E. Pian, J. Rhoads, G. Ricker, J. D. Salmonson, L. Stella, G. Tagliaferri, N. Tanvir, E. van den Heuvel, R. A. M. J. Wijers, and F. M. Zerbi. On the jet structure and magnetic field configuration of GRB 020813. *A&A*, 422:121–128, July 2004a. doi: 10.1051/0004-6361:20035951.

D. Lazzati, E. Rossi, G. Ghisellini, and M. J. Rees. Compton drag as a mechanism for very high linear polarization in gamma-ray bursts. *MNRAS*, 347:L1–L5, January 2004b. doi: 10.1111/j.1365-2966.2004.07387.x.

D. Lazzati, C. H. Blackwell, B. J. Morsony, and M. C. Begelman. X-ray flares from propagation instabilities in long gamma-ray burst jets. *MNRAS*, 411:L16–L20, February 2011. doi: 10.1111/j.1745-3933.2010.00984.x.

G. Leloudas, J. P. U. Fynbo, S. Schulze, D. Xu, D. Malesani, S. Geier, Z. Cano, and P. Jakobsson. GRB 130702A: NOT spectroscopy and redshift of the nearby bright galaxy. *GRB Coordinates Network, Circular Service, No. 14983, #1 (2013)*, 4983, 2013.

A. Levinson and D. Eichler. Baryon Loading of Gamma-Ray Burst by Neutron Pickup. *ApJ*, 594:L19–L22, September 2003. doi: 10.1086/378487.

A. Levinson, E. O. Ofek, E. Waxman, and A. Gal-Yam. Orphan Gamma-Ray Burst Radio Afterglows: Candidates and Constraints on Beaming. *ApJ*, 576:923–931, September 2002. doi: 10.1086/341866.

L.-X. Li. Star formation history up to z = 7.4: implications for gamma-ray bursts and cosmic metallicity evolution. *MNRAS*, 388:1487–1500, August 2008. doi: 10.1111/j.1365-2966.2008.13488.x.

L.-X. Li and B. Paczyński. Transient Events from Neutron Star Mergers. *ApJ*, 507:L59–L62, November 1998. doi: 10.1086/311680.

E. Liang, B. Zhang, F. Virgili, and Z. G. Dai. Low-Luminosity Gamma-Ray Bursts as a Unique Population: Luminosity Function, Local Rate, and Beaming Factor. *ApJ*, 662: 1111–1118, June 2007. doi: 10.1086/517959.

E.-W. Liang, S.-X. Yi, J. Zhang, H.-J. Lü, B.-B. Zhang, and B. Zhang. Constraining Gamma-ray Burst Initial Lorentz Factor with the Afterglow Onset Feature and Discovery of a Tight Γ_0-$E_{gamma,iso}$ Correlation. *ApJ*, 725:2209–2224, December 2010. doi: 10.1088/0004-637X/725/2/2209.

A. Lien, T. Sakamoto, S. D. Barthelmy, W. H. Baumgartner, J. K. Cannizzo, K. Chen, N. R. Collins, J. R. Cummings, N. Gehrels, H. A. Krimm, C. B. Markwardt, D. M. Palmer, M. Stamatikos, E. Troja, and T. N. Ukwatta. The Third Swift Burst Alert Telescope Gamma-Ray Burst Catalog. *ApJ*, 829:7, September 2016. doi: 10.3847/0004-637X/829/1/7.

LIGO Scientific Collaboration, J. Aasi, B. P. Abbott, R. Abbott, T. Abbott, M. R. Abernathy, K. Ackley, C. Adams, T. Adams, P. Addesso, and et al. Advanced LIGO. *Classical and Quantum Gravity*, 32(7):074001, April 2015. doi: 10.1088/0264-9381/32/7/074001.

L. Lindegren. Gaia: Astrometric performance and current status of the project. In S. A. Klioner, P. K. Seidelmann, and M. H. Soffel, editors, *Relativity in Fundamental Astronomy: Dynamics, Reference Frames, and Data Analysis*, volume 261 of *IAU Symposium*, pages 296–305, January 2010. doi: 10.1017/S1743921309990548.

V. M. Lipunov, K. A. Postnov, and M. E. Prokhorov. Gamma-Ray Bursts as Standard-Energy Explosions. *Astronomy Reports*, 45:236–240, March 2001. doi: 10.1134/1.1353364.

Y. Lithwick and R. Sari. Lower Limits on Lorentz Factors in Gamma-Ray Bursts. *ApJ*, 555: 540–545, July 2001. doi: 10.1086/321455.

N. M. Lloyd and V. Petrosian. Distribution of Spectral Characteristics and the Cosmological Evolution of Gamma-Ray Bursts. *ApJ*, 511:550–561, February 1999. doi: 10.1086/306719.

N. M. Lloyd and V. Petrosian. Synchrotron Radiation as the Source of Gamma-Ray Burst Spectra. *ApJ*, 543:722–732, November 2000. doi: 10.1086/317125.

N. M. Lloyd-Ronning, X. Dai, and B. Zhang. On the Structure of Quasi-universal Jets for Gamma-Ray Bursts. *ApJ*, 601:371–379, January 2004. doi: 10.1086/380483.

H.-J. Lü, J. Lü, S.-Q. Zhong, X.-L. Huang, H.-M. Zhang, W. Xie, R.-J. Lu, and E.-W. Liang. Extremely bright GRB 160625B with multi-episodes emission: Evidences for long-term ejecta evolution. *ArXiv e-prints*, February 2017.

D. Lynden-Bell. A method of allowing for known observational selection in small samples applied to 3CR quasars. *MNRAS*, 155:95, 1971. doi: 10.1093/mnras/155.1.95.

G. A. MacLachlan, A. Shenoy, E. Sonbas, K. S. Dhuga, B. E. Cobb, T. N. Ukwatta, D. C. Morris, A. Eskandarian, L. C. Maximon, and W. C. Parke. Minimum variability time-scales of long and short GRBs. *MNRAS*, 432:857–865, June 2013. doi: 10.1093/mnras/stt241.

P. Madau and M. Dickinson. Cosmic Star-Formation History. *Annual Review of A&A*, 52: 415–486, August 2014. doi: 10.1146/annurev-astro-081811-125615.

F. Malacrino, J.-L. Atteia, M. Boër, A. Klotz, C. Veillet, J.-C. Cuillandre, and GRB Rtas Collaboration. Constraining the rate of GRB visible afterglows with the CFHTLS very wide survey. *A&A*, 464:L29–L32, March 2007. doi: 10.1051/0004-6361:20066912.

A. Maloney and V. Petrosian. The Evolution and Luminosity Function of Quasars from Complete Optical Surveys. *ApJ*, 518:32–43, June 1999. doi: 10.1086/307260.

R. Margutti, C. Guidorzi, G. Chincarini, M. G. Bernardini, F. Genet, J. Mao, and F. Pasotti. Lag-luminosity relation in γ-ray burst X-ray flares: a direct link to the prompt emission. *MNRAS*, 406:2149–2167, August 2010. doi: 10.1111/j.1365-2966.2010.16824.x.

R. Margutti, G. Bernardini, R. Barniol Duran, C. Guidorzi, R. F. Shen, and G. Chincarini. On the average gamma-ray burst X-ray flaring activity. *MNRAS*, 410:1064–1075, January 2011. doi: 10.1111/j.1365-2966.2010.17504.x.

D. V. Martynov, E. D. Hall, B. P. Abbott, R. Abbott, T. D. Abbott, C. Adams, R. X. Adhikari, R. A. Anderson, S. B. Anderson, K. Arai, and et al. Sensitivity of the Advanced LIGO detectors at the beginning of gravitational wave astronomy. *Physical Review D.*, 93(11): 112004, June 2016. doi: 10.1103/PhysRevD.93.112004.

A. Maselli, A. Melandri, L. Nava, C. G. Mundell, N. Kawai, S. Campana, S. Covino, J. R. Cummings, G. Cusumano, P. A. Evans, G. Ghirlanda, G. Ghisellini, C. Guidorzi, S. Kobayashi, P. Kuin, V. La Parola, V. Mangano, S. Oates, T. Sakamoto, M. Serino, F. Virgili, B.-B. Zhang, S. Barthelmy, A. Beardmore, M. G. Bernardini, D. Bersier, D. Burrows, G. Calderone, M. Capalbi, J. Chiang, P. D'Avanzo, V. D'Elia, M. De Pasquale, D. Fugazza, N. Gehrels, A. Gomboc, R. Harrison, H. Hanayama, J. Japelj, J. Kennea, D. Kopac, C. Kouveliotou, D. Kuroda, A. Levan, D. Malesani, F. Marshall, J. Nousek, P. O'Brien, J. P. Osborne, C. Pagani, K. L. Page, M. Page, M. Perri, T. Pritchard, P. Romano, Y. Saito, B. Sbarufatti, R. Salvaterra, I. Steele, N. Tanvir, G. Vianello, B. Weigand, K. Wiersema, Y. Yatsu, T. Yoshii, and G. Tagliaferri. GRB 130427A: A Nearby Ordinary Monster. *Science*, 343: 48–51, January 2014. doi: 10.1126/science.1242279.

A. Maselli, A. D'Ai, A. Y. Lien, D. M. Palmer, B. Sbarufatti, M. H. Siegel, M. Stamatikos, and T. N. Ukwatta. GRB 151027A: Swift detection of a burst with a bright optical afterglow. *GRB Coordinates Network, Circular Service, No. 18478, #1 (2015)*, 18478, 2015.

N. Matsumura, K. Niinuma, M. Kuniyoshi, K. Takefuji, K. Asuma, T. Daishido, S. Kida, T. Tanaka, T. Aoki, S. Ishikawa, K. Hirano, and S. Nakagawa. The Closely Positioned Three Radio Transients in the Nasu 1.4 GHz Wide-Field Survey. *AJ*, 138:787–795, September 2009. doi: 10.1088/0004-6256/138/3/787.

C. D. Matzner and C. F. McKee. The Expulsion of Stellar Envelopes in Core-Collapse Supernovae. *ApJ*, 510:379–403, January 1999. doi: 10.1086/306571.

A. Maxham and B. Zhang. Modeling Gamma-Ray Burst X-Ray Flares Within the Internal Shock Model. *ApJ*, 707:1623–1633, December 2009. doi: 10.1088/0004-637X/707/2/1623.

M. V. Medvedev. Theory of "Jitter" Radiation from Small-Scale Random Magnetic Fields and Prompt Emission from Gamma-Ray Burst Shocks. *ApJ*, 540:704–714, September 2000. doi: 10.1086/309374.

C. Meegan, G. Lichti, P. N. Bhat, E. Bissaldi, M. S. Briggs, V. Connaughton, R. Diehl, G. Fishman, J. Greiner, A. S. Hoover, A. J. van der Horst, A. von Kienlin, R. M. Kippen, C. Kouveliotou, S. McBreen, W. S. Paciesas, R. Preece, H. Steinle, M. S. Wallace, R. B. Wilson, and C. Wilson-Hodge. The Fermi Gamma-ray Burst Monitor. *ApJ*, 702:791-804, September 2009. doi: 10.1088/0004-637X/702/1/791.

C. A. Meegan, G. N. Pendleton, M. S. Briggs, C. Kouveliotou, T. M. Koshut, J. P. Lestrade, W. S. Paciesas, M. L. McCollough, J. J. Brainerd, J. M. Horack, J. Hakkila, W. Henze, R. D. Preece, R. S. Mallozzi, and G. J. Fishman. The Third BATSE Gamma-Ray Burst Catalog. *ApJ*, 106:65, September 1996. doi: 10.1086/192329.

A. Melandri, B. Sbarufatti, P. D'Avanzo, R. Salvaterra, S. Campana, S. Covino, S. D. Vergani, L. Nava, G. Ghisellini, G. Ghirlanda, D. Fugazza, V. Mangano, M. Capalbi, and G. Tagliaferri. The dark bursts population in a complete sample of bright Swift long gamma-ray bursts. *MNRAS*, 421:1265–1272, April 2012. doi: 10.1111/j.1365-2966.2011.20398.x.

A. Melandri, S. Covino, D. Rogantini, R. Salvaterra, B. Sbarufatti, M. G. Bernardini, S. Campana, P. D'Avanzo, V. D'Elia, D. Fugazza, G. Ghirlanda, G. Ghisellini, L. Nava, S. D. Vergani, and G. Tagliaferri. Optical and X-ray rest-frame light curves of the BAT6 sample. *A&A*, 565:A72, May 2014. doi: 10.1051/0004-6361/201323361.

A. Merloni. All-sky X-ray surveys with eROSITA: Clusters, AGN, active stars and mor. In *Science from the Next Generation Imaging and Spectroscopic Surveys*, page 43, October 2012.

P. Meszaros and M. J. Rees. Relativistic fireballs and their impact on external matter - Models for cosmological gamma-ray bursts. *ApJ*, 405:278–284, March 1993a. doi: 10.1086/172360.

P. Meszaros and M. J. Rees. Gamma-Ray Bursts: Multiwaveband Spectral Predictions for Blast Wave Models. *ApJ*, 418:L59, December 1993b. doi: 10.1086/187116.

P. Mészáros and M. J. Rees. Collapsar Jets, Bubbles, and Fe Lines. *ApJ*, 556:L37–L40, July 2001. doi: 10.1086/322934.

B. D. Metzger, P. K. G. Williams, and E. Berger. Extragalactic Synchrotron Transients in the Era of Wide-field Radio Surveys. I. Detection Rates and Light Curve Characteristics. *ApJ*, 806:224, June 2015. doi: 10.1088/0004-637X/806/2/224.

M. R. Metzger, S. G. Djorgovski, S. R. Kulkarni, C. C. Steidel, K. L. Adelberger, D. A. Frail, E. Costa, and F. Frontera. Spectral constraints on the redshift of the optical counterpart to the γ-ray burst of 8 May 1997. *Nature*, 387:878–880, June 1997. doi: 10.1038/43132.

N. Mirabal, J. P. Halpern, D. An, J. R. Thorstensen, and D. M. Terndrup. GRB 060218/SN 2006aj: A Gamma-Ray Burst and Prompt Supernova at z = 0.0335. *ApJ*, 643:L99–L102, June 2006. doi: 10.1086/505177.

R. Mochkovitch and L. Nava. The E_p - E_{iso} relation and the internal shock model. *A&A*, 577:A31, May 2015. doi: 10.1051/0004-6361/201424490.

E. Molinari, S. D. Vergani, D. Malesani, S. Covino, P. D'Avanzo, G. Chincarini, F. M. Zerbi, L. A. Antonelli, P. Conconi, V. Testa, G. Tosti, F. Vitali, F. D'Alessio, G. Malaspina, L. Nicastro, E. Palazzi, D. Guetta, S. Campana, P. Goldoni, N. Masetti, E. J. A. Meurs, A. Monfardini, L. Norci, E. Pian, S. Piranomonte, D. Rizzuto, M. Stefanon, L. Stella, G. Tagliaferri, P. A. Ward, G. Ihle, L. Gonzalez, A. Pizarro, P. Sinclaire, and J. Valenzuela. REM observations of GRB 060418 and GRB 060607A: the onset of the afterglow and the initial fireball Lorentz factor determination. *A&A*, 469:L13–L16, July 2007. doi: 10.1051/0004-6361:20077388.

B. J. Morsony, D. Lazzati, and M. C. Begelman. Temporal and Angular Properties of Gamma-Ray Burst Jets Emerging from Massive Stars. *ApJ*, 665:569–598, August 2007. doi: 10.1086/519483.

E. Nakar and A. Gal-Yam. Are the Properties of Host Galaxies of Short-Hard GRBs Consistent With an Origin of NS-NS Mergers? In *American Astronomical Society Meeting Abstracts*, volume 37 of *Bulletin of the American Astronomical Society*, page 1418, December 2005.

E. Nakar and T. Piran. Modeling Fluctuations in Gamma-Ray Burst Afterglow Light Curves. *ApJ*, 598:400–410, November 2003. doi: 10.1086/378388.

E. Nakar, T. Piran, and J. Granot. The Detectability of Orphan Afterglows. *ApJ*, 579:699–705, November 2002. doi: 10.1086/342791.

E. Nakar, A. Gal-Yam, and D. B. Fox. The Local Rate and the Progenitor Lifetimes of Short-Hard Gamma-Ray Bursts: Synthesis and Predictions for the Laser Interferometer Gravitational-Wave Observatory. *ApJ*, 650:281–290, October 2006. doi: 10.1086/505855.

E. Nakar, S. Ando, and R. Sari. Klein-Nishina Effects on Optically Thin Synchrotron and Synchrotron Self-Compton Spectrum. *ApJ*, 703:675–691, September 2009. doi: 10.1088/0004-637X/703/1/675.

F. Nappo, A. Pescalli, G. Oganesyan, G. Ghirlanda, M. Giroletti, A. Melandri, S. Campana, G. Ghisellini, O. S. Salafia, P. D'Avanzo, M. G. Bernardini, S. Covino, E. Carretti, A. Celotti, V. D'Elia, L. Nava, E. Palazzi, S. Poppi, I. Prandoni, S. Righini, A. Rossi, R. Salvaterra, G. Tagliaferri, V. Testa, T. Venturi, and S. D. Vergani. The 999th Swift gamma-ray burst: Some like it thermal. A multiwavelength study of GRB 151027A. *A&A*, 598:A23, February 2017. doi: 10.1051/0004-6361/201628801.

P. Natarajan, B. Albanna, J. Hjorth, E. Ramirez-Ruiz, N. Tanvir, and R. Wijers. The redshift distribution of gamma-ray bursts revisited. *MNRAS*, 364:L8–L12, November 2005. doi: 10.1111/j.1745-3933.2005.00094.x.

L. Nava, G. Ghisellini, G. Ghirlanda, F. Tavecchio, and C. Firmani. On the interpretation of spectral-energy correlations in long gamma-ray bursts. *A&A*, 450:471–481, May 2006. doi: 10.1051/0004-6361:20054211.

L. Nava, G. Ghirlanda, G. Ghisellini, and A. Celotti. Spectral properties of 438 GRBs detected by Fermi/GBM. *A&A*, 530:A21, June 2011. doi: 10.1051/0004-6361/201016270.

L. Nava, R. Salvaterra, G. Ghirlanda, G. Ghisellini, S. Campana, S. Covino, G. Cusumano, P. D'Avanzo, V. D'Elia, D. Fugazza, A. Melandri, B. Sbarufatti, S. D. Vergani, and G. Tagliaferri. A complete sample of bright Swift long gamma-ray bursts: testing the spectral-energy correlations. *MNRAS*, 421:1256–1264, April 2012. doi: 10.1111/j.1365-2966.2011.20394.x.

L. Nava, L. Sironi, G. Ghisellini, A. Celotti, and G. Ghirlanda. Afterglow emission in gamma-ray bursts - I. Pair-enriched ambient medium and radiative blast waves. *MNRAS*, 433:2107–2121, August 2013. doi: 10.1093/mnras/stt872.

A. Nicuesa Guelbenzu, S. Klose, A. Rossi, D. A. Kann, T. Krühler, J. Greiner, A. Rau, F. Olivares E., P. M. J. Afonso, R. Filgas, A. Küpcü Yoldaş, S. McBreen, M. Nardini, P. Schady, S. Schmidl, A. C. Updike, and A. Yoldaş. GRB 090426: Discovery of a jet break in a short burst afterglow. *A&A*, 531:L6, July 2011. doi: 10.1051/0004-6361/201116657.

J. P. Norris, R. J. Nemiroff, J. T. Bonnell, J. D. Scargle, C. Kouveliotou, W. S. Paciesas, C. A. Meegan, and G. J. Fishman. Attributes of Pulses in Long Bright Gamma-Ray Bursts. *ApJ*, 459:393, March 1996. doi: 10.1086/176902.

G. Oganesyan, L. Nava, G. Ghirlanda, and A. Celotti. Detection of Low-energy Breaks in Gamma-Ray Burst Prompt Emission Spectra. *ApJ*, 846:137, September 2017. doi: 10.3847/1538-4357/aa831e.

R. O'Shaughnessy, K. Belczynski, and V. Kalogera. Short Gamma-Ray Bursts and Binary Mergers in Spiral and Elliptical Galaxies: Redshift Distribution and Hosts. *ApJ*, 675:566-585, March 2008. doi: 10.1086/526334.

W. S. Paciesas, C. A. Meegan, G. N. Pendleton, M. S. Briggs, C. Kouveliotou, T. M. Koshut, J. P. Lestrade, M. L. McCollough, J. J. Brainerd, J. Hakkila, W. Henze, R. D. Preece, V. Connaughton, R. M. Kippen, R. S. Mallozzi, G. J. Fishman, G. A. Richardson, and M. Sahi. The Fourth BATSE Gamma-Ray Burst Catalog (Revised). *ApJ*, 122:465–495, June 1999. doi: 10.1086/313224.

B. Paczynski. Gamma-ray bursters at cosmological distances. *ApJ*, 308:L43–L46, September 1986. doi: 10.1086/184740.

B. Paczynski and J. E. Rhoads. Radio Transients from Gamma-Ray Bursters. *ApJ*, 418:L5, November 1993. doi: 10.1086/187102.

D. M. Palmer, S. D. Barthelmy, J. R. Cummings, N. Gehrels, H. A. Krimm, A. Y. Lien, C. B. Markwardt, A. Maselli, T. Sakamoto, M. Stamatikos, and T. N. Ukwatta. GRB 151027A: Swift-BAT refined analysis. *GRB Coordinates Network, Circular Service, No. 18496, #1 (2015)*, 18496, 2015.

A. Panaitescu and P. Kumar. Analytic light curves of gamma-ray burst afterglows: Homogeneous versus wind external media. *ApJ*, 543(1):66, 2000. URL `http://stacks.iop.org/0004-637X/543/i=1/a=66`.

A. Panaitescu and P. Kumar. Fundamental Physical Parameters of Collimated Gamma-Ray Burst Afterglows. *ApJ*, 560:L49–L53, October 2001. doi: 10.1086/324061.

A. Panaitescu and P. Kumar. Properties of Relativistic Jets in Gamma-Ray Burst Afterglows. *ApJ*, 571:779–789, June 2002. doi: 10.1086/340094.

A. Panaitescu and P. Mészáros. Gamma-Ray Bursts from Upscattered Self-absorbed Synchrotron Emission. *ApJ*, 544:L17–L21, November 2000. doi: 10.1086/317301.

A. Panaitescu, W. T. Vestrand, and P. Woźniak. An external-shock model for gamma-ray burst afterglow 130427A. *MNRAS*, 436:3106–3111, December 2013. doi: 10.1093/mnras/stt1792.

A. Pe'er. Temporal Evolution of Thermal Emission from Relativistically Expanding Plasma. *ApJ*, 682:463-473, July 2008. doi: 10.1086/588136.

A. Pe'er and B. Zhang. Synchrotron Emission in Small-Scale Magnetic Fields as a Possible Explanation for Prompt Emission Spectra of Gamma-Ray Bursts. *ApJ*, 653:454–461, December 2006. doi: 10.1086/508681.

A. Pe'er, P. Mészáros, and M. J. Rees. The Observable Effects of a Photospheric Component on GRB and XRF Prompt Emission Spectrum. *ApJ*, 642:995–1003, May 2006a. doi: 10.1086/501424.

A. Pe'er, P. Mészáros, and M. J. Rees. Radiation from an Expanding Cocoon as an Explanation of the Steep Decay Observed in GRB Early Afterglow Light Curves. *ApJ*, 652:482–489, November 2006b. doi: 10.1086/507595.

A. Pe'er, F. Ryde, R. A. M. J. Wijers, P. Mészáros, and M. J. Rees. A New Method of Determining the Initial Size and Lorentz Factor of Gamma-Ray Burst Fireballs Using a Thermal Emission Component. *ApJ*, 664:L1–L4, July 2007. doi: 10.1086/520534.

G. N. Pendleton, R. S. Mallozzi, W. S. Paciesas, M. S. Briggs, R. D. Preece, T. M. Koshut, J. M. Horack, C. A. Meegan, G. J. Fishman, J. Hakkila, and C. Kouveliotou. The Intensity Distribution for Gamma-Ray Bursts Observed with BATSE. *ApJ*, 464:606, June 1996. doi: 10.1086/177349.

F.-K. Peng, E.-W. Liang, X.-Y. Wang, S.-J. Hou, S.-Q. Xi, R.-J. Lu, J. Zhang, and B. Zhang. Photosphere Emission in the X-Ray Flares of Swift Gamma-Ray Bursts and Implications for the Fireball Properties. *ApJ*, 795:155, November 2014. doi: 10.1088/0004-637X/795/2/155.

D. Perley, J. S. Bloom, M. Cooper, J. Newman, P. Guhathakurta, J. X. Prochaska, and H.-W. Chen. GRB 050904: Keck I-band imaging. *GRB Coordinates Network*, 3932, 2005.

D. A. Perley, S. B. Cenko, A. Corsi, N. R. Tanvir, A. J. Levan, D. A. Kann, E. Sonbas, K. Wiersema, W. Zheng, X.-H. Zhao, J.-M. Bai, M. Bremer, A. J. Castro-Tirado, L. Chang, K. I. Clubb, D. Frail, A. Fruchter, E. Göğüş, J. Greiner, T. Güver, A. Horesh, A. V. Filippenko, S. Klose, J. Mao, A. N. Morgan, A. S. Pozanenko, S. Schmidl, B. Stecklum, M. Tanga, A. A. Volnova, A. E. Volvach, J.-G. Wang, J.-M. Winters, and Y.-X. Xin. The Afterglow of GRB 130427A from 1 to 10^{16} GHz. *ApJ*, 781:37, January 2014. doi: 10.1088/0004-637X/781/1/37.

D. A. Perley, L. Hillenbrand, and J. X. Prochaska. GRB 151027A: Keck/HIRES redshift. *GRB Coordinates Network, Circular Service, No. 18487, #1 (2015)*, 18487, 2015a.

D. A. Perley, R. A. Perley, J. Hjorth, M. J. Michałowski, S. B. Cenko, P. Jakobsson, T. Krühler, A. J. Levan, D. Malesani, and N. R. Tanvir. Connecting GRBs and ULIRGs: A Sensitive, Unbiased Survey for Radio Emission from Gamma-Ray Burst Host Galaxies at $0 < z < 2.5$. *Apj*, 801:102, March 2015b. doi: 10.1088/0004-637X/801/2/102.

D. A. Perley, T. Krühler, S. Schulze, A. de Ugarte Postigo, J. Hjorth, E. Berger, S. B. Cenko, R. Chary, A. Cucchiara, R. Ellis, W. Fong, J. P. U. Fynbo, J. Gorosabel, J. Greiner, P. Jakobsson, S. Kim, T. Laskar, A. J. Levan, M. J. Michałowski, B. Milvang-Jensen, N. R. Tanvir, C. C. Thöne, and K. Wiersema. The Swift Gamma-Ray Burst Host Galaxy Legacy Survey. I. Sample Selection and Redshift Distribution. *ApJ*, 817:7, January 2016a. doi: 10.3847/0004-637X/817/1/7.

D. A. Perley, N. R. Tanvir, J. Hjorth, T. Laskar, E. Berger, R. Chary, A. de Ugarte Postigo, J. P. U. Fynbo, T. Krühler, A. J. Levan, M. J. Michałowski, and S. Schulze. The Swift GRB Host Galaxy Legacy Survey. II. Rest-frame Near-IR Luminosity Distribution and Evidence for a Near-solar Metallicity Threshold. *ApJ*, 817:8, January 2016b. doi: 10.3847/0004-637X/817/1/8.

R. Perna, D. Lazzati, and F. Fiore. Time-dependent Photoionization in a Dusty Medium. II. Evolution of Dust Distributions and Optical Opacities. *ApJ*, 585:775–784, March 2003. doi: 10.1086/346109.

R. Perna, D. Lazzati, and B. Giacomazzo. Short Gamma-Ray Bursts from the Merger of Two Black Holes. *ApJ*, 821:L18, April 2016. doi: 10.3847/2041-8205/821/1/L18.

A. Pescalli, G. Ghirlanda, O. S. Salafia, G. Ghisellini, F. Nappo, and R. Salvaterra. Luminosity function and jet structure of Gamma-Ray Burst. *MNRAS*, 447:1911–1921, February 2015. doi: 10.1093/mnras/stu2482.

A. Pescalli, G. Ghirlanda, R. Salvaterra, G. Ghisellini, S. D. Vergani, F. Nappo, O. S. Salafia, A. Melandri, S. Covino, and D. Götz. The rate and luminosity function of long gamma ray bursts. *A&A*, 587:A40, March 2016. doi: 10.1051/0004-6361/201526760.

V. Petrosian, E. Kitanidis, and D. Kocevski. Cosmological Evolution of Long Gamma-Ray Bursts and the Star Formation Rate. *ApJj*, 806:44, June 2015. doi: 10.1088/0004-637X/806/1/44.

E. Pian, P. A. Mazzali, N. Masetti, P. Ferrero, S. Klose, E. Palazzi, E. Ramirez-Ruiz, S. E. Woosley, C. Kouveliotou, J. Deng, A. V. Filippenko, R. J. Foley, J. P. U. Fynbo, D. A. Kann, W. Li, J. Hjorth, K. Nomoto, F. Patat, D. N. Sauer, J. Sollerman, P. M. Vreeswijk, E. W. Guenther, A. Levan, P. O'Brien, N. R. Tanvir, R. A. M. J. Wijers, C. Dumas, O. Hainaut, D. S. Wong, D. Baade, L. Wang, L. Amati, E. Cappellaro, A. J. Castro-Tirado, S. Ellison, F. Frontera, A. S. Fruchter, J. Greiner, K. Kawabata, C. Ledoux, K. Maeda, P. Møller, L. Nicastro, E. Rol, and R. Starling. An optical supernova associated with the X-ray flash XRF 060218. *Nature*, 442:1011–1013, August 2006. doi: 10.1038/nature05082.

M. Pierre, I. Valtchanov, B. Altieri, S. Andreon, M. Bolzonella, M. Bremer, L. Disseau, S. Dos Santos, P. Gandhi, C. Jean, F. Pacaud, A. Read, A. Refregier, J. Willis, C. Adami, D. Alloin, M. Birkinshaw, L. Chiappetti, A. Cohen, A. Detal, P.-A. Duc, E. Gosset, J. Hjorth, L. Jones, O. Le Fèvre, C. Lonsdale, D. Maccagni, A. Mazure, B. McBreen, H. McCracken, Y. Mellier, T. Ponman, H. Quintana, H. Rottgering, A. Smette, J. Surdej, J.-L. Starck, L. Vigroux, and S. White. The XMM-LSS survey. Survey design and first results. *Journal of Cosmology and Astroparticle Physics*, 9:011, September 2004. doi: 10.1088/1475-7516/2004/09/011.

T. Piran. The implications of the Compton (GRO) observations for cosmological gamma-ray bursts. *ApJ*, 389:L45–L48, April 1992. doi: 10.1086/186345.

T. Piran. Gamma-ray bursts and the fireball model. *Physics Reports*, 314:575–667, June 1999. doi: 10.1016/S0370-1573(98)00127-6.

T. Piran. The physics of gamma-ray bursts. *Reviews of Modern Physics*, 76:1143–1210, October 2004. doi: 10.1103/RevModPhys.76.1143.

T. Piran, A. Shemi, and R. Narayan. Hydrodynamics of Relativistic Fireballs. *MNRAS*, 263: 861, August 1993. doi: 10.1093/mnras/263.4.861.

L. Piro, E. Troja, B. Gendre, G. Ghisellini, R. Ricci, K. Bannister, F. Fiore, L. A. Kidd, S. Piranomonte, and M. H. Wieringa. A Hot Cocoon in the Ultralong GRB 130925A: Hints of a POPIII-like Progenitor in a Low-Density Wind Environment. *ApJ*, 790:L15, August 2014. doi: 10.1088/2041-8205/790/2/L15.

Planck Collaboration, P. A. R. Ade, N. Aghanim, C. Armitage-Caplan, M. Arnaud, M. Ashdown, F. Atrio-Barandela, J. Aumont, C. Baccigalupi, A. J. Banday, and et al. Planck 2013 results. XXX. Cosmic infrared background measurements and implications for star formation. *A&A*, 571:A30, November 2014. doi: 10.1051/0004-6361/201322093.

C. Porciani and P. Madau. On the Association of Gamma-Ray Bursts with Massive Stars: Implications for Number Counts and Lensing Statistics. *ApJ*, 548:522–531, February 2001. doi: 10.1086/319027.

S. F. Portegies Zwart and L. R. Yungelson. Formation and evolution of binary neutron stars. *A&A*, 332:173–188, April 1998.

A. Pozanenko, E. Mazaeva, A. Volnova, and O. Burhonov. GRB 151027A: Maidanak optical observations. *GRB Coordinates Network, Circular Service, No. 18635, #1 (2015)*, 18635, 2015.

R. D. Preece, M. S. Briggs, R. S. Mallozzi, G. N. Pendleton, W. S. Paciesas, and D. L. Band. The Synchrotron Shock Model Confronts a "Line of Death" in the BATSE Gamma-Ray Burst Data. *ApJ*, 506:L23–L26, October 1998. doi: 10.1086/311644.

J. X. Prochaska, J. S. Bloom, H. W. Chen, K. Hurley, A. Dressler, and D. Osip. GRB 031203: magellan spectrum of possible GRB host. *GRB Coordinates Network*, 2482, 2003.

R. Protassov, D. A. van Dyk, A. Connors, V. L. Kashyap, and A. Siemiginowska. Statistics, Handle with Care: Detecting Multiple Model Components with the Likelihood Ratio Test. *ApJ*, 571:545–559, May 2002. doi: 10.1086/339856.

J. P. Pye and I. M. McHardy. The Ariel V sky survey of fast-transient X-ray sources. *MNRAS*, 205:875–888, November 1983. doi: 10.1093/mnras/205.3.875.

S.-F. Qin, E.-W. Liang, R.-J. Lu, J.-Y. Wei, and S.-N. Zhang. Simulations on high-z long gamma-ray burst rate. *MNRAS*, 406:558–565, July 2010. doi: 10.1111/j.1365-2966.2010.16691.x.

E. Ramirez-Ruiz and E. E. Fenimore. Pulse Width Evolution in Gamma-Ray Bursts: Evidence for Internal Shocks. *ApJ*, 539:712–717, August 2000. doi: 10.1086/309260.

A. Rau, J. Greiner, and R. Schwarz. Constraining the GRB collimation with a survey for orphan afterglows. *A&A*, 449:79–88, April 2006. doi: 10.1051/0004-6361:20054317.

A. Rau, R. Schwarz, S. R. Kulkarni, E. O. Ofek, M. M. Kasliwal, C. Brinkworth, S. B. Cenko, Y. Lipkin, and A. M. Soderberg. The Incidence of Dwarf Novae in Large Area Transient Searches. *ApJ*, 664:474–480, July 2007. doi: 10.1086/518759.

A. Rau, S. R. Kulkarni, N. M. Law, J. S. Bloom, D. Ciardi, G. S. Djorgovski, D. B. Fox, A. Gal-Yam, C. C. Grillmair, M. M. Kasliwal, P. E. Nugent, E. O. Ofek, R. M. Quimby, W. T. Reach, M. Shara, L. Bildsten, S. B. Cenko, A. J. Drake, A. V. Filippenko, D. J. Helfand, G. Helou, D. A. Howell, D. Poznanski, and M. Sullivan. Exploring the Optical Transient Sky with the Palomar Transient Factory. *Publications of the Astronomical Society of Pacific*, 121:1334, December 2009. doi: 10.1086/605911.

M. J. Rees and P. Meszaros. Relativistic fireballs - Energy conversion and time-scales. *MNRAS*, 258:41P–43P, September 1992. doi: 10.1093/mnras/258.1.41P.

M. J. Rees and P. Meszaros. Unsteady outflow models for cosmological gamma-ray bursts. *ApJ*, 430:L93–L96, August 1994. doi: 10.1086/187446.

M. J. Rees and P. Mészáros. Dissipative Photosphere Models of Gamma-Ray Bursts and X-Ray Flashes. *ApJ*, 628:847–852, August 2005. doi: 10.1086/430818.

J. E. Rhoads. How to Tell a Jet from a Balloon: A Proposed Test for Beaming in Gamma-Ray Bursts. *ApJ*, 487:L1–L4, September 1997. doi: 10.1086/310876.

J. E. Rhoads. The Dynamics and Light Curves of Beamed Gamma-Ray Burst Afterglows. *ApJ*, 525:737–749, November 1999. doi: 10.1086/307907.

B. E. Robertson and R. S. Ellis. Connecting the Gamma Ray Burst Rate and the Cosmic Star Formation History: Implications for Reionization and Galaxy Evolution. *ApJ*, 744: 95, January 2012. doi: 10.1088/0004-637X/744/2/95.

P. Romano, S. Campana, G. Chincarini, J. Cummings, G. Cusumano, S. T. Holland, V. Mangano, T. Mineo, K. L. Page, V. Pal'Shin, E. Rol, T. Sakamoto, B. Zhang, R. Aptekar, S. Barbier, S. Barthelmy, A. P. Beardmore, P. Boyd, D. N. Burrows, M. Capalbi, E. E. Fenimore, D. Frederiks, N. Gehrels, P. Giommi, M. R. Goad, O. Godet, S. Golenetskii, D. Guetta, J. A. Kennea, V. La Parola, D. Malesani, F. Marshall, A. Moretti, J. A. Nousek, P. T. O'Brien, J. P. Osborne, M. Perri, and G. Tagliaferri. Panchromatic study of GRB 060124: from precursor to afterglow. *A&A*, 456:917–927, September 2006. doi: 10.1051/0004-6361:20065071.

P. W. A. Roming, T. E. Kennedy, K. O. Mason, J. A. Nousek, L. Ahr, R. E. Bingham, P. S. Broos, M. J. Carter, B. K. Hancock, H. E. Huckle, S. D. Hunsberger, H. Kawakami, R. Killough, T. S. Koch, M. K. McLelland, K. Smith, P. J. Smith, J. C. Soto, P. T. Boyd, A. A. Breeveld, S. T. Holland, M. Ivanushkina, M. S. Pryzby, M. D. Still, and J. Stock. The Swift Ultra-Violet/Optical Telescope. *Space Science Review*, 120:95–142, October 2005. doi: 10.1007/s11214-005-5095-4.

P. Rosati, S. Borgani, R. Gilli, M. Paolillo, and P. Tozzi. The Wide Field X-ray Telescope. *Memorie della Societa Astronomica Italiana Supplementi*, 17:3, 2011.

E. Rossi, D. Lazzati, and M. J. Rees. Afterglow light curves, viewing angle and the jet structure of γ-ray bursts. *MNRAS*, 332:945–950, June 2002. doi: 10.1046/j.1365-8711.2002.05363.x.

E. M. Rossi, D. Lazzati, J. D. Salmonson, and G. Ghisellini. The polarization of afterglow emission reveals γ-ray bursts jet structure. *MNRAS*, 354:86–100, October 2004. doi: 10.1111/j.1365-2966.2004.08165.x.

E. M. Rossi, R. Perna, and F. Daigne. 'Orphan' afterglows in the Universal structured jet model for γ-ray bursts. *MNRAS*, 390:675–682, October 2008. doi: 10.1111/j.1365-2966.2008.13736.x.

G. B. Rybicki and A. P. Lightman. *Radiative Processes in Astrophysics*. June 1986.

F. Ryde. The Cooling Behavior of Thermal Pulses in Gamma-Ray Bursts. *ApJ*, 614:827–846, October 2004. doi: 10.1086/423782.

F. Ryde, M. Axelsson, B. B. Zhang, S. McGlynn, A. Pe'er, C. Lundman, S. Larsson, M. Battelino, B. Zhang, E. Bissaldi, J. Bregeon, M. S. Briggs, J. Chiang, F. de Palma, S. Guiriec, J. Larsson, F. Longo, S. McBreen, N. Omodei, V. Petrosian, R. Preece, and A. J. van der Horst. Identification and Properties of the Photospheric Emission in GRB090902B. *ApJ*, 709:L172–L177, February 2010. doi: 10.1088/2041-8205/709/2/L172.

E. S. Rykoff, F. Aharonian, C. W. Akerlof, K. Alatalo, M. C. B. Ashley, T. Güver, D. Horns, R. L. Kehoe, Ü. Kiziloğlu, T. A. McKay, M. Özel, A. Phillips, R. M. Quimby, B. E. Schaefer, D. A. Smith, H. F. Swan, W. T. Vestrand, J. C. Wheeler, J. Wren, and S. A. Yost. A Search for Untriggered GRB Afterglows with ROTSE-III. *ApJ*, 631:1032–1038, October 2005. doi: 10.1086/432832.

T. Sakamoto and N. Gehrels. Indication of Two Classes in the Swift Short Gamma-Ray Bursts from the XRT X-Ray Afterglow Light Curves. In C. Meegan, C. Kouveliotou, and N. Gehrels, editors, *American Institute of Physics Conference Series*, volume 1133 of *American Institute of Physics Conference Series*, pages 112–114, May 2009. doi: 10.1063/1.3155860.

T. Sakamoto, D. Q. Lamb, C. Graziani, T. Q. Donaghy, M. Suzuki, G. Ricker, J.-L. Atteia, N. Kawai, A. Yoshida, Y. Shirasaki, T. Tamagawa, K. Torii, M. Matsuoka, E. E. Fenimore, M. Galassi, T. Tavenner, J. Doty, R. Vanderspek, G. B. Crew, J. Villasenor, N. Butler, G. Prigozhin, J. G. Jernigan, C. Barraud, M. Boer, J.-P. Dezalay, J.-F. Olive, K. Hurley, A. Levine, G. Monnelly, F. Martel, E. Morgan, S. E. Woosley, T. Cline, J. Braga, R. Manchanda, G. Pizzichini, K. Takagishi, and M. Yamauchi. High Energy Transient Explorer 2 Observations of the Extremely Soft X-Ray Flash XRF 020903. *ApJ*, 602:875–885, February 2004. doi: 10.1086/381232.

T. Sakamoto, G. Sato, L. Barbier, S. D. Barthelmy, J. R. Cummings, E. E. Fenimore, N. Gehrels, D. Hullinger, H. A. Krimm, D. Q. Lamb, C. B. Markwardt, D. M. Palmer, A. M. Parsons, M. Stamatikos, J. Tueller, and T. N. Ukwatta. E_{peak} Estimator for Gamma-Ray Bursts Observed by the Swift Burst Alert Telescope. *ApJ*, 693:922–935, March 2009. doi: 10.1088/0004-637X/693/1/922.

O. S. Salafia, G. Ghisellini, A. Pescalli, G. Ghirlanda, and F. Nappo. Structure of gamma-ray burst jets: intrinsic versus apparent properties. *MNRAS*, 450:3549–3558, July 2015. doi: 10.1093/mnras/stv766.

R. Salvaterra and G. Chincarini. The Gamma-Ray Burst Luminosity Function in the Light of the Swift 2 Year Data. *ApJ*, 656:L49–L52, February 2007. doi: 10.1086/512606.

R. Salvaterra, A. Cerutti, G. Chincarini, M. Colpi, C. Guidorzi, and P. Romano. Short Gamma-ray bursts: a bimodal origin? *MNRAS*, 388:L6–L9, July 2008. doi: 10.1111/j.1745-3933.2008.00488.x.

R. Salvaterra, M. Della Valle, S. Campana, G. Chincarini, S. Covino, P. D'Avanzo, A. Fernández-Soto, C. Guidorzi, F. Mannucci, R. Margutti, C. C. Thöne, L. A. Antonelli, S. D. Barthelmy, M. de Pasquale, V. D'Elia, F. Fiore, D. Fugazza, L. K. Hunt, E. Maiorano, S. Marinoni, F. E. Marshall, E. Molinari, J. Nousek, E. Pian, J. L. Racusin, L. Stella, L. Amati, G. Andreuzzi, G. Cusumano, E. E. Fenimore, P. Ferrero, P. Giommi, D. Guetta, S. T. Holland, K. Hurley, G. L. Israel, J. Mao, C. B. Markwardt, N. Masetti, C. Pagani, E. Palazzi, D. M. Palmer, S. Piranomonte, G. Tagliaferri, and V. Testa. GRB090423 at a redshift of z˜8.1. *Nature*, 461:1258–1260, October 2009a. doi: 10.1038/nature08445.

R. Salvaterra, C. Guidorzi, S. Campana, G. Chincarini, and G. Tagliaferri. Evidence for luminosity evolution of long gamma-ray bursts in Swift data. *MNRAS*, 396:299–303, June 2009b. doi: 10.1111/j.1365-2966.2008.14343.x.

R. Salvaterra, S. Campana, S. D. Vergani, S. Covino, P. D'Avanzo, D. Fugazza, G. Ghirlanda, G. Ghisellini, A. Melandri, L. Nava, B. Sbarufatti, H. Flores, S. Piranomonte, and G. Tagliaferri. A Complete Sample of Bright Swift Long Gamma-Ray Bursts. I. Sample Presentation, Luminosity Function and Evolution. *ApJ*, 749:68, April 2012. doi: 10.1088/0004-637X/749/1/68.

R. Sari and T. Piran. Variability in Gamma-Ray Bursts: A Clue. *ApJ*, 485:270–273, August 1997. doi: 10.1086/304428.

R. Sari and T. Piran. The early afterglow. *A&AS*, 138:537–538, September 1999a. doi: 10.1051/aas:1999342.

R. Sari and T. Piran. Predictions for the Very Early Afterglow and the Optical Flash. *ApJ*, 520:641–649, August 1999b. doi: 10.1086/307508.

R. Sari, R. Narayan, and T. Piran. Cooling Timescales and Temporal Structure of Gamma-Ray Bursts. *ApJ*, 473:204, December 1996. doi: 10.1086/178136.

R. Sari, T. Piran, and R. Narayan. Spectra and Light Curves of Gamma-Ray Burst Afterglows. *ApJ*, 497:L17–L20, April 1998. doi: 10.1086/311269.

R. Sari, T. Piran, and J. P. Halpern. Jets in Gamma-Ray Bursts. *ApJ*, 519:L17–L20, July 1999. doi: 10.1086/312109.

S. Y. Sazonov, A. A. Lutovinov, and R. A. Sunyaev. An apparently normal γ-ray burst with an unusually low luminosity. *Nature*, 430:646–648, August 2004. doi: 10.1038/nature02748.

M. Schmidt. Space Distribution and Luminosity Functions of Quasi-Stellar Radio Sources. *ApJ*, 151:393, February 1968. doi: 10.1086/149446.

M. Schmidt, J. C. Higdon, and G. Hueter. Application of the V/V(max) test to gamma-ray bursts. *ApJ*, 329:L85–L87, June 1988. doi: 10.1086/185182.

R. Schneider, V. Ferrari, S. Matarrese, and S. F. Portegies Zwart. Low-frequency gravitational waves from cosmological compact binaries. *MNRAS*, 324:797–810, July 2001. doi: 10.1046/j.1365-8711.2001.04217.x.

S. Schulze, R. Chapman, J. Hjorth, A. J. Levan, P. Jakobsson, G. Björnsson, D. A. Perley, T. Krühler, J. Gorosabel, N. R. Tanvir, A. de Ugarte Postigo, J. P. U. Fynbo, B. Milvang-Jensen, P. Møller, and D. J. Watson. The Optically Unbiased GRB Host (TOUGH) Survey. VII. The Host Galaxy Luminosity Function: Probing the Relationship between GRBs and Star Formation to Redshift ~ 6. *ApJ*, 808:73, July 2015. doi: 10.1088/0004-637X/808/1/73.

B. F. Schutz. Networks of gravitational wave detectors and three figures of merit. *Classical and Quantum Gravity*, 28(12):125023, June 2011. doi: 10.1088/0264-9381/28/12/125023.

A. Shemi and T. Piran. The appearance of cosmic fireballs. *ApJ*, 365:L55–L58, December 1990. doi: 10.1086/185887.

K. Siellez, M. Boër, and B. Gendre. Simultaneous event detection rates by electromagnetic and gravitational wave detectors in the advanced era of LIGO and Virgo. *MNRAS*, 437:649–655, January 2014. doi: 10.1093/mnras/stt1915.

J. Singal, V. Petrosian, and M. Ajello. Flux and Photon Spectral Index Distributions of Fermi-LAT Blazars and Contribution to the Extragalactic Gamma-Ray Background. *ApJ*, 753:45, July 2012. doi: 10.1088/0004-637X/753/1/45.

J. Singal, V. Petrosian, Ł. Stawarz, and A. Lawrence. The Radio and Optical Luminosity Evolution of Quasars. II. The SDSS Sample. *ApJ*, 764:43, February 2013. doi: 10.1088/0004-637X/764/1/43.

A. M. Soderberg, P. A. Price, D. W. Fox, S. R. Kulkarni, S. G. Djorgovski, E. Berger, F. Harrison, S. Yost, M. Hamuy, S. Shectman, N. Mirabal, and J. Halpern. XRF 020903: supernova. *GRB Coordinates Network*, 1554, 2002.

A. M. Soderberg, E. Berger, M. Kasliwal, D. A. Frail, P. A. Price, B. P. Schmidt, S. R. Kulkarni, D. B. Fox, S. B. Cenko, A. Gal-Yam, E. Nakar, and K. C. Roth. The Afterglow, Energetics, and Host Galaxy of the Short-Hard Gamma-Ray Burst 051221a. *ApJ*, 650:261–271, October 2006a. doi: 10.1086/506429.

A. M. Soderberg, S. R. Kulkarni, E. Nakar, E. Berger, P. B. Cameron, D. B. Fox, D. Frail, A. Gal-Yam, R. Sari, S. B. Cenko, M. Kasliwal, R. A. Chevalier, T. Piran, P. A. Price, B. P. Schmidt, G. Pooley, D.-S. Moon, B. E. Penprase, E. Ofek, A. Rau, N. Gehrels, J. A. Nousek, D. N. Burrows, S. E. Persson, and P. J. McCarthy. Relativistic ejecta from X-ray flash XRF 060218 and the rate of cosmic explosions. *Nature*, 442:1014–1017, August 2006b. doi: 10.1038/nature05087.

J. Sollerman, A. O. Jaunsen, J. P. U. Fynbo, J. Hjorth, P. Jakobsson, M. Stritzinger, C. Féron, P. Laursen, J.-E. Ovaldsen, J. Selj, C. C. Thöne, D. Xu, T. Davis, J. Gorosabel, D. Watson, R. Duro, I. Ilyin, B. L. Jensen, N. Lysfjord, T. Marquart, T. B. Nielsen, J. Näränen, H. E. Schwarz, S. Walch, M. Wold, and G. Östlin. Supernova 2006aj and the associated X-Ray Flash 060218. *A&A*, 454:503–509, August 2006. doi: 10.1051/0004-6361:20065226.

M. Sparre and R. L. C. Starling. A search for thermal X-ray signatures in gamma-ray bursts - II. The Swift sample. *MNRAS*, 427:2965–2974, December 2012. doi: 10.1111/j.1365-2966.2012.21858.x.

K. Z. Stanek, T. Matheson, P. M. Garnavich, P. Martini, P. Berlind, N. Caldwell, P. Challis, W. R. Brown, R. Schild, K. Krisciunas, M. L. Calkins, J. C. Lee, N. Hathi, R. A. Jansen, R. Windhorst, L. Echevarria, D. J. Eisenstein, B. Pindor, E. W. Olszewski, P. Harding, S. T. Holland, and D. Bersier. Spectroscopic Discovery of the Supernova 2003dh Associated with GRB 030329. *ApJ*, 591:L17–L20, July 2003. doi: 10.1086/376976.

R. L. C. Starling, K. L. Page, A. Pe'Er, A. P. Beardmore, and J. P. Osborne. A search for thermal X-ray signatures in gamma-ray bursts - I. Swift bursts with optical supernovae. *MNRAS*, 427:2950–2964, December 2012. doi: 10.1111/j.1365-2966.2012.22116.x.

D. Svinkin, S. Golenetskii, R. Aptekar, D. Frederiks, P. Oleynik, M. Ulanov, A. Tsvetkova, A. Lysenko, A. Kozlova, and T. Cline. Konus-Wind observation of GRB 160625B. *GRB Coordinates Network, Circular Service, No. 19604, #1 (2016)*, 19604, 2016.

J. C. Tan, C. D. Matzner, and C. F. McKee. Trans-Relativistic Blast Waves in Supernovae as Gamma-Ray Burst Progenitors. *ApJ*, 551:946–972, April 2001. doi: 10.1086/320245.

N. R. Tanvir, D. B. Fox, A. J. Levan, E. Berger, K. Wiersema, J. P. U. Fynbo, A. Cucchiara, T. Krühler, N. Gehrels, J. S. Bloom, J. Greiner, P. A. Evans, E. Rol, F. Olivares, J. Hjorth, P. Jakobsson, J. Farihi, R. Willingale, R. L. C. Starling, S. B. Cenko, D. Perley, J. R. Maund, J. Duke, R. A. M. J. Wijers, A. J. Adamson, A. Allan, M. N. Bremer, D. N. Burrows, A. J. Castro-Tirado, B. Cavanagh, A. de Ugarte Postigo, M. A. Dopita, T. A. Fatkhullin, A. S. Fruchter, R. J. Foley, J. Gorosabel, J. Kennea, T. Kerr, S. Klose, H. A. Krimm, V. N. Komarova, S. R. Kulkarni, A. S. Moskvitin, C. G. Mundell, T. Naylor, K. Page, B. E. Penprase, M. Perri, P. Podsiadlowski, K. Roth, R. E. Rutledge, T. Sakamoto, P. Schady, B. P. Schmidt, A. M. Soderberg, J. Sollerman, A. W. Stephens, G. Stratta, T. N. Ukwatta, D. Watson, E. Westra, T. Wold, and C. Wolf. A γ-ray burst at a redshift of $z\tilde{}8.2$. *Nature*, 461:1254–1257, October 2009. doi: 10.1038/nature08459.

N. R. Tanvir, A. J. Levan, A. Cucchiara, and D. B. Fox. GRB 120422A: Gemini redshift of candidate host. *GRB Coordinates Network, Circular Service, No. 13251, #1 (2012)*, 3251, 2012.

M. Tavani. A Shock Emission Model for Gamma-Ray Bursts. II. Spectral Properties. *ApJ*, 466:768, August 1996. doi: 10.1086/177551.

C. C. Thoene, J. P. U. Fynbo, J. Sollerman, B. L. Jensen, J. Hjorth, P. Jakobsson, and S. Klose. GRB060505: VLT observations of the optical afterglow. *GRB Coordinates Network*, 5161, 2006.

K. Toelge, H.-F. Yu, and C. A. Meegan. GRB 151027A: Fermi GBM observation. *GRB Coordinates Network, Circular Service, No. 18492, #1 (2015)*, 18492, 2015.

T. Totani and A. Panaitescu. Orphan Afterglows of Collimated Gamma-Ray Bursts: Rate Predictions and Prospects for Detection. *ApJ*, 576:120–134, September 2002. doi: 10.1086/341738.

E. Troja, G. Cusumano, V. Laparola, V. Mangano, and T. Mineo. Swift observations of GRB 051109B. *Nuovo Cimento B Serie*, 121:1599–1600, December 2006. doi: 10.1393/ncb/i2007-10324-8.

E. Troja, A. M. Read, A. Tiengo, and R. Salvaterra. XMM-Newton Slew Survey Observations of the Gravitational Wave Event GW150914. *ApJ*, 822:L8, May 2016. doi: 10.3847/2041-8205/822/1/L8.

E. Troja, V. M. Lipunov, C. G. Mundell, N. R. Butler, A. M. Watson, S. Kobayashi, S. B. Cenko, F. E. Marshall, R. Ricci, A. Fruchter, M. H. Wieringa, E. S. Gorbovskoy, V. Kornilov, A. Kutyrev, W. H. Lee, V. Toy, N. V. Tyurina, N. M. Budnev, D. A. H. Buckley, J. González, O. Gress, A. Horesh, M. I. Panasyuk, J. X. Prochaska, E. Ramirez-Ruiz, R. Rebolo Lopez, M. G. Richer, C. Roman-Zuniga, M. Serra-Ricart, V. Yurkov, and N. Gehrels. Significant and variable linear polarization during the prompt optical flash of GRB 160625B. *Nature*, 547:425–427, July 2017. doi: 10.1038/nature23289.

R. Tsutsui, D. Yonetoku, T. Nakamura, K. Takahashi, and Y. Morihara. Possible existence of the E_p-L_p and E_p-E_{iso} correlations for short gamma-ray bursts with a factor 5-100 dimmer than those for long gamma-ray bursts. *MNRAS*, 431:1398–1404, May 2013. doi: 10.1093/mnras/stt262.

Z. L. Uhm and A. M. Beloborodov. On the Mechanism of Gamma-Ray Burst Afterglows. *ApJ*, 665:L93–L96, August 2007. doi: 10.1086/519837.

M. V. Ulanov, S. V. Golenetskii, D. D. Frederiks, R. L. A. E. P. Mazets, A. A. Kokomov, and V. D. Palshin. Fast spectral variability of GRBs with known redshifts. *Nuovo Cimento C Geophysics Space Physics C*, 28:351, May 2005. doi: 10.1393/ncc/i2005-10058-8.

C. M. Urry and R. A. Shafer. Luminosity enhancement in relativistic jets and altered luminosity functions for beamed objects. *ApJ*, 280:569–573, May 1984. doi: 10.1086/162027.

A. J. van der Horst, Z. Paragi, A. G. de Bruyn, J. Granot, C. Kouveliotou, K. Wiersema, R. L. C. Starling, P. A. Curran, R. A. M. J. Wijers, A. Rowlinson, G. A. Anderson, R. P. Fender, J. Yang, and R. G. Strom. A comprehensive radio view of the extremely bright gamma-ray burst 130427A. *MNRAS*, 444:3151–3163, November 2014. doi: 10.1093/mnras/stu1664.

H. van Eerten, A. van der Horst, and A. MacFadyen. Gamma-Ray Burst Afterglow Broadband Fitting Based Directly on Hydrodynamics Simulations. *ApJ*, 749:44, April 2012. doi: 10.1088/0004-637X/749/1/44.

H. J. van Eerten and A. I. MacFadyen. Synthetic Off-axis Light Curves for Low-energy Gamma-Ray Bursts. *ApJ*, 733:L37, June 2011. doi: 10.1088/2041-8205/733/2/L37.

J. van Paradijs, P. J. Groot, T. Galama, C. Kouveliotou, R. G. Strom, J. Telting, R. G. M. Rutten, G. J. Fishman, C. A. Meegan, M. Pettini, N. Tanvir, J. Bloom, H. Pedersen, H. U. Nørdgaard-Nielsen, M. Linden-Vørnle, J. Melnick, G. van der Steene, M. Bremer, R. Naber, J. Heise, J. in't Zand, E. Costa, M. Feroci, L. Piro, F. Frontera, G. Zavattini, L. Nicastro, E. Palazzi, K. Bennett, L. Hanlon, and A. Parmar. Transient optical emission from the error box of the γ-ray burst of 28 February 1997. *Nature*, 386:686–689, April 1997. doi: 10.1038/386686a0.

S. D. Vergani, R. Salvaterra, J. Japelj, E. Le Floc'h, P. D'Avanzo, A. Fernandez-Soto, T. Krühler, A. Melandri, S. Boissier, S. Covino, M. Puech, J. Greiner, L. K. Hunt, D. Perley, P. Petitjean, T. Vinci, F. Hammer, A. Levan, F. Mannucci, S. Campana, H. Flores, A. Gomboc, and G. Tagliaferri. Are long gamma-ray bursts biased tracers of star formation? Clues from the host galaxies of the Swift/BAT6 complete sample of LGRBs . I. Stellar mass at z $<$ 1. *A&A*, 581:A102, September 2015. doi: 10.1051/0004-6361/201425013.

W. T. Vestrand, J. A. Wren, A. Panaitescu, P. R. Wozniak, H. Davis, D. M. Palmer, G. Vianello, N. Omodei, S. Xiong, M. S. Briggs, M. Elphick, W. Paciesas, and W. Rosing. The Bright Optical Flash and Afterglow from the Gamma-Ray Burst GRB 130427A. *Science*, 343:38–41, January 2014. doi: 10.1126/science.1242316.

F. J. Virgili, E.-W. Liang, and B. Zhang. Low-luminosity gamma-ray bursts as a distinct GRB population: a firmer case from multiple criteria constraints. *MNRAS*, 392:91–103, January 2009. doi: 10.1111/j.1365-2966.2008.14063.x.

F. J. Virgili, B. Zhang, K. Nagamine, and J.-H. Choi. Gamma-ray burst rate: high-redshift excess and its possible origins. *MNRAS*, 417:3025–3034, November 2011a. doi: 10.1111/j.1365-2966.2011.19459.x.

F. J. Virgili, B. Zhang, P. O'Brien, and E. Troja. Are All Short-hard Gamma-ray Bursts Produced from Mergers of Compact Stellar Objects? *ApJ*, 727:109, February 2011b. doi: 10.1088/0004-637X/727/2/109.

A. von Kienlin, C. A. Meegan, W. S. Paciesas, P. N. Bhat, E. Bissaldi, M. S. Briggs, J. M. Burgess, D. Byrne, V. Chaplin, W. Cleveland, V. Connaughton, A. C. Collazzi, G. Fitzpatrick, S. Foley, M. Gibby, M. Giles, A. Goldstein, J. Greiner, D. Gruber, S. Guiriec, A. J. van der Horst, C. Kouveliotou, E. Layden, S. McBreen, S. McGlynn, V. Pelassa, R. D. Preece, A. Rau, D. Tierney, C. A. Wilson-Hodge, S. Xiong, G. Younes, and H.-F. Yu. The Second Fermi GBM Gamma-Ray Burst Catalog: The First Four Years. *ApJS*, 211:13, March 2014. doi: 10.1088/0067-0049/211/1/13.

K. C. Walker, B. E. Schaefer, and E. E. Fenimore. Gamma-Ray Bursts Have Millisecond Variability. *ApJ*, 537:264–269, July 2000. doi: 10.1086/308995.

D. Wanderman and T. Piran. The luminosity function and the rate of Swift's gamma-ray bursts. *MNRAS*, 406:1944–1958, August 2010. doi: 10.1111/j.1365-2966.2010.16787.x.

D. Wanderman and T. Piran. The rate, luminosity function and time delay of non-Collapsar short GRBs. *MNRAS*, 448:3026–3037, April 2015. doi: 10.1093/mnras/stv123.

F. Y. Wang. The high-redshift star formation rate derived from gamma-ray bursts: possible origin and cosmic reionization. *A&A*, 556:A90, August 2013. doi: 10.1051/0004-6361/201321623.

X. Wang and A. Loeb. Variability of Gamma-Ray Burst Afterglows due to Interstellar Turbulence. *ApJ*, 535:788–797, June 2000. doi: 10.1086/308888.

Y.-Z. Wang, H. Wang, S. Zhang, Y.-F. Liang, Z.-P. Jin, H.-N. He, N.-H. Liao, Y.-Z. Fan, and D.-M. Wei. Evaluating the Bulk Lorentz Factors of Outflow Material: Lessons Learned from the Extremely Energetic Outburst GRB 160625B. *ApJ*, 836:81, February 2017. doi: 10.3847/1538-4357/aa56c6.

J. Wilms, A. Allen, and R. McCray. On the Absorption of X-Rays in the Interstellar Medium. *ApJ*, 542:914–924, October 2000. doi: 10.1086/317016.

A. Wolter, A. Caccianiga, R. della Ceca, and T. Maccacaro. Luminosity functions of BL Lacertae objects. *ApJ*, 433:29–38, September 1994. doi: 10.1086/174622.

S.-W. Wu, D. Xu, F.-W. Zhang, and D.-M. Wei. Gamma-ray bursts: the isotropic-equivalent-energy function and the cosmic formation rate. *MNRAS*, 423:2627–2632, July 2012. doi: 10.1111/j.1365-2966.2012.21068.x.

K. Yamaoka, A. Endo, T. Enoto, Y. Fukazawa, R. Hara, Y. Hanabata, S. Hong, T. Kamae, C. Kira, N. Kodaka, M. Kokubun, S. Maeno, K. Makishima, R. Miyawaki, K. Morigami, T. Murakami, Y. E. Nakagawa, K. Nakazawa, N. Ohmori, M. Ohno, K. Onda, G. Sato, E. Sonoda, S. Sugita, M. Suzuki, M. Suzuki, H. Tajima, T. Takahashi, T. Takahashi, H. Tanaka, T. Tamagawa, M. S. Tashiro, Y. Terada, T. Uehara, Y. Urata, M. Yamauchi, A. Yoshida, K. Hurley, V. Pal'shin, T. Sakamoto, and J. Cummings. Design and In-Orbit Performance of the Suzaku Wide-Band All-Sky Monitor. *PASJ*, 61:S35–S53, January 2009. doi: 10.1093/pasj/61.sp1.S35.

R. Yamazaki, D. Yonetoku, and T. Nakamura. An Off-Axis Jet Model For GRB 980425 and Low-Energy Gamma-Ray Bursts. *ApJ*, 594:L79–L82, September 2003. doi: 10.1086/378736.

B. Yang, Z.-P. Jin, X. Li, S. Covino, X.-Z. Zheng, K. Hotokezaka, Y.-Z. Fan, T. Piran, and D.-M. Wei. A possible macronova in the late afterglow of the long-short burst GRB 060614. *Nature Communications*, 6:7323, June 2015. doi: 10.1038/ncomms8323.

S.-X. Yi, S.-Q. Xi, H. Yu, F. Y. Wang, H.-J. Mu, L.-Z. Lü, and E.-W. Liang. Comprehensive Study of the X-Ray Flares from Gamma-ray Bursts Observed by Swift. *ApJ*, 224:20, June 2016. doi: 10.3847/0067-0049/224/2/20.

D. Yonetoku, T. Murakami, T. Nakamura, R. Yamazaki, A. K. Inoue, and K. Ioka. Gamma-Ray Burst Formation Rate Inferred from the Spectral Peak Energy-Peak Luminosity Relation. *ApJ*, 609:935–951, July 2004. doi: 10.1086/421285.

D. Yonetoku, T. Nakamura, T. Sawano, K. Takahashi, and A. Toyanago. Short Gamma-Ray Burst Formation Rate from BATSE Data Using E_p -L_p Correlation and the Minimum Gravitational-wave Event Rate of a Coalescing Compact Binary. *ApJ*, 789:65, July 2014. doi: 10.1088/0004-637X/789/1/65.

H. Yu, F. Y. Wang, Z. G. Dai, and K. S. Cheng. An Unexpectedly Low-redshift Excess of Swift Gamma-ray Burst Rate. *ApJS*, 218:13, May 2015a. doi: 10.1088/0067-0049/218/1/13.

H.-F. Yu, J. Greiner, H. van Eerten, J. M. Burgess, P. Narayana Bhat, M. S. Briggs, V. Connaughton, R. Diehl, A. Goldstein, D. Gruber, P. A. Jenke, A. von Kienlin, C. Kouveliotou, W. S. Paciesas, V. Pelassa, R. D. Preece, O. J. Roberts, and B.-B. Zhang. Synchrotron cooling in energetic gamma-ray bursts observed by the Fermi Gamma-Ray Burst Monitor. *A&A*, 573:A81, January 2015b. doi: 10.1051/0004-6361/201424858.

Y. B. Yu, X. F. Wu, Y. F. Huang, D. M. Coward, G. Stratta, B. Gendre, and E. J. Howell. Fall back accretion and energy injections in gamma-ray bursts. *MNRAS*, 446:3642–3650, February 2015c. doi: 10.1093/mnras/stu2336.

B. Zhang and P. Mészáros. Gamma-Ray Burst Beaming: A Universal Configuration with a Standard Energy Reservoir? *ApJ*, 571:876–879, June 2002. doi: 10.1086/339981.

B. Zhang and P. Mészáros. Gamma-Ray Bursts: progress, problems and prospects. *International Journal of Modern Physics A*, 19:2385–2472, 2004. doi: 10.1142/S0217751X0401746X.

B. Zhang, X. Dai, N. M. Lloyd-Ronning, and P. Mészáros. Quasi-universal Gaussian Jets: A Unified Picture for Gamma-Ray Bursts and X-Ray Flashes. *ApJ*, 601:L119–L122, February 2004a. doi: 10.1086/382132.

B. Zhang, R.-J. Lu, E.-W. Liang, and X.-F. Wu. GRB 110721A: Photosphere "Death Line" and the Physical Origin of the GRB Band Function. *ApJ*, 758:L34, October 2012a. doi: 10.1088/2041-8205/758/2/L34.

B.-B. Zhang, Y.-Z. Fan, R.-F. Shen, D. Xu, F.-W. Zhang, D.-M. Wei, D. N. Burrows, B. Zhang, and N. Gehrels. GRB 120422A: A Low-luminosity Gamma-Ray Burst Driven by a Central Engine. *ApJ*, 756:190, September 2012b. doi: 10.1088/0004-637X/756/2/190.

B.-B. Zhang, B. Zhang, A. J. Castro-Tirado, Z. G. Dai, P.-H. T. Tam, X.-Y. Wang, Y.-D. Hu, S. Karpov, A. Pozanenko, F.-W. Zhang, E. Mazaeva, P. Minaev, A. Volnova, S. Oates, H. Gao, X.-F. Wu, L. Shao, Q.-W. Tang, G. Beskin, A. Biryukov, S. Bondar, E. Ivanov, E. Katkova, N. Orekhova, A. Perkov, V. Sasyuk, L. Mankiewicz, A. F. Żarnecki, A. Cwiek, R. Opiela, A. Zadrożny, R. Aptekar, D. Frederiks, D. Svinkin, A. Kusakin, R. Inasaridze, O. Burhonov, V. Rumyantsev, E. Klunko, A. Moskvitin, T. Fatkhullin, V. V. Sokolov, A. F. Valeev, S. Jeong, I. H. Park, M. D. Caballero-García, R. Cunniffe, J. C. Tello, P. Ferrero, S. B. Pandey, M. Jelínek, R. Sánchez-Ramírez, and A. Castellón. Transition from Fireball to Poynting-flux-dominated Outflow in Three-Episode GRB 160625B. *ArXiv e-prints*, December 2016.

W. Zhang, S. E. Woosley, and A. I. MacFadyen. Relativistic Jets in Collapsars. *ApJ*, 586: 356–371, March 2003. doi: 10.1086/367609.

W. Zhang, S. E. Woosley, and A. Heger. The Propagation and Eruption of Relativistic Jets from the Stellar Progenitors of Gamma-Ray Bursts. *ApJ*, 608:365–377, June 2004b. doi: 10.1086/386300.

X. Zhao, Z. Li, X. Liu, B.-b. Zhang, J. Bai, and P. Mészáros. Gamma-Ray Burst Spectrum with Decaying Magnetic Field. *ApJ*, 780:12, January 2014a. doi: 10.1088/0004-637X/780/1/12.

X. Zhao, Z. Li, X. Liu, B.-b. Zhang, J. Bai, and P. Mészáros. Gamma-Ray Burst Spectrum with Decaying Magnetic Field. *ApJ*, 780:12, January 2014b. doi: 10.1088/0004-637X/780/1/12.

X.-H. Zhao, Z. Li, and J.-M. Bai. The Bulk Lorentz Factors of Fermi-LAT Gamma Ray Bursts. *ApJ*, 726:89, January 2011. doi: 10.1088/0004-637X/726/2/89.

Y.-C. Zou and T. Piran. Lorentz factor constraint from the very early external shock of the gamma-ray burst ejecta. *MNRAS*, 402:1854–1862, March 2010. doi: 10.1111/j.1365-2966.2009.15863.x.

Y. C. Zou, X. F. Wu, and Z. G. Dai. Estimation of the detectability of optical orphan afterglows. *A&A*, 461:115–119, January 2007. doi: 10.1051/0004-6361:20064853.

Y.-C. Zou, Y.-Z. Fan, and T. Piran. A Revised Limit of the Lorentz Factors of Gamma-ray Bursts with Two Emitting Regions. *ApJ*, 726:L2, January 2011. doi: 10.1088/2041-8205/726/1/L2.